University of Wisconsin Milwaukee
UWM Digital Commons

Theses and Dissertations

May 2022

Terrestrial Perspective on the Formation, Evolution, and Detection of Zeolites in Lacustrine Environments on Early Mars

Gayantha Roshana Loku Kodikara
University of Wisconsin-Milwaukee

Follow this and additional works at: https://dc.uwm.edu/etd

Part of the Geographic Information Sciences Commons, Geology Commons, and the Paleontology Commons

Recommended Citation

Loku Kodikara, Gayantha Roshana, "Terrestrial Perspective on the Formation, Evolution, and Detection of Zeolites in Lacustrine Environments on Early Mars" (2022). *Theses and Dissertations*. 2921.
https://dc.uwm.edu/etd/2921

This Dissertation is brought to you for free and open access by UWM Digital Commons. It has been accepted for inclusion in Theses and Dissertations by an authorized administrator of UWM Digital Commons. For more information, please contact scholarlycommunicationteam-group@uwm.edu.

TERRESTRIAL PERSPECTIVE ON THE FORMATION, EVOLUTION, AND DETECTION OF ZEOLITES IN LACUSTRINE ENVIRONMENTS ON EARLY MARS

by

Gayantha R. L. Kodikara

A Dissertation Submitted in

Partial Fulfillment of the

Requirements for the Degree of

Doctor of Philosophy

in Geosciences

at

The University of Wisconsin-Milwaukee

May 2022

ABSTRACT

TERRESTRIAL PERSPECTIVE ON THE FORMATION, EVOLUTION, AND DETECTION OF ZEOLITES IN LACUSTRINE ENVIRONMENTS ON EARLY MARS

by

Gayantha R. L. Kodikara

The University of Wisconsin-Milwaukee, 2022
Under the Supervision of Professor Lindsay J. McHenry

This study evaluates the possible formation and evolution mechanisms of zeolites on early Mars with possible explanations for their limited detections using Earth analogs. This study focuses on the formation of zeolites in the closed basin lakes where the largest relatively pure concentrations of natural zeolites are found on Earth. Five working hypotheses were formulated to explore the limited detection of zeolites in closed basin lakes on Mars and different styles of scientific reasoning with suitable examples were used to test the independent, converging lines of inquiry. Zeolites may not be identifiable in certain locations on Mars using orbital data if, 1) they are absent, or 2) they were originally present and later removed by chemical processes (e.g. dissolution and alteration), or 3) they are present but are covered by or mixed with other materials, or 4) they are present, but the methods applied are not capable of detecting and mapping them, or 5) they are present, but we are not looking in the correct places. The first possibility was tested using geochemical modeling, while the second possibility and part of the third possibility were tested both using geochemical modeling and analog sites on Earth. A "textbook" example, paleolake Tecopa, was selected as the primary analog site. The fourth possibility was tested using hyperspectral (Hyperion) and multispectral (ASTER) orbital remote sensing data (visible to shortwave infrared and thermal infrared wavelength range) at Lake Tecopa with different spectral mapping techniques and ground

truth data. Fieldwork was conducted during October 2018 and 2019 and 56 soil and rock samples were collected representing different surface materials over the area. X-ray Diffraction (XRD), X-ray Fluorescence (XRF), and Scanning Electron Microscopy-Energy Dispersive X-ray Spectrometry (SEM-EDS) were used to identify the bulk mineral composition and elemental composition of these samples. Spectral deconvolution with deep learning were applied to identify and estimate mineral abundances in zeolite-bearing mineral mixtures. A data-driven fuzzy-based weights-of-evidence method was adopted to identify favorable areas to look for zeolites on Mars, as a solution for the fifth possibility. The geochemical modeling shows that zeolites can form at low temperatures under potential early Martian conditions, both from basaltic and high silica starting materials, and some zeolites (e.g. clinoptilolite) are dissolved over time when other zeolites (e.g. analcime) precipitate as commonly observed on Earth. Field studies along with literature surveys show that most zeolite beds in paleolakes on Earth are thin, covered by other beds, or mixed with other materials due to physical weathering. Orbital and laboratory spectral studies show the difficulty of identifying non-analcime zeolites from mineral mixtures using spectral methods alone. The spectral and spectral resolution of the orbital images, atmospheric components, and dust cover also limit the detection of zeolites in orbital images. The predictive model created during this study shows favorable areas for the formation and/or presence of zeolites and this map could serve as a guide for further searches for zeolites using detailed orbital spectral image analysis and future in situ observations. The overall study shows that analcime is more likely to be found than other zeolite minerals because of it is chemically stable and easy identify using spectral data. The results imply that the paucity of detected zeolites on Mars does not preclude their wider presence, either beneath other materials, obscured by surface dust, or mixed with more spectrally dominant phases. The best way to confirm their presence is to “follow the zeolite on Mars” using future in situ observations.

© Copyright by Gayantha R. L. Kodikara, 2022
All Rights Reserved

To my loving father Sumanadasa Loku Kodikara.

TABLE OF CONTENTS

LIST OF FIGURES **x**

LIST OF TABLES **xxi**

LIST OF ABBREVIATIONS **xxiv**

Introduction **1**

Zeolites 1

Mars 3

Main Objective 7

1 Models, modeling, scientific reasoning, and terrestrial perspective on formation of zeolites on early Mars. **12**

Abstract 13

1.1 Introduction 13

1.2 Scientific reasoning 15

1.3 Evaluation 40

1.4 Closing Comments 45

Acknowledgements 48

2 The study of the paleolake basin at Lake Tecopa using orbital and Mars rover-like instrument data. **49**

Abstract 49

2.1 Introduction 50

2.2 Study area 55

2.3 Data and overall methodology 59

2.4 Results and discussion 63

2.5 Lessons Learned 90

Acknowledgements 93

3 Spectral mapping of zeolite bearing paleolake deposits at Lake Tecopa, California and its implications for mapping zeolites on Mars. 1. VNIR-SWIR wavelength region. 94

Abstract . . . 95
3.1 Introduction . . . 96
3.2 Study area . . . 102
3.3 Data and Methods . . . 107
3.4 Results . . . 123
3.5 Discussion . . . 131
3.6 Implications for Mars . . . 133
3.7 Conclusions . . . 136
Acknowledgements . . . 137

4 Spectral mapping of zeolite bearing paleolake deposits at Lake Tecopa, California and its implications for mapping zeolites on Mars. 2. TIR wavelength region. 138

Abstract . . . 139
4.1 Introduction . . . 140
4.2 Study area . . . 141
4.3 Data Sets . . . 145
4.4 Spectral Analysis . . . 147
4.5 Image Analysis . . . 149
4.6 Spectral Mapping . . . 158
4.7 Implications for Mars . . . 166
4.8 Assumptions and limitations . . . 170
4.9 Conclusions . . . 173
Acknowledgements . . . 174

5 Application of deep learning and spectral deconvolution for estimating mineral abundances of zeolite, Mg-sulfate and montmorillonite mixtures and its implications for Mars. 175

Abstract . . . 176
5.1 Motivation and background . . . 177
5.2 Spectral Analysis . . . 181
5.3 Spectral Deconvolution . . . 189
5.4 Deep learning . . . 195
5.5 5. Accuracy assesment . . . 201

5.6 Conclusions 206
Acknowledgement 207

6 Self-Organizing Maps for identification of zeolitic diagenesis patterns in closed hydrologic systems on the Earth and its implications for Mars. 208
Abstract 208
6.1 Introduction 209
6.2 Dataset 214
6.3 Approach 220
6.4 Results and discussion 225
6.5 Implications for Mars 232
6.6 Conclusion 234
Acknowledgements 234

7 Possible formation pathways for zeolites in closed-basin lakes on Noachian Mars: Insights from geochemical modeling. 235
Abstract 235
7.1 Introduction 237
7.2 Previous models 238
7.3 Model Description 239
7.4 Results and discussion 250
7.5 Conclusion 268
Acknowledgement 269

8 Data-driven Fuzzy Weights-of-Evidence model for identification of potential zeolite-bearing environments on Mars. 270
Abstract 271
8.1 Introduction 272
8.2 Datasets 275
8.3 Methods 282
8.4 Results and discussion 304
8.5 Conclusion 313
Acknowledgement 314

Conclusion 315

References 318

Appendices

A Non-Marine Tuff Deposits **386**

B Spectral Angle Mapper Results **393**

C Deep Leaning Model **395**

D Self-Organizing Maps **409**

E Geochemical Modeling **414**

LIST OF FIGURES

1 Schematic cross-sectional diagram showing the patterns of zeolite zoning in tuff deposits in different environments. 2

2 Geological activity as a function of time on Mars (Modified after Wordsworth et al., 2021). The approximate boundaries of major time periods on Mars and similar major time subdivisions in Earth history are also shown. . . . 5

1.1 Diagenetic zones of (a) Lake Tecopa, Inyo County, California (after Sheppard and Gude, 1968) (b) Big Sandy Formation, Mohave County, Arizona (after Sheppard and Gude, 1973), (c) Karlovassi basin, Samos, Greece (after Stamatakis, 1989), and (d) Gila Conglomerate near Buckhorn, New Mexico. Dark tones of each litholgy type in the map indicate the approximate extent of diagenetic zones, whereas the light tones (letter (i) after the lithology type in the legend) indicate the inferred extent of zones prior to erosion (after Gude and Sheppard, 1988) 18

1.2 Reaction sequence of lateral mineral changes typical of saline-alkaline lake deposits 19

1.3 Relative mineral abundance in each cluster derived from Self-Organizing Maps (SOM) 27

1.4 Temporal changes in pH with precipitation of secondary minerals during weathering of buckskin sample exposed to rainwater in closed systems at 25 ^oC and 1 bar at 0.25 W/R ratio. Solution is equilibrated with 1.3 bar CO_2 and 0.0147 mbar of O_2 30

1.5 The frequency of occurrence of analcime, chabazite, clinoptilolite, erionite, mordenite, and phillipsite during geologic time. 34

1.6 Spectra of clinoptilolite-montmorillonite (a), and clinoptilolite-epsomite (b) binary mineral mixtures. The letter C in the legend indicates clinoptilolite, M indicates the montmorillonite, and E indicates epsomite. Two integers after each letter indicate the mineral weight proportions in 10 scale . . . 38

1.7 (a) A false-color composite image captured by the Curiosity Rover shows the inerior deposits of Gale Crater and Mount Sharp (Image: NASA/JPL), (b) Field photoghaph of Lake Tecopa area showing general stratigraphy, (c) zoomed area showing the erosional features with zeolite (tuff) bed (P), green mudstone bed (Q), gravel pavement (S), and sandstone/siltstone bed (S), and (d) exposed zeolitized tuff bed showing chemical and physical weathering. 44

1.8 The relationship beween the real world, conceptual model, and the methods of inferences. 46

2.1 (a) Pluvial lakes in basins of the Amargosa, Mojave, and Owens Rivers (modified after Anderson, 2005) RU: Lake Russell, LV: Long Valley, OL: Ownes Lake, CH: China Lake, SL: Searles Lake, PN: Panamint Lake, MN: Lake Manly, LT: Lake Tecopa, DM: Lake Dumont, MJ: Lake Mojave, CR: Cronese Lakes, CF: Confidence Flat sub-basin, MX: Lake Manix. Amargosa River basin is shown in tan color. (b) Map of the Lake Tecopa basin and surrounding mountains, Amargosa river, roads, and study areas. S1 shows the area shown in Figure 3. S2 is the area shown in Figure 4 and Figure 5. 58

2.2 Comparison between the NED DEM (a) and SRTM DEM (b). The accuracy of both DEMs was assessed using handheld GPS in the field (c). 63

2.3 a) Hillshade map derived from NED DEM of the Lake Tecopa area, b) Drainage network (dark blue), Amargosa River (light blue), Catchment area (yellow), and proposed outlet (red) draped over the NED hillshade image, c) Drainage network (dark blue) and 550m contour line (yellow) draped over the NED hillshade image, and d) lake boundary from the Hillhouse (1987) published map (pink), Amargosa River (dark blue), and derived lake boundary map from this study (red) draped on NAIP and NED hillshade image. 66

2.4 a). NAIP image of the study area. Band combinations: Red 3, Green 2, Blue 1. Sample locations and vicinity of the field pictures discussed in this text are shown in the triangles. The green arrows show the places and directions from which the photos were taken. The bases of the traingles opposite to the green arrows show the sections shown in Figure 2.4 (b), Figure 2.5, and Figure 2.6. Sample locations are shown by red dots. The sample number is shown in blue text. b) Elevation profile of the line A-A', and c) Geomorphology map created based on the Figure 4 (a). Map is overlain on the NED DEM. See the text for legend descriptions. 69

2.5 3-dimensional (3-D) view of the study area. A mosaiced high-resolution NIAP image was draped onto NED DEM. 71

2.6 Field photos showing sections B-B' and C-C' marked in Figure 4 (a). . . 73

2.7 3-D Anaglyph photo of the field site D-D' view shown in Figure 2.4 (a). Anaglyph glasses are required to view in 3-D. 73

2.8 Interpretation of sedimentary structures seen from a distance photograph. A person standing there can be seen in the middle of the picture as a scale. The photo was taken at 100m distance. 75

2.9 Depositional environments and sedimentary structures in the middle of Lake Tecopa. a) saline mudflat, b) mudflat with ripple marks showing shallow water wave actions, c) dry mudflat showing wetting and drying process, and d) ripple mark preserved on a tuff bed. 77

2.10 Sedimentary beds in upper levels of Lake Tecopa. Less altered welded tuff beds (a), zeolitized tuff beds (b), clay beds (c), and sandstone beds (d). . 78

2.11 (a) Fresh vitric tuff bed T45, (b) Microphotographs of zeolitized tuff sample T27. (c) Microphotograph of altered tuff sample T25. (d) Microphotograph of T30 mudstone sample. 79

2.12 Scanning electron micrographs (SEM) of fresh tuff sample T45. (a) SEM image showing large lithic fragments and welded glass matrix, (b) silica in a cavity. Yellow X indicates the location of energy dispersive X-ray (EDS) spectra that assist with mineral identification, (c) Opal-CT and feldspar crystal growth in a cavity, and (d) phillipsite and silica. 81

2.13 XRD patterns for selected field samples 83

2.14 a) The plot $(Na_2O + K_2O)/(Al_2O_3 + TiO_2)$ versus $SiO_2/(Al_2O_3 + TiO_2)$ in the fresh tuff, zeolitized tuff, sandstone and mudstone samples from the study area, and b) The relations between $(CaO + MgO)/(Al_2O_3 + TiO_2)$ and $(Na_2O + K_2O)/(Al_2O_3 + TiO_2)$ ratios of samples analyzed in this study. 86

2.15 Reflectance spectra of collected samples. The position of Mastcam-Z multispectral filters are shown as black dots. The light gray region indicates a gap in SuperCam passive coverage. The collected ASD spectra extend to 2.5 um, though the SuperCam passive IR range extends to 2.6 um. 88

2.16 Plots of absorption band depths versus water content in the region of a) 1.422 um region, b) 1.910 um region and c) 2.800 um region. Dashed lines show the best fil line of all the samples. 89

3.1 RELAB spectra of zeolite minerals (particle size $<$ 45 um) including analcime (laze57), phillipsite (laze23), chabazite (laze17), erionite (laze25), mordenite (laze29), heulandite (laze31), clinoptilolite (laze27), and stilbite (laze21), and polyhydrated sulfate epsomite (799f366). 102

3.2 Location and geology of Lake Tecopa study area, (a) Location of the study area, (b) sample locations, Tuff beds A, B, and C, and Hyperion image coverage overlay on the ASTER true color composite data (Sample (M): Locations of field samples with their mineral assemblages identified by XRD, Sample (SM): Locations of field samples with their mineral assemblages identified by XRD and spectral data, Tuff: Locations of samples T27 (abandoned quarry reference location), T30, T37 and T45 are shown in the figure; Locations of Tuff bed exposures selected from the Hillhouse (1987) geological map, NoTuff: Locations of the NoTuff class points, Gravel: Locations of the Gravel class points. Additional information in Section 3.5), (c) geological map (after Hillhouse (1987)), (d) diagenetic facies map (after Sheppard and Gude (1968)) with the sample locations, (e) Allogroup Map (after Morrison (1999)) with the sample locations, and (f) USGS National Elevation DEM image of the area with the sample locations (elevation in meters). 105

3.3 Field photos of Lake Tecopa study area showing (a) general stratigraphy, (b) erosional features of the area, (c) thin layer of zeolitic tuff bed covered by thin layer of gravel bed (washes), (d) mixing of zeolitic tuff bed with surrounding mudstone and sandstone beds due to physical weathering. P = Zeolite (tuff) bed, Q = Green mudstone bed, R = gravel pavement, S = sandstone/siltstone beds, and T = mixed sediments from all beds due to erosion and deposition. 107

3.4 XRD patterns for field samples T27 (zeolite bearing altered tuff), T30 (green mudstone), T37(siltstone) and T45 (less altered tuff). 109

3.5 Correction of errors associated with calculation of band depths using a continuum line. (a) Original T37 spectrum with its continuum line, (b) band depth spectra after continuum correction. This shows some artifacts with negative band depth values, (c) original spectra after removing unnecessary points and adding some points at local maxima, and (d) band depth spectra after continuum line correction. 111

3.6 Reflectance spectra of samples and library spectra of sample minerals (panels a, c, e, and g) over the wavelength range 0.3 - 2.5 um, and their continuum removed spectra (panels b, d, f, and h) showing the band depth, over the wavelength range 1.3 - 2.5 um 125

3.7 Sample spectra (black), Hyperion convolved sample spectra (green), ASTER convolved sample spectra (red), Hyperion image pixel spectra of sample location (pink) and ASTER image pixel spectra of sample location (blue). Hyperion and ASTER convolved spectra were 5 percent offset from each other for clarity. Plot T45 shows the spectral bandpasses of Hyperion and ASTER sensors. 126

3.8 ASTER and Hyperion VNIR-SWIR mapping results. (a) Natural color composite of ASTER image. The red arrow in the map points to the location of an abandoned quarry (T27 sample site), (b) Geological map of the area (Hillhouse (1987)), (c) Map of the tuff beds, sample locations, and Hyperion image coverage (Sam (M): Locations of field samples with their mineral assemblages identified by XRD, Sam (SM): Locations of field samples with their mineral assemblages identified by XRD and spectral data), (d) Natural color composite of Hyperion image, (e) ASTER band indices, (f) ASTER Minimum Noise Fraction (MNF) bands, (g) ASTER Spectral Angle Mapper (SAM) rule images, (h) ASTER linear unmixing bands, (i) Hyperion band indices, (j) Hyperion MNF bands, (k) Hyperion SAM rule images, and (l) Hyperion unmixing bands. Selected band combinations are shown in the legend. 128

3.9 Importance scores of attribute images derived from ASTER and Hyperion image data for predicting the Tuff beds. 131

4.1 RELAB spectra of zeolite minerals (particle size < 45 um) including analcime (laze57), phillipsite (laze23), chabazite (laze17), erionite (laze25), mordenite (laze29), heulandite (laze31), clinoptilolite (laze27), and stilbite (laze21). 141

4.2 Location and geology of Lake Tecopa study area, (a) Location of the study area,(b) geological map (after Hillhouse (1987)), (c) sample locations, Tuff beds A, B, and C, and Hyperion image coverage overlay on the ASTER true color composite data (Sample (M): Locations of field samples with their mineral assemblages identified by XRD, Sample (SM): Locations of field samples with their mineral assemblages identified by XRD and spectral data, Tuff: Locations of samples T27 (abandoned quarry reference location), Locations of Tuff bed exposures selected from the Hillhouse (1987) geological map, NoTuff: Locations of the NoTuff class points, Gravel: Locations of the Gravel class points, and (d) Hillshade map of the study area derived from USGS National Elevation DEM. 144

4.3 Emissivity spectra of samples with the RELAB laboratory emissivity spectra of constituent minerals over the 5.0 - 15 um wavelength range. 148

4.4 TIR sample spectra with resampled ASTER image pixel spectra after different processing levels and methods. 155

4.5 Comparison of different TES methods. (a) Emissivity normalization (EN) and Reference Channnel Emissivity (RCE) methods, (b) Alpha Residuals (AR) method, and (c) Temperature calculated from EN and RCE methods 157

4.6 ASTER TIR mapping results. (a) Emissivity bands calculated using the Reference Channel Emissivity method, (b) Emissivity bands calculated using the Emissivity Normalization method, (c) Emissivity bands calculated using the Alpha residuals method, (d) decorrelation stretched image of ASTER band 10, 13, and 14, (e) Geology map of the area, (f) ASTER TIR band indices, (g) ASTER TIR MNF bands, (h) ASTER TIR SAM image, and (i) ASTER TIR linear spectral mixture analysis results. Selected band conbinations are shown in the legend. 159

4.7 The effects of thermal atmospheric correction on the selected band indices. 162

4.8 Importance scores of attribute images derived from ASTER TIR image data for predicting the Tuff beds. 166

4.9 Spectral bandpasses of the THEMIS IR subsystem and the ASTER TIR subsystem. Spectral bandpasses of ASTER bands 10, 11, 12, 13, and 14 are plotted in red, green, blue, purple, and black, respectively. Center wavelength of THEMIS IR bands are shown with dotted lines. Band widths of each THEMIS IR bands are shown in gray color. Emissivity spectra of zeolitied tuff (T27) is shown in gold. 168

5.1 Schematic ternary diagram for mixtures of clinoptilolite, montmorillonite and epsomite. Blue points show the sample points of physical mineral mixtures prepared to collect reflectance spectra. The sample ID for each mixture is shown near the sample point. 183

5.2 Reflectance spectra of mineral end members (spectral endmembers) used in this study. 184

5.3 Original mineral mixture spectra (a) and after applying the multiplicative scatter correction (b). 186

5.4 Binary mineral mixtures showing absorption feature variations associated with varied mineral abundances. Each subplot shows the binary mineral mixture clinoptilolite - montmorillonite (a), clinoptilolite - epsomite (b), and montmorillonite - epsomite (c). F1, F2, and F3 are the wavelength regions of the absorption features selected for this study. Letter C in the legend indicates clinoptilolite, M indicates montmorillonite, and E indicates epsomite. Two integers after each letter indicate the mineral weight proportions on a 10 ponit scale. 188

5.5 Example of Gaussian curve fitting for F1 (a), F2 (b), and F3 (c) of mineral mixture T53 (60 percent clinoptilolite, 20 percent montmorillonite, and 20 percent epsomite) 191

5.6 Ternary plots showing the calculated Gaussian curve parameters of feature 1 (F1). a) Amplitude of Gaussian curve 1 of F1 (F1G1-AMP), b) Center wavelength of Gaussian curve 1 of F1 (F1G1-CNT), c) Width of Gaussian curve 1 of F1 (F1G1-SGM), d) Amplitude of Gaussian curve 2 of F1 (F1G2-AMP), e) Center wavelength of Gaussian curve 2 of F1 (F1G2-CNT), f) Width of Gaussian curve 2 of F1 (F1G2-SGM). Linear interpolation was applied between sample points to fill the colors in small triangles in the plots. 193

5.7 Ternary plots showing the amplitude of Gaussian curve 1 of feature 2 (F2G1-AMP, plot a), maximum band depth of feature 2 (F2BD-MAX, plot b), wavelength at maximum band depth of feature 2 (F2WL-MAX, plot c), and amplitude of Gaussian curve 1 of feature 3 (F3G1-AMP, plot d). Linear interpolation was applied between the sample points to fill the colors in small triangles in the plots. 194

5.8 An MLP with eight inputs, two hidden layers containing six hidden units, and three outputs. 197

5.9 Noise added versions of spectrum T53, resampled to CRISM spectral resolution. Savitzky-Golay Smoothed spectra are shown in black. 200

5.10 Ternary plot showing the original composition of the mineral/mineral mixture with their predicted compositions. Arrowheads show the predicted composition of each mineral mixture. 203

5.11 Continuum removed spectra of F1 (plot a), F2 (plot b), and F3 (plot c) of end member spectra (dashed lines) and library spectra, which shows the highest prediction error. 205

6.1 Reported mineral abundances in saline-alkaline paleolakes. Each sedimentary bed type in the concentric graph shows the abundance of each mineral type (color coded), along with the relative frequency of samples that contain it. Frequency is depicted by the height of the each bar. The data were normalized for each sediment type to its maximum frequency. 218

6.2 Self-Organizing Map (SOM) training progress. 223

6.3 Self-Organizing Map (SOM) Results. a). Mapping positions of all 1648 tuff bed samples in ten-by-ten (nodes) Self-Organizing Map (100 nodes), based on their 14 mineral assemblages. Big circles indicate the nodes, while small circles inside each node show the nodes onto which samples have been mapped. No samples have been mapped to six nodes. b) Neighbor distance plot shows the distance between each node and its neighbors. Areas with low neighbor distance (shown in dark red) indicate the groups of nodes that are similar, while more dissimilar nodes are indicated by a lighter color. c) Plot of codebook vectors for the mapping of the glass class with 12 clusters. Nodes of the different colors represent the different clusters. The size of the fans inside each node represents the magnitude of each variable in the weight vector (In this case frequency of each abundance class for glass assigned to each node). 224

6.4 Relative mineral abundance in each Cluster. 226

6.5 Decision Tree showing the clustering rules. 229

6.6 Diagenetic zones of (a) Lake Tecopa, Inyo County, California (after Sheppard and Gude, 1968) (b) Big Sandy Formation, Mohave County, Arizona (after Sheppard and Gude, 1973), (c) Karlovassi basin, Samos, Greece (after Stamatakis, 1989), and (d) Gila Conglomerate near Buckhorn, New Mexico (after Gude and Sheppard, 1988). Dark color of each lithology type in the map (d) indicates the approximate extent of diagenetic zones, whereas the light colors (letter (i) after the lithology type in the legend) indicate the inferred extent of zones prior to erosion. 232

7.1 Total alkali vs. SiO_2 diagram (TAS diagram) showing the geochemical classification of Martian rocks analyzed by rover missions (Pathfinder, Opportunity, Spirit, and Curiosity) and Martian meteorites. Chemical composition of fresh tuff samples collected from the saline-alkaline paleolakes where zeolites are observed also added to the plot for easy comparison (Dataset with references can be found in Table E.1 in the Appendix E) . 247

7.2 Dissolution of primary minerals (a and e), concentration of elements in the aqueous phase (b and f), precipitation of secondary minerals (c and g), total mass of mineral destroyed and created with mass of H_2O lost from aqueous phase (d and h) during weathering of Buckskin sample under rainwater in closed systems at 25 ^oC and 1 bar at 0.24 W/R ratio. Plots (a, b, c, and d) are for hydrologic system A and plots (e, f, g, and h) are for hydrologic system B. Both solutions are equilibrated with 1.3 bar CO_2 and 0.0147 mbar of O_2. 253

7.3 Precipitation of secondary minerals during weathering of the Buckskin sample in closed systems using a solution containing 50000 umole/L H_2SO_4 and 9600 umole HCl at 25 ^oC and 1 bar at 0.25 W/R ratio. Initial pH of solution is 1.36. 255

7.4 Effects of water/rock mass ratio on pH (a) and secondary mineral precipitation (b) during weathering of the Buckskin sample in a closed system at 25^oC and 1 bar. Horizontal lines in Figure 4 (b) represent the time intervals at which minerals are present in different W/R ratio. 258

7.5 Schematic profile showing alteration zoning of two genetic types of zeolite formation patterns discussed in this study. The minerals showed in the legend are the main minerals formed in the calculated models. Rainwater 1: "pure" rainwater adopted in hydrologic system A, Rainwater 2: rainwater during volcanic eruption (hydrologic system B), Acid water: $H_2SO_4 - HCl$ acid water (hydrologic system C). 267

8.1 Hydrous mineral detections on Mars. Each point represents the position of a hydrous mineral exposure detected by CRISM and/or OMEGA. Background is a grayscale hillshade map created from MOLA DEM. Point density plot shows on the left side of the map. 283

8.2 Venn diagram for the relations between binary patterns. 286

8.3 Calculation of fuzzy membership functions using different methods. The geology map (tn_geomp) was used as the example in this figure. The Weights W^+ x-axis refers to Method 1 (Zimmermann, 1991), and Method 4 developed in this study, while the Contrast C x-axis refers to Method 2 (Cheng and Agterberg, 1999) and Method 3 (Porwal et al., 2003). 291

8.4 Calculated fuzzy membership values as a function of time (geological units). eNh: Early Noachian highland, eNhm: Early Noachian highland massif, mNh: Middle Noachian highland, mNhm: Middle Noachian highland massif, Nve: Noachian volcanic edifice, Nhe: Noachian highland edifice, Nhu: Noachian highland undivided, lNH: Late Noachian highland, lNv: Late Noachian volcanic, HNb: Hesperian and Noachian basin, ANa: Amazonian and Noachian apron, HNt: Hesperian and Noachian transition, HNhu: Hesperian and Noachian highland undivided, Htu: Hesperian transition undivided, Ht: Hesperian transition, eHh: Early Hesperian highland, eHb: Early Hesperian basin, eHv: Early Hesperian volcanic, eHt: Early Hesperian transition, Hve: Hesperian volcanic edifice, Hto: Hesperian transition outflow, lHv: Late Hesperian volcanic, lHb: Late Hesperian basin, lHl: Late Hesperian lowland, lHvf: Late Hesperian volcanic field, lHt: Late Hesperian transition, AHtu: Amazonian and Hesperian transition undivided, AHv: Amazonian and Hesperian volcanic, AHi: Amazonian and Hesperian impact, eAb: Early Amazonian basin, mAl: Middle Amazonian lowland, Aa: Amazonian apron, Av: Amazonian volcanic, Ave: Amazonian volcanic edifice, lAa: Late Amazonian apron, lAv: Late Amazonian volcanic, lAvf: Late Amazonian volcanic field. 293

8.5 Fuzzification process showing the original MOLA DEM (a), classified MOLA DEM (b), and a map after assigning the fuzzy membership values for each elevation class (c). 294

8.6 Integrated fuzzy membership maps. a) Max_physical (eq. 8.25), and b) Min_physical (eq. 8.24). 297

8.7 Fuzzy algebraic product (FAP) and fuzzy algebraic sum (FAS) maps of map combination 6 (FAP_6 and FAS_6) listed in Table 8.4. 298

8.8 A graph of fuzzy membership obtained by combining two fuzzy membership values versus gamma. 299

8.9 Percentage accuracy and spatial coverage in each map combination (F2 and F6) against different gamma values. 301

8.10 a) Favorability map for hydrous minerals (Map Fz_06_0.84). Areas ranked according to fuzzy membership values. The fuzzy set comprises those locations that satisfy the proposition favorable for hydrous minerals. Fuzzy membership ranges from 0 to 1 (less favorable to highly favorable). b) Favorability class map derived from map (a) showing the potential area for hydrous minerals on Mars up to 40 degrees latitude. 302

8.11 The map shows the thickness of possible ash deposits modelled by Kerber et al. (2013), pyroclastic ash deposits (black outline) compiled by Broz et al. (2020) and open and closed basins (black filled areas) compiled by Goudge et al. (2016). Values in the legend are fuzzy membership values corresponding to the thickness of the modeled ash deposits. 303

8.12 The fuzzy inference engine used to crate map Fz_06. 304

8.13 Potential zeolite bearing terrains calculated using the data driven fuzzy weights-of-evidence method. Value range indicates the possibility of finding zeolite based on the calculations. 1 = highest possibility, 0 = Lowest possibility. Background is a hillshade from MOLA DEM. 305

8.14 The favorability map of zeolites in open- and closed-paleolake basins cataloged by Goudge et al.(2016) in Arabia Terra region, Mars. Color range indicates the possibility of finding zeolites based on the present calculation. 0.9 = highest possibility, 0 = lowest possibility. Background is Viking color image. 310

B.1 Spectral Angle Mapper classification results from ASTER and Hyperion images, using sample spectra for classification without spectral subset (a), using pixel spectra for classification without spectral subset (b), and using sample spectra after spectral subset (c). 393

C.1 Ternary plots showing the center wavelength of Gaussian curve 1 of feature 2 (a), gamma value of Gaussian curve 1 of feature 2 (b), sigma value of Gaussian curve 1 of feature 2 (c), amplitude of Gaussian curve 2 of feature 2 (d). Linear interpolation was applied between the sample points to fill the colors in small triangles in the plots. 406

C.2 Ternary plots showing the center wavelength of Gaussian curve 2 of feature 2 (a), gamma value of Gaussian curve 2 of feature 2 (b), amplitude of Gaussian curve 2 of feature 3 (c), sigma value of Gaussian curve 2 of feature 3 (d). Linear interpolation was applied between the sample points to fill the colors in small triangles in the plots. 407

LIST OF TABLES

1 Typical unit-cell formula of most common zeolites in saline-alkaline lakes. After Breck (1974); Mumpton (1977); Hay (1966); Passaglia and Sheppard (2002). 2

2 Basic data about Earth and Mars. Data sources: Grotzinger et al. (2013); Taylor et al. (2018). 3

3 Minerals detected on Mars from landed and orbital data. 6

1.1 Three mode of inference 25

2.1 Science instruments onboard the Curiosity (Grotzinger et al., 2012) and Perseverance rovers (Farley et al., 2020). 51

2.2 Source and dating of Lake Tecopa ash beds 56

2.3 Earth data/instruments used in this study with their complementary Mars data/instruments. 61

2.4 Bulk mineral composition of the selected field samples 83

2.5 Elemental compositions of the selected field samples 84

3.1 Mineralogy of selected samples 109

3.2 Performance of the ASTER VNIR-SWIR and Hyperion Instruments (Hubbard and Crowley, 2005; Pearlman et al., 2003). 112

3.3 Radiometric correction parameters used in this study. 114

3.4 RBD and simple band ratios used in this study. 120

4.1 Summary characteristics of the ASTER TIR subsystem (Tonooka, 2005) 146

4.2 Radiometric correction parameters used in this study. 150

5.1 Absorption band assignment for clinoptilolite, montmorillonite and epsomite (sources: Cloutis et al. (2002); Bishop et al. (1994); Clark (1995); Hunt and Salisbury (1970); Gendrin et al. (2005); Cloutis et al. (2006)). 184

5.2 Root Mean Square Error (RMSE) of different models adopted in this study. All models were run for 10,000 epochs. 198

5.3 Library spectra used to test the accuracy of the model. 201

6.1 Reported mineral paragenesis. 212
6.2 Number of samples in each type of sedimentary beds in selected sites . . 216
6.3 Most common mineral combinations found in the dataset. 220
6.4 Major group of clusters identified by SOM and DT rules. 229

7.1 Calculated rock recipe for 1 kg of Buckskin sample, number of moles in mineral present, density, specific surface area, rate of mineral dissolution (first order reaction), and activation energy of each mineral. Density values from Gribble (2005). The dissolution rates and activation energy of primary minerals were adopted from Palandri and Kharaka (2004). 247
7.2 Secondary minerals formed in models (Thermodynamic data are from EQ36 database). 251
7.3 Mass of the secondary minerals formed after 1000 years of reaction with the solution and volume percentage of each mineral with respect to the total volume of the secondary minerals formed. 256
7.4 Time intervals (in years) of zeolites present under different water/rock ratios (W:R). Once formed, chabazite and analcime remain throughout the modeled duration. The time interval when clinoptilolite forms and subsequently re-dissolves is indicated by the time interval shown. 259
7.5 Comparison of the input parameters and output secondary minerals for selected models in previous studies. Prominent characteristic secondary minerals of interest in this study are grouped into three bins showing three stages during the reaction progress. Stages were chosen based on the reaction time or W/R ratio of models and therefore minerals in each bin might not be directly comparable. 264

8.1 Factor maps used in this study. 284
8.2 Slope a values used in Logistic membership functions (eq. 8.9 and 8.12). 290
8.3 Fuzzy membership values (fzm) in map classes of maps of valley networks (ga_vlnet) and ash thickness map (lk_pyash). 293
8.4 Input map combinations used to create 12 map combinations. FAP: fuzzy algebraic product. FAS: fuzzy algebraic sum. 298
8.5 List of calculated 25 maps using different map combination and gamma values. 300
8.6 Test and train accuracy (success rate) of each map combinations. This shows the number of hydrous mineral detections in each class as a percentage with respect to the total number of data points. The train dataset is indicated by letters "_trn" after the fuzzy map Fz_02_0.84 or Fz_06_0.84, while the test dataset indicated by letters "_tst". 301

8.7 Selected open-closed basins in the Arabia Terra region. 310

A.1 Database of non-marine tuff deposits from literature. 387

C.2 Deep leaning prediction results 407

E.1 Database used to create Total alkali vs. SiO_2 diagram (TAS diagram) in Chapter 7. 415

E.2 Thermodynamic Database (from EQ3/6 software). 424

E.3 Secondary minerals formed in models (Thermodynamic data are from EQ36 database). 427

LIST OF ABBREVIATIONS

1-D . . . . . One dimensional

2-D . . . . . Two dimensional

3-D . . . . . Three dimensional

ANN . . . . . Artificial Neural Network

APXS . . . . . Alpha Particle X-ray Spectrometer

AR . . . . . Alpha Residuals

ASTER . . . . Advanced Spaceborne Thermal Emission and Reflection Radiometer

AVIRIS . . . . Airborne Visible/ Infrared Imaging Spectrometer

CCF . . . . . Calibration Correction Factors

CIA . . . . . Collision-Induced Absorption

CRISM . . . . Compact Reconnaissance Imaging Spectrometer for Mars

CTX . . . . . Context Camera

DEM . . . . . Digital Elevation Model

DL . . . . . Deep Learning

DNN . . . . . Deep Neural Network

DOM . . . . . Digital Outcrop Model

DT . . . . . Decision Tree

EBM . . . . . Energy Balance Model

EDS . . . . . Energy Dispersive X-ray Spectrometry

EN . . . . . Emissivity Normalization

GDAL . . . . . Geospatial Data Abstraction Library

GPS . . . . . Global Positioning System

GRC . . . . . Ground Resolution Cell

GRS . . . . . Gamma-Ray Spectrometer

HiRISE . . . . High Resolution Imaging Science Experiment

ICDD PDF . . International Center for Diffraction Data Powder Diffraction File
IFOV . . . . . Instantaneous Field of View
ILWIS . . . . . Integrated Land and Water Information System
ISIS . . . . . Integrated Software for Imagers and Spectrometers
k-CV . . . . . k-fold Cross-Validation
LN-EH . . . . Late Noachian to Early Hesperian
LSMA . . . . . Linear Spectral Mixture Analysis
LSU . . . . . Linear Spectral Unmixing
LVQ . . . . . Learning Vector Quantization
MAHLI . . . . Mars Hand Lens Imager
MFF . . . . . Medusae Fossae Formation
MGM . . . . . Modified Gaussian Model
MGS . . . . . Mars Global Surveyor
ML . . . . . Machine Learning
MLP . . . . . Multilayer Perception
MNF . . . . . Minimum Noise Fraction
MOC . . . . . Mars Orbital Camera
MOLA . . . . Mars Orbiter Laser Altimeter
MRO . . . . . Mars Reconnaissance Orbiter
MSC . . . . . Multiplicative Scatter Correction
MSE . . . . . Mean Squared Error
NAIP . . . . . National Agricultural Inventory Program
NCC . . . . . Natural Color Composite
NED . . . . . National Elevation Data
NIR . . . . . Near InfraRed
OMEGA . . . Observatoire pour la Minelralogie, liEau, les Glaces et IiActivitei
PIXL . . . . . Planetary Instrument for X-ray Lithochemistry
PSF . . . . . Point Spread Function
RBD . . . . . Relative Band Depth
RCE . . . . . Reference Channel Emissivity
RMSE . . . . . Root Mean Squared Error

RTM . . . . . Radiative Transfer Models

SAM . . . . . Spectral Angle Mapper

SEM . . . . . Scanning Electron Microscopy

SNR . . . . . Signal to Noise Ratio

SOM . . . . . Self-Organizing Maps

SRTM . . . . . Shuttle Radar Topography Mission

SWIR . . . . . Shortwave InfraRed

TES . . . . . Thermal Emission Spectrometer

TES . . . . . Temperature Emissivity Separation

THEMIS . . . Thermal Emission Imaging System

TIR . . . . . Thermal InfraRed

TST . . . . . Transition-State Theory

UCC . . . . . Unit Conversion Coefficients

USGS . . . . . United States Geological Survey

VNIR . . . . . Visible to Near InfraRed

WEM . . . . . Weights-of-Evidence Method

XRD . . . . . X-ray Diffraction

XRF . . . . . X-ray Fluorescence

ACKNOWLEDGEMENTS

First and foremost, I would like to express my sincere appreciation and thanks to you, my advisor, Dr. Lindsay McHenry. I am very much grateful to you, for your encouragement, advice, friendship, and moral support throughout my PhD.

I would also like to extend many thanks to my thesis committee members, Dr. Timothy J. Grundl, Dr. Freek van der Meer, Dr. Mark T. Harris, and Dr. Julie A. Bowles for your encouragement, guidance, and insightful comments. I express my gratitude to all the faculty and administrative staff at the Department of Geosciences for your continuous support in my graduate studies, and to all my friends at the University of Wisconsin-Milwaukee for your friendship and encouragement.

Because this is the culmination of education, I will also take this opportunity to thank my undergraduate supervisors: Dr. Jagath Gunathilake and Dr. H.A. Dharmagunawardane of the University of Peradeniya, Sri Lanka, for inspiring my enthusiasm in the field of geology. My M.Sc supervisors Dr. Tsehaie Woldai and Dr. Frank van Ruitenbeek of ITC (Faculty of Geo-information Science and Earth Observation, University of Twente), Netherlands, thank you so much for extending my research interest from field-based geology to remote sensing geology. My M.Tech Degree supervisors Dr. P. K. Champati Ray, Dr. R. S. Chatterjee, and Dr. Prakash Chauhan from IIRS (Indian Institute of Remote Sensing), India, thank you for introducing me to planetary remote sensing. I also take this opportunity to thank all the teachers who taught me on this journey.

Thanks to Jason Carman, Mark Eskritt, and Kaitlin Krause for your incredible support during the field visits to Lake Tecopa. A big thank you to Dr. Thomas McCollom at the University of Colorado, and Dr. Takahiro Hiroi from the RELAB facility at Brown University for acquiring spectral data of my field samples. To Dr. Heather Owen from the Department of Biological Sciences, University of Wisconsin-Milwaukee, thank you for being so generous with your time and teaching Scanning Electron Microscopy (SEM).

Dr. Nalaka Ranasinghe and Dr. Suniti Karunathillake, thank you for your encouragement to apply to graduate schools in the USA to achieve my childhood dream to be a planetary scientist.

Thank you to all the free and open-source code and software developers (FOSS). More than 90% of my work is done using FOSS software.

Of course, all my academic success counts back on the love, help, support, and encouragement that I got from my parents, relatives, and friends. Thank you to all my Sri Lankan friends at University of Wisconsin-Milwaukee and Marquette University, and the Sri Lankan community in Milwaukee.

Thank you so much, Chase Glenister. Since my first day at the University of Wisconsin-Milwaukee, I have been so lucky to have you as my best friend.

A big thanks to my sister Inosha Kodikara and her family, who take care of my father, when I am on the other side of the globe. I dedicate this work to my father, I love you. Finally, to my mother, who isn't here anymore but whom I know would be incredibly proud.

Thank you to all the living and nonliving things in this universe. This piece of work is a result of all your kind support and encouragement.

Gayantha R. L. Kodikara
Department of Geosciences, UW-Milwaukee
20 January 2022

Introduction

Zeolites

The term "Zeolite" was introduced by the swedish mineralogist Cronstedt (1756) from the Greek zeo = boil and lithos = stone for minerals which expel water when heated and hence seem to boil (Gottardi and Galli, 1985). The definition of the Zeolite given by the Commission on New Minerals and Mineral Names (CNMMN)(Coombs et al., 1998, 1997) is,

> "A zeolite mineral is a crystalline substance with a structure characterized by a framework of linked tetrahedra, each consisting of four O atoms surrounding a cation. This framework contains open cavities in the form of channels and cages. These are usually occupied by H_2O molecules and extra-framework cations that are commonly exchangeable. The channels are large enough to allow the passage of guest species. In the hydrated phases, dehydration occurs at temperatures mostly below about 400^oC and is largely reversible. The framework may be interrupted by (OH, F) groups; these occupy a tetrahedron apex that is not shared with adjacent tetrahedra."

The general formula for zeolites is $M_xD_y[Al_{x+2y}Si_{n-(x+2y)}O_{2n}]\ .\ mH_2O$, where M are monovalent and D are divalent cations. The content in square brackets represents the tetrahedral framework and is characterized by an overall negative charge that increases as the Al:Si ratio increases. The formula outside the square bracket consists of exchangeable extraframework cations, which balance the framework's negative charge, and water molecules that often coordinate the extraframework cations (Passaglia and Sheppard, 2002).

Based on their geological and hydrological environments, zeolite occurrences in sedimentary rocks on Earth can be classified into six classes: 1) saline-alkaline lakes, 2) alkaline soils and land surfaces, 3) deep sea sediments, 4) open hydrologic systems, 5) as products of hydrothermal alteration, and 6) burial diagenesis or low-metamorphic environments (Fig. 1)(Langella et al., 2001; Hay and Sheppard, 2001). Zeolites are both

common and widespread in ash deposits of saline-alkaline lakes and the largest relatively pure concentrations of natural zeolites are found in these environments (Hay and Sheppard, 2001; Hay, 1966). The most common zeolites in saline-alkaline lake environments (closed hydrologic systems) are listed in Table 1.

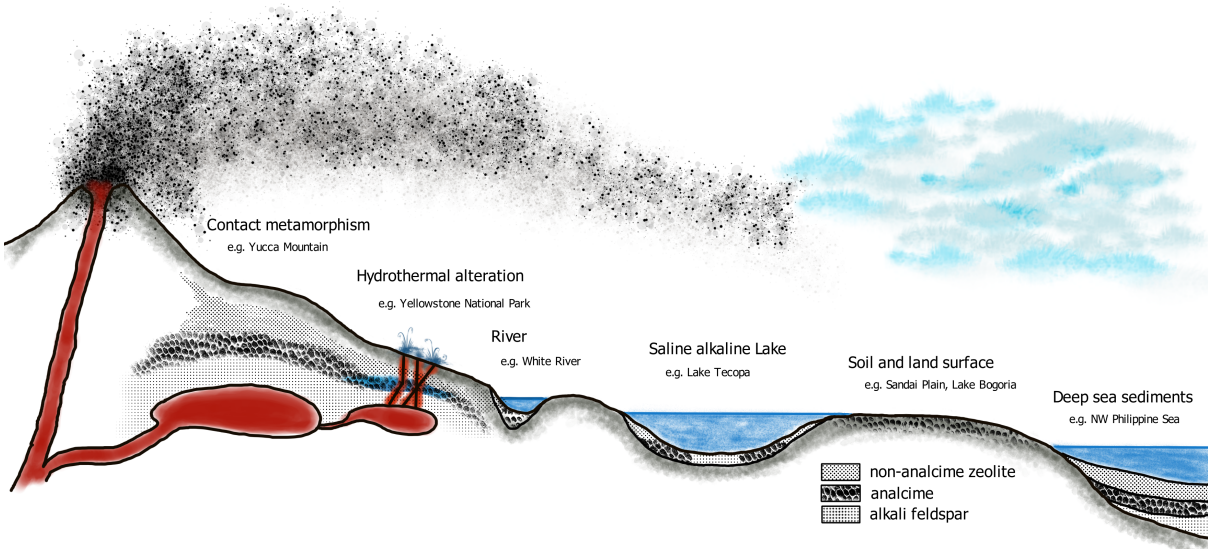

Figure 1: Schematic cross-sectional diagram showing the patterns of zeolite zoning in tuff deposits in different environments.

Table 1: Typical unit-cell formula of most common zeolites in saline-alkaline lakes. After Breck (1974); Mumpton (1977); Hay (1966); Passaglia and Sheppard (2002).

Mineral	Na	Ca	K	Al:Si	Unit-cell Formula
Analcime	x	-	x	1.8 - 2.8	$Na_{16}[(AlO_2)_{16}(SiO_2)_{32}].16H_2O$
Chabazite	-	x	-	1.6 - 3.0	$Ca_2[(AlO_2)_4(SiO_2)_8].13H_2O$
Clinoptilolite	x	x	x	4.25-5.25	$Na_6[(AlO_2)_6(SiO_2)_{30}].24H_2O$
Erionite	x	x	x	3.0 - 3.5	$(Ca, Mg, Na_2, K_2)_{4.5}[(AlO_2)_9(SiO_2)_{27}].27H_2O$
Phillipsite	x	x	x	1.7 - 2.4	$(Ca, K_2, Na_2)_5[(AlO_2)_{10}(SiO_2)22].20H_2O$

Tuffs deposited in and near saline-alkaline lakes will be altered to different degrees depending on their position within the lake basin, with, 1) an outer zone of glass and/or smectite, where pore fluids are relatively dilute, 2) a non-analcime zeolite zone reflecting elevated pH and salinities, 3) a zone of analcime reflecting higher salinities, and 4) the zone of highest salinity, where tuffs may be altered to K-feldspar, generally located in the central part of the basin (Hay and Sheppard, 2001; Langella et al., 2001). Thus, zeolites in saline-

alkaline lacustrine environments can be used to reconstruct lake history (e.g., McHenry et al. (2020)) and also for climate proxy studies (e.g., Arnold et al. (2021)) on Earth and even on Mars where paleolake environments have been identified using Mars orbital and rover data.

Mars

Mars, the fourth planet from the sun, is one of the most explored bodies in our solar system. Mars is a geologically heterogeneous planet on which have operated many geological processes similar to Earth. Interactions between atmospheric and geologic processes influence the composition and morphology of the planetary surface, which records the evolution of the planet's surface and variations in climate history (Grotzinger et al., 2013). Many fundamental differences can also be observed between these two planets (Table 2). On Earth, plate tectonics are the main cause of uplift, subsidence, basin formation, and sediment deposition. On Mars, plate tectonics never occurred and instead volcanic loading and impact processes provide the elevation differences, subsidence, and basins that are required for sediment formation, transport, and deposition (Taylor and McLennan, 2009). Mars possessed a dynamic sedimentary rock cycle for most of its history, like that of Earth. But the sedimentary rock cycle on Mars is dominated by the sulfur cycle (and sulfates) rather than the carbon cycle (and carbonates) which dominates on Earth (McLennan, 2012; Taylor and McLennan, 2009).

Table 2: Basic data about Earth and Mars. Data sources: Grotzinger et al. (2013); Taylor et al. (2018).

	Earth	Mars
Mean distance from Sun	1.496 x $10^8 km$	2.279 x $10^8 km$
Comparative solar distance	1	1.524
Orbital period	1	1.881
Rotational period	23.9345 hours	24.6229 hours
Equatorial radius	6378 km	3397 km
Mass	5.97 x $10^{24} kg$	0.642 x $10^{24} kg$
Relative Mass	1	0.107
Gravity	9.8 ms^{-2}	3.7 ms^{-2}
Mean surface Temperature	288 K	214 K
Atmospheric pressure(surface)	1 bar	6.1 mbar
Atmospheric composition		
Nitrogen (N_2)	78.08%	2.7%

	Earth	Mars
Oxygen (O_2)	20.95%	almost zero
Carbon Dioxide (CO_2)	0.035%	95.3%
Water vapour (H_2O)	~1%	0.03%
Other gases	almost zero	2% (mostly Ar)
Composition of Crust		
Exposed crust (SiO_2)	66%	49%
Exposed crust dominant material	Quartz, plagioclase, K-feldspar	Plagioclase, pyroxene, olivine

Surface features of Mars have been divided into three age groups (Noachian, Hesperian, and Amazonian) based on their cross-cutting relationships and the number of superimposed impact craters (Hartmann and Neukum, 2001; Tanaka et al., 2014a) (Fig. 2). Surface conditions during the pre-Noachian are little known since that geologic record has been almost completely erased (Carr and Head, 2010). The Noachian age is characterized by high rates of cratering, erosion, valley formation, and the widespread presence of phyllosilicate minerals (Carter et al., 2013; Craddock and Howard, 2002). Fe-/Mg- smectites are the most common phyllosilicate minerals on Mars, identified in more than 75% of locations in which any hydrated silicate mineral is detected (Ehlmann et al., 2013). The main characteristics of the Hesperian period are volcanism and the formation of extensive lava plains, low rates of valley formation compared to the Noachian, formation of largest outflow channels and their terminal lakes or seas, extremely low rates of erosion, an extreme decline of rock alteration to form phyllosilicates, and accumulations of sulfate-rich deposits (Carr and Head, 2010). This transition from phyllosilicate to sulfate deposition can be explained as the combined outcome of increasing planetary oxidation, decreasing groundwater availability, and a waning bolide impactor flux (Wordsworth et al., 2021). The most distinguishing characteristic of the Amazonian is the formation of features that have been attributed to the presence, accumulation, and movement of ice, particularly at mid to high latitudes (Carr and Head, 2010).

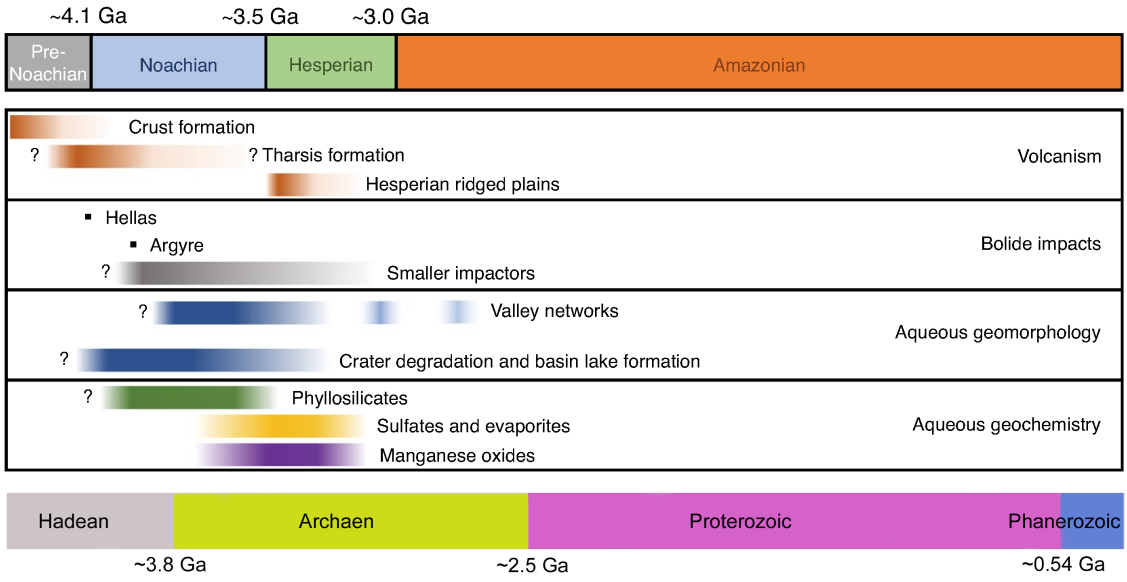

Figure 2: Geological activity as a function of time on Mars (Modified after Wordsworth et al., 2021). The approximate boundaries of major time periods on Mars and similar major time subdivisions in Earth history are also shown.

Bibring et al. (2006) suggested three sequential eras for Martian history based on the surface alteration products identified by global mineralogical mapping of Mars using OMEGA (Observatoire pour la Mineralogie, l'Eau, les Glaces et l'Activite) orbital data. Similarly, ten stages of mineralogical evolution have been proposed for Earth (Hazen et al., 2008). The stages of mineral evolution on Earth arise from three primary mechanisms: 1) the progressive separation and concentration of elements from the relatively uniform composition of the solar nebula, 2) increase in range of intensive variables (e.g., pressure, temperature, and activities of H_2O, CO_2, and O_2), 3) the generation of far-from-equilibrium conditions by living organisms (Hazen et al., 2008). For Mars, mineralogical evolution was likely controlled largely by the amount and composition of near-surface water available for surficial processes (McLennan, 2012). The alteration history proposed by Bibring et al. (2006) includes 1) the Phyllosian era (Early and Mid-Noachian): non-acidic aqueous alteration indicated by phyllosilicates, 2) the Theiikian era (Late Noachian to Early Hesperian): acidic aqueous alteration indicated by sulfate, and 3) the Siderikian era (Late Hesperian to Amazonian): atmospheric aqueous-free alteration indicated by ferric oxides (Bibring et al., 2006; McLennan, 2012).

Over the past 45 years, the amount of data coming from orbiters, rovers, and landers on Mars has greatly increased. Many minerals were identified and mapped on the surface of Mars (Table 3). Their origin is not well constrained and they could have formed by different processes such as pedogenic weathering, in situ alteration, diagenesis, and hydrothermal alteration due to volcanism or impacts (Ehlmann et al., 2013).

Table 3: Minerals detected on Mars from landed and orbital data.

	Class	Group/Mineral	Reference
Primary	Framework silicate	Olivines	
		Orthophyroxene	
		Clinopyroxene	
		Plagioclase feldspar	
		Alkali feldspar	
	Sulfides	Pyrrhotite	
		Pyrite	
	Oxides	Magnetite	
		Ilmenite	
Secondary	Oxides	Hematite	Christensen et al. (2000)
		Goethite	Morris et al. (2006)
		Akaganeite	
	Phyllosilicates	Fe/Mg smectite	Poulet et al. (2005)
		(e.g., nontronite, saponite)	
		Al smectite	Poulet et al. (2005)
		(e.g., montmorillonite)	
		Kaolinite group	Gondet et al. (2006)
		(e.g., kaolinite, halloysite)	
		Chlorite	Mustard et al. (2008)
		Serpentine	Ehlmann et al. (2010)
		Muscovite/ illite	Mustard et al. (2008)
	Zeolites	Analcime	Ehlmann et al. (2009)
	Silicates	Opaline silica, quartz	Squyres et al. (2008)
		Prehnite	Ehlmann et al. (2009)
	Carbonates	Mg/Fe carbonates	Bandfield et al. (2003)
		Ca carbonates	Boynton et al. (2009)
	Sulfates	Kieserite	Arvidson et al. (2005)
		Mg-polyhydrated sulfates	Bishop et al. (2009)
		Szomolnokite	Bishop et al. (2009)
		Fe-polyhydrated sulfates	Bishop et al. (2009)
		Gypsum	Bibring et al. (2005)
		Bassanite	Wray et al. (2010)
		Anhydrite	Vaniman et al. (2018)
		Alunite	Swayze et al. (2008)
		Jarosite	Klingelhofer et al. (2004)

Class	Group/Mineral	Reference
Chlorides	Chlorides	Osterloo et al. (2010)
Perchlorates	Perchlorates	Hecht et al. (2009)

Note: Numerous papers have been published on these and therefore the references listed here are for the first paper (based on literature survey) reporting the detections with robust justification.

Na-zeolite analcime has also been identified in several locations on Mars (e.g., Ehlmann et al. (2009); Carter et al. (2013); Sun and Milliken (2015)). These studies show that zeolite detections are not widespread and discussed the difficulty of confirming zeolite detections due to spectral similarity to polyhydrated sulfate spectra. Zeolites have not yet been reported in Martian meteorites or in data from in situ landers or rovers. Zeolites may not be identifiable using orbital remote sensing at certain locations on Mars, because

1. they are absent, or
2. they were originally present and later removed by chemical processes (e.g., dissolution and alteration), or
3. they are present but are covered by or mixed with other materials, or
4. they are present, but the methods applied are not capable of detecting and mapping them, or
5. they are present, but we are not looking in the correct places.

The main objective, specific objectives, and related research questions are defined to assess which of the possibilities discussed above are most likely.

Main Objective

The main objective of this research is to evaluate the possible formation and evolution mechanisms of zeolites on early Mars with possible explanations for their limited detections using Earth analogs.

Specific Objectives and associated research questions of this study are as follows:

Specific Objective 1:

Explore the use of multiple hypotheses and different scientific reasoning styles for planetary geology research.

Research Questions:

1. Why are zeolites not commonly observed in paleolake basins on Mars?
2. Can analog reasoning, modeling, and models be used to address their limited detection?

Specific Objective 2:

Identify the capabilities, limitations, and uncertainties associated with identifying and mapping zeolites and other authigenic mineral assemblages in zeolite-bearing paleolacustrine deposits on Earth using remotely sensed data.

Research Questions:

1. What are the main remote sensing attributes that can help to identify and characterize the zeolites and associated sediments on paleolacustrine environments on Earth?
2. What are the capabilities, limitations, and uncertainties associated with mapping zeolites and other authigenic mineral assemblages using remote sensing data?

Specific Objective 3:

Explore possible zeolite diagenetic patterns in closed hydrologic systems on Earth.

Research Questions:

1. What are the most common diagenetic pathways of zeolite formation in saline-alkaline lacustrine environments on Earth?
2. How can machine learning be applied to identify the most common diagenetic patterns using bulk mineralogy data?

Specific Objective 4:

Examine the effects of the composition of starting material, starting solution chemistry and pH, solution/rock ratio, and timing of rock alteration for the formation of zeolites on early Mars.

Research Questions:

1. How do the chemistry and pH of the solution, solution/rock ratio, and primary rock composition affect zeolite mineral formation in hydrologically closed environments on early Mars?
2. What are the possible zeolites that can be expected to form in hydrologically closed environments on early Mars with the given environmental conditions?

Specific Objective 5:

Explore the possible zeolite-bearing environments on Mars using orbital remote sensing data.

Research Questions:

1. What are the main remote sensing attributes that can help to identify potential zeolite-bearing areas on Mars?
2. How can geocomputational predictive models be used to identify potential target locations for detailed studies?

It is hypothesized that the knowledge gained by characterizing the formation and fate of zeolites in paleolacustrine deposits on Earth using mineralogic, geochemical, geomorphologic, and remotely sensed data can be transferable to identify zeolite-bearing paleolacustrine deposits on Mars. This assumes that late Noachian to early Hesperian Mars was warm and wet and that the processes and interactions involved in the formation and fate of zeolites on lacustrine environments on Mars are like the processes and interactions observable in modern and ancient environments on Earth.

Specific objective 1 is addressed in Chapter 1, while specific objective 2 is addressed in Chapters 2, 3, 4, and 5. Chapter 1 explores the use of multiple hypotheses and different scientific reasoning styles for planetary geology research. This research was conducted to find possible answers for the main research question of this study: *"Why are zeolites not commonly observed in paleolake basins on Mars?"*.

Chapter 2 presents the data, methods, and techniques used to identify and reconstruct paleolake basins on Earth using data like that used in orbital and ground-based studies on Mars. Paleolake Tecopa in California was chosen as an analog environment for this study. This chapter also applies digital elevation models (DEM), high-resolution multispectral images, ground-based images, X-ray diffraction (XRD), X-ray fluorescence (XRF), and Visible to near infrared - Shortwave infrared (VNIR-SWIR) reflectance spectroscopy to identify paleolake deposits on Earth and discusses its implications for Mars.

Chapter 3 applies multispectral and hyperspectral orbital images in the VNIR-SWIR wavelength region to identify zeolite-bearing lacustrine sediments in Lake Tecopa and discusses its implications for Mars.

Chapter 4 applies multispectral orbital images in the Thermal infrared Wavelength (TIR) region to identify zeolite-bearing lacustrine sediments in Lake Tecopa and discusses its implications for Mars.

Chapter 5 proposes a technique for estimating clinoptilolite, montmorillonite, and epsomite mineral abundances from reflectance spectra of mineral mixtures using a spectral deconvolution and deep neural network, following the difficulties in identifying zeolites using VNIR-SWIR spectra discussed in Chapter 3.

Chapter 6 addresses specific objective 3 by applying the Kohonen Self-Organizing Maps (SOM) to identify the most common diagenetic patterns that occur in the saline-alkaline lacustrine environments on Earth where volcaniclastic beds are associated with zeolite.

Specific objective 4 is addressed in Chapter 7. This chapter applies geochemical modeling to identify zeolite phases that could have formed in closed lake basins on late Noachian Mars.

Specific objective 5 is addressed in Chapter 8, which provides a map of potential zeolite-bearing terrains on Mars calculated using the data-driven fuzzy based weights-of-evidence method.

"The mainspring of scientific thought is not an external goal toward which one must strive, but the pleasure of thinking"

-Albert Einstein, 1918-

1

Models, modeling, scientific reasoning, and terrestrial perspective on formation of zeolites on early Mars.

Contents

Abstract **13**
1.1 Introduction **13**
1.2 Scientific reasoning **15**
1.2.1 Analogical reasoning 22
1.2.2 Categorization and classification 26
1.2.3 Hypothetical modeling 28
1.2.4 Historical-based evolutionary reasoning 32
1.2.5 Experimental evaluation 36
1.2.6 Probabilistic and statistical reasoning 38
1.3 Evaluation **40**
1.3.1 Independent, converging lines of inquiry. 40
1.3.2 Inference to the best explanation 41
1.3.3 Ground Truthing 42
1.4 Closing Comments **45**
Acknowledgements **48**

1. Models, modeling, scientific reasoning, and terrestrial perspective on formation of zeolites on early Mars.

Abstract

The main objective of this chapter is to explore the use of multiple hypotheses and different scientific reasoning styles for planetary geology research. The entire project was built to address one research question; "Why are zeolites not commonly observed in paleolake basins on Mars?". Five working hypotheses were formulated and different styles of scientific reasoning with suitable examples were used to discuss the importance of the independent, converging lines of inquiry. Selected scientific reasoning methods include analogical reasoning, categorization and classification, hypothetical modeling, historical-based evolutionary reasoning, experimental evaluation, and probabilistic and statistical reasoning. This dissertation also discusses the advantages and limitations of each scientific reasoning method and /or the examples used for each method in the context of assessing alternative hypotheses. Based on the selected examples, the study validates each hypothesis and finally argues that the absence or paucity of detected zeolites in paleolake basins on Mars does not preclude their wider presence, since there is no valid reasoning to infer their absence. Zeolites might be present on Mars but covered by dust or other sediments or cannot be definitively identified using orbital data. Overall, the study demonstrates the importance of understanding the philosophy of science and scientific reasoning for studies of comparative planetary geosciences.

1.1 Introduction

Zeolites are among the most common authigenic silicate minerals found in sedimentary rocks on Earth (Hay, 1966). Most zeolite occurrences on Earth can be categorized into several classes based on the associated geologic environment or hydrologic system; 1) saline-alkaline lakes (e.g., Lake Tecopa, California; Sheppard and Gude (1968)), 2) soils and land surfaces (e.g., Lake Bogoria basin, Kenya; Renaut (1993)), 3) deep sea sediments (e.g., North-West Pacific; Lee (1988)), 4) open hydrologic systems (e.g., White river sequence, Wyoming, USA; Lander and Hay (1993)), 5) hydrothermal alteration (e.g., Yucca Mountain, Nevada, USA; Sheppard et al. (1988)), and 6) burial diagenesis (e.g., Mogami district, Yamagata, Japan; Iijima (1988)). All these occurrences show

characteristic mineral zoning patterns, as an example, saline-alkaline lake deposits, places where the largest relatively pure concentrations of natural zeolites are found, show mainly lateral variations reflecting the chemical gradients in the original lake water (Hay and Sheppard, 2001). The formation and stability of zeolites are strongly dependent on the geochemical condition (e.g., pH) of the hydrologic system (Chipera and Apps, 2001). Therefore, the presence of zeolite is a good probe to reconstruct the geological and hydrological history of zeolite-bearing environments of the Earth (Surdam and Eugster, 1976; Bish and Carey, 2001; Chipera and Apps, 2001).

Zeolites have also been postulated to be components of martian regolith (e.g., Ming and Gooding (1988); Basu et al. (1998); Berkley and Drake (1981); Bish et al. (2003); Dickinson and Rosen (2003); Tokano and Bish (2005); Cannon et al. (2015)). Ming and Gooding (1988) argue that Si-poor zeolites (e.g., analcime, phillipsite, and chabazite) would be favored to form over Si-rich zeolites (e.g., clinoptilolite) on Mars due to the mafic nature of the martian surface. They also suggested that, if zeolites do exist on the surface of Mars, they would probably have formed in a paleo weathering environment on Mars or have been removed from an erosional surface and deposited on the surface due to eolian processes. Basu et al. (1998) argue that diagenetic processes that might have operated on Mars should have produced zeolites in volcaniclastic rocks on Mars.

Ruff (2004) documents spectral evidence for zeolite in Mars dust using Mars Global Surveyor Thermal Emission Spectrometer (TES) data based on the absorption features at 6.134 μm and 12.048 μm wavelength regions of the TES spectral data. This could be an indication of widespread abundance of zeolites on the surface of Mars. However, the presence of zeolite in Mars dust is uncertain and disputed (Bandfield et al., 2003). Michalski et al. (2005) proposed the presence of silica-rich alteration products such as Al- or Fe- bearing opal, clay minerals, clay precursors or certain zeolites in dark region of Mars using spectral observation of TES data. Ehlmann et al. (2009) identified spectral signatures of analcime, a Na-zeolite, near the Antoniadi basin west of Nili Fossae using several images of Compact Reconnaissance Imaging Spectrometer for Mars (CRISM) hyperspectral data. They used the strong absorption features at 1.42 μm, 1.91 μm, and 2.52 μm with a weak absorption feature at 1.79 μm, which are characteristic for the

analcime, for this identification. Wray et al. (2009) also suggested the presence of analcime in the Nili Fossae area using CRISM data. Ehlmann et al. (2009), Wray et al. (2009), Carter et al. (2013), and Sun and Milliken (2015) discussed the difficulties of discriminating zeolites from polyhydrated sulfates using spectral data. Carter et al. (2013) conducted a global-scale investigation of the distribution, composition, age, and geomorphic settings of hydrous minerals on Mars using OMEGA (Observatoire pour la Mineralogie, l'Eau, la Glace et l'Activite) and CRISM data. They noted that the only way to discriminate zeolite from sulfates is the position of the 2.3 - 2.4 μm shoulder and the shape of the 1.9 μm absorption feature. Based on these criteria, they found that most (> 80 %) of the minerals detected within the zeolite/sulfate class are likely to be zeolites. Sun and Milliken (2015) presented a global survey of 633 crater central peaks to asses the presence of hydrous minerals using CRISM data. They classified analcime occurrences as zeolites, and spectra that only show 1.4 μm and 1.9 μm absorption features as unidentified hydrous phases. Based on that criterion, they have identified zeolites in only 4.5 % of observed central peaks. It is also important to note that zeolites have not yet been reported in Martian meteorites or data from in-situ landers or rovers.

The previous studies show that the detection of zeolite minerals with their abundance is based on the observation criteria and instrument used. Therefore, this essay will discuss the importance of critical understanding of scientific reasoning for developing hypotheses to study the presence/absence of zeolites in paleolake basins on Mars. Since the zeolite occurrences on Earth span a very wide spectrum of geologic and hydrologic conditions, this study focused only on the possibility of formation and presence of zeolites in closed basin lakes on Mars, with analog studies of zeolites occurrences in closed basin lakes on Earth.

1.2 Scientific reasoning

First, we will start our discussion with the "what if" reasoning (conceptual simulation). "What if" reasoning allows the construction of multiple alternative hypothesis, which may be useful in generating predictions or explanations when precise quantitative information is not available, or when we attempt to develop a general understanding of a system Trickett and Trafton (2007). Chamberlin (1965) stressed the need to generate multiple

working hypotheses and the risk of having a single ruling hypothesis (e.g., the probability of being wrong will increase). Trickett and Trafton (2007) proposed a three-step process for "what if" thinking, 1) visualizing a situation, 2) carring out an operation on the visualization, and 3) seeing what happened.

Zeolites may not be identifiable in certain locations on Mars using orbital data if,

H1) they are absent, or H2) they were originally present and later removed by chemical processes (e.g., dissolution and alteration), or H3) they are present, but are covered by or mixed with other materials, or H4) they are present, but the methods applied are not capable of detecting and mapping them, or H5) they are present, but we are not looking in the correct places.

In this discussion, we will try to address whether zeolite is absent (H1) and if so, *why* it is absent. H2 and H3 will be addressed as we consider *How* and *When* it could have been removed. H4 will relate with *what* types of instruments and methods are used and what problems they face in detecting zeolites, and H5 will address *where* we need to look for zeolites on Mars. The hypotheses formulated here can be addressed by the five most common "W-H" questions. Each hypothesis will be addressed separately or combined with others and applied to different scientific methods discussed in following sections.

Giere (1999) argued that scientific reasoning is to a large extent model-based reasoning. Constructing models is part of the process of figuring out how the world works. Scientist are always trying to create a best fit model/s to simulate or understand the problems they seek to solve. Maps are the most common representational model used in the field of Geosciences. A map is a spatial classification that projects information about physical features at or near the planetary surface for a defined purpose. Maps involve the definition of classes or units by grouping or division, logical synthesis or analysis, induction or deduction (Varnes, 1974). A common problem in making maps is the isolation and identification of the attributes that are necessary and sufficient to define the units to be mapped. The attributes that need to be mapped may be absolute (i.e categorical data), or exist in degrees (i.e. continuous data) that are measurable qualitatively or quantitatively, or may be immeasurable (Varnes, 1974). The continuous data can be classified into groups (units) based on their physical, chemical, temporal, spatial, or relational attributes. Figure

1. Models, modeling, scientific reasoning, and terrestrial perspective on formation of zeolites on early Mars.

1.1 shows mineral zoning maps of four paleolake basins; 1) Lake Tecopa, Inyo County, California (Map (a), after Sheppard and Gude (1968)), 2) Big Sandy Formation, Mohave County, Arizona (Map (b), after Sheppard and Gude (1973)), 3) Karlovassi basin, Samos, Greece (Map (c), after Stamatakis (1989a)), and 4) Gila Conglomerate near Buckhorn, New Mexico (after Gude and Sheppard (1988)). These four maps only represent a few minerals and phases of interest including zeolites, K-feldspar, and glass, and do not imply that these minerals cover 100 % of their respective areas. These minerals might be highly abundant in respective map classes, and it is also possible that in a certain location, the represented mineral in the map class might be minimal or even absent. It is also possible that we can find two minerals shown in two classes at one location near the class boundaries. Simply, a map represents the spatial similarities between the map and the region mapped with regards to the attribute being mapped. Therefore, similarity is context dependent. Similarity can be specified based on what is said to be similar to what, in what ways, and to what degree. As an example, our field experience at Lake Tecopa shows that the most abundant minerals in these classes are other minerals such as clay minerals, quartz, and calcite, while the map classes are represented by fresh-glass, zeolites and K-feldspar. The attributes of maps are defined with a particular purpose in mind to convey certain information and to omit certain information. Therefore a geological/ mineralogical map is an interpretation, whereas a spectral image acquired by an orbital or airborne sensor records the physical and chemical properties of the land surface as it is. Therefore it is also important to find the relation between the mapping results derived from remote sensing data and the geologic map (representation model), since both record information from two different entities.

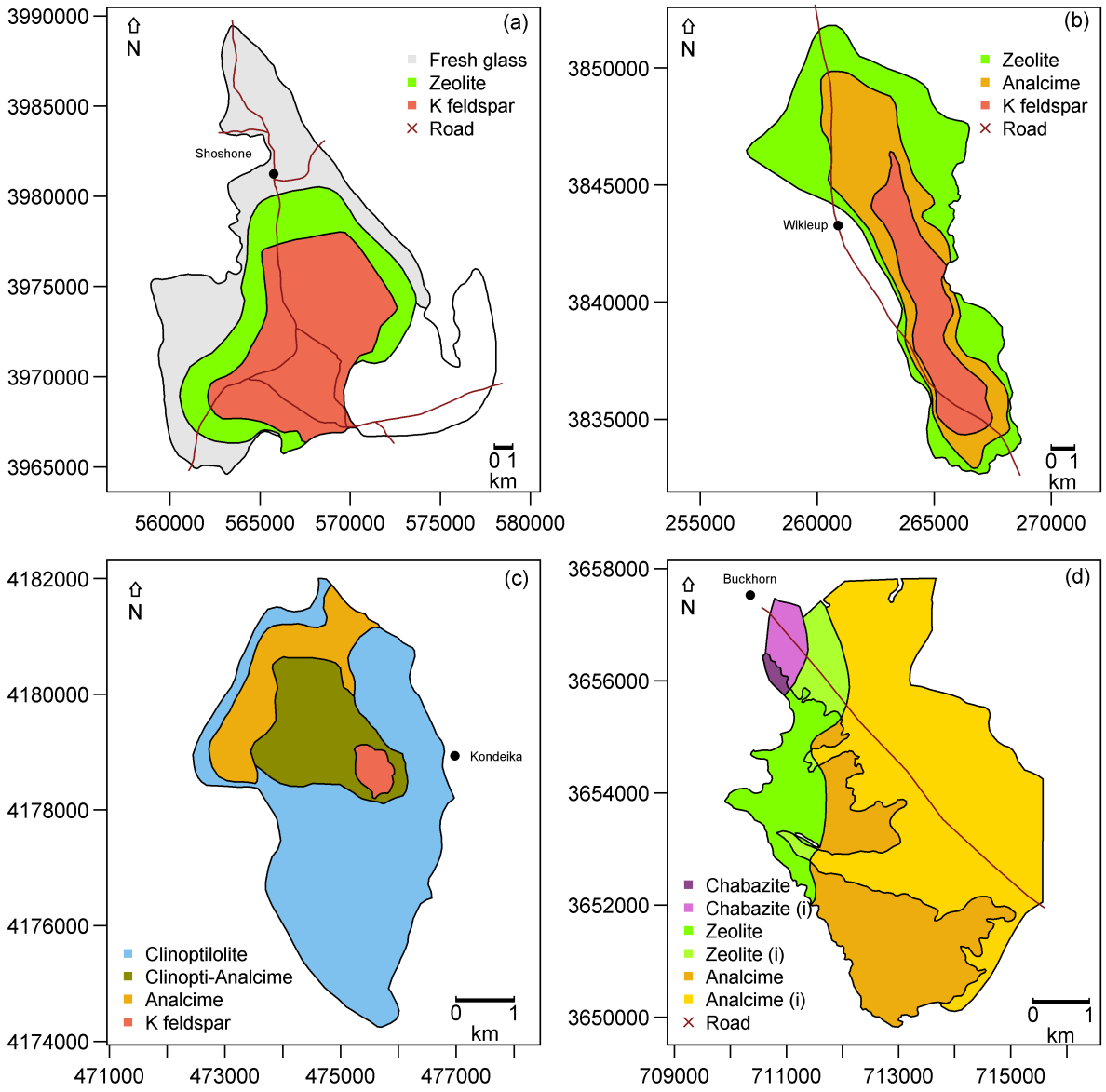

Figure 1.1: Diagenetic zones of (a) Lake Tecopa, Inyo County, California (after Sheppard and Gude, 1968) (b) Big Sandy Formation, Mohave County, Arizona (after Sheppard and Gude, 1973), (c) Karlovassi basin, Samos, Greece (after Stamatakis, 1989), and (d) Gila Conglomerate near Buckhorn, New Mexico. Dark tones of each litholgy type in the map indicate the approximate extent of diagenetic zones, whereas the light tones (letter (i) after the lithology type in the legend) indicate the inferred extent of zones prior to erosion (after Gude and Sheppard, 1988)

The maps in Figure 1.1 represent the formation, evolution, and fate of zeolites in closed basin lacustrine environments. Maps are not linguistic entities. Saline-alkaline lakes form in closed hydrographic basins where evaporation exceeds precipitation. Glassy volcanic ash deposited in these lakes provides the settings and ideal parent materials for accumulation of rather pure zeolite deposits. Volcanic material falling into these lakes

slowly react with solutions entering the basin. The concentric zonation of water results from shrinkage of the water-filled portion of the basin mainly due to evaporation, causing an increase in salinity and pH from the periphery to the center of the basin resulting in zoned mineral deposits, 1) an outer zone of glass and/or smectite, where the pore fluid was relatively dilute, 2) a non-analcime zeolite zone with mostly phillipsite, clinoptilolite, erionite, etc., reflecting elevated pH and salinity, 3) a zone of analcime reflecting higher salinity, and 4) the zone of highest salinity, where tuffs may be altered to K-feldspar, generally located in the lowest part of the basin (Hay and Sheppard, 2001; Langella et al., 2001). More siliceous zeolites such as clinoptilolite and mordenite are the most common alteration products of silicic glasses in freshwater environments, whereas less silicious phillipsite and erionite are more common in saline alkaline lakes (Mariner and Surdam, 1970). The formation of different zeolites depends on the different proportions of $Al : Si$, and $Na : Ca$ and/or $K : Ca$ ratios in the precursor volcanic ash and/or in the pore fluids. Analcime crystallized from volcanic ash with relatively high $Al : Si$ ratios and solutions with high $Na : Ca$ ratio, while clinoptilolite forms from ash with lower $Al : Si$ ratios and solutions lower $Na : K + Ca$ ratios. This linguistic-theoretical model can also be represented by following flow diagram (Fig 1.2),

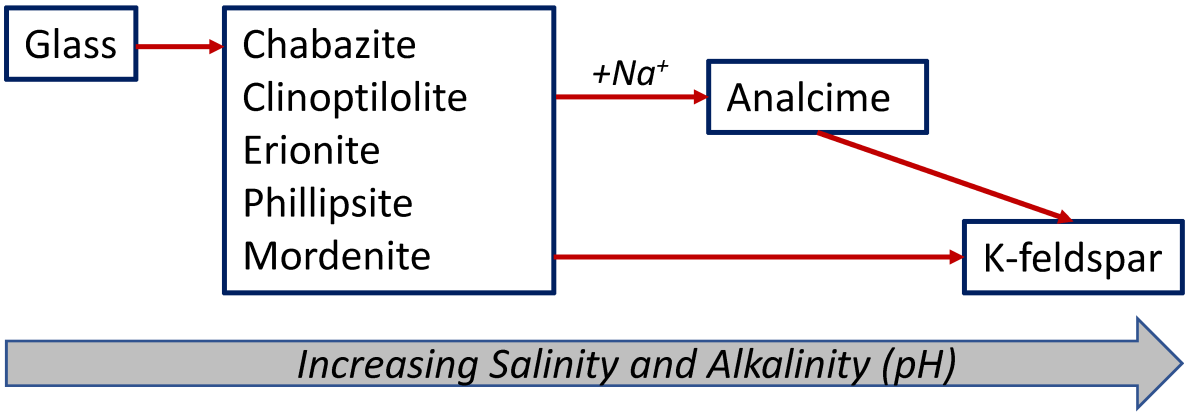

Figure 1.2: Reaction sequence of lateral mineral changes typical of saline-alkaline lake deposits

However, lakes (like Lake Magadi, Kenya, Surdam and Eugster (1976)) located in a narrow trough or other more restricted locations may not develop these zones as readily as those situated on wide playas.

1. Models, modeling, scientific reasoning, and terrestrial perspective on formation of zeolites on early Mars.

Geological observations and interpretations of Late Noachian to Early Hesperian (LN-EH) Mars show that it is characterized by impact craters with degraded crater rims, shallow floors, and lack of visible ejecta deposits and central peaks (Craddock and Howard, 2002). Valley networks, channels, alluvial fans, deltas, and open- and closed-basin lakes, also found in LN-EH exposures, are interpreted to be formed mainly due to rainfall and overland flow (Craddock and Howard, 2002; Palumbo et al., 2020; Ramirez and Craddock, 2018). Based on these geological and geomorphological studies, the early Martian climate has been characterized as "warm and wet" (e.g., Ramirez and Craddock (2018)). However, climate modeling has struggled to successfully recreate the long-lived "warm and wet" early Mars, given that faint young sun paradox, and instead suggests a long-lived "cold and icy" Mars (e.g., Kasting (1991); Wordsworth et al. (2013)). It is difficult to explain the occurrence of rainfall-related erosional features in a "cold and icy" climate scenario, and therefore some researchers have suggested that these fluvial and lacustrine activities may have occurred during periods of punctuated heating induced by impact events, volcanism, orbital variation, summer melting, and transient greenhouse gas-rich atmospheres (Wordsworth et al. (2017); Palumbo et al. (2020), and references therein). We assume a warm and semi-arid climate model for LN-EH Mars, since this model is consistent with both geological and climate evidence, as argued by Ramirez and Craddock (2018).

Data from orbital and in situ remote sensing methods and Martian meteorites indicate that the Martian crust is dominated by basalt and related ultramafic rocks (McSween, 2015; McSween et al., 2009). Therefore, sediments sourced from mafic-rich precursors are enriched in olivine, pyroxene, and calcic plagioclase in contrast to the quartzofeldspathic sediments commonly found on Earth. However, high-silica deposits have also been identified on Mars (e.g., Bandfield (2006); Bandfield and Rogers (2008); Bedford et al. (2019); Broz et al. (2020); Czarnecki et al. (2020); Ehlmann et al. (2009); Morris et al. (2016); McSween (2015)). Wilson and Head (2007) modeled the eruption and dispersal of tephra under current Mars atmospheric conditions and showed that an explosive eruption could produce thick, widespread ash deposits like those thought to have formed due

to mantling deposits in several regions of Mars. Broz et al. (2020) reviewed the broad spectrum of observations supporting the evidence of explosive volcanism on Mars.

Whether zeolites will form and if they do, which zeolite will form depends on 1) the composition of the starting materials, 2) the composition of the solutions to which they are exposed, 3) hydrologic conditions, and 4) kinetic factors (e.g., Langella et al. (2001); Hay (1966)). If LN-EH Mars had a warm and semi-arid climate capable of producing rain,and if the composition of starting solutions and kinetic factors were suitable for producing zeolites, then zeolites likely formed in closed basin on Mars, at least where pyroclastic materials were present. Throughout this work, we hypothesize that LN-EH Mars was warm and semi-arid and that the processes and interactions involved in the formation and fate of authigenic minerals on Mars are similar to the processes and interactions observed in ancient and modern environments on Earth. Even when thinking only about the studies of terrestrial geology, with out these assumptions (assumptions of uniformity), no geological explanation is possible (Kravitz, 2013). In geology, as in any other scientific discipline, we must assume the uniformity of the laws of nature (and geology) (Kravitz, 2013; Frodeman, 1995).

The methodology of geological studies is divided into three classes: logical inference, hermeneutics (theory of interpretation), and historical methods (Engelhardt and Zimmermann, 1988; Frodeman, 1995). Logical inference includes inductive, deductive, and abductive reasoning. Hermeneutics consists of recursive reasoning, forestructures of understanding, and the historical nature of human understanding. Alistair Crombie's three-volume, 20-year study of *Styles of Thinking in the European Tradition* (Crombie, 1994) listed six styles of scientific reasoning (Scientific thinking) drawn from the neglected field of scholarship undertaken in the cognitive history of sciences (Osborne, 2018). These are, 1) the method of postulation represented by Greek mathematical sciences, 2) the experimental argument, both to control postulation and to explore by observation and measurements, 3) hypothetical modeling, 4) categorization and classification, 5) probabilistic and statistical analysis, and 6) historical-based evolutionary reasoning. The rest of this essay discuss how these reasoning methods can be used to evaluate the formulated hypotheses using selected examples.

1.2.1 Analogical reasoning

Geologists and philosophers (e.g., Frodeman (1995); Schumm (1991); Baker (2014); Gilbert (1896); Gilbert (1886)) have noted that geoscientists frequently reason by analogy. Analogy in science assumes that if two things are similar in some respects, then they must be similar in others (Schumm, 1991). Sibley (2009) argue that the cognitive processes in thinking and reasoning with analogies are the same as those involved in thinking and reasoning with scientific models, because both: 1) are based on recognizing relational characteristics of the analog and target, 2) map similarities and differences between them, and 3) support inferences about the target based on the relational similarities between them. Baker (2014) discussed the importance of analogical reasoning for the formulation of genetic hypotheses in planetary geology. Grove Karl Gilbert, an early pioneer of planetary geology, states:

> "The unexplained phenomenon on which the student fixes his attention resembles in some of its features another phenomenon of which the explanation is known. Analogic reasoning suggests that the desired explantion is similar in character to the known, and this suggestion constitutes the production of a hypothesis" Gilbert (1896), p. 2

On December 27, 1885, during the presidential address of the American Society of Naturalists at Boston, he explained the geological hypothesis generation via analogical reasoning, as follows:

> "Given a phenomenon, A, whose antecedent we seek. First we ransack the memory for some different phenomenon, B, which has one or more features in common with A, and whose antecedent we know. Then we pass by analogy from the antecedent of B, to the hypothetical antecedent of A, solving the analogic proportion-as B is to A, so is the antecedent of B to the antecedent of A." Gilbert (1886), p. 287

Adopting Gilbert's logic, we first identify the zonation of mineral deposits from glass, zeolites, and K-feldspar towards the center of a hypothetical paleolake basin on Mars (A), for which we are seeking to identify the responsible mechanism/s for formation of this pattern. Then we will seek places where a similar mineral zonation pattern is observed on Earth (B), which has key attributes in common with A, and for which we truly know the

formation mechanism of these patterns. If the mineral zonation patterns of A and B are similar, we can infer the possible or likely causes for A, since we know the cause/s of B.

A complete scientific explanation consists of the logical connection between the statements describing the controlling state of affairs (Case, A), the statement of law (Rule, L), and the statements describing the resulting state of affairs (Result, B) (Engelhardt and Zimmermann, 1988; Baker, 2014). Scientific explanation is called a deductive-nomological model (DN-model), because it draws conclusion B from A, using a law L, in the logical form of deduction. The term 'nomological' refers to 'pertaining to laws of nature'. The application of induction, abduction, and deduction inferences according to deductive-nomological model, each using or arriving the same rule (L), is discussed below.

Induction

> "The controlling states of affairs (A) and the resulting states of affaires (B) are known. A law (L) is sought which will unite (A) and (B) in accordance with the deductive-nomological model. This is the process of induction." Engelhardt and Zimmerann (1988), p. 80

Example

1. Result (B):

We find an example of a closed basin having concentric mineralogic zoning from volcanic glass to non-analcime zeolites, to analcime, to K-feldspar, towards the center of a basin on Earth.

2. Case (A):

We know that this kind of mineral zoning pattern can be found in tuff beds in saline-alkaline lake deposits on the Earth.

3. Rule (L):

We generalize that volcanic material falling into saline-alkaline lakes on Earth will produce a concentric mineralogic zoning from glass to non-analcime zeolites, to analcime, to K-feldspar, towards the center of the basin.

1. Models, modeling, scientific reasoning, and terrestrial perspective on formation of zeolites on early Mars.

Deduction

> "The controlling states of affairs (A) and laws (L) are known. Resulting states of affairs (B) are sought, which will be explained by (A) and (L) according to the deductive-nomological model. This is the process of deduction." Engelhardt and Zimmerann (1988), p. 80

Example

1. Rule (L):

Volcanic material falling into saline-alkaline lakes on Earth will produce a concentric mineralogic zoning from glass to non-analcime zeolites, to analcime, to K-feldspar due to a series of progressive reactions as a function of increasing salinity.

2. Case (A):

We find examples of closed basin paleolakes filled with volcanic materials (tuff) on Mars.

3. Result (B):

We conclude that we will find concentric mineral zoning with fresh glass, zeolites, and K-feldspar on Mars.

Abduction

> "Resulting states of affairs (B) and laws (L) are known. The controlling states of affairs (A) are sought which when united with (L) and (B) will satisfy the model of deductive-nomological explanation. This is the process of abduction." Engelhardt and Zimmerann (1988), p. 80

Example

1. Result (B):

We find an example of a closed basin having concentric mineralogic zoning from volcanic glass to non-analcime zeolites, to analcime, to K-feldspar, towards the center of a basin on Mars.

2. Rule (L):

We know that volcanic material falling into a saline-alkaline lake on Earth will produce concentric mineral zoning from fresh volcanic glass to non-analcime zeolites, to analcime, to K-feldspar, towards the center of the basin.

3. Case (A):

We conclude that this is an example of a saline-alkaline paleolake on Mars.

The following table presents the three modes of inference we used.

Table 1.1: Three mode of inference

	Induction	Abduction	Deduction
Premises	A	B	L
	B	L	A
Conclusions	L	A	B

Abbreviations are:

A = controlling state of affairs (Case),

B = resulting state of affairs (Result),

L = law (Rule).

One can argue that analogical reasoning cannot be directly applied from the Earth to Mars, even though we hypothesize that the geology and environmental conditions of LN-EH Mars were similar to the Earth, because of other inherent differences (e.g., gravity, distance from sun, orbital inclination, orbital period, etc.). However, we cannot provide such accuracy with analogical reasoning, since there are no identical things in nature. There is a chicken-and-egg paradox which can be expressed as follows: an argument from analogy depends on induction from known laws connecting the properties of each analog and therefore all such arguments are inductive. On the other hand, inductive arguments depend on recognizing similarities between instances. However, in practice no instances will be exactly the same as others. Therefore, all such arguments are also analogical (Hesse, 1966). The importance of analog reasoning in geology is stressed by

Baker (2014); Frodeman (1995); Sibley (2009); Gilbert (1886), who indicate the need for a more in-depth consideration of methodology in terms of both strengths and weaknesses. Frodeman (1995) claims that geological reasoning consists of a combination of logical procedures in addition to the classic deductive-nomological method of the experimental sciences. He also argues that geological reasoning provides another model of scientific reasoning based on the historical sciences and the techniques of hermeneutics.

1.2.2 Categorization and classification

Categorization and classification are the ordering of variety by comparison, differentiation, and taxonomy (Kind and Osborne, 2017). In geology, ordering into categories is often derived from a theory of causal ordering independent of a criterion of experimental reproducibility (Ault, 1998).

> "In a profession more observational and comparative than experimental, the ordering of diverse objects into sensible categories becomes a sine qua non of cuasal interpretation. A taxonomy is not a mindless allocation of objective entities into self-evident pigeon-holes, but a theory of causal ordering. Gould (1986), p. 63

Previous studies show that identifying the most prominent mineral zoning pattern in zeolite-bearing paleolake deposits is often difficult because they often do not show prominent first order similarities. Chapter 6 identifies the most common authigenic minerals and their paragenetic relations in saline-alkaline paleolake systems on Earth using a combination of two machine learning methods, Self-Organizing Maps (SOM) and Decision Tree (DT) analysis. The published bulk mineral abundance data from 1648 zeolitic tuff bed samples from thirteen paleolake deposits from the USA, Mexico, Greece, and Tanzania were used. The SOM and DT algorithms captured the zeolitic diagenetic patterns defining clear class boundaries between fresh glass, non-analcime zeolites, analcime, and K-feldspar, even without prescribing any specific interpretation (Fig 1.3). This shows the capability of statistical learning methods for categorizing and classifying of mineral composition data to reveal the most prominent geochemical behaviors in these paleolake deposits.

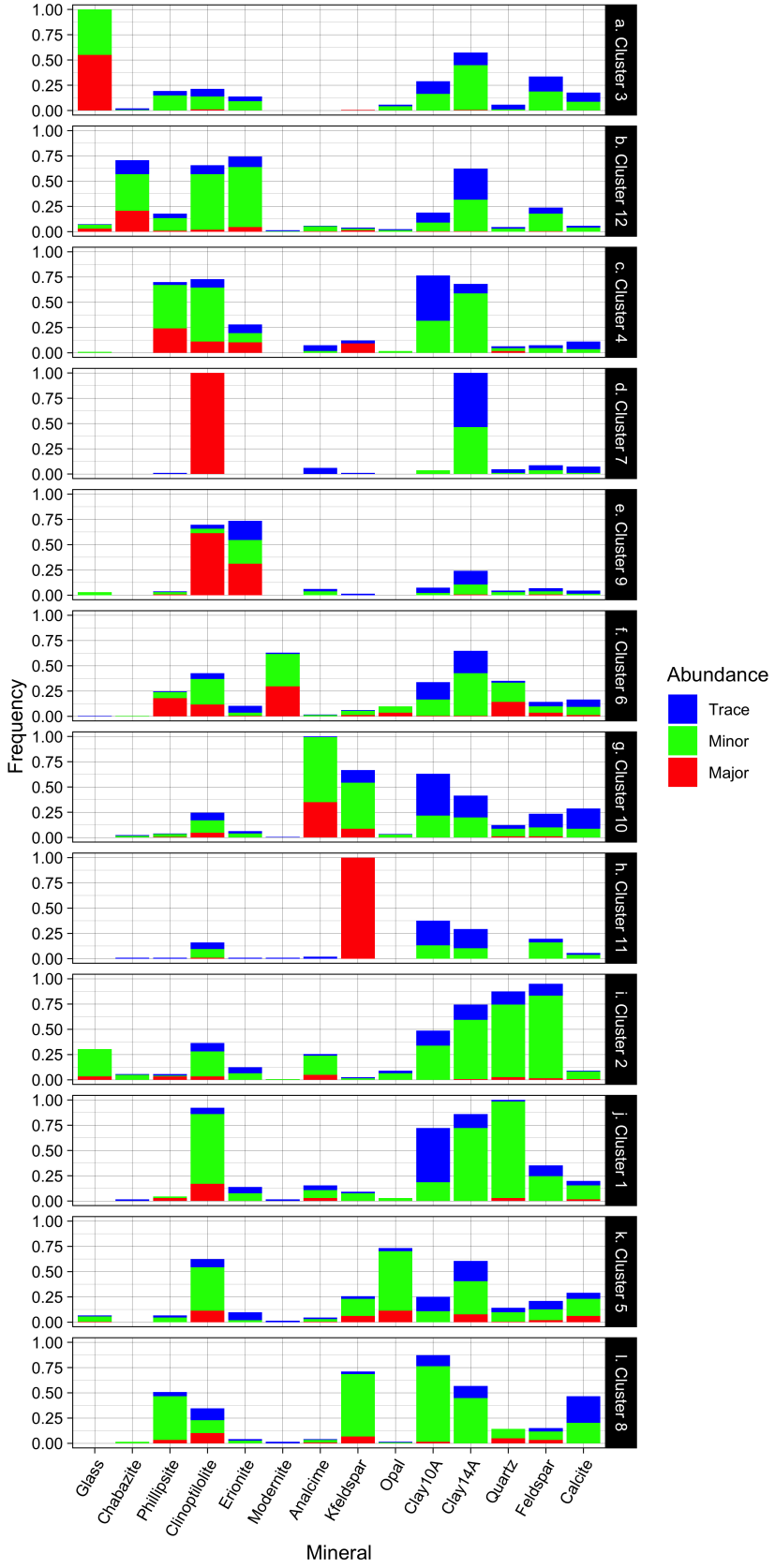

Figure 1.3: Relative mineral abundance in each cluster derived from Self-Organizing Maps (SOM)

1.2.3 Hypothetical modeling

Hypothetical modeling is the construction of analogical or hypothetical models to represent the world. Hypothetical modeling has a lineage to early modern perspective painting and then to engineering, and finally to science as a method of analysis and synthesis by construction of analogies (Crombie, 1994).

> "The imitation of nature by art then became an art of inquisition; rational design for construction became rational modeling for inquisitorial trial." Cromie (1994), Vol. I, p. 84

What is a model?

> "A model is a theoretical construct that begins with a concept (the conceptual model) and might be portrayed mathematically or diagrammatically or physically or by analogy. It is always a simplification, and idealization, a picture of how we think about some aspect of physical phenomena. In one sense, it is always incorrect because it is never complete or exact. In another sense, it may be correct because it might be our best understanding or approaximation of something at a perticular time in history" Nordstrom (2012), p. 1903

Philosophers and scientists have proposed many classifications to categorize models, some examples are, 1) material and mathematical models (Rosenblueth and Wiener, 1945), 2) verbal moldes, physical models, graphical models, mathematical models, and computer models (Futuyma, 2006), 3) concrete, mathematical, and computational models (Weisberg, 2015),and 4) scale models, analog models, theoretical models (Giere, 1991). How we characterize and classify the models informs our approach to understanding their representational capacities and the epistemic work that they do (Downes, 2021). Geochemical modeling was taken as an example here. A geochemical model is a chemical model that can calculate the chemical properties and processes such as the thermodynamics and kinetics of a geologic system.

Geochemical models have been developed to investigate the interactions between acidic solutions with Martian basalts in the Noachian epoch (e.g., McAdam et al. (2008); Viennet et al. (2017); Zolotov and Mironenko (2007); Zolotov and Mironenko (2016)). Zolotov and Mironenko (2016) used the composition of Martian Adirondack-type olivine basalt as a staring material. They selected pure water, solutions equilibrated with current Mars

atmospheric CO_2 (5.3 $mbar$) and O_2 (7.6 μbar), and an acidic $H_2SO_4 - HCl$ solution (0.05 molal H_2SO_4 and 9.6 millimolal HCl) as staring solutions. They calculated the chemical equilibria using the GEOCHEQ code. They observed the precipitation of Mg-Fe phyllosilicates, Ca sulfates, zeolites, and minor carbonates with neutral to alkaline solutions. Saponite, zeolites, gypsum form at low W/R ratio and pH 7-12, and 1 bar CO_2 atmospheric pressure. Higher W/R ratios with a pH < 7 resulted in kaolinite, montmorillonite, siderite, and amorphous silica. Although the Martian crust has an average composition equivalent to subalkaline Fe-rich basalt, locally more evolved silicic composition also observed (McLennan et al., 2019). For this study, a LN-EH atmosphere of Mars with 1.3 bars of CO_2 (90 - 99 %) and a small amount of H_2 (1 - 10 %) is assumed. The atmospheric O_2 pressure of early Mars is assumed to be same as today (Daswani et al., 2016; Mahaffy et al., 2013; Trainer et al., 2019). The modeling is restricted to 25^oC, due to limited thermodynamic data for most of the minerals. The simulation was run under 1.013 bar pressure, even though the HCO_3^- concentration was measured under 1.3 bar P_{CO_2}, since there is insufficient thermodynamic data for 1.3 bar. A simplified version of the chemical composition of the high-silica Buckskin sample of the Murray Formation, Mars was chosen as a starting material since zeolites found in saline-alkaline paleolake deposits on Earth are mostly associated with altered silicic tuffs, and thus the model can be easily validated using Earth analogs. The calculation was done using the EQ3/6 code (Wolery, 2013). A detailed description of the model can be found in Chapter 7.

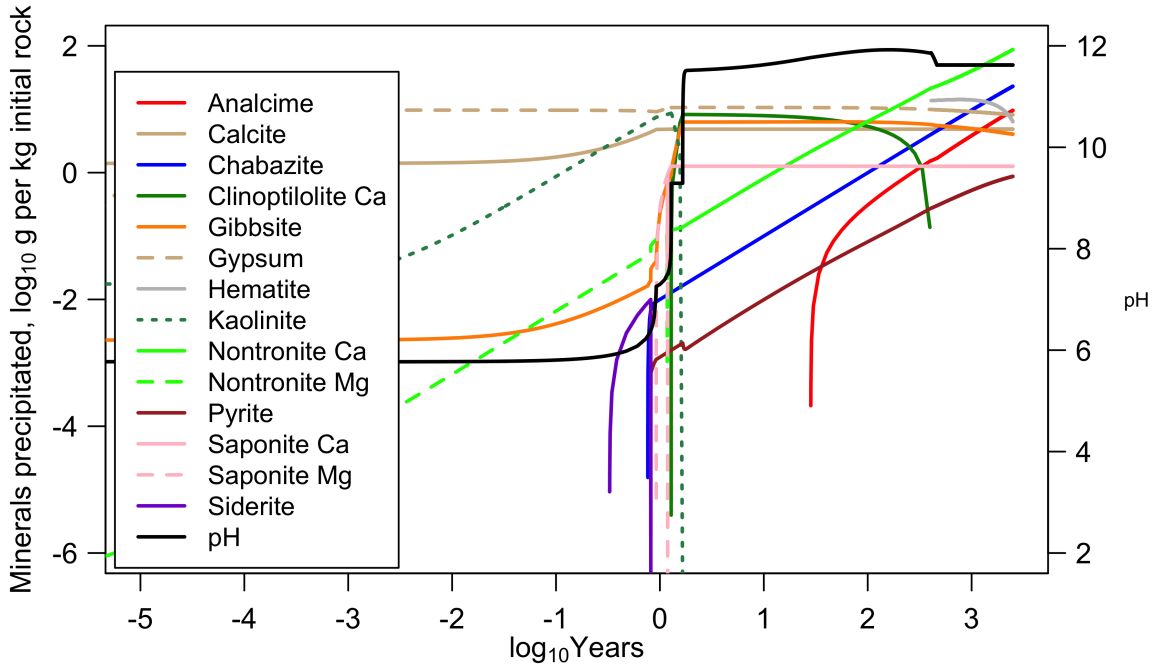

Figure 1.4: Temporal changes in pH with precipitation of secondary minerals during weathering of buckskin sample exposed to rainwater in closed systems at 25 ^oC and 1 bar at 0.25 W/R ratio. Solution is equilibrated with 1.3 bar CO_2 and 0.0147 mbar of O_2

According to the model (Fig 1.4), in early stages of the reaction path (less than a year after the reaction starts; $\sim$ zero in log_{10} years scale), kaolinite precipitation increases, and with the increase of pH it redissolves. Mg-nontronite continuously precipitates with time and after around a year Ca-nontronite appears, most likely due to cation exchange. Similarly, Mg-saponite starts to form at the end of this early stage and later transforms to Ca-saponite. Gypsum, gibbsite and calcite form and remain until the end of the reaction process. In the later stage of the reaction path (after around one year), chabazite, clinoptilolite, pyrite, analcime, and hematite form. After $\sim$ 100 years, clinoptilolite starts to redissolve when analcime starts to precipitate.

This shows that even though the starting material (basic vs. felsic), starting solution (acidic vs. near neutral), environmental conditions (e.g., low atmospheric CO_2 vs. high atmospheric CO_2), and the governing equations of the adopted code (free energy minimization approach vs. equilibrium constant approach) are different, overall the first-order mineral precipitation pattern for both models is similar and both resulted in Fe/Mg-phylosilicate and zeolites as secondary minerals, which suggests that zeolites are likely

to from on Mars. Calculations in this study show that while clinoptilolite formed it will be replaced by the analcime, and that chabazite and analcime would be the only stable zeolite after around 1000 year of reaction progress.

Nordstrom (2012) reviewed the science and philosophy of models, model validation, and prediction in the context of geochemistry, and proposed guidelines to improve our perceptions and ensure proper utilization of models. Chipera and Apps (2001) discussed the advances and limitations of thermodynamic modeling for identifying the stability relationships among various zeolites as a function of temperature, pressure, and chemical potentials of the participating components. The mineralogy and crystal chemistry of naturally occurring zeolites are complex. Zeolites commonly show multiple, coupled solid solutions, ion exchange, variable degrees of hydration, hydration/dehydration reactions, order-disorder, second order displacive phase transitions, and anomalous expansivities and compressibilities (Chipera and Apps, 2001). It is important to consider these properties under early Martian conditions, if we are going to calculate precisely the thermodynamic and kinetic factors controlling zeolite stability. However these properties are unknown or little known even for most zeolite phases on the Earth. Small deviations in the thermodynamic values used in an equilibrium calculation can lead to significant shifts in calculated equilibria (Chipera and Apps, 2001). Selecting the most appropriate "representative" chemical formulas and thermodynamic data of minerals for the models is thus essential. While existing thermodynamic data are not accurate enough for strict quantitative analysis of the stability of zeolites, the general trends and relative stability relationships can be readily calculated, and these trends can be used to predict the stability of zeolites in hypothesized closed basin lakes on Mars.

In the earth sciences, models are often tested by seeing how well they match historical data. If a model fails to correctly explain the natural world, there is often no simple way to identify the problem. The problem might arise from the hypothesis being tested, but can come from a faulty piece of equipment, mistaken model assumptions, or even from a bug in computer code (Oreskes, 2000). This is more complicated when modeling extraterrestrial environments (e.g., Mars in this study) because of the lack of historical data, or detailed knowledge from which to derive model assumptions and due to the

lack of reliable ways to validate the results. In modeling, we tune the model until it fits with the given set of observational data (a process called calibration). We reject the model as false if it does not match the observational data. However, a model that matches with the available data could still be false.

1.2.4 Historical-based evolutionary reasoning

Geologists explore the history of the earth using historical methodologies, which include, 1) uniformitarianism (the assumption that present day geologic processes operate in a similar manner to those of the past: "the present is key to the past"), 2) place substituting for time in stage-theorizing, 3) relic interpretation (the examination of oddities or complexly superimposed events), 4) constructing proper taxonomies, and 5) evaluating independent lines of inquiry for convergence (Park and Park, 2013; Ault, 1998).

Stephen Jay Gould, in his "Wonderful Life" book states that,

> "..... the"scientific method" involves a set of concepts and procedures tailored to the image of a man in a white coat twirling dials in a laboratory–experiment, quantification, repetition, prediction, and restriction of complexity to a few variables that can be controlled and manipulated. These procedures are powerfull, but they do not encompass all of nature's variety. How should scientists operate when they must try to explain the results of history, those inordinately complex events that can occur but once in detailed glory? Many large domains of nature–cosmology, geology, and evolution among them–must be studied with the tools of history. The appropreate methods focus on narrative, not experiment as usually concieved." Gould (1989), p. 277

Nature's laws are defined by their invariance in space and time. The science of history use a different mode of explanation, in the form of narrative. Narrative logic is a type of understanding where details are made sense of in terms of the overall structure of a story (Frodeman, 1995). An historical explanation does not rest on direct deductions from laws of nature. Any major changes in any step of the sequence can alter the final result. Therefore the final result is dependent, or contingent, upon everything that came before, the unerasable and determining signature of history (Gould, 1989). One of the major goals of the study of geology is to chronicle the particular events that occurred at a given location, in addition to understanding the general laws that form and shape the

planetary body. However, most of the geological processes including the study described here (formation of zeolites in saline-alkaline lakes) cannot be directly observed on the human time scale. One way to solve this problem is by arranging the stages of processes by selecting different places as substitutes for time (place substitute for time).

As an example, a database of 150 non-marine zeolite deposits from multiple continents was compiled using available published studies that documented the time period of their formation. Figure 1.5 shows the frequency of occurrence of analcime, chabazite, clinoptilolite, erionite and phillipsite as a function of geologic age, derived from that database. The database can be found in Appendix A (Table A.1). It shows that these minerals are mostly documented in late Pleistocene to early Miocene deposits, with the highest number of documented occurrences in deposits of Miocene age. The frequency of occurrence of these minerals decreases with age after Miocene. Analcime is seen over the entire age range (recent to early carboniferous), while other minerals disappear with time. This also shows that the number of zeolite types decreases with age. Hay (1966) argues that, while the number of zeolite species decreases with age, the diversity of non-zeolite silicate minerals may increase as a function of age in deposits containing Na-carbonate minerals. Analcime is the most stable zeolite mineral in these environments.

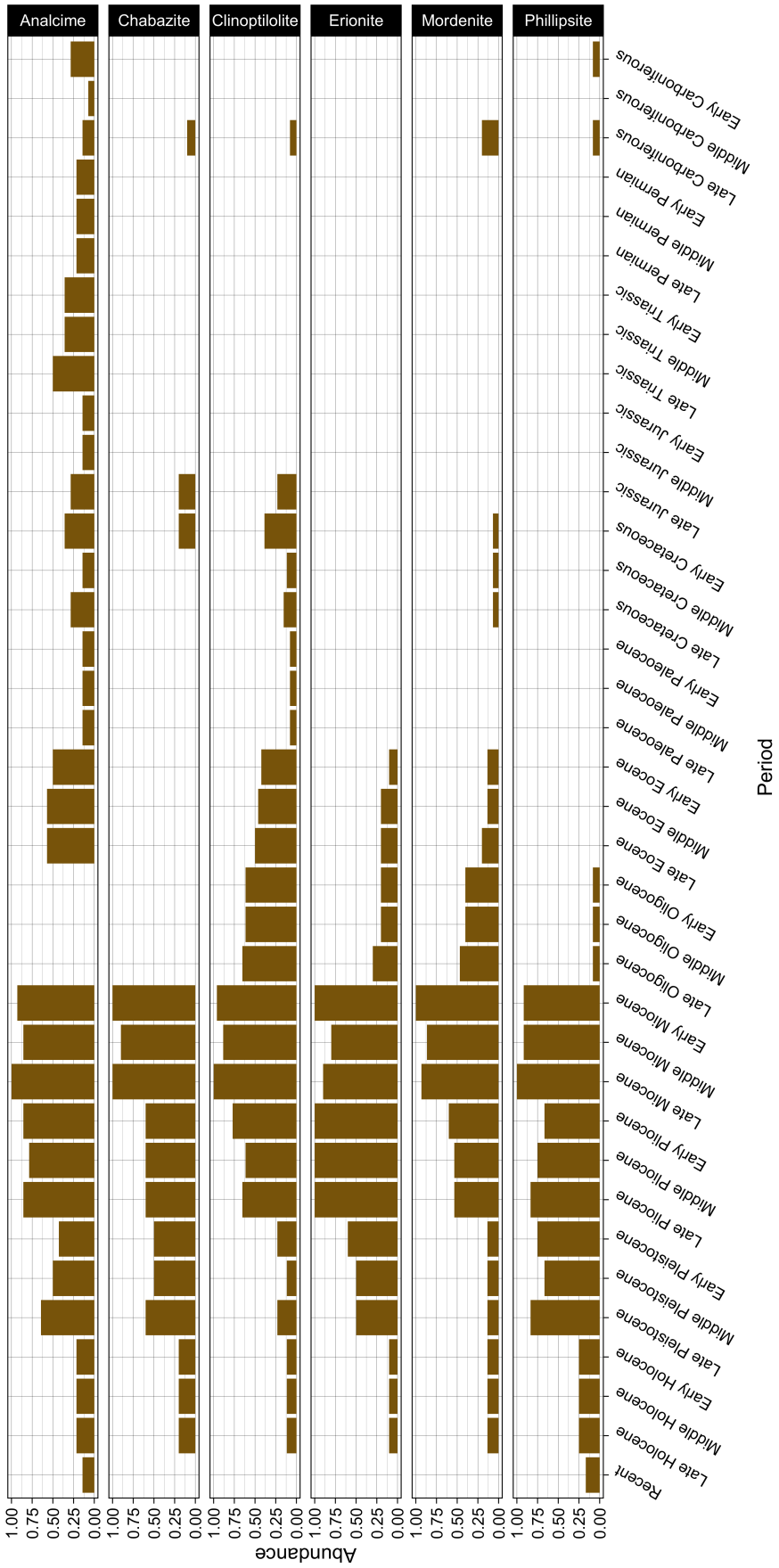

Figure 1.5: The frequency of occurrence of analcime, chabazite, clinoptilolite, erionite, mordenite, and phillipsite during geologic time.

1. Models, modeling, scientific reasoning, and terrestrial perspective on formation of zeolites on early Mars.

Several studies attempted to calculate the formation time of zeolites in a natural setting using absolute or relative age dating techniques. Taylor and Surdam (1981) determined that the upper ash bed of Teels Marsh, Nevada, which is characterized by highly saline-alkaline waters, was completely altered to phillipsite in 1000 years. An eolian nephelinite tuff of Bed V at Olduvai Gorge, Tanzania, was completely zeolitized within the past 8,000 to 20,000 years (Hay, 1963). Rhyolitic tuff from various levels of mud at Searles lake, California altered to phillipsite over 10,000 to 20,000 years (Smith, 1979). These studies are important to assess whether the proposed time durations of water activity on Mars are enough to form zeolites in closed basins and to validate the geochemical modeling results.

As discussed in the section on geochemical modeling, the presence of a specific mineral or mineral assemblage in a closed-basin lake can be attributed to thermodynamic equilibrium reactions due to changing water chemistry (Hay, 1966) and to kinetically controlled dissolution and precipitation reactions (Dibble and Tiller, 1981). Therefore, changes in zeolite assemblage over time in paleolake deposits can be used to track changes in paleoenvironment. Trauth et al. (2001) analyzed a 60 m thick sedimentary sequence in the Ol Njorowa Gorge at the margin of the Naivasha basin, Kenya, using vertical variations of authigenic mineral phases to define the lake level fluctuations and alkalinity changes during last 175,000 - 60,000 year period. Fresh water episodes were characterized by diatomite, unaltered volcanic glass, and the absence of authigenic silicates, while transitions to alkaline episodes ($\sim$ 9 pH) were characterized by silicic glass, montmorillonite, and occasional chabazite and phillipsite. Higher alkalinity resulted in the formation of clinoptilolite while the most alkaline pore waters formed analcime. McHenry et al. (2020) studied the mineral assemblages of three paleolacustrine cores from Olduvai Gorge, Tanzania. They reconstructed lake chemistry over time, based on the type of zeolites and their abundance in the lakebed sediments. These studies show the importance of evolutionary reasoning (e.g., relic interpretation) for reconstruction of geological and hydrological history.

It is important to note that there are many first-order similarities and differences observed for the sedimentary records of Earth and Mars. Some first-order similarities include facies relationships, groundwater diagenesis, and recycling (McLennan et al., 2019). On Earth, forces associated with plate tectonics are the main cause of uplift,

subsidence, basin formation, and large scale architecture of sedimentary deposits. With the absence of plate tectonics on Mars, large-scale thermal subsidence appears to be mostly absent. However, volcanic loading and impact cratering create basins and subsidence that are required for sediment formation, transport, accumulation and preservation (Taylor and McLennan, 2009). Therefore, even though examples from Earth cannot be directly compared to Mars, underlying physical and chemical processes identified by careful examination of the evolution of these basins can be compared.

1.2.5 Experimental evaluation

Empirical evidence is used to test whether scientific ideas can be falsified and to substantiate or critique arguments. While most geological processes and concepts cannot be tested under laboratory conditions due to their complex nature and the requirements of great spans of time, simplified version of some processes can be tested to understand the governing physical and/or chemical laws.

As discussed earlier, analcime is the only zeolite group mineral identified on Mars based on its distinctive broad absorption band centered at $\sim 2.5\ \mu m$ and a weaker absorption at $\sim 1.8\ \mu m$. Identifying other zeolite species is complicated by the lack of diagnostic absorption bands in the visible-shortwave infrared (VIS-SWIR) region, their spectral similarity with polyhydrated Mg-sulfates, and whether the target mineral is mixed with other minerals. Experimental methods can be used to empirically evaluate how the factors discussed above affect the identification of zeolites using reflectance spectra.

Clinoptilolite, montmorillonite, and the polyhydrated Mg-sulfate mineral epsomite were used for this study. These minerals were individually ground and dry-sieved to a size fraction $< 150\ \mu m$. The purity of these mineral end members was assessed using X-ray diffraction (XRD). Binary mineral mixtures (clinoptilolite-montmorillonite and clinoptilolite-epsomite) were prepared at 10 % increments, and reflectance spectra of mineral mixtures were acquired using an ASD Field spec reflectance spectrometer at the University of Colorado. The entire study was done under ambient laboratory conditions. The spectra of binary mineral mixtures used in this study are shown in Figure 1.6. The letter C in the legend indicates clinoptilolite, while M indicates montmorillonite and E

indicates epsomite. Two integers after each letter indicate the respective weight proportion of each mineral in 10 scale. This shows that absorption bands around 1.4 μm, 1.9 μm, and 2.2 μm vary linearly with mineral abundance. Though the shape and position of the 1.4 μm and 1.9 μm absorption bands in the clinoptilolite - montmorillonite mineral mixtures (Fig 1.6a) do not change with the changes of mineral weight proportion, the 2.2 μm absorption band associated with montmorillonite disappears only in the pure clinoptilolite spectra. Thus clinoptilolite might not be identifiable in reflectance spectra even in a mineral mixture that contains $\sim$ 90 % clinoptilolite if it is associated with montmorillonite. The spectra of clinoptilolite - epsomite mineral mixtures shown in Figure 1.6b demonstrate the lack of diagnostic absorption feature/s to differentiate these two minerals, except for minute changes in absorption band shape and the position of 1.4 μm and 1.9 μm bands, which are difficult to differentiate in orbital spectral data.

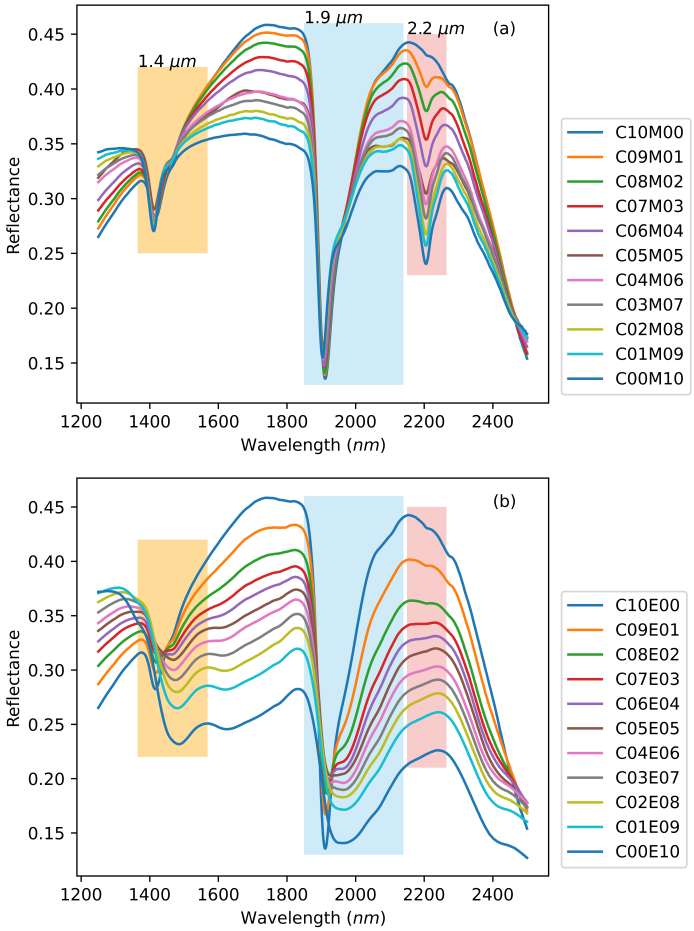

Figure 1.6: Spectra of clinoptilolite-montmorillonite (a), and clinoptilolite-epsomite (b) binary mineral mixtures. The letter C in the legend indicates clinoptilolite, M indicates the montmorillonite, and E indicates epsomite. Two integers after each letter indicate the mineral weight proportions in 10 scale

1.2.6 Probabilistic and statistical reasoning

Probabilistic and statistical reasoning uses statistical analysis of regularities in populations to identify patterns and to calculate their probability (Kind and Osborne, 2017). One of the widely used statistical and probabilistic reasoning methods in geosciences is predictive modeling for mineral exploration. Predictive modeling can be defined as "making descriptions, representations, or predictions about an indirectly observable and complex real-world system via (quantitative) analysis of relevant data" (Carranza, 2009). Induction and deduction are the two approaches used in predictive modeling. Predictive modeling can be divided into two categories: mechanistic and empirical. Mechanistic modeling uses

the fundamental or theoretical knowledge of predictor variables and their interactions to predict or understand the target variable of interest, while empirical modeling uses the empirical model equations derived through data to predict or understand the system of interest. Therefore, mechanistic modeling generally follows a deductive approach while empirical modeling follows an inductive approach (Carranza, 2009). Empirical modeling can also be divided into two categories: quantitative and qualitative, based on the sufficiency of data for the target variable. Quantitative empirical modeling is appropriate when enough data for the target variable is available. The qualitative empirical modeling can be used when insufficient target variable is available for statistically significant results. In mapping of prospective areas, quantitative empirical modeling is also known as data-driven modeling, while qualitative empirical modeling is known as knowledge-driven modeling (Carranza, 2009).

The philosophy of some common early mineral exploration methods will also be discussed in this essay. Some examples, as discussed by Bailly (1972), are 1) the "Elephant Country" approach, which assumes that deposits of a certain type tend to occur in areas where similar deposits are already known, 2) the "Grass Root Exploration", which usually refers to exploration starting with the reconnaissance of areas not known to be mineralized, regardless of field procedures, 3) the "Grasshopper" approach, which characterizes the explorer who limits his work to visual examination of mineral showings, and 4) the philosophy of "Drillitis", in which the explorer believes the only way to explore is systematic drilling in large favorable areas. Earlier exploration methods thus also used a wide range of inference methods from inductive, deductive, and abductive, and even with no inference at all. The geocomputational modeling follows the specific steps starting with defining a conceptual model of exploration targets followed by, identifying suitable spatial datasets (factor maps), enhancement or extraction of evidential features from each dataset, selection of appropriate methods for mapping evidential features, creating predictor maps, integrating predictor maps using suitable methods, and creating a predictive model or map (Carranza, 2011).

Chapter 8 uses the data-driven fuzzy based weights-of-evidence method, a geocomputational predictive model, to delineate the best areas to look for zeolites on Mars. The

weights-of-evidence method uses the Bayesian theory of conditional probability to quantify spatial associations between the evidence layers and known mineral occurrences (Bonham-Carter, 1994). The model used the global mineralogical, geological, geomorphological, physical, and elemental abundance maps derived from the orbital data as evidence maps with the locations of the detected hydrous minerals using orbital data for the known mineral occurrences. The results map the other locations where hydrous minerals can be found. The map of the pyroclastic ash distribution, modeled by Kerber et al. (2013), used to delineate the areas where zeolites can be found with higher probabilities based on the conceptual model created in this study.

1.3 Evaluation

1.3.1 Independent, converging lines of inquiry.

The founder of the *Journal of Geology*, T. C. Chamberlin, developed the method of multiple working hypotheses (Chamberlin, 1965) with particular emphasis on geological examples. He stated that:

> "In the use of the multiple method, the re-action of one hypothesis upon another tends to amplify the recognized scope of each, and their mutual conflicts whet the discriminative edge of each. The analytic process, the development and demonstration of criteria, and the sharpening of discrimination, recieve powerfull impulse from the co-ordinate working of several hypotheses."
>
> "Each hypothesis suggests its own criteria, its own means of proof, its own methods of developing the truth; and if a group of hypotheses encompass the subject on all sides, the total outcome of means and of methods is full and rich". Chamberlin (1965), p. 756

Owing to the complexity of the system studied and the impossibility of conducting controlled experiment, as discussed before, arguments over the descriptive categories often leads to debate. Therefore, generating independent multiple lines of inquiry to evaluate the degree to which they converge to a common answer increases the confidence of the final solution (Park and Park, 2013; Ault, 1998). This study introduces five working hypotheses with different lines of inquiry (reasoning) to answer why zeolites are not identified (except orbital identification of analcime) in the basins of Mars.

1.3.2 Inference to the best explanation

The above examples illustrate the difficulties involved in finding the best explanation to a given problem. What makes one explanation the best? Which criteria or methodological values of a hypothesis must be satisfied to make it superior to others? Faye (2002) listed some of the criteria we can examine to assess the best hypothesis, 1) precision (a hypothesis must be precise in the sense that the implications that may be derived from it must agree with the experimental and observation results), 2) observational range (a hypothesis must have the same implications as alternative hypotheses and must be able to explain all the relevant facts), 3) fertility (a hypothesis must be conductive to future research and theoretical development), 4) previous success (a hypothesis must be able to explain previous observations), 5) inter-theoretical support (a hypothesis must agree with background knowledge and other hypotheses), 6) uniformity (a hypothesis may not be able to explain all relevant facts, however those deviating facts must at least be systematic), 7) consistency (a hypothesis must not be self contradictory), 8) coherence with metaphysical assumptions (a hypothesis must agree with generally accepted ontological principles), 9) simplicity (a hypothesis must contain as few concepts and laws as possible), 10) qualitative formulizability, and 11) its ability to make new predictions. Due to the space limitations of this essay, only simplicity will be discussed as an example. Simple systems are easier to test. Ockham's Razor principle ("All things being equal, the simplest solution tends to be the best one") can be useful in sorting through multiple hypotheses (Tibbetts, 2013). However, sometimes it is difficult to apply Ockham's razor, because as we expand our knowledge on the possible processes and phenomena we wish to explain, the theories that describe those behaviors will also become more complicated (Tibbetts, 2013), as we saw in the geochemical model example. One way to simplify the model is based on the continuum theory, in which a material with heterogeneous parts is treated as if it were a single homogeneous entity (Oreskes, 2000). However, making this simplification, fine scale details will be lost.

1. Models, modeling, scientific reasoning, and terrestrial perspective on formation of zeolites on early Mars.

1.3.3 Ground Truthing

Ground truthing is the best way to assess the results. Field geologists go to the field to examine samples and rock outcrops in detail and collect samples for detailed laboratory studies. In geological mapping, they synthesize laboratory studies with field observations. In contrast, planetary geologists first study the planetary body globally through orbital remote sensing at low resolution, followed by high-resolution imagery for detailed studies for a selected location/s. Sample and outcrop studies can only come much later and only for one or a few discrete locations, if an in situ rover/lander mission is implemented. Orbital observations provide a first order prediction of mineralogy, mineral transition and geomorphology in a broad context, while in situ rover observations provide higher resolution details from a ground perspective. It is also important to understand that, even though orbital and in situ observations are often consistent, sometimes there might be gaps between these two types of observations. The Vera Rubin ridge (VRR) at Gale cater, Mars provide an excellent example of how more detailed and higher resolution observations lead to changes of hypothesis (Sheppard et al., 2021b). The identification of an isolated hematite-bearing layer at VRR from orbital data initially led to the hypothesis that it preserved a redox interface (Vaniman et al., 2014), however data from the CheMin instrument on the Curiosity rover identified widespread hematite at Mount Sharp below VRR, which was not detected in the orbital data. Based on that, Fraeman et al. (2020a) argued that it might formed by interactions with late stage diagenetic fluids, instead of a localized interval of iron oxidation as originally hypothesized. As another example, in Gale cater Mg-sulfates are only observed in orbital data, while Ca-sulfates are only observed from in situ data (Sheppard et al., 2021b). Although both orbital and in situ observations provide great details for understanding the sedimentary history of pleolake basins, the future sample return mission will provide an invaluable opportunity to extract more details (such as absolute dating) through the high-precision analytical instruments on Earth, which may change the current hypotheses about how these deposits formed.

Chapter 3 and 4 explore other possible reasons for limited orbital detection of zeolites in paleolake environments on Mars, using a saline-alkaline zeolite bearing paleolake deposit, Lake Tecopa, California as an analog site (Fig 1.7a & 1.7b). This study demonstrates

the difficulties in identifying and mapping zeolites based solely on orbital spectral data. Field studies showed that most zeolite-rich beds are buried by other beds (Fig 1.7c) or that the areas of exposed beds are mostly smaller than the ground resolution cell of the satellite (Fig 1.7d), leading to limited detection. Laboratory analyses further showed that zeolites are usually present in mixtures with other more spectrally-dominant minerals, further complicating their detection.

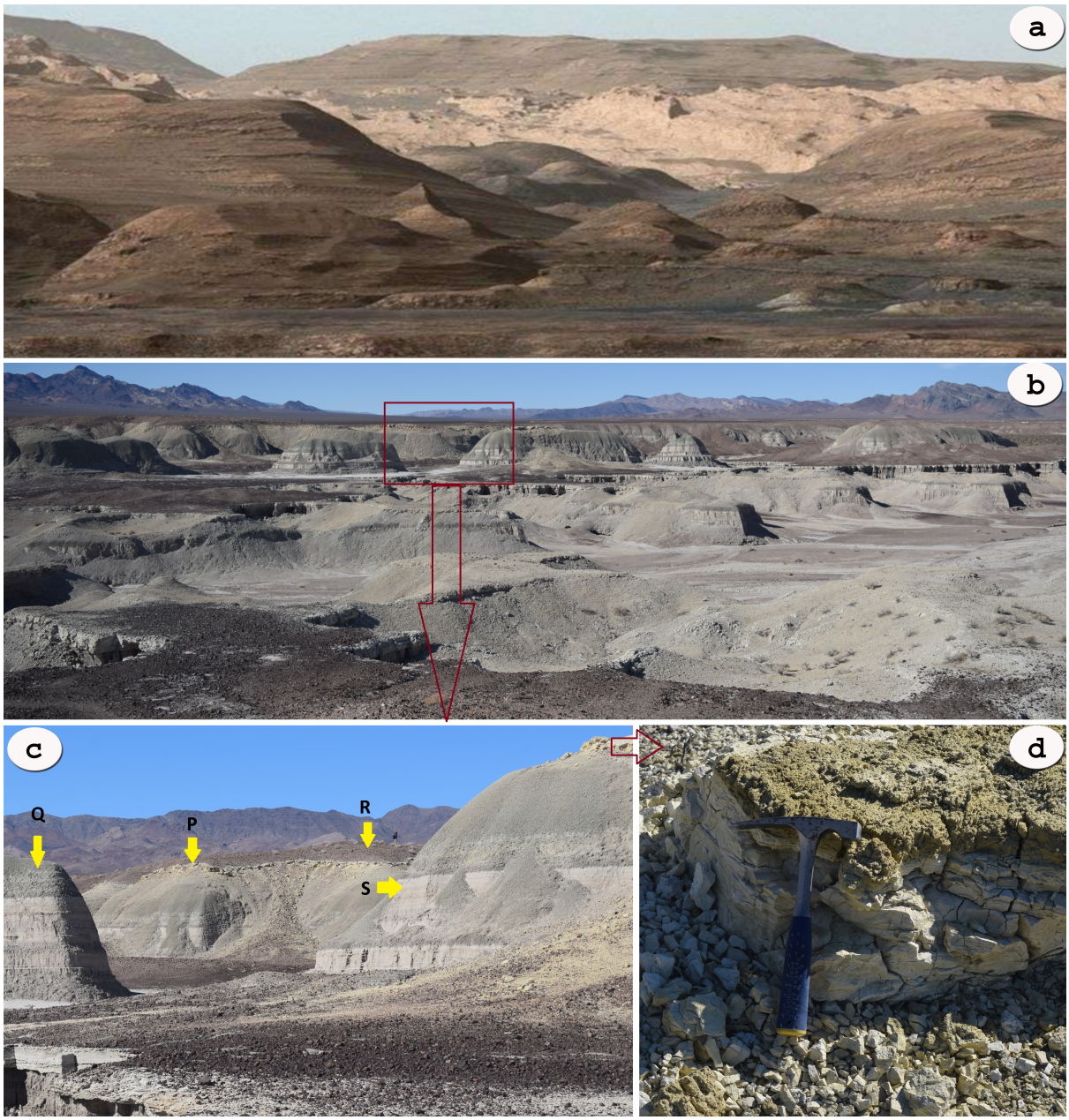

Figure 1.7: (a) A false-color composite image captured by the Curiosity Rover shows the inerior deposits of Gale Crater and Mount Sharp (Image: NASA/JPL), (b) Field photoghaph of Lake Tecopa area showing general stratigraphy, (c) zoomed area showing the erosional features with zeolite (tuff) bed (P), green mudstone bed (Q), gravel pavement (S), and sandstone/siltstone bed (S), and (d) exposed zeolitized tuff bed showing chemical and physical weathering.

It is worthy to end this discussion with a final quotation from Chamberlin (Chamberlin, 1897),

> "The studies of the geologist are peculiarly complex. It is rare that his problem is a simple unitary phenomenon explicable by a single simple cause. Even when it happens to be so in a given instance, or at a given stage of work, the subject is

> quite sure, if pursued broadly, to grade into some complication or undergo some transition. He must therefore ever be on the alert for mutations and for the insidious entrance of new factors. If therefore there are any advantages in any field in being armed with a full panoply of working hypotheses and in habitually employing them, it is doubtless the field of the geologist." Chamberlin (1897), p. 848

1.4 Closing Comments

This chapter was written to discuss the importance of critical understanding of scientific reasoning for developing hypotheses to study the presence/absence of zeolites in paleolake basins on Mars. I present five alternative hypotheses to asses why zeolites may not be identifiable in certain locations on Mars using orbital data, through "what-if" reasoning. This chapter discusses the application of philosophical and scientific methods, such as the use of inference methods, the application of different styles of scientific reasoning, the advancement of independent converging lines of inquiry, inference to the best explanation, etc., instead of deriving the final results (best explanation, hypothesis) using these methods. The study used at least one example for each styles of reasoning, and those examples will be used to draw the closing comments of this discussion. The overall concept of the study discussed is show in Figure 1.8.

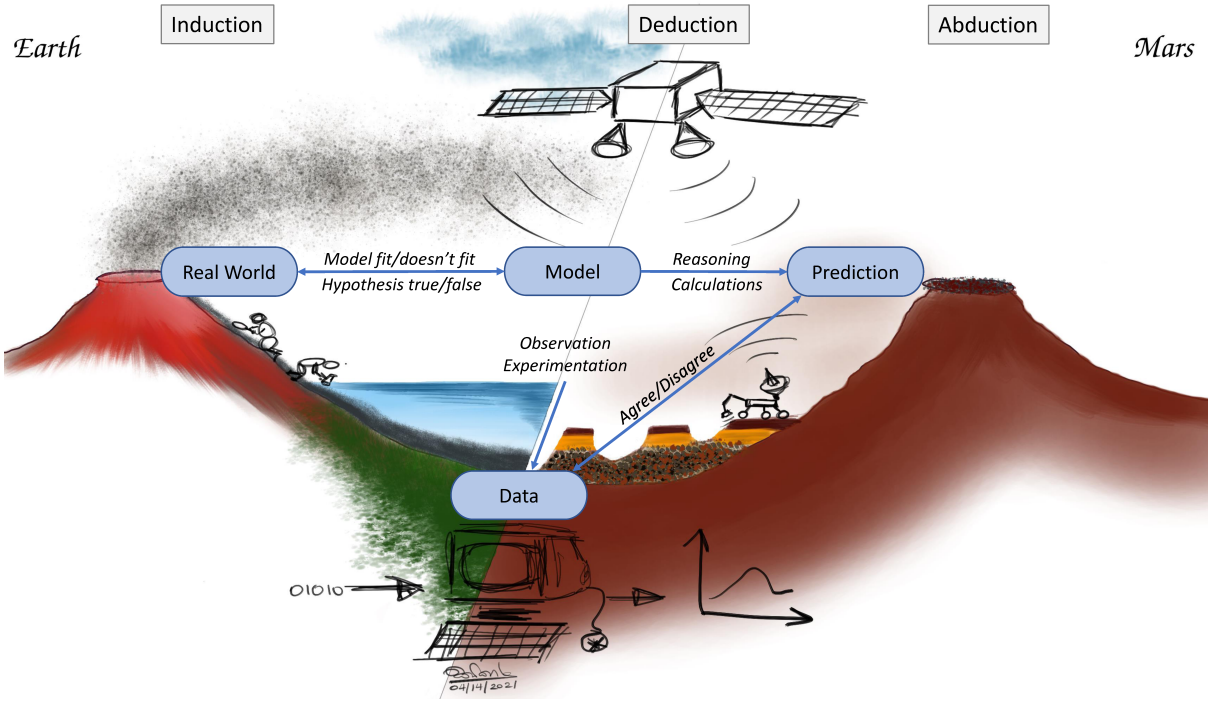

Figure 1.8: The relationship beween the real world, conceptual model, and the methods of inferences.

Previous studies document the detection of analcime, a Na-zeolite from orbital data, though the presence of zeolites on Mars is not yet confirmed by in situ observation or from Martian meteorites. Those identified analcime detections are hypothesized to form by hydrothermal alteration (e.g., Ehlmann et al. (2009)). However, geochemical modeling shows that these zeolites can also form at law temperature (0 - 25^oC), both from basaltic and high silica starting materials. Therefore, based on the orbital detection of "analcime" and this thermodynamic point of view, there is no reason to accept hypothesis 1 (H1), that "zeolites are absent". In the geochemical modeling we found that some zeolites (e.g., clinoptilolite) are dissolved over time and other zeolites (e.g., analcime) precipitate. Previous modeling studies yielded the same trend as discussed before. The frequency of occurrence of zeolites as a function of geological age on Earth (Fig 1.5) shows that analcime is more stable than the other zeolites (also suggested by geochemical modeling based on the Ostwald rule, e.g., Dibble and Tiller (1981)). While analcime might be the most common zeolite detected on Mars, this does not mean that other zeolites are absent, as they might be present but less abundant. The experimental study on the

spectra of binary mineral mixtures shows that our ability to recognize zeolites from reflectance spectra is suppressed when zeolites are mixed with clay minerals. Therefore, if zeolites are mixed with clay minerals, as is commonly observed in Lake Tecopa and other saline-alkaline terrestrial sites described in the categorization and classification section, they will be difficult to identify using orbital data. The Lake Tecopa analog study area showed that most zeolite-rich tuff beds are covered by other types of beds in this depositional environment and later mixed with other beds due to erosion and/or formed as an accessory phase in claystone. Burial of thinner beds due to later deposition (e.g., layering) or dust and erosion are also common processes in sedimentary environments on Mars. We also saw from the experimental data from binary mineral mixtures that it is difficult to spectrally distinguish non-analcime zeolites from Mg-sulfate minerals as several previous studies already established (e. g. Sheppard et al. (2021a)).

This study also demonstrates that VNIR-SWIR spectroscopy is not the best method to identify non-analcime zeolite minerals due to the lack of characteristic absorption features. The example of mineral potential mapping using the "Data-driven fuzzy weights-of-evidence" method, discussed under the probabilistic and statistical reasoning methods section, provides a potential method to look for the most suitable places for detailed analysis. This study also discusses the importance of in situ observation for developing the most accurate hypothesis. As an example, based on in situ observations, we can reject most of the hypotheses discussed here (e.g., if the zeolite beds are covered by other materials,they cannot observed by orbital VNIR-SWIR sensors, but could be detected by in situ rover missions). Therefore, the probabilistic and statistical reasoning methods will also help to identify the best sites for in situ missions to look for zeolites. Based on the given examples, we can reject hypothesis 1 and hypothesis 2 can be modified (even though some zeolite facies dissolve or alter with time, some zeolite facies will remain or form). Hypothesis 5 will need to be studied in detail and hypotheses 2, 3, and 4 can be fully answered only by using in situ observations. Karl R. Popper (Popper, 1959) argues that it is impossible to prove the correctness of a hypothesis, however one can disprove it by one failure. We can infer that the absence (or paucity of detected) zeolites in paleolake basins on Mars does not preclude their (wider) presence, since there is no

valid hypothesis to infer their absence. Kuhn (1962) make a valid point that it is possible to view scientific problems in different ways based on a person's prevailing social and scientific climates, training, background, and personnel views. We tend to see what we are trained to see. In this study we look at the formation of zeolites in paleolake basins with the view of near-surface temperature processes, while those who work/train in hydrothermal environments can see the same deposit in the view of hydrothermal alteration (high temperature) process, especially when there is insufficient background information available as in this case (the presence of some associated key minerals, such as prehnite, has been used to infer the hydrothermal origin for some of the detected analcime). Even multiple working hypothesis can lead to erroneous conclusions (e.g., Gilbert (1896)), when there is not enough information available.

Acknowledgements

I thank all the philosophers for their great ideas, researchers and geologists for documenting and sharing their field and lab observations, and programmers (FORTRAN, python, and R) for sharing their codes and algorithm freely.

"...boundaries between scientific disciplines are largely a matter of conventional division of labor between scientists."

-Benoit Mandelbrot, The Fractal Geometry of Nature, 1982, p.27.-

2

The study of the paleolake basin at Lake Tecopa using orbital and Mars rover-like instrument data.

Contents

Abstract **49**
2.1 Introduction **50**
2.2 Study area **55**
2.3 Data and overall methodology **59**
2.4 Results and discussion **63**
2.4.1 Imaging observations from orbital data (spatial resolution ~ 1m/pixel to ~ 100m/pixel) 64
2.4.2 Imaging observations from in situ data (spatial resolution ~ 1 cm to ~ 1 m) 71
2.4.3 Imaging observations from in situ data (spatial resolution ~ 1 nm to ~ 1 cm) 79
2.4.4 non-imaging observations 81
2.5 Lessons Learned **90**
Acknowledgements **93**

Abstract

The synergies of orbital and in situ field methods for understanding the geological features and processes in lacustrine deposits were evaluated via the study of a Mars

analog paleolacustrine basin at Lake Tecopa, using instruments approximating those of current and future rover missions on Mars. The dataset used in this study includes high-resolution multispectral aerial orthorectified NAIP (National Agricultural Inventory Program) Plus images, National Elevation Data (NED) Digital Elevation Model (DEM) data, Shuttle Radar Topography Mission (SRTM) DEM data, ground-based photographs, high-resolution micro images, Scanning Electron Microscopy (SEM) images with Energy Dispersive X-ray Spectrometry (EDS) spectra of selected field samples, X-ray Diffraction (XRD), X-ray Fluorescence (XRF), and Visible to near Infrared - Shortwave Infrared (VNIR-SWIR) spectroscopy data of selected samples. Different mapping techniques (e.g., 2-dimensional and 3-dimensional) were used to extract information of landforms and processes of the basin while ground-based images were used to identify the sedimentary structures, textures, and fabrics. Compositional information was extracted from the XRD, XRF, and VNIR-SWIR data. This study demonstrates the importance of ground-based observations including the field-based mapping, sampling, and analysis by human geologists, and the synergy of using ground-based and orbital remote sensing data for the identification of paleolake basins on the Earth and its implications for Mars.

2.1 Introduction

Lakes are time capsules (Cabrol and Grin, 2010). They capture the record of geological, hydrological, and climatological variations over a wide range of temporal and spatial scales. The existence of lakes on ancient Mars is widely accepted (e.g., Cabrol and Grin (2010); Alemanno et al. (2021); Goudge et al. (2012); Goudge et al. (2016); Quay et al. (2020); Goudge et al. (2015); Matsubara et al. (2011); Wharton et al. (1995); Cabrol and Grin (2002); Fassett and Head (2008); Cabrol and Grin (1999); Hargitai et al. (2018); Zhao et al. (2020)). Paleolakes on Mars are fed by valley networks (e.g., Fassett and Head (2008); Quay et al. (2020)) and groundwater sources (e.g., Wray et al. (2011); Hargitai et al. (2018)). Paleolakes have been divided into two types based on their hydrology; 1) open-basin (balanced fill) lakes having both inlet and outlet valleys, abd 2) closed-basin (endorheic) lakes having only the inlet valley/s (Cabrol and Grin, 1999; Fassett and Head, 2008). Open lakes on Earth are fresher, while closed lakes become

progressively more saline due to evaporation. Paleolakes on Mars have been identified based on the presence of topographic lows, inlet and/or outlet channels, benches, and shoreline features such as delta-shaped terminal deposits (Hargitai et al., 2018; Zhao et al., 2020; Fassett and Head, 2008; Goudge et al., 2016). Zhao et al. (2020) proposed a framework to identify paleolakes on Mars with three different confidence levels; 1) Confident: Basin connected with a network of inlet valleys or single inlet valley with sedimentary landforms or aqueous minerals, 2) Probable: Basins connected with inlet valley network without sedimentary landforms or aqueous minerals, and 3) Possible: Basin with single inlet valley without sedimentary landforms or aqueous minerals. Previous studies (e.g., Alemanno et al. (2021); Zhao et al. (2020); Goudge et al. (2012); Goudge et al. (2015)) reported aqueous alteration minerals in open and closed-basin lakes on Mars, with limited evaporite mineral detections. They argued that this is due to the short-lived period of lacustrine activity in the observed open and closed paleolakes on Mars. However, these limited detections can also be due to the presence of spectrally obscuring resurfacing units and due to the limited spectral and spatial coverage.

The ability to identify minerals and classify rocks on Mars depends on the capabilities of the available instruments (e.g., spectral and spatial resolution, detection limits, etc.) and environmental conditions (e.g., viewing angle, dust, etc.). The currently serving Curiosity and Perseverance rovers on Mars are equipped with an excellent suite of imaging, geochemical, and mineralogical instruments for geological investigations (Table 2.1).

Table 2.1: Science instruments onboard the Curiosity (Grotzinger et al., 2012) and Perseverance rovers (Farley et al., 2020).

Rover	Science Instruments	Name	Use
Curiosity	Cameras	Mastcam (Mast Camera)	Panoramic color images of the surface and the terrain ahead of the rover
		MAHLI (Mars Hand Lens Imager)	Microscopic imaging of minerals, textures, and structures in rocks and soil

2. The study of the paleolake basin at Lake Tecopa using orbital and Mars rover-like instrument data.

Rover	Science Instruments	Name	Use
	Spectrometers	APXS (Alpha Particle X-ray Spectrometer)	Analyze chemical elements in rock and soil (regolith) up close
		ChemCam (Chemistry and Camera)	Analyze chemical composition of rocks and soil from distance
		CheMin (Chemical and Mineralogy)	Analyze mineralogy and chemical composition of sampled rocks and soil
Perseverance	Cameras	Mastcam-Z	High-definition video, panoramic color, and 3D images of the surface
		Supercam	Identify the chemical composition of rocks and soils
		PIXL (Planetary Instrument for X-ray Lithochemistry)	Measure the chemical makeup of rocks at a very fine scale
		SHERLOC (Scanning Habitable Environments with Raman & Luminescence for Organics & Chemicals)	Fine-scale detection of minerals
		WATSON (Wide Angle Topographic Sensor for Operations and eNgineering)	Fine-scale textures and structures in rocks, soil, and dust

Ten locations on Mars have so far been visited by rovers or landers: Chryse Planitia (Viking 1), Utopia Planitia (Viking 2), Ares Vallis (Mars Pathfinder), Meridiani Planum (Opportunity), Gusev Crater (Spirit), Vastitas Borealis (Phoenix), Gale crater (Curiosity), Elysium Planitia (Insight), Jezero crater (Perseverance), and Utopia Planitia (Zhurong). Three of them landed in candidate paleolake basins (Gusev crater, Gale crater, and Jezero crater) and Gale and Jezero crater show substantial evidence for hydrological evolution of the lakes (e.g., Hurowitz et al. (2017); Mangold et al. (2021); Williams et al. (2013)). Rounded pebbles in a conglomerate identified in Mastcam images from the Curiosity rover at Gale crater indicated the substantial fluvial abrasion (Williams et al., 2013), and desiccation cracks identified by Mastcam and Mars Hand Lens Imager (MAHLI)

provide evidence for a lake drying on Mars (Stein et al., 2018). Mastcam-Z images from the Perseverance rover at Jezero crater also reveal an ancient delta-lake system with flood deposits (Mangold et al., 2021). The conglomerates in Jezero crater likely required much higher energy environments than those of Gale crater. Although Gusev crater has long been considered as a lake basin based on orbital imagery, the Spirit rover found no apparent evidence of lake deposits. However, based on the evidence of alteration of the Comanche outcrop in the Columbia Hills, (Ruff et al., 2014) suggested that it might have contained an ephemeral lake recharged by multiple episodes.

Stack et al. (2016) systematically compared orbital geologic interpretations to detailed ground-based geological observation from the Curiosity rover at Aeolis Palus, Gale crater to examine the validity of geologic interpretation from orbital data. They demonstrate the difficulty of making process-based depositional interpretations from orbital mapping alone. Orbital stratigraphic interpretation commonly produces simple "layer cake" stratigraphic models with layers of constant thickness, horizontal deposition, and lateral continuity at least at the scale of the drafted cross-section (Stack et al., 2016). In contrast, ground-based observations will capture stratigraphic information from the vertical profile but cannot provide the horizontal view on a regional scale that is important for understanding the type of environment based on the spatial associations of landform features. The three-dimensional (3-D) digital outcrop models (DOMs) facilitate virtually reconstructing geological/geomorphological features of varying size, from mm-scale geological samples to km-scale landforms. Barnes et al. (2018) developed new 3-D visualization software (PRo3D) for geological analysis of Martian rover-derived DOMs and demonstrate the advancement of using 3-D models to interpret the surface geology captured from rovers. Caravaca et al. (2020) reconstruct a DOM of the Kimberley outcrop at Gale crater using images taken by four different cameras aboard Curiosity rover and HiRISE (High Resolution Imaging Science Experiment) orbital images from the Mars Reconnaissance Orbiter (MRO). The DOM was integrated with a Virtual Reality environment allowing real-scale visualization of the simulated outcrop, for both research and educational purposes. Sheppard et al. (2021b) and Fraeman et al. (2020b) recently compared the results from orbital and ground

observation data for Gale crater, Mars, and discussed the importance of ground-truthing to better understand how to interpret orbital data.

Analog studies provide the next level of accuracy assessment. These can be conducted with rover-like instruments to assess their capabilities and limitations for interpreting geological environments on Mars. Black and Hynek (2018) analyzed 100 hydrothermally altered basalts from Costa Rica, Nicaragua, and Iceland with Mars analog Visible to near Infrared- Shortwave Infrared (VNIR-SWIR) spectroscopy, X-ray diffraction (XRD), and Raman laser spectroscopy, and emphasized the importance of XRD for bulk mineral analysis. Martin et al. (2020) studied a Mars analog field site in the Mojave Desert near Lake Tecopa using Mars-2020 Perseverance rover-like instruments. They found that the Mars-2020 instruments are well suited and complement each other and can explore and identify interesting units to help select samples to cache. Mangold et al. (2017) developed a classification scheme for sedimentary and igneous rocks in Gale crater based on the texture captured by ChemCam Remote Micro Imager (RMI), MAHLI, and Mastcam, and geochemical information from the Alpha Particle X-ray Spectrometer (APXS) and ChemCam instruments.

Sedimentological investigations can identify and characterize paleolakes on Earth and employ a host of stratigraphic, petrographic, and paleontological observations (McLane, 1995). By identifying and characterizing the relicts of sedimentary subenvironments present in a paleolake basin and how they were arranged in space and time, it is possible to reconstruct the history of the paleolake. This study aims to develop a simple framework to identify and reconstruct paleolake basins on Mars, using an analog site in Lake Tecopa, California, using orbital remote sensing and data acquired from instruments similar to those available on current rover missions.

The study was guided by the questions formulated below,

1) How do I interpret landforms using orbital and ground-based images?
2) What methods and techniques can I use to extract more information from these data?
3) What landforms are present and how were they formed?

2. The study of the paleolake basin at Lake Tecopa using orbital and Mars rover-like instrument data.

2.2 Study area

Pliocene-Pleistocene Lake Tecopa is in the southeastern part of Inyo Country, California, about 30 km southeast of Death Valley (Fig 2.1). The Lake Tecopa paleolake basin is bordered by highlands, with Resting Spring Range to the east, Nopah Range and Alexander Hills to the southeast, Sperry Hills to the south, Ibex Hills to the southwest, and Dublin Hills to the west (Fig 2.1b). Lake Tecopa had a drainage area of about 8,300 km^2 and most of its water came from its headwaters in the Yucca, Timber, and Shoshone Mountains and Paiute Mesa (Morrison, 1999; Anderson, 2005). For more than 5 m.y., Lake Tecopa's depth and area fluctuated repeatedly with changes in climatic and tectonic conditions. Playa and shallow-lake conditions persisted until about 1 m.y. ago, followed by a trend of gradually higher lake levels with many intervening lake recessions. Around 186,000 years ago, Lake Tecopa reached its maximum water level. It breached soon afterwards, which initiated the dissection of the basin fill, eventually exposing one of the longest and most complete climatic-stratigraphic records in the southwestern United States (Morrison, 1999). With the breach of the Tecopa basin, the upper Amargosa river drainage basin became integrated with the lower Amargosa river providing through-flow to Death Valley (Fig 2.1a). Currently, the Lake Tecopa area is a hot, near-hyperarid desert. Precipitation is highly variable and much of the erosion occurs due to occasional summer rainstorms.

Sheppard and Gude (1968) first examined the distribution and genesis of authigenic silicate minerals in the Lake Tecopa area. They identified three diagenetic facies (fresh glass, zeolites, and K-feldspar) based on the main alteration minerals in three widespread marker tuff beds, which they named Tuff A, Tuff B, and Tuff C (Table 2.2). The fresh glass facies lies along the lake margin and is succeeded basinward by the zeolite facies, followed by K-feldspar facies in the center of the basin (Fig 2.1b). This concentric mineralogic zoning pattern represents a series of progressive reactions as a function of increasing salinity (Hay and Sheppard, 2001), reflecting the hydrological and hydrochemical history of the lake. Hillhouse (1987) first described and mapped the Quaternary geology of the Tecopa valley in detail. Morrison (1999) described the history of Lake Tecopa using four alloformation groups. Allostratigraphc units are defined based on physical, mappable boundary criteria

(not based on lithology). The boundaries can be time-transgressive (e.g., marker beds or widespread mappable unconformities) or isochronous (e.g., tuff layers). For mapping purposes, Morrison (1999) used Tuffs A, B, and C as boundaries for the alloformation groups. The allogroups he identified are, 1) Spanish Trail Alloformation, 2) Greenwater Fan Alloformation, 3) Shoshone Spring Alloformation, and 4) Amargosa Alloformation. He interpreted four main phases of lakes in the Tecopa basin: 1) an early Pleistocene shallow lake younger than Tuff C, 2) a large lake terminating with the deposition of Tuff B, 3) another large lake coeval with the deposition of Tuff A, and 4) a younger very large lake possibly with two high stands early in MIS (Marine Isotopic Stage) 6.

Table 2.2: Source and dating of Lake Tecopa ash beds

Ash bed	Source of air-fall ash	Dating	Reference
Tuff A	Lava Creek B ash, Lava Creek Tuff of the Yellowstone Group	631 ka	Matthews et al. (2015)
Tuff B	Bishop Tuff, Long Valley caldera, California	765 ka	Bogaard and Schirnick (1995)
Tuff C	Huckleberry Ridge Tuff of the Yellowstone Group	1.25 Ma	Scott and Deino (2014)

Larsen (2008) examined the stratigraphy and authigenic mineralogy of Lake Tecopa to assess the effects of sedimentary, chemical, and hydrological processes in controlling the types and distributions of authigenic minerals. Larsen and Olson (2019) interpreted the sedimentary facies and their distributions in terms of eleven depositional environments: 1) open-water lacustrine, 2) shallow-water lacustrine, 3) lacustrine margin, 4) mudflat and sandflat, 5) fluvial delta, 6) fan delta, 7) perennial streams, 8) floodplain and distal alluvial fan, 9) alluvial fan, 10) eolian deposits, and 11) groundwater discharge deposits. Reheis et al. (2020) established a lake-level history based on the uranium series and luminescence dating of shoreline deposits. Also, water chemistry and source(s) of water were inferred using the presence and distribution of ostracodes. Ostracodes are small crustaceans that live in most aquatic environments. Their distribution is typically controlled by the water chemistry (e.g., total dissolved solutes and the ratio of carbonate alkalinity to calcium) (Reheis et al., 2020).

2. The study of the paleolake basin at Lake Tecopa using orbital and Mars rover-like instrument data.

Depositional facies in the Lake Tecopa beds include a variety of mudstone, siltstone, sandstone, conglomerate, and tuff. The clastic sediment in the Lake Tecopa beds likely derived from four main sources, 1) the ancestral Amargosa River, 2) locally derived epiclastic sediments, 3) eolian silt and sand, and 4) volcanic ash (Larsen, 2008). Post Lake Tecopa dissections proceeded through four major erosion cycles (stream incision, followed by pedimentation, alluviation, and soil development), forming four widespread pediment-terrace surfaces exposing a complex, thick (~100 m) stratigraphic record (Morrison, 1999). These 3-D badland landforms make it possible to trace strata/stratigraphic units through various changes in lithofacies (e.g., from deep-lake to shore to alluvial facies). The wide spread marker beds enable precise stratigraphic correlations within the basin, which help to reconstruct the lake history (Morrison, 1999; Larsen, 2008; Larsen and Olson, 2019).

2. The study of the paleolake basin at Lake Tecopa using orbital and Mars rover-like instrument data.

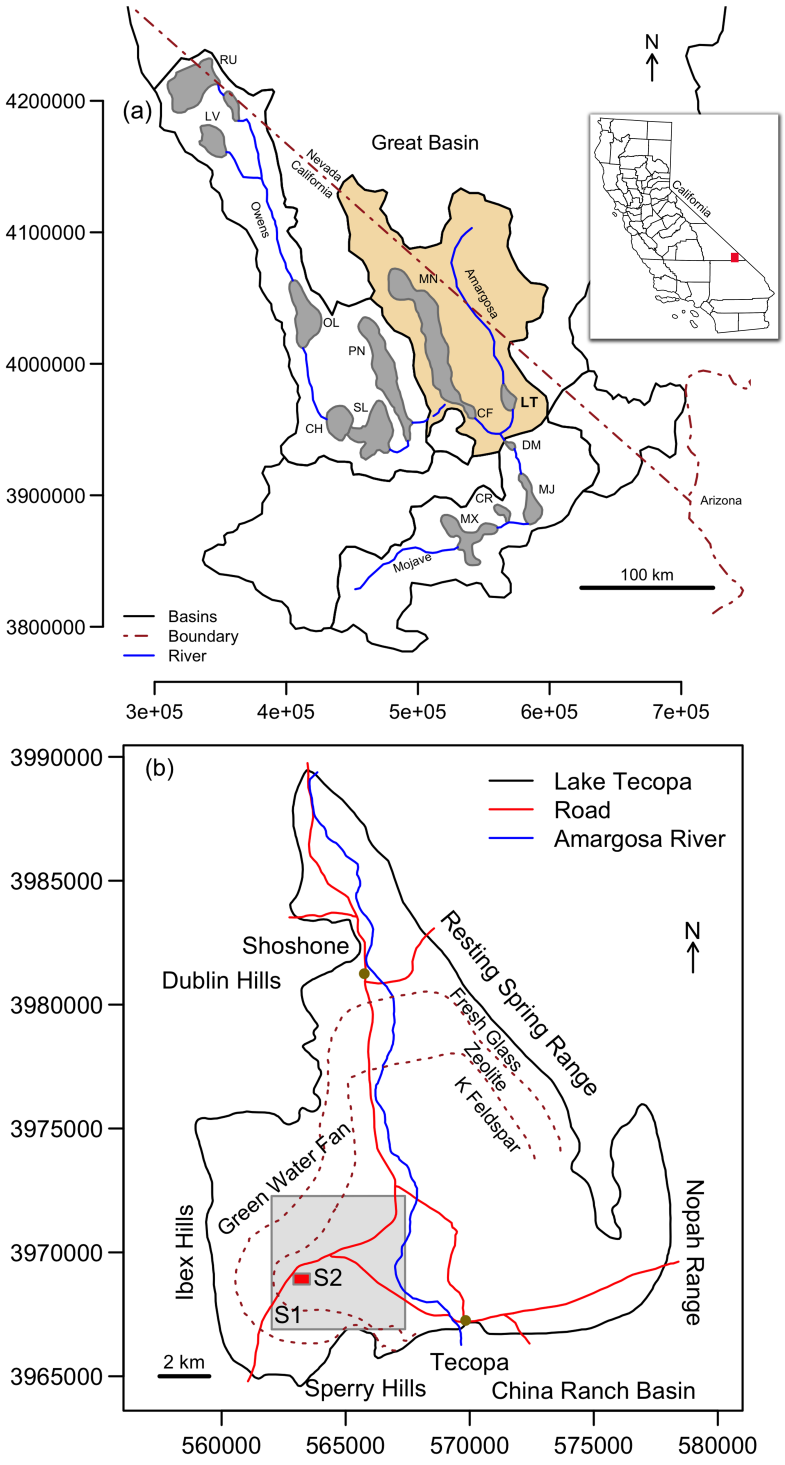

Figure 2.1: (a) Pluvial lakes in basins of the Amargosa, Mojave, and Owens Rivers (modified after Anderson, 2005) RU: Lake Russell, LV: Long Valley, OL: Ownes Lake, CH: China Lake, SL: Searles Lake, PN: Panamint Lake, MN: Lake Manly, LT: Lake Tecopa, DM: Lake Dumont, MJ: Lake Mojave, CR: Cronese Lakes, CF: Confidence Flat sub-basin, MX: Lake Manix. Amargosa River basin is shown in tan color. (b) Map of the Lake Tecopa basin and surrounding mountains, Amargosa river, roads, and study areas. S1 shows the area shown in Figure 3. S2 is the area shown in Figure 4 and Figure 5.

2. The study of the paleolake basin at Lake Tecopa using orbital and Mars rover-like instrument data.

2.3 Data and overall methodology

Fieldwork was conducted during October 2018 and 2019. The target field locations were identified before the field visits using published geological maps and orbital image data of the area. During the field expeditions, a total of 56 rock and soil samples were collected representing different surface materials over the area. Every sampling location was documented with detailed field descriptions of morphological features, lithology, thicknesses of the beds, location information (GPS), elevations, and field photographs. Field photographs were taken from the Nikon D3300 DSLR (f = 18 - 55 mm) camera.

The laboratory methods include the processing of image data, acquisition and processing of spectral data, and acquisition and analysis of X-ray diffraction (XRD) and X-ray fluorescence (XRF) data. The orbital and airborne image data used in this study were downloaded from the USGS (United States Geological Survey) EarthExplorer (`https://earthexplorer.usgs.gov`) and processed and analyzed using ILWIS 3.8 software. The ILWIS (Integrated Land and Water Information System: `https://www.itc.nl/ilwis/`) is a Windows-based GIS & Remote Sensing software, developed by the Faculty of Geo-Information Science and Earth Observation (ITC), University of Twente, the Netherlands.

The USGS National Agricultural Inventory Program (NAIP Plus) images were used for the detailed terrain analysis. The aerial orthorectified NAIP Plus digital photography is multispectral 4 band (red, green, blue, and near infrared) imagery with ~1 m/pixel resolution. The National Elevation Data (NED) from USGS is a seamless raster product (Digital Elevation Model-DEM) developed by merging the highest-resolution and best quality elevation data available across the USA. The NED employs a multi-resolution structure, coverage for the continental US at a grid spacing of 1-arc-second (~ 30m/pixel), and higher resolutions (1/3 and 1/9 arc-seconds) for some areas based on the availability of very high-resolution source data such as LIDAR DEM (Gesch, 2007). The 1/3-arc-second (~ 10m/pixel (9.33m/pixel)) NED data was used for this study. The Shuttle Radar Topography Mission (SRTM) flown on Space Shuttle Endeavour from 11 to 22 February 2000 was a joint project of NASA and NGA (National Geospatial Intelligence Agency) with the German Aerospace Center (DLR) and Italian Space Agency (ASI)

(Rabus et al., 2003; Yang et al., 2011). SRTM flew at an altitude of 233 km with two InSAR instruments of C-band (5.6cm) and X-band (3.1cm) (Yang et al., 2011). SRTM was derived from the InSAR (interferometric synthetic aperture radar) at resolution levels of 1 and 3 arc-seconds. The DEM Visualization script in ILWIS 3.8 software was used to create DEM shadow images to visualize the morphology of the area. The script creates three shadow maps (West, North-West, and North) using shadow filters and uses RGB (red-green-blue) color composite to visualize relief of the area after linear stretching of these three maps, ignoring 5% (ITC-ILWIS, 2001).

Anaglyphs and 3-D morphology models were created using GIMP (`https://www.gimp.org`) and Blender (`https://www.blender.org`) software packages, respectively. GIMP and Blender are cross-platform free and open-source software packages used for image editing and 3D modeling, respectively. Targeted landscapes were captured by two different looking angles to create anaglyph images. Microphotographs of collected field samples were taken using an AmScope MU1803 (18 megapixels) camera mounted on Zeiss Stereomicroscope. Scanning Electron Microscopy (SEM) and Energy Dispersive X-ray Spectroscopy (EDX) images of the selected samples were taken using the Hitachi S-4800 FE-SEM facilities at the Department of Biological Sciences at the University of Wisconsin-Milwaukee. Selected samples were glued on glass slides and carbon-coated using an Edwards vacuum coating unit.

The mineral assemblages of field samples were identified using XRD. Samples for XRD analysis were cleaned, powdered by hand, and quantitatively mixed with crystalline Cerium (IV) oxide powder ($CeO_2 < 5\ \mu m$) using a 100: 1 ratio (by weight) of sample to internal standard. Samples were analyzed using a Bruker D8 Focus XRD system (Cu K α X-ray radiation, 1s per step, 0.01^o 2θ per step,2°-60° range, scintillation detector) and results were compared against the ICDD PDF-2 (International Center for Diffraction Data Powder Diffraction File) library using Bruker's EVA software. Intensities of the characteristic peak of each mineral were measured and relative abundances were calculated based on the normalized relative intensity of the CeO_2 peak at 28.585 $2\theta^o$. Based on the mineral compositions, ten samples were selected representing commonly observed paleolacustrine deposits of the area.

2. The study of the paleolake basin at Lake Tecopa using orbital and Mars rover-like instrument data.

For XRF analysis, around fifteen grams of the same ten samples were cleaned, ground, weighed and then dried overnight at 105^oC. Samples were weighed again to calculate the water content of each sample. One gram of each sample was mixed with 1g of ammonium nitrate (oxidizer) and 10g of a 50:50 lithium metaborate: lithium tetraborate flux, with 1% LiBr as a non-wetting agent. The mixtures were fused at ~1050^oC in a Claisse M4 fluxer to make fused beads and each bead was analyzed for major, minor and some trace elements using a Bruker S4 Pioneer XRF system. Loss on ignition (LOI) was measured by heating ~ 1g of each dried sample in a muffle furnace at 1050^oC. The XRD and XRF analysis were done at the Department of Geosciences, University of Wisconsin-Milwaukee.

The reflectance spectra of these ten samples (bulk) were acquired using an ASD TerraSpec HALO reflectance spectrometer at the University of Colorado. The maps and all the plots shown in this study were created using R statistical software packages (`https://www.r-project.org`). The summary of the instruments/datasets used in this study with their complementary Mars instruments/datasets are listed in the table 2.3.

Table 2.3: Earth data/instruments used in this study with their complementary Mars data/instruments.

No	Type	Earth Data/Instruments	Complementary Mars Data/Instruments
01	Orbital	High Resolution Images: NAIP Plus Images (60 cm/pixel)	HiRISE (30 cm/pixel)
02		DEM: NED (~ 10 m/pixel)	CTX (6 m/pixel)
03		DEM: SRTM (~ 30 m/pixel)	MOLA (~ 463 m/pixel)
04	In-situ	Site Photographs: Nikon D3300 HDSLR camera (24.2 megapixels)	Mastcam (-Z) (2 megapixel)
05		Microphoto-Surface: Zeiss Stereomicroscope with AmScope (18 megapixels) camera	MAHLI (13.9 microns/pixel)
06		Microphoto-SEM: Hitachi S-4800 with Bruker EDS	PIXL
07		X-ray Diffraction: Bruker D8 Focus (2-60°, Cu-Kα)	CheMin (5-50°, Co-Kα)
08		X-ray Fluorescence: Bruker S4 Pioneer	APXS
09		VNIR-SWIR Spectroscopy: TerraSpec HALO Spectrometer (350-2500 nm)	SuperCam (400-900 nm, 1300-2600 nm)

The first exercise of this study was to identify and demarcate the catchment area and paleolacustrine boundary using DEM data. The NED and SRTM DEM datasets were

assessed for morphological mapping and catchment extraction. The study area selected for accuracy assessment is shown in Figure 2.2 (S1 coverage in Fig 2.1b). The ~10m spatial resolution NED DEM (Fig 2.2a) clearly shows depositional and erosional features by water including badlands fringed by cliffy rock mountains, mesa-like ridges, and channels. It is difficult to identify these features in the 30m spatial resolution SRTM DEM product (Fig 2.2b) due to noise. Guth (2006) compared the quality of the SRTM (30m) and NED DEM using about 500,000 sample areas over the United States, and Shortridge and Messina (2011) used the same approach with 90m SRTM DEM using over 240,000 locations to access the errors associated with SRTM DEM. Both studies concluded that all SRTM DEMs suffer from radar speckle and random noise in the elevations and more noise in flat areas (Fig 2.2b). Yang et al. (2011) discussed the causes of typical radar artifacts including 1) geometric artefacts such as foreshortening, layover, and radar shadow, 2) specular reflection of water, 3) phase unwrapping artifacts and artifacts due to the influence of the dielectric constants of the imaged surface. Filtering by averaging the nearby pixels lessens the effect of radar speckle, but also averages the terrain by lowering the peaks and ridges and raising the valleys (Guth, 2006). Therefore, a comparison of NED and SRTM DEM at Lake Tecopa shows the effect of DEM sources and their spatial resolution on the identification of the type of geological settings based on landforms. The accuracy of the DEM elevation was assessed using elevation data acquired from hand-held GPS during the field visits. It is assumed that the hand-held GPS elevation data are accurate enough. Twenty-eight (28) field elevation values were used to assess the accuracy of the NED and SRTM data (Fig 2c). The highest accuracy is achieved by the NED DEM ($R^2 = 0.9616$). Based on the above reasons NED DEM was selected for the rest of the study.

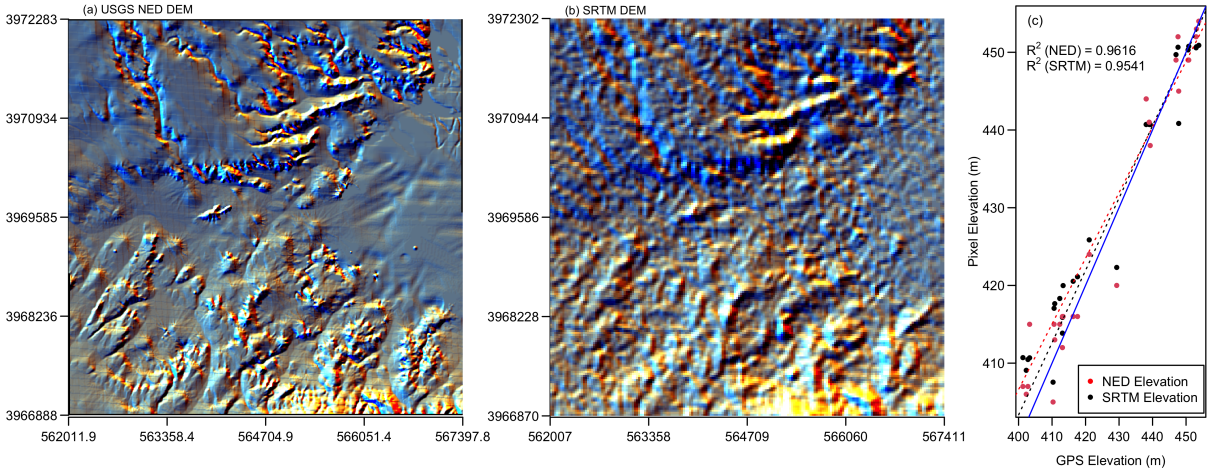

Figure 2.2: Comparison between the NED DEM (a) and SRTM DEM (b). The accuracy of both DEMs was assessed using handheld GPS in the field (c).

The drainage network extraction process was done using the "DEM Hydroprocessing" operation in ILWIS 3.8 as follows. 1) The fill sink operation was used to clean the DEM by removing the local depressions, 2) the flow direction operation was used to determine into which neighboring pixel any water in a central pixel will flow naturally in a sink-free DEM, 3) a flow accumulation map was created to extract the basic drainage network with a stream threshold of 1000, 4) the drainage network ordering map was created, and 5) catchment extraction was conducted by selecting the narrowest valley point of the basin as the outlet.

2.4 Results and discussion

Results will be presented in five steps equivalent to the geological observations implemented on the surface of Mars using orbital and rover missions. 1) regional-scale hydrological analysis using DEM data, 2) local-scale geomorphological mapping using high-resolution image and elevation data, 3) initial outcrop investigation using field photos, 4) microscopic imaging of composition, textures, and structures of selected rock and soil samples, and 5) in-depth mineralogical and chemical assessment using VNIR spectroscopy, XRD, and XRF.

2. The study of the paleolake basin at Lake Tecopa using orbital and Mars rover-like instrument data.

2.4.1 Imaging observations from orbital data (spatial resolution ~ 1m/pixel to ~ 100m/pixel)

A hillshade map generated from NED DEM is shown in Figure 2.3 (a). It shows the difficulty of identifying the catchment area and the topographic low in which water would have ponded using only visual image interpretation of hillshade image data. The drainage network pattern derived using NED DEM is shown in Figure 2.3 (b), which shows that the DEM-generated drainage network (dark blue lines) closely follows the Amargosa River (light blue line). The boundary of the catchment area (yellow line) was delineated, assigning the outlet to the narrowest point of the basin (red point). It is important to note that the complete catchment area is not represented by the extent shown in the image.

Identifying the lake margin (shoreline) using remote sensing data is the next challenge. Shoreline deposits such as deltas, beaches, spits, bars, platforms, and carbonate mounds can be used to identify the margins of the paleolake basin (Smoot and Lowenstein, 1991). On Mars, lake boundaries are typically demarcated using the highest closed contour in the basin before it spilled into the outlet canyon (Quay et al., 2021; Fassett and Head, 2008). However, this method cannot be used in this study since the lake was breached completely, forming a valley. In previous work, the maximum lake level of paleolake Tecopa was identified using shoreline deposits, based on the exposure of horizontal to inclined beds of rounded sand and gravels (Larsen and Olson, 2019; Larsen, 2008; Reheis et al., 2020). However, the timing and maximum water level of the basin are debated (Morrison, 1999; Larsen, 2008; Reheis et al., 2020). The resolution of NAIP images is not enough to identify the shoreline deposits based on their sediment textures or fabric. The NAIP image in Figure 2.3 (d) shows some light tone/ white color deposits in the middle of the basins up to a certain elevation on the basin margin. Several lake margins were derived based on the maximum extent of these deposits and compared against the published lake boundaries derived from shoreline deposits. The ~550m contour line was found to best match the published boundary lake. Morrison (1999) estimated the maximum water level (before breached) as 549m, and Reheis et al. (2020) identified a high lake level up to 525m, both based on detailed field and laboratory data. However, the 550m contour line shows the lake boundary beyond the published lake boundary due

to the breach of the lake. Therefore, in this case, the intersection of 550m contour with the catchment boundary map created the paleolake boundary with high spatial accuracy (Fig 2.3d). The calculated paleolake boundaries based on the DEM and on the published geological map are shown in red and pink polygons, respectively. The lessons learned from this exercise are: 1) identifying of paleolakes can be difficult depending on the type of breach (complete or partial), 2) possible paleolake areas can be estimated using the catchment extraction with DEM data, 3) identifying paleolake boundaries is difficult using remote sensing data, if there are no visible shoreline deposits or if these deposits are difficult to identify using remote sensing data due to the limitations of spatial and spectral resolutions, and 4) identifying paleolake basins using remote sensing data can yield false positive or false negative errors based on the type of basin.

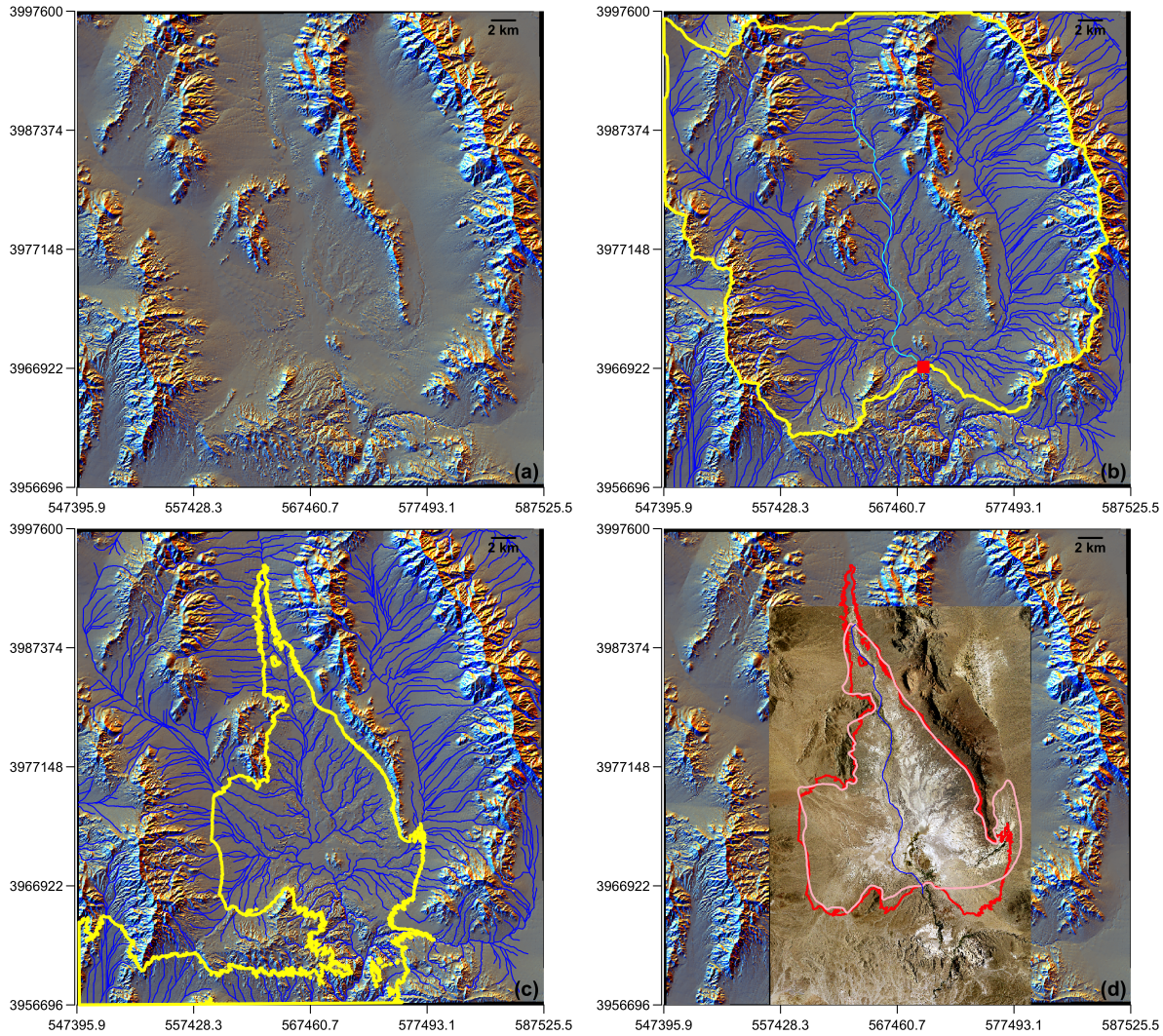

Figure 2.3: a) Hillshade map derived from NED DEM of the Lake Tecopa area, b) Drainage network (dark blue), Amargosa River (light blue), Catchment area (yellow), and proposed outlet (red) draped over the NED hillshade image, c) Drainage network (dark blue) and 550m contour line (yellow) draped over the NED hillshade image, and d) lake boundary from the Hillhouse (1987) published map (pink), Amargosa River (dark blue), and derived lake boundary map from this study (red) draped on NAIP and NED hillshade image.

Geomorphology is an observationally framed, interpretative science that analyzes landscape forms, patterns processes, and their evolution (Brierley and Fryirs, 2014; Schumm, 1991; Frodeman, 1995). It records the materials of which landforms are composed and an indication of the process-response geomorphic systems associated with their formation (Knight et al., 2011). The approach used to create geologic maps of Mars has been mainly based on the surface morphology interpreted by orbital image data and digital elevation models derived from MOLA data. The geologic map is a two-dimensional (2-D)

representation of spatial and temporal relationships of lithologic or chronostratigraphic units of the area investigated. Tanaka et al. (2009) assessed the planetary geologic mapping techniques for Mars using terrestrial analog at the SP mountain area of the San Francisco volcanic field, Arizona. They defined their mapping units and stratigraphic relations primarily based on geomorphology, color contrasts, and cross-cutting relationships. Stack et al. (2016) used the term "orbital facies" instead of "geologic unit" or "geomorphologic unit" since the interpretation was made based on the tone, color, and texture of the orbital images. Figure 2.4 (a) shows the high-resolution NAIP image of the study area. The location of the study area in the Lake Tecopa basin is demarcated by polygon S2 in Figure 2.1 (b). Samples collected for this study (red dots and sample numbers in blue) and the field photo locations (green arrows show the direction of photographs taken while yellow triangles show the vicinity of the photo) are also shown in Figure 2.4 (a).

Terrain analysis by aerial/orbital photography is the systematic study of visual elements relating to the origin and composition of distinct landscape units that appear in the image. The elements used to study the terrain include topographic relief, elevation, drainage patterns, gully characteristics, erosional features, landform boundaries, color, tone, and texture (Way, 1978). These elements were used to create a geological map of the area. The study area shows terraces, erosional slopes, alluvial fans, mesas, buttes, pediments, valleys, and braided channels. Different terraces can be identified based on the tone and the texture. The A-A' elevation profile in Figure 2.4 (b) clearly shows two prominent terraces with two prominent valleys. Figure 2.4 (c) shows the interpreted geology based on the NIAP image and NED DEM image of the area. It shows four terraces (L1, L2, P1, P2), two dry stream beds (R1 and R2), and four erosional surfaces (S1, S2, S3, S4). It shows that the dark color L1 terrace is the highest terrace in the area and the dark brown color of the surface is due to the fan-gravel deposits. The principal source of the gravel is problematic (Morrison, 1999). P1 is the second terrace and is covered by erosional sediments and gravels coming from L1. L2 is the third terrace which is also mostly covered by gravel beds. P2 is the lowest terrace of the area. Pediments (shallow slopes) and slope foots of these terraces are represented by S1, S2, S3, and S4. S1 represents the erosional slope of terrace L1, and S3 represents the erosional surface of L2. The S2 and

2. The study of the paleolake basin at Lake Tecopa using orbital and Mars rover-like instrument data.

S3 pediments are mostly covered by gravel. Without the elevation model (cross-section), it may be difficult to identify the different levels of terraces of the area.

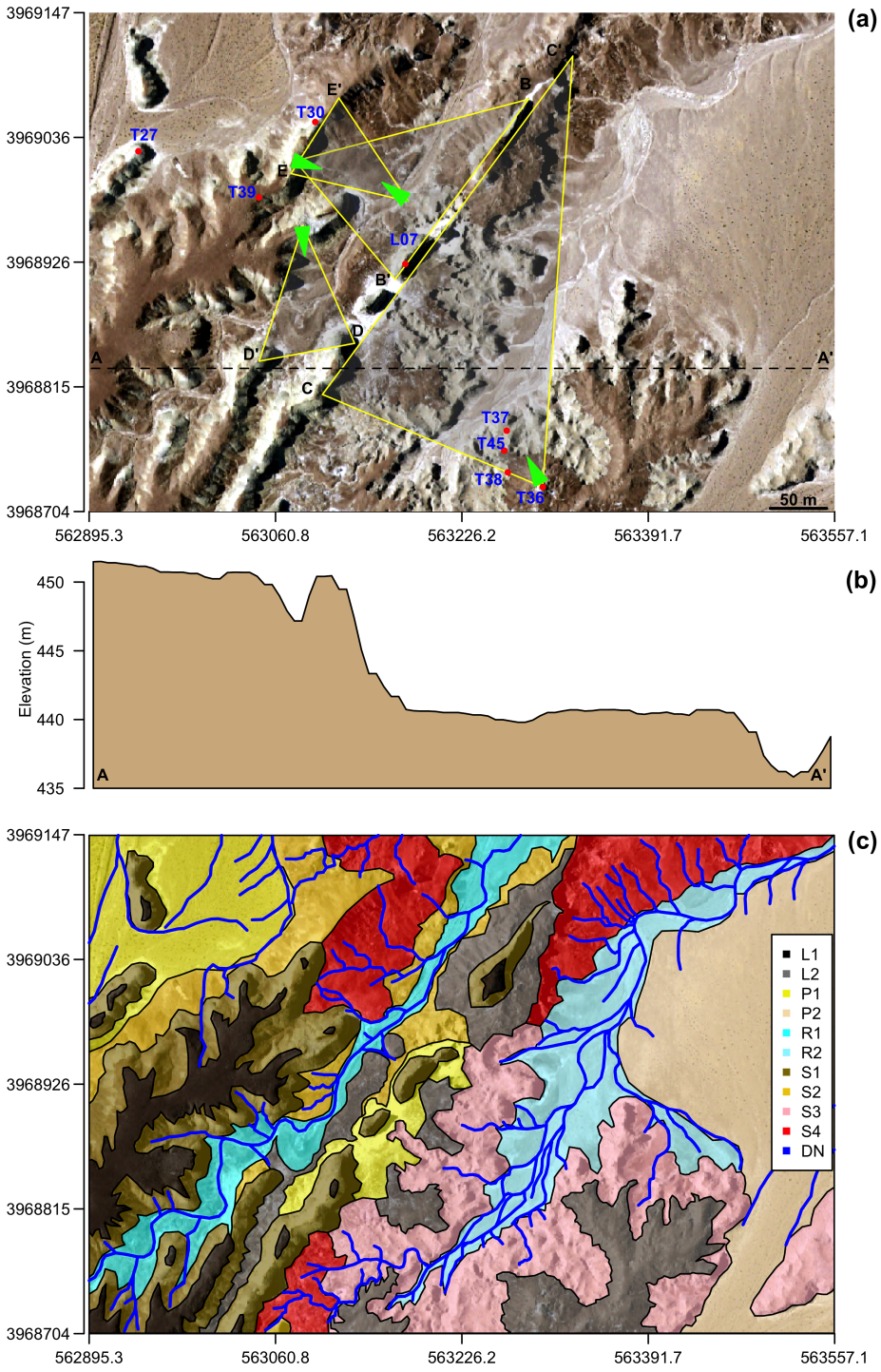

Figure 2.4: a). NAIP image of the study area. Band combinations: Red 3, Green 2, Blue 1. Sample locations and vicinity of the field pictures discussed in this text are shown in the triangles. The green arrows show the places and directions from which the photos were taken. The bases of the traingles opposite to the green arrows show the sections shown in Figure 2.4 (b), Figure 2.5, and Figure 2.6. Sample locations are shown by red dots. The sample number is shown in blue text. b) Elevation profile of the line A-A', and c) Geomorphology map created based on the Figure 4 (a). Map is overlain on the NED DEM. See the text for legend descriptions.

2. The study of the paleolake basin at Lake Tecopa using orbital and Mars rover-like instrument data.

One of the most sophisticated ways to identify the erosional and depositional features of the area is the use of 3-D models. Two snapshots of the 3-D model created in this study are shown in Figure 2.5. It demonstrates that 3-D models provide more information such as the geometry and dimensions of sedimentary structures and landforms, therefore making it easier to interpret the morphological features of the area compared to using 2-D map products. It provides the ability to roam the landform or outcrop to view features of interest from different view angles. It also helps to define the best traverses for manned and robotic missions in planetary exploration. Though the high-resolution images provide more information compared to other map bases, morphologic and stratigraphic information was not always distinctive even when the high-resolution image is draped over the DEM to create a 3-D model. This is largely due to surface color, texture, spatial resolution, and illumination angle, which commonly contributed to ambiguous image information (Fig 2.5). Lake deposits are commonly interbedded with or otherwise closely associated with fluvial and alluvial deposits (McLane, 1995). Though the fluvial and alluvial deposits may be identifiable from the orbital data, interbedded lake beds will not be identifiable from the nadir-looking orbital data if the slopes are vertical or near-vertical. In this case, ground-based photographs are needed to explore the bedding style, sedimentary structures, lithology, and texture, which are essential for paleoenvironmental reconstruction.

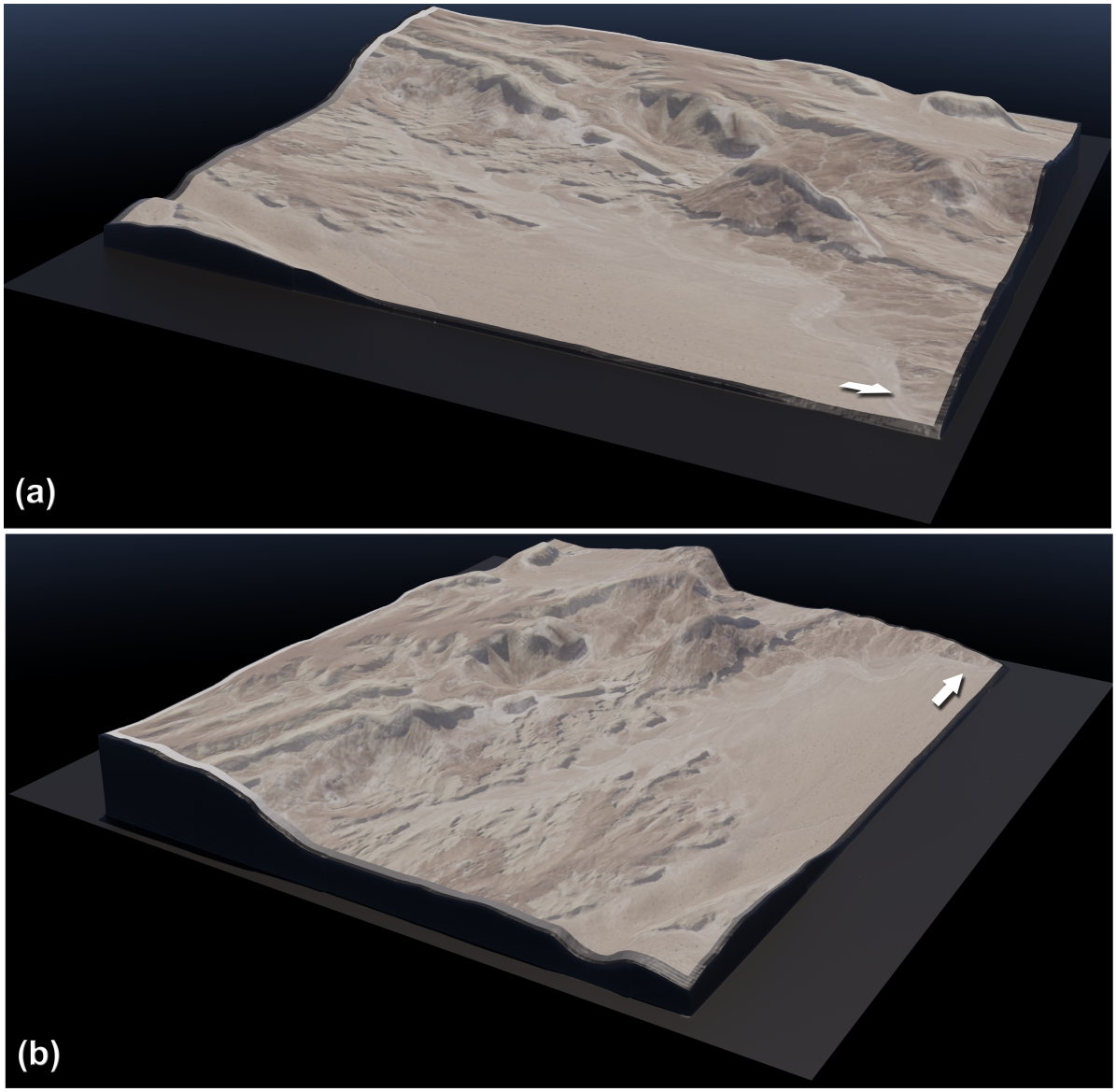

Figure 2.5: 3-dimensional (3-D) view of the study area. A mosaiced high-resolution NIAP image was draped onto NED DEM.

2.4.2 Imaging observations from in situ data (spatial resolution ~ 1 cm to ~ 1 m)

Figure 2.6 shows the field photographs of the area from two view directions. Figure 2.6 (a) shows the view direction B-B' shown in Figure 2.4 (a), while Figure 2.6 (b) shows the view direction C-C' in Figure 2.4 (a). These two field photographs show the extensive badlands observed in the 3-D model and the gravel-capped terraces and mesas. Gravel caps are beds of ancient washes (Morrison, 1999). It also shows that, where gravel caps

are absent, bare rounded mudstone hills can be observed. Three terraces of the area can be identified in Figure 2.6 (b). Many lake deposits are bedded or laminated and show frequent vertical changes in lithology and color. The main reasons for this are 1) lakes and their sediments are little affected by waves and currents, and 2) they are very sensitive to changes in climate and other environmental factors (Einsele, 2000). These landforms and processes can easily be interpreted from the combination of 3-D models and field photographs. It is also possible to create a 3-D view from the field photographs using field photographs of a site/landscape looking from two different directions. Figure 2.7 shows the anaglyph (3-D photograph) created from D-D' view direction shown in Figure 2.6 (a). It clearly shows the buttes, pediments, layering, and erosional and depositional features. The extensive badlands are mostly butte-like gravel-capped ridges with steep side slopes. Thick sedimentary beds indicate an increased sedimentation rate.

2. The study of the paleolake basin at Lake Tecopa using orbital and Mars rover-like instrument data.

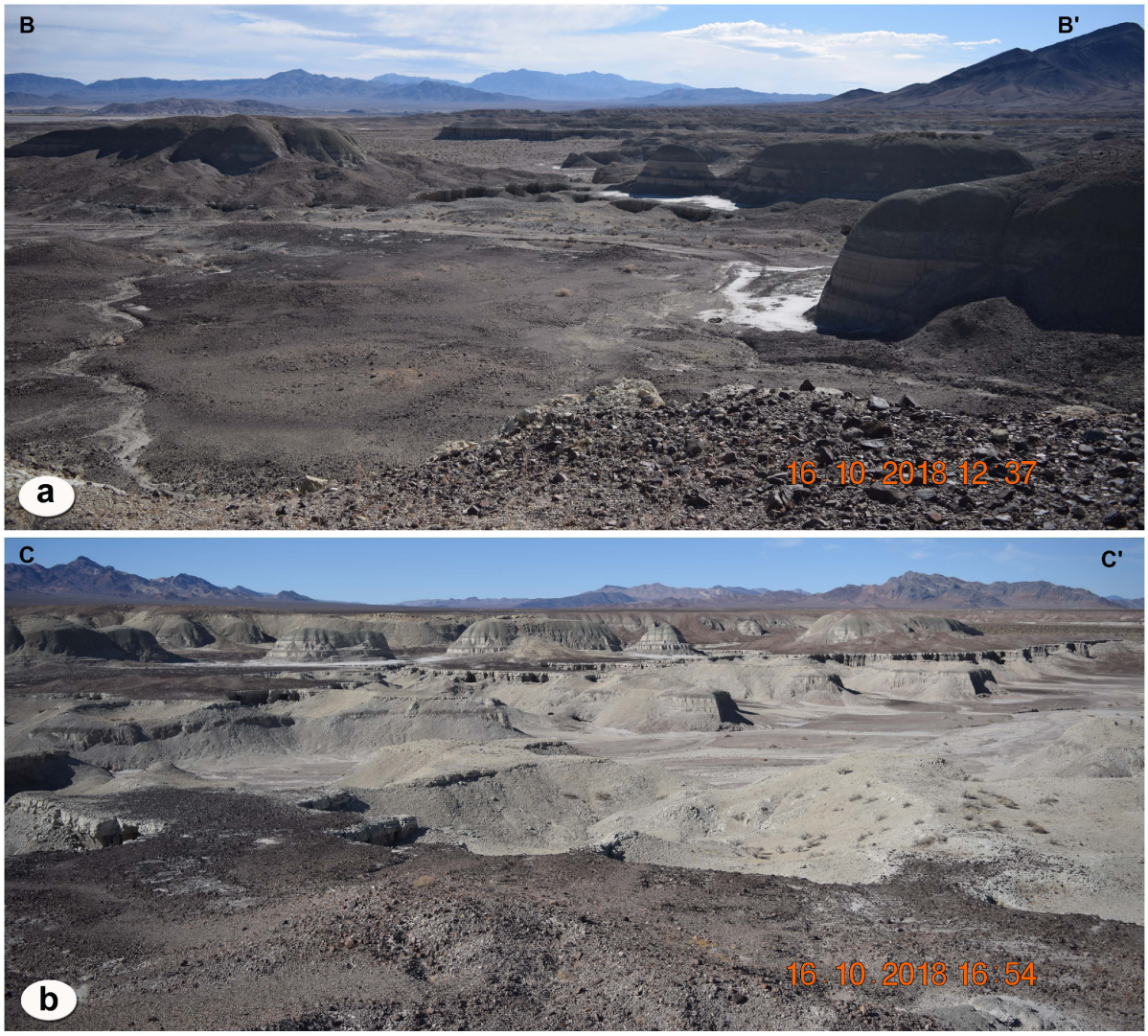

Figure 2.6: Field photos showing sections B-B' and C-C' marked in Figure 4 (a).

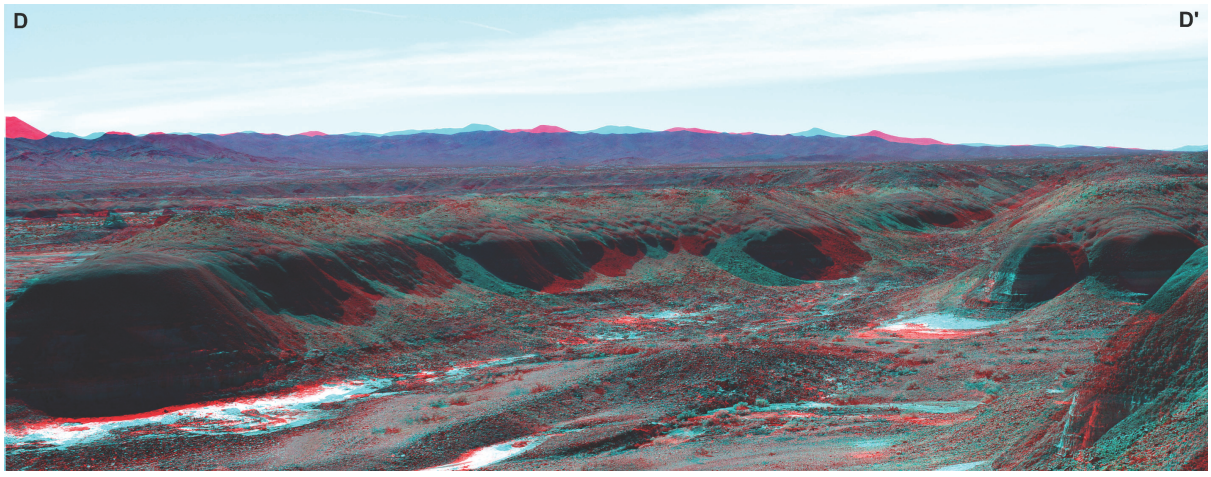

Figure 2.7: 3-D Anaglyph photo of the field site D-D' view shown in Figure 2.4 (a). Anaglyph glasses are required to view in 3-D.

2. The study of the paleolake basin at Lake Tecopa using orbital and Mars rover-like instrument data.

Composition and texture are the basis for the classification of sedimentary rocks. The composition refers to the mineralogy of grains, matrix, and chemical cements, while texture refers to absolute and relative sizes of grains and their shapes and the quantity of matrix (McLane, 1995). Sedimentary structure refers to larger aspects of grain aggregates, features that are imposed by sedimentary processes acting collectively upon many grains at once (e.g., cross-bedding, ripples, graded bedding, etc.) (McLane, 1995). The composition, texture, and structures are controlled by the parent materials, nature of transporting media, distance and duration of transport, the physical, chemical, and biological conditions under which they formed, and the nature and extent of post-depositional processes (McLane, 1995). Identifying and characterizing sedimentary structures and textures using ground-based imaging will be discussed hereafter. This study does not attempt to address the traversability challenges for the rovers while identifying the target locations and collecting the samples.

Figure 2.8 shows a sedimentary structure seen from a distance photograph. The image was taken at ~100m distance from the target location and the person sitting in the middle of the sedimentary structure (right edge on the black box in the main photograph) can be used as a scale. The zoomed figure inset shows mainly four sedimentary beds with different thicknesses and fabrics. The second layer from the top shows the conglomerate bed, while the two beds above and below are finer grained. The conglomerate bed and its concave shape can be interpreted as a paleochannel. A paleochannel can be identified using channel lag deposits and point bar deposits. A channel lag deposit is a lenticular sheet composed of the coarsest or heaviest materials available to the river (e.g., gravel, mud clasts, pieces of wood, bone, and shells). A point bar deposit is an arcuate or crescentic body of sand and maybe some gravel that forms by lateral accretion on the convex bank of a channel (McLane, 1995). It also shows the decrease of grain sizes upwards in point bars, which is one of the most distinctive characteristics of a fluvial sandstone. It is clear that this is the depositional feature (e.g., channel) formed during a certain lake level and the elevation of this point can be found from the NED DEM since, in this study, the ground observations are coordinated with the orbital data. The elevation of this point is 450.7 m.

2. The study of the paleolake basin at Lake Tecopa using orbital and Mars rover-like instrument data.

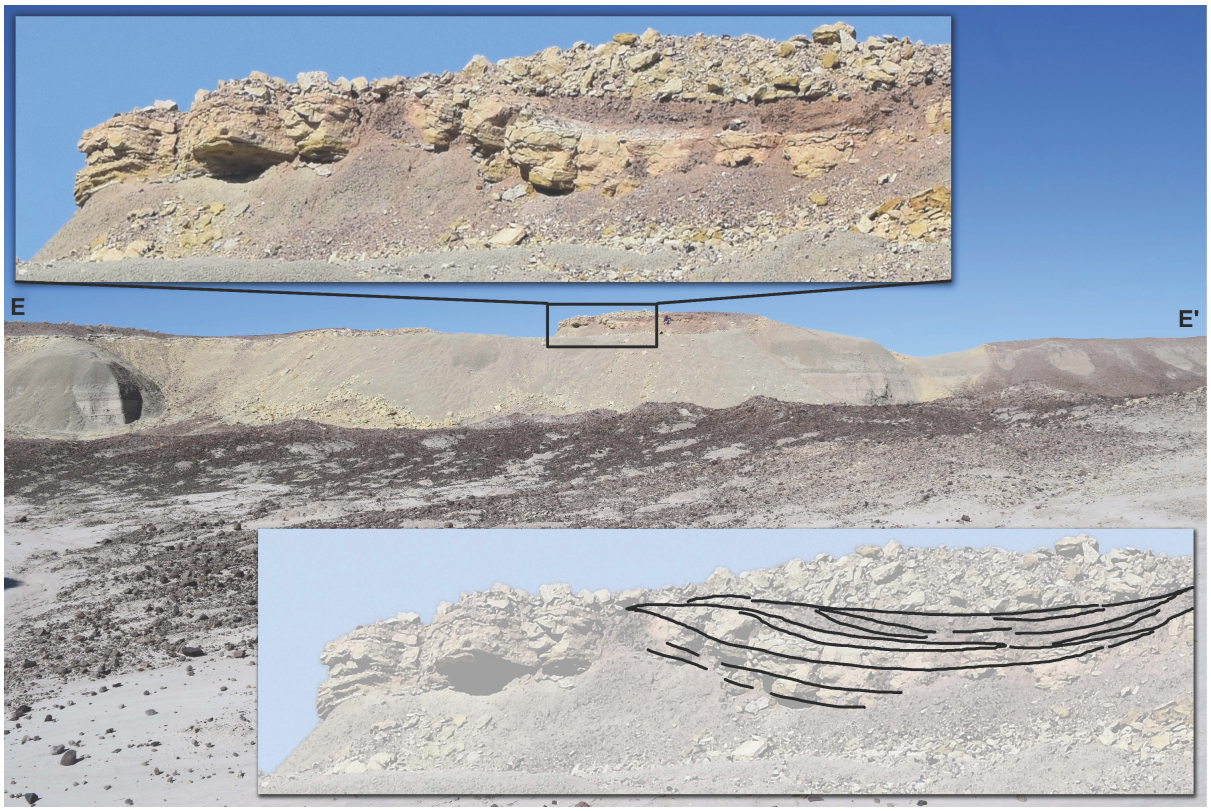

Figure 2.8: Interpretation of sedimentary structures seen from a distance photograph. A person standing there can be seen in the middle of the picture as a scale. The photo was taken at 100m distance.

A facies is a body of sediment with specified characteristics that can be distinguished from the adjacent sediments (McLane, 1995). The distribution and types of sedimentary facies in lake basins mainly depend on the hydrology and climate (Smoot and Lowenstein, 1991). Therefore, the distribution and spatial arrangement of these facies in a lake basin can be used to reconstruct the paleohydrologic and paleoclimatic conditions of the area. The most common and characteristic sedimentary environments in a saline lake basin from the center of the basin toward the margin are, 1) saline mudflats, 2) dry mudflat, 3) sandflat, 4) shoreline features, and 5) alluvial fan (Calvo et al., 1999; Hardie et al., 1978; Smoot and Lowenstein, 1991; Shaw and Thomas, 1989). A saline mudflat can be found in the center of the Lake Tecopa basin (Fig 2.9a). Saline mudflats are narrow fringes or broad extensive flats of fine-grained sediment commonly marginal to saline pans and perennial saline lakes. Saline mudflats are formed by a combination of fluvial, lacustrine, and aeolian processes. Hardie et al. (1978) documented three basic types of mudflats,

each produced by a different combination of depositional processes resulting in a different kind of layering, 1) sheet washed mudflats, 2) ponded water mudflats, and 3) exposed old perennial lake bottom mudflats. The types of evaporite minerals formed in saline mudflats depend on 1) the stage of the chemical evolution of groundwater brine, 2) the sinking of surface brine, and 3) the mixing of groundwater brine and surface-derived brine (Smoot and Lowenstein, 1991). Therefore, the identification of evaporite minerals present in the mudflat can be used to characterize the chemistry of the groundwater. Ripple marks on the mudflat (Fig 2.9b) indicate agitation by water currents or waves. Dry mudflats are characterized by polygonal mud cracks with thin saline crusts that result from repeated wetting and drying (Hardie et al., 1978; Smoot and Lowenstein, 1991). Sandflat is the flat, unchanneled sandy apron at the toe of an alluvial fan. The main constituent of a sandflat is sand, which occurs as planer parallel horizontal laminae and wavy laminated beds (Smoot and Lowenstein, 1991). Ripple marks preserved on the tuff bed are shown in Figure 2.6 (d). The interbedded mudstone and laminated or wave-ripple cross-laminated very fine to fine-grained sandstone and tuff indicate the shallow-water lacustrine environment (Larsen, 2008). Therefore, while the texture and structure of sediments and sedimentary rocks reflect the hydraulics of the environments under which they were deposited, grain size and sorting infer the strength of currents and turbulence in the depositional environments (McLane, 1995).

2. The study of the paleolake basin at Lake Tecopa using orbital and Mars rover-like instrument data.

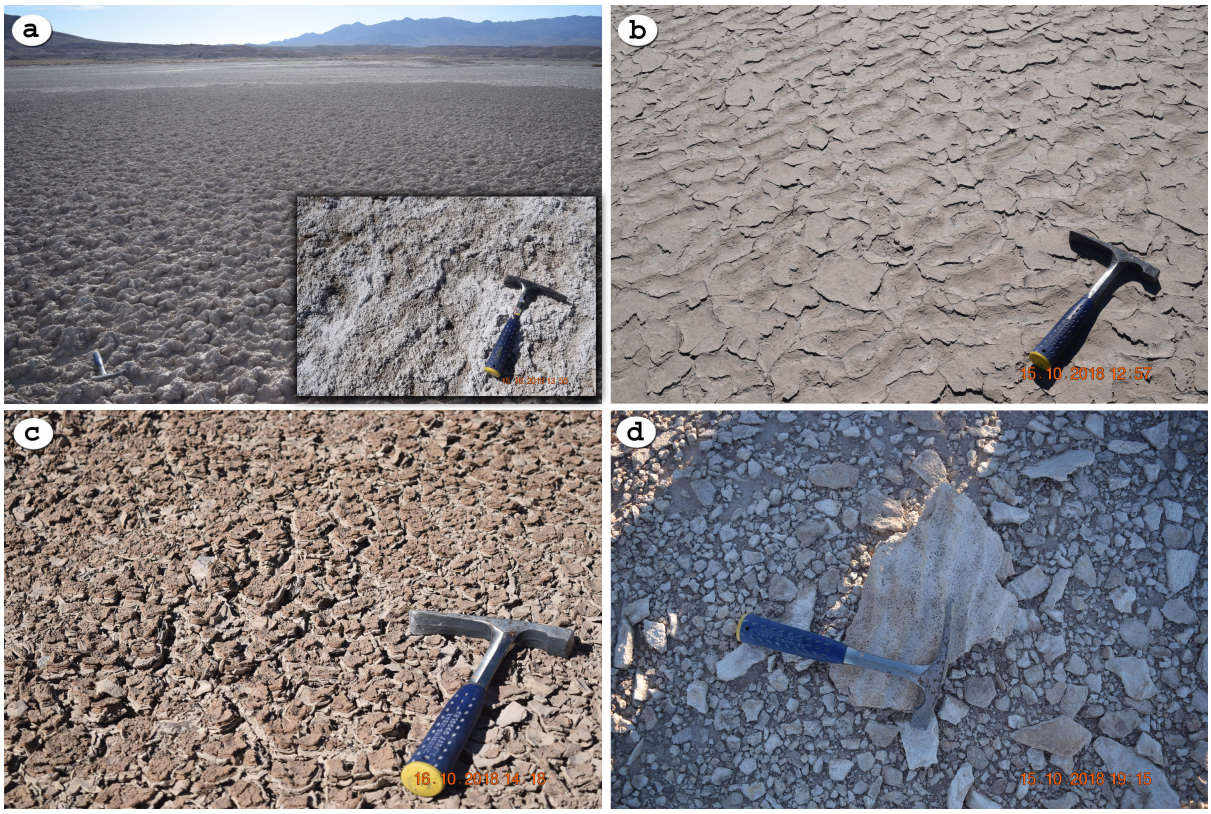

Figure 2.9: Depositional environments and sedimentary structures in the middle of Lake Tecopa. a) saline mudflat, b) mudflat with ripple marks showing shallow water wave actions, c) dry mudflat showing wetting and drying process, and d) ripple mark preserved on a tuff bed.

Four main sedimentary facies identified in the study area are shown in Figure 2.10. The identified sedimentary facies include, 1) fresh tuff (Fig 2.10a), 2) zeolitized tuff (Fig 2.10b), 3) greenish-gray mudstone (Fig 2.10c), and sandstone (Fig 2.10d). The tuff can be further classified based on the nature of the dominant particles (vitric, lithic, crystal), chemical and petrographic composition (e.g., acid tuff, andesitic tuff), manner of transport (e.g., ash-flow tuff), and environment of deposition (e.g., submarine tuff) (Greensmith, 1989). However, the tuff showed in Figure 2.10 (a) will be difficult to classify only based on the photograph. High-resolution images (to identify the grain size) and compositional information are required. These tuff layers are important as marker beds since deposition from one eruptive phase can extend over a wide region. Therefore, these layers can be used for correlative and chronological purposes, areas of study known as tephrostratigraphy and tephrochronology, respectively (Greensmith, 1989). When ash is laid down on the bodies of water, they show a range of sedimentary structures, such as bedding, lamination,

cross-bedding, slumps, grading, and diagenetic concretions (Greensmith, 1989). These structures can be seen in zeolitized tuff beds (Fig 2.10b). Zeolitized tuff beds also help reconstruct the hydrochemistry of the lake and the environmental conditions during the alteration of fresh tuff to zeolite (Hay and Sheppard, 2001). Figure 2.10 (c) shows the green mudstone. The most characteristic feature of this mudstone is the "popcorn" texture implying the presence of expandable clay minerals such as montmorillonite (McLane, 1995). The composition of the mudstone is partly controlled by the composition of the parent rock and the content of alkalis (Na, K), and alkaline earths (Ca, Mg). Therefore, the basic igneous rocks with abundant Ca and Mg are more likely to make smectites while granites and syenites rich in alkalis favor the production of illite (McLane, 1995). Sandstone is a sedimentary rock mainly composed of quartz sand. It can also contain significant amounts of feldspar, and sometimes silt and clay. Sandstones shown in Figure 2.10 (d) are pale brown and thin-bedded, with some ripple marks.

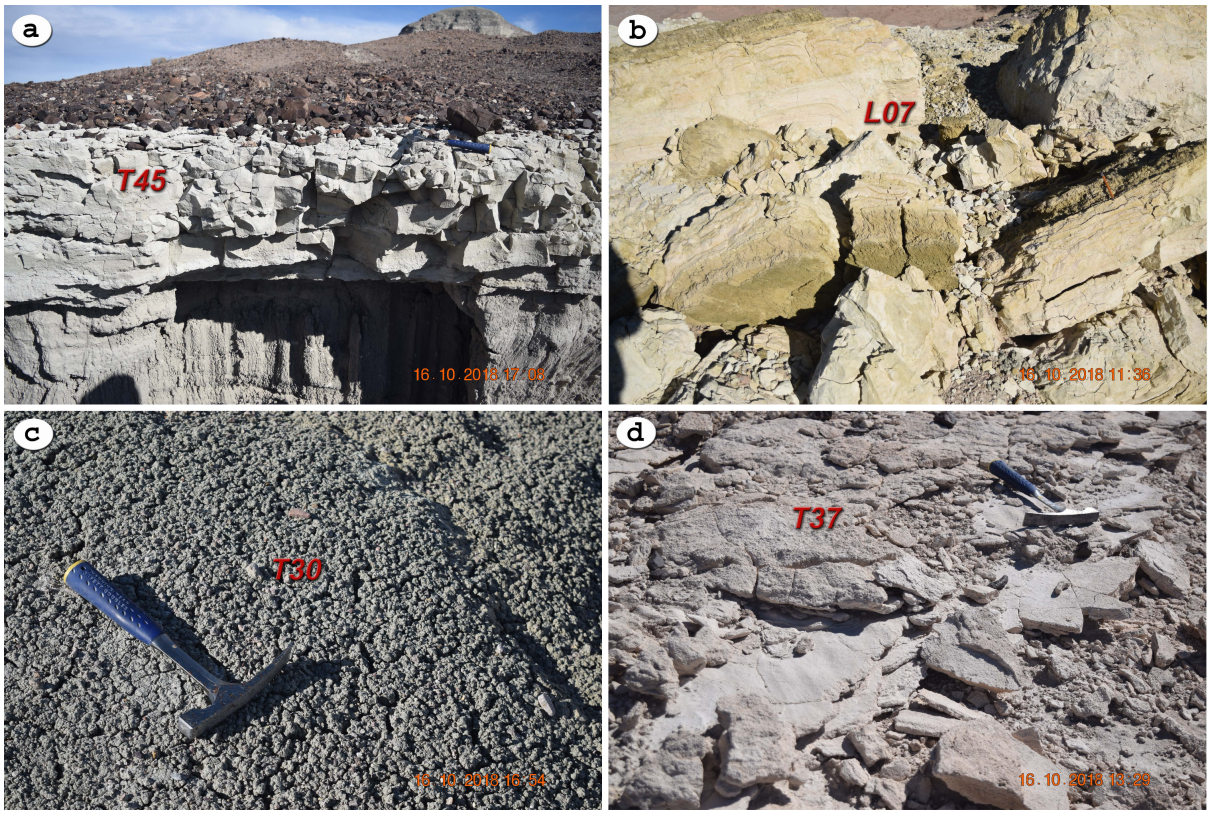

Figure 2.10: Sedimentary beds in upper levels of Lake Tecopa. Less altered welded tuff beds (a), zeolitized tuff beds (b), clay beds (c), and sandstone beds (d).

2.4.3 Imaging observations from in situ data (spatial resolution ~ 1 nm to ~ 1 cm)

Figure 2.11 shows the microphotographs of tuff, altered tuff, zeolitized tuff, and mudstone for detailed textural analysis. Tuff sample T45 (Fig 2.11a) shows layering with different colors and cavities. The layering in this rock might indicate different ash beds with compositional, textural, or time differences. This tuff is a vitric tuff, but also contains varying amounts of crystal and rock fragments. Altered tuff in Figure 2.11 (b) shows pastel shades of yellow, orange, and green color, and the original textures and sedimentary structures of the tuffs are preserved in the zeolite bed. Figure 2.11 (c) shows the fine-grained altered tuff bed T25. The microphotograph of mudstone is shown in Figure 2.11 (d) and is characterized by earthy luster and light green or pale greenish-yellow color.

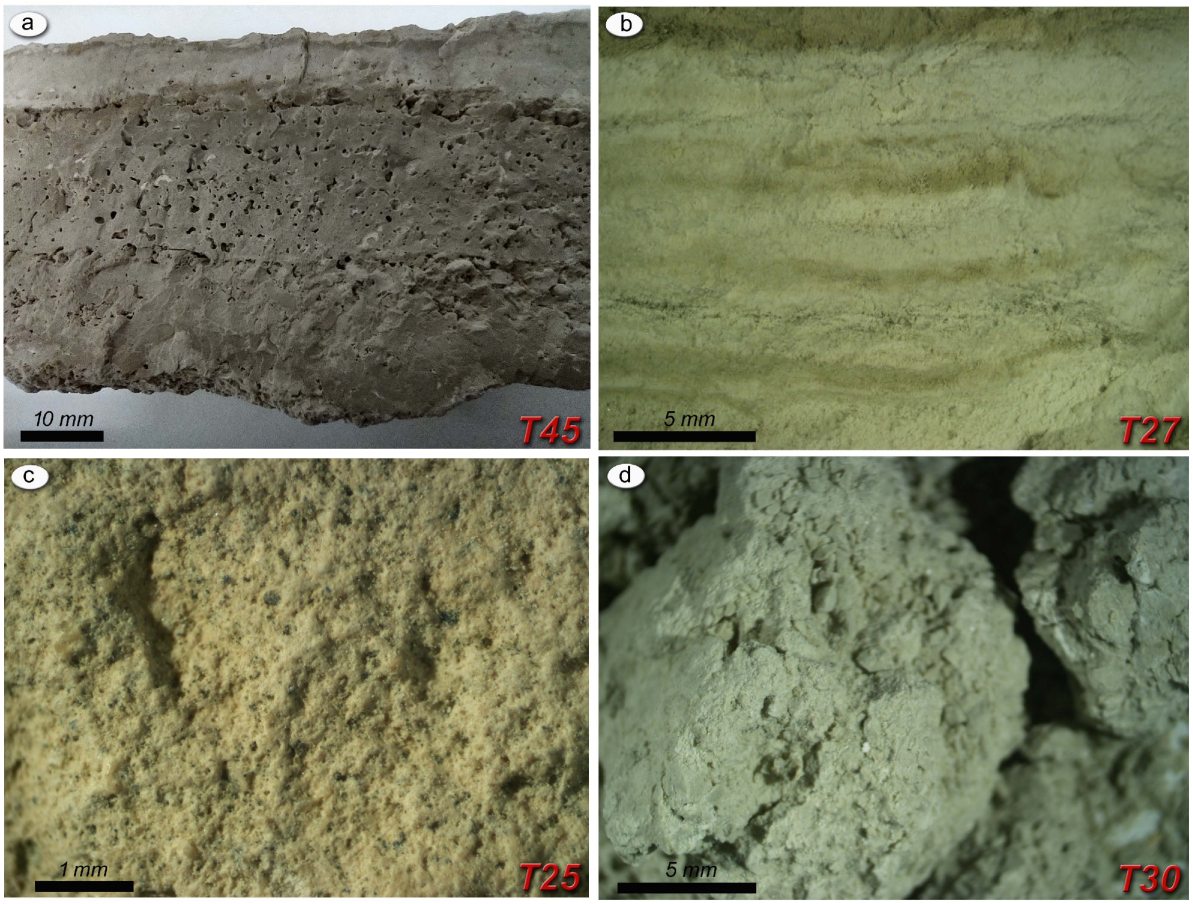

Figure 2.11: (a) Fresh vitric tuff bed T45, (b) Microphotographs of zeolitized tuff sample T27. (c) Microphotograph of altered tuff sample T25. (d) Microphotograph of T30 mudstone sample.

2. The study of the paleolake basin at Lake Tecopa using orbital and Mars rover-like instrument data.

The SEM images of the T45 fresh tuff sample are shown in Figure 2.12. Lithic fragments and glass matrix of the sample is shown in Figure 2.12 (a). Silica (Fig 2.12b), opal-CT and Feldspar (Fig 2.12c), and phillipsite (Fig 2.12d) can be identified based on their crystal morphologies captured by SEM and chemical composition analyzed by EDS. Opal-CT shows lepispheres (a Greek word for spheres of blades) composed of microspherical interpenetrating plates or blades (Dixon and Weed, 1989). It shows that Opal-CT formed after the deposition of volcanic ash. The opal-CT (cristobalite) can form from the Si with the dissolution of pyroclastic glass, pre-existing quartz, biogenic opal, siliceous microfossils, or clay minerals, depending on local chemical and physical environmental conditions (Dixon and Weed, 1989). Intergrowth of feldspar with opal-CT implies that feldspar also authigenically formed under these conditions. Authigenic feldspar has been identified in Tecopa tuff samples using SEM and XRD methods in previous studies (e.g., Larsen (2008)). The alteration product of tuff, authigenically formed phillipsite, was also identified in these cavities (Fig 2.12d). This shows the commonly observed authigenic mineral formation process in saline-alkaline lakes starting with fresh glass to zeolite minerals (phillipsite in this case) and then to authigenic K-feldspar, with the increase of salinity of water in the pore spaces (cavities) of these samples.

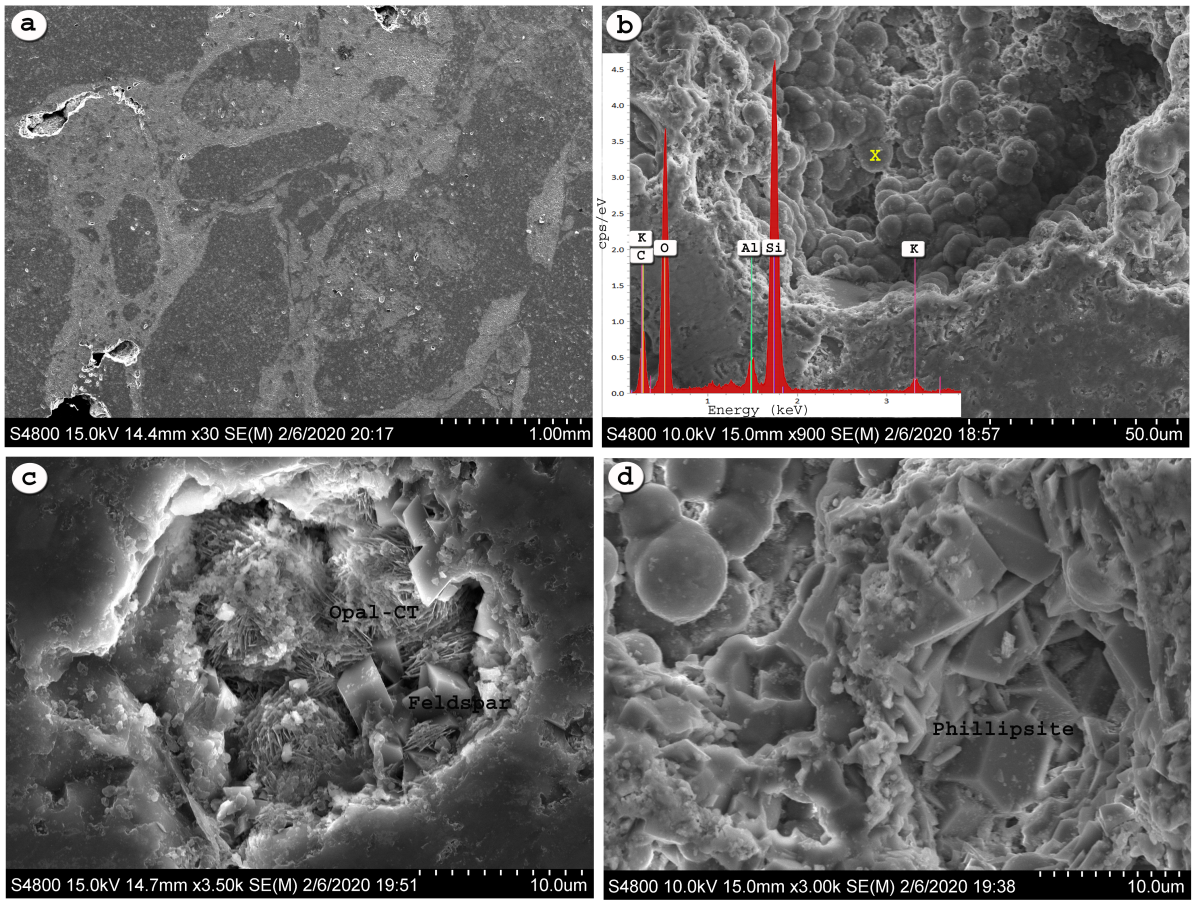

Figure 2.12: Scanning electron micrographs (SEM) of fresh tuff sample T45. (a) SEM image showing large lithic fragments and welded glass matrix, (b) silica in a cavity. Yellow X indicates the location of energy dispersive X-ray (EDS) spectra that assist with mineral identification, (c) Opal-CT and feldspar crystal growth in a cavity, and (d) phillipsite and silica.

2.4.4 non-imaging observations

Mineralogical study using XRD

The XRD patterns of eight representative samples (T25, T27, T29, T30, T37, T38, T39, and T45) are shown in Figure 2.13. Sample T25 is altered tuff beds with symmetrical ripple marks (Fig 2.9d). This sample mainly consists of K-feldspar, in addition to illite, smectite, and albite. Sample T27, from the yellow altered tuff bed, contains mainly clinoptilolite and phillipsite. Sample T29 is the fine-grained sandstone+tuff found between the tuff bed and sandstone. Searlesite ($NaBSi_2O_5.H_2O$) is observed in this sample in addition to phillipsite, K-feldspar, smectite, quartz, and calcite. Sheppard and Gude (1968) found that searlesite is commonly associated with zeolites and/or K-feldspar in Lake Tecopa tuff

beds. They also observed the replacement of phillipsite by K-feldspar and searlesite in thin sections of some Tecopa tuff beds. Sample T30 was selected from the green mudstone bed and contains mainly calcite and smectite. As documented by Larsen (2008); Sheppard and Gude (1968); Nelson et al. (2001), greenish to gray mudstone commonly contains more trioctahedral smectite and calcite than in other mudstone, suggesting open-deep water conditions. Sample T37, a light-gray to pinkish-gray sandstone sample, interbedded with mudstone, mainly contains quartz, calcite, phillipsite, and albite, and a small amount of smectite. It represents the shallow lacustrine environment according to Larsen and Olson (2019). Sample T38, a light-green sandstone sample, mainly contains quartz and phillipsite. Altered light green tuff sample T39, which shows lamination and bedding, is composed of calcite, phillipsite, K-feldspar, smectite, and opal-CT. Phillipsite, K-feldspar, and opal-CT were also identified in SEM images of fresh tuff sample T45. Sample T45, a white sample from the tuff bed, consists mainly of sanidine and various silica varieties. Though the SEM image of T45 shows phillipsite, the XRD pattern did not capture it most likely due to very low abundance. Relative mineral abundances in each sample are tabulated in Table 2.4, which shows that illite tends to dominate the K-feldspar and albite mineral facies. The formation of illite is favored by a high K/Mg ratio and salinity, and likely results from neoformation from the most saline pore-fluid compositions (Hover and Ashley, 2003). The association of authigenic K-feldspar and illite in the central part of the Tecopa basin are interpreted to reflect reaction with the most concentrated pore waters as in other saline-alkaline environments (Larsen, 2008; Turner and Fishman, 1991; Stamatakis, 1989a).

However, illite, kaolinite, chlorite, and dioctahedral aluminous smectite have been described as common detrital clay components of terrigenous mud in many modern lake basins (Calvo et al., 1999). Chamley (1989) noted that clay associations in many modern saline lakes are detrital and simply reflect the mineral suites resulting from river discharge, rain wash, and aeolian transport. The distinction between detrital and authigenic clay minerals is often difficult (Calvo et al., 1999). Therefore, the presence of zeolite and their spatial distribution in the basin can be used to infer the origin of these deposits. It is also important to note that in ancient lake deposits, the highly soluble minerals are often missing due to dissolution by circulating groundwater or dissipated by diffusion into

neighboring rocks. In addition, some primary salt minerals may have been replaced by secondary, diagenetic minerals (e.g., dolomite, glauberite, and gaylussite) (Einsele, 2000).

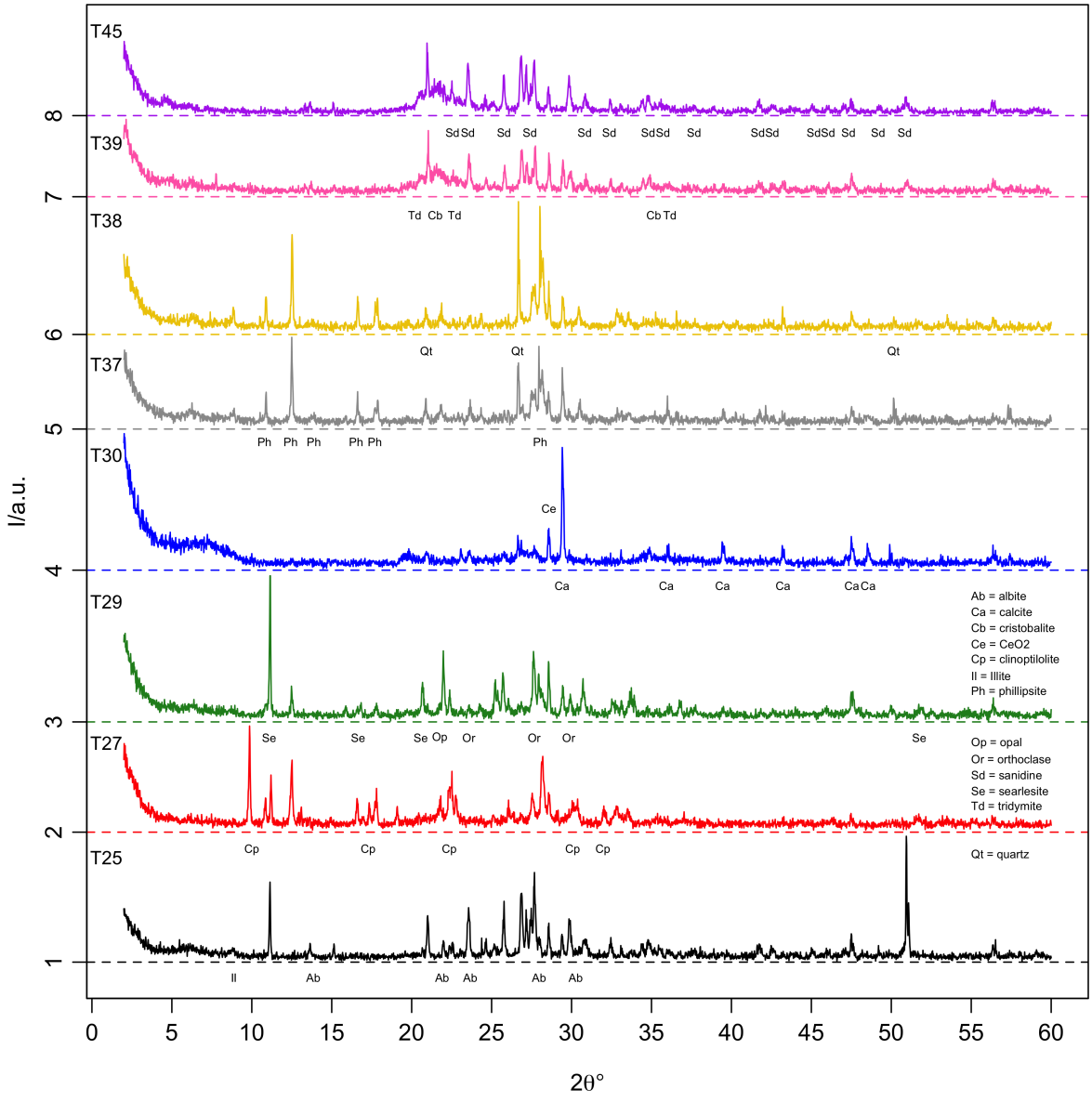

Figure 2.13: XRD patterns for selected field samples

Table 2.4: Bulk mineral composition of the selected field samples

Sample	T25	T27	T29	T30	T37	T38	T39	T45
Lithology	tuff	tuff	ss+tuff	mdst	ss	ss	tuff	tuff
Quartz			x	x	xx	xx		
Calcite			x	xxx	xx	x	x	
Phillipsite		xx	x		xx	xx	x	
Clinoptilolite		xxx						

Sample	T25	T27	T29	T30	T37	T38	T39	T45
Albite	x				xx	x		
Orthoclase	xxx		x	x			x	
Sanidine								x
Illite	xx	x		x	x	x		
Smectite	x		x	xx	x	x	x	
Searlesite			xx					
Tridymite								x
Opal-CT							x	x
Cristobalite								x

Lithological Abbreviations: ss - sandstone, mdst - mudstone, tuff - tuffaceous, Abundance: xxx - abundant, xx - minor, x - trace.

Geochemical study using XRF

Bulk chemical analyses of selected field samples are given in Table 2.5. All samples analyzed by XRF have around 50 % or more SiO_2. The Al_2O_3 percentage was lowest in the green mudstone (T30), whereas the samples with feldspar (T25 and T37) or zeolite (T27, T38) have higher Al_2O_3 percentages, as expected. Sample T29, which contains abundant searlesite, has the highest amount of Na_2O from all samples. The highest percentage of K_2O is found in the altered tuff rich in K-feldspar (T25). The highest percentages of MgO and CaO are in T30 mudstone sample, due to its high calcite abundance. T45, the fresh tuff sample, has a rhyolitic composition. The total Fe is reported as Fe_2O_3 and no samples have Fe_2O_3 higher than 4 percent.

Table 2.5: Elemental compositions of the selected field samples

Sample	T25	T27	T29	T30	T37	T38	T39	T45
SiO_2	59.14	66.80	57.62	47.48	57.61	60.97	70.60	79.81
Al_2O_3	12.04	12.50	8.06	6.77	12.93	13.32	8.39	8.79
Na_2O	2.90	4.59	7.76	2.39	2.39	3.45	0.55	0.36
K_2O	9.82	4.96	4.51	4.01	5.20	5.46	7.12	7.88
MgO	1.67	0.54	1.56	11.15	2.03	1.72	1.14	0.21
CaO	3.13	0.26	2.42	10.87	6.46	3.27	3.78	0.29
Fe_2O_3	1.44	1.85	1.54	2.36	2.28	2.19	1.60	0.28
TiO_2	0.15	0.14	0.15	0.24	0.35	0.33	0.12	0.02
P_2O_5	0.05	0.03	0.03	0.06	0.10	0.08	0.03	0.01
MnO	0.06	0.03	0.04	0.06	0.05	0.06	0.04	0.01

Sample	T25	T27	T29	T30	T37	T38	T39	T45
Total	95.83	98.82	92.24	99.13	98.10	97.41	98.38	99.37
Other	0.10	0.10	0.14	0.22	0.20	0.17	0.17	0.18
LOI	5.32	7.02	8.40	13.52	8.50	6.38	4.84	1.53
H_2O	0.71	7.24	2.81	4.18	3.09	4.04	1.19	0.95

To infer chemical variations during lake diagenesis, the compositions of these samples were compared based to their SiO_2, alkali and alkaline-earth elements. Oxide ratios were used in this analysis. Al and Ti oxides were assumed to be immobile during the alteration process due to their low solubility. Therefore, $Al_2O_3 + TiO_2$ values were used as the denominator. Plots are shown in Figure 2.14. Fresh vitric tuff T45 has the highest $SiO_2/(Al_2O_3 + TiO_2)$ ratio, while T29, a sandstone+tuff sample, has the highest $(Na_2O + K_2O)/(Al_2O_3 + TiO_2)$ ratio due to the presence of searlesite. Sample T25, an altered tuff mainly composed of K-feldspar and illite, has a relatively high $(Na_2O+K_2O)/(Al_2O_3+TiO_2)$ ratio. This shows that $SiO_2/(Al_2O_3+TiO_2)$ and $(Na_2O+K_2O)/(Al_2O_3 + TiO_2)$ ratios decrease with increasing degree of alteration in tuff from fresh tuff (T45) to highly zeolitized tuff (T27). Figure 2.15 (b) shows the relations between $(CaO + MgO)/(Al_2O_3 + TiO_2)$ and $(Na_2O + K_2O)/(Al_2O_3 + TiO_2)$ ratios of samples. A comparison for alkali and alkaline-earth elements shows a significant loss of alkalis from alteration of tuff to zeolites. Sample T30, a green mudstone, has the highest concentration of alkaline-earth elements, mostly due to the presence of calcite. In plot b, four clearly demarcated clusters can be seen: 1) quartz rich sandstone with a low concentration of alkali elements, 2) Na rich searlesite containing tuff+sandstone, 3) tuff samples with different degrees of alteration, and 4) mudstone with high concentrations of calcium (due to the presence of calcite).

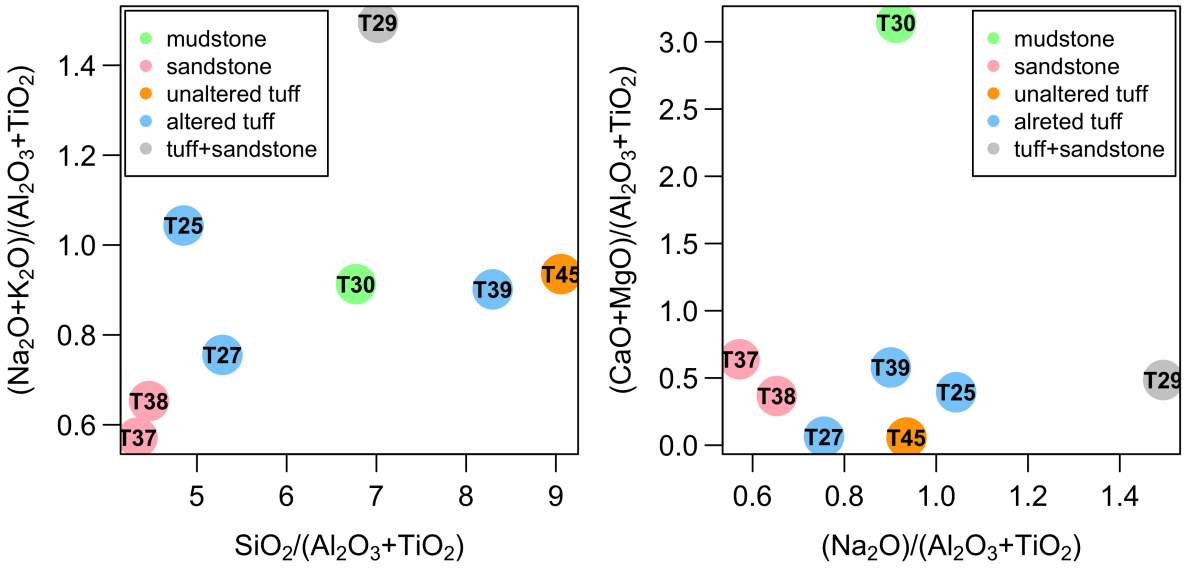

Figure 2.14: a) The plot $(Na_2O + K_2O)/(Al_2O_3 + TiO_2)$ versus $SiO_2/(Al_2O_3 + TiO_2)$ in the fresh tuff, zeolitized tuff, sandstone and mudstone samples from the study area, and b) The relations between $(CaO + MgO)/(Al_2O_3 + TiO_2)$ and $(Na_2O + K_2O)/(Al_2O_3 + TiO_2)$ ratios of samples analyzed in this study.

Smykatz-Kloss and Roy (2010) discussed the applicability of the simple geochemical approach of using the ratios of soluble/insoluble elements to characterize the paleoclimatological events, especially in arid environments where lack of preservation of biological proxies such as pollen, diatoms, and ostracodes are available. Thorpe et al. (2021) calculated the chemical index of alteration (CIA) for weathering profiles and fluvial sediments to better constrain the relationship between climate and chemical weathering in mafic terrains using samples from Idaho and Iceland and data from Gale crater, Mars. Their results show that the CIA values of terrestrial sediments from basaltic watersheds can be reliably used as a climate proxy and extended to Mars. Therefore, chemical indices calculated from elemental compositions of the field samples can be used to reconstruct the hydrological and climatological conditions in the lake history.

VNIR-SWIR Spectral Analysis

Reflectance spectroscopy is the study of light as a function of wavelength that has been reflected or scattered from a solid, liquid, or gas (Clark, 1995). This technique has been widely used to remotely identify the mineral composition, water-ice content, and

atmospheric composition of terrestrial and extraterrestrial environments. Goudge et al. (2017) studied the ~ 40,000 years old lake sediment record from Lake Towuti, Indonesia using VNIR reflectance spectroscopy and showed its capability for reconstructing paleolake environments on Earth and its potential for paleolakes on Mars. Arnold et al. (2021) demonstrated the use of the reflectance spectra (0.25 - 17 μm wavelength range) of 35 lacustrine sediment core samples from the Chew Bahir Basin, southern Ethiopia for climate proxy studies. They identified four absorption bands at 2.2 μm (Al-OH), at 2.3 μm (Mg-OH), at 1.16 μm (analcime), and at 3.98 μm (calcite) as spectral indicators for paleoclimate reconstructions and showed the very good agreement between the geochemical and hyperspectral mineralogical results.

Figure 2.15 shows the reflectance spectra collected for this study. The spectra show prominent absorption features at 0.62 μm, ~1.00 μm, 1.42 μm, 1.80 μm, 1.91 μm, 2.21 μm, 2.31 μm and 2.39 μm. All spectra show absorption features at 1.4 μm and 1.9 μm, due to the presence of hydroxyl ($O-H$) and/or water ($H-O-H$) in samples. The absorption bands around 0.62 μm and 1 μm in sample T27 and T39 indicate more Fe^{2+} and Fe^{3+} content. This could be visible using multispectral Mastcam-Z data on the Mars Perserverance rover at Jezero crater (multispectral band positions of Mastcam-Z are shown in black points in Figure 2.15). The absorption features near 1.417 μm and 1.910 μm are due to the bound water typical of montmorillonite (Hunt and Salisbury, 1970; Bishop et al., 1994). The absorption band near 2.2 μm is due to the OH stretch plus Al-OH bend in montmorillonite (Bishop et al., 1994). A broad absorption feature at 2.2 μm observed in T45 is attributable to Si-OH rotation plus stretching (Rice et al., 2013). The absorption feature at 2.3 μm, observed in spectra of T30, T38, and T39 can be attributed to the combination tones involving vibrations of the carbonate group (Clark et al., 1990; Gaffey, 1987). However, sample T37 does not show a clear absorption feature at 2.3 μm, though the sample contains calcite. Perseverance's SuperCam IR passive range of 1.3 - 2.6 μm extends beyond the maximum range of the ASD spectrometer, providing the opportunity to identify carbonate minerals based on the absorption feature centered from 2.5 - 2.6 μm (Martin et al., 2020). Sample T27, a zeolitized tuff sample containing phillipsite and clinoptilolite, does not show characteristic absorption features in the measured wavelength

region. The spectral data shows the difficulty of identifying mineral composition based solely on spectral data due to the complex nature of mineral mixing.

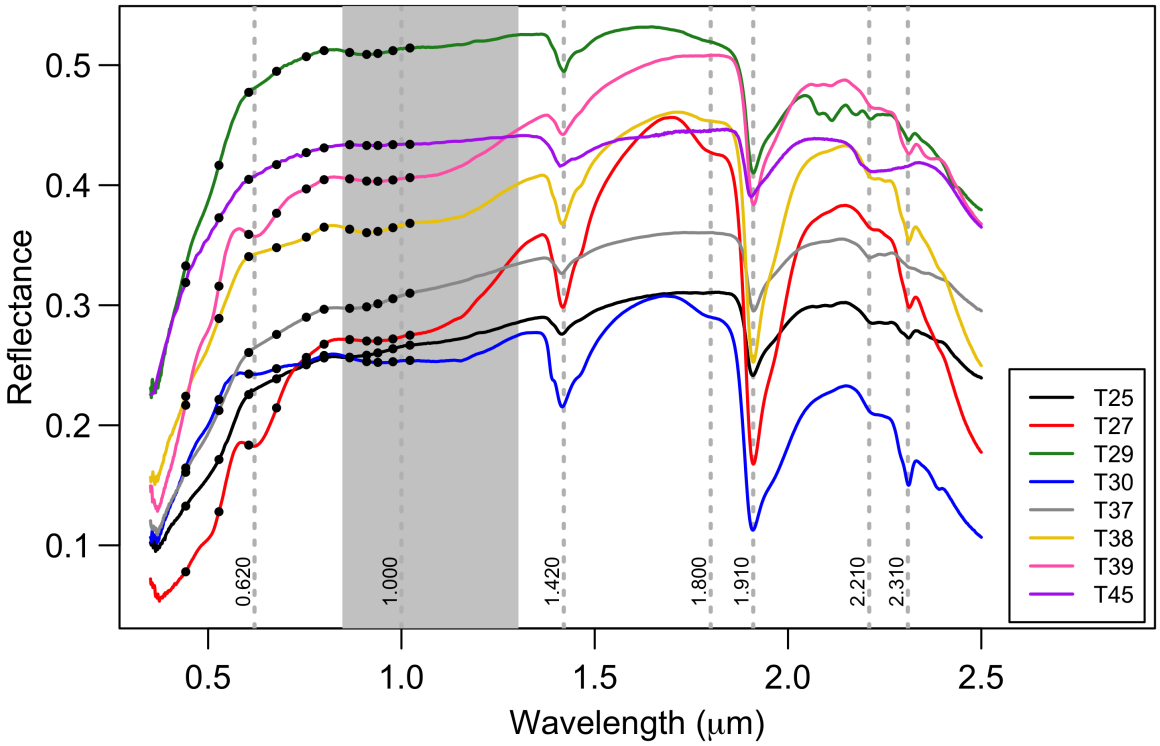

Figure 2.15: Reflectance spectra of collected samples. The position of Mastcam-Z multispectral filters are shown as black dots. The light gray region indicates a gap in SuperCam passive coverage. The collected ASD spectra extend to 2.5 um, though the SuperCam passive IR range extends to 2.6 um.

Understanding how 1.4 μm and 1.91 μm absorption features change as a function of water content will provide a useful tool for mapping surface hydration on Mars (Milliken and Mustard, 2005; Pommerol and Schmitt, 2008; Rice et al., 2013). Figure 2.16 shows the correlation between the absorption band depths at 1.422 and 1.910 μm of each sample with their water content. The coefficient of determination values (R^2) of best fit lines is also shown in each plot. The absorption band depth at 1.910 μm shows higher correlation with the water content than the absorption band depth at 1.422 μm. Spectra acquired from sample T30 show more dispersed data points, likely due to the water adsorbed on the grain surfaces (humidity). Clay minerals can hold varying amounts of H_2O, including water that is bound to the inter-layer (between tetrahedral-octahedral-tetrahedral) surface,

inter-layer cations, bound to other water molecules, and adsorbed on the grain surfaces (Bishop et al., 1994). The zeolite is a framework silicate consisting of interlocking SiO_4 and AlO_4 tetrahedra that form large open channels and voids in their structure in which H_2O can be stored (Milliken and Mustard, 2005; Armbruster and Gunter, 2001). The depth of these absorption features is changed not only due to the water content in the sample, but also due to the particle size, sample albedo, and nature of sample mixing and also depends on the criterion used to calculate the band strength (Pommerol and Schmitt, 2008). More discussions on the spectral identification and quantification can be found in Chapter 3 and 5, respectively.

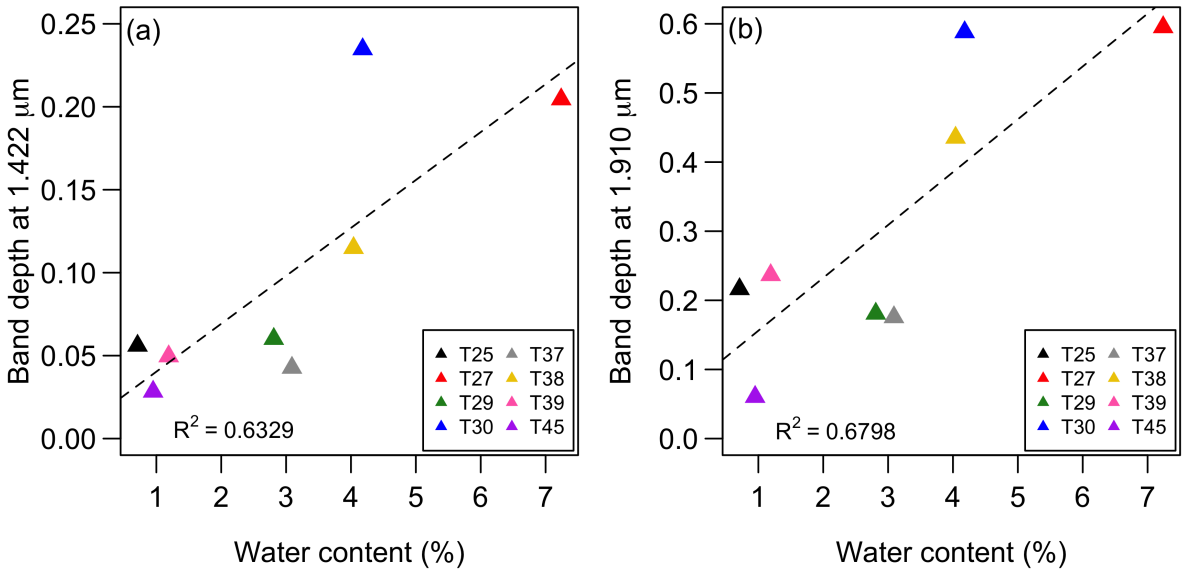

Figure 2.16: Plots of absorption band depths versus water content in the region of a) 1.422 um region, b) 1.910 um region and c) 2.800 um region. Dashed lines show the best fil line of all the samples.

In this study, the identification of an "unidentified" (presumed) paleolake basin starts with hydrological modeling using a DEM to try to determine how water flows and accumulates in the area. For Tecopa, the area resembles a valley instead of a basin due to extensive erosion at the outlet. Extensive fieldwork by Morrison (1999) noted that it is impossible to determine whether the breaching was due to lake overflow or stream erosion or both because relevant deposits and landforms have been entirely eroded from the threshold area. The varying elevations of shorelines (and their associated

shoreline deposits) at Lake Tecopa have long complicated the reconstruction of its lake history, even with substantial fieldwork (e.g., Reheis et al. (2020); Morrison (1999); Larsen (2008)). Previous studies used different techniques to reconstruct the lake history including sedimentological approaches (e.g., Morrison (1999)), sedimentological and mineralogical approaches (e.g., Larsen (2008)), biological indicators (e.g., ostracodes), and uranium-series and luminescence dating (e.g., Reheis et al. (2020)).

At the orbital scale, it was difficult to identify shoreline features and therefore different elevation values were tested with the published map to identify the maximum lake water level and then the boundary of the lake area. The orbital and ground-based images show deep erosion and extensive badlands, exposing a complex stratigraphic record. Different erosional and depositional features with their relative sizes and associations were identifiable using the 3-D model created. Four depositional terraces were identified. Sedimentary environments and structures, such as saline mudflat, dry mudflat, mud cracks, alluvial fans, paleo-channels, ripple marks, and horizontal bedding were observed by ground-based images, confirming the existence of a paleolake. The mineralogy identified from Lake Tecopa beds in this study includes detrital and diagenetic (authigenic) components. The detrital minerals are present as individual grains or in polymineralic rock fragments (e.g., quartz, plagioclase feldspar, mafic silicates), while diagenetic and authigenic minerals precipitate within the sediments due to chemical reactions between pore water and sediments (e.g., zeolites, searlesite, authigenic K-feldspar) (Larsen, 2008). Most of the clays in continental environments are of detrital origin and are supplied to basins in periodic flooding or episodic discharges (Calvo et al., 1999). The presence of authigenic silicate minerals such as zeolites and authigenic K-feldspar, along with their distribution, can be used to infer the ancient lake level and thus paleohydrology.

2.5 Lessons Learned

Lessons learned during this study are as follows,

1) Digital Elevation Models (DEMs) can be used to create geomorphological maps more quickly than by field survey. DEMs are essential for identifying and mapping

paleolake basins and associated erosional and depositional landforms. However, the spatial resolution and noise associated with DEMs may limit their use for identifying and characterizing paleolake basins, leading to false-negative errors. Identifying paleolake margins from orbital data depends on the presence of shoreline deposits and their "visibility" to orbital sensors. Therefore, DEMs cannot substitute the experience and outcomes of field mapping, and remote observations should be ground-truthed where possible in test areas.

2) High-resolution orbital data are useful for identifying erosional and depositional landforms in paleolake deposits. The identification of terraces, erosional slopes, alluvial fans, mesas, buttes, pediments, valleys, and braided channels is important to reconstruct the history of the basin. 3-D models created from high-resolution data with DEMs substantially improve the ability to read landscapes.

3) High resolution images cannot always be used to identify sedimentary facies, mostly due to limited spatial resolution. The textural characteristics of an outcrop, including lithology, grain size, and internal structures, are important to characterize the depositional environment and, cannot be readily extracted from orbital images. Ground-based observations, in this case, provide the best platform to identify and characterize sedimentary facies and structures.

4) The nadir-looking viewing geometry of orbital imaging sensors also limits the amount of information that can be extracted from orbital data since 3-D outcrops are difficult to observe using nadir-looking data. Though the ground-based observations provide a breadth of surface coverage with fine-detailed observations, they provide only limited visual range and cannot provide the coverage available from horizontal viewing geometry. Therefore, the combination of orbital and ground-based observations provides the best set of information to reconstruct the history of paleolake.

5) High-resolution close image data provides more information on sedimentary texture and fabric, which are important to interpret the origin of those sediments. High resolution images are also important for classifying sedimentary rocks based on their

grain sizes (e.g., clay, silt, sand). Grain size, shape, and composition are important to infer the maturity of sediments and their formation.

6) XRD is better suited than reflectance spectroscopy to identify the mineralogical composition of the collected samples. Though reflectance spectroscopy provides a quick, non-destructive, and remotely sensed method for mineral identification, spectral mixing limits its ability to identify constituent minerals in a mineral mixture. The chemical indices calculated from the elemental compositions of field samples acquired using the XRF method help to reconstruct the hydrological and climatological conditions over a lake's history.

7) Three diagenetic facies (fresh-glass, potassium feldspar, and zeolite) identified by Sheppard and Gude (1968) are difficult to recognize in the field. Though tuff of the fresh glass facies can be distinguished from those of the zeolite facies from ground-based images, the tuff of the zeolite facies cannot be positively distinguished from those of the K-feldspar facies in the field. Therefore, mineral identification is essential to identify these diagenetic facies.

8) Evidence from SEM and XRD analysis suggests that most of the hydrous minerals in the lacustrine facies are authigenic. Comparison to multi-billion year ancient hydrous minerals on Mars requires consideration of the effects of diagenentic alteration that may modify or obscure primary spatial and stratigraphic mineralogical patterns.

9) To unravel the history of a paleolake basin requires more information, and ultimately field-based mapping, sampling, and analysis by human geologists either physically present or using remotely operated robot geologists.

10) Geologists must deal with systems in which complexity is an essential character at different levels. It is important to understand not only the substances that constitute the grains, matrix, cements, and interstitial fluids of sedimentary rocks but also the ways these minerals are made, organized, and assembled into bodies of rock. It is more difficult in extraterrestrial studies since it is difficult to get a clear picture of

2. The study of the paleolake basin at Lake Tecopa using orbital and Mars rover-like instrument data.

the entire system with the same details as we have in the field. 3-D digital outcrop models with virtual reality might help.

Acknowledgements

Field work was supported by a grant from the Wisconsin Space Grant Consortium to Dr. Lindsay J. McHenry. The authors also would like to thank NASA for making orbital image data freely available for research and Thomas McCollom at University of Colorado for acquiring spectral data of samples. Many thanks to the developers who created free and open-source software which I used in this study. Thanks are extended to Dr. John Isbell for a helpful discussion.

"One [way] would be to ascribe to the hypothesis a certain probability–perhaps not a very precise one–on the basis of an estimate of the ratio of all the tests passed by it to all the tests which have not yet been attempted. But this way too leads nowhere. For this estimate can, as it happens, be computed with precision, and the result is always that the probability is zero."

-Karl Popper, 1968, 257-

3

Spectral mapping of zeolite bearing paleolake deposits at Lake Tecopa, California and its implications for mapping zeolites on Mars. 1. VNIR-SWIR wavelength region.

Contents

Abstract **95**
3.1 Introduction **96**
3.1.1 Spectral Identification of Zeolites 99
3.2 Study area **102**
3.3 Data and Methods **107**
3.3.1 Field methods 107
3.3.2 Laboratory methods 108
3.3.3 VNIR-SWIR sample spectra 110
3.3.4 ASTER and Hyperion image data 112
3.3.5 Mapping Methods 118
3.3.6 Attribute Maps 122
3.4 Results **123**
3.4.1 Laboratory Spectra 123
3.4.2 Image Spectra 125
3.4.3 Mapping Results 126
3.4.4 Finding the best mapping product(s) 129
3.5 Discussion **131**
3.6 Implications for Mars **133**
3.7 Conclusions **136**
Acknowledgements **137**

3. Spectral mapping of zeolite bearing paleolake deposits at Lake Tecopa, California and its implications for mapping zeolites on Mars. 1. VNIR-SWIR wavelength region.

Abstract

Zeolites are among the most common authigenic silicate minerals in sedimentary rocks on Earth and are particularly abundant in deposits of saline, alkaline, nonmarine environments. The zeolite mineral analcime has also been detected on the surface of Mars using orbital data. Zeolite detections on Mars are not widespread and most studies conclude that they do not provide evidence for in situ aqueous alteration in open and closed basin paleolakes. This is often attributed to the difficulty of confirming non-analcime zeolite detections due to spectral similarity with polyhydrated sulfate spectra.

Here, other possible reasons that could lead to limited detections of zeolites in paleolake environments were studied using orbital data and a "textbook" terrestrial example, Paleolake Tecopa, California. The spaceborne hyperspectral Hyperion and multispectral ASTER data were used to identify zeolites following X-ray Diffraction (XRD) and visible-near infrared and shortwave infrared (VNIR -SWIR) spectral analysis of collected samples containing zeolites and other associated minerals. Four of the most common spectral mapping methods were used: 1) band ratios, 2) minimum noise fraction, 3) spectral angle mapper, and 4) linear spectral unmixing. The zeolite-rich tuff beds were mapped using the spectral characteristics of the pixels corresponding to a small, abandoned, zeolite-rich quarry in the study area. Field investigations showed that most zeolite-rich beds are buried by other beds or that the areas of exposed beds are mostly smaller than the ground resolution cell (GRC) of the satellite, leading to limited detections. The results imply that the paucity of detected zeolites on Mars, as we see at Lake Tecopa, does not preclude their wider presence, either beneath other materials, obscured by surface dust, or mixed with more spectrally dominant phases.

3. Spectral mapping of zeolite bearing paleolake deposits at Lake Tecopa, California and its implications for mapping zeolites on Mars. 1. VNIR-SWIR wavelength region.

3.1 Introduction

Zeolites are among the most common authigenic silicate minerals in sedimentary rocks on Earth and are particularly abundant in deposits of saline, alkaline nonmarine environments (e.g., Hay (1966)). Zeolites can originate from a variety of precursor materials including volcanic and impact glass, aluminosilicate gels, and aluminosilicate minerals including other zeolites, smectites, kaolinites, feldspars, and feldspathoids (Hay and Sheppard, 2001). Zeolite occurrences on Earth can be classified into six classes: 1) saline-alkaline lakes, 2) alkaline soils and land surfaces, 3) deep sea sediments, 4) open hydrologic systems, 5) products of hydrothermal alteration, and 6) burial diagenesis or low-grade metamorphic environments (Hay and Sheppard, 2001; Langella et al., 2001). Zeolites are both common and widespread in volcanic ash deposits in saline-alkaline lakes and the largest relatively pure concentrations of natural zeolites are found in these environments (Hay, 1966; Hay and Sheppard, 2001). Tuffs deposited in and near saline-alkaline lakes will be altered to different degrees depending on their position within the lake basin, with, 1) an outer zone of glass and/or smectite, where pore fluids are relatively dilute, 2) a zeolite zone of alteration with phillipsite, clinoptilolite, erionite, etc., reflecting elevated pH and salinities, 3) a zone of analcime reflecting higher salinities, and 4) the zone of highest salinity, where tuffs may be altered to K-feldspar, generally located in the central part of the basin (Hay and Sheppard, 2001; Langella et al., 2001). Trauth et al. (2001) analyzed a 60m thick sedimentary sequence in the Ol Njorowa Gorge at the margin of the Naivasha basin, Kenya, using vertical variations of authigenic mineral phases to define the lake level fluctuations and alkalinity changes during last 175,000 - 60,000-year period. Fresh water episodes were characterized by diatomite, unaltered volcanic glass, and the absence of authigenic silicates, while transitions to alkaline episodes (~ 9 pH) were characterized by silicic glass, montmorillonite, and occasional chabazite and phillipsite. Higher alkalinity resulted in the formation of clinoptilolite while the most alkaline pore waters formed analcime. McHenry et al. (2020) studied the mineral assemblages of three paleolacustrine cores from Olduvai Gorge, Tanzania. They reconstructed lake chemistry over time, based on the type of zeolites and their abundance in the lakebed sediments. Zeolites are thus a

useful indicator of saline-alkaline lacustrine environments, which can help us investigate past and present environments of Earth (e.g., Bish and Carey (2001); Chipera and Apps (2001); Surdam and Eugster (1976)) and even Mars (e.g., Bish et al. (2003); Ming and Gooding (1988); Tokano and Bish (2005); Viennet et al. (2017)).

Zeolites have been postulated to be components of Mars regolith (Ackiss et al., 2018; Allen et al., 1981; Basu et al., 1998; Berkley and Drake, 1981; Bish et al., 2003; Cannon et al., 2015; Dickinson and Rosen, 2003; Ehlmann et al., 2009, 2011; Ming and Gooding, 1988; Ruff, 2004; Tokano and Bish, 2005; Viennet et al., 2017). Ruff (2004) documented spectral evidence for zeolites in Mars dust using Mars Global Surveyor Thermal Emission Spectrometer (TES) data, based on their absorption features at 6.134 and 12.048 μm. This could indicate their widespread abundance on the surface of Mars. However, the presence of zeolite in Mars dust is uncertain and disputed (e.g., Bandfield et al. (2003)). Michalski et al. (2005) proposed that silica-rich alteration products such as Al- or Fe-bearing opal, clay minerals, clay precursors, or certain zeolites may be present in dark colored regions of Mars, based on TES data. Bandfield (2008) identified an isolated high silica surface in western Hellas Basin and proposed that the minerals there may be opal, phyllosilicates, or zeolites. Wray et al. (2009) suggested that analcime may be present in the Nili Fossae area based on strong absorption features at 1.4 μm, 1.9 μm and a broad absorption at around 2.5 μm, using Compact Reconnaissance Imaging Spectrometer for Mars (CRISM) hyperspectral data. Ehlmann et al. (2009) identified analcime at craters near the Antoniadi basin, west of Nilli Fossae using CRISM data. Several authors have described the difficulties of discriminating zeolites from polyhydrated sulfates using spectral data (e.g., Ehlmann et al. (2009); Wray et al. (2009); Carter et al. (2013)). Sun and Milliken (2015) presented a global survey of 633 crater central peaks to assess their hydrous minerals using CRISM data and identified zeolites in only 4.5% of cases. They also emphasized the difficulty of identifying and distinguishing zeolites from sulfates and therefore the only zeolite they specifically classified was analcime, classifying the other potential zeolites as unidentified hydrous phases instead. Viviano-Beck et al. (2017) documented zeolites in eastern Tharsis Rise, using subtle spectral differences in 3.4 and 3.9 μm to distinguish zeolite + Mg-phyllosilicate from carbonate spectra. Ackiss et al.

(2018) examined the mineral assemblages detected on possible glaciovolcanic edifices in the Sisyphi Planum region and interpreted the spectral class as a mixture of phases, including smectite, zeolites, and Fe-oxides, based on absorption features at 0.54, 0.94, 1.45, 1.78, 1.93, 2.21, and 2.46 μm of CRISM image spectra. These studies show that zeolites are difficult to identify using VNIR-SWIR and Thermal Infrared (TIR) data. They also show that zeolite detections on Mars are not widespread. Zeolites have not yet been reported in Martian meteorites (Viennet et al., 2017) or in data from landers or rovers.

The climate and hydrochemistry of early Mars remains an intriguing mystery. The ancient terrains of Mars reveal a warmer and wetter climate preserved in a wide array of surface fluvial features including open and closed basin lakes, channels, modified craters, alluvial fans and deltas, though climate models have difficulty generating sufficiently warm conditions to form such features (e.g., Ramirez and Craddock (2018)). Orbital spectral observations of the Martian surface indicate uneven occurrences of aqueously formed minerals in geological formations of different ages (e.g., Noachian alkaline fluids and Hesperian acidic fluids, Zolotov and Mironenko (2016)). Identifying possible paleolakes and ponds on Mars is important because they record the hydrological history of Mars (e.g., neutral, saline, saline-alkaline, or acidic), seasonal and orbital cyclic changes, and geological processes that occurred in the catchment area during their lifetimes (Cabrol and Grin, 2002). Remote sensing orbital data suggest that large bodies of standing water existed on the surface of Mars in its early history (e.g., Cabrol and Grin (2002); Fassett and Head (2008); Goudge et al. (2015); Goudge et al. (2012)). Goudge et al. (2015); Goudge et al. (2012) noted the lack of evidence for widespread in situ aqueous alteration and mineral precipitation (i.e. evaporites) in the open and closed paleolake systems they studied. They interpreted this lack of evidence of alteration minerals and mineral precipitates as due to either water chemistry that was not conducive to their formation, or a short-lived period of lacustrine activity for most lake basins on Mars that did not provide enough time for such deposits to accumulate. Identifying zeolites in these paleolake basins could address both of these arguments.

Zeolites may not be identifiable using orbital remote sensing in certain locations on Earth or Mars, because 1) they are absent or were originally present and later removed

by chemical or physical processes at that location (e.g., resurfacing, dissolution, etc.), or 2) they are present, but difficult to detect and map. In this Chapter, the second possibility is addressed by examining how well orbital remote sensing can identify and map zeolites in paleolake environments on Earth. The hyperspectral Hyperion and multispectral ASTER orbital image data, supplemented by VNIR-SWIR spectroscopy and X-ray Diffraction (XRD) analysis of collected samples, were used to study zeolites and related minerals in a paleolacustrine deposit at Paleolake Tecopa, California. Five fundamental questions to be considered when using orbital remote sensing data to identify and map certain minerals or lithologies were defined: 1) does the mineral in question have unique absorption features that can be used to identify it and distinguish it from other minerals?, 2) are the data sufficiently well calibrated to yield diagnostic spectral shape information?, 3) are the spectral resolution, spatial resolution, and radiometric precision of the data sufficient to identify materials of interest without any field observations and field samples?, 4) is the mineral in question sufficiently abundant to be detected from orbit or are the spectral characteristics of that mineral masked by the spectral features of other minerals in the deposit?, and 5) which spectral mapping methods are most suitable for detecting, identifying, and mapping those mineralogical and lithological variations based solely on the available data?

To answer these questions, the physical and chemical properties of the zeolite minerals with their spectral characteristics is discussed in section 1. Section 2 presents the geology of the Paleolake Tecopa area. Questions 2, and 3, pertaining to the sufficiency of the calibration and resolution of the available data, are addressed in Sections 3 and 4. Questions 4 and 5, regarding the spatial resolution and the selection of mapping methods, are discussed in Sections 4 and 5. Section 6 discusses the implications for Mars and section 7 describes the conclusions of this study.

3.1.1 Spectral Identification of Zeolites

The spectral characteristics of the most common zeolite minerals in closed hydrologic systems are discussed here. The spectra were taken from the RELAB Spectral Database (`http://www.planetary.brown.edu/relab/`). Figure 3.1 shows the reflectance spectra

of selected species in the VNIR-SWIR wavelength range (0.3 - 4.0 μm). A polyhydrated sulfate spectrum (epsomite) is also included in the plot to show the spectral similarities between zeolites and polyhydrated sulfate spectra. Heulandite and stilbite show weak absorption features in the 0.97 μm region. This feature is attributed to the second overtone of the O-H stretch (Clark et al., 1990). Most of the zeolite spectra exhibit a weak, narrow absorption feature near 1.160 μm. This can be attributed to a combination of a symmetric O-H stretch (v_1), an asymmetric O-H stretch (v_3), and the H-O-H bending fundamental (v_3) (Bishop et al., 1994; Cloutis et al., 2002; Hunt and Salisbury, 1970). Cloutis et al. (2002) noted that the wavelength position of the 1.16 μm band generally increases as the major cation weight percent in the mineral increases. In Na- and K-rich zeolites, the band occurs between 1.155 and 1.160 μm, while in Ca-rich zeolites it occurs between 1.160 and 1.180 μm. This absorption feature occurs at generally longer wavelength in those zeolites with larger voids, consistent with less hydrogen bonding to cations expected in such zeolites (Cloutis et al., 2002). All the spectra show a strong absorption band near 1.427 μm and a weak absorption band near 1.460 μm. The 1.427 μm band is attributed to a bound H_2O combination band, while the 1.460 μm band is assigned to an adsorbed H_2O combination band (Bishop et al., 1994). These features involve an H_2O stretch plus the first overtone of the H_2O bend ($v_w + \delta_w$) (Bishop et al., 1994; Cloutis et al., 2002). Spectral absorption due to H_2O stretching vibrations are labelled v_w and those due to H_2O bending vibrations are labelled δ_w. Zeolites also exhibit a weaker absorption band near 1.78 μm ($2\delta + v_1$ or v_3) (Cloutis et al., 2002). Absorption bands near the 1.9 μm wavelength region are due to a combination of the H_2O stretching and bending modes ($v_w + \delta_w$) (Clark, 1999; Hunt et al., 1973). The Ca bearing zeolites show an absorption feature near 2.465 μm, and the Na- and K- bearing zeolites display an absorption feature near 2.68 μm (Cloutis et al., 2002). All the reflectance spectra selected for this study, except for analcime, show a broad absorption feature near 2.55 μm, which appears as a prominent inflection on the short wavelength wing of the fundamental H_2O band (Cloutis et al., 2002). Analcime shows a distinctive narrow absorption band at 2.54 μm, which has been used to distinguish analcime from other phyllosilicate minerals (e.g., Sun and Milliken (2015)). The broad region of intense absorption with minima near 2.774 and

3.06 μm are assigned to H_2O stretching vibrations and the first overtone of the H_2O bending vibration, respectively (Bishop et al., 1994; Clark et al., 1990). This shows that the VNIR-SWIR spectra of naturally occurring zeolites are dominated by the vibrational absorption features associated with zeolitic waters, as in other hydrous minerals.

It is important to note that one of the characteristic absorption features of zeolites, centered at ~ 2.5 μm, is not covered by either ASTER or Hyperion image data. Additionally, absorption features around 1.4 and 1.9 μm are not well covered because of the effects of strong water vapor absorption by Earth's atmosphere. Since both phyllosilicate and zeolite minerals show similar absorption features around 1.4 and 1.9 μm, these two absorption feature are not typically helpful for distinguishing zeolite minerals from other hydrous minerals from orbital data. Despite this limitation it is still possible to distinguish phyllosilicate minerals from zeolites using the characteristic absorption features of phyllosilicates observed near 2.2 to 2.3 μm, which do not appear (or occasionally appear as weak features) in the zeolite minerals identified in this study area. However, if zeolites are mixed with phyllosilicate minerals, they may be difficult to identify them using their mixed spectra.

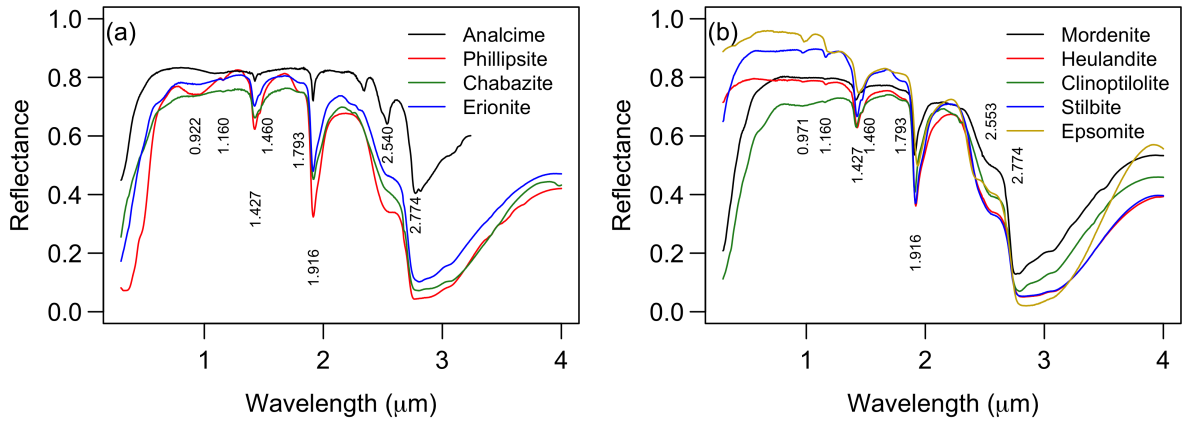

Figure 3.1: RELAB spectra of zeolite minerals (particle size < 45 um) including analcime (laze57), phillipsite (laze23), chabazite (laze17), erionite (laze25), mordenite (laze29), heulandite (laze31), clinoptilolite (laze27), and stilbite (laze21), and polyhydrated sulfate epsomite (799f366).

3.2 Study area

The Tecopa basin in the southeastern part of Inyo County, California is a well-documented example of a terrestrial paleolake sedimentary environment. The early Pleistocene (ca. 2.4 - 1.0 Ma) deposits of the Lake Tecopa beds record deposition in small saline and alkaline lakes and playas with surrounding mudflats, sandflats and alluvial fans (Hillhouse, 1987; Nelson et al., 2001; Sheppard and Gude, 1968). The basin is bordered by Resting Spring Range on the east, Nopah Range on the southeast, Sperry Hills on the south, Ibex Hills on the southwest, and Dublin Hills on the northwest (Fig 3.2a). Rocks exposed in the study area are limestone and rhyolitic to basaltic flows and tuffs in the Dublin Hills and quartzite, limestone, dolostone, volcanic rocks, and several fanglomerate (conglomerate formed from sediments deposited on alluvial fans) units in the Sperry Hills (Morrison, 1999). The sedimentary deposits of the lake are ~100 meters thick and contain at least fifteen ash layers deposited by airfall and redeposited into the lake by fluvial processes (Martin and Bindeman, 2009) along with other fluvial and lacustrine sediments. The general stratigraphy of the Tecopa beds was established by Hillhouse (1987) and Sheppard and Gude (1968) and refined by Morrison (1999), Larsen (2008), and Larsen and Olson (2019). The paleolake beds are currently exposed by erosion across an extensive area,

and the modern desert climate minimizes vegetation cover, making it an excellent site for mineralogical analysis using orbital remote sensing techniques.

Tuff layers are particularly prominent and widespread marker beds in Lake Tecopa, making up about 8-12 percent of the stratigraphic sections (Hillhouse, 1987; Sheppard and Gude, 1968). Sheppard and Gude (1968) designated these tuff layers as Tuff A (Lava Creek B), Tuff B (Bishop ash bed), and Tuff C (Huckleberry Ridge). Tuffs A and Tuff C are light gray and vitric where fresh, and white or orange where altered to zeolites (Hillhouse, 1987; Larsen and Olson, 2019). Tuff B is white and pumiceous with sparse sanidine and biotite crystals where fresh and white to multicolored where altered (Hillhouse, 1987). Tuff B in the southern part of the study area is mostly associated with deep water mudstone (Hillhouse, 1987). Sheppard and Gude (1968) also identified three diagenetic facies in the tuffs of the Lake Tecopa deposits. Tuffs nearest the lake margins are characterized by fresh glass and named the fresh glass facies (Glass in Fig 3.2d). Tuffs in the central part of the lake basin are characterized by potassium feldspar and/or searlesite, and referred to as the potassium feldspar facies (Feldspar in Fig 3.2d). Tuffs between the fresh-glass facies and the potassium feldspar facies are characterized by zeolites and termed the zeolite facies. In the zeolite facies, the tuffs were replaced by zeolites, clay minerals, and locally opal. While thin tuff layers mostly contain one zeolite mineral, most commonly phillipsite, thick tuff layers mostly contain two or more zeolites, most commonly phillipsite and clinoptilolite, in addition to the nearly ubiquitous authigenic clay minerals (Sheppard and Gude, 1968). Calcite and authigenic clay minerals occur in all tuffs throughout the basin regardless of facies, but opal is found only in the zeolite and potassium feldspar facies.

Hillhouse (1987) mapped the late tertiary and quaternary geology of the Lake Tecopa area. The geology of the study area is shown in figure 3.2c. Map units covered by the study area include Holocene alluvium (Qa1), Quaternary alluvium (Qa2), Conglomerate unit (Qtc), and Lacustrine mudstone unit (Qtlm). The Holocene (younger) alluvial deposits consist of unconsolidated sand, silt, and conglomerate in active and recently active stream channels. The washes near the ranges contain a mixture of sand, sub granular cobbles, and boulders of dolomite, quartzite, and basalt (Hillhouse, 1987). In the central part of the Tecopa beds, the recent deposits consist of loose silt and clay, which

form a small playa. The Quaternary (older) alluvium units consist of remnants of alluvial fans that now form prominent mesas and raised areas capped by desert pavement (Fig 3.3). These remnants are generally 1- 10 m high above the active washes and are no longer receiving sediments (e.g., Greenwater Valley). Thickness of this alluvium ranges from a thin gravelly veneer (~ 30 cm) in the central basin to thick wedges (~ 100 m) of bouldery conglomerate at the range front. The clasts consist of sub granular dolomite, quartzite, and silicic volcanic rocks from the surrounding range and zeolitic tuff from the lakebed. The Qa2 is deeply dissected by the modern washes, forming fingerlike mesas near the margin of the lake beds (Fig 3.3c). A distinguishing feature of the Qa2 in the study area is its surface of desert pavement consisting of planar surfaces of densely packed pebbles and cobbles, mostly 2-5 cm in diameter (Hillhouse, 1987). The conglomerate unit, Qtc, covers a very small portion of the study area, at the foot of the Sperry Hills (Fig 3.2c). The unit consists of fanglomerate and pebbly fluviatile deposits that interfinger with the lacustrine mudstone units. The lacustrine mudstone unit (Qtlm) is the most interesting unit for this study since it contains most of the tuff beds (Fig 3.3a and 3.3d). The sediments in this unit have pastel colors ranging from buff and pink near the lake margins to green and brown in the central basin (Hillhouse, 1987). The dominant lithology in the mudstone unit contains clay, silt, and minor amount of sand. The mudstone unit contains calcite, clay minerals, authigenic zeolites, potassium feldspar, and rock fragments. The predominant detrital clay minerals are montmorillonite, illite, and saponite (Starkey and Blackmon, 1979). Sediments along the lake perimeter tend to be richer in calcite than sediments at the center of the basin (Hillhouse, 1987).

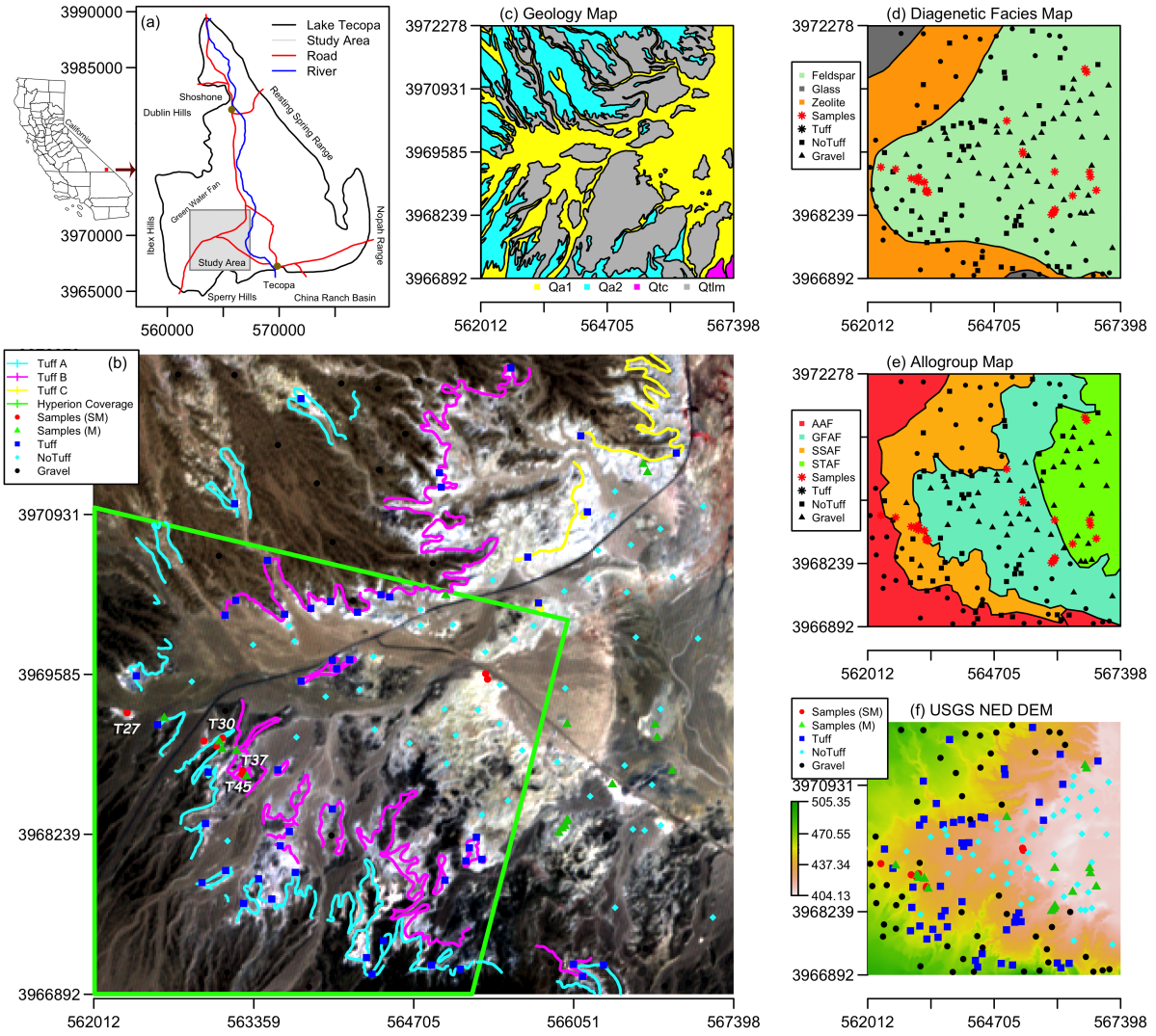

Figure 3.2: Location and geology of Lake Tecopa study area, (a) Location of the study area, (b) sample locations, Tuff beds A, B, and C, and Hyperion image coverage overlay on the ASTER true color composite data (Sample (M): Locations of field samples with their mineral assemblages identified by XRD, Sample (SM): Locations of field samples with their mineral assemblages identified by XRD and spectral data, Tuff: Locations of samples T27 (abandoned quarry reference location), T30, T37 and T45 are shown in the figure; Locations of Tuff bed exposures selected from the Hillhouse (1987) geological map, NoTuff: Locations of the NoTuff class points, Gravel: Locations of the Gravel class points. Additional information in Section 3.5), (c) geological map (after Hillhouse (1987)), (d) diagenetic facies map (after Sheppard and Gude (1968)) with the sample locations, (e) Allogroup Map (after Morrison (1999)) with the sample locations, and (f) USGS National Elevation DEM image of the area with the sample locations (elevation in meters).

Morrison (1999) used the Tuff beds to define the allostratigraphic units in the Tecopa basin based on the physical and mappable boundary criteria instead of lithology, inferred time, or climate, etc. (Fig. 3.2e). The mapped allostratigraphic units are, 1) the Spanish

Trail Alloformation (STAF); the lowest unit in the Lake Tecopa Allogroup (LTAG), including all playa, lacustrine, and subaerial sediments located below the 2.1 Ma Tuff C, 2) the Green Water Fan Alloformation (GFAF), bounded at its base by Tuff C and capped by the 758 ka Tuff B, representing 1.34 Ma, 3) the Shoshone Spring Alloformation (SSAF) between Tuff B and the 665 ka Tuff A, spanning only 93 ka. Uppermost is the Amargosa Alloformation (AAF), comprising all sediments above the base of Tuff A. The AAF spans about 479 ka (Morrison, 1999). The STAF exposures are entirely basin-lowland sediments and consist of siltstone, claystone, mudstone, and some very fine to fine grained sandstones. All exposed strata of this LTAG have undergone various degrees of authigenesis, transforming their original detrital composition into new mineral assemblages. The unit has little quartz but contains authigenic sepiolite, smectite, potassium feldspar, calcite, dolomite, zeolites (mainly clinoptilolite and phillipsite), halite, gypsum, and other saline minerals (Morrison, 1999). The GFAF is composed of three members; 1) lower 10-14 m thick member composed of alternating beds of sandstone, siltstone, and mudstone, 2) 4-10 m thick middle layer consisting of well to thin bedded to laminated mudstone, some siltstone and rarely fine-grained sandstone, and 3) the 10-12 m thick upper member dominated by light to pale gray thin-bedded siltstone, mudstone, and claystone, with some thin- to thick bedded fine to medium grained sandstone, and rarely, pebbly sand and/or pebble gravel (Morrison, 1999). The SSAF on Greenwater Fan, in the northeast part of our study area, consists of gray, thin-bedded, fine grained sandstone rhythmically alternating with laminated siltstone and mudstone (playa and playa margin sediments). The lower part of the Greenwater Fan contains abundant local carbonate and volcanic detritus, and other parts of the SSAF are mostly associated with the deep-water mudstone (Morrison, 1999). The AAF includes pebble gravel, snd, silt, and clay, and these sediments are much less affected by authigenesis than other groups.

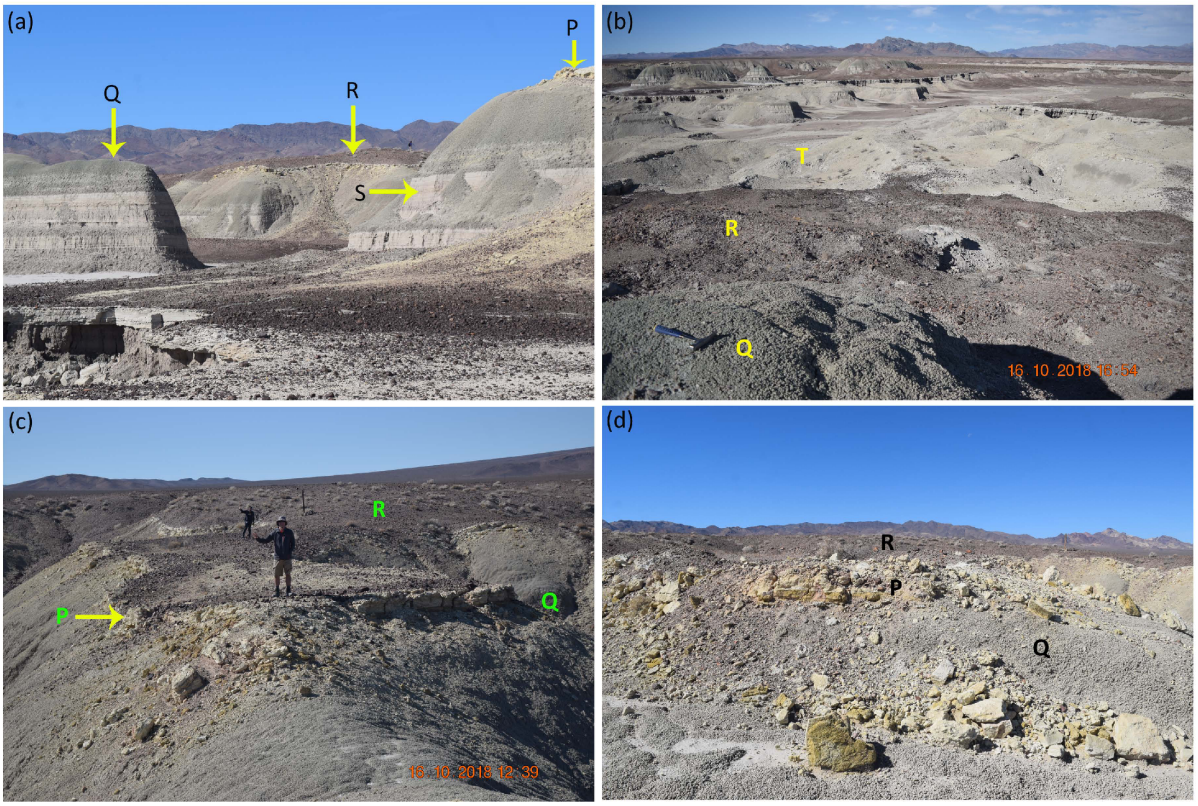

Figure 3.3: Field photos of Lake Tecopa study area showing (a) general stratigraphy, (b) erosional features of the area, (c) thin layer of zeolitic tuff bed covered by thin layer of gravel bed (washes), (d) mixing of zeolitic tuff bed with surrounding mudstone and sandstone beds due to physical weathering. P = Zeolite (tuff) bed, Q = Green mudstone bed, R = gravel pavement, S = sandstone/siltstone beds, and T = mixed sediments from all beds due to erosion and deposition.

3.3 Data and Methods

3.3.1 Field methods

Fieldwork was conducted during October 2018 and 2019. Before the field visits, we identified target field locations using the unsupervised classification mapping results of ASTER and Hyperion image data along with the published geological maps of the area. During the field expeditions, we collected a total of 56 rock and soil samples representing mudstone, siltstone, sandstone, unaltered tuff beds, zeolitized tuff beds, gravels, etc. Every sampling location was documented with detailed field descriptions of morphological features, lithology, thicknesses of the sedimentary beds, location information (GPS), elevations, and field photographs. Rock and soil samples were collected from the center of

patches of relatively homogeneous bare land surface having a spatial extent of at least 20 m radius. Sample T27, from an abandoned quarry in the study area (Fig 3.2b), was selected as a reference site for zeolites due to its large coverage of exposed, relatively fresh zeolitic tuff.

3.3.2 Laboratory methods

The mineralogy of field samples were identified using XRD method. Samples for XRD analysis were powdered by hand and quantitatively mixed with crystalline Cerium (IV) oxide powder ($CeO_2 < 5$ μm) using a 100: 1 ratio of sample to internal standard. Samples were analyzed using a Bruker D8 Focus XRD system (Cu Ka radiation, 1 s per step, 0.01^o 2θ per step,$2^o - 60^o$ range, scintillation detector) and results were compared against the ICDD PDF-2 (International Center for Diffraction Data Powder Diffraction File) library using Bruker's EVA software. Intensities of the characteristic peak of each mineral were measured and relative abundances were calculated based on the normalized relative intensity of the CeO2 peak at 28.585 $2\theta^o$ (Table 3.1).

Figure 4 shows the XRD patterns of four representative samples: T27, T30, T37, and T45. Sample T27 is composed almost entirely of the zeolite minerals clinoptilolite and phillipsite, representing completely altered tuff beds. Sample T30, from a green mudstone bed, contains mainly calcite and smectite. Larsen (2008), Larsen and Olson (2019), and Sheppard and Gude (1968) all found that the greenish to gray mudstone in the Tecopa beds commonly contains more trioctahedral smectite and calcite than in other mudstones in the area, suggesting reactions with less saline water during times with relatively open-deep water conditions. Sample T37, a light gray to pinkish-gray siltstone sample, interbedded with mudstone, mainly contains quartz, calcite, the zeolite mineral phillipsite, and albite, and minor smectite. This represents the shallow lacustrine environment, according to Larsen and Olson (2019). Sample T45 is a white sample from a welded tuff bed that consists of mainly sanidine and different silica polymorphs.

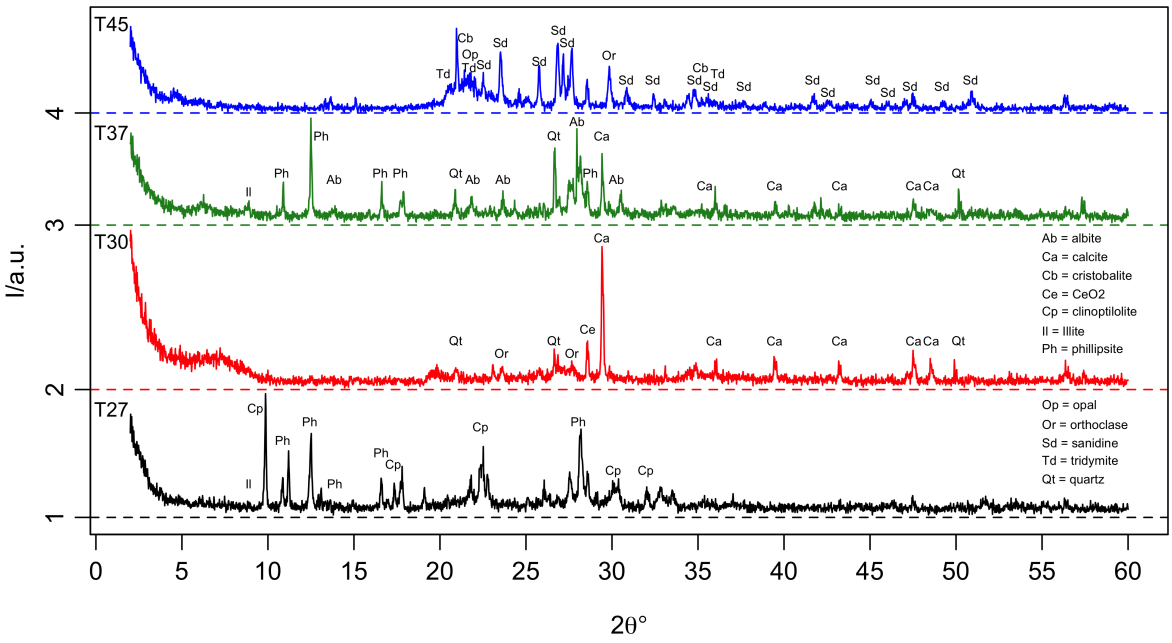

Figure 3.4: XRD patterns for field samples T27 (zeolite bearing altered tuff), T30 (green mudstone), T37(siltstone) and T45 (less altered tuff).

Table 3.1: Mineralogy of selected samples

Sample	T25	T26	T27	T29	T30	T37	T38	T39	T40	T45
Lithology	tuff	ss	tuff	ss+tuff	mdst	ss	ss	tuff	tuff	tuff
Quartz		xxx		x	x	xx	xx			
Calcite		xx		x	xxx	xx	x	x	x	
Phyllipsite			xx	x		xx	xx	x	x	
Clinoptilolite			xxx						xx	
Albite	x	xx				xx	x			
Orthoclase	xxx	x		x	x			x	x	
Sanidine										x
Illite	xx	x	x		x	x	x			
Smectite	x			x	xx	x	x	x	x	
Searlsite				xx						
Tridymite										x
Opal-CT								x		x
Cristobalite										x

Lithological Abbreviations: ss - sandstone; mdst - mudstone; tuff - tuffaceous,

Abundance: xxx – abundant, xx – minor, x – trace.

3.3.3 VNIR-SWIR sample spectra

To characterize the spectral features of the selected samples listed in Table 3.1, preliminary spectra of ten field samples (bulk) were collected using an ASD Field spec reflectance spectrometer at the University of Colorado. After analyzing the spectral characteristics, and considering the sample mineral assemblages and bulk geochemistry, four representative samples (T27, T30, T37, T45) were selected for the rest of the study. These samples were ground to less than 150 μm particle size and their bidirectional reflectance and thermal infrared spectra were measured at the Brown University RELAB facility to acquire the full wavelength range spectra from 0.3 μm to 25 μm. More information on the spectral acquisition procedure are available in the RELAB User's Manual and Instructions (`http://www.planetary.brown.edu/relabdocs/RelabManual2006a.pdf`).

Processing of spectral data

The position, depth, width, area, and shape of absorption features of a given spectrum are mainly controlled by the composition and crystal structure of the absorbing species (e.g., Clark (1999); Van der Meer (2004)). Different spectral analysis techniques such as curve matching (e.g., Clark (1999)), curve fitting (e.g., Brown (2006)), and curve deconvolution (e.g., Sunshine et al. (1990)) were used to identify the mineral composition and their abundances from the spectra. The curve matching method was used here to identify the possible mineral assemblages based on the characteristics of the absorption features using "pure" endmember mineral spectra. A library spectral database was created representing the minerals identified in the study area. Differences in the sample preparation and spectrometry techniques used (along with optical arrangement, scanning time, references used, etc.) for spectral acquisition can make it difficult to compare spectral features from one study to another (Bishop et al., 1994; Clark et al., 1990; Hunt, 1979). Therefore, mineral spectra acquired from powdered samples in the RELAB spectral library database were collected to create our spectral library. The library and sample spectra were imported into the R statistical software package to create a spectral database using the "hsdar" package (Lehnert et al., 2018). Spectra were continuum removed to enhance the absorption features. Two kinds of continuum removal methods are commonly

used: the "upper convex hull" (Green and Craig, 1985) and the "segmented upper hull" (Clark et al., 1987). The main difference between these two is that the resulting continuum line in convex hull must be convex while the resulting continuum line of segmented hull can be convex or concave. Both methods were tested, and the segmented hull method was chosen based on the reduced artifact formed from the continuum line. However, it was found that sometimes this may not represent some local maxima in the original reflectance spectra and can lead to artifacts when the spectrum is divided by its continuum line as shown in Figure 3.5 (a) and 3.5 (b). Therefore, those artifacts were removed by manually removing and adding some points to the continuum line (Fig 3.5c and 3.5d).

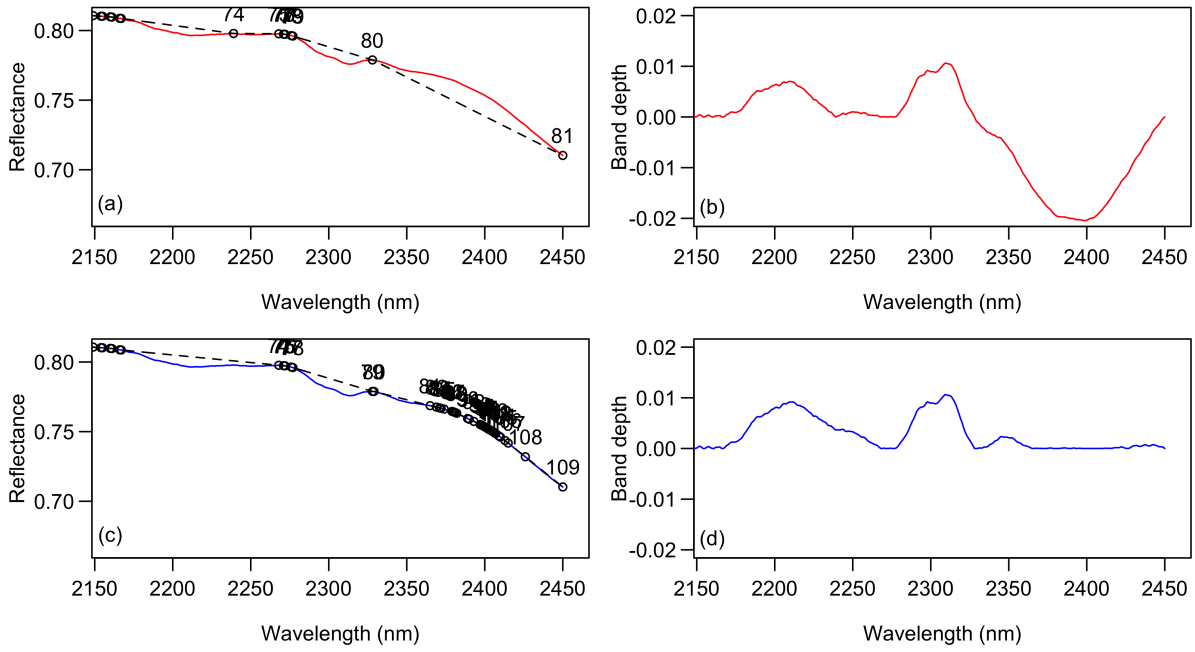

Figure 3.5: Correction of errors associated with calculation of band depths using a continuum line. (a) Original T37 spectrum with its continuum line, (b) band depth spectra after continuum correction. This shows some artifacts with negative band depth values, (c) original spectra after removing unnecessary points and adding some points at local maxima, and (d) band depth spectra after continuum line correction.

Band depth (BD) is one of the most widely used parameters for determining the relative strength of absorption features and is usually calculated relative to the continuum, $R_c(\lambda)$:

$$BD(\lambda) = 1 - (R_b(\lambda))/(R_c(\lambda)) \quad \text{(eq. 3.1)}$$

Where $R_b(\lambda)$ is the reflectance at the bottom of the spectral absorption feature and $R_c(\lambda)$ is the reflectance of the continuum line at the same wavelength as $R_b(\lambda)$

(Clark and Roush, 1984). The absorption depth is related to the abundance of the absorber and the grain size of the material concerned (Clark, 1999). The band position is the wavelength of $R_b(\lambda)$. The band position changes with the composition of the material concerned (e.g., Clark (1999)).

3.3.4 ASTER and Hyperion image data

The Advanced Spaceborne Thermal Emission and Reflection Radiometer (ASTER) was developed by the Ministry of International Trade and Industry (METI), Japan and launched onboard NASA's Terra satellite in 1999 (Kato et al., 2014; Yamaguchi et al., 1998). The instrument has three separate optical subsystems: the visible and near-infrared (VNIR) radiometer, shortwave-infrared (SWIR) radiometer, and the thermal infrared (TIR) radiometer (Arai and Tonooka, 2005). Table 3.2 summarizes the characteristic features of the ASTER subsystems (Yamaguchi et al., 1998). The characteristic features of the ASTER TIR subsystem were not included in the Table 3.2, since this study focuses on the VNIR and SWIR bands.

The Hyperion was the first space-based imaging spectrometer onboard NASA's Earth Observing 1 (EO-1) under the New Millennium Program (NMP), launched in November 2000 (Kruse et al., 2003; Pearlman et al., 2003). The Hyperion instrument was designed as a technology demonstration and equipped with a single telescope and two grating spectrometers: a VNIR spectrometer and a SWIR spectrometer. Hyperion is a pushbroom instrument and captured the 256 spectra each with 242 spectral bands at approximately 10 nm spectral resolution over a 7.5 km wide swath (Table 3.2).

Table 3.2: Performance of the ASTER VNIR-SWIR and Hyperion Instruments (Hubbard and Crowley, 2005; Pearlman et al., 2003).

Sensor	Subsystem	Band No	Spectral range (μm)	Digitization	SNR	Spatial Resolution (m)
ASTER	VNIR	1	0.52 - 0.60	8 bits	370/1	15
		2	0.63 - 0.69		306/1	
		3N	0.78 - 0.86		202/1	
	SWIR	4	1.600 - 1.700	8 bits	466/1	30
		5	2.145 - 2.185		254/1	
		6	2.185 - 2.225		229/1	
		7	2.235 - 2.285		234/1	

Sensor	Subsystem	Band No	Spectral range (μm)	Digitization	SNR	Spatial Resolution (m)
		8	2.295 - 2.365		258/1	
		9	2.360 - 2.430		231/1	
Hyperion	VNIR	1 - 70	0.355 - 1.006	12 bits	161/1	30.38
	SWIR	70 - 242	0.902 - 2.500		40/1	

Preprocessing of ASTER data

The VNIR and SWIR bands were treated separately and then all bands were resampled into VNIR band pixel sizes using the nearest neighbor resampling method. The geometrically and radiometrically corrected level 1B ASTER image product, acquired on 14th September 2000 (Image ID: AST_L1T_00308142000185402_20150411012044510 19), was processed as follows.

1. Conversion of the image DN values to radiance using Unit Conversion Coefficients (UCC). A DN value of 0 in 8-bit VNIR and SWIR bands are allocated to dummy pixels while the DN value of 1 is allocated to zero radiance. A DN value of 255 is allocated to saturated pixels. Therefore, DN values are linearly correlated with the radiance over the range 1:254. Therefore the radiance at sensor, $L_{sen}(Wm^{-2}sr^{-1}\mu m^{-1})$ can be calculated from the level 1B or 1T data using,

$L_{sen} = UCC * (DN - 1)$ ———- (eq. 3.2)

UCC values used in this study are listed in Table 3.3. Note that band 1 and band 2 of the selected image show high gain while other bands shows low gains. UCC values were set pre-launch and have not changed.

2. Biggar et al. (2005) and Iwasaki et al. (2002) have found that the light incident to band 4 in SWIR subsystem is reflected at the detector and filter boundary and then transported to the other bands by multiple reflections in the focal plane area, producing crosstalk components on the images. SWIR bands radiance data were crosstalk-corrected using ASTER Crosstalk Correction Software (Blackburn and Dennen, 1988).

3. Biggar et al. (2005) have also found that the effect of the crosstalk can only be partially removed by applying a crosstalk correction program. They identified that, as many spacecraft optical sensors do, the response of ASTER SWIR subsystem also changed at launch or after extended operation in space. An independent method of investigating any change in the radiometric calibration other than on-board sources or methods is called vicarious calibration (Arai, 2001; Biggar et al., 2005; Dinguirard and Slater, 1999). The calibration correction factors (CCF) calculated by Biggar et al. (2005) were applied to the Crosstalk-Corrected data. Mars and Rowan (2010) observed that these radiance correction factors were successful in adjusting the ASTER SWIR bands for better retrieval of surface reflectance spectra. The adopted factor values (CCF) are listed in Table 3.3.

$L_{swir} = L_{sen}(SWIR) * CCF$ ..... (eq. 3.3)

Here it is assumed that the radiometric calibration parameters for each pixel are known.

Table 3.3: Radiometric correction parameters used in this study.

Subsystem	Band No.	UCC	CCF
VNIR	1	0.676	
	2	0.708	
	3N	0.862	
SWIR	4	0.2174	1.046
	5	0.0696	1.016
	6	0.0625	0.937
	7	0.0597	0.919
	8	0.0417	0.900
	9	0.0318	0.875

The radiance reaching the sensor L_{sen} from the ground surface within a single pixel is given by,

$L_{sen}(\lambda_j) = L_{BB}(\lambda_j, T)\tau(\lambda_j)\epsilon(\lambda_j) + \tau(\lambda_j)\rho L\downarrow(\lambda_j) + L\uparrow(\lambda_j)$ ..... (eq. 3.4)

where, L_{sen} is in units of $Wm^{-3}sr^{-1}$, and;

L_{BB} = Blackbody radiance $[Wm^{-3}]$

ϵ = surface emissivity [unitless]

τ = sensor-surface atmospheric transmissivity [unitless]

$L \uparrow$ = upwelling atmospheric path radiance $[Wm^{-3}sr^{-1}]$

$L \downarrow$ = downwelling atmospheric irradiance $[Wm^{-3}]$

ρ = surface reflectance [unitless]

λ_j = wavelength of the band j [m]

Equation 3.4 shows that there is a significant attenuation along the sun-surface-sensor pathway due to the thick atmosphere between the surface, sun, and the sensor. Several methods and strategies have been developed to "correct" or "compensate" for the effect of the atmosphere on the remotely sensed images. These methods can be divided in to two categories, 1) model based methods such as Atmospheric REMoval program (ATREM) (Mees et al., 2005), Atmospheric CORrection Now (ATCOR) (Richter, 1996; Richter and Schlapfer, 2002) and Fast Line-of-sight Atmospheric Analysis of Spectral Hypercubes (FLAASH) (Adler-Golden et al., 1998), and 2) empirical based methods, including Flat Field (Goetz and Srivastava, 1985), Internal Average Relative Refelctance (IARR) (Savitzky and Golay, 1964), Empirical Line (Conel et al., 1987), and Log Residuals (Green and Craig, 1985). The model based methods use the radiative transfer (RT) models to calculate the radiance at the sensor. These methods only require basic information such as the acquisition date and time of the image, sensor altitude, location and local visibility, and no field measurements are required (Ben-Dor et al., 2004; Kruse, 2004). The empirical based methods rely only on scene information. Related information for the atmospheric correction can be obtained from the simultaneous atmospheric measurements, or from radiometric measurements over calibrated ground areas or from statistical calculations or modeling (Duggin and Robinove, 1990). The advantages and limitations of each methods discussed and summarized in many studies (e.g., Kruse (2004); Ben-Dor et al. (1994)).

4. Atmospheric correction of the radiometric corrected ASTER VNIR and SWIR bands were performed using 6S FORTRAN Code. The 6S (Second Simulation of the Satellite Signal in the Solar Spectrum) code is an improved version of 5S (Simulation of the Satellite Signal in the Solar Spectrum) developed by the Laboratoire d'Optique Atmospherique, France (Tanre et al., 1979). The code predicts a satellite signal between 0.25 - 4.0 μm assuming cloudless atmosphere (Vermote et al., 2006). In

this code, the apparent reflectance at the satellite level for a Lambertian surface, (ρ_{TOA}) is given by,

$$\rho_{TOA}(\theta_s, \theta_v, \phi_s - \phi_v) = T_g(\theta_s, \theta_v)[\rho_{R+A} + T\downarrow(\theta_s)T\uparrow(\theta_v)\frac{\rho_s}{1-S\rho_s}] \ldots\ldots \text{(eq. 3.4)}$$

where,

ρ_s = lambertian homogeneous target reflectance at sea level altitude θ_s = solar zenith angle ϕ_s = solar azimuth angle θ_v = sensor zenith angle ϕ_v = sensor azimuth angle ρ_{R+A} = intrinsic reflectance of the molecule+aresole layer $T\downarrow(\theta_s)$ = total transmission of the atmosphere on the path between the sun and surface $T\uparrow(\theta_v)$ = total transmission of the atmosphere on the path between the surface and sensor S = spherical albedo of the atmosphere T_g = gaseous transmission for the H_2O, CO_2, O_2 and O_3. This is the non-linear function of the effective amount of absorptive matters in the atmosphere and depends also on pressure and temperature profile (Vermote et al., 1997; Tanre et al., 1979; Mees et al., 2005).

ASTER subroutines written in the 6S FORTRAN code were used to calculate the atmospheric correction parameters for each band.

Hyperion Preprocessing

A Hyperion Level 1R image acquired on June 08, 2002 (Image ID: EO1H0400352002159 110KI) was processed as follows, with details on the preprocessing steps explained in Datt et al. (2003). The following preprocessing steps were done using ENVI and the R statistical software package:

1) Setting Bad Bands: The Hyperion VNIR sensor has 70 bands, and the SWIR has 172 bands providing 242 potential bands. Some of the 242 bands are not calibrated in Level 1R data. Some of the bands were not activated in the Hyperion arrays (called zero bands; Band 1-7,58-76, 225-242), some had low signal levels (Band 121,122,126,127, 167-178,224) and some other bands are duplicated in the VNIR-SWIR overlap regions (Band 77-78). Those bands were removed and remaining 179 unique bands were further processed.

2) Fixing Bad Pixels: Due to the nature of pushbroom image acquisition mode, a single band image in Hyperion data is made up from 256 along-track image columns and each one was measured by one across track detector element in the detector array. However, detector-to-detector radiometric miscalibration, temperature change, or functional failure of individual detector elements during acquisition lead to the vertical stripes or "streaks" in certain pixels of an image band. Pixels that contain little or no valid data are identified as bad pixels (Datt et al., 2003). When the pushbroom sensor moves forward, a given pixel creates a "column" of data along-track (vertical) direction of the image. The bad pixel list identifies about 17 pixels out of the total 242 x 256 pixels as bad. These pixels were corrected by replacing them with an average value of the adjacent pixels.

3) De-streaking radiance data: After fixing the bad pixels identified on the image, less severe vertical stripes were corrected using destriping method. Such striping is often seen in data acquired from pushbroom sensors and may be caused by factors such as detector non-linearities, movement of the slit with respect to the focal plane, and temperature effects (Kruse et al., 2003). Destriping methods can be classified roughly into three categories, 1) digital filtering, 2) histogram matching, and 3) moment matching (Sun et al., 2008). Digital filtering suppress the stripes by filtering the images in either spatial or frequency domain (Pan and Chang, 1992). The method assume the stripes are spatially periodic with a frequency distinct from those contributed by the scene variations. The striping observed in Hyperion images does not show the periodic pattern and therefore digital filtering can not be applied. Histogram matching techniques assumes that the subscenes measured by separate detector elements for the same band have approximately the same histogram (Horn and Woodham, 1979). The concept of the moment matching techniques is similar to the histogram matching and they compare the moment statistics such as the mean and standard deviation of the pixel columns in a given band. Datt et al. (2003) categorized the moment machine techniques into two categories, global destriking and local destriking methods. The global method estimates the reference moment statistics by spatially smoothing the moment statistics of the adjacent pixel columns,

while the global method uses the whole band of the image to calculate the moment statistics. The global destriking method was implemented to destrike the image data.

4) Recalibration: The Hyperion Level 1R data is provided as scaled radiance data in a signed integer format. The calibrated radiance ($W/m^2/sr/\mu m$) values for bands 1-70 have been multiplied by a factor of 40 and bands 71-242 have been multiplied by a factor of 80 to maintain the precision. Therefore, bands 1-70 were divided by 40 and 71-242 were divided by 80, to return to the absolute radiance.

5) Geometric Correction: Image to image map registration was done using the first-order polynomial transformation methods. VNIR bands of the ASTER image was selected as the base map. Accuracy of map registration was assessed by overlaying the road vector map of the area.

6) Atmospheric correction: The 6S RT code does not have the capability to correct the Hyperion data yet. Therefore, a FORTRAN code (subroutine) was written to the 6S RT code using the band response information of the Hyperion data. Modified 6S RT code was used to do the atmospheric correction of Hyperion bands with the same basic parameters used for the ASTER image.

7) EFFORT Polishing: Empirical Flat Field Optimized Reflectance Transformation (EFFORT) is a correction method used to remove residual calibration errors and atmospheric effects from a reflectance data (Boardman, 1998). The EFFORT correction method selects Hyperion spectra that match a low-order polynomial estimate in a least-squares sense as representative featureless spectra. These spectra are then averaged, and a mild gain factor is determined to remove systematic, coherent noise present in every spectrum (ENVI, 2009).

3.3.5 Mapping Methods

Most spectral mapping techniques work on a pixel by pixel basis to match the reflected spectra of possible surface materials of the area with unknown pixel spectra to derive

surface composition. Algorithms used to map, enhance, or delineate geology from the spectral images can be grouped into five basic categories, 1) Band ratios and indices (Sultan et al., 1987), 2) principle components and enhancement/display based methods such as Minimum Noise Fraction (Green et al., 1988), 3) shape-fitting based algorithms such as Spectral Angle Mapper (Kruse et al., 1993), 4) Linear Spectral Unmixing (Kruse et al., 1993) and, 5) Machine Learning methods (e.g., Hu et al. (2019)).

Because the objective of this paper is to assess how well zeolites or zeolite-bearing rocks can be identified and mapped using remote sensing methods, four most commonly used and well-established spectral mapping techniques, representing different levels of information extraction methods, were selected. The first two methods assume there is no field information (e.g., geology, types of minerals) from our study area, which is similar to mapping minerals on most areas of Mars. The third method assumes that limited information on the study area are available, such as the reflectance spectra of known sample(s) or the image spectra of the target location(s). Fourth method assumes that more information on the study area is available, including spectral endmembers or locations of possible endmembers to collect the image endmember spectra. The methods include, 1) band indices, 2) Minimum noise fraction, 3) Spectral angle mapper, and 4) Linear spectral unmixing. Machine learning represents a wide spectrum of algorithms (e.g., supervised, unsupervised, linear, nonlinear, rule based models, classification trees, etc). Therefore, no machine learning methods were selected.

1. Band ratios are designed to display the spectral contrast of specific absorption features and have been used extensively in geologic remote sensing (e.g., Rowan and Mars (2003)). Relative absorption band depth (RBD) images (Crowley et al., 1989) are three-point ratio formulations to detect diagnostic mineral absorption features on the spectral image, while minimizing the reflectance variations related to topographic slope and albedo differences. For each absorption feature, the numerator is the sum of the bands representing both shoulders (Band A and Band C), while the denominator is the band located nearest the absorption feature minimum (Band B) (Crowley et al., 1989).

$$RBD = ((BandA + BandC))/BandB \quad \text{(eq. 3.5)}$$

Commonly used ASTER spectral band ratios for lithological mapping are listed in Kalinowski and Oliver (2004), Rajendran and Nasir (2019) and Rowan and Mars (2003). Six band indices were selected based on the identified mineralogy of the area (Table 3.4).

Table 3.4: RBD and simple band ratios used in this study.

Index Name	Index Formula for ASTER	Index Formula for Hyperion	Feature
RBD_{CaCO3}	(B7 + B9)/ B8	(B167 + B179)/ B174	Carbonate-chlorite-epidote
$RBD_{CaMgCO3}$	(B6 + B8)/ B7	(B161 + B174)/ B167	Dolomite
RBD_{Clay1}	(B5 + B7)/ B6	(B157 + B167)/ B161	Sericite-muscovite-illite-smectite
RBD_{Clay2}	(B4 + B6)/ B5	(B118 + B161)/ B157	Alunite-kaolinite-pyrophillite
BR_{Fe3}	B2 / B1	B24 / B14	Ferric iron, Fe^{3+}
BR_{Alt}	B4 / B5	B118 / B157	Alteration

2. The Minimum Noise Fraction transformation (MNF), introduced by Green et al. (1988), is used to determine the inherent dimensionality of the image data. The eigenvalue of each MNF transformed band provides a measure of its information content, with progressively noisier bands approaching eigenvalues near zero (Hubbard and Crowley, 2005). The MNF transformation was applied to the Hyperion and ASTER image data. After visually analyzing each of the MNF bands, two band combinations from each image were selected to show the lithological variations over the study area.

3. The Spectral Angle Mapper (SAM) tool measures spectral similarity by calculating the angle between two spectra and treating them as vectors in n-dimensional space (Kruse et al., 1993). The calculation consists of taking the arccosine of the dot product of the spectra.

$$\text{SAM} = COS^{-1}\left(\frac{\sum_{i=1}^{n} t_i r_i}{(\sum_{i=1}^{n} t_i^2)^{1/2}(\sum_{i=1}^{n} r_i^2)^{1/2}}\right) \quad \text{(eq. 3.6)}$$

where n is the number of bands, t is the test spectrum and r is the reference spectrum. The test spectrum can be the image spectrum or field sample spectrum. The reference

spectrum can be the spectrum acquired from 1) the field sample, 2) the published standard spectral libraries, or 3) the image to be classified itself (Kruse et al., 1993). A small spectral angle (SA) between two vectors shows that the two spectra closely match each other, while the large angle shows a poor match. The SAM is insensitive to gain factors because the angle between two vectors is invariant with respect to the length of the vectors and is therefore insensitive to the topographic illumination effects (Kruse et al., 1993).

In this study, we have tested three different mapping scenarios including: 1) SAM classification using field sample spectra (T27, T30, T37, T45) for both ASTER and Hyperion images with all bands, 2) SAM classification using the corresponding pixel spectra (T27P, T30P, T37P, T45P) for both images with all bands, and 3) SAM classification using 9 bands of the Hyperion image, which are comparable to the ASTER bands, with their corresponding pixel spectra (T27P, T30P, T37P, T45P). SAM results were assessed using the Class point map.

The results show that the image spectra give better results than the sample spectra and that ASTER gives better results than Hyperion, likely because of the high noise inherent to the Hyperion image (Appendix B, Fig B.1).

4. The linear spectral unmixing (LSU) methods generally assume that the spectral signature of a mixed pixel is represented by the weighted sum of the endmember spectra and that the weights associated with the endmembers are given by the corresponding proportional area coverage in the pixel (Shi and Wang, 2014). A mixed pixel signal can be described as a linear combination of pure spectral signatures (endmembers) of its constituent components, weighted by their subpixel fraction cover (Adams and Smith, 1986).

$R_i = \sum_{j=1}^{N} F_j R_{i,j} + \epsilon_i \; i = 1, ...LL \; \ldots\ldots\ldots\ldots$ (eq. 3.8)

where R_i is the reflectance of the mixed spectrum in image band i for each pixel, f_j is the fraction of each endmember j calculated band by band, N is the number of endmembers, L is the number of bands, and ϵ_i is the residual error for band i of the fit of N spectral endmembers (Adams and Smith, 1986). Selecting endmembers involves identifying the correct number of endmembers, type of endmembers, and their corresponding spectral

signatures (Somers et al., 2011). Too many endmembers and spectrally similar endmembers leads to physically inaccurate endmember fraction images (Adams et al., 1993). The spectral signatures of the endmembers can be derived from the spectra collected from the field or spectra acquired in laboratories from field samples or directly from the image data itself. The most common method to extract endmembers from the image data is the AIG (Analytical Imaging and Geophysics) endmember selection method (included in the ENVI image analysis software) (Kruse et al., 2003). The method includes spectral data reduction using the MNF transformation (Green et al., 1988), spatial data reduction using the Pixel Purity Index (Boardman, 1993), an n-Dimensional Visualizer to determine image endmembers (Boardman, 1993), and identification of endmembers using their reflectance spectra. This procedure was applied for both ASTER and Hyperion images to extract endmembers but did not get satisfactory results (representative and informative endmembers with reasonable pixel coverage), most likely due to mixed pixels.

Image endmembers can also be selected based on the spatial context or field experience. The only requirement for selecting correct endmembers is that their mixtures reproduce the spectra of other pixels. Based on that requirement, five endmember spectra were selected including the image spectra selected for the SAM analysis and the image spectra representing gravel beds over the study area. A "full constrained" Linear Spectral Unmixing module in ENVI was used to calculate the fraction image data.

3.3.6 Attribute Maps

Previous studies of Lake Tecopa, as discussed in section 2, used different criteria such as diagenetic facies and allostratigraphy to simplify the complex geology of the area, hence the spatial distribution of those map units differ between studies. A geologic map is an interpretation, whereas a spectral image records the physical and compositional properties of the land surface as it is. Therefore, the geological/lithological classes defined by interpretation of remote sensing data should correspond to the kinds of units that one would map on the ground.

Previous work along with field studies emphasizes that 1) Tuff beds A, B, and C are clearly visible in the field and can be used to correlate sections across the basin.

Zeolites are primarily identified as major constituents in these altered tuff beds, 2) the dominant lithologies are mudstone or calcareous silty or sandy variants (Fig 3.3a and 3.3b), 3) Conglomerate, sandstone, and siltstone mainly occur along the lake margin and these coarse clastic sediments interdigitate basinward with the predominant mudstone, 4) surrounding hilly areas are mainly covered by rhyolitic to basaltic flows, volcaniclastic materials, or desert pavement consisting of planar surfaces of densely packed pebbles and cobbles (Fig 3.3c), and 5) the boundaries between the facies discussed above are laterally gradational and difficult to recognize in the field. Therefore, for this study, the mappable units of the area were simplified into three units named Tuff, NoTuff, and Gravel. The point map was created with 50 points for each unit after visual analysis of maps in Figure 3.2 (c, d, and e), Hyperion, ASTER (Fig 3.2b), DEM data (Fig 3.2f), and based on the field observations. Fifty (50) Tuff points were selected where the Tuff A, B, and C layers are exposed and zeolite-rich deposits have been mapped in previous studies (e.g., Hillhouse (1987)) or visually observed (based on their yellowish color) during the field visit. Tuff A, Tuff B and Tuff C map layers were also digitized from the published geological map (Hillhouse, 1987) (Fig 3.2b). Places where the surface is exposed without tuff layers were designated as NoTuff unit. Map unit Gravel is assigned to the dark color areas of the image where the surface is covered by gravels, volcanic flows, or desert pavements. Gravel points were randomly selected only based on the visual interpretation of the image data and the published maps. Spatial distribution of those points is shown in Figure 3.2 (b, d, e, and f). This point map was named as Class point map for easy reference. These vector files were imported to the R statistical software package for spatial analysis and visualization.

3.4 Results

3.4.1 Laboratory Spectra

Figure 3.6 (a) shows the reflectance spectra of sample T27 with library spectra of clinoptilolite and phillipsite. The absorption bands near 0.49 μm and 0.65 μm indicate higher Fe^{2+} and Fe^{3+} contents in the sample. The two most intense absorption features near 1.4 and 1.9 μm are the common OH stretching overtone and the stretch-bend

combination respectively, typical for the presence of molecular water in hydrous minerals including zeolites (Hunt et al., 1973). Figure 3.6 (b) shows the absorption band depth of the spectra shown in Figure 3.6 (a) over the 1.3 μm - 2.5 μm wavelength range. Figure 3.6 (c) and 3.6 (d) show the spectral characteristics of sample T30 and spectra of its constituent minerals. The sample consists of mostly calcite and montmorillonite (Fig 3.4 and Table 3.1). Sample spectra show prominent absorption features near 1.417 μm, 1.910 μm, 2.2 μm, 2.3 μm and 2.393 μm. The absorption features near 1.417 μm and 1.910 μm are due to the bound water typical of montmorillonite (Bishop et al., 1994; Hunt and Salisbury, 1970). The absorption band near 2.2 μm is due to the OH stretch plus $Al-OH$ bend in montmorillonite (Bishop et al., 1994). The combination and overtone bands of the CO_3 fundamentals in calcite occur in the near IR region. The two strongest are at 2.50 - 2.55 μm and 2.30 -2.35 μm (Clark et al., 1990; Gaffey, 1987). Therefore, the absorption feature at 2.3 μm is due to combination tones involving vibrations of the carbonate group. The reflectance spectrum of T37 shows four absorption features including two strong absorption features at 1.42 and 1.91 μm, and two very weak absorption features near 2.2 and 2.3 μm (Fig 3.6e and 3.6f). The absorption features at 1.4 and 1.7 μm may be due to phillipsite, while absorption features near 2.2 and 2.3 μm may be due to incipient alteration and calcite in the sample, respectively. Quartz does not show any absorption features in this region (Rice et al., 2013). Tuff sample T45 contained mainly K-feldspar, opal, and quartz. The reflectance spectrum of T45 shows three weak absorption features near 1.4, 1.9, and 2.2 μm. Opal may contain up to 8 wt % H_2O and it is possible to recognize the presence of both molecular water and Si-OH groups in near infrared spectra (Aines and Rossman, 1984). The absorption bands near 1.4 and 1.9 μm are due to the molecular water in opal, and the absorption feature at 2.2 μm is attributable to $Si-OH$ rotation plus stretching (Rice et al., 2013).

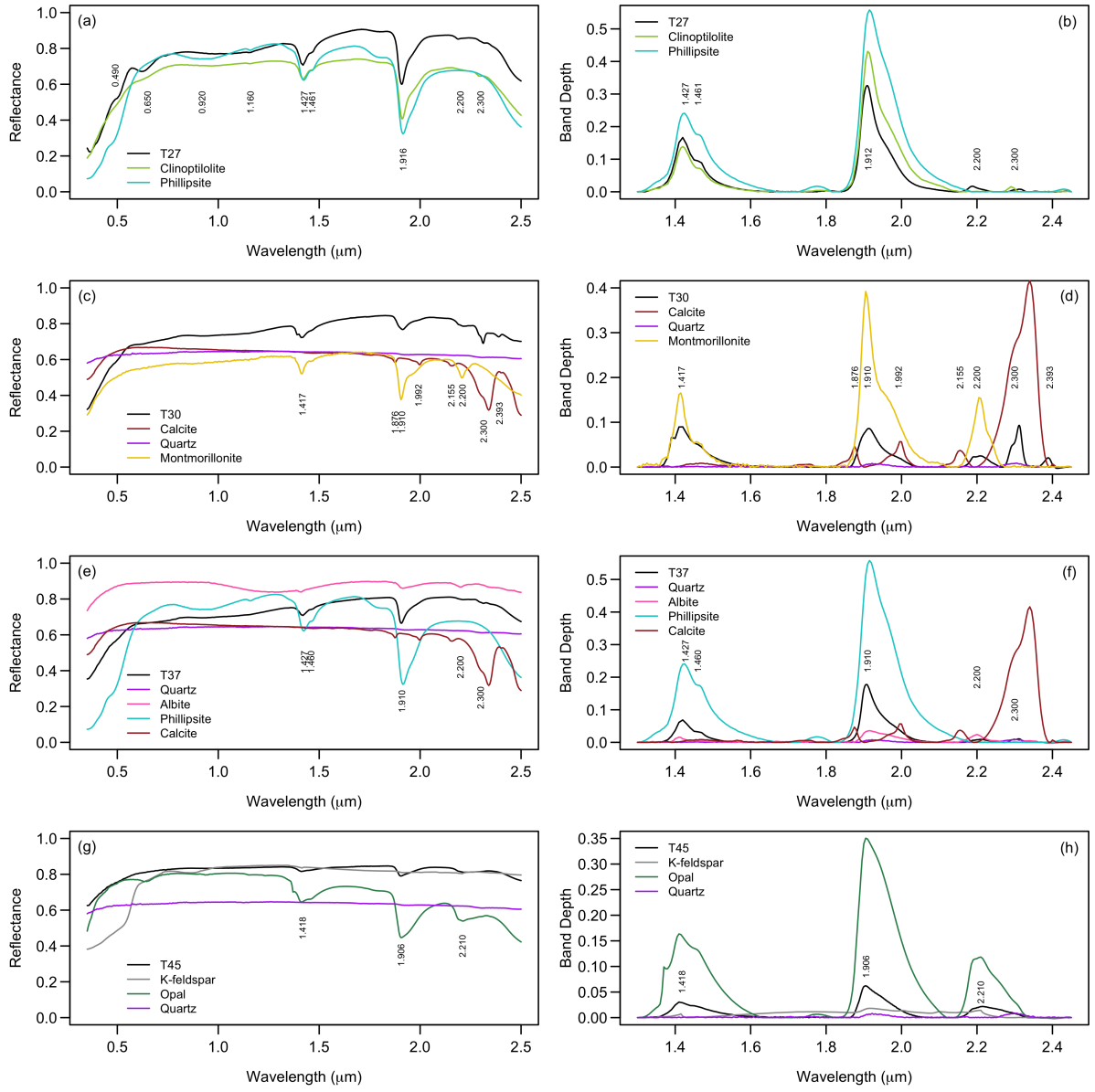

Figure 3.6: Reflectance spectra of samples and library spectra of sample minerals (panels a, c, e, and g) over the wavelength range 0.3 - 2.5 um, and their continuum removed spectra (panels b, d, f, and h) showing the band depth, over the wavelength range 1.3 - 2.5 um

3.4.2 Image Spectra

Figure 3.7 shows the sample spectra, ASTER and Hyperion resampled sample spectra, and their pixel spectra. Sample spectra were resampled into ASTER and Hyperion bandpasses using the spectral response characteristics of those sensors. All Hyperion pixel spectra show an absorption feature near 2.2 μm, stronger than that of the sample spectra. The 2.2 μm bands are diagnostic of aluminum-bearing clays that commonly

occur in altered materials and which are absent from most unaltered geologic materials (Hunt, 1979). ASTER image spectra also show the 2.2 μm absorption band as in Hyperion data. Hyperion image spectra show a 2.3 μm absorption feature in different strengths, even though it is not evident in corresponding ASTER image spectra. The Hyperion image pixel spectra at sample T45 show a 2.3 μm absorption feature though the T45 sample spectrum does not show a 2.3 μm absorption feature, likely due to weathering rinds and coatings of the rock or other rocks in the area.

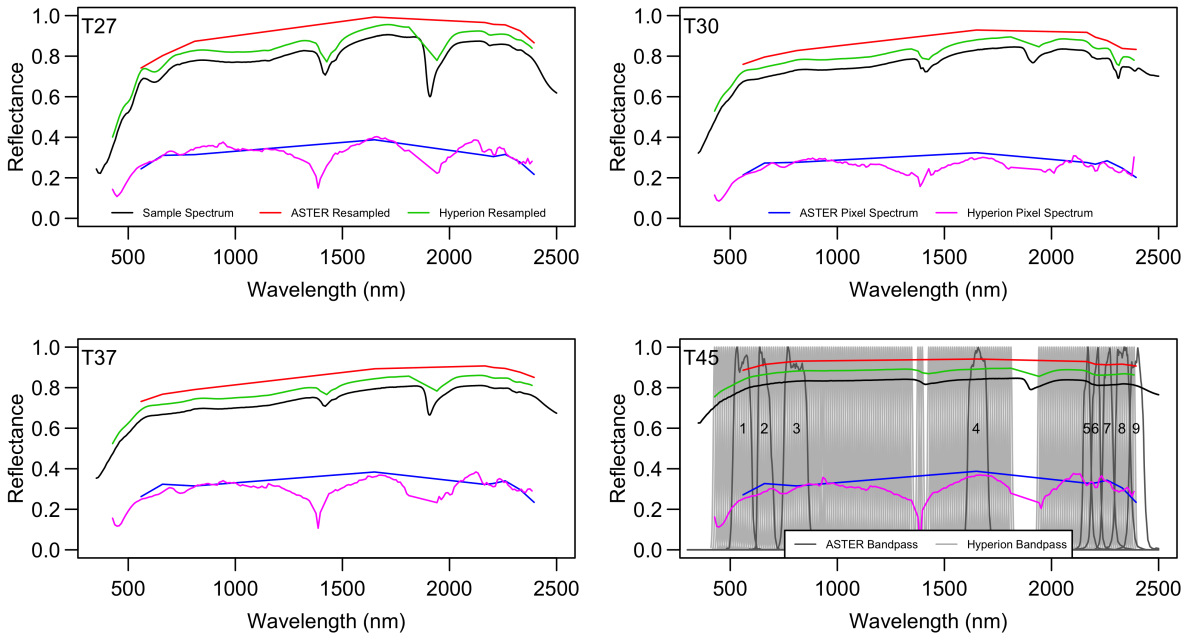

Figure 3.7: Sample spectra (black), Hyperion convolved sample spectra (green), ASTER convolved sample spectra (red), Hyperion image pixel spectra of sample location (pink) and ASTER image pixel spectra of sample location (blue). Hyperion and ASTER convolved spectra were 5 percent offset from each other for clarity. Plot T45 shows the spectral bandpasses of Hyperion and ASTER sensors.

3.4.3 Mapping Results

We found that band index BR_{Fe3} and BR_{Alt} give the lowest index values for the tuff bed area; of these two indices, BR_{Fe3} shows clear spatial distribution of those pixels due to the higher spatial resolution of ASTER bands 2 and 3. RBD_{CaCO3} and RBD_{Clay1} also show more interesting results compared to the other applied band indices. Therefore, band index RBD_{Clay1}, RBD_{Fe3} and RBD_{CaCO3} images were selected for further analysis and are shown in Figure 3.8 (e) and 3.8 (i) as color composite images. All images displayed in

Figure 3.8 were linearly stretched to the same range to compare easily with each other. The accuracy of radiometric and atmospheric correction applied to the both images can be assessed by comparing the very similar color patters of ASTER and Hyperion band index images . Alluvial gravels on the Greenwater Fan are shown in green in both images (Fig 3.8e and Fig 3.8i), depicting higher ferric iron content. Blue in both images shows higher calcite abundances, spatially associated with tuff bed areas. Red represents the clay minerals (e.g., smectite), which are mostly associated with the blue area and washes from the west side. The T27 sample location shows a combination of calcite and clay minerals. Previous studies (e.g., Hillhouse (1987); Larsen (2008); Larsen and Olson (2019); Sheppard and Gude (1968)) and our field visits (Fig 3.3a) showed that the tuff beds are interlayered with the mudstone beds within a pixel resolution leading to mixed pixels. The pink area next to the Greenwater fan in Figure 3.8 (e) and 3.8 (i) represents the recent bare, brown clay soils with thin slopewash veneer (Morrison, 1999).

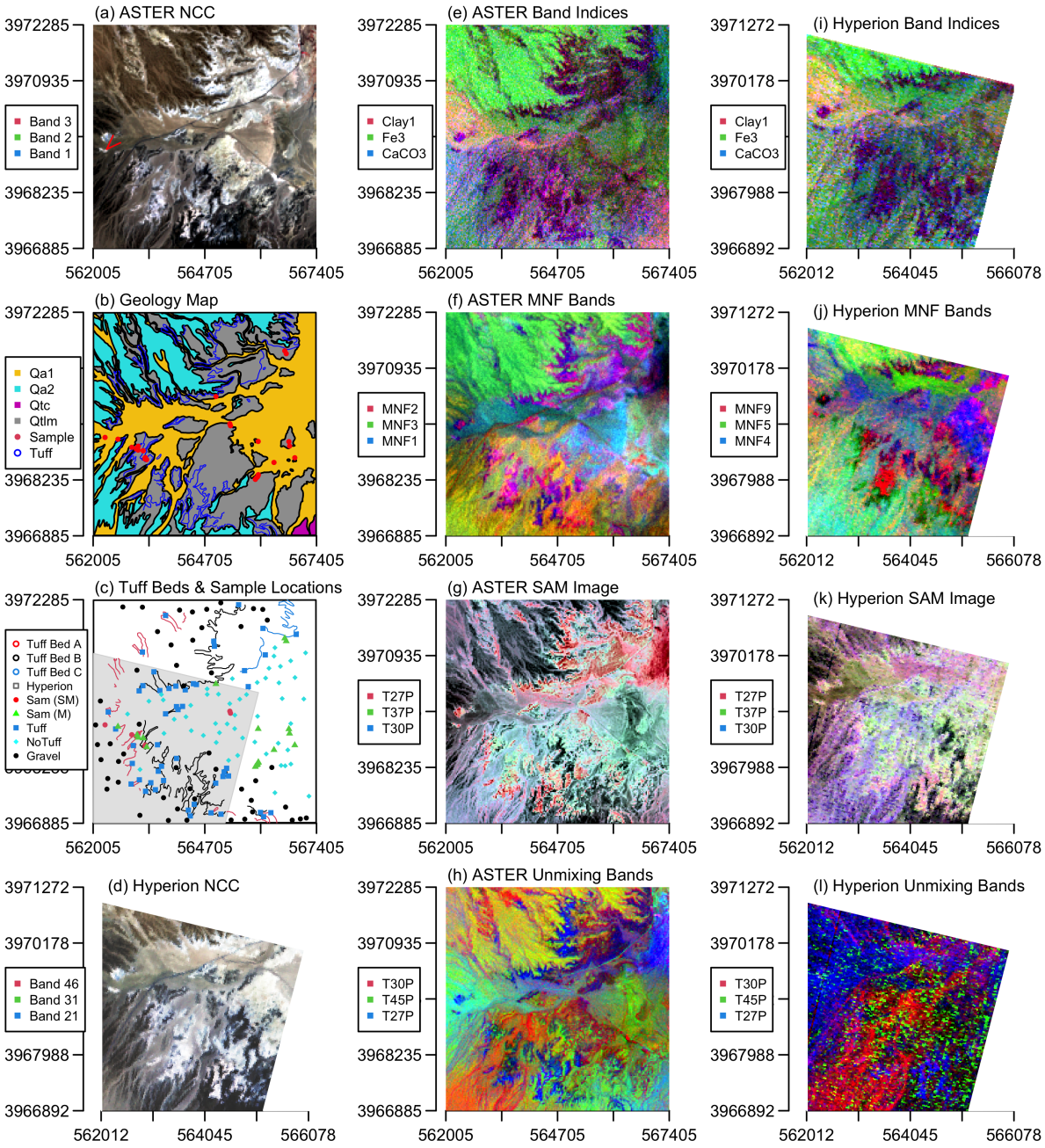

Figure 3.8: ASTER and Hyperion VNIR-SWIR mapping results. (a) Natural color composite of ASTER image. The red arrow in the map points to the location of an abandoned quarry (T27 sample site), (b) Geological map of the area (Hillhouse (1987)), (c) Map of the tuff beds, sample locations, and Hyperion image coverage (Sam (M): Locations of field samples with their mineral assemblages identified by XRD, Sam (SM): Locations of field samples with their mineral assemblages identified by XRD and spectral data), (d) Natural color composite of Hyperion image, (e) ASTER band indices, (f) ASTER Minimum Noise Fraction (MNF) bands, (g) ASTER Spectral Angle Mapper (SAM) rule images, (h) ASTER linear unmixing bands, (i) Hyperion band indices, (j) Hyperion MNF bands, (k) Hyperion SAM rule images, and (l) Hyperion unmixing bands. Selected band combinations are shown in the legend.

Figures 3.8 (f) and 3.8 (j) show the selected MNF band combinations in ASTER and Hyperion images, respectively. The zeolite-rich tuffs at the abandoned small quarry (T27) and tuff beds over the area are shown in red - magenta on these selected MNF band color composite images. The Greenwater Fan is represented by green in the ASTER image, whereas quartzite, limestone, dolostone, and volcanic materials in the Sperry Hills are represented by yellow-orange. Younger alluvial fan deposits in the area are represented by light blue in the ASTER MNF band image (Fig 3.8f).

The false color composite images of SAM rule images (grayscale images showing intermediate classification results) calculated from all ASTER and Hyperion bands are shown in Figure 3.8 (g) and 3.8 (k). The spectrally most similar pixels to the reference spectra have the lowest pixel values in SAM rule images, therefore, the values in rule images were inverted to show the mineral assemblages based on their RGB colors. Red areas in Figure 3.8 (g) show places where pixel spectra are similar to the pixel spectra at the abandoned quarry (T27) and also show high spatial correlation with the locations of Tuff beds and identified zeolite rich exposed tuff bed locations (Fig 3.8c). Blue-green areas show younger erosional deposits, while dark colors show gravel pavements. The SAM results of the Hyperion image (Fig 3.8k) do not show very clear spatial distribution of those materials, compared to ASTER.

The selected fraction images are shown in Figure 3.8 (h) and 3.8 (l). The ASTER unmixing bands T30P, T45P and T27P in red, green, blue false color composite clearly shows most of the Tuff bed areas in blue. High fractions of T30 end member are located in most of the erosional features of the area (in red). Greenwater Fan alluvial deposits are shown in yellow, the mixture of T30 and T45. The Hyperion unmixing bands do not show clear results, and the fraction image T45P (Fig 3.8i) captures the noise (random and column) from the image bands.

3.4.4 Finding the best mapping product(s)

All of the image products created using the different mapping techniques described above are referred to from here onwards as “attribute maps” for easy reference. All attribute maps created above are not equally useful for identifying the tuff layers containing zeolites,

as some attributes are more significant than others. Therefore, it is important to select the most important attribute map to create a geological model of the area and to characterize these attributes for the identification of zeolitized tuff layers. This can be performed by determining the degree of positive association, or clustering, within and between the selected attribute maps, and using a measure of the lack of clustering, called a confusion index. The clustering and confusion index can be viewed as indicators of the effect of selected attributes on the classification (Brodaric et al., 2004). Here, the learning vector quantization (LVQ) neural network technique (Kohonen, 2001) was adopted to determine the importance of attribute maps using the clustering technique. Learning vector quantization (LVQ) is a family of algorithms for statistical pattern classification, which aims at learning codebook vectors; a list of numbers having the same input and output attributes as training data, representing class regions (Nova and Estevez, 2014). Cross-validation (CV) techniques are used to evaluate and compare more models, various training algorithms, or to identify optimal model parameters (James et al., 2017). The k-fold Cross-validation method was used. This approach involves randomly dividing the set of observations into k groups (in our case ten groups) of approximately equal size. The first fold is treated as the validation set, while the method is fit on the remaining k -1 groups. The mean squared error (MSE) is computed on the observations in the held-out group. This procedure is repeated k times and each time a different group of observations is treated as a validation test. At the end, the k-fold CV estimate is computed by averaging the MSE value in each repeat. The k-fold CV method was repeated three times for each attribute map for robust results. The highest importance scores of twelve attribute maps for each class are shown in Figure 3.9.

The results show that the band index BR_{Fe3} calculated using ASTER image was able to differentiate Tuff and Gravel classes with high accuracy. It is important to note that ASTER bands 1 and 2 have higher SNR than other bands, except for band 4 (Table 3.2). The unmixing results of T45 and T37 and the spectral angle mapping results of T45 and T27 derived from the ASTER image are better able to differentiate the Gravel class from the Tuff. The Spectral Angle Mapper rule images of T27, T30, and T37 was able to classify the Gravel, NoTuff, and Tuff classes with high accuracies using Hyperion

image data. It also shows that band index BR_{Fe3} is one of the most important Hyperion image products for classifying the area into these classes. One of the main reasons for this could be the higher SNR ratio in the VNIR region of the Hyperion data compared to the SWIR region (Table 3.2), as apparent even in the image spectra (Fig 3.7). The NoTuff class shows the least important score in each classification method, due to the class overlap between the Tuff and NoTuff classes. Hyperion results show less overall accuracy than the ASTER image products, even though the spectral resolution is high in the Hyperion image. This could be because of the SNR, since ASTER has a higher SNR ratio than the Hyperion image (Table 3.2). It is noteworthy that for the Hyperion T27SAM image, the pixel spectrum collected from the zeolite area for the SAM was able to differentiate these three classes with the highest overall score, implying that zeolite is a potential factor for differentiating the Tuff class from NoTuff.

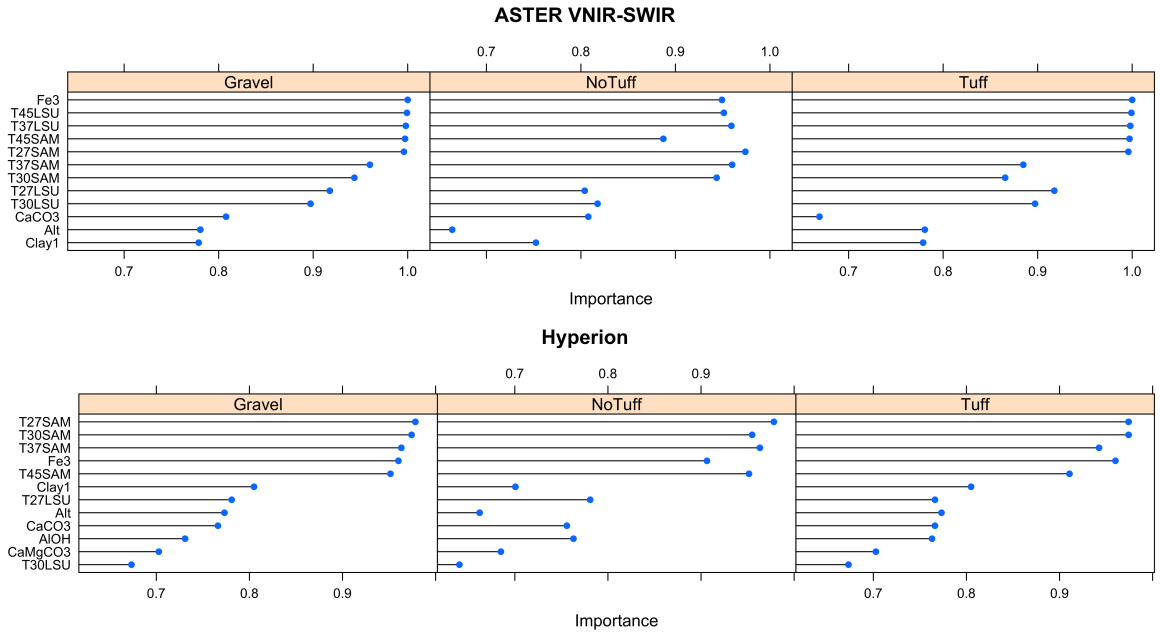

Figure 3.9: Importance scores of attribute images derived from ASTER and Hyperion image data for predicting the Tuff beds.

3.5 Discussion

The most prominent absorption features of zeolites (non-analcime) in the studied wavelength region (VNIR-SWIR: 350-2500 nm) form due to $O-H$ vibrations in hydroxyl (~1.4

μm) and $H-O-H$ stretching and bending vibrations in mineralogic water (~1.9 μm). The intermediate or associated products of tuff alteration, such as Fe/Mg-smectite and Al-smectite clay minerals, also show prominent absorption features at ~1.4 μm and ~1.9 μm due to hydroxyl and molecular water in the minerals. These phyllosilicate minerals show additional characteristic absorption features around 2.2 μm and 2.3 μm due to Metal-OH bending vibrations (e.g., Al-OH, Mg-OH, Fe-OH), which zeolites typically lack. However, occasionally, zeolites can also show weak absorption features in these two wavelength regions due to Metal-OH bending vibrations (e.g., AlFe-OH, NaAl-OH). The identification of zeolites using orbital and lab spectroscopy is complicated when zeolites are present in mudstone and sandstone beds that also contain clays (e.g., T37, T38, T39 in Table 1).

As depicted in Figure 3.7, the laboratory spectrum collected from the sample is not well represented by the pixel spectra of the sample location, likely due to several factors: 1) Geometric factors. Illumination and detection geometry of the lab setup for measuring reflectance spectra are standardized to optimize spectral contrast and to compare spectra from different materials. But satellite images show variations in zenith angle, local incidence angle due to roughness of the surface, topography, slope and slope aspects (slope angle and the direction that slope faces), and local exitance angle, such as nadir vs. off-nadir viewing. Therefore, even if the pixel coverage contains an apparently homogeneous surface, recorded radiance can show variations due to the above reasons (Duggin and Robinove, 1990). 2) Laboratory spectral measurements and orbital spectral measurements use completely different calibration methods, which will affect the final results. 3) The spectral effects due to atmospheric scattering and absorption are completely different in these two methods. In laboratory measurements, atmospheric attenuations are minimized by using short optical path lengths and using the standard reference, which cannot be applied for orbital sensors. 4) Spectral resolution and spatial coverage are not the same in both systems. Most laboratory measurements show higher spectral and spatial coverage while orbital sensors show low spectral and spatial resolution and coverage. 5) Even though the samples used for this study were selected based on the spatial coverage and abundance in the area, we cannot expect the same spectral behavior from the satellite image because of the spatial resolution. Most of the image

pixels represented the combination of different materials with different proportions and textures, such as debris and fans- in this case, cannot be simulated in the lab for spectral acquisition. Though the "pure" materials were collected to identify the mineralogy and acquire spectra, at the land surface these materials are contaminated by impurities, stains, coatings and different degrees of physical and chemical weathering. 6) Even the laboratory spectra acquired using the same setup show different spectral variability for the same mineral or rock type due to the variability of physical properties (e.g., polished surfaces, rough surfaces, particulates), chemical composition (e.g., minor element composition) and their crystal structures (e.g., site distortions and site symmetry) (Cloutis, 1996; Gaffey, 1986; Hunt, 1979). Therefore, we cannot expect one reference spectrum to represent the entire category such as calcite or basalt (Adams and Gillespie, 2006).

Kruse et al. (2003) compared the mineral mapping results from Airborne Visible/Infrared Imaging Spectrometer (AVIRIS) data with the Hyperion mineral mapping results at northern Death Valley test site, California and Nevada. Minerals mapped include calcite, dolomite, muscovite, silica and zeolites. They used the MTMF (Mixture Tuned Matched Filtering) mapping methods and came up with 92.96 % accuracy of mapping zeolite using Hyperion data with an overall accuracy of approximately 76 % for the Hyperion mapping compared to AVIRIS.

In this study, we observed that the different mapping methods are sensitive to the different surface composition over the area. The Unmixing and SAM methods gave better results than the Band indices and MNF band combinations for identifying zeolite rich exposed tuff layers. However, since unmixing and SAM methods only achieved better results with the scene-derived endmember spectra instead of laboratory spectra, these methods work well only when ground truth data is available. The study also shows the importance of finding the best mapping result using ground truth and cross validated machine learning methods.

3.6 Implications for Mars

Even though the spectral characteristics of certain zeolite minerals should be common to Earth and Mars, due to the variations in grain size effects, impurities, atmospheric

effects, weathering and alteration conditions, coatings, etc., it might be difficult to identify zeolite minerals at the species level or to distinguish them from other minerals such as polyhydrated sulfates. From this study we found that one of the biggest limitations of mapping zeolite, in addition to the spectral coverage and spectral characteristics, is the spatial resolution of the orbital image data. It was able to identify and map the large exposure of zeolite-rich tuff using the scene-derived endmember spectrum from a well-exposed abandoned quarry in the study area. Most of the other exposed zeolitic tuffs in the area are located on the top of mesas (e.g., Fig 3.3a) and most have an areal extent less than the pixel coverage. Zeolitic tuff beds varied in thickness from meters to centimeter scale (e.g., Fig 3.3c), which cannot be detected using spaceborne sensors, even if zeolite has very prominent characteristic spectral features, which could be captured by the orbital sensor with high SNR. Most of the zeolitic beds were covered by other sedimentary beds or gravel pavements (e.g., Fig 3.3c and 3.3d), or mixed with neighboring mudstone and sandstone beds due to physical weathering (e.g., Fig 3.3d). Minerals that are apparent in image spectra only indicate the minerals from the upper few hundreds of micrometers of the observable surface. Therefore, our minerals of interest could easily be masked by dust or other mineral phases. A lack of detected zeolites therefore does not preclude their presence, either beneath other materials, masked by surface dust, or mixed with more spectrally dominant phases. Similar phenomena could also affect zeolite detection on Mars, if zeolites are located in paleolake basins that are already subjected to erosion, deposition, and resurfacing (e.g., Goudge et al. (2015); Goudge et al. (2012)).

We have seen that both ASTER SAM and Unmixing images show materials similar to the zeolite rich tuff in the middle of the paleolake basin (Red in ASTER SAM image and Blue in ASTER Unmixing image), likely due to sediment transport processes. Therefore, special attention needs to be paid during the interpretation of these authigenic minerals with respect to their origin (e.g., transformation vs. neoformation). It also shows the importance of the different mapping methods to extract more information from the image data and the importance of comparing the results of different mapping methods to validate the mapping results when there is no ground truth available.

The adopted 6S atmospheric code assumed that the atmosphere is not turbulent, but rather consists of a series of steady-state, layered media, with discrete and constant aerosol, molecular, and particle concentrations (Duggin, 1985). The code also assumes that the surface is of uniform Lambertian reflectance and that the atmospheric water content is constant over the area (Vermote et al., 2006, 1997). Atmospheric correction on Mars also assumes the Lambertian surface and reflected solar flux is isotropic and depends only on the surface reflectance and the incident angle (Bultel et al., 2015; Itoh and Parente, 2021). Multiple scattering in the vicinity of a given pixel can lead to cross irradiance and cross radiance. Therefore, the adjacent terrain can contribute to the radiance of the observed pixel and thus reduce the contrast between targets of different reflectance (Teillet, 1986). Atmospheric attenuation, backscatter, and self-radiance will serve to reduce the signal-to-noise ratio at the sensor and to reduce the highest spatial frequencies that might be observed from the upwelling radiance field (Duggin and Robinove, 1990). Atmospheric attenuation and scattering due to Mars dust and aerosols in a certain place and time are unknown. Therefore, weak but characteristic absorption features might not be observed or hidden by noise of the spectra. In addition, zeolitized tuff beds in the study area show different alteration and weathering conditions. Some only contained the zeolites (completely altered), whereas others are partly altered containing different proportions of zeolites, glass, and authigenic clay minerals. Therefore, it is not possible to find a representative spectrum to characterize/ identify the zeolite-bearing tuff layers from the remote sensing data in this type of paleolake environment.

Though the orbital and in situ observations are often consistent, sometime there might be gaps between these two types of observations. In Gale crater, Mars, in situ observations by the Curiosity rover found abundant Ca-sulfate throughout Mount Sharp, which has not yet been identified in the orbital spectra. Most of the orbital sulfate detections in Mount Sharp are interpreted as Mg-sulfate, which has not yet been clearly identified in CheMin data from Curiosity rover (Sheppard et al., 2021b). The orbital spectroscopy identified an isolated hematite-bearing layer at Vera Rubin ridge (VRR) at Gale cater, Mars, however data from the CheMin instrument indicate widespread hematite at Mount Sharp below VRR, which was not detected in the orbital data (Sheppard et al., 2021b;

Fraeman et al., 2020b). Fraeman et al. (2020b) noted that dust, subpixel mixing, surface textures, photometric angles, and atmospheric contribution could influence the strength and interpretation of orbital spectral signatures, and they emphasized the importance of in situ observations for refining orbital observations. While ground truthing is a valuable check on interpretations made using terrestrial orbital spectroscopy, it unfortunately cannot be applied widely on Mars given the small number of landed and rover missions.

3.7 Conclusions

In this study, it was able to map zeolite-rich tuff beds using carefully selected band indices, MNF band combinations, and the pixel spectra corresponding to a zeolitic abandoned quarry area. The spectral characteristics of zeolites in zeolite-rich pixels are masked by phyllosilicates (e.g., smectite) present on the GRC, making it difficult to identify zeolites solely based on zeolite spectra. Spectral detectability is also a function of local lighting and atmospheric conditions, instrument noise, target-background spectral contrast, and spectral sampling characteristics. Therefore, it is important to understand that the spectral variability of the ground is usually far greater than the spectra collected using field spectrometers or for collected samples using laboratory spectrometers. However, once we identify the zeolites or zeolite-rich materials on the ground, the spectrum of the pixel covered by that region can be successfully used to map compositionally similar areas. This work emphasizes the importance of ground investigations to interpreting orbital data. Even using the pixel endmember spectra, most of the zeolite-rich beds could not be detected, since tuff beds in most terrestrial paleolakes are thin and mostly masked by dust or other mineral phases. Therefore, a lack of detected zeolites does not preclude their presence, either beneath other materials, surface dust, or mixed with more spectrally dominant phases. These same limitations would affect our ability to identify zeolites on Mars, if zeolites were present in its paleolake basins.

Acknowledgements

This work was supported by a grant from the Wisconsin Space Grant Consortium to Lindsay J. McHenry. The authors also would like to thank NASA for making the Hyperion and ASTER image data freely available for research and Brown University (Relab) and Thomas McCollom at University of Colorado for acquiring spectral data for field samples. Also thank to Mark Eskritt, Kaitlin Elizabeth Krause, and Jason Benjamin Carman for their support during the field visits. Many thanks to the 6S code developers, R Core Team, and Rstudio for making them as free and open source, and all the R library developers for their effort and contribution.

"The limits of the possible can only be defined by going beyond them into the impossible"

-Arthur C. Clarke-

4

Spectral mapping of zeolite bearing paleolake deposits at Lake Tecopa, California and its implications for mapping zeolites on Mars. 2. TIR wavelength region.

Contents

Abstract **139**
4.1 Introduction **140**
4.1.1 Spectral Identification of Zeolites 140
4.2 Study area **141**
4.3 Data Sets **145**
4.3.1 Field Sample XRD 145
4.3.2 TIR spectra of field samples 145
4.3.3 ASTER image data 146
4.4 Spectral Analysis **147**
4.5 Image Analysis **149**
4.5.1 Preprocessing of ASTER TIR data 150
4.5.2 Temperature and Emissivity Separation (TES) 152
4.6 Spectral Mapping **158**
4.6.1 Finding the best mapping product(s) 165
4.7 Implications for Mars **166**
4.8 Assumptions and limitations **170**
4.9 Conclusions **173**
Acknowledgements **174**

4. Spectral mapping of zeolite bearing paleolake deposits at Lake Tecopa, California and its implications for mapping zeolites on Mars. 2. TIR wavelength region.

Abstract

This study explores the effects of spatial and spectral resolution, and the method of emissivity information extraction from orbital thermal infrared (TIR) data, on the detectability of zeolite-bearing paleolake deposits on Earth and their implications for Mars. Earth-orbiting Advanced Spaceborne Thermal Emission and Reflection Radiometer (ASTER) data were used to map zeolite-bearing tuff beds at paleolake Tecopa, California. The thermal emission spectral analysis was conducted for the collected field samples containing zeolites and other associated minerals, after mineral assemblages confirmed by X-ray Diffraction. Three different temperature-emissivity separation (TES) algorithms were implemented for the ASTER TIR data and results were compared against laboratory emissivity spectra. Four different spectral mapping methods including: 1) band indices, 2) minimum noise fraction (MNF), 3) spectral angle mapper (SAM), and 4) linear spectral mixture analysis (LSMA) were applied to the thermal atmospheric corrected data. Accuracy assessment was done by selecting 150 pixels covering tuff beds, gavel beds, and other associated sedimentary deposits identified during field visits, using published maps, and using high-resolution orbital data. Band indices including relative band depth at band 13 (RBD13) and mafic indices (MIn) yield better results than MNF, SAM and LSMA. Field investigations showed that most zeolite-rich beds are buried by other beds, or that the areas of exposed beds are mostly smaller than the ground resolution cell (GRC) of the ASTER TIR instrument, or that zeolites are present in small amounts mixed with other more spectrally-dominant minerals. Implications of the lessons learned from this study for identifying zeolite-bearing deposits on Mars are also discussed. The results of this study infer that the paucity of detected zeolites on Mars, like their apparent absence from remotely sensed spectra for Lake Tecopa, does not preclude their wider presence, either beneath other materials, in small exposures, or mixed with other spectrally dominant phases.

4. Spectral mapping of zeolite bearing paleolake deposits at Lake Tecopa, California and its implications for mapping zeolites on Mars. 2. TIR wavelength region.

4.1 Introduction

Zeolites, a group of authigenic framework alumino-silicate minerals, are both common and widespread with relatively pure concentrations in volcanic ash deposits in saline-alkaline lakes on Earth (Hay, 1966; Hay and Sheppard, 2001). Zeolites have also been postulated to be components of the martian regolith (e.g., Ackiss et al., 2018; Crisp et al., 1990; Basu et al., 1998; Berkley and Drake, 1981; Bish et al., 2003; Cannon et al., 2015; Dickinson and Rosen, 2003; Ehlmann et al., 2009, 2011; Ming and Gooding, 1988; Ruff, 2004; Tokano and Bish, 2005; Viennet et al., 2017). Goudge et al. (2012) and Goudge et al. (2015) studied open and closed paleolake basins on Mars and reported a lack of evidence for widespread in situ aqueous alteration and mineral precipitation (i.e. evaporites), interpreted as due to either water chemistry that was not conducive to their formation, or a short-lived period of lacustrine activity. Identifying zeolites in these paleolake basins could address both hypotheses. However, previous studies show that zeolite detections on Mars are extremely difficult (except for analcime) since they are spectrally similar to polyhydrated sulfates in the visible to near infrared - shortwave infrared (VNIR-SWIR) wavelength region (e.g., Ehlmann et al., 2009; Sun and Milliken, 2015; Wray et al., 2009; Carter et al., 2013).

Therefore, this chapter explores how well orbital thermal infrared (TIR) multispectral remote sensing data can be used to identify and map zeolites in paleolake deposits. The laboratory and spaceborne TIR spectroscopy analyses, supplemented by X-ray Diffraction (XRD) analysis of collected samples, was conducted to study zeolites and related minerals in a Mars analog paleolacustrine deposit at Lake Tecopa, California.

4.1.1 Spectral Identification of Zeolites

The thermal infrared spectral characteristics of most common zeolite minerals in closed hydrologic systems are discussed here. The spectra were taken from the RELAB spectral database (`http://www.planetary.brown.edu/relab/`). The spectral behaviors of zeolite in the TIR wavelength region are shown in Figure 4.1 (a) and (b). These spectra have a prominent peak at 6.134 μm, which is indicative of bound water (Lagroix and Banerjee, 2004). The second most prominent peak in these spectra is the Christiansen frequency

feature located near 7.810 μm. The Cristiansen frequency feature occurs in a wavelength region where the real part of the refractive index of the mineral passes through unity; it is present on the short wavelength wing of an absorption feature (Cloutis et al., 2002; Salisbury and Walter, 1989). The wavelength position of the Christiansen frequency is positively correlated with the Al:(Al+Si) ratio (Cloutis et al., 2002). However, this feature can vary as a function of viewing geometry, grain size, particle packing, and atmospheric pressure (Salisbury and Walter, 1989; Cloutis et al., 2002). Spectra additionally show two major broad peaks near 8.7 μm and around 10 μm, assigned to asymmetric stretches due to O-Si-O and O-Al-O bends (Cloutis et al., 2002). The most intense absorption feature in the spectra of all silicates occurs between 8 to 12 μm and is generally referred as "Si-O stretching region" (Christensen et al., 1986). This transparency peak (emissivity minimum) forms due to the enhanced volume scattering in fine grained materials (Salisbury and Walter, 1989; Cloutis et al., 2002). The general shape of the analcime spectra slightly deviates from those of other zeolites.

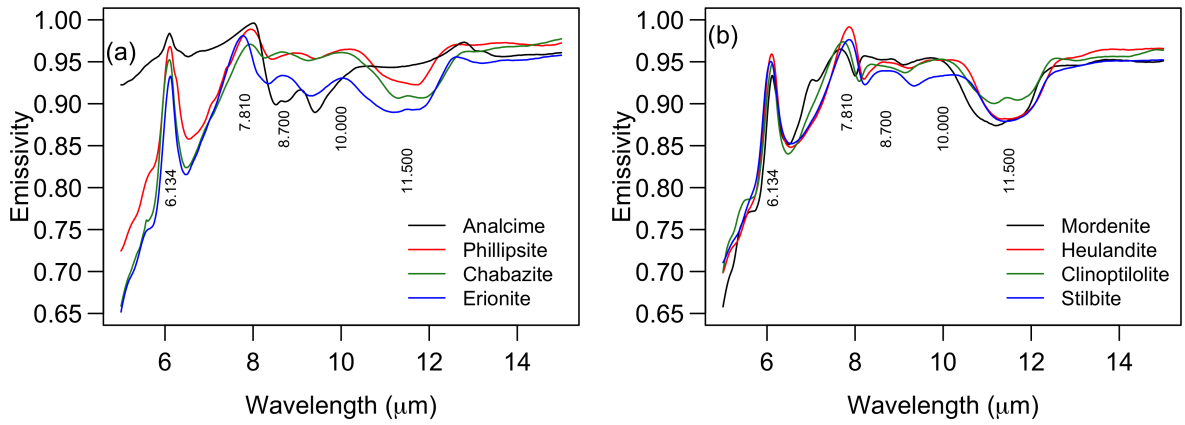

Figure 4.1: RELAB spectra of zeolite minerals (particle size < 45 um) including analcime (laze57), phillipsite (laze23), chabazite (laze17), erionite (laze25), mordenite (laze29), heulandite (laze31), clinoptilolite (laze27), and stilbite (laze21).

4.2 Study area

Pleistocene Lake Tecopa in Southeastern California is a well-documented "textbook" example of a terrestrial paleolake sedimentary environment, containing modern playa evaporites, paleolacustrine sedimentary beds, alluvial fans, and badlands fringed by

mountains. The incised badlands expose paleolake beds with characteristic alkaline minerals, including authigenic silicate minerals such as smectite, phillipsite, clinoptilolite, Opal C-T, potassium feldspar, and illite, and provide an opportunity to reconstruct the climatic history of the area based on clearly exposed eroded stratigraphy (Morrison, 1999). The gypsum beds suggest a shallow lacustrine evaporitic environment (Hillhouse, 1987). The sedimentary deposits of the lake are 100 meters thick and contain at least 15 ash layers (tuff beds) deposited by airfall and redeposited into the lake by fluvial processes making up about 8-12 percent of the stratigraphic sections (Sheppard and Gude, 1968; Hillhouse, 1987; Martin and Bindeman, 2009), along with other fluvial and lacustrine sediments. Sheppard and Gude (1968) designated three main tuff layers as Tuff A, Tuff B, and Tuff C. Tuffs A and C are light gray and vitric where fresh, and white or orange where altered to zeolites (Hillhouse, 1987; Larsen and Olson, 2019). Tuff B is white and pumiceous with sparse sanidine and biotite crystals where fresh and white to multicolored where altered (Hillhouse, 1987). Tuffs nearest to the lake margins are characterized by fresh glass and named as fresh-glass facies (Glass in Fig 4.2 (a)). Tuffs in the central part of the lake basin are characterized by potassium feldspar and/or searlsite, referred to as the potassium feldspar facies (Feldspar in Fig 4.2 (a)). Tuffs between the fresh-glass facies and the potassium feldspar facies are characterized by zeolites and termed as zeolite facies. In zeolite facies, the tuffs were replaced by the zeolites, clay minerals, and locally by opal.

Hillhouse (1987) published the late tertiary and quaternary geology of the Lake Tecopa area (Fig 4.3 (c)). Map units covered by the study area include Holocene alluvium (Qa1), Quaternary alluvium (Qa2), Conglomerate unit (Qtc), and Lacustrine mudstone unit (Qtlm). The Holocene (younger) alluvial deposits consist of unconsolidated sand, silt, and conglomerate in active and recently abundant stream channels. The Quaternary (older) alluvium units consist of remnants of alluvial fans that now form prominent mesas and raised areas capped by desert pavement. A distinguishing feature of the Qa2 in the study area is its surface of desert pavement consisting of planar surfaces of densely packed pebbles and cobbles, mostly 2-5 cm in diameter (Hillhouse, 1987). The conglomerate unit, Qtc, covers a very small portion of the study area, at the foot of the Sperry Hills (Fig 4.2c). The unit consists of fanglomerate and pebbly fluviatile deposits that interfinger with the

lacustrine mudstone units. The lacustrine mudstone unit (Qtlm) is the most interesting unit in the study because most of the tuff beds are in this unit. The mudstone unit contains calcite, clay minerals, authigenic zeolites, potassium feldspar, and rock fragments. The predominant detrital clay minerals are montmorillonite, illite, and saponite (Starkey and Blackmon, 1984). Sediments along the lake perimeter tend to be richer in calcite than sediments at the center of the basin (Hillhouse, 1987).

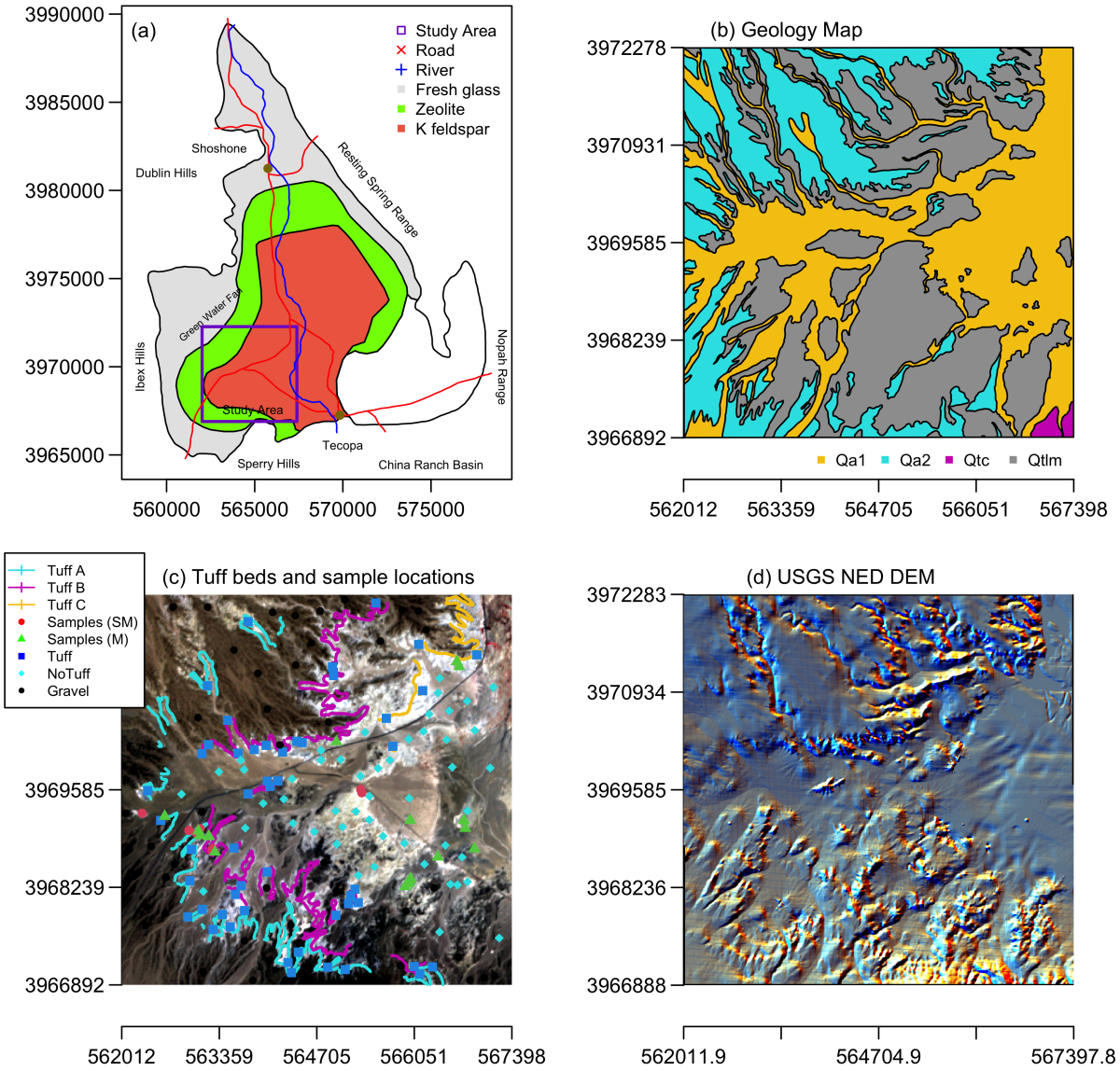

Figure 4.2: Location and geology of Lake Tecopa study area, (a) Location of the study area,(b) geological map (after Hillhouse (1987)), (c) sample locations, Tuff beds A, B, and C, and Hyperion image coverage overlay on the ASTER true color composite data (Sample (M): Locations of field samples with their mineral assemblages identified by XRD, Sample (SM): Locations of field samples with their mineral assemblages identified by XRD and spectral data, Tuff: Locations of samples T27 (abandoned quarry reference location), Locations of Tuff bed exposures selected from the Hillhouse (1987) geological map, NoTuff: Locations of the NoTuff class points, Gravel: Locations of the Gravel class points, and (d) Hillshade map of the study area derived from USGS National Elevation DEM.

4.3 Data Sets

The data sets include X-ray diffraction (XRD) data and TIR spectra of selected field samples and ASTER TIR image data. Fieldwork was conducted during October 2018 and 2019. During the field expeditions, a total of 56 rock and soil samples representing mudstone, siltsone, sandstone, tuff beds, zeolites, gravels, etc. were collected. Every sampling location was documented with detailed field descriptions of morphological features, lithology, location information (GPS), elevations, and field photographs. Rock and soil samples were collected from the center of relatively homogeneous bare land surface exposures.

4.3.1 Field Sample XRD

Samples for XRD analysis were powdered by hand and quantitatively mixed with crystalline Cerium (IV) oxide powder ($CeO_2 < 5$ μm) using a 100: 1 ratio of sample to internal standard. Samples were analyzed using a Bruker D8 Focus XRD system (Cu Ka radiation, 1 s per step, 0.01^o 2θ per step, $2^o - 60^o$ range, scintillation detector) and results were compared against the ICDD PDF-2 (International Center for Diffraction Data Powder Diffraction File) library using Bruker's EVA software. Based on the mineralogical results of XRD analysis, four samples (T27, T30, T37, and T45) were selected for TIR spectral acquisition. Sample T27, collected from a yellow altered tuff bed, contains mainly zeolites (clinoptilolite and phillipsite). Sample T30, sampled from the green color mudstone bed, contains mainly calcite and smectites. Sample T37, a light gray to pinkish-gray siltstone sample interbedded with mudstone, mainly contains quartz, calcite, phillipsite and albite, with a small amount of smectite. Sample T45, a white sample from a vitric tuff bed, consists of mainly sanidine and silica polymorphs.

4.3.2 TIR spectra of field samples

Samples T27, T30, T37, and T45 were ground to less than 150 μm particle size and their thermal infrared spectra were measured at the Brown University RELAB facility. Samples were measured with the RELAB Nicolet Nexus 870 FTIR spectrometer collecting biconical reflectance from 0.83 to 25 μm. More information on the spectral acquisition procedure is

available in the RELAB User's Manual and Instructions (`http://www.planetary.brown.edu/relabdocs/RelabManual2006a.pdf`). The reflectance spectra from 5 μm - 25 μm were converted to the emissivity using Kirchhoff's law (eq. 4.1) assuming that the thermal gradient and radiant flux transmitted through the sample are negligible with the given thickness of the sample (Rivard et al., 1993; Siegel and Howell, 1981).

$$E = 1 - R \quad \text{(eq. 4.1)}$$

where E is total emittance and R is total reflectance.

4.3.3 ASTER image data

The Advanced Spaceborne Thermal Emission and Reflection Radiometer (ASTER), which was developed by the Ministry of International Trade and Industry (METI), Japan, was launched onboard NASA's Terra satellite in 1999 (Yamaguchi et al., 1998; Kato et al., 2014). The instrument has three separate optical subsystems with their own telescopes with independent pointing and different detector technologies and onboard calibration (OBC) systems: the visible and near-infrared (VNIR) radiometer, shortwave-infrared (SWIR) radiometer, and the thermal infrared (TIR) radiometer (Arai and Tonooka, 2005). The three VNIR bands are used for assessing vegetation and iron-oxide minerals in surface materials. The spectral bandpasses of the six SWIR bands were designed for mapping phyllosilicate and carbonate minerals. Emissivity patterns derived from the five TIR bands are used to estimate silica content (Yamaguchi et al., 1998). Table 4.1 summarize the characteristic functions of the ASTER TIR subsystem.

Table 4.1: Summary characteristics of the ASTER TIR subsystem (Tonooka, 2005)

Band No	Spectral range (μm)	Digitization	Spatial Resolution (m)	Swath (km)
10	8.125 - 8.475	12 bits	90	60
11	8.475 - 8.825			
12	8.925 - 9.275			
13	10.25 - 10.95			
14	10.95 - 11.65			

4.4 Spectral Analysis

The position, depth, width, area, and shape of absorption features of a given spectrum are mainly controlled by the composition and crystal structure of the absorbing species (e.g., Van der Meer (2004); Clark (1999)). Different combinations of techniques such as curve matching (e.g., Clark (1999)), empirical curve fitting (e.g., Clark and Roush (1984)), and curve deconvolution (e.g., Clark and Roush (1984)) are used to identify the mineralogy and to derive physical and chemical information from the spectra. Curve matching is done by comparing one spectrum to others and is mostly done visually. In empirical curve fitting, spectra are curve fit systematically using polynomials fit about the minima or centers of absorption and those minima or centers are compared against similar curve fits performed using laboratory spectra of calibrated standards or calibrated mixtures. Curve deconvolution is a quantitative approach to extract the absorption parameters by fitting the Gaussian curves with selected spectra. In this work, simple curve matching was adopted to study spectral features of each sample spectrum using the corresponding library mineral spectra. The mineral spectra acquired from powdered samples in the RELAB spectral library database were selected to minimize the grain size and instruments effects on both spectra. The library and sample spectra were then converted to comma separated values (.csv) file format and imported into the R statistical software package to create a spectral database using the "hsdar" package (Lehnert et al., 2018).

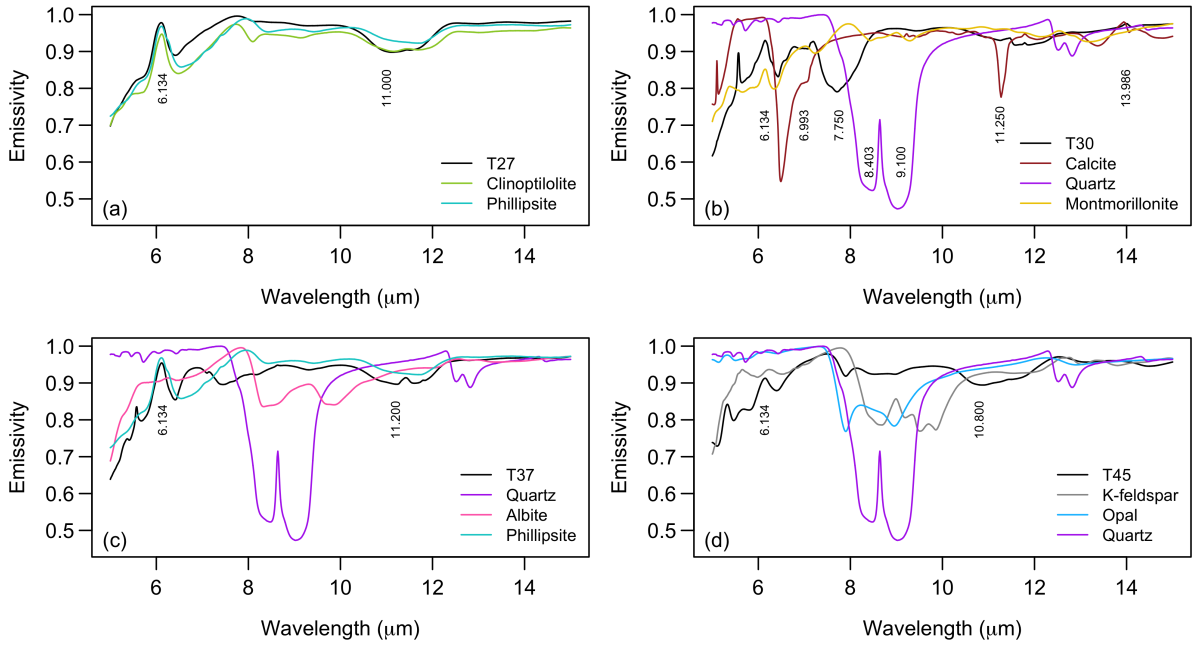

Figure 4.3: Emissivity spectra of samples with the RELAB laboratory emissivity spectra of constituent minerals over the 5.0 - 15 um wavelength range.

The sample spectra have the first emissivity peaks at 6.134 μm indicating the bound water in the samples (Fig 4.3). The emissivity spectra of sample T27 matches well with the library emissivity spectra of clinoptilolite and phillipsite (Fig 4.3a). The Christiansen frequency feature (7.810 μm) is prominent in T27 and T45. Calcite has three prominent characteristic features due to the internal vibrations of the carbonate ions; a fundamental absorption band near 6.9 μm, a CO_3 bending restrahlen band near 11.25 μm, and a third band at 13.98 μm (Salisbury and D'Aria, 1992; Christensen et al., 1986). Although sample T30 has abundant calcite, the emissivity spectra only show minimal spectral signatures in the 6.9 and 13.9 μm wavelength regions. The feature at 11.25 μm may be suppressed or masked by the spectral signatures of the other constituent minerals or due to grain size and texture (Kirkland et al., 2003; Sabol et al., 1992; Wehrens and Kruisselbrink, 2018). The emissivity spectrum of T30 most closely matches the montmorillonite library spectra except for the broad absorption feature near 7.75 μm. The "Si-O stretching region" is prominent in all sample spectra. This absorption feature shifts to shorter wavelengths as bond strength increases for isolated, chain, sheet, and framework tetrahedron silicates (Christensen et al., 1986). The spectrum of sample T37

shows more contribution from phillipsite than from quartz and albite (Fig 4.3c). The T45 spectrum shows more contribution from K-feldspar and opal than from quartz (Fig 4.3d). It is noteworthy that while sample T30, T37, and T45 contain quartz as identified by XRD, we do not see its most prominent reststrahlen band in the sample spectra and it might be obscured by the other mineral spectra, as is often the case for sedimentary rocks (e.g., Rivard et al. (1993)) and desert varnish (e.g., Salisbury and D'Aria (1992)). In addition, the spectral contrast of restrahlen bands decreases with increasing surface roughness (due to cavity effect) or decreasing particle size (due to volume scattering) (Wehrens and Kruisselbrink, 2018). Therefore, the spectral band depth is not a function of composition alone, but also the physical properties of the sample.

4.5 Image Analysis

An imaging sensor records scene as a composite of adjacent non-overlapping picture elements (pixels) and each pixel records the instantaneous field of view (IFOV) of the scene. The area recorded by the IFOV is referred to as the ground resolution cell (GRC). A single GRC may contain an assemblage of different scene elements with different optical anisotropies (Duggin and Robinove, 1990). Therefore, the average value of the spectral emissivity record in the image pixel will depend on the content of the GRC, its heterogeneity, topography, slope, and aspect (Duggin and Robinove, 1990). The point-spread function (PSF) of a sensor describes the phenomenon whereby the central portion of the IFOV has a higher sensitivity than the outer portions of the IFOV (Duggin, 1985). If the GRC contains different scene components with different emissivity anisotropies, changes of IFOV by a fraction of a pixel will produce a considerable change in sensor output (Duggin, 1985). It is assumed that the radiance recorded in the image pixel represents the optical properties of those features on the ground in which we are interested (Duggin and Robinove, 1990). Therefore, the accurate and quantitative interpretation of remote sensing data requires radiometric, geometric, and atmospheric correction prior to image analysis.

4. Spectral mapping of zeolite bearing paleolake deposits at Lake Tecopa, California and its implications for mapping zeolites on Mars. 2. TIR wavelength region.

4.5.1 Preprocessing of ASTER TIR data

The geometrically and radiometrically corrected level 1B ASTER TIR image product, acquired on 14th September 2000 (Image ID: AST_L1T_00308142000185402_20150411012044 51019), was processed as follows.

Tonooka et al. (2004) has showed that the sensor response to input radiance for ASTER TIR bands has been decreasing since launch due to degradation of optics or electronics. Sensor response to band 12 has decreased most rapidly and had reduced to 80% by 12th March 2000, while the sensor response to the band 10 decreased most slowly (Tonooka et al., 2004). For all TIR bands, odd and even detectors show different rates of sensor response decrements. Therefore, L1 products do not always satisfy the specified accuracy and those errors will often lead to a critical error on higher processing levels that use band to band comparison, such as in temperature-emissivity separation (TES) methods (Gillespie et al., 1998). Tonooka et al. (2004) have developed a recalibration method to apply to radiometrically correct ASTER TIR data (e.g., Coll et al. (2007)).

$R_{new} = A_{RCC} * R_{sen} + B_{RCC}$ ..... (eq. 4.2)

A_{RCC} and B_{RCC} values were taken from the Tonooka Laboratory ASTER TIR Recalibration Coefficient database (www.tonolab.cis.ibaraki.ac.jp/ASTER/RECAL/) and are listed in Table 4.2.

Table 4.2: Radiometric correction parameters used in this study.

Band No.	UCC	A_{RCC}	B_{RCC}
10	0.006822	0.999113	0.0044
11	0.00678	0.999005	0.0052
12	0.00659	0.998844	0.0063
13	0.005693	0.998755	0.0073
14	0.005225	0.998647	0.0079

Thermal Atmospheric correction was performed to approximate and remove the atmospheric contribution of the ASTER TIR radiance data using ENVI software. The algorithm used in ENVI is like the In-Scene Atmospheric Compensation algorithm (ISAC) developed by Johnson and Young (1998).

The radiance reaching the sensor L_{sen} from the ground surface within a single pixel is

given by,

$L_{sen}(\lambda_j) = L_{BB}(\lambda_j, T)\tau(\lambda_j)\epsilon(\lambda_j) + \tau(\lambda_j)\rho L\downarrow(\lambda_j) + L\uparrow(\lambda_j)$ ..... (eq. 4.3)

where, L_{sen} is in units of $Wm^{-3}sr^{-1}$, and;

L_{BB} = Blackbody radiance $[Wm^{-3}]$

ϵ = surface emissivity [unitless]

τ = sensor-surface atmospheric transmissivity [unitless]

$L\uparrow$ = upwelling atmospheric path radiance $[Wm^{-3}sr^{-1}]$

$L\downarrow$ = downwelling atmospheric irradiance $[Wm^{-3}]$

ρ = surface reflectance [unitless]

λ_j = wavelength of the band j $[m]$

Equation 4.3 can be simplified by collecting terms containing τ. The spectral radiance reaching the sensor can then be defined as,

$L_{sen} = \tau[\epsilon L_{BB} + \rho L\downarrow] + L\uparrow$ .....(eq. 4.4)

The atmospheric correction algorithm assumes that the atmosphere is a uniform, single layer over the data scene and that a near-blackbody surface exists within the scene ($\epsilon \approx 1$). No reflected downwelling radiance is assumed. Therefore, equation 4.4 can be simplified to

$L_{sen} = \tau L_{BB} + L\uparrow$ ..... (eq. 4.5)

The total amount of radiation emitted over a hemisphere from a perfectly emitting (blackbody) surface at any given wavelength, L_{BB}, is described by Planck function as,

$L_{BB}(\lambda_j T) = \frac{C_1}{\lambda_j^5}.\frac{1}{(e^{C_2/\lambda_j T}-1)}$ .....(eq. 4.6)

where the radiation constant $C_1 = 3.7417 * 10^{16}(Wm^2)$ and $C_2 = 1.4387 * 10^{-2}(mK)$.

If the transmission (τ) and upwelling radiance ($L\uparrow$) are estimated, brightness temperature (T_b) of the surface can be estimated by rearranging equation 4.5 and substituting the Planck function (eq. 4.6).

$T_b = C_2[\lambda_j(ln[\frac{C_1}{\lambda_j^5(\frac{L_{sen}-L\uparrow}{\tau})}] + 1)]^{-1}$ .....(eq. 4.7)

The radiance values of each pixel (L_{sen}) are first converted to brightness temperature (T_b), as in equation 4.7. Then, at each pixel, the band with the highest T_b is tabulated, and for the entire image the band with the greatest number of records is determined.

Scatter plots will be made for each band using the pixels with highest T_b. The measured spectral radiance-at-sensor (L_{sen}) is then plotted against the spectral radiance of a black body (L_{BB}). According to equation 4.5, the atmospheric upwelling ($L\uparrow$) and transmission (τ) can be derived from the slope and offset of the best fitted line of the plot (Hernandez-Baquero, 2000; Young et al., 2002).

Young et al. (2002) found that, in the ISAC method, the band for which T_b is largest is not the same for all pixels. This non-uniqueness in wavelength of maximum T_b leads to inconsistencies in the definition of the compensation parameters.

4.5.2 Temperature and Emissivity Separation (TES)

Planck's law, discussed in equation 4.6, describes the spectral distribution of the radiation from a perfectly emitting black body. As most natural surfaces do not behave as perfect emitters, the total amount of emitted radiation at any given wavelength, L_{em}, is better described by,

$L_{em} = L_{BB}.\epsilon = \frac{C_1}{\lambda^5}.\frac{\epsilon}{(e^{C_2/\lambda T}-1)}$ .....(eq. 4.8)

where, L_{em} is in units of Wm^{-3}.

Inversion of equation 4.8 yields temperature,

$T = \frac{C_2}{\lambda}.\frac{1}{ln[\frac{C_1\epsilon}{\lambda^5 L_{em}+1}]}$ .....(eq. 4.9)

Equation 4.9 shows the non-linear relationship between T, λ, ϵ and surface-emitted radiation. This non-linear behavior leads to more complex effects of atmospheric scattering, emission effects in scenes with more complex geometries such as slope, aspects and sun-surface-sensor geometries, heterogeneity of scene elements, and heterogeneity of the atmosphere (Rolim et al., 2016; Collins et al., 1999). It also demonstrates the inherently under-determined problem of retrieving T and ϵ separately. The ϵ is wavelength dependent and thus measurements of n wavelengths are always accompanied by at least $n+1$ degrees of freedom (n emissivities for each band with a temperature), even if the pixel is isothermal, compositionally homogeneous, and quantities characterizing the atmosphere ($\tau, L\uparrow, and L\downarrow$) are known (Hook et al., 1992; Mushkin et al., 2005; Becker and Li, 1995). Different approaches have been applied to extract the emissivity from thermal multispectral and hyperspectral data. Some of them are the day/night method (Becker

and Li, 1990), the gray body emissivity method (Barducci and Pippi, 1996), the reference channel emissivity method (Kahle et al., 1980), the emissivity normalization method (Gillespie, 1985), the spectral ratio method (Watson, 1992), and the alpha residuals method (Kealy and Gabell, 1990). The methods listed above calculate the absolute or relative emissivity values for the quantitative analysis. The following three methods were applied for the atmospheric corrected ASTER TIR image using ENVI software.

1) Reference Channnel Emissivity

The simplest temperature-emissivity separation (TES) method is the reference channel emissivity (RCE) method developed by (Kahle et al., 1980). This method assumes that the emissivity in one band (i) has a constant value for each pixel. The selection of this band is subject to prior knowledge of the target area and the variations of emissivity values of those materials in different bands. Knowing the atmospheric parameters ($\tau_i, L\uparrow_i, L\downarrow_i$) of the selected band, it is possible to derive the temperature ($T_{s,i}$) for each pixel based on its radiance ($L_{sen,i}$), using the inverse of equation 4.3.

$$T_{s,i} = L^{-1}_{BB,i}\left[\frac{L_{sen,i}-(1-\epsilon_i)\tau_i L\downarrow_i - L\uparrow_i}{\epsilon_i \tau_i}\right] \quad \text{.....(eq. 4.10)}$$

This temperature is then used to derive the emissivity values for rest of the TIR bands, according to equation 4.3,

$$\epsilon_i = \frac{L_{sen,i}-L\uparrow_i-\tau_i L\downarrow_i}{\tau_i(L_{BB,i}(T_{s,i})-L\downarrow_i)} \quad \text{.....(eq. 4.11)}$$

ASTER band 12 was selected as a reference band with an emissivity value of 0.95, after analyzing the emissivity spectra of field samples.

2) Emissivity Normalization Method

The Emissivity Normalization Method (EN), developed by (Gillespie, 1985), calculates the apparent surface temperatures in all bands using an assumed reference emissivity value (ϵ_r) across all bands. The highest of these apparent temperature (T_{max}) is used as the land temperature (T_s). The temperature is calculated by,

$$T_{\lambda,i} = L^{-1}_{BB,\lambda}\left[\frac{L_{sen,\lambda,i}-(1-\epsilon_r)\tau_\lambda L\downarrow_\lambda - L\uparrow_\lambda}{\epsilon_r \tau_\lambda}\right] \quad \text{.....(eq. 4.12)}$$

where, ϵ_r is the reference emissivity, $L_{sen,\lambda,i}$ is the radiance measured in the band λ for pixel i.

Then, T_s is used to re-calculate the emissivities in each of the remaining bands by,

$\epsilon_{\lambda,i} = \frac{L_{sen,\lambda,i} - L\uparrow_\lambda - \tau_\lambda L\downarrow_\lambda}{\tau_\lambda (L_{BB,\lambda}(T_s) - L\downarrow_\lambda)}$ .....(eq. 4.13)

The value 0.95 is selected for ϵ_r as in the RCE method.

3) Alpha Residuals (AR)

This method was developed by (Kealy and Gabell, 1990) based on the Wien's approximation of the Planck function given by equation 4.6. Taking the natural logarithms of the $L_{BB}(\lambda, T)$ by Planck function and eliminating the surface temperature (T_s) by subtracting natural logarithms of one band from its mean of total N bands, α for band j can be calculate according to equation 4.8,

$\alpha_j = \lambda_j ln\epsilon_j - \frac{1}{N}\sum_{i=1}^{N} \lambda_j ln\epsilon_j$ .....(eq. 4.14)

It should be noted that the alpha residual spectra are not directly comparable to laboratory emittance spectra (Fig 4.3).

Figure 4.4 compares the sample spectra (black) along with ASTER TIR convolved sample spectra (red), pixel spectra after thermal atmospheric correction (green), and pixel spectra of adopted TES methods (RCE: cyan, EN: blue, and AR: pink). Pixel spectra after thermal atmospheric correction were divided by 20 to plot in the same plot. Emissivity spectra of RCE, EN, and AR were also linear stretched to enhance the band depths. The fundamental absorption feature of quartz, which dominates in felsic rocks, appears around 8 - 9 μm (Salisbury and D'Aria, 1992; Ninomiya et al., 2005) in the RCE and EN pixel spectra of T27, T30, and T37. In silicate rocks, this feature shifts to longer wavelength as the SiO_2 content (weight percent) decreases (Christensen et al., 1986). Major carbonate minerals show spectral minima in ASTER band 14, but this is not evident in either the RCE or EN pixel spectra or sample spectra of T30 (Fig 4.3b). The emissivity spectra (RCE and EN) of T45 shows signatures for both felsic and ultramafic materials (Fig 4.4d) (Ninomiya et al., 2005). The results show that the scene-derived emissivity spectra are mostly mixed with the spectra of surrounding felsic and mafic materials.

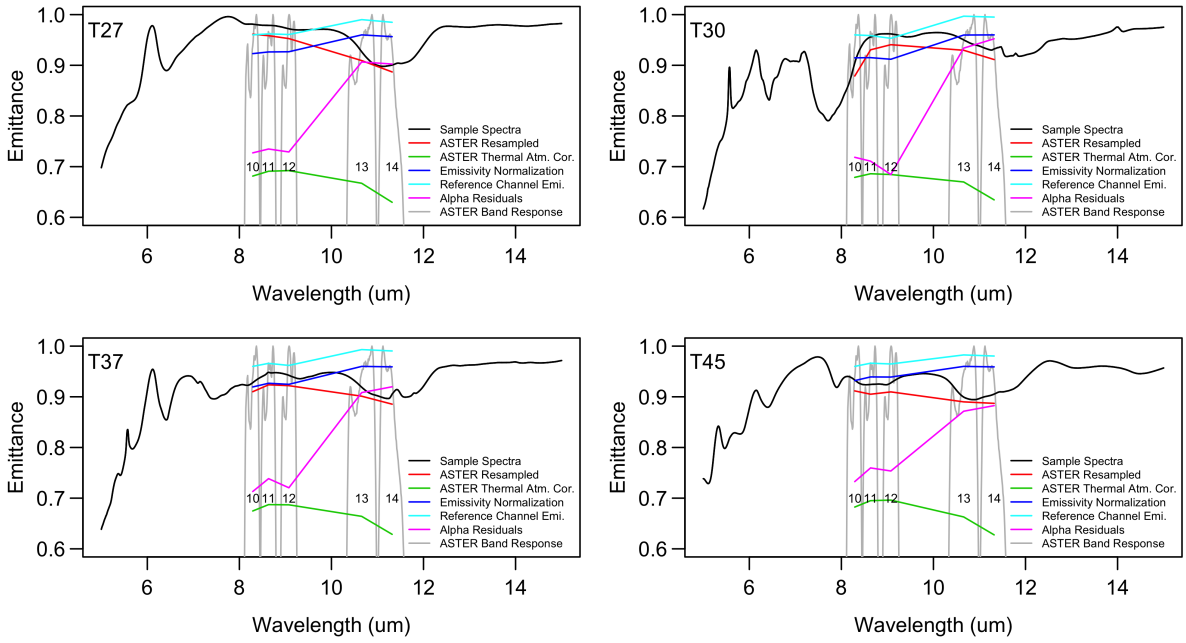

Figure 4.4: TIR sample spectra with resampled ASTER image pixel spectra after different processing levels and methods.

Although the overall objective of this study is to detect and map zeolite minerals using orbital TIR data, the field visit indicates that fully zeolitized tuff beds with spatial coverage larger than 90 m × 90 m are very limited in the area. Therefore, an attempt was made to identify and map the tuff beds in which the zeolites mostly occur. The surface materials of the area were grouped into three first order units named $Tuff$, $NoTuff$ and *Gravel*. The point map was created with 50 points for each unit after visual analysis of published maps, the ASTER VNIR NCC (visible to near infrared natural color composite) image, along with our field data. The $Tuff$ points were selected from the field data and places where the area is exposed and Tuff A, B, and C have been identified. The $NoTuff$ unit was assigned for the exposed areas where no tuff beds are identified. Map unit *Gravel* is assigned to the dark color areas of the image where the surface is covered by gravels, volcanic flows, or desert pavements. Spatial distribution of those points is shown in Figure 4.2 (c). The point map was imported to the R statisitcal software package for spatial and statistical analysis and visualization.

The differences in derived emissivity (ϵ) values in each class were compared after applying the temperature emissivity separation (TES) using emissivity normalization

(EN) and reference channel emissivity (RCE) methods (Fig 4.5a). Data points represent the mean ϵ value in each class. This shows that ϵ values of $Tuff$ and $NoTuff$ classes overlap with each other in all bands, whereas *Gravel* class can be distinguished from $Tuff$ and $NoTuff$ classes in Band 10, 11 and 12, based on their ϵ values. However, it is difficult to select the best TES method using this graph since the mean ϵ values and their standard deviations in each class and method do not follow any specific pattern. Alpha Residual method (Fig 4.5b) also shows a similar pattern to the EN and RCE methods, such as $Tuff$ and $NoTuff$ classes overlapping each other while the *Gravel* class can be recognized from the other two with some accuracy. One way to check the accuracy of the EN and RCE methods is to compare the temperature calculated from both methods (Fig 4.5c). All *Gravel* pixels show similar temperature values in both methods, while some of the $Tuff$ and $NoTuff$ pixels show higher temperature values in the RCE method than in the EN method.

Band 14 was selected as a reference channel for the RCE method with an ϵ value of 0.95 (Fig 4.5a). The temperature image was then calculated using those pixel values. The emissivity normalization method first used one reference ϵ value (0.95) for all bands to create temperature maps for each band (eq. 4.8), and the highest temperature pixels were then used to create the final temperature map. The EN algorithm found the highest temperature pixels from *Gravel* class in band 14 (Fig 4.5c) for the given ϵ value (0.95). Therefore, both EN and RCE methods calculate the same temperature values for the *Gravel* points in both cases. Some of the $Tuff$ and $NoTuff$ pixels had higher temperature estimates from RCE or lower temperature from EN, probably due to the overestimation of ϵ values for those pixels in RCE or underestimation of ϵ for the EN method. This result implies that both the RCE and EN methods have several limitations; 1) it is difficult to find a unique emissivity value that is appropriate for all surface materials in one reference channel using the RCE method. Li et al. (1999) noted that 1 % uncertainty in the emissivity in the RCE method can result in an error of about 0.5 K in temperature, and emissivity errors of 1 - 2 % in other channels. Incorrect assumptions for ϵ will either decrease or increase the absolute value of the spectrum and rotate the spectrum clockwise or counter clockwise about the assumed band, based on whether the value assumed is

overestimated or underestimated (Hook et al., 1992). 2) The unique ϵ value was selected for band 14 and therefore there is no emissivity spatial information in this band. 3) When the bands are highly correlated with the reference band, the data in the adjacent band is also forced towards the constant value (Band 13, Fig 4.5a), and any noise differences between the two bands are enhanced (Band 10, 11, 12 in Fig: 4.5a) (Hook et al., 1992), 4) If the data in the constant band contains noise, this noise is introduced into other bands, as part of the algorithm (Hook et al., 1992). The EN method assumes that the maximum emissivity value in all pixels in the image is constant, but the band with maximum emissivity may differ pixel by pixel (Becker and Li, 1995). The advantage of the AR method is thar this method is scene-independent and no noise is propagated from one band to another (Hook et al., 1992). The biggest drawback of the AR method is that the spectra can not be directly compared to sample emissivity spectra (Fig 4.4). For the above reasons and the recommendations of previous researchers (e.g., Kealy and Hook (1993); Li et al. (1999)), the EN method was selected for further analysis.

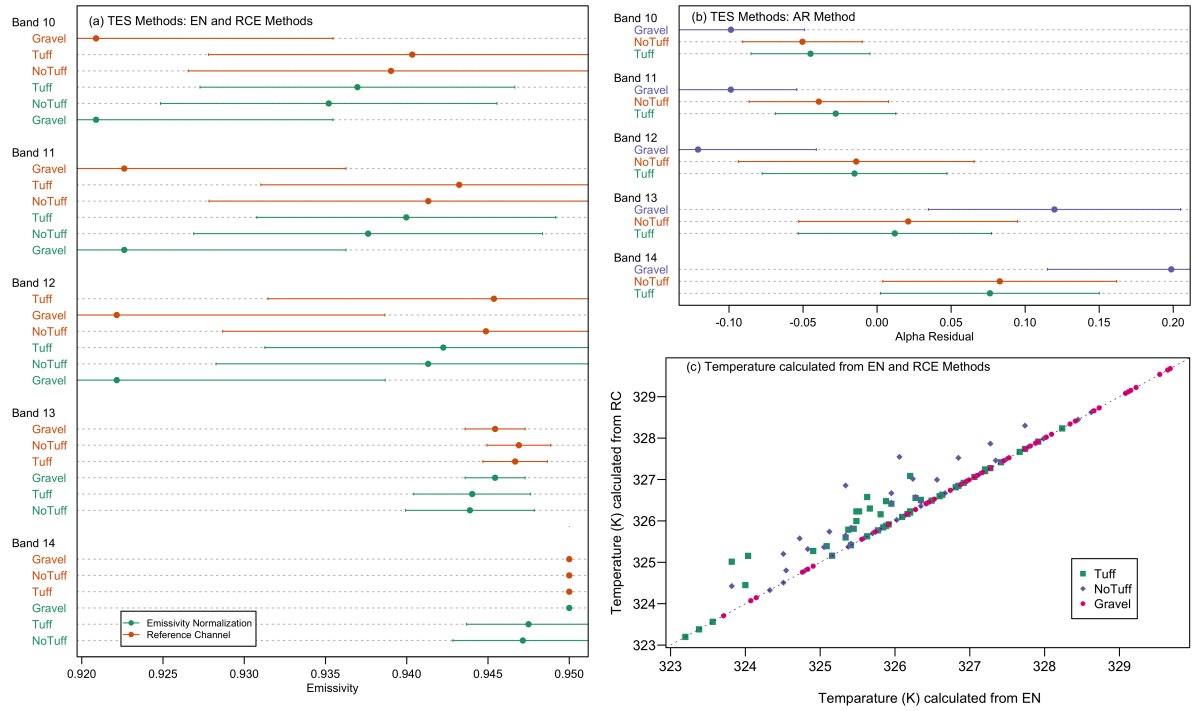

Figure 4.5: Comparison of different TES methods. (a) Emissivity normalization (EN) and Reference Channnel Emissivity (RCE) methods, (b) Alpha Residuals (AR) method, and (c) Temperature calculated from EN and RCE methods

4.6 Spectral Mapping

Spectral mapping algorithms used to map, enhance or delineate geology from spectral images and can be grouped into five basic categories, 1) Band ratios and indices (Sultan et al., 1987), 2) principle components and enhancement/display based methods such as Principle Component analysis (Crosta and Moore, 1989), Minimum Noise Fraction (Green et al., 1988), decorrelation stretched (Soha and Schwartz, 1978), false color composite (Harding et al., 1989), or IHS transformation (Gillespie et al., 1986), 3) shape-fitting based algorithms such as Spectral Angle Mapper (Kruse et al., 1993), Matched Filtering (Harsanyi and Chang, 1994) and Mixture Tuned Matched Filtering (MTMF) (Boardman and Kruse, 2011), 4) Spectral Unmixing methods (e.g., Kruse et al. (1993)), and 5) Machine Learning methods (e.g., Hu et al. (2019)).

To assess their capabilities for identifying and mapping zeolite-bearing deposits using thermal infrared remote sensing data, four most commonly used spectral mapping techniques were selected representing different levels of information extraction. The methods include 1) band indices, 2) Minimum noise fraction (MNF), 3) Spectral angle mapper (SAM), and 4) Linear spectral mixture analysis (LSMA). The band indices and MNF methods were adopted assuming that there is no field information (e.g., geology and mineralogy), which is similar to mapping minerals in most areas on Mars. The SAM method was implemented assuming that limited information is available on the study area such as the emissivity spectra of known sample/s or the image spectra of the target location/s. The LSMA method was applied assuming that more information is available including the spectral endmembers or locations of possible endmembers to collect scene-derived endmember spectra of the study area.

Figure 4.6 (a, b, and c) compares the results of the three adopted TES methods. All images shown in Figure 4.6, except the lithology map (e) and SAM classification map (h), are linearly stretched for visual comparison. Emissivity values extracted using the RCE method shows more noise than the other two methods as discussed before. The band combination Band 11, 13, and 14 was used for RGB color composite to enhance the lithological variations in the area. An abandoned quarry in the west of the study area

in Figure 4.6 (b), indicated by the bright red spot, has exposed zeolitic tuff beds. The band combination selected for the EN method shows the exposed tuff beds in red and washes of these tuff materials and surrounding sandstone and mudstone beds are seen in the middle of the paleolake deposits as discussed by Morrison (1999).

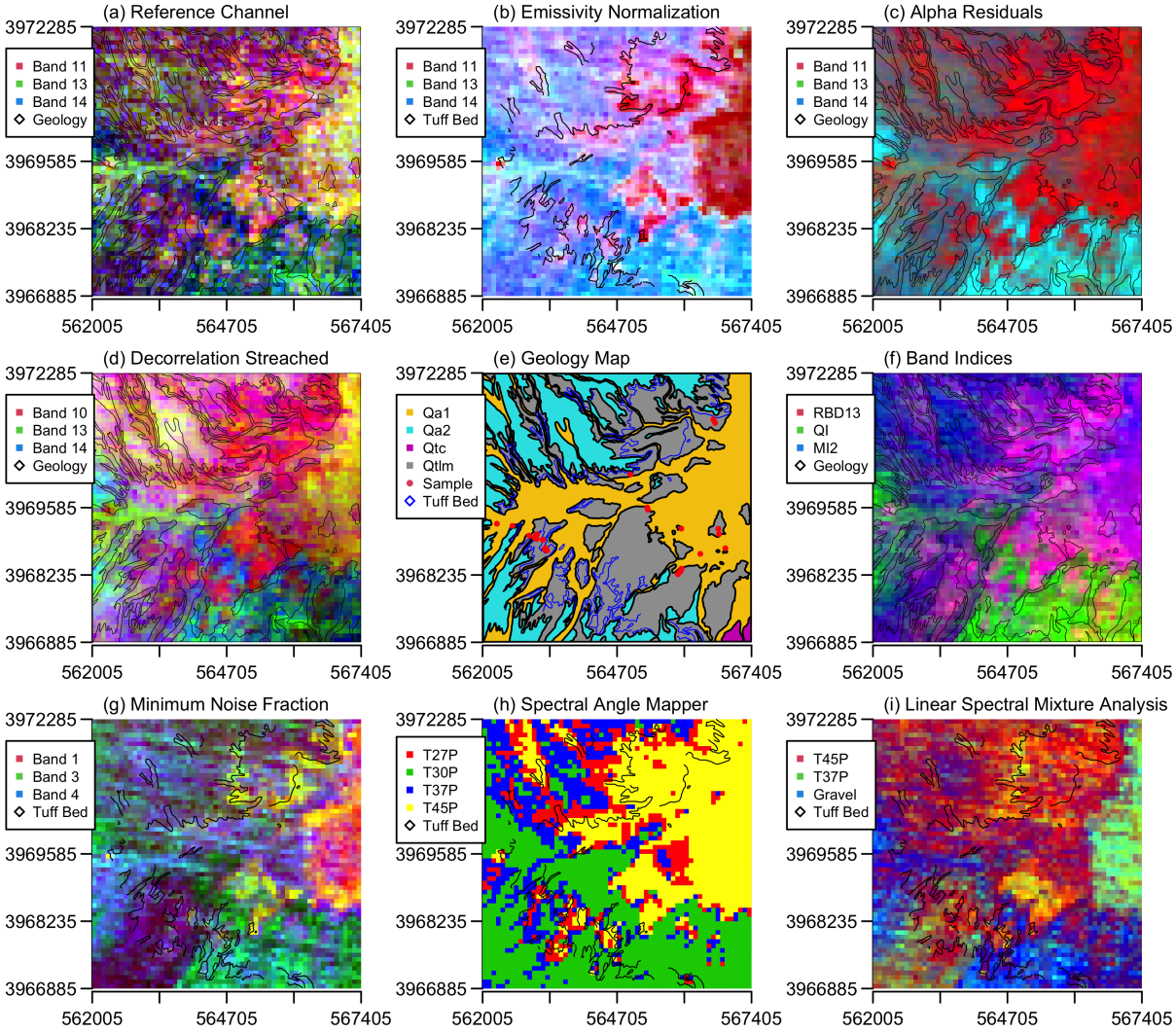

Figure 4.6: ASTER TIR mapping results. (a) Emissivity bands calculated using the Reference Channel Emissivity method, (b) Emissivity bands calculated using the Emissivity Normalization method, (c) Emissivity bands calculated using the Alpha residuals method, (d) decorrelation stretched image of ASTER band 10, 13, and 14, (e) Geology map of the area, (f) ASTER TIR band indices, (g) ASTER TIR MNF bands, (h) ASTER TIR SAM image, and (i) ASTER TIR linear spectral mixture analysis results. Selected band conbinations are shown in the legend.

The spectral ratio method (SR) is based on the concept that though spectral radiance is very sensitive to small changes in temperature, the ratios are not (Watson, 1992). Therefore, only an approximate value of temperature is enough to determine the emissivity ratio with

high precision. Ninomiya et al. (2005) introduced several mineralogical indices that can be used even with atmospherically uncorrected radiance-at-sensor ASTER data. Seven band indices were adopted including six band indices introduced by Ninomiya et al. (2005).

Major carbonate minerals show spectral emissivity minima near 11.2 μm (ASTER band 14) due to the CO_3 bending reststrahlen feature (Salisbury and D'Aria, 1992). Therefore, the Carbonate Index (CI) for ASTER-TIR data is defined as,

$CI = B_{13}/B_{14}$ ..... (eq. 4.15)

Band 13 is assigned as the numerator because the major terrestrial siliceous and felsic rocks have strong absorption features in the band 10 to 12 spectral region and it is common to see mixed pixels of carbonate rocks with siliceous and felsic rocks in nature (Ninomiya and Fu, 2019).

Quartz Index (QI) enhances the spectral feature of quartz in ASTER bands 10-12. The emissivity of quartz at the ASTER band 11 is convex upward in ASTER band 10-12 spectral region.

$QI = \frac{B_{11}*B_{11}}{B_{10}*B_{12}}$ .....(eq. 4.16)

Mafic Index (MI) is negatively correlated to the SiO_2 content in silicate rocks and defined as,

$MI = \frac{B_{12}}{B_{13}}$ ..... (eq. 4.17)

MI is also sensitive to carbonates. To avoid that, a series of MI, separated from carbonate, is defined as,

$MI_n = \frac{B_{12}}{B_{13}*CI^n} = \frac{B_{12}*B_{14^n}}{B_{13^{n+1}}}$ ..... (eq. 4.18)

where n is the isolation degree for carbonates.

The relative band depth at band 13 (RBD13) will give high DN values for mafic-ultramafic lithologies (Rowan et al., 2005).

$RBD_{13} = \frac{B_{12}+B_{14}}{B_{13}*B_{13}}$ .....(eq. 4.19)

These band indices were calculated before and after the thermal atmospheric correction. This shows that the atmospheric correction decreases the variance in index values (low SD) and rescales the band ratios (Watson, 1992) (Fig 4.7a). This also shows that the thermal atmospheric correction decreases the systematic and random variations in the

radiance data. Therefore, the band indices calculated after the atmospheric correction were selected. The fundamental limitation of the band ratioing method is that it enhances the high spatial frequencies, due to their low signal to noise ratio (Watson, 1992). The Greenwater Fan, shown in blue (Fig 4.6f) indicates mafic minerals in the area while younger alluvial deposits and exposures (Greenwater wash) are shown in purple-magenta. MI is expected to be high for some iron oxides and halite (Ninomiya et al., 2005). The lowest portion of the study area shows high values on MI indicating the presence of halite as thin crust of evaporites. RBD13 is more sensitive to the tuff in the area (Fig 4.6d). Sperry Hills in the southern portion of the study area is shown in green, indicating a high abundance of quartz. The tuff-rich area is indicated by yellow due to the combination of RBD13 and QI. Ninomiya et al. (2005) noted that, while the QI and MI are insensitive to the temperature, CI is highly affected by temperature differences even under good atmospheric conditions. Therefore, CI will not be a good index to map carbonates in rugged terrain such as in this study area, due to shadowing effects.

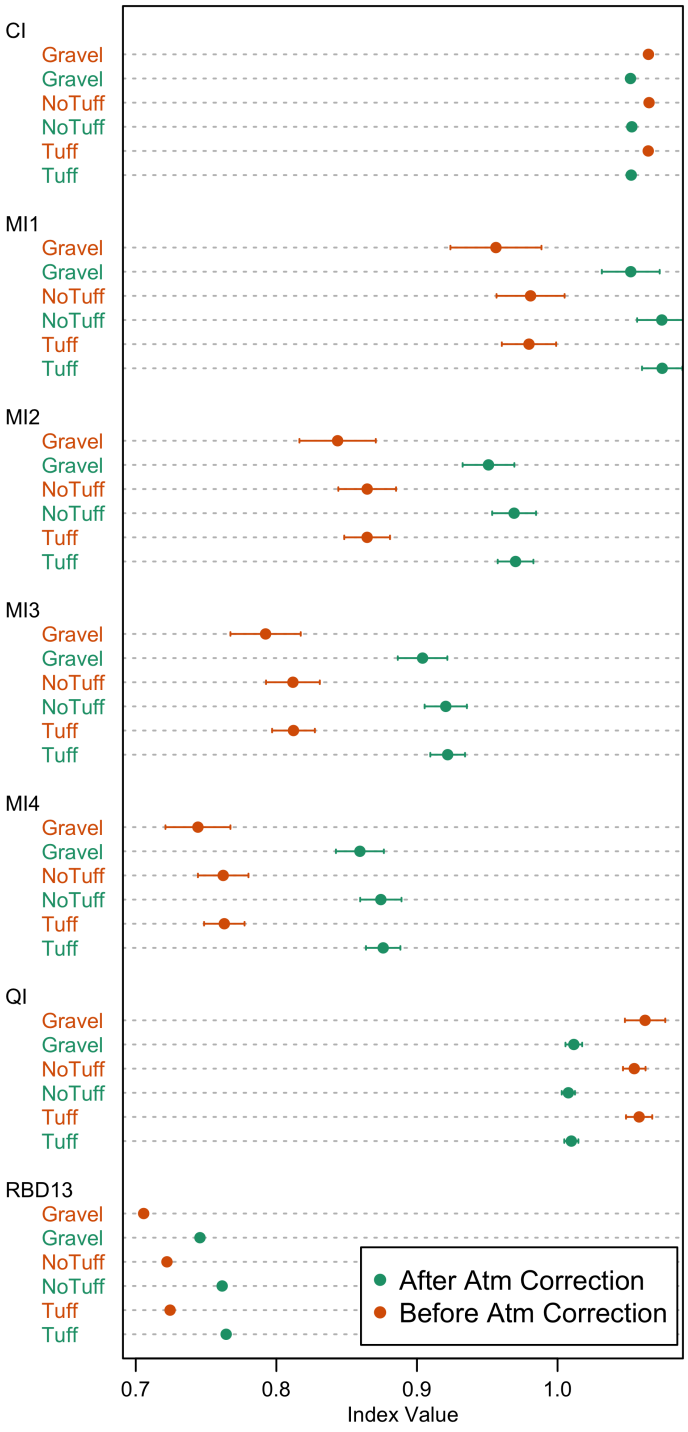

Figure 4.7: The effects of thermal atmospheric correction on the selected band indices.

The Minimum Noise Fraction transformation (MNF), introduced by Green et al. (1988), is used to determine the inherent dimensionality of the image data. The eigenvalue of each MNF transformed band provides a measure of its information content, with

progressively noisier bands approaching eigenvalues near zero (Hubbard and Crowley, 2005). The MNF transformation was applied to the ASTER TIR image data. After visually analyzing each of the MNF bands, MNF bands 1, 2, and 3 was selected as the best band combination. The MNF results do not show clear spatial correlation with tuff beds or published geological maps of the area (Fig 4.6g).

The Spectral Angle Mapper (SAM) measures spectral similarity by calculating the angle between two spectra and treating them as vectors in n-dimensional space (Kruse et al., 1993). The calculation consists of taking the arccosine of the dot product of the spectra.

$$\text{SAM} = COS^{-1}\left(\frac{\sum_{i=1}^{n} t_i r_i}{(\sum_{i=1}^{n} t_i^2)^{1/2}(\sum_{i=1}^{n} r_i^2)^{1/2}}\right) \quad \text{..... (eq. 4.20)}$$

where n is the number of bands, t is the test spectrum and r is the reference spectrum. A small spectral angle between two vectors shows that the two spectra closely match each other, while the large angle shows a poor match. The SAM is insensitive to gain factors because the angle between two vectors is invariant with respect to the length of the vectors and therefore, it is insensitive to the topographic illumination effects (Kruse et al., 1993). Hecker et al. (2008) demonstrated the influence of different sources of reference spectra on SAM classification results and noted that the image spectra works better than either library or sample spectra. The scene-derived endmember spectra of sample locations T27, T30, T37, and T45 were used as reference spectra in each category. The SAM result does not demarcate the tuff beds or lithology of the area, instead it demarcates the exposed sedimentary deposits, washes, and gravel beds at Greewater Fan and Sperry hills (Fig 4.6h).

The spectral unmixing methods can be broadly categorized into two groups as linear spectral unmixing models and non-linear spectral unmixing models, according to the mathematical formulation for describing the underlying mixing process (Shi and Wang, 2014; Bioucas-Dias et al., 2012). The linear spectral mixture analysis (LSMA) predicts the areal fraction of endmember components in a spectrum measured for a mixture (Bandfield and Rogers, 2019; Gillespie, 1992b). It is a form of multivariate linear regression and can be generally expressed as,

$$Y_i = \sum_{j=1}^{n} \beta_j X_{i,j} + e_i \quad \text{.....(eq. 4.21)}$$

where Y_i is the reflectance of the mixed spectrum in image band i for each pixel, β_j is the fraction of each endmember j calculated band by band, n is the number of endmembers,

and e_i is the residual error for band i of the fit of n spectral endmembers (Bandfield and Rogers, 2019). As in the SAM, the spectral endmembers can consist of laboratory measured spectra, scene-derived spectra, synthetic spectra, or modeled derived spectra. However, this study and previous studies show that scene-derived spectra perform better than laboratory measured spectra and therefore five scene-derived endmember spectra were chosen. Scene-derived endmember spectra were extracted from the corresponding pixels of sample locations T27, T30, T37, T45, and average spectra of *Gravel* class. The residual error e map is used to determine the quality of fit. The LSMA shows more complex mapping results (Fig 4.6i), indicating more tuff and sandstone layers in yellow, and more gravels in blue. Recent washes towards the basin center show combination of all sediments (cyan), as seen in the field.

Kahle et al. (1980) found that an image color enhancement method decorrelation stretched can be used to visualize the temperature and emissivity variations of the image. The decorrelation stretched method (DS), introduced by Soha and Schwartz (1978), produces a stretched image that exaggerates color saturation (Gillespie et al., 1986; Campbell, 1996). This technique is based on a principal component transformation in which the transformed variables are contrast stretched and then retransformed into the original coordinate system to display. The process can be described in three stages, 1) the original bands are first transformed to their principal components, 2) the transformed variables are then stretched separately, and 3) the inverse of the principal component transformation is applied (Campbell, 1996; Gillespie et al., 1986; Gillespie, 1992a). Previous research found that the false-color composition (RGB) of decorrelation stretched TIR images shows emissivity differences as color variations while temperature information is seen as intensity variations (Hook et al., 1992; Rolim et al., 2016; Kahle et al., 1980). The decorrelation stretched image was created from the atmospheric corrected ASTER TIR bands using the R software package. The color composite from bands 10 (R), 13 (G), and 14 (B) was selected for the final decorrelation stretched image after visualizing all possible band combinations, based on the spatial variability of color and intensity over the study area. It shows the erosional stream deposits and lowland sediments in yellow and tuff bed areas in red (Fig 4.6d).

4.6.1 Finding the best mapping product(s)

All the map products created above using different mapping techniques (Fig 4.6) are not equally important for identifying zeolites or zeolite bearing tuff beds over the study area. Therefore, it is important to find the best mapping product to create a geological model of the area. The learning vector quantization (LVQ) neural network technique (Kohonen, 2001b) was adopted to determine the importance of each mapping product using a clustering technique. The k-fold cross-validation (k-CV) method is used to evaluate and compare the mapping results. This approach involves randomly dividing the set of observations into k groups (10 groups in this case) of approximately equal size. The first group is treated as the validation set, while the method is fit on the remaining k -1 groups. The mean squared error (MSE) is computed on the observations in the held-out group. This procedure is repeated k times and each time a different group of observations is treated as a validation test. At the end, the k-fold CV estimate is computed by averaging the MSE value in each repeat. The k-fold CV method was repeated three times for each attribute map to find the best results. The highest importance scores of 12 attribute maps of each class ($Tuff, NoTuff$, and $Gravel$) is shown in Figure 4.8. The $RBD13$, with its relative band depth near 10.5 μm (Table 4.1), is the best mapping technique to differentiate these classes. The absorption band depth near 10.5 μm is the most prominent Si-O absorption feature, which changes with the type of silicate minerals as discussed before. This absorption band depth also varies due to other minerals present in the area (Salisbury and D'Aria, 1992) and due to the desert varnish (Rivard et al., 1993). It is interesting to note that the importance (separability) of the MI series linearly decreases with the increase of series, with its highest accuracy for MI1. Ninomiya et al. (2005) noted that the MI3 shows good separation of carbonate from silicates. This study could not identify the signature of carbonate well (i.e. lowest important values in CI band index and T30LSU in Fig 4.8), though carbonates are abundant in most beds (based of field and XRD analysis).

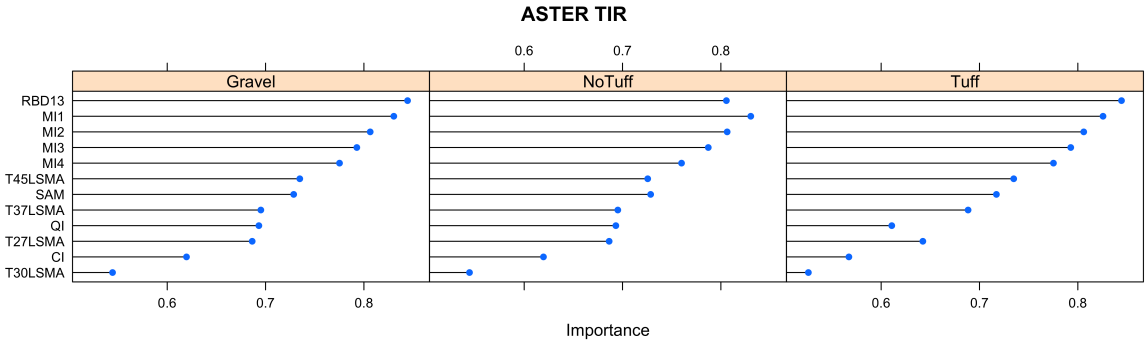

Figure 4.8: Importance scores of attribute images derived from ASTER TIR image data for predicting the Tuff beds.

4.7 Implications for Mars

Thermal infrared observation of Mars can be used to determine the surface mineralogy and is sensitive to some minerals not detectable in the near infrared wavelength region, such as feldspar and anhydrous silica. The Mars Global Surveyor (MGS) Thermal Emission Spectrometer (TES) was designed to address a wide range of science objectives including identification of surface minerals, volatile abundance and history, and atmospheric dynamics (Christensen et al., 1992). The TES instrument is equipped with a Michelson interferometer (~ 6 - 50 μm) and bore sighted solar reflectance and thermal radiance channels to measure albedo and thermophysical properties at a spatial resolution of ~3 km × 6 km (Christensen et al., 1992). The Thermal Emission Imaging System (THEMIS) onboard 2001 Mars Odyssey followed the MGS TES and Mars Orbiter Camera (MOC) experiments, providing substantially higher spatial resolution IR multispectral data. THEMIS is composed of a visible subsystem with five channels with a maximum resolution of ~ 18 m × 18 m, and an uncooled, infrared subsystem consisting of nine ~ 1 μm wide channels in the wavelength region from 6.8 to 14.9 μm with a spatial resolution of ~ 100 m × 100 m (Christensen et al., 2004).

Ruff (2004) documented spectral evidence for zeolites in Mars dust using TES data, based on their absorption features at 6.134 and 12.048 μm. This could indicate their widespread abundance on the surface of Mars. However, the presence of zeolite in Mars dust is uncertain and disputed (e.g., Bandfield et al. (2003)). Michalski et al. (2005)

proposed that silica-rich alteration products such as Al- or Fe- bearing opal, clay minerals, clay precursors, or certain zeolites may be present in dark regions of Mars, based on TES data. Bandfield (2008) identified an isolated high silica surface in western Hellas Basin and proposed that the minerals there may be opal, phyllosilicates, or zeolites. Michalski and Fergason (2009) analyzed the thermal infrared surface properties of the Mawrth Vallis area, Mars using TES and THEMIS data. Geologic units of their study area have been devided into three classes based on the TES albedo measurements: light-toned surface, intermediate-toned surface, and dark-toned surface. Their spectral unmixing results point to a more silica-rich nature for the light-toned units. Modeled mineralogy of the averaged light-toned surface spectrum includes 16% plagioclase feldspar, 37% high silica material, 13% zeolites, 11% clay minerals, and other minor components of oxides and sulfates. Based on these results they suggested that the light-toned deposits might have formed through aqueous sedimentary origins from a combination of sedimentary and pyroclastic processes. However, zeolites detected with TES data are not corroborated by the near infrared data, likely due to their coexistence with more spectrally dominant clay minerals (Michalski and Fergason (2009), chapter 3 and 5 of this thesis).

Owing to their similar spectral and spatial resolutions, ASTER TIR bands can be used as a proxy for THEMIS IR bands. Figure 4.9 compares the spectral band passes of the THEMIS IR subsystem to the spectral band passes of the ASTER TIR subsystem. Emissivity spectra of zeolitized tuff (T27) is also plotted. This shows that ASTER bands 13 and 14 are located between THEMIS IR bands 6 and 7, and 7 and 8, respectively. This study found that the relative band depth at band 13 (RBD13) of ASTER TIR band indices performed better in identifying zeolitied tuff. Based on this information along with the emissivity spectral characteristics of T27 (Fig 4.9), the following band index can be implemented as a first order (theoretical) analysis with the THEMIS IR data.

$RBD_{IR} = \frac{B_5+B_7}{B_6*B_6}$.....(eq. 4.21)

However, it is important to note that the proposed band index could lead to incorrect results if other minerals in an area have similar spectral signatures between 10 - 12 μm (e.g., augite and olivine).

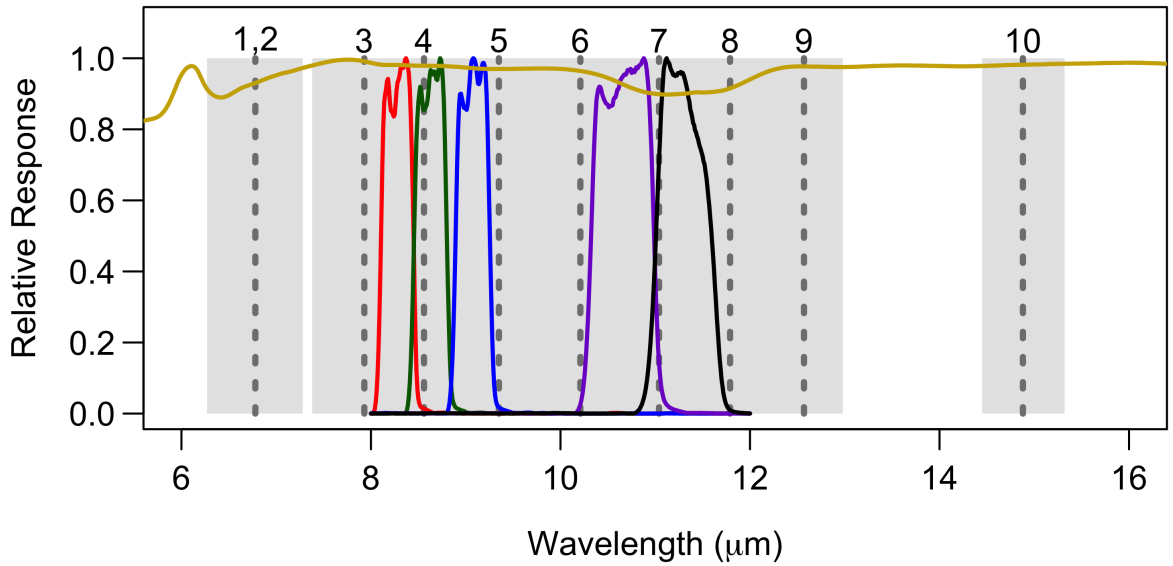

Figure 4.9: Spectral bandpasses of the THEMIS IR subsystem and the ASTER TIR subsystem. Spectral bandpasses of ASTER bands 10, 11, 12, 13, and 14 are plotted in red, green, blue, purple, and black, respectively. Center wavelength of THEMIS IR bands are shown with dotted lines. Band widths of each THEMIS IR bands are shown in gray color. Emissivity spectra of zeolitied tuff (T27) is shown in gold.

The field studies show that most of the exposed zeolite-rich tuff beds are on the top of mesas with a spatial coverage less than the pixel coverage (90 m $\times$ 90 m). Also, most of the zeolite-bearing tuff beds were covered by other sedimentary beds, dust or gravel pavements or mixed with adjacent mudstone and sandstone beds due to physical weathering. This study shows disagreements between lab-based emissivity spectra acquired from fine grained ($< 150\ \mu m$) field samples and the image spectra extracted from orbital data. Previous studies show that the spectral effects tied to particle size and surface roughness can make mineral deposits substantially more difficult to detect and map than is generally understood (e.g., Kirkland et al. (2003); Wagner and Schade (1996); Engelbrecht (2002)). Paleolake deposits are characterized by erosional and depositional features from kilometers to millimeter scale, as observed in lake Tecopa (e.g., mesa, butte, gullies, rills, pop-corn texture in mudstone due to swelling clays, grain textures, and coatings). This surface roughness causes multiple surface reflectances and makes a target less detectable (decreases the spectral contrast) and increases the emissivity (Kirkland et al., 2003). In general, the smoother the surface, the higher the spectral contrast and more readily the

material is detected. Therefore, the effects of surface roughness (and texture) at multiple scales must be considered when interpreting thermal remote sensing data of the surface of Mars. Also, care should be taken during the linear spectral mixture analysis (LSMA) approach to model the mineral abundances since different materials have different surface textures that can change the band depth (and volume scattering can change the band shape). Therefore, observed band depth and/or band shape alone should not be used for identifying minerals or for measuring their abundances. Proper selection of image end members for LSMA is also important. Image end member emissivity spectra provide a better deconvolution model fit than laboratory spectra since all the data were collected with the same instrument under the same atmospheric and viewing conditions.

Wright and Ramsey (2006) analyzed the ASTER TIR data of Meteor Crater as a proxy for examining THEMIS IR data of similar-sized craters on Mars. They also noted the limitation of linear deconvolution of multispectral TIR data. Further, they conclude that, in cases on Earth and Mars where the distribution of lithologic endmembers is less than 15 % of the entire area or where there are no large-scale outcrops, the spectral deconvolution approach will not detect their presence. Kirkland et al. (2003) demonstrate that substantial, well-crystalline, regional mineral deposits with even 100% exposure (including rock outcrops) can remain undetected at the sensitivity of TES/THEMIS. They also noted that materials with optically rough surfaces will be underrepresentated while optically smooth surfaces will be overrepresented in TES and/or THEMIS data.

This study also shows the difficulty of identifying carbonate through lab based and orbital TIR spectral data, though the study area contains carbonate-bearing mudstone (e.g., T30). Wagner and Schade (1996) studied the spectral contrast of the carbonate band at $\sim 4\ \mu m$ for various amounts of carbonates (siderite and dolomite/ankerite) in two Mars soil analogs (palagonite and tholeiite). Their study shows that the detectability of carbonates strongly depends on the surface temperature and the grain size. The spectral detectability of carbonates at the $\sim 4\ \mu m$ wavelength is reduced for material coarser than $\sim 25\ \mu m$, and for surface temperature near 300 K. Kirkland et al. (2003) demonstrate the spectral contrast variation of 11.25 μm band of carbonate using laboratory spectra of intensely lithified hand samples of calcrete and airborne spectrum of a region

covered with calcrete boulders. Hanna et al. (2012) demonstrate how sensitive the TIR emissivity spectra of plagioclase feldspar is to the environmental conditions (temperature and pressure) under which they are measured (e.g., Earth-like, Mars-like, lunar-like). Therefore, it is also important to conduct more research to understand the spectral behaviors of zeolites under Mars environmental conditions.

4.8 Assumptions and limitations

The most common assumptions used in this study and in planetary remote sensing studies in general are listed here. It is important to note that each assumption/limitation may affect to different degrees or in different combinations and that inaccuracies associated with each assumption/limitation may be accumulated in the final result.

1) The objective of this study was to identify zeolite bearing beds using thermal infrared spectral mapping methods. From the total collected field samples (65), four representative samples (geologically and mineralogically) were selected as end members for the spectral and image analysis. It is assumed that selected samples represent the spectral characteristics of zeolites and associated sediments of the area. One can argue that increasing the number of end members will better represent the study area. However, the number of end members is limited by the mapping algorithm used (e.g., SAM, LSMA), accessibility for sample collection and limitations associated with spectral acquisition.

2) Selected samples were ground to 150 μm to acquire TIR spectra to compare against existing library spectra of similar grain size. It is assumed that laboratory conditions during sample collection and optical arrangement of the instruments are similar to the conditions used to collect library spectra. It is also assumed that chemical composition (e.g., minor element composition, cation exchanged species, etc.) and crystal structures (e.g., site distortions and site symmetry) of the samples and samples used for the library spectra are similar.

3) The emissivity spectra were calculated from the acquired reflectance spectra using Kirchhoff's law (eq. 4.1) by assuming that the thermal gradient and radiant flux transmitted through the sample are negligible with the given thickness of the sample (Rivard et al., 1993; Siegel and Howell, 1981). The thermal gradient may cause its spectral emittance to depart substantially from its reflectance and therefore, deriving emissivity spectra from reflectance spectra using Kirchhoff's law must be done carefully (Salisbury et al., 1987). Salisbury et al. (1994) showed that even though the emissivities calculated from lab measurements of directional hemispherical reflectance and emissivities calculated from laboratory measurements of emittance are equally valid, a measurement of emissivity is far more complex compared to a measurement of reflectance, due to the multiple sources of error involved.

4) It is well known that the decrease of intensity or spectral contrast of the fundamental molecular vibration bands with decreasing particle size and increasing porosity is a major drawback of using thermal infrared for remote sensing of planetary bodies (Salisbury et al., 1987; Lane and Christensen, 1998). However, detailed observation of the fundamental/combination/overtone absorption bands and transparency features with their relative depths can provide insight into their effective particle size and composition (Lane and Christensen, 1998).

5) An emissivity value of 0.95 was assigned for band 14 in the RCE method and as the maximum emissivity of the area for EN method for Temperature-Emissivity Separation (TES). Both methods create uncertainties by calculating the temperature and deriving the apparent emissivity from these derived pixel temperatures.

6) At the 90 m $\times$ 90 m scale of ASTER TIR pixels, surfaces are covered by multiple components having different emissivities and temperatures. Each component adds to the number of unknowns, while the number of measurements is constant (5 bands). The number of bands in the ASTER TIR subsystem is not sufficient to estimate all unknowns. Therefore, the effective temperature and ϵ spectrum for each pixel was calculated by assuming that pixel coverage is homogeneous (Gillespie et al., 1998).

7) The scene-derived endmember spectra were collected assuming the ground surface area is correctly represented by the pixel. However, the scene-derived endmembers are typically a mixture of more basic components, regardless of how well they are chosen. Therefore those basic components may change in proportion in each each pixel, creating another level of complication.

8) The underlying assumptions for the LSMA method adopted include that 1) the library spectra (scene-derived endmember spectra in this case) used to model each pixel spectrum contains all the endmembers present in the area, and that 2) the spectral emissivity of each endmember in the mixture contributes to the mixed spectrum in proportion to its true areal abundance, at each image band. The second assumption is true for optically thick grains or crystals (i.e. photon path length $<$ thickness of the grain). There is the potential to over- or underestimate a phase in LSMA if the library spectrum of a certain phase was measured from much smaller or larger grains than the other phases in the library. Additionally, weakly absorbing minerals, such as halite in this case, or very thin coatings ($<\sim$ 10 μm) can preclude calculating an accurate abundance for that phase or for the abundance of other phases with which they are mixed. Systematic instrument errors and anisothermality can also affect the pixel spectrum, adding potential uncertainty to identifying minerals and measuring their abundance (Bandfield and Rogers, 2019). A detailed discussion of the complexities inherent in spectral mixture analysis is beyond the scope of this chapter.

9) This study assumes that the atmosphere is not spatially variable over the ASTER TIR scene. Atmospheric dust and gasses attenuate and scatter surface emitted radiance and emit their own radiance into the measurement field of view. The atmospheric emitted radiance reflected from the surface must pass again through the atmosphere in the the measurement field of view. Therefore, even with excellent knowledge of the atmospheric conditions, this will create extraordinary complexity (Bandfield and Rogers, 2019).

10) The accuracy of the classified image is usually assessed by means of statistical procedures by calculating the correctly and incorrectly identified areas using ground truth data. The statistical conclusions assume that the ground information is totally correct and that classification criteria used for ground data are the same as the classification criteria used for the image data. The most correlated factor maps with the tuff layers are not directly related to the spectral signatures of the tuff. Therefore, even if the statistical test gives high accuracy for classification, the interpreter must understand that the mapping results may not be directly correlated with the ground attribute of interest.

4.9 Conclusions

This study discussed the spectral characteristics of zeolites in the TIR wavelength region and how well spectral libraries can be used to identify the constituent minerals in samples from paleolake deposits. This study also discussed how well orbital pixel spectra can be calibrated to an apparent emissivity for comparison with laboratory spectral end members using different temperature-emissivity separation (TES) methods. It shows that instrument calibration, atmospheric compensation uncertainties, and variations in the contribution of surface materials in GRC increase the difficulty of making a direct comparison with library/laboratory spectra. Also, the band depth and shape of emitted spectra varies with the grain size, weathering, texture, and roughness of the surface.

The field studies along with laboratory and orbital spectral studies reveal critical spectral effects not typically observed in laboratory spectra. Therefore, identification of minerals and their abundance using library spectra and spectral mapping methods such as linear spectral mixture analysis (LSMA) could lead to incorrect results. Though the results derived from remote sensing images are surprisingly effective, the interpreter and user always need to recognize the limits of the data acquiring processes, data, and the limits of the analysis to be made. The results might change with the new instrumentation and or with detailed ground observations.

Overall, this study concludes that the limited or no detection of a certain mineral using TIR remote sensing data does not preclude their wider presence. Zeolites could be

present, either beneath other materials, surface dust, in deposits of small areal extent, or mixed with other spectrally dominant phases, or might not be detectable due to their roughness, surface texture, or grain size.

Acknowledgements

This work was supported by a grant from the Wisconsin Space Grant Consortium to Prof. Lindsay J. McHenry. I also thank NASA for making the Hyperion and ASTER image data freely available for research and Brown University (Relab) for acquiring spectral data for field samples. Also, thank to Mark Eskritt, Kaitlin Elizabeth Krause, and Jason Benjamin Carman for their support during the field visits. Many thanks to the R Core Team, and Rstudio for making them as free and open source, and all the R library developers for their effort and contribution.

"Sometimes it is the people no one can imagine anything of who do the things no one can imagine."

-Alan Turing-

5

Application of deep learning and spectral deconvolution for estimating mineral abundances of zeolite, Mg-sulfate and montmorillonite mixtures and its implications for Mars.

Contents

Abstract **176**
5.1 Motivation and background **177**
5.2 Spectral Analysis **181**
5.2.1 Sample preparation 181
5.2.2 Spectral Aqusition 183
5.2.3 Selection of spectral features 186
5.3 Spectral Deconvolution **189**
5.4 Deep learning **195**
5.5 5. Accuracy assesment **201**
5.6 Conclusions **206**
Acknowledgement **207**

5. Application of deep learning and spectral deconvolution for estimating mineral abundances of zeolite, Mg-sulfate and montmorillonite mixtures and its implications for Mars.

Abstract

A technique for estimating clinoptilolite, montmorillonite, and epsomite mineral abundances from a reflectance spectrum of mineral mixtures using spectral deconvolution and a deep neural network is proposed. Sixty-six ternary mineral mixtures were physically prepared with $< 150\ \mu m$ grain size with different weight percentages of minerals. A combination of normal and skewed Gaussian curves was fitted to the absorption bands at 1.4 μm, 1.9 μm, and 2.2 μm of the acquired reflectance spectra of these mineral mixtures. Six Gaussian curve parameters with maximum absorption band depth $\sim 1.9\ \mu m$, and wavelength at the maximum band depth, were used (along with mineral abundances) to train multilayer perceptron deep neural network (MLP-DDN) models. Forty-eight models with different DNN architectures and different hyperparameters were trained and the results were validated to find the best models. Winning models were tested with twenty-five samples including fourteen library spectra from RELAB and USGS spectral databases, a spectrum from a different sample, five varying amounts of noise-added spectra simulating CRISM (Compact Reconnaissance Imaging Spectrometer for Mars) orbital spectral data, and five mixed spectra derived from linear mixtures of laboratory minerals. The best model was able to predict mineral mixture composition with higher accuracies; three of five montmorillonite and four of the five epsomite library spectra with more than 90 % of accuracy. However, clinoptilolite samples show less than 50 % accuracy and always predicted as mixture of clinoptilolite and epsomite. This shows the difficulties of identifying non-analcime zeolites (e.g., clinoptilolite) from Mg-polyhydrated minerals, as discussed by authors who mapped hydrous minerals on Mars using hyperspectral image data. Random artifacts introduced by noise sometime leads to predictions of completely different and incorrect mineral abundances. The study also discusses the possible reasons for the incorrect prediction of mineral abundances and how to overcome these difficulties. Overall, the study shows the advantage of spectral deconvolution with deep neural network for calculating mineral abundance form mixed mineral spectra.

5. Application of deep learning and spectral deconvolution for estimating mineral abundances of zeolite, Mg-sulfate and montmorillonite mixtures and its implications for Mars.

5.1 Motivation and background

As photons enter a mineral, some are absorbed by the grain, some are reflected from the grain surface, and some pass through it. When photons enter an absorbing medium, they are absorbed according to Beers Law,

$$I = I_o e^{-kx} \text{ ——————(5.1)}$$

where I is the observed intensity, I_o is the original light intensity, k is an absorption coefficient, and x is the distance traveled through the medium. This equation holds for a single wavelength, while for different wavelengths the absorption coefficient will be different. Differences in absorption coefficients in a certain wavelength range lead to intensity differences, creating absorption bands. Many minerals exposed to solar reflected light wavelengths (0.3 - 3 μm) show characteristic absorption bands due to vibrational overtones, electronic transitions, charge transfer, and conduction processes (Hunt, 1977). Very broad absorption bands in the ~ 0.3 - 0.9 μm wavelength region are typically caused by electronic transitions while the absorption bands in the ~ 0.9 - 3 μm wavelength region are typically caused by overtones, and combinations of the fundamentals of the absorptions form due to OH^-, H_2O, and CO_3^{2-}, which occur at longer wavelengths. The characteristics of these absorption band (e.g., position, shape, and depth) in reflectance spectra are a powerful tool for remote identification of surface composition on Earth and other planetary bodies.

Based on the spectral characteristics captured by the orbital spectral sensors, hydrous minerals, such as smectites, kaolinite, sulfates, carbonates, zeolite, opaline silica, chlorites, serpentine, prehnite, and epidote have been identified on the surface of Mars (Carter et al., 2013; Ehlmann et al., 2009, 2013). Ehlmann et al. (2009) identified the Na-zeolite analcime in the Nili Fossae region on Mars using Compact Reconnaissance Imaging Spectrometer for Mars (CRISM) data. Analcime is the only zeolite group mineral specifically identified on Mars based on its distinctive broad absorption band centered at ~ 2.5 μm and a weaker absorption at ~ 1.8 μm (Cloutis et al., 2002; Ehlmann et al., 2009). Ehlmann et al. (2009), Wray et al. (2009), Carter et al. (2013), and Sun and Milliken (2015) have discussed the difficulties associated with identifying other zeolite minerals using spectral

data. Identifying other zeolite species is complicated by the lack of diagnostic absorption bands in the visible-shortwave infrared (VIS-SWIR) region (Cloutis et al., 2002), spectral similarity with Mg-polyhydrated sulfates (Ehlmann et al., 2009), and residual atmospheric effects at wavelengths longer than 2.5 μm (Murchie et al., 2007). Carter et al. (2013) noted that the only ways to discriminate polyhydrated sulfates from zeolites are to use the position of the 2.3 - 2.4 μm shoulder and the shape of the 1.9 μm absorption. In most studies non-analcime and polyhydrated sulfates are thus commonly categorized as an unidentified hydrous phases (e. g. Sun and Milliken (2015)), or as zeolite and sulfate group (e. g. Carter et al. (2013), Wray et al. (2009)).

Gendrin et al. (2005) identified hydrated sulfates including kieserite, polyhydrated sulfate, and gypsum on light-toned layered terrain in Valles Marineris, Margaritifer Sinus, and Terra Meridiani on Mars, based on the vibrational absorption bands between 1.3 and 2.5 μm wavelength of OMEGA (Observatoire pour la Mine'ralogie, l'Eau, les Glaces et I'Activite') hyperspectral data. It is important to note that for most of the locations where sulfates are identified, monohydrated sulfate layers coexist with polyhydrated sulfates layers in an interbedded sulfate stratigraphy (Wang et al., 2016; Roach et al., 2009), or sulfates minerals and clays occur together (e.g., Milliken et al. (2010); Weitz et al. (2015); Wray et al. (2011)). On Earth, evaporitic sulfate minerals commonly occur together with detrital clays and/or authigenically precipitated clay minerals in modern and ancient saline lakes and playa environments (Warren, 2016). Zeolites are the most common authigenic silicate minerals in saline, alkaline lakes associated with detrital or authigenic clay minerals (Hay, 1966). Therefore, it is not unexpected that the same may be true for Mars. Orbital reflectance spectroscopy provides an effective way to map the spatial distribution of these minerals to assess the activity, timing, duration, and extent of aqueous processes over Martian history. However, questions remain about how reliably these mineral components can be detected and their relative abundances estimated, given the difficulties observed in previous studies.

The process of identifying minerals and determining their quantitative abundances from the reflectance spectra of mineral mixtures is not always straightforward. Efforts to identify minerals and their abundances are hindered by the complexities introduced by

particle size effects, variations in viewing and illumination geometry, surface roughness, and regolith or weathering alteration on reflectance spectra (Mustard and Pieters, 1989). Multiple theoretical and empirical approaches have been introduced to estimate mineral abundances from the reflectance spectra of mineral mixtures under laboratory conditions and on planetary surfaces. Radiative transfer models (RTMs) are one of the most common theoretical models used to describe how light intensity changes as it enters, interacts with, and exits a specific medium (Robertson et al., 2016). Hapke (Hapke (1981); Hapke (1993)) and Shkuratov (Shkuratov et al. (1999)) RTM models have been commonly used for modeling spectra of laboratory mineral mixtures (e.g., Stack and Milliken (2015); Robertson et al. (2016); Cahill et al. (2010); Liu et al. (2015)) and planetary surfaces (e.g., Trang and Lucey (2019); Cahill et al. (2009)). Hapke's model is designed for intimate mixtures of particulates, while the Shkuratov RTM treats particles as a one-dimensional layer (Robertson et al., 2016). Stack and Milliken (2015) examined the VNIR reflectance properties of a suite of binary mineral mixtures containing epsomite mixed with varying proportions of Fe, Mg and Al- smectites, and assessed the ability of linear and non-linear (Hapke) models to reproduce spectra of these mineral mixtures. Robertson et al. (2016) assessed the efficacy of the Hapke and Shkuratov RTMs for estimating mineral abundances from gypsum-montmorillonite binary mineral mixtures. RTMs are useful as diagnostic tools for mixtures of specific minerals, though they are limited to applications that only involve the minerals studied (Sunshine et al., 1990).

Curve fitting is the classic empirical approach to model reflectance spectra and resolve single absorption bands within complex absorption features. The reflectance spectra can be modeled by a linear combination of overlapping absorption bands superimposed onto a background continuum (Clark and Roush, 1984). Because of that, curve fitting methods have been extensively used to decompose reflectance spectra of mineral mixtures to identify their constituent minerals both in laboratory mineral mixtures (e.g., Parente et al. (2011); Sunshine et al. (1990); Noble et al. (2006)) and planetary surfaces (e.g., Kodikara et al. (2016); Parente et al. (2011); Brown (2006)). Spectral deconvolution resolves spectra into individual absorption bands with discrete mathematical distributions.

5. Application of deep learning and spectral deconvolution for estimating mineral abundances of zeolite, Mg-sulfate and montmorillonite mixtures and its implications for Mars.

The absorption bands can be modeled using Gaussian, Lorentz, or Voight (mixed Gaussian-Lorentz) curves (Clark, 1981; Sunshine et al., 1990; Brown, 2006). These curves are all symmetrically shaped and decay from a central peak, and different decay rates may represent different physical processes (Brown, 2006). Curve fitting of spectra can estimate the central wavelength, width, amplitude, and asymmetry of the absorption band, and is typically achieved using an iterative least square method (Brown, 2006). The modified Gaussian model (MGM), developed by Sunshine et al. (1990), provides an accurate mathematical description of the shape of isolated electronic transition absorption bands, and Sunshine and Pieters (1993) noted that this can estimate modal abundances from spectra of unknown pyroxene mixtures without the use of end member spectra. Roush et al. (2015) used four absorption parameters (center, width, depth, and asymmetry) of reflectance spectra from saponite + montmorillonite with pyroxene, and saponite with palagonitic soil mixtures, in the wavelength region of 2.1 - 2.3 μm to extract the clay abundances from the mixed mineral spectra. They found that the absorption band depth is the most indicative of saponite/montmorillonite abundance in the mixtures.

Deep learning (DL) methods, a subfield of machine learning (ML), are representation-learning methods with multiple levels of representation (layers), obtained by a composite of simple non-linear modules that each transform the representation at one level (from input layer) into a representation at a higher, slightly more abstract levels (hidden layers to output layer) (LeCun et al., 2015). The key feature of DL is that these layers of features are not designed by humans, they are learned automatically from exposure to training data using a learning algorithm. DL is very good at discovering intricate structures in high-dimensional data and therefore it is used in many fields, but not limited to science, image recognition, speech recognition, business, natural language processing, robotics, etc. Review of deep learning and its evolution can be found in LeCun et al. (2015) and Schmidhuber (2015), respectively. Recently, Kodikara and McHenry (2020) examined the ability of ML algorithms, adopting 9 ML algorithm representing linear, non-linear, classification trees, and rule based models to determine the physical and mineralogical properties of lunar soil using the reflectance spectra of lunar soils.

5. Application of deep learning and spectral deconvolution for estimating mineral abundances of zeolite, Mg-sulfate and montmorillonite mixtures and its implications for Mars.

Here we assess the efficacy of a combination of spectral deconvolution and deep learning to estimate mineral abundances of zeolite, Mg-sulfate, and montmorillonite mixtures using their reflectance spectra. Our study was limited to the absorption features formed caused by vibrational overtones and combinations in the reflected light portion of the spectrum located within the 1.4 to 2.5 μm region.

The rest of this chapter is organized as follows: Section 2 discusses the details of sample preparation, spectral acquisition, and preprocessing of the collected spectral data. Section 3 outlines the identification of spectral features for Gaussian curve deconvolution, parameter estimation, and feature selection. Section 4 discusses the selection of the best deep learning model using its hyperparameters and validation process. Section 5 reports an accuracy assessment using test data. Section 6 concludes this study. The entire study was conducted using several python modules (numpy, math, lmfit, matplotlib, and pytorch) implemented in Rstudio IDE (integrated development environment) (`https://www.rstudio.com`). An opensource machine learning framework pytorch (`https://pytorch.org/`) was used to build deep learning models.

5.2 Spectral Analysis

5.2.1 Sample preparation

The end member minerals selected for this study are clinoptilolite, montmorillonite, and epsomite. Clinoptilolite ($(Na, K, Ca)_{2-3}Al_3(Al, Si)_2Si_3O_{36}.12H_2O$) was purchased from www.Kelp4less.com, montmorillonite

$$((Na_{0.27}K_{0.04}Ca_{0.07})(Al_{1.65}Mg_{0.26}Fe^{3+}_{0.17})(Si_{3.84}Al_{0.06})O_{10}(OH)_2.nH_2O)$$

was purchased from Wards collection (No.46E0438), which was collected from Panther Creek, Colorado. The commercial USP grade synthetic salt Epsomite ($MgSO_4.7H_2O$) was also purchased from a local store. These samples were individually ground and dry-sieved to a size fraction of < 150 μm. The purity of these mineral end members was determined using a Bruker D8 Focus X-ray diffraction (XRD) system. XRD patterns were compared against the ICDD PDF-2 (International Center for Diffraction Data Powder Diffraction

File) library using Bruker's EVA software. The montmorillonite sample contains minor amounts of albite and quartz, while the clinoptilolite sample contains minor cristobalite. The epsomite sample contains a minor amount of hexahydrite, most likely due to the dehydration of epsomite. Epsomite transforms readily to hexahydrite by loss of extra-polyhedral water at 298 K and ~ 50 - 55 % relative humidity conditions (Vaniman et al., 2004). Since more than 90 % of each sample is represented by the major mineral of interest, these samples were considered as "end members" for the purpose of this study.

Sixty-six ternary mineral mixtures, each totaling 2.00g, were prepared. The mineral abundances (weight percentage) of each end member mineral in each mixture are represented by the blue points on the ternary plot in Figure 5.1, and Figure C. 1 and C.2 in the Appendix C. Mineral proportions for each sample were weighed separately, accurate to 0.005 g, and then mixed well to ensure homogeneous mixing. Samples were prepared under ambient laboratory conditions.

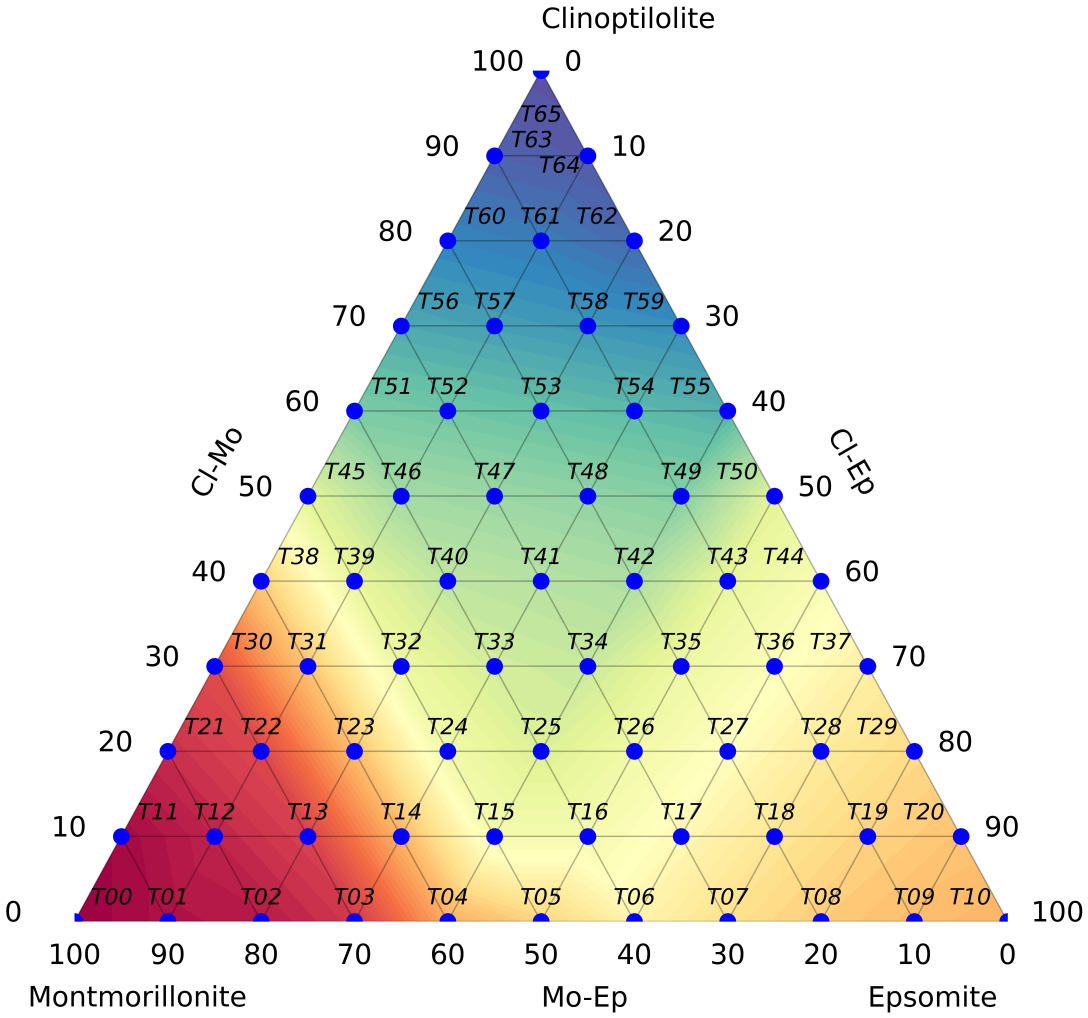

Figure 5.1: Schematic ternary diagram for mixtures of clinoptilolite, montmorillonite and epsomite. Blue points show the sample points of physical mineral mixtures prepared to collect reflectance spectra. The sample ID for each mixture is shown near the sample point.

5.2.2 Spectral Aqusition

The VIS-SWIR reflectance spectrum of each mineral mixture was collected using an ASD Field spec reflectance spectrometer at the University of Colorado under ambient laboratory conditions. The spectral ID of each mineral mixture is the same as the sample ID shown in Figure 5.1. Reflectance spectra of mineral end members (spectral endmembers) are shown in Figure 5.2. In hydrous minerals, water molecules occur in different contexts. They can be bound to the interlayer surface, as interlayer cations as in montmorillonite, or can occur singly or in clusters forming an essential part of the crystal lattice as in various

hydrates in Mg-sulfates (e.g., epsomite and hexahydrite), occupying specific sites in the crystal structure without being essential to its structure, as in clinoptilolite, or physically adsorbed on the surfaces of mineral grains (Hunt and Salisbury, 1970; Bishop et al., 1994). Water molecules have three fundamental vibrational modes, the symmetric O-H stretch, the asymmetric O-H stretch, and the H-O-H bend. Absorption band assignments for clinoptilolite, montmorillonite, and epsomite are shown in Table 5.1.

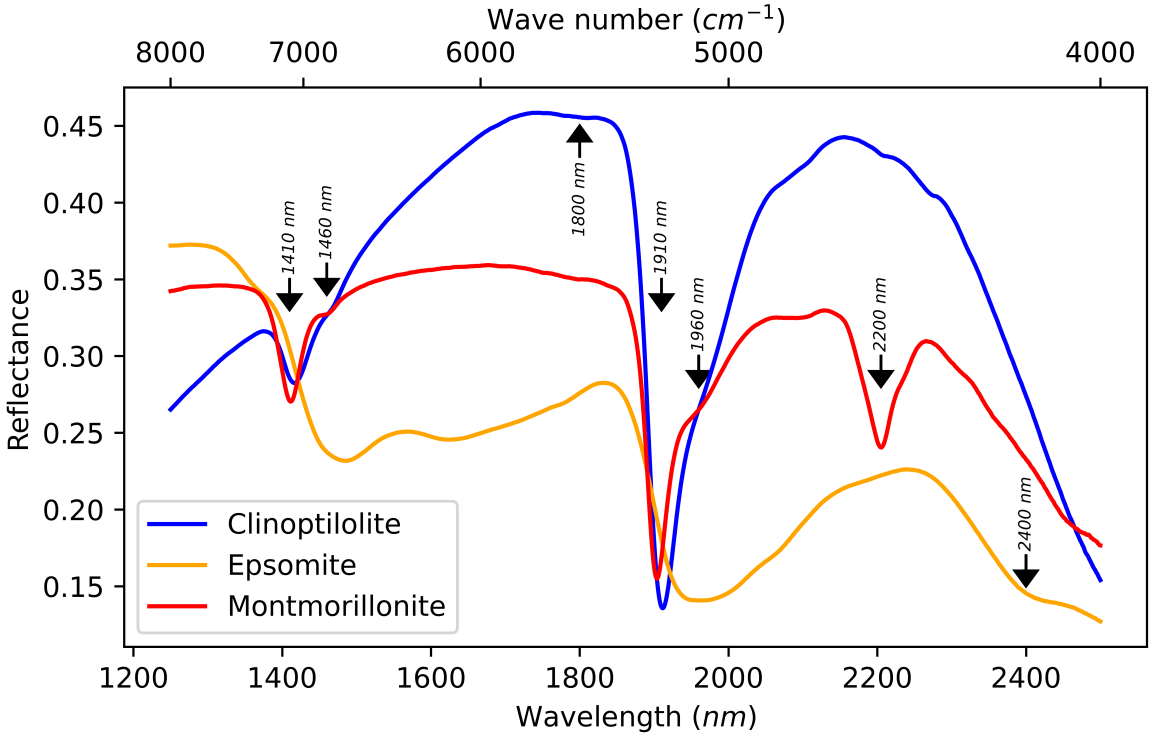

Figure 5.2: Reflectance spectra of mineral end members (spectral endmembers) used in this study.

Table 5.1: Absorption band assignment for clinoptilolite, montmorillonite and epsomite (sources: Cloutis et al. (2002); Bishop et al. (1994); Clark (1995); Hunt and Salisbury (1970); Gendrin et al. (2005); Cloutis et al. (2006)).

Wavelength, μm	Assignment	Mineral
1.41	H_2O stretch + first overtone of H_2O bend	CLI, MON
1.46	H_2O stretch + second overtone of H_2O bend	CLI, EPS, MON
1.80	Symmetric or asymmetric H_2O stretch	CLI
1.91	H_2O stretch + H_2O bend	CLI, EPS, MON
1.97	H_2O combinations	EPS
2.20	OH stretch + bend ($Al_2 - OH$)	MON

Wavelength, μm	Assignment	Mineral
2.40	$(SO_4)^{2-}$ stretch	EPS

Note: CLI = Clinoptilolite, EPS = Epsomite, and MON = Montmorillonite.

It is important to note that due to relatively high iron impurities (~ 1.7 w% Fe_2O_3) in the clinoptilolite sample, the reflectance spectrum of clinoptilolite shows a spectral slope on the left side of left shoulder of the 1.4 μm absorption band due to the broad absorption band near 0.9 μm formed due to the Fe^{2+} crystal field transition. While care was taken to handpick the purest mineral chips to grind, some iron oxide remains. The dominant absorption bands between 1.2 - 2.5 μm are formed mainly due to vibrational processes (Table 5.1), and therefore iron content of the sample does not affect the current study.

The original spectra of mineral mixtures are shown in Figure 5.3 (a). The spectra show different intensity variations making it difficult to visually analyze the spectra to select which absorption bands are best for determining relative mineral abundances. Therefore, these spectra were corrected using multiplicative scattering correction algorithm (MSC) (Geladi et al., 1985). MSC compensates for the multiplicative effects caused by light scattering effects and changes in path length. The MSC corrected spectra (X_{MSC}) are shown in Figure 5.3 (b). The MSC corrected spectra were calculated using,

$X_{MSC} = (x - a)/b$ ————-(5.2)

where x = the spectrum of a sample.

a and b were estimated using ordinary least-squares regression of spectrum x versus $\bar{x}$, using equation 5.3.

$x = a + b\bar{x} + e$ ————(5.3)

where $\bar{x}$ = spectrum of the "ideal" sample (mean spectrum in this case), e = residual spectrum.

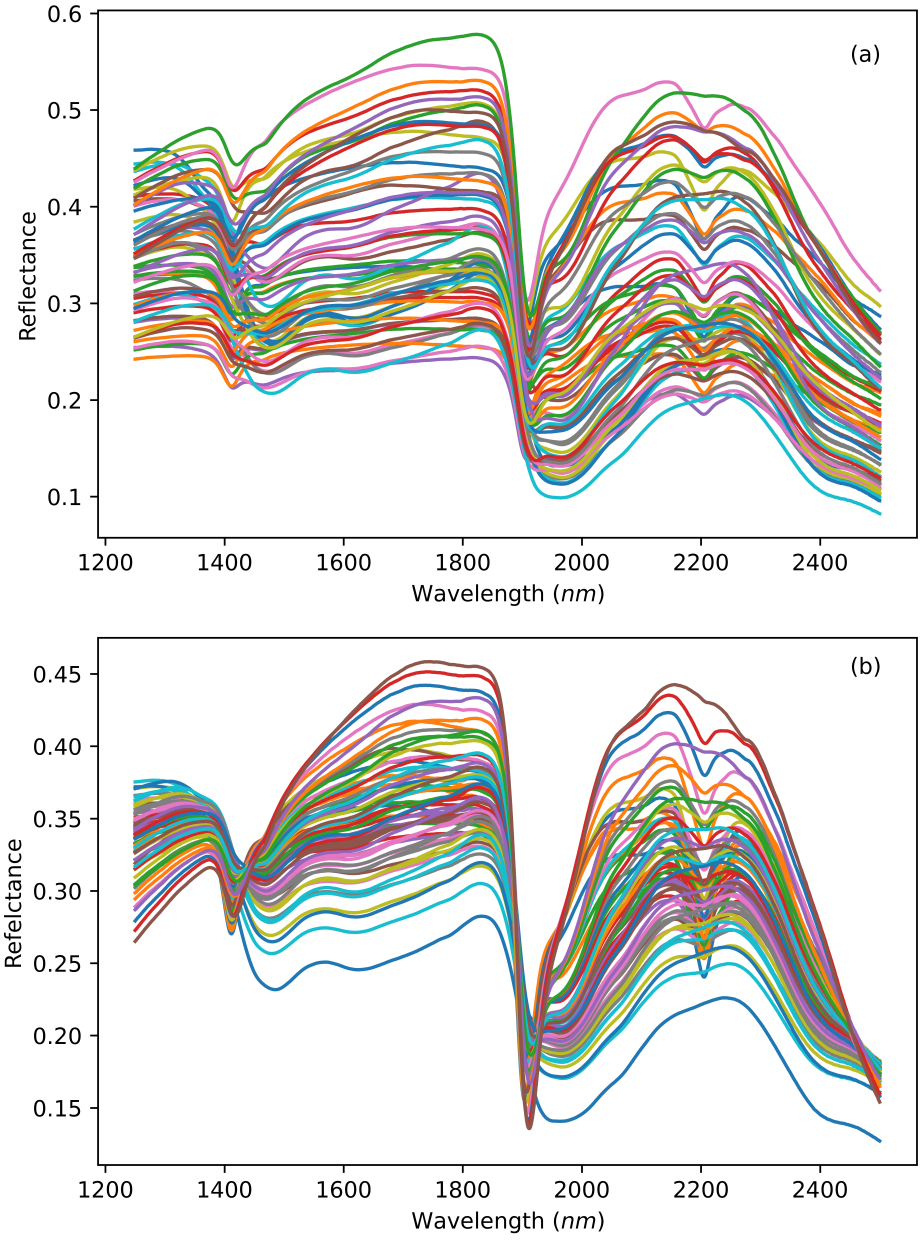

Figure 5.3: Original mineral mixture spectra (a) and after applying the multiplicative scatter correction (b).

5.2.3 Selection of spectral features

The spectra of binary mineral mixtures were used to find the important absorption bands which vary with mineral abundance (Figure 5.4). The letter C in the legend indicates clinoptilolite, M indicates montmorillonite, and E indicates epsomite. Two integers after each letter indicate the respective weight proportion of each mineral on

a scale of 10. This shows that absorption bands around 1.4 μm, 1.9 μm, and 2.2 μm vary linearly with their mineral abundances. The shape of the absorption bands at 1.4 μm and 1.9 μm does not vary much with the changes of mineral weight proportion for the clinoptilolite-montmorillonite binary mineral mixture (Fig 5.4a), while the depth and shape of these absorption bands varies greatly for the clinoptilolite-epsomite and epsomite-montmorillonite binary mineral mixtures due to broad spectral features of epsomite. The absorption band at 2.2 μm increases with increased montmorillonite as expected for both the clinoptilolite-montmorillonite (Fig 5.4a) and montmorillonite-epsomite (Fig 5.4c) binary mineral mixtures. Based on the spectral characteristics of the absorption bands discussed here, three wavelength regions covering absorption bands at 1.4 μm, 1.9 μm, and 2.2 μm were selected and referred to here as F1 (feature 1), F2 (feature 2), and F3 (feature 3), respectively. The wavelength ranges for features F1, F2, and F3 were determined based on the extreme convex points on either side of the respective feature shoulders. To compare and implement the curve fitting to these features, a piecewise straight-line continuum was removed from the spectra across the F1, F2, and F3 regions. The continuum is a mathematical function used to isolate a particular absorption feature for analysis of a spectrum (Clark and Roush, 1984).

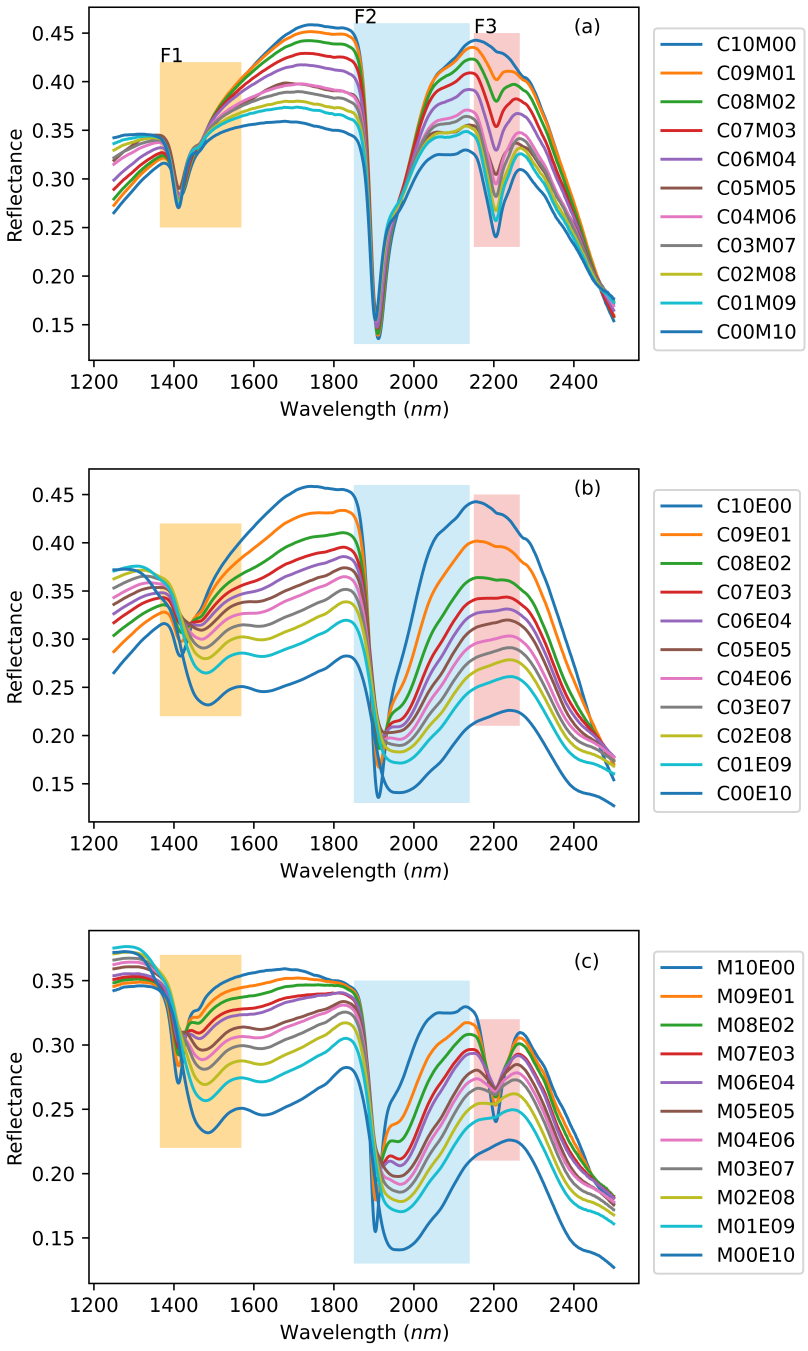

Figure 5.4: Binary mineral mixtures showing absorption feature variations associated with varied mineral abundances. Each subplot shows the binary mineral mixture clinoptilolite - montmorillonite (a), clinoptilolite - epsomite (b), and montmorillonite - epsomite (c). F1, F2, and F3 are the wavelength regions of the absorption features selected for this study. Letter C in the legend indicates clinoptilolite, M indicates montmorillonite, and E indicates epsomite. Two integers after each letter indicate the mineral weight proportions on a 10 ponit scale.

5.3 Spectral Deconvolution

To represent mathematically the reflectance spectra of selected wavelength regions as linear combinations of absorption bands that occur around discrete energies, it is necessary to carry out the Gaussian model of absorption bands in log reflectance and energy space (Sunshine et al., 1990). Therefore, the reflectance spectra were converted to apparent absorbance by taking the logarithm of the reflectance,

$$\text{apparent absorbance} = log_{10}(\text{reflectance}) \quad \text{——— (5.4)}$$

The original spectra were recorded in wavelength space; therefore, they were converted to energy space in cm^{-1} (wavenumbers). Converting to energy space also eliminates the asymmetry due to display on a constant interval wavelength abscissa (Rossman, 1988).

$$\text{frequency } (cm^{-1}) = \frac{10000}{wavelength(\mu m)} \quad \text{———(5.5)}$$

The underlying assumption of the Gaussian model is that absorption bands observed in VIS-SWIR spectra are composed of absorption features that are inherently Gaussian in shape. If this is true, these spectral features can be resolved into absorption bands by curve fitting using Gaussian distributions (Sunshine et al., 1990). Roush and Singer (1986) pointed out that a Gaussian deconvolution should produce a unique fit for a given mineral under certain reasonable constraints. Even if is not firmly tied to a physical mechanism, this can provide some useful information to analyse absorption bands (Sunshine et al., 1990).

Several curve fitting algorithms including Gaussian, Lorentzian and Vogit were tested using the lmfit python module, and the Gaussian models provide a better fit for the selected absorbance regions of mineral end members and mixtures. A Gaussian distribution in a random variable x, $f(x; A, \mu, \sigma)$, can be expressed in terms of its amplitude (strength of the peak); A, center (centeroid of the curve); μ, sigma (width of the peak); σ.

$$f(x; A, \mu, \sigma) = \frac{A}{\rho\sqrt{2\pi}} e^{[-(x-\mu)^2/2\sigma^2]} \quad \text{———-(5.6)}$$

A Levenberg-Marquardt (L-M) algorithm (Levenberg, 1944; Marquardt, 1963) was used to find the best fit curve. Brown (2006) used the L-M algorithm for spectral curve fitting in the shortwave infrared (SWIR) region. Parente et al. (2011) adopted the L-M and Total Inversion (Tarantola and Valette, 1982) methods for curve fitting modeling of reflectance spectra for Martian meteorites and CRISM spectral image data. They found

that both L-M and total inversion methods perform similarly on low-noise spectra, though L-M is more stable when its parameters are varied. The main advantage of the L-M algorithm in curve fitting is that uncertainties of the model parameters can be included in the form of ranges of values. The range of initial values for the width, strength, and centers for each feature were provide at first and then the fitting procedure iteratively adjusts these parameters until a negligible improvement in the overall fit is obtained.

Two normal Gaussian curves appear to be sufficient to achieve good least squares fit for Feature 1 (example in Fig 5.5a), though Feature 2 is best represented by combining a normal Gaussian curve and a skewed Gaussian curve (Fig 5.5b). Feature 3 can be represented by a normal Gaussian curve (Fig 5.5c).

The Skewed Gaussian model can be represented by

$f(x; A, \mu, \sigma, \gamma) = \frac{A}{\rho\sqrt{2\pi}} e^{[-(x-\mu)^2/2\sigma^2]}\{1 + erf[\frac{\gamma(x-\mu)}{\sigma\sqrt{2}}]\}$ ——————(5.7)

where A = amplitude, μ = center, σ = width of the peak, γ = skewness, and $erf[]$ is the error function.

The amplitude of the peak (A), central frequency of the peak (μ), width of the peak (σ) and skewness (γ, in the case of skewed Gaussian model) were calculated for all fitted Gaussian curves of Features F1, F2, and F3. Since the absorption bands at F1 (near 1.4 μm) and F2 (near 1.9 μm) are composed of multiple, overlapping molecular water features, the band shape, band depth and band strength are all important to find the relation between constituent mineral abundance and their spectra.

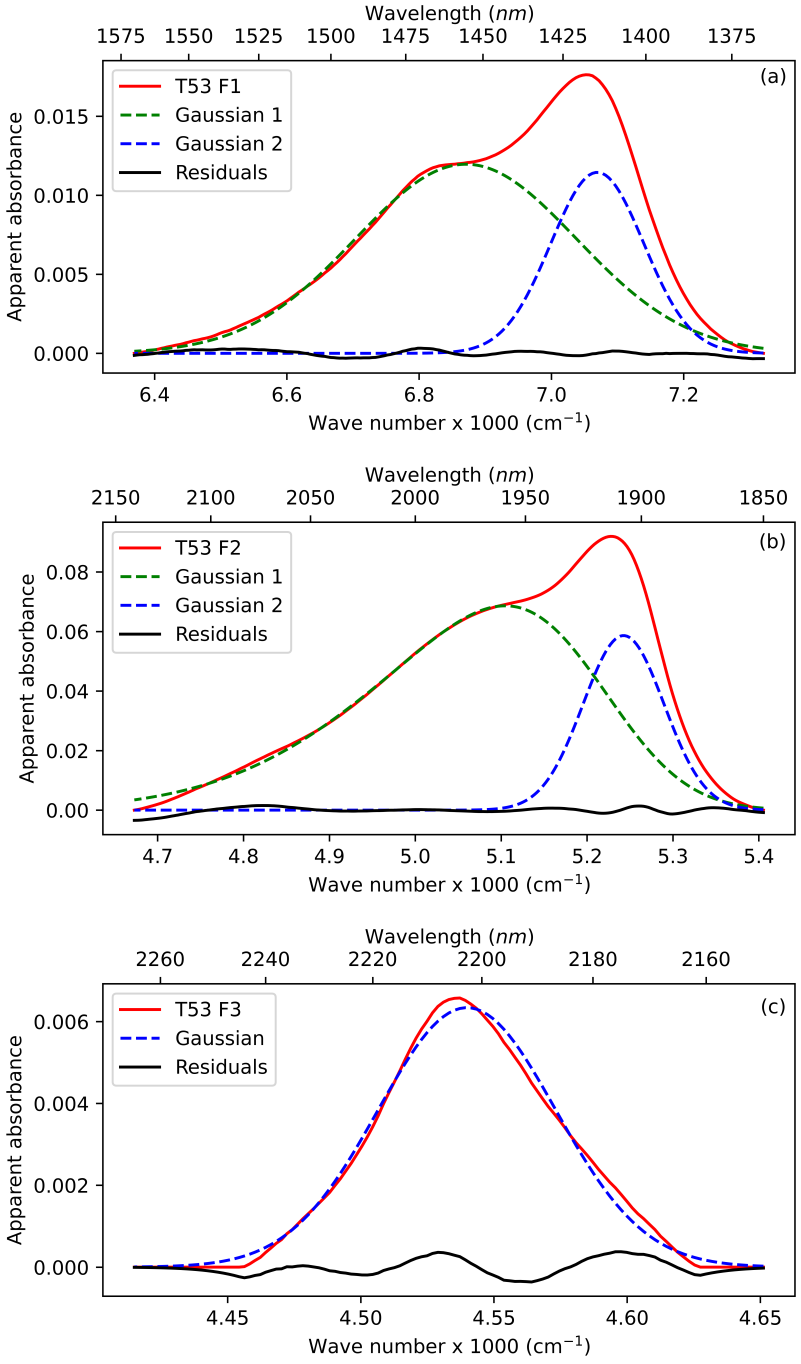

Figure 5.5: Example of Gaussian curve fitting for F1 (a), F2 (b), and F3 (c) of mineral mixture T53 (60 percent clinoptilolite, 20 percent montmorillonite, and 20 percent epsomite)

Calculated Gaussian parameters for F1 are shown in Figure 5.6. This shows that the amplitude and center wavelength of Gaussian curve 1 (F1G1_AMP; plot a, and F1G1_CNT; plot b, respectively) and Gaussian curve 2 (F1G2_AMP; plot d, and F1G2_CNT; plot e) show a relatively clear linear trend over the ternary diagram.

The amplitude of Gaussian curve 1 increases towards epsomite, while the amplitude of Gaussian curve 2 increases towards montmorillonite. The center frequencies of Gaussian curves are converted to wavelength space for easy reference. The center wavelength of both Gaussian curve 1 (F1G1_CNT, plot b) and curve 2 (F1G2_CNT, plot e) of F1 increase towards epsomite. The width of the peaks (σ) of Gaussian curve 1 (F1G1_SGM, plot c) and Gaussian curve 2 (F1G2_SGM, plot f) of F1 do not show general linear variations over the plot.

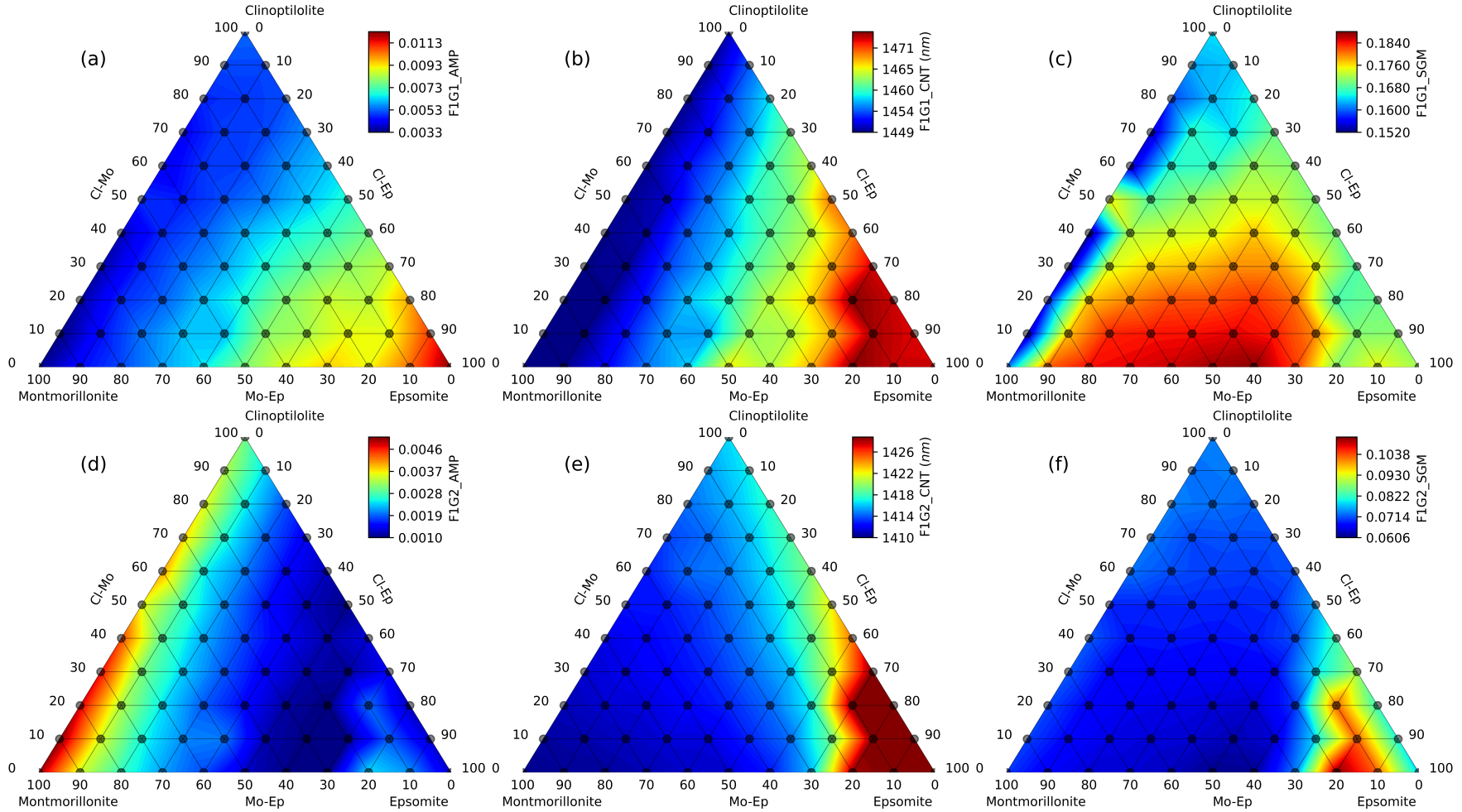

Figure 5.6: Ternary plots showing the calculated Gaussian curve parameters of feature 1 (F1). a) Amplitude of Gaussian curve 1 of F1 (F1G1-AMP), b) Center wavelength of Gaussian curve 1 of F1 (F1G1-CNT), c) Width of Gaussian curve 1 of F1 (F1G1-SGM), d) Amplitude of Gaussian curve 2 of F1 (F1G2-AMP), e) Center wavelength of Gaussian curve 2 of F1 (F1G2-CNT), f) Width of Gaussian curve 2 of F1 (F1G2-SGM). Linear interpolation was applied between sample points to fill the colors in small triangles in the plots.

5. Application of deep learning and spectral deconvolution for estimating mineral abundances of zeolite, Mg-sulfate and montmorillonite mixtures and its implications for Mars.

Figure 5.7 shows the amplitude of Gaussian curve 1 of F2 (F2G1_AMP, plot a), maximum band depth of F2 (F2BD_MAX; entire feature without using spectral deconvolution, plot b), wavelength at the maximum band depth (F2WL_MAX, plot plot c), and amplitude of Gaussian curve 1 of F3 (F3G1_AMP, plot d). It shows that the maximum band depth of F2 increases towards epsomite while the wavelength of the maximum band depth increases towards clinoptilolite. Gaussian curve 1 of F3 increases towards montmorillonite as expected. The rest of the parameters do not show clear patterns over the ternary plots (Appendix C).

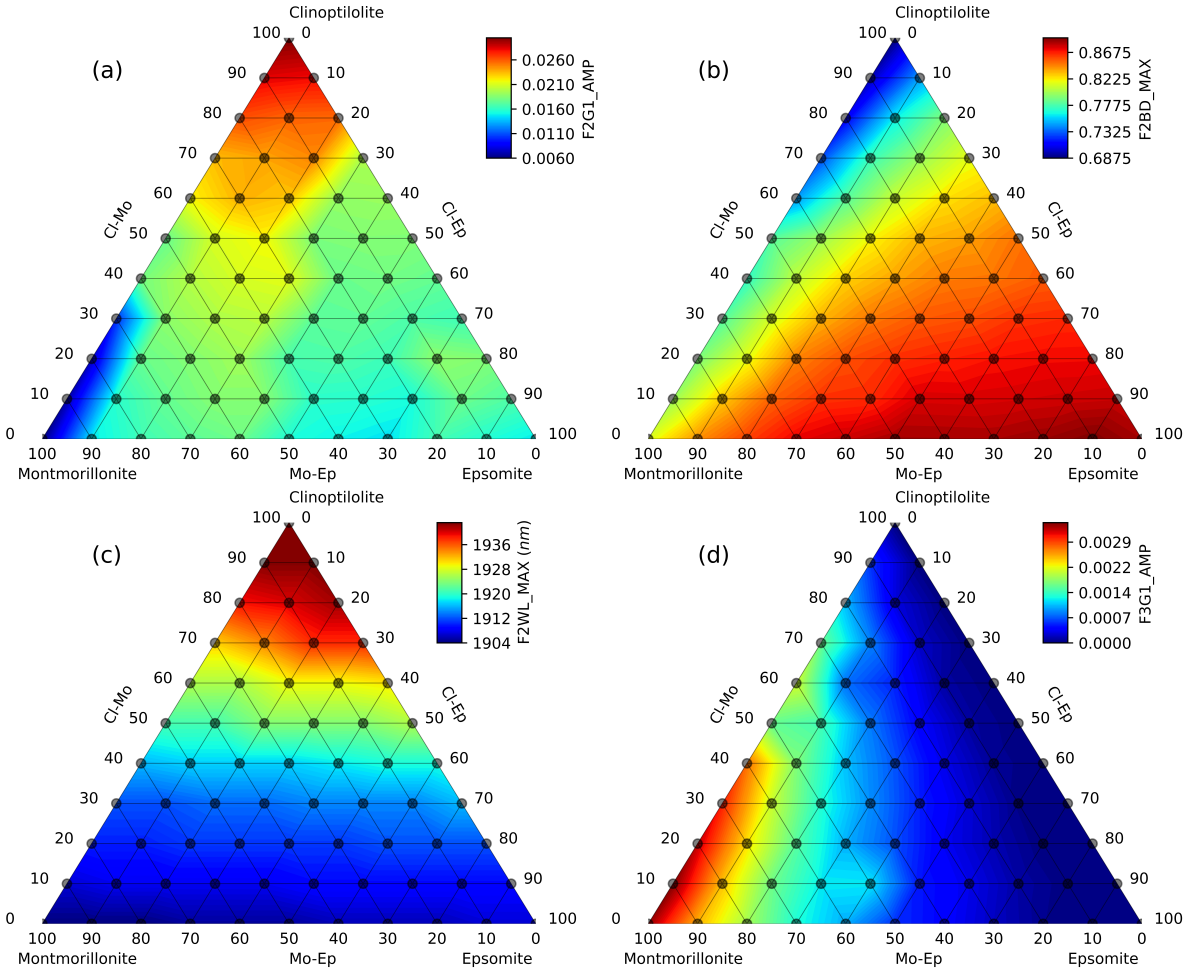

Figure 5.7: Ternary plots showing the amplitude of Gaussian curve 1 of feature 2 (F2G1-AMP, plot a), maximum band depth of feature 2 (F2BD-MAX, plot b), wavelength at maximum band depth of feature 2 (F2WL-MAX, plot c), and amplitude of Gaussian curve 1 of feature 3 (F3G1-AMP, plot d). Linear interpolation was applied between the sample points to fill the colors in small triangles in the plots.

This shows that some of the Gaussian curves and spectral parameters have clear linear

trends on the in the ternary plots while other do not. Therefore, eight parameters that depict clearer patterns in the ternary diagrams were selected as input parameters for the DL model. The selected parameters are F1G1_AMP, F1G1_CNT, F1G2_AMP, and F1G2_CNT shown in Figure 5.6, and F2G1_AMP, F2BD_MAX, F2WL_MAX, and F3G1_AMP shown in Figure 5.7. The process of selecting the most useful features to train among existing features is called feature selection in the ML realm. Feature selection is an effective way to identify the important features in a dataset and discard others as irrelevant and redundant. Irrelevant and redundant features in the training dataset can result in highly unstable models and poor performance (e.g., Kodikara and McHenry (2020)).

5.4 Deep learning

Picking the right deep neural network (DNN) architecture is more an art than a science, while there are some best practices and principles, only practice can help to select the best DNN architecture for a specific use (Chollet and Allaire, 2018). The Multilayer Perceptrons (MLP) neural network, the simplest deep neural network, consisting of a stack of many fully connected (also called densely connected) layers on top of each other, was adopted for this study. Each layer feeds into the layer above it, starting with the input layer in which we feed the data. It may consists of one or more hidden layers and the uppermost layer is the output linear predictor. Figure 5.8 shows the MLP with eight inputs, three outputs, and two hidden layers containing six units per layer. Hidden layers can be explained by,

$$H_1 = \sigma_1(XW_1 + b_1) \text{ ——————(5.8)}$$

Where, H_1 is the first hidden layer that can be denoted by matrix $H_1 \in \Re^{n \times h}$, H is a matrix with a minibatch of n examples with h hidden units. The matrix X input layer has n examples with d input features ($X \in \Re^{n \times d}$). Since hidden and output layers are fully connected, first hidden weights and bias can be represented by $W_1 \in \Re^{d \times h}$ and $b_1 \in \Re^{1 \times h}$, respectively. The weights (also called trainable parameters) contain the information learned by the network when exposed to training data. A nonlinear activation function for hidden layer 1 is denoted by σ_1. Activation functions decide whether a neuron should be activated or not based on the calculated weighted sum after adding bias. Two

of the most popular activation functions, ReLU and Sigmoid, were tested. ReLU (rectified linear unit) provides a very simple nonlinear transformation for a given element x.

$$ReLU(x) = max(x, 0) \text{ ——————(5.9)}$$

It retains only positive elements and discards all negative elements by setting the corresponding activations to 0. The Sigmoid function transforms its inputs to outputs in the interval 0 to 1.

$$Sigmoid(x) = \sigma(x) = \frac{1}{1+exp(-x)} \text{ ——————} (5.10)$$

Finally, output layer $O \in \Re^{n \times q}$ is calculated as follows,

$$O = H_2W_3 + b_3 \text{ ——————(5.11)}$$

Two common optimization algorithms including Stochastic Gradient Decent (SGD) and Adam (Kingma and Ba, 2015) were used. The term stochastic refers to the fact that each batch of the data is drawn at random. The algorithm computes the outputs and the errors for each batch, then computes the average gradients and adjusts the weights accordingly. This process is repeated for each batch from the training dataset until the loss (mismatch between the prediction and expected target) is minimum (Chollet and Allaire, 2018; LeCun et al., 2015). Adam (name derived from adaptive moment estimation) is also an efficient stochastic optimization algorithm that computes individual adaptive learning rates for different parameters from estimates of first and second moments of the gradients (Kingma and Ba, 2015). The method combines the advantages of two popular optimization algorithms; the ability to deal with sparse gradients in AdaGrad, and the ability to deal with non-stationary objectives in RMSProp (Kingma and Ba, 2015).

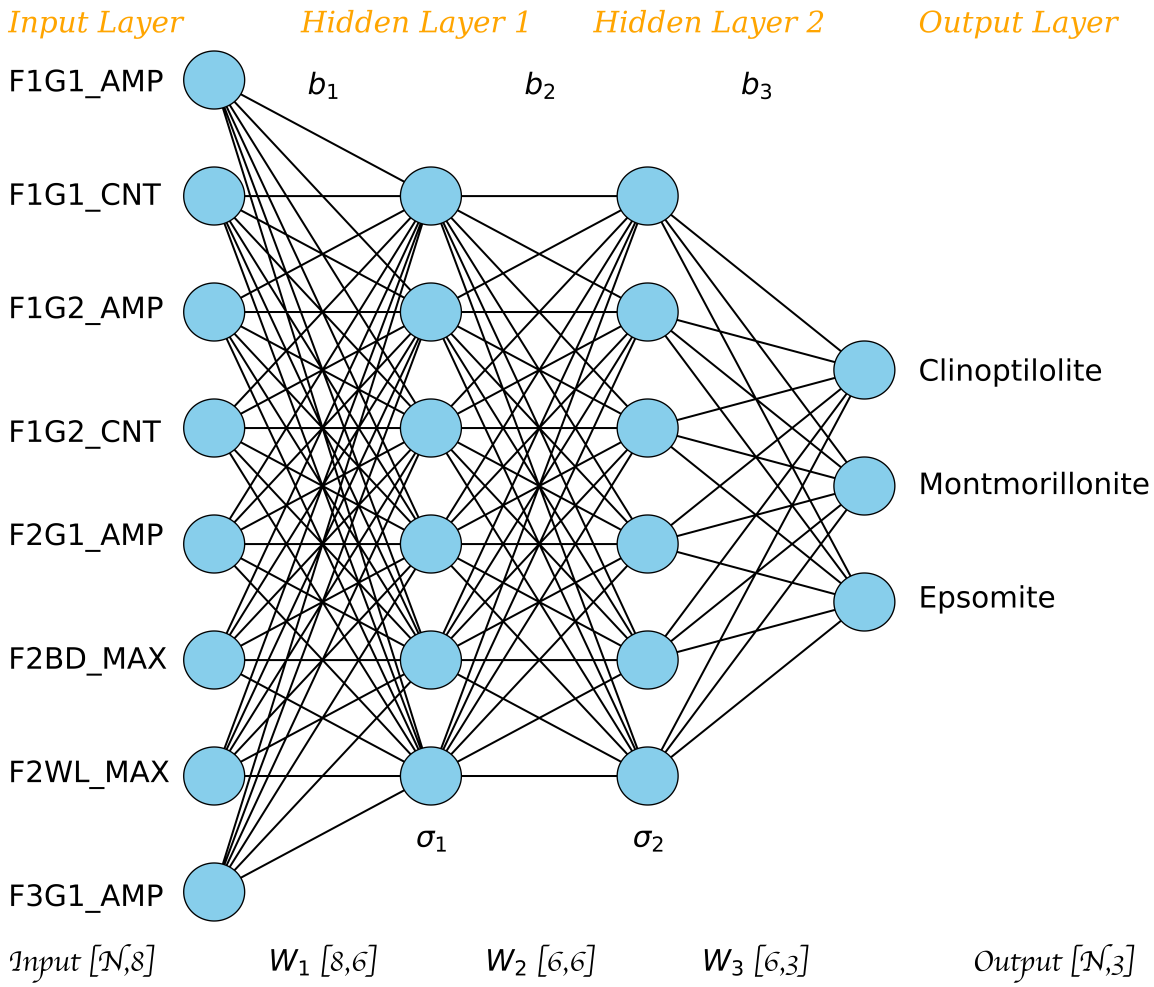

Figure 5.8: An MLP with eight inputs, two hidden layers containing six hidden units, and three outputs.

The number of training samples is a key factor in ML. Fewer training samples are more likely to overfit the model. With the increase in the amount of training data, the generalization error typically decreases. The generalization error measures how accurately the trained model can predict the outcome for previously unseen data. It is also crucial that the training set used is representative of the cases to which we want to generalize. For this reason, the spectral parameters for another 100 points were derived, interpolating from the nearest three sample points in the ternary plots. Derived sample points represent the middle point of each small triangle. The interpolations were done only for the eight selected parameters. Spectral parameters for five data points (T89, T120, T131, T134,

and T155) were kept aside to test the model. The rest of the samples (160) were randomly divided into two sets, a training dataset containing 66 % of the dataset and the rest assigned as a validation dataset. The validation dataset was used to calculate the accuracy (root mean square error; RMSE) of the model after training the DNN using the training dataset. To determine the best DNN model for estimating the most accurate mineral abundances for the given spectral data, 48 models were run changing DNN architecture and its hyperparameters: adding different numbers of hidden layers (2 and 3 layers) and changing the number of units in each hidden layer (6 and 10 units), changing the activation function (Sigmoid and ReLU), and changing the optimization algorithm (SGD and Adam). Each model was tested with four learning rates (0.0001, 0.001, 0.01, 0.1), each with 10,000 epochs. The RMSE errors of the model runs are shown in Table 5.2. This shows that two hidden layer architecture (with six units in each hidden layer) with ADAM optimization and Sigmoid activation function performed better than the others. From that architecture, the two lowest RMSE were archived under 0.001 and 0.01 learning rates (bold numbers in Table 5.2). Therefore, these two models were evaluated by the test dataset to find the most generalized model.

Table 5.2: Root Mean Square Error (RMSE) of different models adopted in this study. All models were run for 10,000 epochs.

DNN Architecture	Learning Rate	ADAM with Sigmoid	ADAM with RELU	SGD with Sigmoid	SGD with RELU
8 x 6 x 6 x 3					
	0.0001	0.426	0.684	1.276	0.264
	0.001	**0.176**	0.434	2.400	2.504
	0.01	**0.278**	0.367	2.510	2.501
	0.1	2.509	2.496	2.668	2.528
8 x 6 x 6 x 6 x 3					
	0.0001	0.353	0.699	0.214	1.711
	0.001	0.202	0.358	2.230	2.249
	0.01	2.231	0.377	2.213	2.250
	0.1	2.215	2.512	2.437	2.255
8 x 10 x 10 x 3					
	0.0001	0.294	0.380	2.592	0.266
	0.001	0.211	0.245	0.325	2.331

DNN Architecture	Learning Rate	ADAM with Sigmoid	ADAM with RELU	SGD with Sigmoid	SGD with RELU
	0.01	0.283	0.288	2.302	2.301
	0.1	2.340	2.350	2.297	2.438

The test dataset consisted of twenty-five samples including spectral parameters derived from the five points that were kept aside before. This was used to assess how well the model identifies mineral mixtures calculated under similar experimental conditions. Fifteen reflectance spectra from available spectral databases were used to assess how well this worked to identify mineral end members from different samples. Five noise added spectra simulated the effects of the signal to noise (S/N) ratio on the identification of constituent mineral abundances. The library spectra were taken from the RELAB spectral database (www.planetary.brown.edu/relab), USGS spectral library (www.usgs.gov/labs/spec-lab), and a spectrum acquired by the author (Table 5.3). Library spectra were resampled into laboratory spectra and processed in the same way to derive the spectral parameters. The spectrum of sample T53 was resampled to CRISM spectral bandpass and then random noise was added to simulate the spectral quality of these mixtures as seen from orbital data. Five different percentages of random noise with a Gaussian distribution having a zero mean were added to the original spectra.

$$R_n(\lambda) = R_{T53}(\lambda) + N(\lambda) \quad \text{——————(5.12)}$$

$$N(\lambda) = \left(\frac{1}{\sqrt{2\pi\sigma^2}} e^{-\frac{(x-\mu)^2}{2\sigma^2}}\right) * percentage \quad \text{———(5.13)}$$

where μ is the mean, σ is the standard deviation, and x is the size (number of data points). The percentages of added noise are 5 %, 10 %, 25 %, 50 %, 75 %. Noise added spectra were smoothed using Savitzky-Golay filter (Savitzky and Golay, 1964) to get more realistic results. The Savitzky-Golay smoothing function fit a low-degree polynormial through the data points within the local spectral window to derive the processed signal values from the polynormial function. The resultant spectra were resampled again into the original laboratory bandpass to derive the Gaussian curve parameters (Fig 5.9).

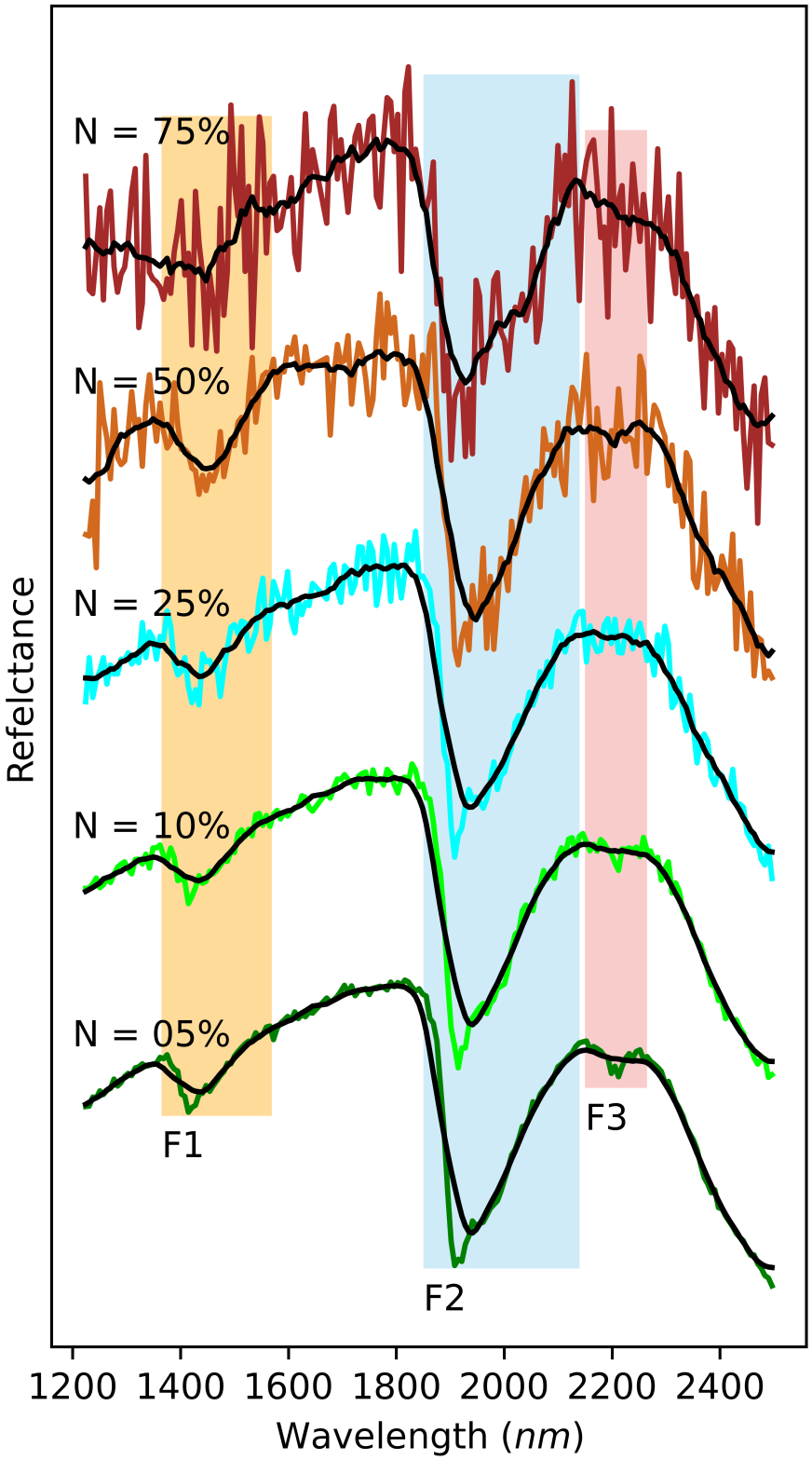

Figure 5.9: Noise added versions of spectrum T53, resampled to CRISM spectral resolution. Savitzky-Golay Smoothed spectra are shown in black.

Table 5.3: Library spectra used to test the accuracy of the model.

Spectral ID	Mineral	Specimen Size	Source
T27U	Clinoptilolite + Phillipsite	150 μm	personal collection
gds152-5841	Clinoptilolite	–	USGS
gds2-5896	Clinoptilolite	–	USGS
c1ze27	Clinoptilolite	0 - 45 μm	RELAB
c1ze28	Clinoptilolite	0 - 45 μm	RELAB
gds149-7646	Epsomite ($MgSO_4.7H_2O$)	–	USGS
c1cc19	$MgSO_4$ (anhydrous)	0 - 25 μm	RELAB
c1cc31	$MgSO_4$ (hydrous)	0 - 25 μm	RELAB
c1jb366	Epsomite $MgSO_4.7H_2O$	0 - 45 μm	RELAB
c1jb711	Starkeyite $MgSO_4.4H_2O$	–	RELAB
c1gr02	Montmorillonite	0 - 100 μm	RELAB
c1jb186	Montmorillonite - SWy-2	–	RELAB
c1jb13	Montmorillonite - SWy-1	0 - 125 μm	RELAB
c1jb899	Montmorillonite	0 - 0.2 μm	RELAB
cm27-14440	Montmorillonite	–	USGS

5.5 5. Accuracy assesment

From the two selected models, two hidden layer architectures (with 6 hidden units) with ADAM optimization, Sigmoid activation function, and 0.001 learning rate model gave the best results with the lowest RMSE. The architecture of the winning model is shown in Figure 5.8. The accuracy of the predicted results is shown in figure 5.10. This shows that mineral mixtures derived from the interpolated data (T89, T120, T131, T134, and T155) provide more than 90 % accuracy based on their predicted mineral abundances. Three out of five montmorillonite and four of five epsomite samples also gave more than 90 % of accuracy with the predicted data. However, clinoptilolite samples show less than 50 % accuracy and were always predicted as mixture of clinoptilolite and epsomite. One of the epsomite samples was also predicted as a mixture of clinoptilolite and epsomite (with ~ 10 % of montmorillonite). Although the original T53 spectra was collected from a mineral mixture with 60% clinoptilolite, 20% montmorillonite and 20% epsomite, four out of five noise added T53 spectra predicted as it contained more than 95% of clinoptilolite and montmorillonite. The remaining spectra predicted mainly a mixture of epsomite ($>$ 80%) and montmorillonite ($<$ 20%) with not clinoptilolite. The 50% noise added

spectra shows an absorption feature at F3, created by the added noise (Fig 5.9). The original spectrum shows very low band depth at F3 (Fig 5.5c) compared to the noise added spectra (Fig 5.11c). Also, F1 and F2 of the T53 50% noise added spectral features are like the features of the epsomite endmember (Fig 5.11). The spectral features of most deviated clinoptilolite (gds125-5841) and montmorillonite (gds149-7646) spectra from their respective endmembers show similar spectral behaviors (Fig 5.11a and b). The band strengths of the most deviated predicted compositions are higher than the band strengths of the modeled spectral features (Fig 5.11). This could be overcome by normalizing spectral parameters (especially amplitudes and widths of Gaussian curves) using a certain parameter, such as taking the ratio of amplitudes of two different Gaussian curves in the same feature (e.g., F1G1_AMP/F1G2_AMP), or normalizing by a Gaussian curve parameter from another feature (e.g., F1G1_AMP/F2G1_AMP). Prediction results (values) can be found in Table C.1 in Appendix C.

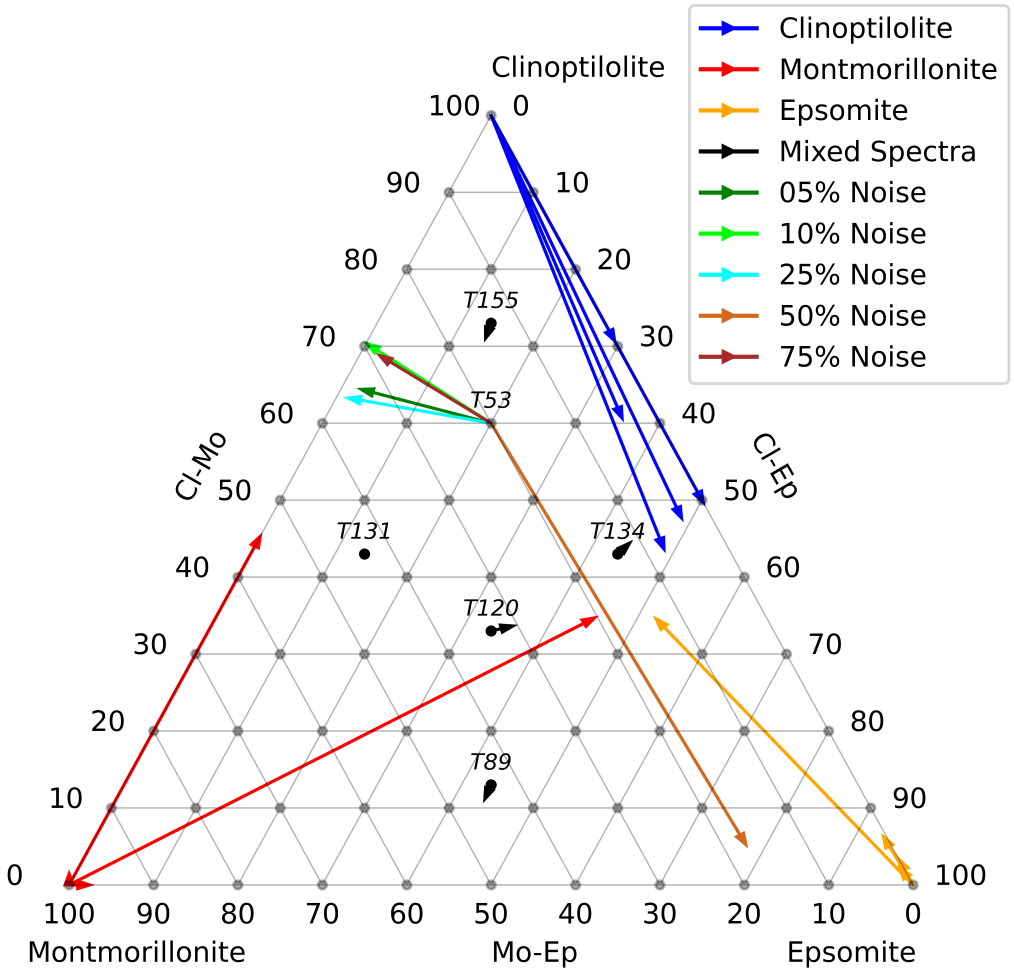

Figure 5.10: Ternary plot showing the original composition of the mineral/mineral mixture with their predicted compositions. Arrowheads show the predicted composition of each mineral mixture.

Even though the overall spectral shape is similar for different samples of the same mineral, grain size variations influence the strength of absorption bands and continuum levels for each sample (Swayze et al., 2003; Robertson et al., 2016). The selected library spectra were taken from different grain sizes, which influence the prediction accuracy. Hunt et al. (1972) observed that the 1.4 μm band depths are strongly influenced by the grain size of the mineral and contaminants. The strength of an absorption is also related to the amount of absorber in the optical path. Clark et al. (1990) noted that the position of the $\sim$ 2.2 μm absorption band of montmorillonite shift to a longward position with increasing

Ca content. Absorption bands in reflectance spectroscopy are also sensitive to hydration state and cation substitution. The reflectance spectra of variably cation-exchanged SWy montmorillonite show that their absorption band depth at 1.9 μm increases with respect to the absorption band at 2.2 μm from Na-Swy to Fe^{3+}-SWy to $natural(Na/Ca)$-SWy, to Ca-SWy, and to Mg-SWy (Bishop et al., 1994). Cloutis et al. (2002) also observed a general increase in the wavelength position of the 1.4 μm absorption feature from 1.420 μm in K-bearing zeolites, to 1.422 μm in Na-bearing zeolites, and to 1.427 μm in Ca-bearing zeolites. Previous studies show that the position of the 1.9 μm band of montmorillonite shifts to longer wavelength during hydration (e.g., Pommerol et al. (2009); Bishop et al. (1994)). Bishop et al. (1994) also noted that Mg and Na montmorillonite measured under a H_2O-purged environment exhibit slightly asymmetric bands centered at 1.91 μm, and under moist conditions, the same samples show a much stronger band at 1.91 μm along with a strong shoulder at 1.97 μm. The shoulder near 1.97 μm is present under moist conditions as it forms due to adsorbed H_2O. Milliken and Mustard (2005) collected spectra from five materials including Na-Ca montmorillonite, Mg-exchaged montmorillonite, clinoptilolite, palagonite, and a reagent-grade $MgSO_4.nH_2O$ with initial water contents ranging from 6 to 20 wt% to identify the relationships between the absolute water content and water-related absorption bands. There appears to be no correlation between water absorption at 1.9 μm and absolute water content. The 1.9 μm band is also weaker for amorphous material than for well-ordered materials with similar water content. Cloutis et al. (2002) document an increase in the 1.9 μm band position for zeolites from K-bearing zeolites (1.911 μm average) to Na-bearing zeolites (1.913 μm average) to Ca-bearing zeolites (1.922 μm average). Dalton (2003) showed the spectra of different hydration stages of magnesium sulfates ($MgSO_4.nH_2O$ for n = 0,1,1.5,2,3,4,5,6,and 7) and noted that, with the increase of hydrate stage (n), the spectral features near 1.4 and 1.9 μm begin to merge and combine creating broad absorption features. Sheppard et al. (2021a) measured the changes in near-infrared spectral absorptions of powdered montmorillonite and Mg sulfate mixtures exposed to Mars relevant conditions in a controlled lab setting. They observed that the presence of amorphous Mg sulfate is difficult to identify in physical mixtures that contain more than $\sim$ 10 % montmorillonite by weight.

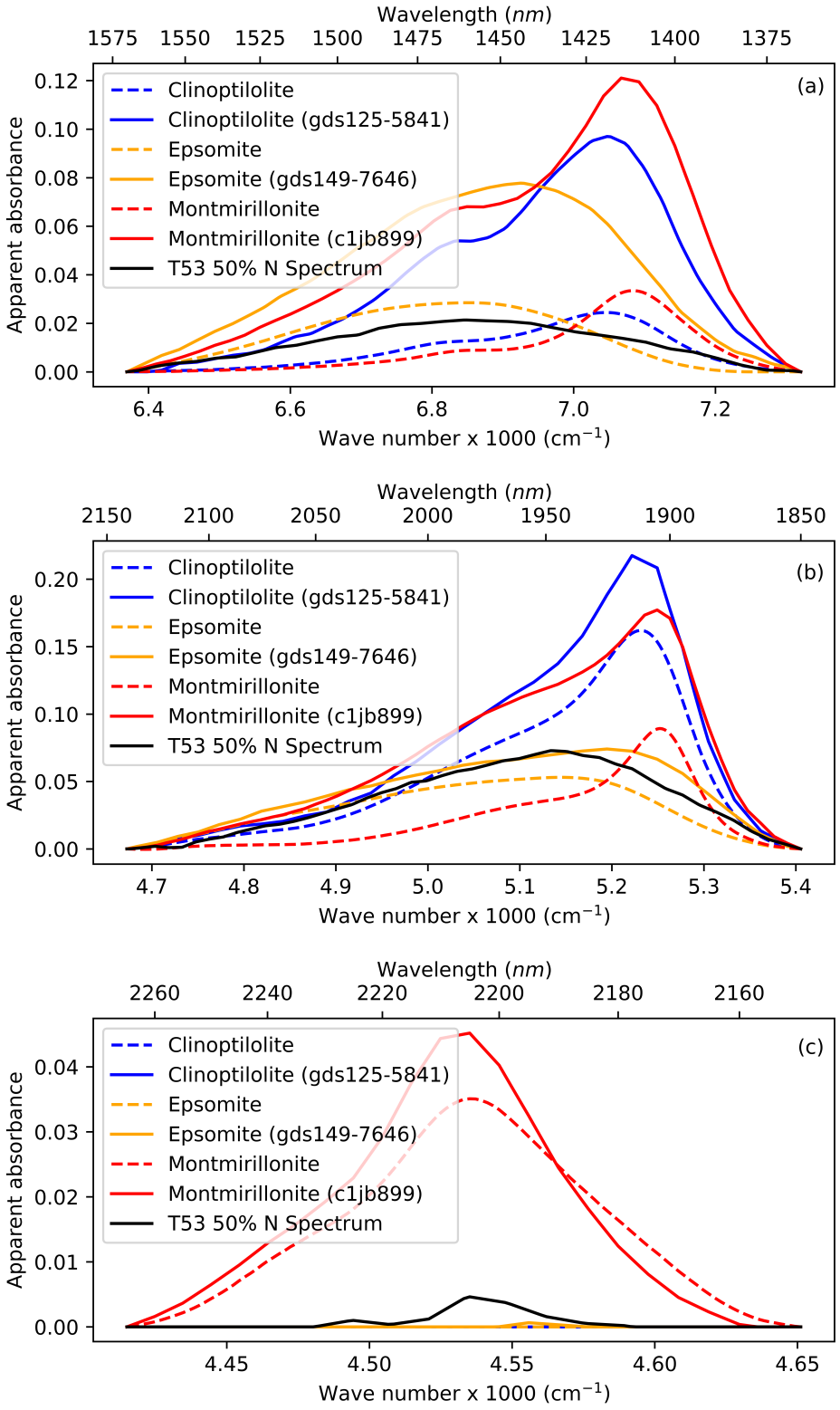

Figure 5.11: Continuum removed spectra of F1 (plot a), F2 (plot b), and F3 (plot c) of end member spectra (dashed lines) and library spectra, which shows the highest prediction error.

5. Application of deep learning and spectral deconvolution for estimating mineral abundances of zeolite, Mg-sulfate and montmorillonite mixtures and its implications for Mars.

Though the shape and position of 1.4 μm and 1.9 μm absorption bands in clinoptilolite - montmorillonite mineral mixtures (Fig 5.4a) do not change with the changes of mineral weight proportion, the 2.2 μm absorption band disappears only in the pure clinoptilolite spectra. Since the absorption band at 2.2 μm is unique for montmorillonite in this mineral assemblage, even though mineral mixture contains ~ 90% of clinoptilolite, it may not be identifiable from the reflectance spectra if it is associated with montmorillonite. The spectra of clinoptilolite - epsomite mineral mixtures shown in Figure 5.4 (b) shows that the lack of diagnostic absorption feature/s to differentiate these two minerals, except the minute changes of absorption band shape and position of the 1.4 μm, 1.9 μm bands, makes them difficult to differentiate using orbital spectral data. This discrepancy is evident in orbital and in-situ observation from Gale crater data. While only Mg-sulfates were visible in the orbital observations, only Ca-sulfates have been seen in in-situ data at certain locations (Sheppard et al., 2021b).

Results from previous and current experiments and modeling demonstrate the strong effects of albedo, particle size, water content, and cation substitution for the band parameters (band depth, band width, and band shape) of the 1.4, 1.9 and 2.2 μm absorption bands, in addition to the contribution from constituent mineral abundances. When two opposite correlations are superposed, as seen on real planetary surfaces, this may lead to an even more complex situation, making it more difficult to derive the correct mineral abundances using band parameters. As an example, band strength is positively correlated to surface albedo, though variation of particle size introduces a negative correlation between band strength and surface albedo (Pommerol and Schmitt, 2008). When noise is added into this already complex situation, predicted mineral abundances can be completely incorrect, even using a well-trained DNN. Therefore, it is also important to incorporate the contribution from albedo, particle size, water content, and cation substitution for future models.

5.6 Conclusions

In this study, the efficacy of a combination of spectral deconvolution and deep neural network techniques was examined to estimate mineral abundances of zeolite, Mg-sulfate,

5. Application of deep learning and spectral deconvolution for estimating mineral abundances of zeolite, Mg-sulfate and montmorillonite mixtures and its implications for Mars.
and montmorillonite mixtures using their reflectance spectra. Key findings are as follows,

1. The presence of at least ~ 10% of montmorillonite in a clinoptilolite-montmorillonite mixture can entirely mask the presence of clinoptilolite in SWIR spectral data.

2. If a sample contains higher than ~ 20 % montmorillonite in an epsomite-montmorillonite mixture, the montmorillonite will mask the presence of epsomite in SWIR spectral data.

3. The results show the difficulties of distinguishing clinoptilolite from epsomite even for the spectra acquired under laboratory conditions.

4. The absorption bands at 1.4 μm, 1.9 μm, and 2.2 μm were able to mathematically deconvolve using two normal Gaussian curves, a normal Gaussian curve with a skewed Gaussian curve, and a normal Gaussian curve, respectively.

5. Selecting the correct input features, architecture of DNN, and hyperparameters helps to predict the mineral abundances with higher accuracies.

6. Care must be taken when estimating mineral abundance from a new dataset, even from a well-trained DNN. The new dataset must have similar characteristics to the training dataset to achieve the best results. Normalizing the spectral parameters before feeding it to the DNN might be a good approach, if working with a wide variety of datasets.

7. It is also important to incorporate the contribution from albedo, particle size, water content, and cation substitution for future models.

Acknowledgement

Many thanks to Thomas McCollom at University of Colorado for acquiring spectral data for field samples, and to USGS and RELAB. Also, thanks to python, pytorch and other python modules, and Rstudio developers.

"We are what we think. All that we are arises with our thoughts. With our thoughts, we make the world."

-Gothama Buddha-

6

Self-Organizing Maps for identification of zeolitic diagenesis patterns in closed hydrologic systems on the Earth and its implications for Mars.

Contents

Abstract **208**
6.1 Introduction **209**
6.2 Dataset **214**
6.3 Approach **220**
6.3.1 Self-Organizing Map 220
6.3.2 Hierarchical Clustering 224
6.4 Results and discussion **225**
6.5 Implications for Mars **232**
6.6 Conclusion **234**
Acknowledgements **234**

Abstract

A survey of zeolite occurrences in saline-alkaline paleolake deposits on Earth was conducted to identify the most prominent zeolite alteration patterns and to characterize the most common authigenic minerals and their paragenetic relationships. The bulk mineral

assemblages (from previous and our studies) as identified by X-ray Diffraction from zeolitic tuff beds and associated sedimentary beds were collected from thirteen paleolake deposits from the USA, Mexico, Greece, and Tanzania. The Kohonen Self-Organizing Maps (SOM) was applied to look for interesting patterns in the tuff bed mineral assemblages without prescribing any specific interpretation, and for information reduction and classification. Decision Tree (DT) method was applied to characterize these clusters. The method was able to define clear class boundaries between fresh glass, non-analcime zeolites, analcime, and K feldspar. The non-analcime zeolites were further grouped into several classes based on mineral type. Potential implications for Mars also discussed. It shows that the mineral assemblages of diagenetic facies identified by SOM and DT can be used to test or validate the orbital, in situ, or modeling results, while the trained SOM provides a robust generalized ability to classify the new mineral assemblage data into the most common diagenetic facies identified in saline-alkaline paleoenvironments that contain zeolites. The study concludes that generalizing the complex geochemical behaviors using unsupervised statistical learning methods can help to identify the most prominent geochemical behaviors.

6.1 Introduction

Zeolites are one of the most common authigenic silicate minerals found in paleolacustrine environments on the Earth. The most common zeolites in saline-alkaline paleolakes are analcime ($Na(AlSi_2O_6).H_2O$), chabazite ($Ca_2[Al_4Si_8O_{24}].13H_2O$), clinoptilolite ($(Na_2, Ca, K_2)_3(Si_{30}Al_6)O_{72}.20H_2O$), erionite ($(Na_2, Ca, K_2)_5(Si_{26}Al_{10}O_{72}).30H_2O$), mordenite ($(Na_2, Ca, K_2)_4(Al_8Si_{40})O_{96}.28H_2O$) and phillipsite ($(Na_2, Ca, K_2)_3(Si_{10}Al_6)O_{32}$. $12H_2O$) (Hay, 1966; Chipera and Apps, 2001). The spatial and stratigraphic patterns of authigenic minerals found in paleolakes are potentially diagnostic for their lacustrine origin. Several factors are influential in determining whether zeolites, clay minerals, or feldspars will form when pore solutions react with vitric material in the host rock. These are, 1) salinity, 2) pH, 3) activity of water (a_{H_2O}), 4) activity of silica ($a_{SiO_2(aq)}$), and 5) relative proportions of the alkali (Na^+, K^+) and alkaline earth (Ca^{2+}, Mg^{2+}) cations (Hay, 1966; Sheppard and Gude, 1968; Mariner and Surdam, 1970; Hay and Sheppard, 2001). Therefore the presence of a certain mineral, mineral assemblage, and/or mineral zonation

in a saline-alkaline paleolake can be attributed to thermodynamic equilibrium reactions due changing water chemistry (Hay, 1966), and to kinetically controlled precipitation and dissolution reactions (Dibble and Tiller, 1981). Thus, changes in zeolite assemblages over time in paleolake deposits can be used to track changes in paleoenvironment (e.g., Trauth et al. (2001); McHenry et al. (2020)).

Zeolites have been proposed to be components of Mars regolith (e.g., Berkley and Drake (1981); Ming and Gooding (1988); Basu et al. (1998); Bish et al. (2003); Dickinson and Rosen (2003); Ruff (2004); Tokano and Bish (2005); Ehlmann et al. (2011); Cannon et al. (2015); Viennet et al. (2017); Ackiss et al. (2018)), and have been detected on the Martian surface using orbital data (e.g., Ehlmann et al. (2009); Michalski et al. (2005); Bandfield (2008); Wray et al. (2009); Sun and Milliken (2015); Viviano-Beck et al. (2017)). These detections were mostly associated with hydrated silica, Fe-, Mg-rich phyllosilicates, or carbonates. Basu et al. (1998) argued that diagenetic processes that likely operated on Mars should have produced zeolites in Martian volcanoclastic rocks. Ming and Gooding (1988) infer that clinoptilolite and mordenite are more likely to be present on Mars compared to Si-poor zeolite species such as analcime, phillipsite and chabazite. Bristow and Milliken (2011) discussed the importance of recognizing spatial and stratigraphic trends in the types of authigenic mineral phases that formed in standing bodies of water on Mars, probably with elevated pH.

Sun and Milliken (2015) conducted a global survey of central peaks of 633 craters on Mars to assess their hydrous minerals using orbital spectral data. They have identified seven mineral groups: Fe/Mg smectite, chlorite, hydrated/opaline silica, zeolite, sulfate, Al-phyllosilicates, and unidentified hydrous phases. Analcime is the most commonly detected zeolite on Mars based on its distinctive broad absorption feature centered at ~2.5 μm and a weak absorption feature at ~1.8 μm (Ehlmann et al., 2009). Identification of non-analcime zeolites is complicated by the lack of diagnostic absorption features in the Visible-Near Infrared (VNIR) wavelength region. Therefore, Sun and Milliken (2015) classified the potential analcime detections as zeolite, and spectra that only exhibit the 1.4 and 1.9 μm absorption peaks as unidentified hydrous phases, which could include non-analcime zeolites along with other hydrous phases, such as polyhydrated sulfates. Based on this criteria,

they have identified analcime in 4.5% of the central peaks studied. However, if zeolites are formed in closed hydrologic systems and analcime and non-analcime zeolites are not present together in same diagenetic environment, it is possible that non-analcime zeolites could be present in other central peaks, but cannot at present be identified using orbital data.

Since orbital and most in-situ spectral methods capture the spectra from a mineral mixture (due mostly to limited spatial resolution), understanding spectral behaviors of mineral mixtures possibly present in the target area (along with their relative abundances) is important for correct identification. In addition, if a targeted mineral does not have a characteristic absorption feature/s or if the spectra of two different minerals appear too similar in the wavelength range analyzed (e.g., spectra of most zeolites look similar in VNIR, Cloutis et al. (2002)), we have to rely on a different wavelength region or a different observation technique to identify those minerals. Therefore, it is important to identify the most prominent zeolite alteration patterns and mineral assemblages in saline-alkaline paleolake systems. The objective of this study, therefore, is to identify the most common authigenic minerals and their paragenetic relations in saline-alkaline paleolake systems on Earth, assuming that Earth and Mars underwent similar geological processes in the past.

For that, a literature survey was done to collect data on patterns of mineral paragenesis reported covering a wide spectrum of paleolacustrine environments on Earth. These studies have identified mineral paragenesis patterns mainly based on petrographic and scanning electron microscopy and X-ray diffraction methods. The data shows that mineral paragenesis in closed hydrologic systems on the Earth is often complex and difficult to study, since mineral assemblages are not representative and vary widely even within the same site/same bed (13 selected sites show at least 45 mineral paragenesis patterns: Table 6.1). These differences can be attributed to the composition of the starting material and the solution interacting with them, hydrologic conditions of the environment, and kinetic factors (Langella et al., 2001). In addition, most of the mineral paragenetic patterns were observed at the micron scale (e.g., SEM images), which may not represent the large scale (basin-wide) generalized pattern/s. Therefore, the bulk mineral assemblages (identified by XRD) from the same published studies was used for this study.

Table 6.1: Reported mineral paragenesis.

No	Mineral Sequence	References
1	Glass → Chabazite → Analcime → K feldspar	Gude and Sheppard (1986)
2	Glass → Chabazite → Clinoptilolite → Mordenite	Gude and Sheppard (1986)
3	Glass → Chabazite → Erionite → Calcite	Sheppard (1994)
4	Glass → Chabazite → Erionite → Clinoptilolite	Gude and Sheppard (1986)
5	Glass → Clinoptilolite → Analcime → K feldspar	Gude and Sheppard (1986)
6	Glass → Clinoptilolite → K feldspar	Sheppard (1994); Boles and Surdam (1979)
7	Glass → Clinoptilolite → Mordenite → Erionite → Opal	Pablo-Galan and Chavez-Garcia (1996)
8	Glass → Clinoptilolite → Opal	Pablo-Galan and Chavez-Garcia (1996)
9	Glass → K feldsper → Opal	Pablo-Galan and Chavez-Garcia (1996)
10	Glass → Mordenite → Analcime → K feldspar	Gude and Sheppard (1986)
11	Glass → Opal → Clinoptilolite	Sheppard (1991)
12	Glass → Phillipsite → Analcime → K feldspar	Gude and Sheppard (1986)
13	Glass → Phillipsite → Clinoptilolite → Erionite	Gude and Sheppard (1986)
14	Glass → Phillipsite → Clinoptilolite	Gude and Sheppard (1986)
15	Glass → Phillipsite → Clinoptilolite → Mordenite	Gude and Sheppard (1986)
16	Glass → Phillipsite → Erionite	Gude and Sheppard (1986)
17	Glass → Phillipsite → Erionite → Chabazite	Gude and Sheppard (1986)
18	Glass → Smectite → Analcime → K feldspar	Sheppard (1994)
19	Glass → Smectite → Chabazite → Clinoptilolite → Erionite	Sheppard (1994)
20	Glass → Smectite → Chabazite → Erionite	Gude and Sheppard (1986); Gude and Sheppard (1988); Sheppard and Gude (1969b); Sheppard (1994)

No	Mineral Sequence	References
21	Glass → Smectite → Chabazite	Gude and Sheppard (1988)
22	Glass → Smectite → Chabazite → Erionite → Analcime	Gude and Sheppard (1988)
23	Glass → Smectite → Chabazite → Clinoptilolite	Sheppard and Gude (1969b); Sheppard and Gude (1973); Gude and Sheppard (1986)
24	Glass → Smectite → Clinoptilolite → Analcime → K feldspar	Stamatakis (1989b)
25	Glass → Smectite → Clinoptilolite → Mordenite	Sheppard (1991); Sheppard (1994); Gude and Sheppard (1988); Sheppard and Gude (1969b)
26	Glass → Smectite → Clinoptilolite → Opal	Sheppard (1991)
27	Glass → Smectite → Clinoptilolite → Calcite	Sheppard (1991); Sheppard (1994)
28	Glass → Smectite → Clinoptilolite → Quartz → Calcite	Sheppard (1991)
29	Glass → Smectite → Clinoptilolite → Erionite	Sheppard (1991); Gude and Sheppard (1988); Sheppard and Gude (1973)
30	Glass → Smectite → Clinoptilolite → Quartz	Sheppard (1991); Sheppard (1994); Sheppard and Gude (1969b); Sheppard and Gude (1973)
31	Glass → Smectite → Clinoptilolite	Sheppard (1994); Gude and Sheppard (1988); Gude and Sheppard (1986); Sheppard (1991)
32	Glass → Smectite → Clinoptilolite → Analcime	Sheppard (1994); Gude and Sheppard (1988)
33	Glass → Smectite → Clinoptilolite → Mordenite → Erionite	Sheppard (1994)
34	Glass → Smectite → Erionite	Sheppard (1991)
35	Glass → Smectite → Erionite → Clinoptilolite	Gude and Sheppard (1986)
36	Glass → Smectite → Erionite → Analcime	Gude and Sheppard (1988)
37	Glass → Smectite → Mordenite	Sheppard (1994); Gude and Sheppard (1988)
38	Glass → Smectite → Mordenite → K feldspar	Sheppard (1994)

No	Mineral Sequence	References
39	Glass → Smectite → Opal	Pablo-Galan and Chavez-Garcia (1996)
40	Glass → Smectite → Opal → Clinoptilolite	Sheppard (1991)
41	Glass → Smectite → Phillipsite → Clinoptilolite → Erionite	Sheppard (1991)
42	Glass → Smectite → Phillipsite → Clinoptilolite	Sheppard (1994); Sheppard and Gude (1969b); Sheppard and Gude (1973); Gude and Sheppard (1986)
43	Glass → Smectite → Phillipsite → Erionite	Sheppard (1994)
44	Glass → Smectite → Phillipsite → Opal	Sheppard (1994)
45	Glass → Smectite → Phillipsite → Clinoptilolite → Erionite → Analcime	Sheppard (1994)

6.2 Dataset

Published bulk mineral abundance data from zeolitic tuff beds and associated sandstone, siltstone, mudstone, and carbonates were collected from thirteen paleolake deposits from the USA, Mexico, Greece, and Tanzania. Bulk mineral assemblages of samples collected from Paleolake Tecopa, California during 2018 and 2019 field visits also incorporated. Sites where field and laboratory studies show that diagenesis took place at near-surface temperatures and pressures were only selected. Eliminated sites include open hydrologic systems (e.g., White River sequence, Wyoming (Lander and Hay, 1993)) and sites that have been affected by other diagenetic processes such as hydrothermal processes (e.g., Yucca Mountain, Nevada (Sheppard et al., 1988), Ngakuru zeolite deposits, New Zealand (Brathwaite, 2003), Mecsek mountains, SW of Hungary (Polgari et al., 1997), and Kaiserstuhl volcanic complex, SW Germany (Weisenberger and Spurgin, 2009)). Some saline-alkaline lacustrine deposits also eliminated due to inconsistency between the reported data or insufficient reported data. Some of the volcanoclastic zeolite deposits on Earth are interpreted to have formed in lagoonal or marine environments (e.g., Cinerite of central northern Apennines, Italy (Passaglia and Vezzalini, 1985) and most of the zeolite deposits in Bulgaria and Slovakia (Kirov et al., 2011)), and these sites were also not considered. Therefore, the adopted dataset includes only saline-alkaline lacustrine

deposits formed in closed hydrologic systems, for which sufficient data has been published. The data compiled from different published sources is listed in Table 6.2. Most of the data was collected from the studies of Richard A. Sheppard and Arthur J. Gude, and they conveniently categorized clay minerals into two groups, named Clay10Å (including authigenic illite and pyrogenic biotite from older volcanic rocks) and Clay14Å (including smectite minerals, most commonly montmorillonite or mixed-layered montmorillonite-illite). The same approach for other datasets were applied for consistency. All feldspar types reported were grouped into either authigenic K feldspar (orthoclase), referred to here as K feldspar or others (albite, plagioclase, and anorthoclase), named "feldspar". Fourteen minerals common to all datasets were selected, and others were grouped into the "Other" mineral class. In addition, different authors have used different scales for the mineral abundance (e.g., 0-10 scale, 0-4 scale, and 0-3 scale), and therefore all of the abundance data were re-scaled into four categories including Absent, Trace, Minor and Major. The "absent" and "trace" categories were retained as they were used in all of the collected datasets, while the rest of the data were re-scaled into the minor and major categories.

Table 6.2: Number of samples in each type of sedimentary beds in selected sites

Site	Age	Tf	Ss	St	Md	Cb	Total	Reference
Barstow Formation, California, USA	Miocene	102	-	-	-	-	102	Sheppard and Gude (1969b)
Big Sand Formation, Arizona, USA	Pliocene	265	37	5	40	-	347	Sheppard and Gude (1973)
Buckhorn, New Mexico, USA	Pliocene(?)	45	3	4	10	-	62	Gude and Sheppard (1988)
Chalk Hill Formation, Idaho, USA	Miocene	183	26	8	33	-	250	Sheppard (1991)
Durkee, Oregon, USA	Miocene	326	19	5	45	-	395	Gude and Sheppard (1986)
Eastgate Zeolite Deposit,Nevada, USA	Pliocene	72	-	-	5	-	77	Sheppard and Gude (1980)
Harney Lake, Oregon, USA	Miocene	171	30	7	2	13	223	Sheppard (1994)
Karlovassi Basin, Samos Island, Greece	Miocene	83	-	-	-	-	83	Stamatakis (1989b); Stamatakis (1989a)
Lake Tecopa, California, USA	Pleistocene	258	8	4	31	-	301	Larsen (2008); Sheppard and Gude (1968);this study
Little Humboldt River, Nevada, USA	Miocene	45	-	-	-	-	45	Sheppard and Gude (1983)

Site	Age	Tf	Ss	St	Md	Cb	Total	Reference
Mexican Volcanic Belt, Guanajuato, Mexico	Miocene	10	-	-	-	-	10	Pablo-Galan and Chavez-Garcia (1996)
Olduvai Gorge, Nothern Tanzania	Pleistocene	34	27	-	316	24	401	McHenry et al. (2020)
Rome, Oregon, USA	Pliocene	54	-	-	13	-	67	Sheppard and Gude (1969a)
	Total	1648	150	33	495	37	2363	

Tf = Tuff, Ss = Sandstone, St = Siltstone, Md = Mudstone, Cb = Carbonate

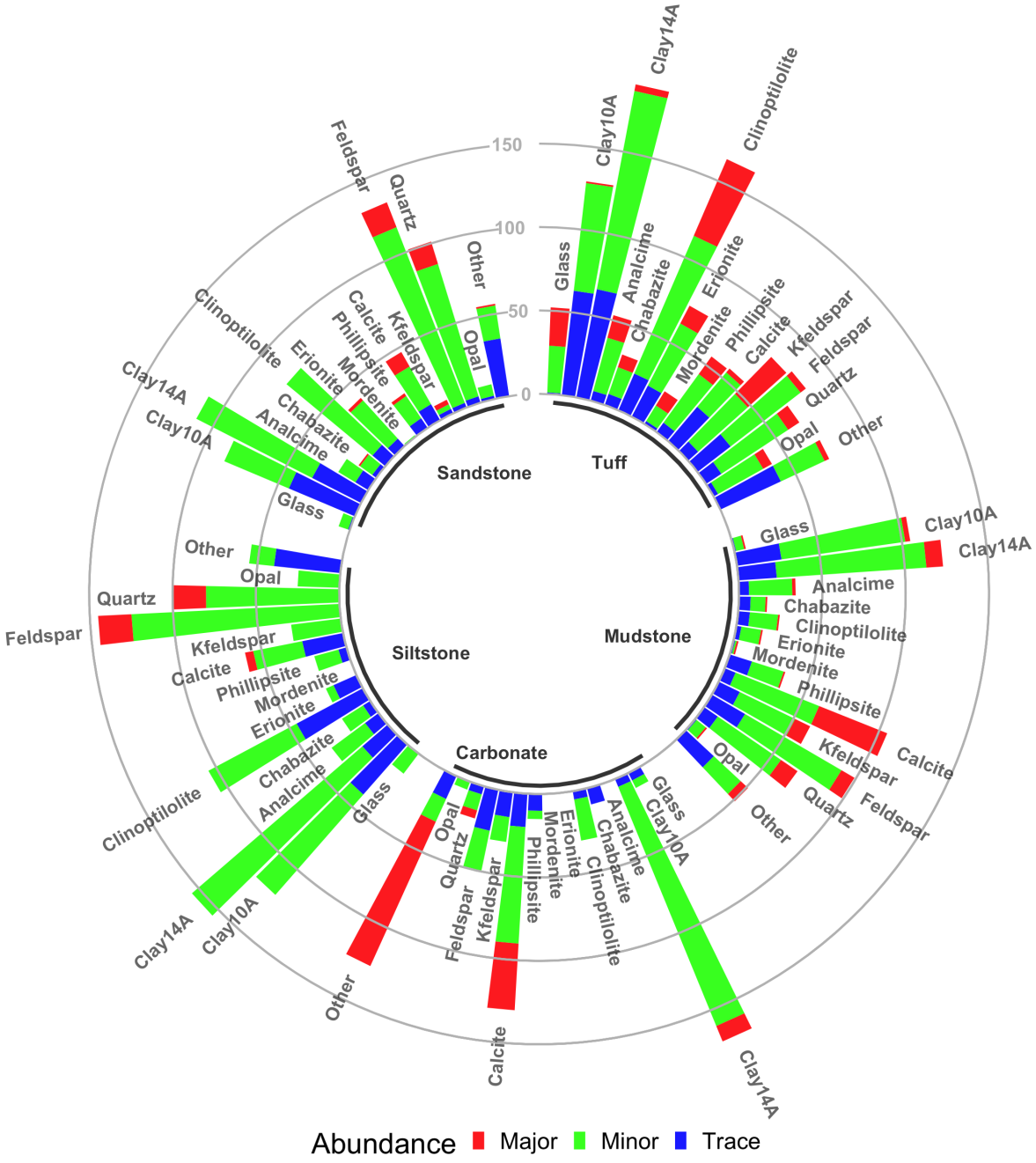

Figure 6.1: Reported mineral abundances in saline-alkaline paleolakes. Each sedimentary bed type in the concentric graph shows the abundance of each mineral type (color coded), along with the relative frequency of samples that contain it. Frequency is depicted by the height of the each bar. The data were normalized for each sediment type to its maximum frequency.

Figure 6.1 shows the relative mineral abundances of saline-alkaline paleolake beds of selected sites. It shows the frequency of three assigned mineral abundance classes (color coded, for Major, Minor, and Trace) of each mineral in each sediment type. The

height of each bar shows the relative frequency of that mineral in that sediment type. The entire dataset contained different numbers of total samples in each sedimentary rock type (Table 6.2). Therefore,the dataset was normalized to the maximum frequency in each class (for presentation). According to the reported data, clay14Å is the most frequently present mineral in the tuff beds. Clinoptilolite is frequently present in tuff as a major or minor mineral. K feldspar is frequently identified as a major constituent in tuff samples. Glass appears most often in tuff beds, as expected. Calcite was most likely to be identified as a major mineral constituent in mudstone and carbonate beds. Clay10Å, clay14Å, and feldspar are also present as minor minerals in mudstone beds. Overall, clay14Å is more abundant and more frequently observed than clay10Å. This accounts for the commonly seen "popcorn" texture developed by the swelling properties of smectite on weathered mudstone. Carbonate beds usually contained minor amounts of clay14Å. Calcite is the major mineral in the carbonate beds. The "other" mineral category is also abundant in many carbonate beds, since dolomite is included in this category. Siltstone beds mostly contained feldspar and quartz as a major mineral, with clay10Å, clay14Å, and clinoptilolite as frequent minor minerals. Sandstone beds usually contained feldspar and quartz as major minerals, and in general have similar mineral assemblages to those observed in siltstone beds.

It should be noted that the number of samples of different kinds of sediment from different sites are not equally distributed (Table 6.2). As an example, around 64% of the mudstone samples came from Olduvai Gorge, Tanzania, while most of the other sites did not report mudstones. Field identification of sandstone, siltstone, and mudstone might vary between different studies (e.g., some researchers might lump siltstones and claystones into "mudrocks"). The sandstone, siltstone, and carbonate beds also yielded fewer samples compared to tuff beds (less than 10%), which is insufficient for the application of statistical learning methods. Therefore, only the tuff bed samples were selected for further analysis. These samples also contain the most volcanic glass, a common precursor for zeolite formation in saline-alkaline lakes.

All mineral assemblages reported in tuff beds samples were examined based on whether a particular mineral is present (Trace, Minor or Major) or absent. The dataset contains

552 different mineral assemblages, around 3.4 % of the total statistically possible mineral assemblages (16383 ($2^{14} - 1$)). The ten most frequently found mineral assemblages are shown in Table 6.3. The most frequently observed mineral assemblage is only observed in 63 samples (~3.8% of all samples), which shows that finding the most common or representative mineral paragenesis pattern using basic statistical methods is not feasible (even without considering relative abundances). Therefore, the Self-Organizing Maps (SOM), a statistical learning method, was applied with two main requirements in mind, 1) to look for "interesting patterns" in the dataset without prescribing any specific interpretation (exploratory data analysis) and, 2) to look for information reduction and structuring of sets of entities for simplification (complexity reduction for classification).

Table 6.3: Most common mineral combinations found in the dataset.

Mineral combination	# samples	Percentage %
Caly14A + Clinoptilolite	63	3.82
Clinoptilolite	29	1.75
K feldspar	28	1.69
Clay14A + Clinoptilolite + Erionite	28	1.69
Clinoptilolite + Erionite	26	1.57
Clay14A + Clinoptilolite + Opal	24	1.45
Clay10A + K feldspar	23	1.39
Glass + Clay14A + Feldspar	21	1.27
Clay10A + Analcime + K feldspar	20	1.21
Erionite	19	1.15

6.3 Approach

6.3.1 Self-Organizing Map

Teuvo Kohonen developed an algorithm called Self-Organizing Map (SOM) to imitate the brain's ability to organize itself in response to external stimuli (Kohonen, 1982, 2001a). The SOM is a mapping algorithm that forms an ordered non-linear smooth projection of n-dimensional input data onto a 2-dimensional grid of nodes and the entire learning process is performed through the iterative process (Kohonen, 2001a; Wehrens and Buydens, 2007). It does not require a priori information to establish relationships in the dataset. SOMs are different from other artificial neural network (ANN) methods since they apply competitive

learning instead of error-correction learning, such as backpropagation, and they organize the clusters in a two dimensional space according to the similarity of the cluster centroids themselves (Dowla and Rogers, 1995; Wehrens and Buydens, 2007). SOMs can be applied in every field of geosciences including geochemistry (e.g., Penn (2005)), petrology (e.g., Chang et al. (2002)), seismology (e.g., Kohler et al. (2009)), GIS (e.g., Bacao et al. (2005)) and remote sensing (e.g., Ehsani and Quiel (2009)), geomorphology (e.g., Bue and Stepinski (2006)), volcanology (e.g., Ersoy et al. (2007)),and marine geology (e.g., Ferentinou et al. (2012)). SOMs can be used for both continuous and categorical data. Since this dataset contains only the categorical data showing the four abundance classes, these factor classes were converted into a class matrix. The entire study was done using R statistical package. The "Kohonen" package developed by Wehrens and Buydens (2007) was mainly used.

SOM mapping algorithm is defined as an incremental, stepwise correction process and the overall learning process accomplished though the following iterative process (Dowla and Rogers, 1995; Wehrens and Buydens, 2007),

1. Set the random values for weight vectors.

$w_i^{m,n} = random$, for $n = 0,\ldots,N_n$; $m = 0,\ldots,N_m$; $i = 0,\ldots,N_F$,

where, N_n and N_m are the number of rows and columns of the map. N_F is the number of features in each node.

Set the initial $\eta(0) = 1$.

2. For each input patterns, x^i, identify the node that is closest to the kth input. This winning node is also called as the Best Matching Unit (BMU). Tanimoto distance calculation was adopted since our data were categorical.

$(n_0, m_0) = min\{||x^k - w^{j,l}||\}$.

3. Update the weights of the nodes in the neighbourhood of nodes (n, m), N, according to the rule,

$w_i^{n,m}(t-1) \leftarrow w_i^{n,m}(t) + \eta(t)\lambda(n,m)[x_i^k - w_i^{n,m}(t)],\ (n,m) \in N.$

where $\lambda(n,m)$ represent the window function (i.e. amount of change in the weights as a function of the distance from the center node $m_{0,0}$).

Weight updates only applied to the weight vectors in a neighbourhood of the winner selected in previous step. The neighbourhood size is gradually reduced over the course of iterations. The adaptation step size also reduced over the course of iterations.

4. Decrement the gain term,

$\eta(t+1) = \mu\eta(t),$

where μ is the learning rate.

5. Repeat the process from step 2 until convergence or N number of iterations.

After experimenting with SOM results of this dataset using different numbers of iterations, 2000 iterations was chosen. Figure 6.2 shows the training process as measured by the mean distance to the object from the closest codebook vector unit. After around 1700 iterations, the training is merely fine-tuned. The graph shows that the clay14Å, clay10Å, clinoptilolite, and feldspar categories show poorer training progress than the other minerals, most likely due to their more random patterns of abundance. It also showed that chabazite, mordenite, glass, and opal are clustered well, most likely due to their limited abundance or more characteristic abundance patterns.

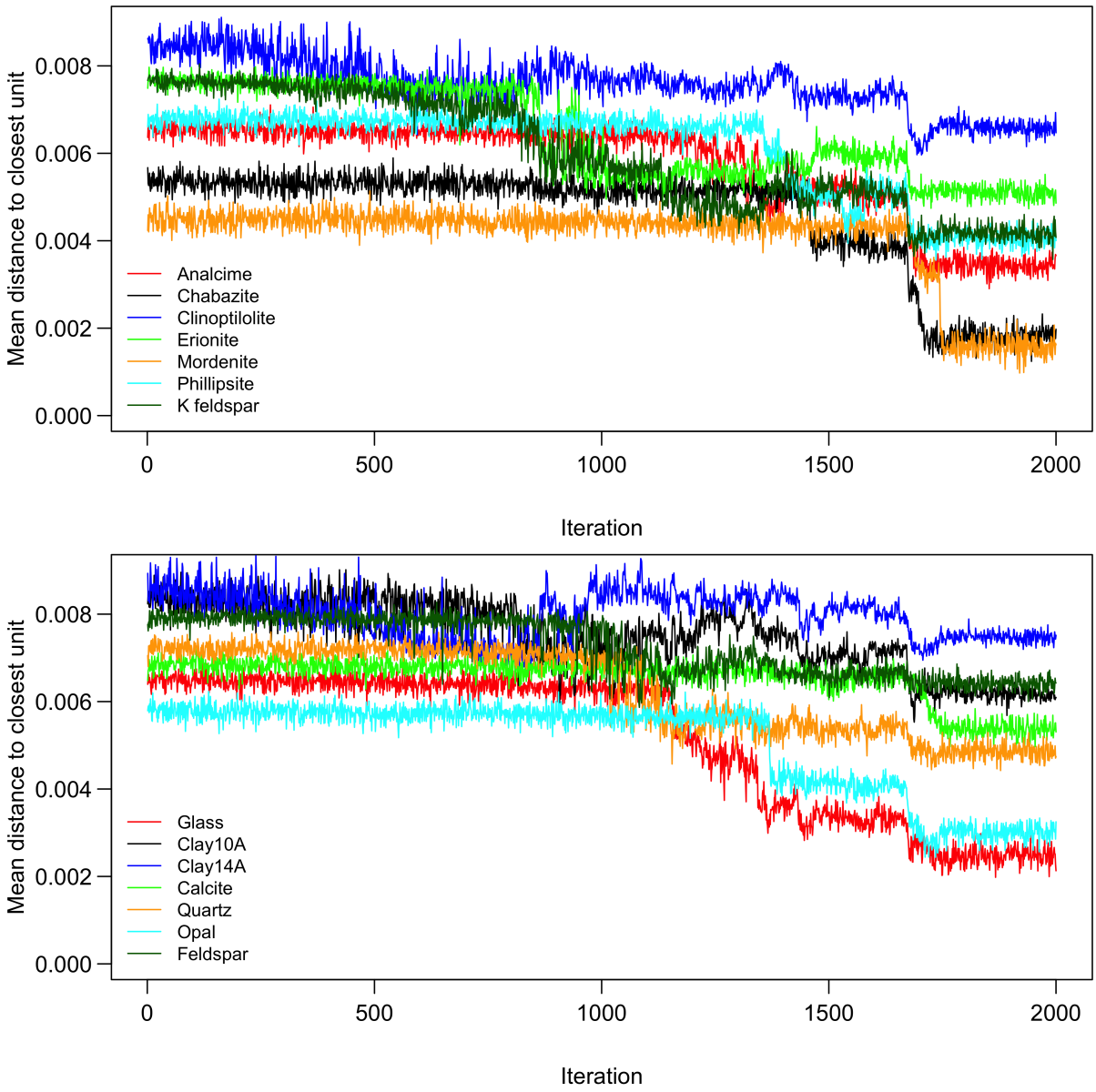

Figure 6.2: Self-Organizing Map (SOM) training progress.

When a certain sample is similar to a certain node's weight vector, that sample is mapped to that node. Patterns in the distribution of samples and variables can be seeing by visualizing the weight vectors on the map (Fig 6.3). The Mapping plot (Fig 6.3a) shows the positions of all samples. Areas with large distances in the Neighbor distance plot (Fig 6.3b) indicate that the nodes are much more dissimilar, whereas lower values indicate more similar nodes. This also depicts the natural boundaries between node clusters. The plot of the codebook vectors of the glass is shown in Figure 6.3 (c) as an example. Major and minor abundances of glass in the samples are clustered in the bottom right corner of the map.

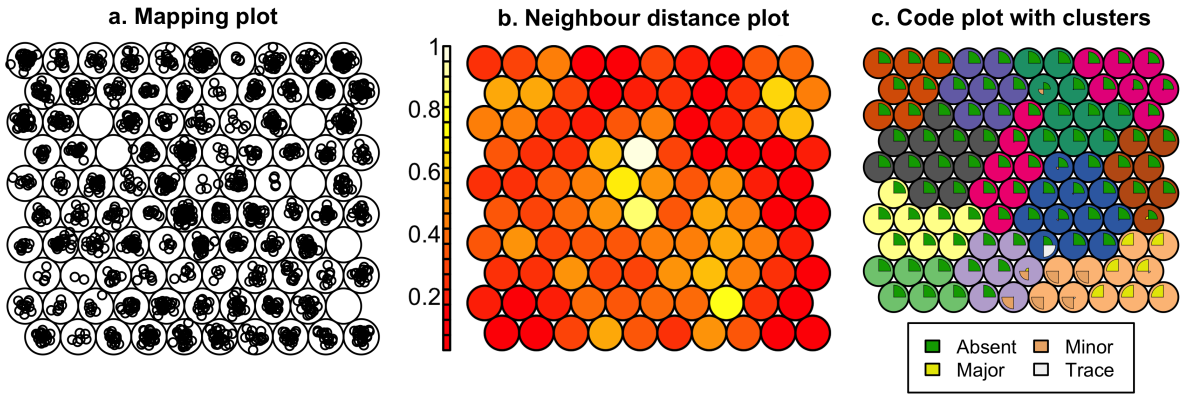

Figure 6.3: Self-Organizing Map (SOM) Results. a). Mapping positions of all 1648 tuff bed samples in ten-by-ten (nodes) Self-Organizing Map (100 nodes), based on their 14 mineral assemblages. Big circles indicate the nodes, while small circles inside each node show the nodes onto which samples have been mapped. No samples have been mapped to six nodes. b) Neighbor distance plot shows the distance between each node and its neighbors. Areas with low neighbor distance (shown in dark red) indicate the groups of nodes that are similar, while more dissimilar nodes are indicated by a lighter color. c) Plot of codebook vectors for the mapping of the glass class with 12 clusters. Nodes of the different colors represent the different clusters. The size of the fans inside each node represents the magnitude of each variable in the weight vector (In this case frequency of each abundance class for glass assigned to each node).

6.3.2 Hierarchical Clustering

To implement the connectivity constraints,the positional distance from one cluster to another on the SOM grid was calculated. This positional distance matrix was multiplied by the higher dimensional distance matrix determined by the variables in the dataset. The elbow (Thorndike, 1953), silhouette (Rousseeuw, 1987) and the gap statistics (Tibshirani et al., 2001) were calculated to determine the optimal number of clusters from the dataset. The results indicate that it is difficult to find the optimal numbers of clusters using these methods, most likely due to more fuzzy cluster boundaries. Therefore, the different numbers of clusters were manually assigned to the Ward hierarchical clustering method and examined the results to identify more meaningful cluster arrangements. The Ward2 method was adopted here, and more information on this method can be found in (Murtagh and Legendre, 2014). It was found that twelve clusters provided the most informative clustering results for this dataset. The clusters assigned are demarcated using the background colors of nodes in Figure 6.3 (c). The hierarchical clustering result was then fed to the decision tree (DT) to understand the clustering rules in a more descriptive manner.

6.4 Results and discussion

Mineral abundances in each cluster identified by SOM and DT results are shown in Figure 6.4 and 6.5, respectively. The cluster positions in Figure 6.4 were rearranged to better describe the general pattern of mineral paragenesis observed in saline-lacustrine environments. Graphs a-h shows the main trend of the minerals with major abundance and graphs i-l show the similar trend in minor abundance. Cluster 3 (Fig 6.4a) shows glass as a major component associated with a minor amount of clay14Å (montmorillonite) and a very small amount of phillipsite, clinoptilolite and erionite. Based on the relative mineral abundances in this class, this can be categorized as the first stage of glass alteration, during which glass is partially altered into smectite and early stage zeolites. The early formation of montmorillonite was probably favored by a relatively low $a_{Na^+ + K^+} : a_{H^+}$ ratio (Sheppard and Gude, 1968). However, clay14Å is observed in all clusters (diagenetic facies), indicating that it is formed (or remains stable) under different chemical conditions. Smectites have been found throughout most of the basins regardless of facies (e.g., Sheppard and Gude (1968); McHenry (2010)). Formation of montmorillonite or subsequent solution of the glass would have increased the pH and the concentration of alkali ions. The further increase of the $a_{Na^+ + K^+} : a_{H^+}$ ratio provides a more favorable chemical environment for the formation of zeolites instead of additional montmorillonite (Sheppard and Gude, 1973).

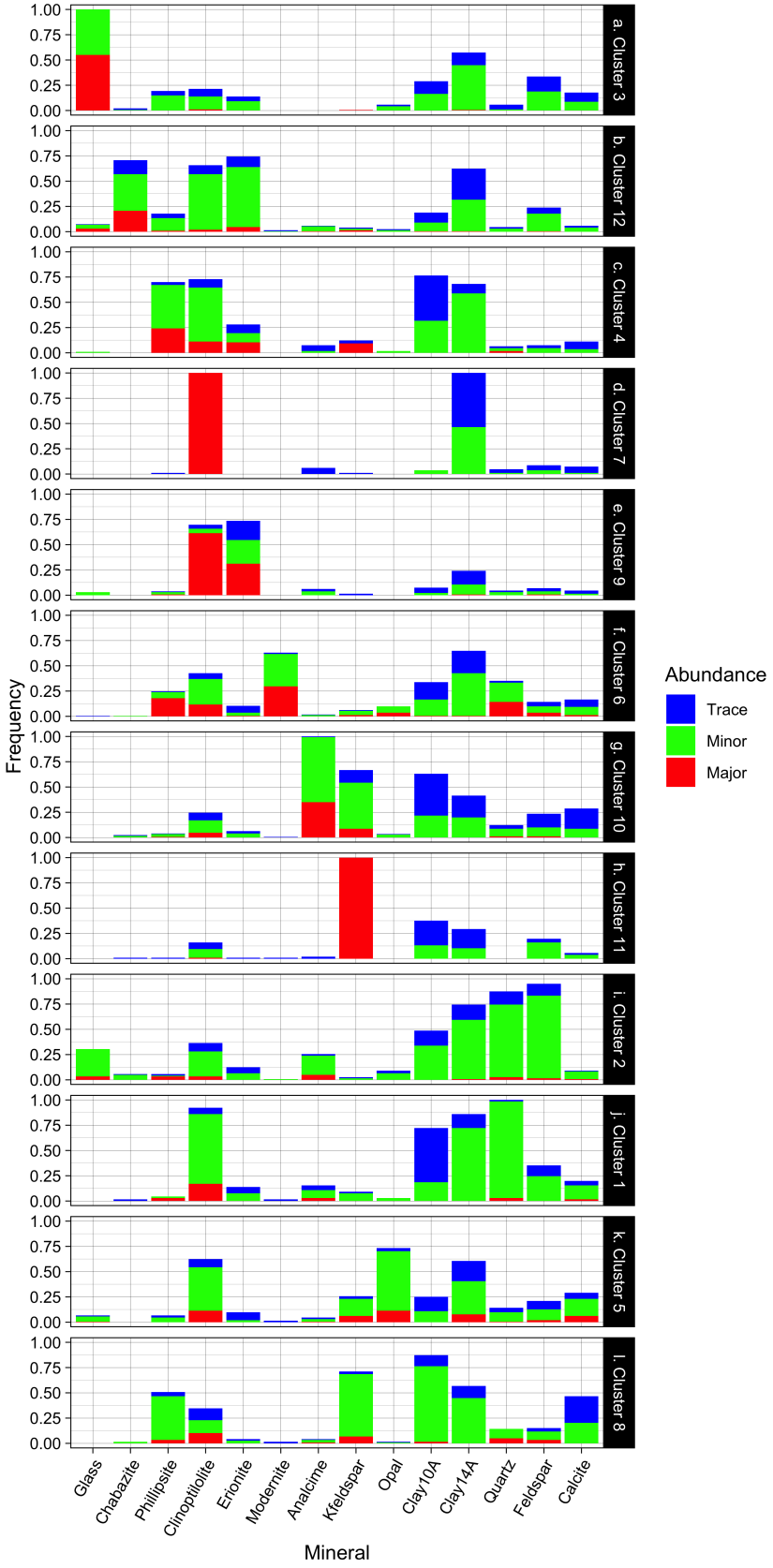

Figure 6.4: Relative mineral abundance in each Cluster.

Cluster 12 has chabazite as a frequent major mineral, while clinoptilolite, erionite and clay14Å are frequently present as minor minerals. Chabazite and phillipsite have higher H_2O contents and lower $Si : Al$ ratios, and a relatively low calcium content compared to clinoptilolite. Therefore, chabazite and/or phillipsite should be favored over clinoptilolite by a relatively low $Si : Al$ ratio and high a_{H_2O} (Mariner and Surdam, 1970; Sheppard and Gude, 1973).

Cluster 4 (Fig 6.4c) has phillipsite as a major mineral, while chabazite is absent. Minor clinoptilolite, erionite and K feldspar are also present. Cluster 7 has clinoptilolite as a major mineral, with clay14Å as a minor mineral. Continued dissolution of the glass along with the early crystallization of phillipsite or chabazite (clusters 12 and 4) probably enrich the Si and Ca^{2+} in the pore water. With the increase of Si, the $Si : Al$ ratio may increase and the a_{H_2O} decreases to levels suitable for the formation of clinoptilolite instead of phillipsite or chabazite (Fig 6.4d). An increase of the $Ca : (Na + K)$ ratio during dissolution also favor the formation of clinoptilolite over the phillipsite (Sheppard and Gude, 1973).

Cluster 9 has clinoptilolite (but less than in Cluster 7) as a frequent major mineral along with erionite, which is slightly less frequent than clinoptilolite. It also shows a decrease in clay14Å. Gundogdu et al. (1996) argued that, in addition to the above factors, variations in the grain size or pore size and the permeability of tuffs also favor the formation of clinoptilolite at this stage. Erionite is favored by high a_{Na^+} and $a_{SiO_2(aq)}$ combined with exceptionally low activities of the alkaline earths (Surdam and Eugster, 1976). Equilibrium activity diagrams calculated for the zeolites by (Birsoy, 2002) show that erionite is stable over a limited range of thermochemical conditions due to its high sensitivity to alkalinity.

In Cluster 6 mordenite appears as a major mineral, while the frequency of clinoptilolite and erionite decreases. Sheppard (1991) noted that relatively high $Na : K$ ratios favor mordenite over clinoptilolite. Sheppard and Gude (1969b) noted that mordenite is favored over clinoptilolite when the $a_{SiO_2(aq)}$ reached a maximum. Mordenite is only observed in Cluster 6. A slight increase in salinity and pH of the pore water would increase the $Na^+ : H^+$ ratio and decrease the $Si : Al$ ratio, and an increase of Na and Si should favor the crystallization of analcime (Sheppard and Gude, 1973). That transition can be seeing in Cluster 10 (Fig 4g). At this stage, frequent or abundant non-analcime zeolite minerals do

not appear, but K-feldspar is often observed as a minor mineral. In Cluster 11, K-feldspar is frequently observed as a major mineral while analcime has completely disappeared. Formation of K-feldspar from precursor zeolites may be governed by a relatively low a_{H_2O}, a relatively high $K^+ : H^+$ ratio, and a relatively high $a_{SiO_2(aq)}$ (Sheppard and Gude, 1973). At this stage, all the analcime and other precursor non-analcime zeolite minerals and montmorillonite can be converted into K-feldspar.

Clusters 2, 1, 5, and 8 (~30% of the total samples) show similar patterns but with minor (rather than major) abundances of minerals, highlighting a more intermediate step in the formation of non-analcime zeolites. These clusters show different abundances of phillipsite, clinoptilolite, and erionite along with lower glass abundance, most likely indicating the dissolution of glass during mineral paragenesis. For all clusters, clays are generally more abundant in samples that contain non-analcime zeolites than in samples that contain analcime and/or K-feldspar. This trend is consistent with the initial dissolution of glass and the formation of clays and non-zeolite feldspars, followed by the alteration of non-zeolite feldspars and clays to form analcime and eventually K-feldspar.

The above explanations were derived assuming that only chemical factors are responsible for the formation of those minerals. Dibble and Tiller (1981) examined the general thermodynamic and kinetic constraints that influence glass dissolution and mineral growth reactions. According to them, the overall process of tuff alteration involves an Ostwald series of metastable reactions that occur with the solution in a series of irreversible steps. Clays and gels (less stable disordered minerals) form in regions and during times of maximum supersaturation with respect to more stable phases generated by relatively rapid glass dissolution. Alkali zeolites crystallize in regions of intermediate to high supersaturation, possibly after glass dissolution rates have diminished. Analcime and K-feldspar (more stable, ordered minerals) grow in regions of lowest supersaturation, after all glass has disappeared.

The DT results are shown in Figure 6.5. The SOM method classified the fresh tuffs with abundant glass into clusters 2 and 3. Samples with major or minor amounts of analcime are grouped into cluster 10. Samples with chabazite are grouped into cluster 12, whereas the samples with abundant K-feldspar are grouped into cluster 11. Cluster 6 was demarcated

based on abundant mordenite. Samples with abundant erionite are grouped into cluster 9. Clinoptilolite is abundant in clusters 7 and 9. Cluster 7 has only clinoptilolite and clay14Å as major minerals. Samples with phillipsite are grouped into cluster 4. The DT shows that clay10Å and calcite are not important for the above classification. It also shows that the boundaries between the clinoptilolite, erionite, and phillipsite mineral classes are more fuzzy, probably due to their strong and complex associations (as shown in Fig 6.4). Therefore, based on the DT, we can easily identify six mineral groups with clear boundary definitions (Table 6.4). The percentage of samples in each of the groups was calculated based on the total number of tuff samples analyzed (1648). Most of the samples (~ 65%) were dominated by the intermediate zeolite minerals, while the rest of the samples show glass, analcime, and K-feldspar in decreasing order of percentage (~19%, 10%, and 6%).

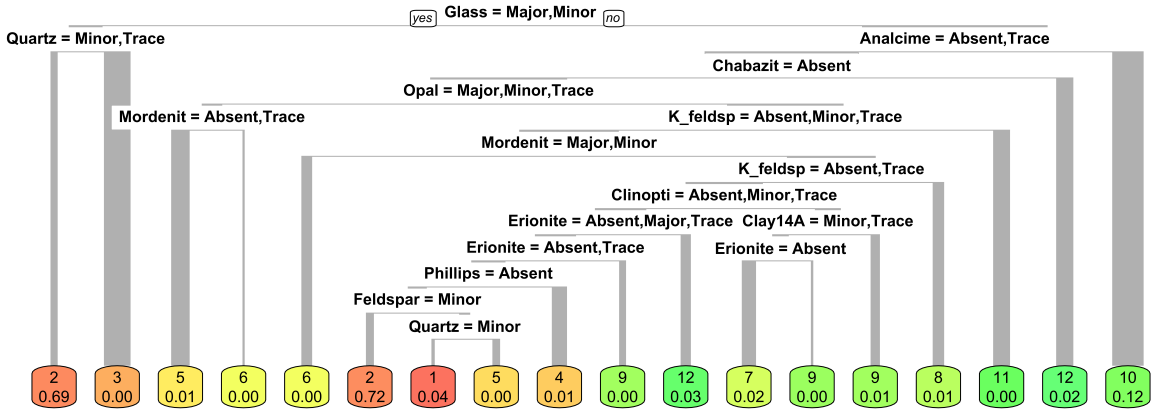

Figure 6.5: Decision Tree showing the clustering rules.

Table 6.4: Major group of clusters identified by SOM and DT rules.

Group	Mineral combination	Cluster No	# samples	Percentage %
01	Glass	2 and 3	308	18.7
02	Chabazite	12	202	12.2
03	Phillipsite+Clinoptilolite+Erionite	1, 4, 5, 7, 8, 9	699	42.4
04	Mordenite	6	162	9.8
05	Analcime	10	171	10.3
06	K-feldspar	11	106	6.43

The main characteristics of mineral assemblages observed from DT are: 1) zeolite minerals were present when the glass was absent or only present as a trace constituent.

Dissolution of glass is a major precursor for zeolites in tuff beds in these environments, as glass dissolves, zeolites form. 2) Non-analcime zeolites are present only when analcime is not present as a major or minor phase. Petrographic evidence from many of the previous studies indicates that the earlier zeolites were replaced by analcime (e.g., Sheppard and Gude (1973); Gude and Sheppard (1988)). 3) Chabazite is rarely abundant in samples that contain other zeolite minerals. The reported studies shows that the sample location within the basin affects the presence of chabazite and its association with other zeolite minerals. 4) Mordenite does not show a clear association with other zeolite minerals. Experimental studies indicate that mordenite is favored over clinoptilolite at higher temperatures and at higher $Na : K$ ratios (Hawkins, 1981; Kusakabe, 1982). 5) Phillipsite, clinoptilolite and erionite are often randomly associated, producing fuzzy boundaries between the clusters. 6) When K-feldspar is present as a major mineral, analcime is usually the only zeolite mineral observed. Textural and field evidence from those studies suggests that K-feldspar formed from early zeolites, and most likely from analcime, which would have formed from precursor intermediate zeolites.

This study shows that regardless of the geographic location and regional geology of the sample locations, the entire dataset reflects the general diagenetic facies discussed in the literature. The diagenetic facies identified by this study can also be visualized spatially in most of the places cited here (e.g., Fig 6.6). The pattern in which unaltered glass, zeolites, and K-feldspar successively appear from peripheral to central parts of a basin is well shown at Lake Tecopa, California (Fig 6.6a) (Sheppard and Gude, 1968). The analcime facies is absent in this example, where zeolites consist of mainly phillipsite and clinoptilolite, with the K-feldspar facies at the center of the basin. The Big Sandy Formation, in Mohave County, Arizona, shows analcime facies between the non-analcime zeolite and K-feldspar facies (Fig 6.6b) (Sheppard and Gude, 1973). In the Karlovassi basin, Samos, in Greece, Stamatakis (1989a) mapped four irregular concentric zones with zeolites and K-feldspar; 1) a clinoptilolite facies, 2) a clinoptilolite-analcime facies, 3) an analcime facies and, 4) a central boron-bearing K-feldspar facies (Fig 6.6c). Figure 6.6 (d) shows the lateral diagenetic mineral facies of the Gila conglomerate, near Buckhorn, Grant County, New Mexico. It shows chabazite at the margin where unaltered vitric

glass was observed, then clinoptilolite, and then clinoptilolite and analcime towards the interior of the basin (Gude and Sheppard, 1988).

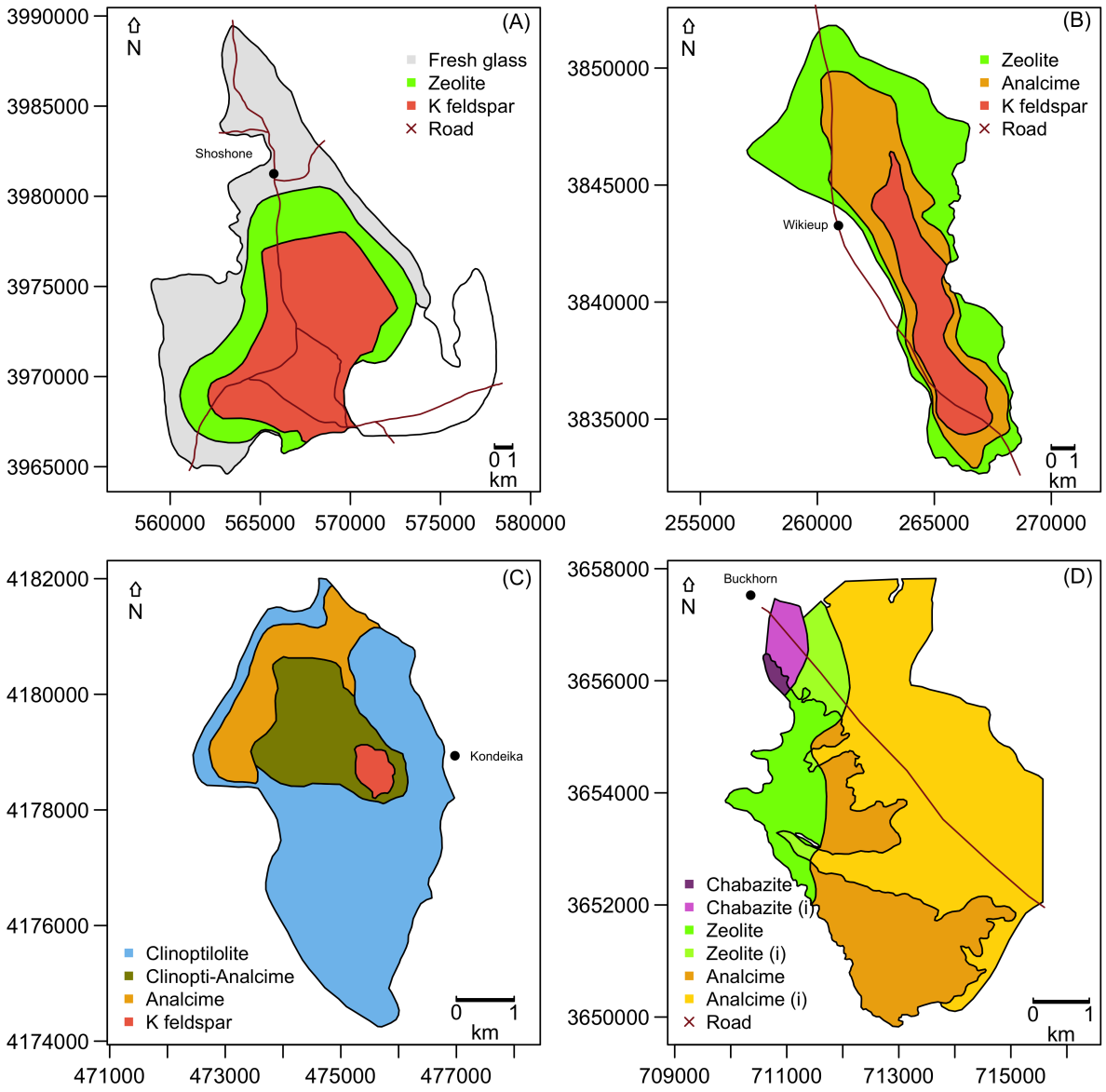

Figure 6.6: Diagenetic zones of (a) Lake Tecopa, Inyo County, California (after Sheppard and Gude, 1968) (b) Big Sandy Formation, Mohave County, Arizona (after Sheppard and Gude, 1973), (c) Karlovassi basin, Samos, Greece (after Stamatakis, 1989), and (d) Gila Conglomerate near Buckhorn, New Mexico (after Gude and Sheppard, 1988). Dark color of each lithology type in the map (d) indicates the approximate extent of diagenetic zones, whereas the light colors (letter (i) after the lithology type in the legend) indicate the inferred extent of zones prior to erosion.

6.5 Implications for Mars

The study shows that the analcime and non-analcime zeolites are rarely present together in the same diagenetic environment. Since analcime is the only zeolite detectable and

detected (using orbital spectral data) in survey of Martian crater central peaks, done by Sun and Milliken (2015), it is possible that non-analcime zeolites (currently labeled as unidentified hydrous minerals) could be present in other central peaks of craters on Mars. These ambiguous detections can be inferred using our trained SOM model based on their association with other hydrous minerals identified.

The Noachian-aged Jezero crater, where Perseverance rover is landed, is interpreted as an open basin paleolake (Fassett and Head, 2005). Raman Spectroscopy, one of the next generation planetary exploration techniques, is included on the Perseverance rover (Williford et al., 2018). Since it is difficult to identify zeolitic mineral mixture using VNIR-SWIR, it is important to study how well mixtures of these zeolite species (with other zeolites, or other associated minerals) can be identified using Raman Spectroscopy. Diagenetic facies identified by SOM clusters can be used to select the end members since these clusters represent the most frequent minerals assemblages found in tuff beds of closed hydrologic systems on the Earth. Once we characterize the mineral assemblages using Raman Spectroscopy, the trained SOM can be used to automate the in-situ identification of hydrochemical stage/diagenetic facies of the area.

The growing availability of high-dimensional big geoscience in situ and orbital data from Mars offers immense potential for Machine Learning methods. More data coming from Mars shows more complex geological and geochemical processes. Therefore, generalizing the complex geochemical behaviors using unsupervised exploratory data analysis (e.g., SOM) can help to identify the most prominent geochemical behaviors. The mineral assemblages identified by SOM can also be used for thermodynamic-kinetic modeling to validate the modeling results or as candidate mineral assemblages for models. Building expert knowledge systems using machine learning methods for geological interpretation, as we demonstrated here, can be used in future missions for the rover itself (autonomously) to find interesting target locations while traveling without waiting for commands from the Earth, which could not be performed in real time. In addition to that, this study shows potential applications of SOM clustering method for terrestrial sedimentary studies such as finding sediment source contribution for comprehensive catchment management

(e.g., Du et al. (2019)) and finding mineralogical signatures and sources of sediments in modern lakes (e.g., Ontiveros-Cuadras et al. (2018)).

6.6 Conclusion

The SOM was able to capture the prominent zeolitic alteration stages starting from dissolution of glass followed by the formation of clays, non-analcime zeolites, analcime, and eventually K-feldspar. The study also shows potential implications for the identification of diagenetic facies/hydrochemical conditions of zeolite occurrences on Mars. SOM results can be used to test or validate orbital, in situ, or modeling results, while the trained SOM provides a robust generalized ability to classify new mineral assemblage data to diagenetic facies identified.

Acknowledgements

Many thanks to all the researchers in this field for making their research data accessible and to the R Core Team, Rstudio, and all the R library developers.

"Although irreversible in an overall sense, any geochemical process can be represented by a succession of partial equilibrium states, each reversible with respect to the next, but all irreversibly related to the initial state of the system. Because the compositional changes resulting from a geochemical process are path dependent functions, they cannot be evaluated by considering only the initial and final states of the system."

-Harold C. Helgeson, 1968, p. 853-

7

Possible formation pathways for zeolites in closed-basin lakes on Noachian Mars: Insights from geochemical modeling.

Contents

Abstract **235**
7.1 Introduction **237**
7.2 Previous models **238**
7.3 Model Description **239**
7.3.1 Selection of the model 240
7.3.2 Selection of environmental parameters 241
7.3.3 Selection of starting material 244
7.3.4 Selection of solutions 248
7.4 Results and discussion **250**
7.4.1 Effects of different solutions 251
7.4.2 Effects of different Water/Rock ratio 257
7.5 Conclusion **268**
Acknowledgement **269**

Abstract

Zeolites are among the most common and widespread authigenic silicate minerals found in saline-alkaline paleolacustrine environments on Earth. Analcime, a Na-zeolite, has been

detected on crustal outcrops in Mars using orbital spectral image data. Identifying other zeolite species is complicated by the lack of diagnostic absorption features in spectral data and spectral similarity to some polyhydrated sulfates. Therefore, analcime is the only zeolite species so far widely identified as present on Mars. The presence of certain zeolite mineral species or assemblages in a closed basin paleolake can be used to track hydrological changes in that basin. This chapter discusses the application of geochemical modeling to identify zeolite phases that could have formed in closed lake basins of late Noachian Mars. The composition of the high-silica Buckskin sample is used as a starting material because 1) most zeolite-rich assemblages in closed hydrologic systems on Earth originate from the decomposition of high-silica volcanic glass, and 2) geochemical modeling studies are already available for the more common lower silica basalts on Mars. This study, along with previous studies involving basaltic starting materials, allow a comparison between terrestrial and Martian data and an exploration of the differences in secondary mineral precipitation with substrates of different silica contents. The EQ3/6 geochemical modeling code was adopted, and Late Noachian Mars was assumed to be warm and semi-arid, with an atmosphere with 1.3 bars of P_{CO_2} and current Mars P_{O_2} (14.7 μbar). The Buckskin sample was reacted with three different starting solutions including two different rainfall chemistries and an acidic $H_2SO_4 - HCl$ solution, which could have formed through volcanic degassing. The mineral formation and re-dissolution patterns under different Water/Rock (W/R) ratios is also explored.

The results show that near neutral and acidic solutions in closed-basin lakes filled with high-silica volcaniclastic materials could eventually produce zeolite minerals, similar to those in saline-alkaline lakes on Earth. Analcime forms only in water-limited environments (low W/R ratio), while chabazite is present even at relatively high W/R ratio. Clinoptilolite transforms to analcime with an increase in pH, with decreased W/R ratio, and with time. Analcime was found to be the most stable zeolite mineral over the greatest range of conditions in this environment, associated with increased pH, consistent with its presence as a very common constituent of saline-alkaline lake deposits on Earth. The study shows that the mineral precipitation patterns associated with the dissolution of high-silica materials through acid weathering are comparable to the mineral precipitation patterns following the

dissolution of basaltic rocks by acid weathering under $0-25^oC$ conditions or hydrothermal conditions as described in previous laboratory, field, and geochemical modeling studies.

7.1 Introduction

Zeolites are among the most common and widespread authigenic silicate minerals found in saline-alkaline paleolacustrine sedimentary deposits on Earth (Hay, 1966; Hay and Sheppard, 2001). The presence of certain zeolite mineral species or assemblages in a saline-alkaline paleolake can be attributed to the thermodynamic equilibrium reactions due to changing water chemistry (Hay, 1966) and to kinetically controlled nonequilibrium dissolution and precipitation reactions (Dibble and Tiller, 1981). Therefore, spatial and stratigraphic patterns of zeolites and other authigenic minerals in paleolake deposits can be used to track hydrological changes in paleolacustrine environments (e.g, Lander and Hay (1993); McHenry et al. (2020); Trauth et al. (2001)). Bristow and Milliken (2011) discussed the value of identifying spatial and stratigraphic patterns of authigenic mineral phases, such as clays, zeolites, carbonates, and opaline silica that formed in bodies of standing water on Mars. Zeolites have been postulated to be components of Martian regolith (e.g, Ackiss et al. (2018); Basu et al. (1998); Berkley and Drake (1981); Bish et al. (2003); Cannon et al. (2015); Dickinson and Rosen (2003); Ehlmann et al. (2011); Ming and Gooding (1988); Ruff (2004); Tokano and Bish (2005); Viennet et al. (2017)) and have been detected on the surface of Mars using orbital spectral data (e.g, Bandfield (2008); Ehlmann et al. (2009); Michalski et al. (2005); Sun and Milliken (2015); Viviano-Beck et al. (2017); Wray et al. (2009)). Ehlmann et al. (2009) have detected analcime along with Fe/Mg-rich smectites, chlorites and hydrated silica in craters near the Antoniadi basin, west of the Nili Fossae region, Mars, using data from the Compact Reconnaissance Imaging Spectrometer for Mars (CRISM) onboard the Mars Reconnaissance Orbiter (MRO). Sun and Milliken (2015) identified Fe/Mg smectite, chlorite, hydrated/ opaline silica, zeolites, sulfates, Al-phyllosilicates and other unidentified hydrous phases from 633 central peaks of craters on Mars using CRISM data. Analcime is the most commonly detected zeolite on Mars, in part due to its characteristic spectral absorption features (Ehlmann et al., 2009). Non-analcime zeolites share some absorption features with polyhydrated sulfate mineral

phases, making them difficult to identify using Visible-Near Infrared (VNIR) spectral data (Ehlmann et al., 2009; Sun and Milliken, 2015; Wray et al., 2009; Carter et al., 2013; **?**).

The climate and hydrochemistry of early Mars remain a mystery. The wide array of fluvio-lacustrine features including open and closed basin lakes, channels, alluvial fans, and deltas supports a warm and wet early Mars, while climate models have struggled to generate sufficiently warm climates to form these features (e.g, Ramirez et al. (2019)). Goudge et al. (2015) identified 55 basins with sedimentary fan deposits out of 205 closed basins and of these only four basins with Fe/Mg-smectites (3 basins) and hydrated silica (1 basin) were found. Based on the lack of evidence for alteration minerals in investigated closed basin lakes, they suggested that the lacustrine processes in closed basin lakes are too short in duration to produce alteration minerals.

Zeolites and associated authigenic minerals may not be identifiable in these closed basin lakes because 1) they never formed or were originally present and later removed by chemical or physical processes over time (e.g., resurfacing, alteration, dissolution, etc.), or 2) they are present, but the methods applied are not capable of detecting and mapping them. Geochemical modeling provides an alternative to studying analogous terrestrial sites for scenarios of the formation and fate of zeolites in closed basin lakes on Mars. This study addresses the first possibility by developing a kinetic-thermodynamic model to assess the formation of zeolites during the diagenesis of volcanoclastic materials in late Noachian closed basin lakes on Mars. The effects of solution pH and Water/Rock (W/R) ratio on secondary mineralogy, solution chemistry, and timing of rock alteration were explored. Results are compared against similar processes studied on Earth.

7.2 Previous models

Numerical chemical models have been developed to investigate the interactions between acidic solutions and Martian basalts in the Noachian epoch (e.g, McAdam et al. (2008); Viennet et al. (2017); Zolotov and Mironenko (2007); Zolotov and Mironenko (2016)). Zolotov and Mironenko (2016) used the composition of Martian Adirondack-type olivine basalt as a staring material. They selected pure water, solutions equilibrated with current Mars atmospheric CO_2 (5.3 mbar) and O_2 (7.6 μbar), and an acidic $H_2SO_4 - HCl$

solution (0.05 molal H_2SO_4 and 9.6 millimolal HCl) as starting solutions. They calculated the chemical equilibria using the GEOCHEQ code which uses the Gibbs free energy minimization method to calculate chemical equilibrium in solid-solution-gas systems. They observed the precipitation of Mg-Fe phyllosilicates, Ca sulfates, zeolites, and minor carbonates with neutral to alkaline solutions. Saponite, zeolites, and gypsum form at low W/R ratio and pH 7-12, and 1 bar CO_2 atmospheric pressure. Higher W/R ratios with a pH $<$ 7 resulted in kaolinite, montmorillonite, siderite, and amophous silica. McAdam et al. (2008) developed a geochemical model using the same GEOCHEQ code to evaluate the formation of silica by low-temperature acid alteration of Martian rocks using a simplified chemical composition of Adirondack-type olivine basalt, Martian basaltic meteorite Shergotty, and Martian dunite meteorite Chassigny as starting materials representing different SiO_2 content. Their models produced analcime along with stellerite, calcite, gypsum, kaolinite, montmorillonite, saponite, and amorphous silica. Viennet et al. (2017) conducted a laboratory and geochemical simulation to explore the formation of dioctahedral/trioctahedral phyllosilicate, carbonate, and zeolite under different CO_2 content and at 120^oC, with volcanic basaltic glass of tholeiitic composition from Iceland as a starting material. They used the EQ3/6 code for geochemical simulation and ran under similar environmental conditions as used for their laboratory experiments. They observed that trioctahedral clay minerals (e.g, saponite) and zeolites are formed at a pH $>$ 7.2 (at 120^oC), while dioctahedral clay minerals (e.g., montmorillonite, nontronite, kaolinite) and carbonate minerals formed at pH $<$ 7.2 (at 120^oC). Catalano (2013) modeled the hydrothermal alteration of 'Adirondack' rock composition using a reacting fluid composed of water in equilibrium with a 10^{-5} or 10^{-15} bar CO_2 pressure at 100^oC or 250^oC. Their study yielded the alteration products of Fe^{2+} and Mg saponite, serpentine, and zeolites at 100^oC and chlorite, prehnite, and talc at 250^oC.

7.3 Model Description

This study develops a theoretical model to assess the possibility that zeolite minerals could be present in closed-basin deposits of Late Noachian Mars but does not explicitly identify zeolite mineral species or establish the timing of their formation. The starting

composition and solutions were selected to be similar to Earth analogs, so that the results can be compared directly to terrestrial data. The model hypothesizes a closed-basin lake fed by rainfall during the late Noachian period of Mars. To correctly interpret the mineral-forming processes for the crystallization of a specific zeolite, the following information is needed: 1) composition of the starting materials, 2) chemical composition of the associated solutions, 3) hydrologic and environmental conditions, and 4) kinetics of primary mineral dissolution (Langella et al., 2001). The model assumes that 1) secondary minerals are formed from the solutions generated by the dissolution of primary minerals, 2) the system is closed with no mass exchange with the surrounding environment, 3) the volume of pore spaces remains the same during mineral dissolution and precipitation, 4) there is no sediment compaction over time, and 5) temperature and pressure remain the same during the entire process. The model neglects the 1) kinetics (rate constants) of secondary mineral precipitation due to limited kinetic data for the minerals discussed here, 2) differences in grain size and shape of primary and secondary minerals, 3) mineral specific reactive surface area, 4) coatings by secondary minerals/gels, 5) solid solution and intermediate mineral complexes 6) cation exchange reactions and 7) redox reactions. Modeling was done for a representative suite of zeolite minerals commonly recorded in saline-alkaline lake environments on Earth (Chipera and Apps, 2001; Hay, 1966; Langella et al., 2001). Selected zeolite species include analcime, chabazite, clinoptilolite, erionite, and phillipsite.

7.3.1 Selection of the model

EQ3/6, a geochemical modeling code developed by Thomas J. Wolery at the Lawrence Livermore National Laboratory (LLNL) (Wolery, 2013), is used. The software package consists of two major codes: EQ3NR, speciation-solubility code, and EQ6, reaction path modeling code. EQ3NR calculates the distribution of species in the solution and the saturation indices of various reactions of interest. B-dot equation (Helgeson, 1969) was used to calculate activity coefficients.

EQ6 calculates how a model aqueous system changes when it reacts under constant or variable temperature and pressure conditions. It can calculate either the relative rate or the absolute rate for each irreversible reaction. The transition-state theory (TST) rate

law (eq.7.1) was used to calculate the time taken for dissolution/precipitation (Wolery, 2013). TST has the strongest theoretical basis among the rate laws applied in this field (Lasaga, 1998). The TST reaction rate, v_j is defined as,

$$v_j = f_j S_j \sum_{i=1}^{i_{T,+^*,j}} k_{+^*,ij} \left[\prod_{n=1}^{n_{T,+^*,ij}} a_n^{-N+^*_{nij}}\right]\left[1 - e^{\frac{A_{+^*,j}}{\sigma_{+^*,ij}RT}}\right] \text{ ——— eq. 7.1}$$

Where S_j is the total surface area of the phase dissolving in the jth irreversible reaction. f_j represents the proportion of reactive surface area. Species in the reaction are represented by i. The net forward form provides for treating $i_{T,+,j}$ parallel mechanisms. For each, there is the rate constant, a kinetic activity product, and a term that depends on the affinity. The $+^*$ sign represents the forward reaction, and it should be replaced by a negative sign (-) for the backward reactions. $k_{+,ij}$ is the forward rate constant for each dissolving phase (Table 7.1). The backward rate constant is $k_{-,ij}$. The kinetic activity product of each phase, shown in $\left[\prod_{n=1}^{n_{T,+^*,ij}} a_n^{-N+^*_{nij}}\right]$, depends on the thermodynamic activities of $n_{T,+,nij}$ species. The kinetic activity product has a value of unity if $n_{T,+,nij}$ = 0. The affinity factor, $\left[1 - e^{\frac{A_{+^*,j}}{\sigma_{+^*,ij}RT}}\right]$ depends on the absolute temperature (T), gas constant (R), and a stoichiometric factor ($\sigma_{+,ij}$). If the affinity of a macroscopic reaction, ($A_{+,j}$), is positive or zero, the forward equation is evaluated (dissolution), unless the backward equation is used (precipitation). It is assumed that the reactive surface area of a mineral grain is equal to its total surface area ($f_j = 1$).

7.3.2 Selection of environmental parameters

Geological observations and interpretations of Late Noachian to Early Hesperian (LN-EH) Mars show that it is characterized by impact craters with degraded crater rims, shallow floors, and lack of visible ejecta deposits and central peaks (Craddock and Howard, 2002), along with valley networks, channels, alluvial fans, deltas, and open and closed-basin lakes, interpreted to be formed mainly due to rainfall and overland flows (Craddock and Howard, 2002; Palumbo et al., 2020; Ramirez and Craddock, 2018). Kite et al. (2019) report that for a given catchment area, rivers on Mars were wider than rivers on Earth today suggesting precipitation-fed intense runoff production on early Mars. Based on these geological and geomorphological studies, the early Martian climate was identified as “warm and wet” (e.g, Ramirez and Craddock (2018)). However, climate modeling has

struggled to successfully recreate the long-lived "warm and wet" early Mars given the faint young sun, and instead suggests a long-lived "cold and icy" Mars (e.g, Kasting (1991); Wordsworth et al. (2013)). In this "cold and icy" climate scenario, most surface water is predicted to have been trapped in the highlands as snow and ice, making it difficult to explain the occurrence of rainfall-related erosional features. Some researchers have suggested that this fluvial and lacustrine activity could have occurred during periods of punctuated heating induced by impact events, volcanism, orbital variation, summer melting, or transient greenhouse gas-rich atmospheres (Palumbo et al. (2020), Wordsworth et al. (2017), and references therein). However, Ramirez and Craddock (2018) explain that nearly all these mechanisms fail to generate the durations of warming and amount of water required to generate the geomorphological features discussed above.

Ramirez et al. (2014) used a 1-D (one dimension) global climate model to demonstrate that an atmosphere containing 1.3-4 bar of atmospheric CO_2 and water with 5- 20% of H_2 could have produced above-freezing surface temperature on early Mars. Wordsworth et al. (2017) describe the new spectroscopic and 1-D line by line climate calculations to assess the warming potential of reducing climates on early Mars. Their results suggested that with just over 1 bar of atmospheric CO_2, a few percent of H_2 and/or CH_4 would have raised surface temperature on early Mars high enough to explain the erosional and depositional features observed. Bishop et al. (2018) showed that a temperature of 298-323 K may have been sufficient to form the Fe/Mg smectite observed on Mars over a geologically short period of time. However, according to the results of the single-column radiative-convective climate model of Ramirez (2017), as much as 20% H_2 with 1.3 bar or 5% H_2 with 2.5 bar surface pressure would be required to reach 298 K mean surface temperature. The current atmospheric $^{13}C/^{12}C$ measurements from Mars Science Laboratory (MSL) along with in-situ and orbital rock and soil carbonate measurements indicate an early atmosphere with a surface pressure < 1 bar. This could be increased to 1.8 bar if a large amount of carbonate deposition had occurred in open-water systems (Hu et al., 2015). The composition of the Comanche rock outcrop in Gusev crater has been interpreted to have required 0.5 to 2.0 bar pressure to form, assuming the carbonates are a solid solution in thermodynamic equilibrium (ignoring the advection, dispersive, and kinetically-controlled processes) (Berk

et al., 2012). Fukushi et al. (2019) used the exchangeable cation compositions of smectite's interlayer with the presence of secondary minerals found in Yellowknife Bay, Gale crater to estimate the water chemistry of the pore water that interacted with the sediment. Their estimated $Na-Cl$ concentrations reflect hyposaline early lakes developed in 10^4-10^6 years under semiarid climates. Turbet et al. (2020) conducted a series of experiments to predict the surface temperature of early Mars using CO_2+CH_4 and CO_2+H_2 collision-induced absoption (CIA) data. Their result shows that in a CO_2 dominated 2 bar atmosphere, ~6% of H_2 is required to increase the surface temperature above the melting point of water. The energy-balance climate model (EBM) developed by Hayworth et al. (2020) was able to deglaciate Late Noachian Mars with 5-8 % H_2 for surface pressures between 1.2 - 3.0 bars. Ramirez et al. (2019) used an advanced energy balance model (Mars Energy Balance Model-MEMB) to show that the observed surface erosion and valley network formation required mean annual surface temperature near or slightly above the freezing point of water. They show that for an atmosphere with 2.9 bars of CO_2, only 1% H_2 is needed to achieve warm mean surface temperatures. H_2 higher than 3% is required if CO_2 is under 2 bars, which satisfies the suggested paleopressure constraints (e.g., Hu et al. (2015); Kite et al. (2019); Ramirez (2017); Ramirez et al. (2019)).

A CO_2-rich atmosphere should have produced widespread surface carbonate on Mars (Kahn, 1985). However, limited detections of carbonates have been observed from the orbital remote sensing methods (Hu et al., 2015). However, if the early Mars atmosphere was rich in CO_2, the rainwater would be acidic (More details in results section), and surface carbonate could have been dissolved and transported to the subsurface (Hayworth et al., 2020; Ramirez and Craddock, 2018). Carbonate could be more widespread on the Martian surface than assumed based on orbital spectral analysis but is obscured by other materials such as recent soil and dust, or present in high abundance in localized areas that make it difficult to identify remotely given spatial and spectral resolution constraints (e.g, Craddock and Howard (2002); Ramirez and Craddock (2018)). Matsubara et al. (2013) developed a hydrological model to estimate the relative flow rates in valley networks and the distribution of lakes on early Mars based on the annual balance of precipitation, runoff, evaporation, and lake area within any enclosed basin. Their model suggested that

the climate conditions on early Mars were at least as moist as the Great Basin region of USA during the Pleistocene glaciation in terms of the balance between runoff and lake evaporation. Most of the zeolite-bearing terrestrial saline-alkaline paleolakes discussed in this study are in North America and formed during the Pleistocene.

Based on the discussion above, this study also hypothesizes that LN-EH was warm and semi-arid. A LN atmosphere with 1.3 bars of CO_2 (90-99%) and a small amount of H_2 (1 -10%) is assumed. It is also assumed that the atmospheric O_2 pressure of early Mars was same as today (Daswani et al., 2016; Mahaffy et al., 2013; Trainer et al., 2019). The modeling is restricted to 25^oC, due to limited thermodynamic data for most of the minerals. The use of 1.3 bar in our models is preferable to the current Martian atmospheric pressure of 8.46 mbar (Trainer et al., 2019) since early Mars undoubtedly had higher atmospheric pressure than today. However, most of the thermodynamic data used in the model were measured under 1.013 bar pressure and do not support pressure corrections. Therefore, the simulation was run under 1.013 bar pressure, even though the HCO_3^- concentration was measured under 1.3 bar P_{CO_2}.

7.3.3 Selection of starting material

Figure 7.1 shows chemical compositions of Martian meteorites, Martian rocks analyzed by the Pathfinder, Opportunity, Spirit, and Curiosity rover missions, and tuffs from 17 terrestrial saline-alkaline paleolacustrine deposits where zeolites were found (Appendix E, Table E.1). On Earth, silicic volcaniclastic rocks most commonly serve as a precursor for zeolites in saline-alkaline lakes (e.g, Hay (1966); Sheppard (1973)). Data from orbital and in situ remote sensing methods and Martian meteorites indicate that the Martian crust is dominated by basalt and related ultramafic rocks (McSween, 2015; McSween et al., 2009). Sediments sourced from mafic-rich precursors would be enriched in olivine, pyroxene, and calcic plagioclase compared to quartzofeldspathic sediments commonly found on Earth (Fig 7.1b). However, there is evidence for high-silica deposits on Mars (e.g, Bandfield (2006); Bandfield (2008); Bedford et al. (2019); Broz et al. (2020); Czarnecki et al. (2020); Ehlmann et al. (2009); Morris et al. (2016)). Broz et al. (2020) reviewed the broad spectrum of observations supporting the evidence of explosive volcanism on

Mars. They list eight Martian deposits larger than 10^5 km^2 for which a pyroclasitic orign has been proposed. They also emphasize the importance of alternative methods for their confirmation since they cannot be confirmed using remote sensing data alone. The textural features attributed to the volcanic or volcaniclastic rocks may not be visible at the scale of rover observations (McSween, 2015). Wilson and Head (2007) modeled the eruption and dispersal of tephra under current Mars atmospheric conditions and show that an explosive eruption could produce thick, widespread ash deposits like those thought to have formed due to mantling deposits in several regions of Mars. Many rocks analyzed in the Columbia Hills of Gusev crater by Spirit rover are sedimentary or volcaniclastic (McSween, 2015). The fine-grained, extremely low density (2.3 gcm^{-3}) materials in Marias Pass in Murray formation, Gale crater could have been generated from a volcanic eruption of highly evolved silicic magma, and could have generated a thick layer of ash that washed downstream into the lake (Bedford et al., 2019; Morris et al., 2016), or the sediments could have been leached in place by short-lived, mildly acidic, late-stage fluids (Rampe et al., 2017). Based on the orbital detection of hydrated SiO_2 materials and Dynamic Albedo of Neutrons instruments aboard the Curiosity rover, Czarnecki et al. (2020) mapped this high-silica layer for at least 17 km throughout Marias Pass, Gale crater.

A simplified version of the chemical composition of the high-silica Buckskin sample of the Murray Formation was chosen as a starting material since zeolites found in saline-alkaline paleolake deposits on Earth are mostly associated with altered silicic tuffs, and thus the model can be easily validated using Earth analogs. The Buckskin outcrop, sampled on sol 1060, is a ~ 2-3 m thick bed of the Murray Formation exposed in the Marias Pass region, 13 m up section from Confidence Hills of Gale crater (Rampe et al., 2017). The Buckskin sample is classified as a rhyolite rock using a Total alkali vs. SiO_2 (TAS) diagram, like most of the terrestrial lacustrine-deposited tuffs considered in Figure 7.1. However, its $Na_2O + K_2O$ wt.% is lower than most terrestrial paleolacustrine tuffs where zeolites are abundant. The mineral composition of the Buckskin sample was determined by mass balance calculations using CheMin-derived crystalline components and elemental abundances measured by APXS (Morris et al., 2016). The crystalline portion of the sample consists of plagioclase, monoclinic tridymite, sanidine, magnetite,

cristobalite, and anhydrite. The ~ 60% of X-ray amorphous portion is enriched in SiO_2 (opal-A, silica glass, and/or opal-CT), volatiles ($SO_3 + P_2O_5 + Cl$), ferrihydrite, and titanium (Morris et al., 2016; Rampe et al., 2017). Ferrihydrite abundance in the Buckskin sample is limited to ~ 1.7 wt.% (Czarnecki et al., 2020). The minimum abundance of SiO_2 glass in the sample is 15.0 ± 13.5 wt.% (Czarnecki et al., 2020). The Buckskin sample contains no mafic igneous minerals, phyllosilicate minerals, or jarosite, unlike other samples collected from the Murray formation (Rampe et al., 2017). TiO_2, P_2O_5, Cr_2O_3, and MnO, which make up 1.57, 1.25, 0.10, and 0.09 wt.% of the total sample composition, respectively, were ignored, because titanium, phosphorus, chromium, and manganese are not included in the system being modeled. The weight percentages of crystallized minerals and amorphous silica were normalized to 1 kg of sample (Table 7.1).

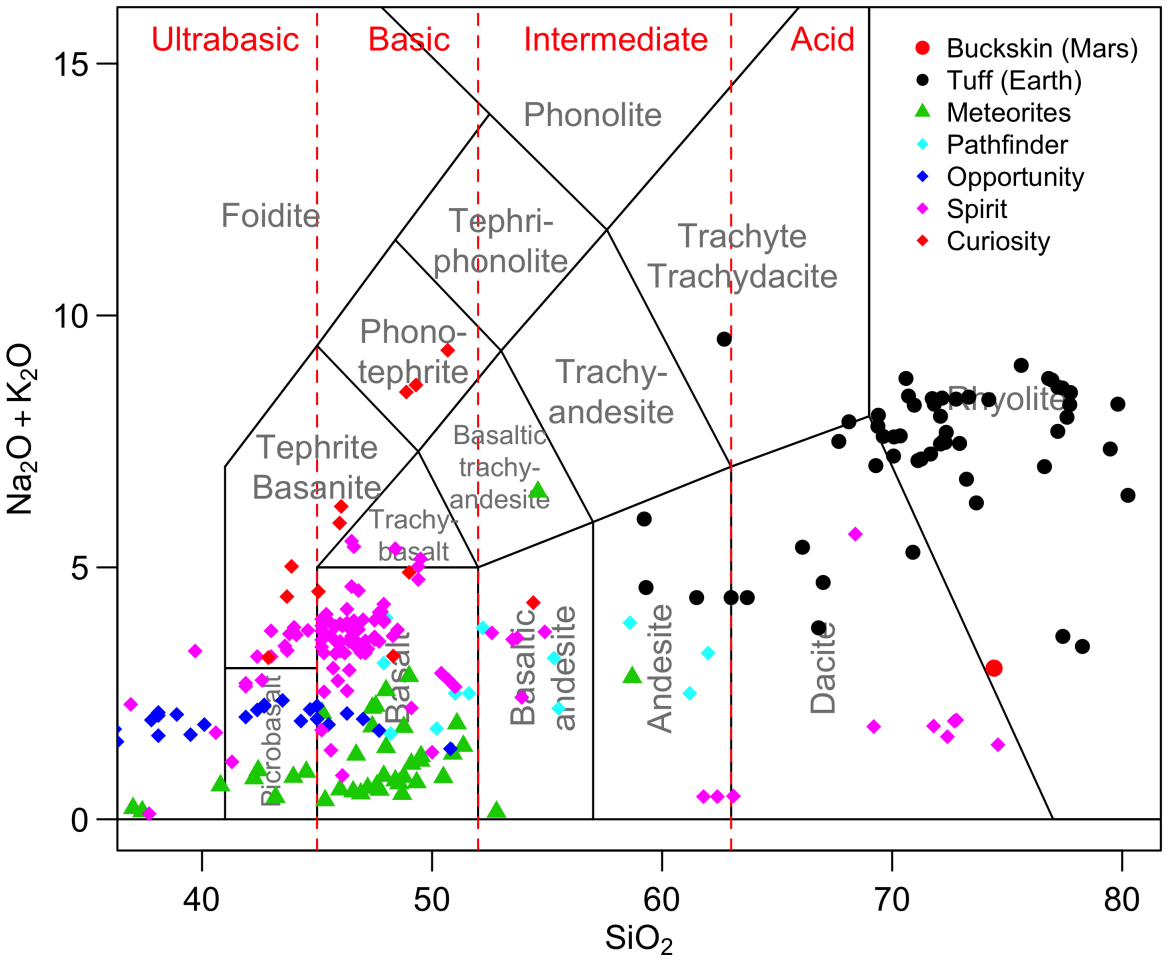

Figure 7.1: Total alkali vs. SiO_2 diagram (TAS diagram) showing the geochemical classification of Martian rocks analyzed by rover missions (Pathfinder, Opportunity, Spirit, and Curiosity) and Martian meteorites. Chemical composition of fresh tuff samples collected from the saline-alkaline paleolakes where zeolites are observed also added to the plot for easy comparison (Dataset with references can be found in Table E.1 in the Appendix E)

Table 7.1: Calculated rock recipe for 1 kg of Buckskin sample, number of moles in mineral present, density, specific surface area, rate of mineral dissolution (first order reaction), and activation energy of each mineral. Density values from Gribble (2005). The dissolution rates and activation energy of primary minerals were adopted from Palandri and Kharaka (2004).

Mineral Name	Mass (g)	# of Moles (moles)	Density ((gcm^{-3}))	Specific surface area (cm^2/g)	log K ($molem^{-2}s^{-1}$)	Activation E ($kjmole^{-1}$)
Albite	127.88	0.48	2.63	182.50	2.75E-17	16.68
Anhydrite	8.01	0.05	2.96	162.16	6.45E-08	3.41
Anorthite	80.22	0.28	2.76	173.91	7.58E-14	4.25
Crisobalite	27.46	0.45	2.38	201.68	4.89E-17	15.53
Hematite	13.72	0.08	5.1	94.11	2.51E-19	15.82

Mineral Name	Mass (g)	# of Moles (moles)	Density ((gcm^{-3}))	Specific surface area (cm^2/g)	log K ($molem^{-2}s^{-1}$)	Activation E ($kjmole^{-1}$)
Magnetite	32.04	0.13	5.2	92.30	1.65E-15	4.44
Orthoclase	26.45	0.09	2.56	187.50	3.89E-17	9.08
$SiO_2(am)$	528.61	8.79	2.25	213.33	5.88E-17	17.80
Tridymite	155.61	2.58	2.26	212.38	7.24E-17	15.03

The particle size and pore size of consolidated volcanic rocks depend on its depositional history, cooling or recrystallization rate, and high or low temperature alteration (Flint and Selker, 2003). Based on the studies of Murai (1964) and Rautman et al. (1995), the median diameter of 125 μm was used for the tuff grains. This also represents the size of grains identified on Mars (Weitz et al., 2018), lunar fines (Sheridan, 1971), and rhyolitic ash flows from non-welded Bishop tuff, USA (Sheridan, 1971). The specific surface area (area per unit mass) is S = $6/\rho$D, where D is the diameter of the grain and ρ is the grain density of each mineral assuming no porosity (Delany et al., 1986). 99 minerals were selected from the EQ3/6 database, based on the extensive review of saline-alkaline paleolacustrine deposits on Earth and minerals identified on Mars and in Martian meteorites (Table E.2 in Appendix E). The dissolution rates and activation energy of primary minerals were adopted from Palandri and Kharaka (2004) (Table 7.1).

It is assumed that all minerals in the sample are spherical monomineralic grains with the same diameter. The hexagonal/orthorhombic regular packing arrangement with 39.5 % porosity was selected to calculate the highest possible water to rock ratio in this model (Parker and Sellwood, 1981) and it was equal to a mass-based W/R ratio of 0.25.

7.3.4 Selection of solutions

The first solution selected is "natural" rainwater. The 25^oC, pure rainwater was reacted in a modeled Mars atmosphere with 1.3 bar CO_2 and 0.0147 mbar of O_2 pressure. The pH of the initial solution was calculated by equilibrating water with high atmospheric CO_2, which yields a value of 3.84. Mars has been reshaped by volcanism throughout its history (Broz et al., 2020), and volcanism is hypothesized to be one of the agents for a (transiently) warm early Mars (Wordsworth et al., 2017). Therefore, acid rain resulting

from volcanic activity is identified as a second solution for this study. The composition of rainfall collected during the eruption at subglacial basaltic Bardarbunga volcano at Holuhraun, Iceland, in 2014 was selected due to its Mars-analogous geologic setting (Ehlmann et al., 2012). The recorded rainfall data from 22 stations, during the Holuhraun eruption, was examined (data from `http://icelandicvolcanoes.is/`). Being an island, rainfall in Iceland is dominated by sea-salt components with the greatest contribution occurring in coastal areas and decreasing inland (Stefánsson et al., 2017). To minimize the sea-salt effect on rainfall, the nearest inland weather stations to the volcano was used. The data collected from Reykjahlio station on 09/28/2014 is used as a starting rainfall composition after closely examining the patterns of the data. The chemical composition of precipitation during the volcanic eruption on an island is mainly influenced by three sources, 1) sea water salt transported by wind from the ocean, 2) dissolution of fine rock aerosol and dust, and 3) volcanic volatiles (Stefánsson et al., 2017). The likely contribution of the seawater spray was removed based on the recommended S/Cl molar ratio (55) of volcanic gas during the eruption and the Na/Cl molar ratio (0.86) of the seawater spray (Stefánsson et al., 2017). The contribution from the rock dust to the precipitation was included since the rock dust in the area is likely similar to the lithology of Mars. The adopted composition of the rainwater in μmole/L is: SiO_2 (19.3), Na^+ (152.2), K^+ (48.3), Ca^+ (74.1), Mg^{2+} (31.1), Al^{3+} (0.2), Fe^{2+} (0.1) , Cl^- (25.8), and SO_4^{2-} (1420). The HCO_3^- and O_2 (aq) was calculated from the modeled Martian atmosphere. The pH of the initial solution was calculated by equilibrating rainwater with high atmospheric CO_2 and the value is 2.63. The third solution used is an acidic $H_2SO_4 - HCl$ solution containing 50,000 μmole/L H_2SO_4 and 9600 μmole HCl. The solution was exposed to the modeled atmospheric CO_2 and O_2, and the initial pH value was 1.36. The S/Cl molar ratio (5.2) of the solution was selected based on the composition of Martian soils at the Viking 1 and 2, Mars Pathfinder, and Spirit rover landing sites (Bruckner et al., 2008; Clark et al., 1982; Foley et al., 2003; Gellert et al., 2006; McSween et al., 2009; Wanke et al., 2001). This solution is similar to the initial solution of Zolotov and Mironenko (2007), and therefore it is easy to compare the difference of secondary mineral assemblages produced by alteration of high silica rock with the low silica rock they used.

The rock and water compositions selected were reacted using the EQ6 reaction path code at 25 ^oC and 1 atm pressure. The geochemical environment modeled here is defined as a system closed to the atmosphere, even though the solutions are initially saturated with atmospheric levels of CO_2 and O_2, when it contacts the atmosphere. 99 minerals were selected based on an extensive review of saline-alkaline paleolacustrine deposits on Earth and minerals identified on Mars and in Martian meteorites (The entire database is given in Table E.2 in Appendix E). Precipitation of quartz and species of dolomite (ordered and disordered) were suppressed due to kinetic constraints (Pokrovsky and Schott, 2001). Delany (1985) adopted EQ3/6 code to investigate the interaction of the Topopah Spring Tuff with well J-13 water and suppressed the silica phases more stable than α-cristobalite (e.g, quartz) to maintain EQ6 simulated silica concentrations consistent with the measured values. Kerrisk (1983) and Bowers and Burns (1990) also found that quartz precipitation needed to be suppressed to form high-silica zeolites such as clinoptilolites and amorphous silica, respectively. The zero backward rate constant was assigned for tridymite in the TST rate equation to eliminate tridymite precipitation, since it does not form under the modeled T-P conditions (Morris et al., 2016). A total of twelve simulations were each run up to 2 x 10^6 steps using an eight node Raspberry Pi single board computer (SBC) cluster.

Three hydrologic systems were tested; the chemical equilibria and mineral precipitation under, 1) pure rainwater, referred to as hydrologic system A, 2) rainwater during the volcanic eruption, referred to as hydrologic system B, and 3) an acidic solution that could have formed through volcanic or impact-induced degassing, referred to as hydrologic system C. These solutions were equilibrated with the modeled Noachian Mars atmosphere, and finally results are compared. The type and timing of secondary minerals formed under a series of water/rock mass ratios, emulating the decrease of porosity with time or depth due to the precipitation of secondary minerals or sediment compaction, were also assessed.

7.4 Results and discussion

Weathering of high-silica materials in acidic water formed under high atmospheric CO_2 causes solution neutralization and consecutive precipitation of carbonates, kaolinite, nontronite, gibbsite, saponite, Fe oxides, sulfates, and zeolites. Major secondary minerals

formed in calculated models are listed in Table 7.2 (chemical formulas and equilibrium constants (log K) values used in the model are also listed in the table. Reaction for which log K is given can be found in Table E.3 in Appendix E).

Table 7.2: Secondary minerals formed in models (Thermodynamic data are from EQ36 database).

Mineral	Formula	log K
Alunite	$KAl_3(OH)_6(SO_4)_2$	-2.40
Analcime	$Na_{0.96}Al_{0.96}Si_{2.04}O_6 : H_2O$	6.00
Calcite	$CaCO_3$	1.84
Chabazite	$K_{0.6}Na_{0.2}Ca_{1.5}Al_{13.8}Si_{8.2}O_{24} : 10H_2O$	10.37
Chalcedony	SiO_2	-3.47
Clinoptilolite Ca	$Ca_{1.7335}Al_{3.45}Fe_{0.017}Si_{14.533}O_{36} : 10.922H_2O$	-5.64
Gibbsite	$Al(OH)_3$	6.96
Gypsum	$CaSO_4.2H_2O$	-4.48
Hematite	Fe_2O_3	0.10
Kaolinite	$Al_2Si_2O_5(OH)_4$	5.95
Magnesite	$MgCO_3$	2.29
Montmorillonite Ca	$Ca_{0.165}Mg_{0.33}Al_{1.67}Si_4O_{10}(OH)_2$	2.40
Nontronite H	$H_{0.33}Fe_2Al_{0.33}Si_{3.67}H_2O_{12}$	-12.05
Nontronite Ca	$Na_{0.33}Fe_2Al_{0.33}Si_{3.67}H_2O_{12}$	-11.10
Nontronite Mg	$Mg_{0.165}Fe_2Al_{0.33}Si_{3.67}H_2O_{12}$	-11.13
Pyrite	FeS_2	-24.65
Saponite Ca	$Ca_{0.165}Mg_3Al_{0.33}Si_{3.67}O_{10}(OH)_2$	27.00
Saponite Mg	$Mg_{3.165}Al_{0.33}Si_{3.67}O_{10}(OH)_2$	26.96
Siderite	$FeCO_3$	-0.19

7.4.1 Effects of different solutions

The results of the reaction path simulations of the Buckskin rock under hydrologic system A and B are shown in Figure 7.2 (a-d) and (e-h), respectively. Figure 7.2 (a-d) shows the dissolution of primary minerals in hydrologic system A (Fig 7.2a), elements released during the dissolution (Fig. 7.2b), formation of secondary minerals (Fig 7.2c), and the amount of primary minerals destroyed, secondary minerals formed, and H_2O loss during the reaction process (Fig 7.2d). Figure 7.2 e-h shows the dissolution of primary minerals under hydrologic system B (Fig 7.2e), dissolved elements (Fig 2f), secondary minerals formed (Fig 7.2g), and the amount of minerals dissolved and precipitated during the reaction progress (Fig 7.2h). In both systems, anhydrite immediately hydrates to

gypsum followed, in order, by dissolution of anorthite, magnetite, amorphous SiO_2, albite, tridymite, orthoclase, cristobalite, and hematite (Fig 7.2a and Fig 7.2e). The dissolution of anorthite begins after around 10 days, releasing Si and Al to the system, and becomes constant after around 1 year in system A, and before 1 year in system B, and continues for another 100 years before starting to increase rapidly (Fig 7.2b and Fig 7.2f). The pH of the system rapidly increases with the dissolution of anorthite. The increase of Al and Si concentrations and pH due to dissolution of anorthite favors precipitation of the zeolite minerals chabazite, clinoptilolite, and analcime under hydrologic system A (Fig 7.2c), and chabazite and analcime under hydrologic system B (Fig 7.2g).

In early stages of the reaction path (less than a year after reaction start; ~ zero in log_{10} years scale) of hydrologic system A, kaolinite continually precipitates until it redissolves with the increase of pH at one year. Mg-nontronite continuously precipitates with time and after around a year Ca-nontronite appears. Similarly, Mg-saponite starts to form at the end of this early stage and later transforms to Ca-saponite. Gypsum starts to precipitate following the dissolution of anhydrite and later equilibrates with the system. Gibbsite and calcite also saturated with the system during the early stages of the reaction progress, with an increased precipitation rate later, again equilibrating with the system at higher concentrations. Magnetite and/or hematite start to release Fe into the solution at a very early stage. After ~ 120 days, siderite starts to precipitate and after ~ 1 year, pyrite started to precipitate with the dissolution of siderite.

In the later stage of the reaction path (after around one year), chabazite, clinoptilolite, pyrite, analcime, and hematite form. The increase of K relative to Na favors the formation chabazite and with the crystallization of chabazite, K decreases. The high-silica zeolite clinoptilolite starts to form with the increase of Si that occurs as anorthite dissolves. After ~100 years, clinoptilolite redissolves when analcime precipitates due to an increase in Na caused by the dissolution of feldspar. However, studies suggested that aqueous silica activity, rather than aqueous Na^+ concentrations, is the predominant factor controlling the reaction of clinoptilolite to analcime (Chipera and Bish, 1997; Kerrisk, 1983). Erionite, phillipsite, or K-feldspar could not form because of the depleted K. Saponite starts to precipitate at pH $>\sim$ 7.

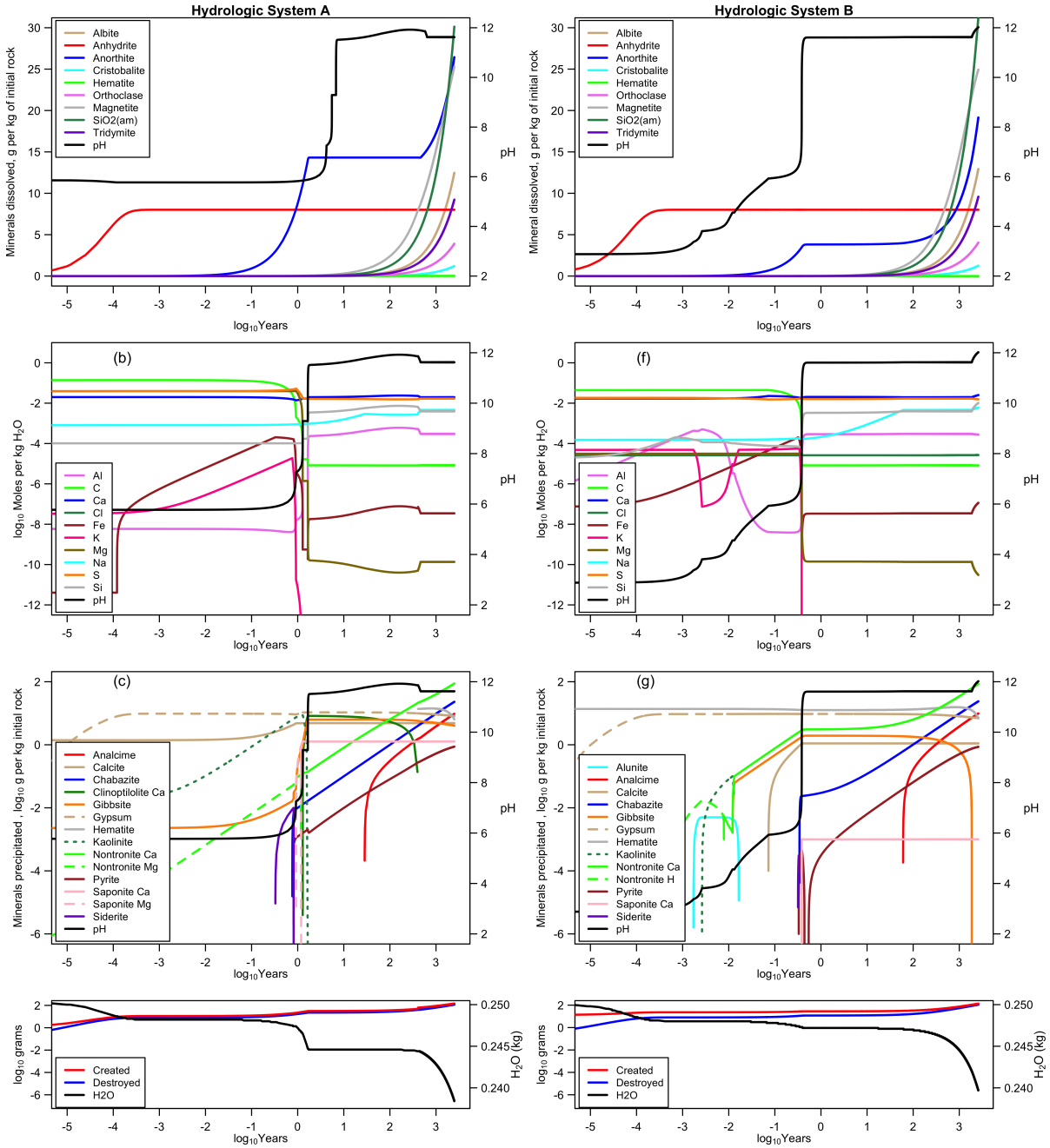

Figure 7.2: Dissolution of primary minerals (a and e), concentration of elements in the aqueous phase (b and f), precipitation of secondary minerals (c and g), total mass of mineral destroyed and created with mass of H_2O lost from aqueous phase (d and h) during weathering of Buckskin sample under rainwater in closed systems at 25 ^oC and 1 bar at 0.24 W/R ratio. Plots (a, b, c, and d) are for hydrologic system A and plots (e, f, g, and h) are for hydrologic system B. Both solutions are equilibrated with 1.3 bar CO_2 and 0.0147 mbar of O_2.

In hydrologic system B, hematite is saturated during the entire modeled period and at the end decreases with increasing pH (Fig 7.2g). With the dissolution of anhydrite, gypsum

starts to precipitate (with an increase of both Ca and S), and later equilibrates with the system. The pH increases rapidly after ~ 100 days of reaction progress, mainly with the dissolution of anorthite, like in hydrologic system A. Alunite, kaolinite, and H-nontronite start to precipitate and are redissolved, forming more stable Ca-nontronite and gibbsite. Al increases over time and then decreases with the formation of gibbsite and phyllosilicate minerals. Gibbsite starts to redissolve after ~ 500 years. The K concentration decreases with the formation of alunite and again increases with alunite dissolution. K is again depleted with the formation of chabazite at pH > ~ 6. Analcime starts to form (Fig 7.2g) as Na increases (Fig 7.2f). Calcite starts to precipitate after ~ 40 days of reaction progress and remains stable after ~ 100 days. In this system, clinoptilolite doesn't appear.

Figure 7.2 (d) and (h) show two prominent steps of water loss during alteration due to the formation of hydrated minerals, first with the formation of gypsum and clay minerals and then with the formation of zeolites. Zeolitization would require the addition of a quantity of water equivalent to approximately 10% of its own mass (Hall, 1998), and this water was taken from the solution. As the alteration progresses, both systems were nearly at saturation as represented by the mass of the minerals destroyed compared to the mass of minerals formed.

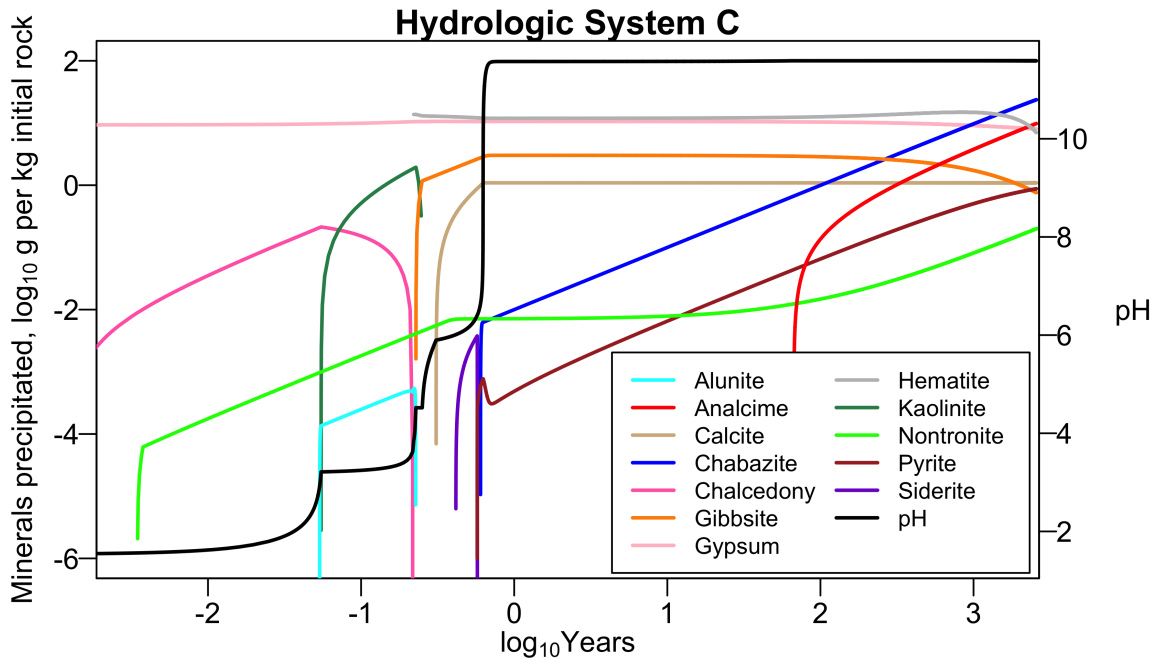

Figure 7.3: Precipitation of secondary minerals during weathering of the Buckskin sample in closed systems using a solution containing 50000 umole/L H_2SO_4 and 9600 umole HCl at 25 ^oC and 1 bar at 0.25 W/R ratio. Initial pH of solution is 1.36.

Acid weathering of the Buckskin sample in hydrologic system C causes neutralization of solution and consecutive precipitation of chalcedony, nontronite, kaolinite, alunite, gibbsite, hematite, calcite, siderite, chabazite, pyrite, and analcime (Fig 7.3). Chalcedony, kaolinite, alunite, and siderite redissolved with the increase of pH. Siderite dissolved with the precipitation of pyrite. Kaolinite and alunite form at pH > ~3 during acid weathering of Buckskin soil and redissolve with the increase of pH. Formation of abundant calcite and zeolites (chabazite and analcime) requires a significant rise in solution (pH > 11) and takes significant time after first precipitation of silica (chalcedony). Chabazite starts to form before 1 year of alteration, however analcime starts to form later, after around 100 years. The precipitation of nontronite, chabazite, and analcime increase over the time, while the precipitation of hematite and gibbsite decrease after 100 years. The model shows that after 1000 years, nontronite, gypsum, hematite, calcite, pyrite, gibbsite, chabazite, and analcime are the secondary minerals.

The three models discussed were compared by calculating the mass of secondary minerals and their percentage of volume with respect to the total volume of secondary

minerals formed after 1000 years of reaction (Table 7.3). This shows that around 8% of the total rock by mass is altered to secondary minerals within 1000 years. Furthermore, after 1000 years, around half of the total secondary mineral volume is represented by nontronite, around 15% by hematite, another ~ 15% by chabazite, and ~ 12% by gypsum. Analcime constituted ~ 5% (by volume) at the end of 1000 years. The amount of analcime and calcite formed decreased with the increase of pH of the initial solution and the maximum amount of zeolite minerals was yielded under hydrologic system B, which models rainwater during volcanic eruptions, a possible scenario for clay formation on early Mars.

Table 7.3: Mass of the secondary minerals formed after 1000 years of reaction with the solution and volume percentage of each mineral with respect to the total volume of the secondary minerals formed.

Mineral	Hydrologic system A	Hydrologic system B	Hydrologic System C
		Mass (g)	
Analcime	3.83	3.79	3.76
Calcite	4.85	1.10	1.09
Chabazite	9.67	9.70	9.68
Gibbsite	4.94	0.64	1.73
Gypsum	9.15	8.03	9.10
Hematite	14.02	15.50	14.82
Nontronite	40.12	34.52	36.32
Pyrite	0.52	0.50	0.50
Saponite	1.26	0.00	0.00
Total	88.36	73.78	77.00
		Volume percentage (%)	
Analcime	4.83	5.86	5.52
Calcite	5.13	1.43	1.34
Chabazite	13.20	16.20	15.33
Gibbsite	6.03	0.96	2.44
Gypsum	11.35	12.20	13.11
Hematite	7.64	10.34	9.38
Nontronite	49.95	52.65	52.54
Pyrite	0.30	0.35	0.34
Saponite	1.57	0.01	0.00
Total	100.00	100.00	100.00

7.4.2 Effects of different Water/Rock ratio

The W/R ratio significantly affects the timing of precipitation and neutralization (Fig 7.4). Higher W/R ratios cause slower neutralization, later precipitation of secondary minerals, and fewer mineral types. High W/R ratios can represent early-stage diagenesis near the surface with high porosity, while porosity decreases through compaction and cementation with depth. The general trend in the results is similar for all cases, though the times of formation differ (Table 7.4). With decreased W/R ratio zeolites begin to form, starting with chabazite, then clinoptilolite and finally analcime. Montmorillonite appears only in the low W/R ratio models. Gypsum also starts to form earlier for lower W/R ratios and does not appear for elevated W/R ratios. Kaolinite redissolves earlier for lower W/R ratios. This shows that the timing of precipitation of some minerals is roughly correlated with the W/R ratios. At the same initial pH (1.36), low W/R ratios cause faster neutralization (Fig 7.4a) and can lead to a diverse secondary mineral assemblage (Fig 7.4b) during a shorter time than at higher W/R ratios, which causes slower neutralization and late precipitation of secondary minerals.

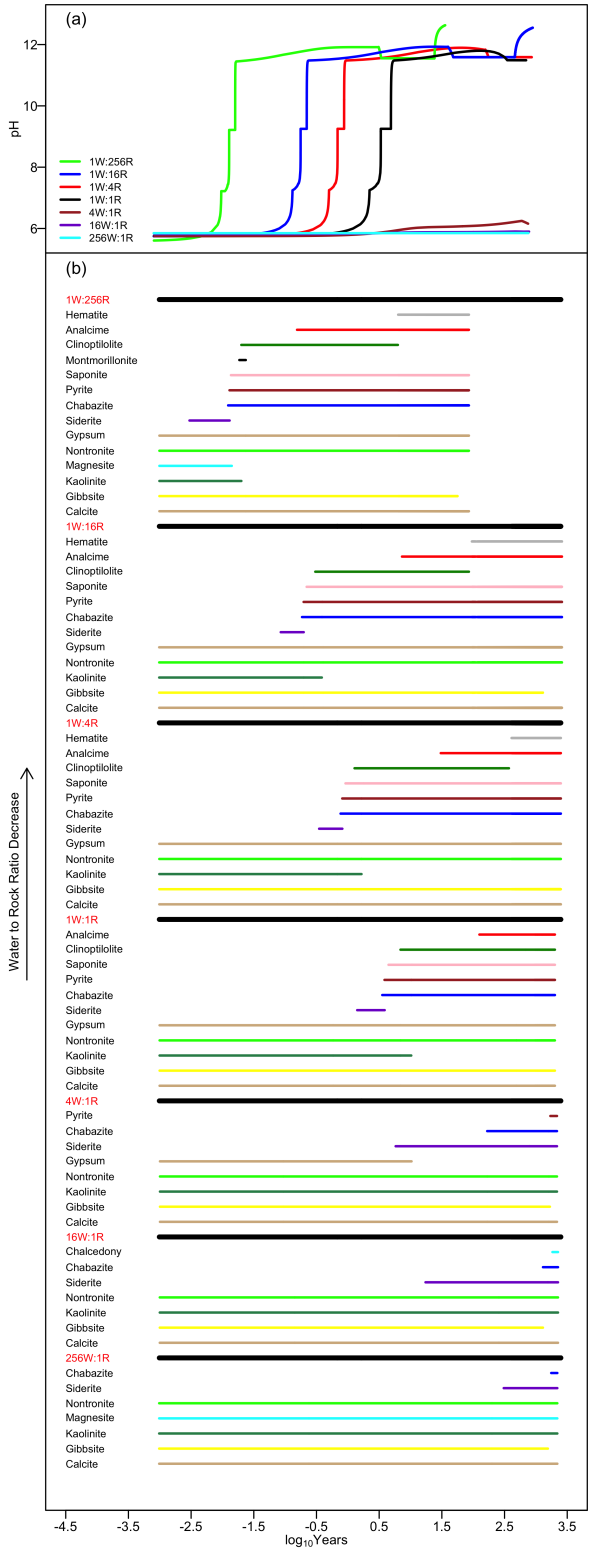

Figure 7.4: Effects of water/rock mass ratio on pH (a) and secondary mineral precipitation (b) during weathering of the Buckskin sample in a closed system at 25^oC and 1 bar. Horizontal lines in Figure 4 (b) represent the time intervals at which minerals are present in different W/R ratio.

7. Possible formation pathways for zeolites in closed-basin lakes on Noachian Mars: Insights from geochemical modeling.

Table 4 shows the time intervals (in years) of zeolite minerals present under different water/rock ratios. Chabazite starts to form early in water limited environments and remains until the end of the modeled time. With increased water in the environment, chabazite starts to form later and remains until end of the modeled period. Clinoptilolite also formed in low W/R (water limited) environments and redissolved later with the formation of analcime. Clinoptilolite and analcime did not develop in the high W/R environments based on this model.

Table 7.4: Time intervals (in years) of zeolites present under different water/rock ratios (W:R). Once formed, chabazite and analcime remain throughout the modeled duration. The time interval when clinoptilolite forms and subsequently re-dissolves is indicated by the time interval shown.

W: R ratio	Chabazite	Clinoptilolite	Analcime
256:1	1757.9		
16:1	1299.1		
4: 1	167.3		
1: 1	3.5	6.9 - 2010.0	125.7
1: 4	0.8	1.3 - 371.2	30.4
1: 16	0.2	0.3 - 85.3	7.3
1: 256	0.01	0.02 - 6.3	0.2

The increase in rates of alteration of tuff with increase in pH and ionic strength is well known (Hay, 1966; Mariner and Surdam, 1970). These calculations show that kaolinite mostly formed with a pH $<\sim$ 7.0, while saponite mostly formed with a pH $>\sim$ 7.0 (Fig 7.2, 7.3 and 7.4). The most common type of alteration in volcanic rocks of felsic composition is the acid-sulfate type characterized by kaolinite-alunite mineral assemblages (Hall, 1998). The Fe-rich smectite nontronite appeared in every hydrologic system modeled and became the most abundant secondary mineral, while kaolinite and montmorillonite (Al-smectite) were less abundant (Table 7.3 and Fig 7.4). The dominant phyllosilicate minerals observed on Mars based on orbital data are Fe/Mg smectites (primarily nontronite and saponite) in crustal material exposed by craters, basin fill, and stratigraphic sections. Al-smectite and kaolinite show limited occurrences in craters and often appear in stratigraphic sections above the Fe/Mg smectite beds (Carter et al., 2013; Ehlmann et al., 2013; Ehlmann and Edwards, 2014). Mawrth Vallis is one of the oldest outflow channels containing one of

the largest exposures of phyllosilicates on Mars. Nontronite, montmorillonite, kaolinite, carbonate, and hydrated silica have been identified there using OMEGA and CRISM orbital data (Bibring et al., 2006; McKeown et al., 2009). Two main stratigraphic units identified in this area are a nontronite-bearing lowermost unit overlain by Al-phyllosilicate unit containing montmorillonite and hydrated silica, with a thin layer of kaolinite and hydrated silica at the top (Bishop et al., 2008; McKeown et al., 2009; Wray et al., 2008). Multiple hypotheses have been proposed for the formation of this stratigraphy including in situ alteration of volcanic ash deposits, transport of clay minerals from outside the Mawrth Vallis region in a large fluvial-lacustrine or marine environment, or formation by pedogenic processes (McKeown et al., 2009). The mostly likely formation scenario, as suggested by McKeown et al. (2009), is that layers of volcanic ash were altered by groundwater circulation after being deposited into a lacustrine (or marine) basin. That scenario can be explained numerically using the geochemical models presented here. The starting material of this study, Buckskin rock from Gale crater, is suggested to be the product of erosion from a high silica volcanic source rock in the Gale Lake catchment (Hurowitz et al., 2017; Morris et al., 2016).

According to the models presented here, zeolites occur after a certain time (based on the W/R ratio) when the solution becomes alkaline, with the availability of Si. Chabazite and clinoptilolite form first and later clinoptilolite is replaced by analcime. The spatial distribution of clinoptilolite and analcime in saline-alkaline paleolake deposits on Earth implies that analcime is produced by replacement of earlier formed zeolites including clinoptilolite (e.g, Hay (1966); Sheppard and Gude (1969b)). The clinoptilolite-analcime transition has been suggested to depend on the concentration of dissolved silica (e.g, Bowers and Burns (1990)). However, using reaction-path calculations, Kerrisk (1983) suggested that clinoptilolite-analcime transition is controlled by the activity of dissolved silica. Ehlmann et al. (2009) identified analcime along with hydrated silica deposits at the craters near the Antoniadi basin, west of Nili Fossae, Mars using CRISM data. In the greater Nili Fossae region, Fe/Mg smectites have been observed over large areas as the lowermost stratigraphic units, and based on such widespread distribution, they exclude the local lacustrine or volcanic hydrothermal processes as the primary formation mechanism

and favor the pedogenic leaching, subsurface hydrothermal activity, or impact processes. Hall (1998) discussed three scenarios that might provide conditions favorable for large scale zeolitization on Earth; 1) volcanic ash deposition in water, 2) reheating of the volcanic ash after the acidity has been removed, or 3) interaction of volcanic ash with alkaline ground water. Many of the large zeolite deposits described from the Western United States were deposited in a lacustrine environment (Hay, 1966; Sheppard, 1974). Lacustrine conditions appear to be highly favorable for zeolitization on Earth due to the tendency of pore water to become alkaline as a result of reaction with volcanic glass (Hall, 1998). Terby impact crater, north of Hellas basin, contains layered deposits interpreted as the thickest paleo-deltaic complex observed at the surface of Mars, composed of Fe/Mg-smectites with local zeolites (or sulfates) present in the lowest sections (Ansan et al., 2011). Though most zeolitic sediments on Earth show evidence of subaqueous deposition or reworking, some are subaerial deposits, such as the zeolitic tuffs of Yucca Mountain, Nevada (Chipera and Bish, 1997), and the highly zeolitized Neapolitan Yellow Tuff, deposited only 12,000 years ago in Italy (Hall, 1998). The zeolitic alteration at Yucca mountain shows four diagenetic zones based on mineralogy; 1) zone I, the shallowest zone, is characterized by vitric tuffs containing unaltered volcanic glass and minor smectite, opal-CT, heulandite, and Ca-clinoptilolite, 2) zone II is characterized by complete replacement of volcanic glass by clinoptilolite with minor amount of opal-CT, smectite, quartz and K-feldspar, 3) zone III consists of analcime, K-feldspar, quartz, and minor calcite and smectite, and 4) zone IV is characterized by albite, K-feldspar, quartz, and minor calcite and smectites (Chipera and Bish, 1997). Thermodynamic modeling by Chipera and Bish (1997) using estimated thermodynamic data for measured chemical compositions of clinoptilolite and analcime at Yucca Mountain concluded that the temperature, relative cation abundances, and silica activity are all important for determining clinoptilolite-analcime equilibria. These results and results presented here are similar, though the present study was done under 25^oC constant atmospheric temperature. Ash deposited in water may be zeolitized either as a result of increased alkalinity resulting from reaction between vitric particles and interstitial water (lacustrine deposits on Earth), or by a rise in temperature associated with burial diagenesis or hydrothermal deposits (e.g, Yellowstone National Park (Bargar and

Beeson, 1981), suggested as a mechanism for the Nili Fossae deposits on Mars (Ehlmann et al., 2009)) (Chipera and Apps, 2001; Hall, 1998).

Carbonate mineral phases including calcite, magnesite, and siderite also formed in the calculated models. Magnesite and siderite redissolve while calcite mostly remains during the entire process. Calcite, magnesite, and siderite have also been detected on Mars using orbital and rover instrument data and from Martian meteorites, though in much lower abundances than on Earth. Fe/Mg-rich carbonates have been identified in several basins on Mars using CRISM orbital spectral data and most of these carbonates are observed mixed with hydrated phases (e.g, Ehlmann et al. (2008); Ehlmann et al. (2009); Horgan et al. (2020)). Magnesite, siderite, and calcite are also identified in Martian meteorite ALH84001 and are hypothesized to have formed at low temperature, possibly in a lacustrine evaporitic environment (e.g, McSween and Harvey (1998); Warren (1998)). Some studies (e.g, Hausrath and Olsen (2013)) have suggested that acidic chemical weathering led to the paucity of carbonate minerals on Mars, and Phillips-Lander et al. (2018) demonstrated that carbonates can also dissolve rapidly in circum-neutral pH sulfate brines. This study shows that siderite redissolves at pH $> \sim 6$. In addition, the hydrated sulfate gypsum and the hydroxylated sulfate alunite are also observed in this model and detected on Mars (e.g, Carter et al. (2013)). Zeolites are also associated with carbonates and Fe/Mg-rich phyllosilicates in Valles Marineris (Viviano-Beck et al., 2017). Several authors have described the difficulties of discriminating zeolites from polyhydrated sulfates using visible to shortwave infrared (VIS-SWIR) spectral data (e.g, Ehlmann et al. (2009); Wray et al. (2009); Carter et al. (2013)). Sun and Milliken (2015) present a global survey of 633 central peaks of craters to assess their hydrous minerals using CRISM data and they identified analcime in 4.5% of central peaks, though other zeolites might be present but not detected due to difficulties of identifying them using orbital VNIR-SWIR data. These detections are mostly associated with unconsolidated sedimentary deposits. Therefore, non-analcime zeolite minerals such as chabazite and clinoptilolites are likely present on the surface of Mars.

Table 7.5 compares the current results with some of the previous models. It is important to note that different models use different factors to represent mineral evolution. While

some models use the reaction progress, others use the calculated time in years or W/R ratio to present their results. Secondary minerals formed in the previous models were arbitrarily grouped into three bins and named stage 1, 2, and 3. These stages were assigned based on the time taken to form or based on the W/R ratios. Two common minerals from each model were listed for easy comparison. Stage 1 represents the early precipitation or minerals formed under high W/R ratios, while stage 3 represents the later precipitation or minerals formed under low W/R ratios. Stage 2 represents the intermediate products. Since selected W/R ratios in each model were different, these stages might not represent the exact hydro-chemical stage of the process for direct comparison. Based on the first order comparison, all models presented here show the same general trend of mineral precipitation, regardless of the staring material composition, starting solution composition, and environmental parameters. The most common general pattern of mineral occurrence is amorphous silica, chalcedony, kaolinite, montmorillonite, nontronite, saponite, and zeolite minerals. The main differences between the previous models and the model calculated here are: 1) previous models used the olivine basalt as the starting material while this model used the silica-rich Buckskin sample, 2) most of the previous models used current atmospheric CO_2 pressure while this model used the modeled late Noachian atmospheric CO_2 pressure. However, the results shows that the overall mineral precipitation pattern is similar. Mineral precipitation under high atmospheric CO_2 leads to the precipitation of carbonate minerals (e.g, calcite, siderite, magnesite) compared to models run with current Martian atmospheric CO_2.

Table 7.5: Comparison of the input parameters and output secondary minerals for selected models in previous studies. Prominent characteristic secondary minerals of interest in this study are grouped into three bins showing three stages during the reaction progress. Stages were chosen based on the reaction time or W/R ratio of models and therefore minerals in each bin might not be directly comparable.

	Zolotov and Mironenko (2007)	*Berger et al. (2009)*	*Bridges et al. (2014)*	*Zolotov and Mironenko (2016)*	*This study*
Starting Material/s	Martian achondrite EETA79001 olivine basalt	Adirondack martian olivine basalt	Portage soil, Gale crater	Adirondack martian olivine basalt	Buckskin, Gale crater
Starting Solution and pH	H2SO4 (0.05 moles) + HCl (0.0096 moles) acid solution, 1.2 pH	Pristine H2SO4 acid, 0.47 pH	Gale Portage Water (GPW) + 0.62 mol of H2CO3	H2SO4 (0.05 moles) + HCl (0.0096 moles) acid solution, 1.2 pH	H2SO4 (0.05 moles) + HCl (0.0096 moles) acid solution, 1.36 pH
Temp. (°C)	0	0	10	0	25
P_{CO_2} **and** PO_2	5.3 mbar CO_2 and 7.6 μbar of O_2	Current martian atmospheric values	-	1 bar CO_2 and 7.6 μbar of O_2	1.3 bar CO_2 and 14.7 μbar of O_2
Simulator	GEOCHEQ	JChess	CHIM-XPT	GEOCHEQ	EQ3/6
Minerals formed at stage 1	Amorphous silica, goethite	Chalcedony, gypsum	Kaolinite, carbonate	Kaolinite, amorphous silica	Chalcedony, kaolinite, alunite
Minerals formed at stage 2	Kaolinite, saponite	Kaolinite, nontronite	Stilbite, chlorite	Siderite, saponite	Siderite, nontronite, hematite

	Zolotov and Mironenko (2007)	*Berger et al. (2009)*	*Bridges et al. (2014)*	*Zolotov and Mironenko (2016)*	*This study*
Minerals formed at stage 3	Stilbite, stellerite	Ca-zeolite, saponite	Stilbite, nontronite	Analcime, stilbite	Chabazite, analcime

7. Possible formation pathways for zeolites in closed-basin lakes on Noachian Mars: Insights from geochemical modeling.

The calculated models show that zeolites could form and their formation pathways on early Mars. The key question is whether these deposits that formed in early Martian hydrologic systems can survive for time spans of hundreds of millions or billions of years. Several studies have evaluated the state of hydration of zeolites (e.g, chabazite, clinoptilolite) along with smectite minerals (e.g, montmorillonite) under present-day Martian surface conditions (e.g, Bish et al. (2003); Fialips et al. (2005); Tokano and Bish (2005)). Bish et al. (2003) noted that, based on the thermodynamic data of hydration of clinoptilolite and smectites, many compositional varieties of these minerals would be at least partially hydrated under the temperature and pressure (H_2O) found on the Martian surface today. The terrestrial petrological investigation of glacial sediments from the Dry Valleys area of Antarctica found authigenic chabazite in the frozen sediments (Dickinson and Rosen, 2003). Thermodynamic calculations by Fialips et al. (2005) showed that under average martian conditions, chabazite would retain between 15 – 22 wt% H_2O. Surface minerals on extraterrestrial bodies are typically identified and mapped using reflectance spectra of those minerals recorded by Earth-based telescopes or orbital sensors. The most prominent absorption features of zeolites are due to O-H vibrations in hydroxyl and H-O-H stretching and bending vibrations in mineralogic water. Therefore, if these minerals were dehydrated or dehydroxylated, they will not not be identifiable using spectral remote sensing methods. Turenne et al. (2022) investigated spectral reflectance properties of eight hydrated minerals including zeolites (heulandite and chabazite), sulfates, and silica-rich sinter under simulated Mars surface conditions. Their results showed that heulandite and chabazite did not exhibit any significant spectral changes under the tested Martian conditions.

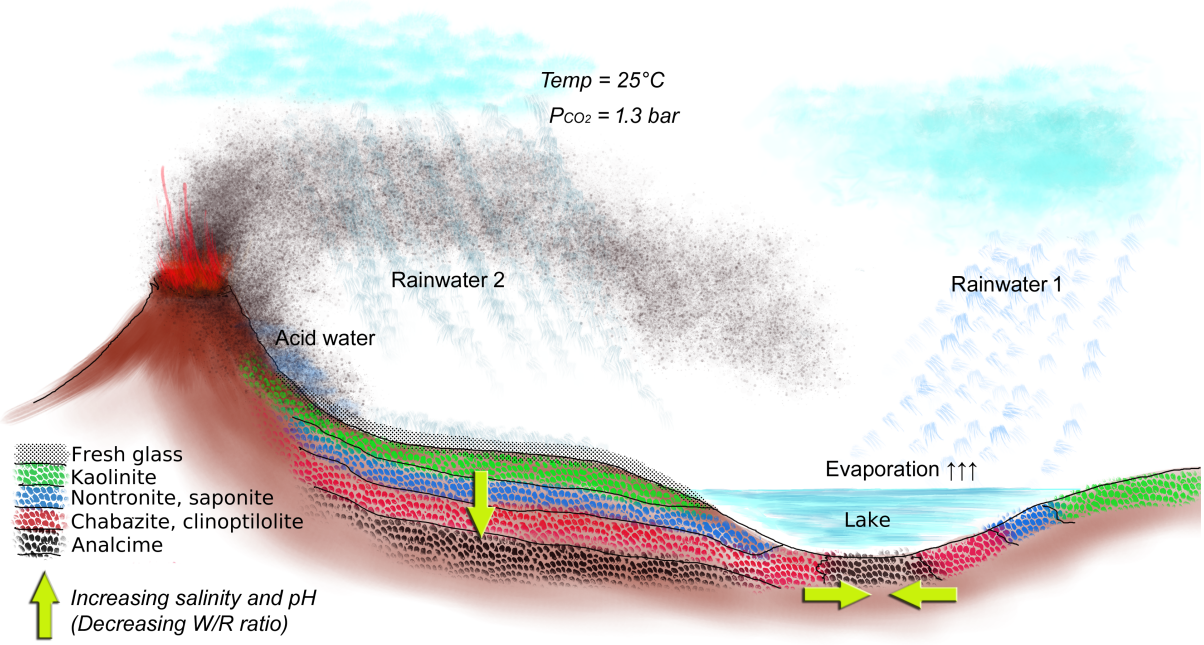

Figure 7.5: Schematic profile showing alteration zoning of two genetic types of zeolite formation patterns discussed in this study. The minerals showed in the legend are the main minerals formed in the calculated models. Rainwater 1: "pure" rainwater adopted in hydrologic system A, Rainwater 2: rainwater during volcanic eruption (hydrologic system B), Acid water: H_2SO_4-HCl acid water (hydrologic system C).

The timescales calculated here are based on the thermodynamic data from literature that was calculated under Earth laboratory conditions. Dissolution rate constants derived from experimental studies have been shown to overestimate the dissolution rate of the material in nature. Experimental dissolution rates for a specific silicate mineral are commonly two to four orders of magnitude faster than field-derived rates (White and Brantley, 2003). Non-analcime zeolites can persist for tens of thousands of years or more depending on reaction rates limited by initial pore-solution chemistry, and analcime commonly crystalizes at the expense of all previously formed phases, but may require hundreds of thousands of years to crystallize in sedimentary environments (Dibble and Tiller, 1981). Calculated models show that analcime starts to form after around 100 years.

Acid water formed due to rainfall during volcanism and/or under high CO_2 atmospheric pressure, or due to volcanic degassing or impact events, will penetrate into the ground or overflow to the (crater) lakes as shown in Figure 7.5. As acid water penetrates into the pyroclastic materials it alters the pyroclastics and in the process becomes more alkaline.

Silica and kaolinite would be formed closest to the surface (at higher W/R ratios and lower pH), followed by Fe-Mg-smectites, non-analcime zeolite, and analcime deeper in the sediments where the W/R ratio low (and pH is high). On the other hand, acid water entering a closed basin where volcanic materials are present can slowly react with volcanic glass and increase the pH and salinity of the solution. Due to the evaporation and shrinkage of the water-filled portion of the basin, W/R ratio may decrease from the edges to the center of the basin leading to an increase of salinity and pH. This will create a concentric pattern of mineral deposits (Fig 7.5) as commonly seen in playa lake deposits on Earth. Both phenomena can be directly explained by the modeling presented here.

7.5 Conclusion

Zeolites, with the confirmed detection of analcime, have been detected in crustal outcrops on Mars using orbital spectral image data. On Earth, zeolites typically form through the alteration of volcanic glass in the presence of water at relatively low temperatures. Studies of the formation and stability of zeolites under different environments are limited by the complexity of the mineralogy and crystal chemistry of naturally occurring zeolites, chemical complexity of the zeolite-forming natural environments, and due to the very slow reaction rates at the low temperatures at which most zeolites form. Therefore, this study used thermodynamic-numerical modeling to study the possible scenarios for formation and fate of zeolites in closed basin lakes on Mars.

The modeling presented here shows that acidic solutions in closed-basin lakes filled with high-silica volcaniclastic materials (similar in composition to the Buckskin outcrop at Gale crater) on late Noachian Mars can produce zeolite minerals, similar to those in saline-alkaline lakes on Earth. Analcime forms only in water-limited environments (low W/R ratio). Chabazite can form in environments with relatively high W/R ratios. Clinoptilolite is replaced by analcime as pH increases, the W/R ratio decreases, and over time. Therefore, analcime was found to be the most commonly formed zeolite mineral in these environments. It is also a very common constituent of saline-alkaline lake deposits on Earth. This study also shows that the mineral precipitation patterns formed from the dissolution of high-silica materials through acid weathering are similar to the

precipitation patterns formed from the dissolution of basaltic rocks by acid weathering under 0-25°C conditions or hydrothermal conditions, reported in previous laboratory, field, and geochemical modeling studies.

While the thermodynamic data used in this study is solely based on Earth observations and the stability fields of zeolite might not be exactly (and quantitatively) represented by these models, the general trends and relative stability relationship should be the same for Mars. Therefore, the trends and relationships observed in these models can lead to a better understanding of the geochemical conditions that produce the observed zeolites and associated mineral assemblages even though the original fluids have long since vanished.

Acknowledgement

Many thanks to Thomas J. Wolery at the Lawrence Livermore National Laboratory (LLNL) for making EQ3/6 code freely available. Also, thanks to R and Rstudio developers.

"as the complexity of a system increases, our ability to make precise and yet significant statements about its behavior diminishes until a threshold is reached beyond which precision and significance (or relevance) become almost mutually exclusive characteristics"

-Lotif A. Zadeh, 1973, p 28 -

8

Data-driven Fuzzy Weights-of-Evidence model for identification of potential zeolite-bearing environments on Mars.

Contents

Abstract **271**
8.1 Introduction **272**
8.2 Datasets **275**
8.2.1 Hydrous mineral Map 275
8.2.2 Geology 276
8.2.3 Elemental abundances 276
8.2.4 Mineralogy 277
8.2.5 Albedo 278
8.2.6 Thermal inertia 278
8.2.7 Dust cover 279
8.2.8 Elevation and slope 280
8.2.9 Valley networks 280
8.2.10 Pyroclastic deposits 281
8.2.11 Open and closed basins 282
8.3 Methods **282**
8.3.1 Preparation of factor maps 282
8.3.2 Weights-of-evidence method 285
8.3.3 Fuzzy Set Theory 288
8.4 Results and discussion **304**
8.5 Conclusion **313**
Acknowledgement **314**

8. Data-driven Fuzzy Weights-of-Evidence model for identification of potential zeolite-bearing environments on Mars.

Abstract

This study used the data-driven fuzzy based weights-of-evidence method to delineate favorable areas to look for zeolites on Mars. The model used the global mineralogical, geological, geomorphological,hydrological, physical, and elemental abundance maps derived from orbital data as evidence maps with the locations of orbitally detected hydrous minerals as the known mineral occurrences. The weights-of-evidence method was used to calculate the weights of each evidential class based on the prior and posterior probabilities. Evidential maps were fuzzified using membership function curves based on the results of a weights-of-evidence model and manually based on expert knowledge of the system concerned. Fuzzified evidential maps were combined through a multi-stage inference engine using fuzzy set operators to generate fuzzy favorability maps. The three-stage inference engines used here consist of three/four parallel networks that sequentially combine collateral fuzzy evidential maps transmitted by the fuzzifier through the fuzzy OR and fuzzy AND operators to yield three/four intermediate fuzzy evidential maps in the first stage. These three/four fuzzy evidential maps were combined using the fuzzy gamma operator to create the synthesized fuzzy favorability map in the second stage. The best hydrous mineral favorability maps were selected after calculating the success rate using train and test datasets. The third stage involved the generation of a favorability map for zeolites by combining the best hydrous mineral favorability fuzzy membership map with ash thickness, pyroclastic deposits, and open and closed-basin maps. Finally, fuzzy favorability maps were defuzzified to demarcate the most favorable areas for hydrous minerals and zeolites. All maps were calculated up to $\pm$ 40° latitudes towards poles. This study also shows the most important and sensitive steps in fuzzy modeling; the selection of fuzzy membership values for the multiclass evidential maps and the selection of fuzzy set operators and appropriate inference networks for synthesizing the evidential map.

8. Data-driven Fuzzy Weights-of-Evidence model for identification of potential zeolite-bearing environments on Mars.

8.1 Introduction

Zeolites are among the most common and widespread authigenic silicate minerals found in sedimentary deposits on Earth (Hay and Sheppard, 2001; Hay, 1966). Zeolite occurrences in sedimentary environments on Earth can be categorized into six groups based on their geologic and hydrologic settings; 1) saline-alkaline lakes (e.g., Lake Tecopa, California; Sheppard and Gude (1968)), 2) soils and land surfaces (e.g., Lake Bogoria basin, Kenya; Renaut (1993)), 3) deep sea sediments (e.g., North-West Pacific; Lee (1988)), 4) open hydrologic systems (e.g., White river sequence, Wyoming, USA; Lander and Hay (1993)), 5) hydrothermal alteration (e.g., Yucca Mountain, Nevada, USA; Sheppard et al. (1988)), and 6) burial diagenesis (e.g., Mogami district, Yamagata, Japan; Iijima (1988)). Zeolites are both common and widespread in volcanic ash deposits in saline-alkaline lakes and the largest relatively pure concentrations of natural zeolites are found in these environments (Hay, 1966). Overall, the highest concentrations of zeolites are found in glass-rich volcaniclastic deposits since volcanic glass is the major precursor of zeolites (Hay and Sheppard, 2001). The formation and stability of zeolites are strongly dependent on the thermodynamic equilibrium of fluid-mineral reactions caused by water chemistry (Chipera and Apps, 2001), and kinetically controlled non-equilibrium growth and dissolution reactions (Dibble and Tiller, 1981). Therefore, the presence and nature of zeolites is a good probe to reconstruct the geological and hydrological history of zeolite-bearing environments on Earth (e.g., Chipera and Apps (2001); McHenry et al. (2020)).

Zeolites have also been postulated to be components of Martian regolith (e.g., Ming and Gooding (1988); Basu et al. (1998); Berkley and Drake (1981); Bish et al. (2003); Dickinson and Rosen (2003); Tokano and Bish (2005); Cannon et al. (2015)). Ehlmann et al. (2009) have identified several analcime detections in deposits also containing Fe/Mg-rich smectites, chlorites, and hydrated silica in craters near the Antoniadi basin, west of the Nili Fossae region, Mars, using Compact Reconnaissance Imaging Spectrometer for Mars (CRISM) orbital data. Based on the associated mineral detections, they infer a hydrothermal origin for the analcime. They described the difficulties of discriminating non-analcime zeolites from polyhydrated sulfates using Visible-near Infrared - Shortwave Infrared (VNIR-SWIR)

spectral data. Carter et al. (2013) conducted a large-scale investigation of hydrous minerals on Mars using CRISM and OMEGA (Observatoire pour la Mineralogie, l'Eau, la Glace et l'Activite) orbital imaging spectrometer data. They categorized zeolites and sulfates into one class due to the difficulty of distinguishing them using orbital data, though they typically form in very different environments. However, based on the shape of the 1.9 μm absorption band, they infer that more than 80% of minerals detected within the zeolite/sulfate class are likely to be zeolites. Sun and Milliken (2015) presented a global survey of 633 crater central peaks to assess their hydrous minerals using CRISM data and identified zeolites in only 4.5% of cases. They also emphasized the difficulty of identifying and distinguishing zeolites from sulfates and therefore the only zeolite specifically identified was analcime, classifying the other potential zeolites as unidentified hydrous phases instead. It is also important to note that zeolites have not yet been reported in Martian meteorites or in situ data from Mars.

Therefore, the identification and delineation of prospective areas for zeolites on the surface of Mars could serve as a guide for further searches for zeolites using detailed orbital spectral image analysis and future in situ observations. Predictive modeling for mineral exploration, a widely used statistical and probabilistic reasoning method in geosciences, can be used in this case. Predictive modeling for mineral exploration follows specific steps starting with defining the conceptual model of the exploration target. Defining a conceptual model of exploration targets for the mineral type sought (zeolite in this study) requires a knowledge of geological and geochemical processes relevant to the formation of the target mineral. This knowledge allows exploration criteria to be defined, followed by the selection of suitable geoscience spatial datasets to be used, the extraction and enhancement of evidential features in each dataset, selecting mapping method(s) for each evidential feature, selecting method(s) for creating predictive map(s) from each evidential feature, and integrating the predictive maps to create a predictive model and/or to map the prospective areas for the target mineral (zeolites) (Carranza, 2011). The preferred predictive model for this study should, 1) accommodate the multiclass and continuous geodata, and 2) be sufficiently robust to handle the "information fuzziness" inherent to remote observational

data (Porwal et al., 2003; Zimmermann, 1991). The combination of weights-of-evidence Method and Fuzzy set theory can fulfill both criteria in a flexible and consistent way.

The weights-of-evidence method commonly applied for the identification and exploration of mineral deposits, landslide susceptibility analysis, and hazard modeling (e.g., Neuhäuser and Terhorst (2007); Bonham-Carter et al. (1989); Bonham-Carter (1994)). The method has also been used for habitat quality assessments (e.g., Romero-Calcerrada and Luque (2006)), and even mapping the potential habitat of underground mushrooms (Yang et al., 2012). In the context of mapping potential mineral deposits, the model uses the location of known mineral occurrences to create spatial information diagnostics for a particular type of mineral, which can be used to map that mineral's potential distribution (Bonham-Carter et al., 1989). Fuzzy set theory is also used for predictive mineral potential mapping since it provides a mathematical framework to combine and analyze qualitative and quantitative data independently of their source or characteristics (Luo and Dimitrakopoulos, 2003; Porwal et al., 2003; Moon, 1998). Cheng and Agterberg (1999) proposed a hybrid fuzzy weights-of-evidence model which allows objective or subjective definition of a fuzzy membership function of evidence augmented by objective definition of conditional probabilities calculated by the weights-of-evidence method. Due to the limited knowledge of the formation conditions (geological, mineralogical, physical, and hydrological) of zeolites on Mars, a data-driven (empirical) approach was used. Data-driven methods typically assume that enough known zeolite occurrences within the study area have been well studied and documented (Porwal et al., 2003). Since there are no well-studied and documented zeolite detections on Mars, this study first models the favorable areas for hydrous minerals and based on that model identifies the favorable areas for zeolites using other information and assumptions.

The conceptual model developed in this study requires: 1) suitable geologic and hydrologic environments for the formation of hydrous minerals, which are commonly formed under lacustrine, hydrothermal, diagenesis/metamorphic, or pedogenic processes, and 2) the presence of volcanic ash (tuff) as a starting material for the formation of zeolites. Therefore, as a first step, this study creates a predictive model (map) for the potential areas for hydrous minerals on the surface of Mars, and then based on the

available information and models of distribution of pyroclastic ash deposits of Mars, create a predictive model (map) for the potential areas for zeolites on the surface of Mars. Finally, this study identifies potential open/closed paleolake basins where zeolite might be present.

The rest of the chapter is arranged as follows. Section two discusses the spatial data sets used in this study. Section three discusses the methodologies used to create evidential features, predictive maps, and integrated predictive model/s (and maps). Sections four and five present the results and discussion and conclusion, respectively.

8.2 Datasets

8.2.1 Hydrous mineral Map

Hydrous minerals are key markers of ancient surface and subsurface conditions on Mars since they contain water in their crystalline structure and provide a clear mineralogical record of water-related processes. Carter et al. (2013) have conducted a global-scale survey of hydrous minerals on Mars using CRISM and OMEGA spectral data and sorted their hydrous detections into nine spectral classes: 1) Fe/Mg - phyllosilicates, 2) chlorites, 3) Al-smectites/micas, 4) Al-rich kaolins, 5) opaline silica, 6) zeolites/sulfates, 7) serpentines/carbonates, 8) prehnite, and 9) epidote. Based on their study, the Fe/Mg-phyllosilicates are the most common hydrous mineral on Mars (~89%), followed by the Al- phyllosilicates (~33%). Over 50% of global hydrous mineral detections by Carter et al. (2013) are associated with an impact structure (e.g., central peaks, rims, walls, or ejecta). Around 20% are associated with horizontal/sub-horizontal sedimentary deposits, while alluvial fans/deltas are about 5% of the cases. Around 20% of the cases are associated with crustal outcrops. Their study found that most craters excavated buried hydrous minerals from various depths. They also identified that for their zeolite/sulfate class, most strong zeolite candidates are associated with impact craters while the strong sulfate candidates are not. The database of detected hydrous mineral locations by Carter et al. (2013) was downloaded form `https://www.cosmos.esa.int/web/psa/mars-maps`.

8. Data-driven Fuzzy Weights-of-Evidence model for identification of potential zeolite-bearing environments on Mars.

8.2.2 Geology

The geologic map of Mars provides unique information on the spatial and temporal sequences of geologic events that dominated the surface of Mars. Tanaka et al. (2014b) applied photogeologic mapping techniques to identify and discriminate 44 geologic units and about ten linear feature types that document the major types and episodes of material emplacement and modification (Tanaka et al., 2014a). The geological units are delineated using morphologic, brightness, and topographic characteristics, and relative ages based on superposition relations and impact crater densities. Similar areas are grouped into geographic (highland, lowland, transition, basin, polar, and apron) and lithologic (volcanic and impact) categories. Each map unit is assigned an age range according to the Martian chronostratigraphic periods (Noachian, Hesperian, and Amazonian) that are subdivided into eight epochs (Early, middle, and late Noachian; Early and late Hesperian; Early, middle, and late Amazonian), based on stratigraphic relations and crater density determinations (Tanaka et al., 2014a; Hartmann, 2005). The geologic map shows the dominance of highland surface modification in the Noachian period, with highland modification and lowland and basin fill in the Hesperian period. The volcanic plains and shield development, polar and localized plains deposition, and scattered impacts are dominant in both Hesperian and Amazonian periods. The geology map, crated by Tanaka et al. (2014b), was downloaded from `https://pubs.usgs.gov/sim/3292/`.

8.2.3 Elemental abundances

The elemental composition of the Martian surface is important to understand the formation and evolution of Mars (Boynton et al., 2007). In situ observations by landers and rovers have yielded more detailed elemental and mineralogic information at a few locations on the surface of Mars, as has the analysis of Martian meteorites. The Gamma Ray Spectrometer (GRS) on the 2001 Mars Odyssey Mission (Boynton et al., 2004) detecting gamma rays produced in near-surface rock and soil materials with higher spatial resolution, providing some element data. The gamma rays measured represent the top few tens of centimeters of the surface and the measurements are complicated by variations in the size and composition of the rocks, the atmosphere, variable amounts of water near the surface,

and composition variations with depth (Evans and Squyres, 1987). Poulet et al. (2007) mapped the concentrations of H, Si, Cl, K, and Th as determined by the GRS for $\pm \sim 45^o$ latitudes assuming that all elements are homogeneously distributed in the top few tens of centimeters of the surface. Detailed discussion of gamma-ray spectral data processing to determine elemental concentrations can be find in Boynton et al. (2004) and Poulet et al. (2007). For this study, two map products by Poulet et al. (2007), $2^o \times 2^o$ and $5^o \times 5^o$ binned point data, were downloaded from `http://grs.lpl.arizona.edu/data`.

8.2.4 Mineralogy

The concept of mineral occurrences and associations is important to infer the identity of unidentified target minerals. Bandfield (2002) produced a global mineral distribution map using data from the Thermal Emission Spectrometer (TES) onboard the Mars Global Surveyor (MGS) spacecraft (Christensen et al., 1992). He used the linear spectral deconvolution method to extract mineral abundance information and to remove atmospheric components from the TES data at 1 pixel per degree (ppd). The method assumes that each TES spectrum can be modeled as a linear combination of both surface and atmospheric endmembers (Bandfield et al., 2000). He selected emissivity spectra of 32 minerals, glass, 6 atmospheric endmembers, and a blackbody spectrum to fit the 73 spectral channels of the TES data. The output was one pixel per degree binned global mineral concentration maps including 1) sheet silicates and high-Si glass, 2) sulfate, 3) plagioclase, 4) hematite, 5) carbonate, 6) K-feldspar, 7) basaltic glass, 8) quartz, 9) High-Ca pyroxene, 10) low-Ca pyroxene, 11) olivine, 12) amphibole, and 13) RMS (root mean square error) maps. Mineral concentrations were calculated based on signal strength relative to the mineral endmembers used in the linear spectral deconvolution method.

The OMEGA imaging spectrometer onboard Mars Express has acquired data from the visible (0.35 μm) to thermal infrared (5.1 μm) wavelength region with a spatial resolution varying from 300 m to 4.8 km per pixel (depending on the pericenter altitude of the spacecraft's elliptical orbit) of the surface of Mars (Bibring et al., 2004; Poulet et al., 2007). Poulet et al. (2007) produced maps of the global distribution of Martian surface material based on the data from one Martian year of OMEGA observations. Global maps of ferric

phases, mafic minerals including pyroxenes and olivine, and hydrated minerals have been derived using spectral parameters. Ody et al. (2012) produced maps detailing the global distribution of these mineral species using the entire OMEGA dataset acquired from orbit insertion in January 2004 to August 2010, until the failure of the 1 - 2.5 μm channel cooler. Since the 1 - 2.5 μm regions are important to discriminate most martian mineralogy, these global maps can be considered the final outcome of OMEGA observations (Ody et al., 2012). Mapping was done at a spatial resolution of 32 ppd (~ 2 km at the equator).

The global mineral abundances maps derived both from TES by Bandfield (2002) and from OMEGA by Ody et al. (2012) were download from `https://www.cosmos.esa.int/web/psa/mars-maps`.

8.2.5 Albedo

A NIR (Near Infrared) 1 μm albedo (lambertian albedo) map produced by Ody et al. (2012) using the I/F/cos(i) value at 1.08 μm (where i = solar incident angle) of OMEGA data from January 2004 to August 2010 was used for this study. The spatial distribution of albedo values observed in this map is consistent with previous space and ground-based data (Ody et al., 2012). The TES bolometric albedo global map with 8 ppd spatial resolution (Christensen et al., 2001) was also used. The surface albedo of Mars has been observed to change significantly from year to year, which is attributable to the redistribution of dust predominantly during global dust storms (Pleskot and Miner, 1981; Putzig and Mellon, 2007).

8.2.6 Thermal inertia

While visible images play a vital role in providing the geological context of morphologic features, certain aspects of the surface materials, such as composition, grain size, and the presence of volatiles in the subsurface, are not readily discenable from the visible image data alone (Putzig and Mellon, 2007). However, they can be studied by using thermal inertia. Thermal inertia is defined as a combination of bulk thermal conductivity k, density, and heat capacity ($I = \sqrt{k}\rho c$). In general, surfaces of unconsolidated, fine-grained materials will have low values of thermal inertia. Cemented surfaces and surfaces

composed of sand-sized grains will have intermediate values, while rocky surfaces and bedrock outcrops will have high values (Putzig and Mellon, 2007). Therefore, the thermal inertia of a certain location on the surface of Mars is generally related to properties such as particle size, abundance of rocks, exposure of bedrock, degree of induration, and the combination of these properties within the field of view (Mellon et al., 2000). Thermal inertia is the key property controlling the diurnal surface temperature variations, which depends on the physical properties of the top few centimeters of the Martian regolith (Putzig and Mellon, 2007). Some of the other factors are albedo, dust opacity, and atmospheric pressure (Mellon et al., 2000). It is also widely accepted that the lowest thermal inertia regions must be covered with dust at least a few centimeters thick (Ruff and Christensen, 2002). Putzig and Mellon (2007) have produced nighttime and daytime seasonal maps of apparent thermal inertia using three years of TES data at 1/20 ppd. They have cropped each of the 36 seasonal maps latitudinally and used the median values to create daytime and nighttime thermal inertia maps. These two maps were downloaded from `https://www.mars.asu.edu/data/`.

8.2.7 Dust cover

The apparent particle size effects observed in TES spectra of bright regions can be used as an indicator for the presence of dust (fine particles) on the surface of Mars (Ruff and Christensen, 2002). Ruff and Christensen (2002) have defined a dust cover index (DCI) to be equal to the average emissivity value from the 1350 to 1400 cm^{-1} wavelength region, which is least affected by atmospheric components. This wavelength region is sensitive to the spectral particle size effects of silicates (Ruff and Christensen, 2002). They have produced a DCI map using nadir-pointing, daytime TES spectral data with brightness temperature $>$ 260 K. The TES were binned at 8 ppd, and any gaps were filled using a linear interpolation between neighboring bins weighted by distance. This DCI map was downloaded from `http://www.mars.asu.edu/~ruff/DCI/dci.html`. The dust index map derived from TES by Bandfield (2002) using the linear spectral deconvolution method was also used. The dust index maps show a remarkable spatial coherence with albedo and thermal inertia maps at many scales. Dust free surfaces can be best identified by

very low albedo values. However, thermal inertia is not well-suited for this due to its complex behavior for mixtures of dust and coarse particles (except for the extremely high values associated with bedrock) (Ruff and Christensen, 2002).

8.2.8 Elevation and slope

The geology of terrestrial planets is mostly related to the morphology of the surface and therefore geological mapping also heavily relies on the morphology. Elevation information of the planetary surfaces is used to derive the morphology of the surface to analyze the landscape forms, processes, patterns, and evolution (Schumm, 1991). The elevation and slope maps were derived from the 463 m/pixel resolution of digital elevation data (DEM) from Mars Orbiter Laser Altimeter (MOLA) onboard the Mars Global Surveyor (MGS) spacecraft (Smith et al., 2001). The MOLA DEM data was downloaded from `https://astrogeology.usgs.gov`.

8.2.9 Valley networks

The study of fluvial systems observed on the surface of Mars is an important factor for determining the aqueous history of Mars. Several global valley network maps on Mars have been produced both manually from Viking data (Carr and Chuang, 1997), MOLA and THEMIS data (Hynek et al., 2010), and THEMIS, CTX and MOLA data (Alemanno et al., 2018), and automated mapping using MOLA data (Luo and Stepinski, 2009). The global valley network map produced by Alemanno et al. (2018) was used in this study. They mapped all Martian valleys with a total length greater than 20 km manually using photographic (THEMIS daytime IR and CTX) and topographic data (MOLA). Mapping classes include 1) valley networks, 2) longitudinal valleys, 3) valleys on volcanoes, 4) valleys adjacent to canyons, 5) single valleys and valley segments, and 6) small outflow channels. The global geologic map of Mars, created by Tanaka et al. (2014b), included three classes of valleys, 1) single valley, 2) small outflow valley, and 3) trough fluvial valley. These segments maps were used in this study.

8.2.10 Pyroclastic deposits

Explosive volcanic eruptions were likely very important in the Noachian and Hesperian periods in Martian history, and basaltic plinian eruptions are likely to have occurred throughout the history of Mars (Wilson and Head, 2007). The fine-grained products of explosive volcanism, pyroclastic deposits, are difficult to identify via remote sensing techniques (Broz et al., 2020). The most commonly used method for identifying potential pyroclastic deposits on Mars includes identifying 1) areas with high friability based on the observation of erosional landforms, 2) a small grain-size inferred from low thermal inertia maps, 3) geographic proximity to potential vent structures, 4) layering, 5) low albedo materials, 6) resurfaced areas near potential volcanic vent/constructs, and 7) mantle-like draping over topography (Broz et al. (2020) and references therein). Potential pyroclastic deposits identified previously based on these characteristics result in a total of ~ 12.4 to 13.4 million km^2 (~ 8.6 - 9.3% of the martian surface) (Broz et al., 2020). The map of Martian deposits larger than $10^5 km^2$, for which a pyroclastic origin has been proposed in the literature, was used for this study (Broz et al., 2020; Tanaka, 2000; Kerber et al., 2012). The mapped deposits include Arabia deposits, Electris deposits, Medusae Fossae Formation, Dorsa Argentea Formation, Hellas deposits, Argyre deposits, Tyrrhena Patera deposits, and Isidis deposits.

Kerber et al. (2013) adopted a planetary global circulation model developed by the Laboratoire de Meteorologie Dynamique (LMD) to simulate explosive eruptions of ancient Martian volcanoes into paleo-atmospheres with higher atmospheric pressures (50 mbar, 0.5 bar, 1 bar, and 2 bar). Most of the explosive volcanic centers on Mars date to the Hesperian period and it has been suggested that the atmospheric pressure at that time was higher than at present (e.g., Ramirez (2017)). The particle size used for their simulation was 35 μm in radius representing small, far-field ash representing the maximum expected areal extent of ash. For this study, a combined ash distribution pattern map created by Kerber et al. (2013) from all major volcanic centers on Mars, assuming that each of them erupted 1.4×10^6 km^3 of ash during their lifetimes under 1 bar of pressure, was selected. It shows that ash was dominantly emplaced along a latitudinal line east or west of the source volcano and would not be expected to travel predominantly north or south.

8. Data-driven Fuzzy Weights-of-Evidence model for identification of potential zeolite-bearing environments on Mars.

8.2.11 Open and closed basins

The study of paleolakes on Mars is critical because these can capture the record of hydrological regimes, geological events that occurred in the catchment area during their lifetime, and the seasonal and orbital cyclic changes through their sedimentary records (Cabrol and Grin, 2002). Possible paleolake basins observed on Mars have been cataloged and categorized into two main groups based on their morphological features: 1) Closed-basin lakes having an inlet valley breaching the basin-confining topography, but no outlet valley, and 2) Open-basin lakes having inlet valleys and outlet valleys that breach the basin-confining topography (Cabrol and Grin, 1999; Fassett and Head, 2008; Goudge et al., 2015, 2012, 2016). For this study, the open and closed-basin lakes catalog compiled by Goudge et al. (2016) was used. The database consists of the locations of 205 closed-basin lakes (Goudge et al., 2015) and 220 open-basin lakes (Goudge et al., 2012; Fassett and Head, 2008). However, this database does not contain potential paleolakes not fed by inlet valleys, such as enclosed basins with shallow lakes in their interiors fed by internal drainage (e.g., Columbus crater; Wray et al. (2011)), even though such types of paleolakes may have been prominent on the surface of early Mars.

8.3 Methods

8.3.1 Preparation of factor maps

All the factor maps discussed above were imported into ILWIS via GDAL and ISIS3. The ILWIS (Integrated Land and Water Information System) is Windows-based GIS & Remote Sensing software, developed by the Faculty of Geo-Information Science and Earth Observation (ITC), University of Twente, the Netherlands (official release of the DOS version 1.0 in 1988). Since 2007, ILWIS is freely available as an open-source software under the 52° North initiative (`https://www.itc.nl/ilwis/`). GDAL (Geospatial Data Abstraction Library) is an open-source translator library for raster and vector geospatial data formats (`https://gdal.org/`). The ISIS3 (Integrated Software for Imagers and Spectrometers - version 3), developed and maintained by the U.S. Geological Survey, is an image processing software package capable of importing raw NASA planetary mission data

into a usable geospatial image product (`https://isis.astrogeology.usgs.gov/`). The entire analysis was done using ILWIS (running on Linux Pop-OS), followed by re-projecting to a common coordinate system (Plate Carree projection system), and resampling into 200 m/pixel resolution using the nearest neighbor method.

Total hydrous mineral locations detected by Carter et al. (2013) are shown in the Figure 8.1. The abundance of those hydrous mineral detections along with the latitudes are shown in the density plot in the Figure 8.1. This shows that more than 90% of the total detections (1735/1855) are in the area between the latitudes 40^oN and 40^oS. The size of a 32-bit global factor map was around 45.5 GB, and most of the maps used in this study are 32-bit (the rest are 8-bit). Much memory space, computational power and computational time is required for map calculations. Each processing step also produces intermediate maps mostly similar in size to the original map. Since the importance of the map classes/area are calculated based on the locations of hydrous mineral detections, the limited detections in the area beyond 40^oN and 40^oS latitudes will be less important. Therefore, to reduce the computational power, time, and memory space, sub maps were created from all the factor maps covering the area between latitudes 40^oN and 40^oS for the rest of the work.

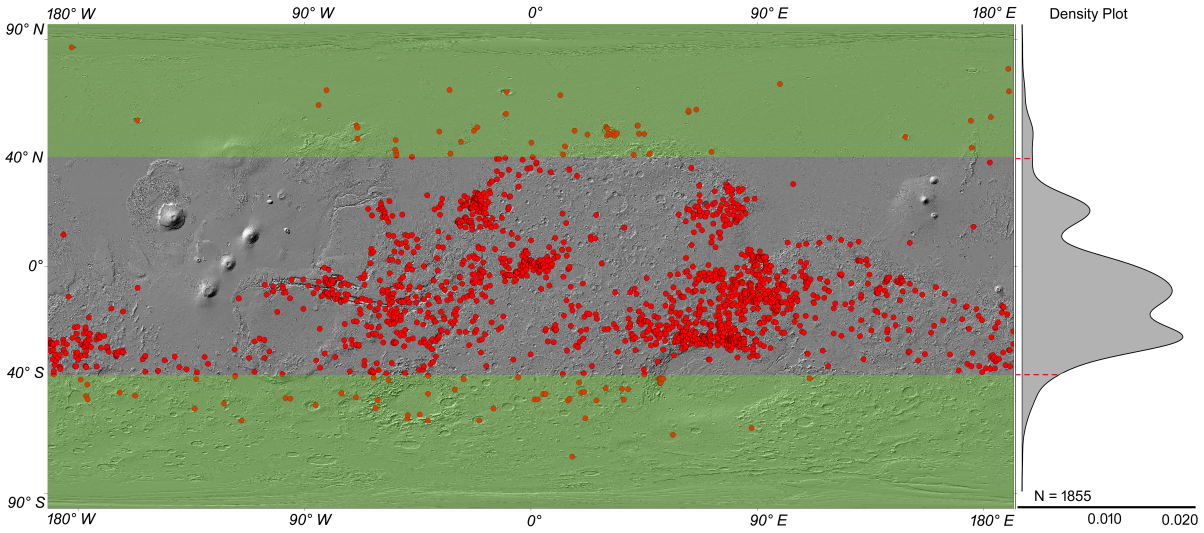

Figure 8.1: Hydrous mineral detections on Mars. Each point represents the position of a hydrous mineral exposure detected by CRISM and/or OMEGA. Background is a grayscale hillshade map created from MOLA DEM. Point density plot shows on the left side of the map.

All the continuous data raster maps (e.g., elevation, dust cover index, elemental abundance, etc.) were reclassified into ten classes after careful examination of their

histograms of the pixel values and based on the discussions in the corresponding literature. The discontinuous data raster maps (categorical maps, e.g., geology map) were imported as is. The ten buffer regions (A: 0 - 200 m, B: 200 - 400 m, C: 400 - 600 m, D: 600 - 800 m, E: 800 - 1000 m, F: 1000 - 2500 m, G: 2500 - 5000 m, H: 5000 - 10000 m, I: 10000 - 100000 m, and J: > 100000 m) were created from the segment maps and then rasterized. Based on the spatial association of buffer regions with the hydrous mineral detections, three buffer maps were selected. The boundaries of all the possible closed and open-basin lakes were manually digitized with the help of MOLA DEM. Two binary maps were created from the ash deposits map (ash deposit = 1, other area = 0) and open and closed paleolake basin map (open/closed basins = 1, other area = 0).

The total hydrous mineral detections within the sub map area (1735 points) were divided into two classes (train and test) using the stratified random sampling method. The H_2O weight percentages at each point location were extracted from the H_2O GRS map for the stratified random sampling method assuming that hydrous mineral abundances at each point location can be represented by the GRS H_2O map. Data partition was done using the "caret" package in R. The train point map contains ~80% (1391 points) of the total points, while the test point map contains the rest of the data points (~20%, 344 points). The factor maps used in this study are listed in Table 8.1, and each factor map is referred to using the MapID in the rest of the text.

Table 8.1: Factor maps used in this study.

#	Platform	Product	MapID	Reference
	RASTER			
1	OMEGA	NIR albedo	om_albdo	Ody et al. (2012)
2		Fe^{3+}	om_fe530	
3		$nphsFe^{3+}$	om_nnphs	
4		Pyroxene	om_pyrox	
5		Olivine Spectral Parameter1	om_osp1m	
6		Olivine Spectral Parameter2	om_osp2m	
7		Olivine Spectral Parameter2	om_osp2m	
8	TES	Albedo	ts_albdo	
9		Amphibole	ts_amphi	Bandfield (2002)
10		Carbonate	ts_carbo	
11		High Calcium Pyroxene	ts_hcpmp	
12		Low Calcium Pyroxene	ts_lcpmp	

#	Platform	Product	MapID	Reference
13		Hematite	ts_hemat	
14		K-feldspar	ts_kfeld	
15		Olivine	ts_olvne	
16		Plagioclase	ts_plgcl	
17		Quartz	ts_quatz	
18		Sulfate	ts_sulft	
19		Dust	ts_dustm	
20		Dust Cover Index (DCI)	ts_dcimp	Ruff and Christensen (2002)
21		Thermal Inertia-Day	ts_tiday	Putzig and Mellon (2007)
22		Thermal Inertia-Night	ts_tingt	
23	GRS	H_2O	gr_h2omp	Boynton et al. (2007)
24		Si	gr_simap	
25		K	gr_kmaps	
26		Cl	gr_clmap	
27		Fe	gr_femap	
28		Th	gr_thmap	
29	VIKING	Global Mosaic 232m v2	vk_color	USGS Astrogeology
30	MGS	MOLA DEM	mg_mldem	Smith et al. (2001)
31		Hilshade map from MOLA	mg_hilsd	
32		Slope map from MOLA	mg_slope	
	VECTOR			
33		Geology Map of Mars 2014	tn_geolo	Tanaka et al. (2014b)
34		Hydrous mineral map	ct_hydst	Carter et al. (2013)
35		Open-closed basins	tg_basin	Goudge et al. (2016)
36		Valley Network	ga_vlnet	Alemanno et al. (2018)
37		Long Valley	ga_logvl	Alemanno et al. (2018)
38		Trough Fluvial	tn_trflu	Tanaka et al. (2014b)
39		Pyroclastic ash distribution	lk_pyash	Kerber et al. (2013)
40		Pyroclastic deposits	pb_pydep	Broz et al. (2020)

8.3.2 Weights-of-evidence method

The weights-of-evidence method (WEM) was originally developed in the field of quantitative medical diagnosis and later applied to the prediction of mineral deposits by Bonham-Carter et al. (1989). This data-driven approach can estimate the relative importance of individual layers (maps) of evidence by statistical means (Bayesian relation) under the assumption that all variables are conditionally independent of mineral occurrences (Pan and Harris, 2000). For simplicity, the integration of two explanatory binary maps by WEM will be discussed. The two explanatory indicator maps, the pyroclastic ash

deposits map and closed basins map as examples in this case, are denoted by A and C, respectively. The single target indicator variable, in this case the location map of detected hydrous minerals, is indicated by H. These maps are regarded as random variables that are either present or absent (binary) in a unit cell. The possible relations between C, A, and H are shown in the Figure 8.2 Venn diagram. $\bar{A}$, $\bar{C}$, and $\bar{H}$ represent the absence status of A, C, and H, respectively.

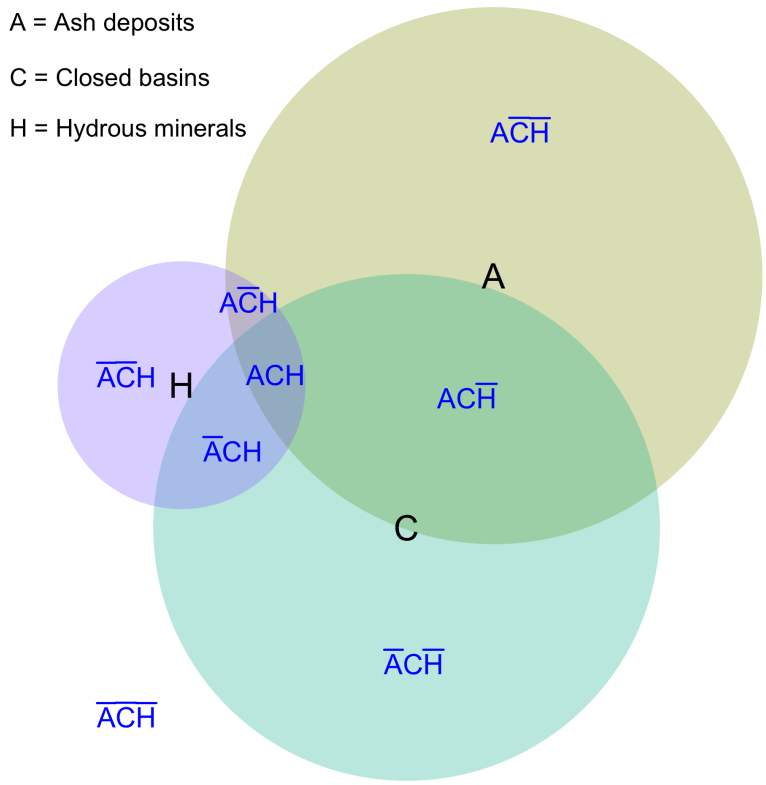

Figure 8.2: Venn diagram for the relations between binary patterns.

The prior probability $p\{H\}$ is the probability of the occurrence of hydrous minerals in the entire study area, which can be calculated using the ratio of detected hydrous mineral pixels (or area), H to the total number of pixels in the study area (or total area), T.

$$p(H) = \frac{H}{T} \quad \text{(eq. 8.1)}$$

The relations between A, C, and H can be expressed by eight probabilities based on the assumption of conditional independence between A and C with respect to H.

$$p(ACH), p(AC\bar{H}), p(A\bar{C}H), p(\bar{A}CH), p(\bar{A}\bar{C}H), p(\bar{A}C\bar{H}), p(A\bar{C}\bar{H}), p(\bar{A}\bar{C}\bar{H})$$

These eight probabilities are mutually related by,

$p(ACH) = p(A|H)p(C|H)p(H)$ ———— (eg. 8.2)

$p(AC\bar{H}) = p(A|\bar{H})p(C|\bar{H})p(\bar{H})$ ———— (eq. 8.3)

Based on the above relations, four conditional probabilities (posterior probabilities) can be calculated. As an example,

$p\frac{(A)}{(H)} = \frac{p(A)\times p(H/A)}{p(H)}$ ————- (eq. 8.4)

where, H is the occurrence of hydrous minerals, A is the pyroclastic deposits map, and $p(H/A)$ is the conditional probability of having hydrous minerals in the area, where pyroclastic deposits are present.

Four weights, W_A^+, W_A^-, W_C^+, and W_C^- can be calculated for each evidence class and these weights are dependent on the spatial relationship between the potential occurrence of hydrous minerals and the selected evidence map.

$W_A^+ = ln\{p(A|H)/p(A|\bar{H})\}$, $W_A^- = ln\{p(\bar{A}|H)/p(\bar{A}|\bar{H})\}$—— (eq. 8.5)

$W_C^+ = ln\{p(C|H)/p(C|\bar{H})\}$, $W_C^- = ln\{p(\bar{C}|H)/p(\bar{C}|\bar{H})\}$—— (eq. 8.6)

W^+ in each evidential map indicates the importance of the presence of the factor class for the occurrence of hydrous minerals. Positive W^+ values for a factor class indicate its favorability for the occurrence of hydrous minerals, while negative W^+ values denote unfavorability. W^- is used to evaluate the importance of the absence of the factor class for the occurrence of hydrous minerals. If W^- is positive, it indicates that the absence of the factor class makes the area more suitable for occurrence of hydrous minerals. When W^- is negative, absence of the factor class is unfavorable. Zero weights do not have correlation between the factor class and hydrous mineral occurrences.

The contrast ($C = W^+ - W^-$) represents the strength of association between the explanatory map (e.g., pyroclastic deposit map, A) and the target map (e.g., detected hydrous mineral location map, H). Large contrast values imply strong association between two factors while small contrast values indicate the opposite. The studentized contrast (C_{std}, also called the normalized contrast) is defined as the ratio of C to its standard deviation ($S(C)$) and is used as an indicator of confidence.

$C_{std} = \frac{C}{\sqrt{S^2(W^+)+S^2(W^-)}}$ ———— (eq. 8.7)

where, $S^2(W^+)$ and $S^2(W^-)$ are the variances of W^+ and W^-, respectively.

The hydrous mineral train points (1391 points) were used to calculate the weight values (W^+, W^-), C, and C_{std} for each class in each map. Based on the weights and C_{std}, the study proceeded with the 30 selected factor maps (Table 8.2). These maps are spatially highly correlated (positively and negatively) with the hydrous mineral detections.

8.3.3 Fuzzy Set Theory

Most of the tools used for formal modeling, reasoning, and computing are crisp, deterministic, and precise in character. It is yes-or-no-type rather than more-or-less type. As an example, zeolite is present-or-not in the closed basin of Mars, instead of more possibility/ less possibility (can be/ cannot be) present. In classical set theory, an element can either belong to a set or not, the same as in optimization, a solution is either feasible or not. Fuzzy set theory, coined by Lotif A. Zadeh (Zadeh, 1965), involves capturing, representing, and working with linguistic notions-objects with unclear boundaries. While the Boolean set theory defines a membership which is either 1 or 0 (true or false), the fuzzy set theory defines a degree of membership in a set, represented by any value between 0 and 1.

Let X be a collection of objects, with a generic element of X denoted by x.

Thus, $\mathrm{X} = \{x\}$.

A fuzzy set A in X is characterized by a membership function (or grade of membership or degree of compatibility or degree of truth) $f_A(x)$ which associates with each object in X a real number in the interval [0,1], with the value of $f_A(x)$ at x representing the *grade of membership* of x in A. The membership function of a fuzzy set A is denoted by μ_A and its form is

$\mu_A : X \rightarrow [0,1]$ ———————— (eq. 8.8)

Typically, a fuzzy model consists of the following feedforward modules, 1) a fuzzifier (encoder: convert input categorical or numerical data into fuzzy values), 2) an inference engine (processor: the mind of the fuzzy model, simulate the human decision-making process), and 3) a defuzzifier (decoder: convert synthesized fuzzy set back to a crisp set using a mathematical function or a subjectively or objectively defined threshold fuzzy value).

Fuzzifier: Fuzzification of Predictor Maps

The value of the membership function can be determined by two methods; 1) calculate the membership function using a membership function curve, 2) assign membership values for each class artificially based on expert knowledge of the system concerned. In this study both methods were adopted. For the factor maps of valley network (ga_vlnet), ash thickness (lk_pyash), and map of open/closed basins (tg_basin), fuzzy membership values were added manually, while the fuzzy membership values for the rest of the maps were calculated using membership function curves.

In this study, four membership functions were modeled, and results were compared to select the best method. The methods include membership function calculation using positive weight (W^+), contrast (C), and studentized contrast (C_{std}) of each map unit calculated using the WEM method.

Method 1 ***(Zimmermann, 1991).***

Logistic membership function, $\mu_A(x)$,

$\mu_A(x) = \frac{1}{1+e^{-a(w_{pij}-b)}}$ ———— (eq. 8.9)

where, w_{pij} is the positive weight of the jth class of the ith evidential map (fuzzy set), b is a specified fuzzy score at cross-over point for the function, a is a specified slope of the function at cross-over point. Slope values, a, used for each factor map are shown in table 8.2. The value of the cross-over point, b, is assigned as 0.5. The logistic membership function transforms the class weights into fuzzy membership values that range from 0 to 1.

Method 2 ***(Cheng and Agterberg, 1999).***

Fuzzy membership values were calculated using the contrast values in each evidential map,

$\mu_A(x) = \frac{C_{ij}-C_{min}}{C_{max}-C_{min}}$ ———— (eq. 8.10)

where, C_{max} and C_{min} are the maximum contrast ($C_{max} = max(W^+ - W^-)$), and the minimum contrast of ith fuzzy set, respectively. C_{ij} is the contrast value of the jth class in the ith evidential map.

Method 3 *(Porwal et al., 2003).*

Porwal et al. (2003) defined the piece-wise linear membership function as the fuzzifier in their model based on the contrast value. The membership value, $\mu_A(x_{ij})$ is calculated using

$$\mu_A(x) = \begin{cases} 0.01 & if \quad C_{ij} = C_{min} \& C_{min} < 0 \\ 0.5 - \frac{C_{ij}}{2 \times C_{min}} & if \quad C_{min} < C_{ij} \leq 0 \\ 0.5 + \frac{C_{ij}}{2 \times C_{max}} & if \quad 0 \leq C_{ij} \leq C_{max} \end{cases} \text{——— (eq. 8.11)}$$

where, C_{ij} is the contrast value of the jth class of ith evidential map, C_{min} and C_{max} are the minimum and maximum contrast values of the ith map.

Method 4 *(this study)*

Logistic membership function, $\mu_A(x)$,

$$\mu_A(x) = \frac{1}{1+e^{-a((w_{pij} \times F)-b)}} \text{ ——— (eq. 8.12)}$$

where, w_{pij} is the positive weight of the the jth class of ith evidential map. b is a specified fuzzy score at the cross-over point for the function, a is a specified slope of the function at the cross-over point. Multiplication factor F was calculated using studentized contrast (C_{std}) of each class in each evidential map.

$$F = \begin{cases} 0.1 & C_{std} < 1.5 \\ 1.0 & C_{std} \geq 1.5 \end{cases} \text{ ———- (eq. 8.13)}$$

The fuzzy membership values must reflect the relative importance of each map, as well as the relative importance of each class (map units) in each map. Therefore, different slope values "a" were chosen for each map based on the importance of each map and their classes (map units) (Table. 8.2). The fuzzy membership function maps are named using the respective MapID followed by prefix fzm_.

Table 8.2: Slope a values used in Logistic membership functions (eq. 8.9 and 8.12).

Map 1 - 10	a	Map 11 - 20	a	Map 21 - 30	a
fzm_gr_femap	1	fzm_ts_kfeld	1	fzm_gr_h2omp	3
fzm_gr_kmaps	1	fzm_ts_olvne	1	fzm_om_fe530	4
fzm_om_osp1m	1	fzm_ts_plgcl	1	fzm_om_nnphs	4
fzm_om_osp2m	1	fzm_ts_sulft	1	fzm_tn_geomp	5
fzm_om_osp3m	1	fzm_gr_simap	2	fzm_gr_clmap	5
fzm_om_pyrox	1	fzm_gr_thmap	2	fzm_mg_mldem	5
fzm_ts_amphi	1	fzm_ts_carbo	2	fzm_om_albdo	5
fzm_ts_hcpmp	1	fzm_ts_quatz	2	fzm_ts_albdo	5
fzm_ts_lcpmp	1	fzm_ts_tiday	2	fzm_ts_dcimp	5

Map 1 - 10	*a*	Map 11 - 20	*a*	Map 21 - 30	*a*
fzm_ts_hemat	1	fzm_ts_tingt	2	fzm_ts_dustm	5

The fuzzy membership values of the different map units in the geologic map calculated using the above four methods are shown in Figure 8.3. This shows that the method developed in this study (Method 4) performs best and was therefore chosen as the fuzzy membership calculation method for this study.

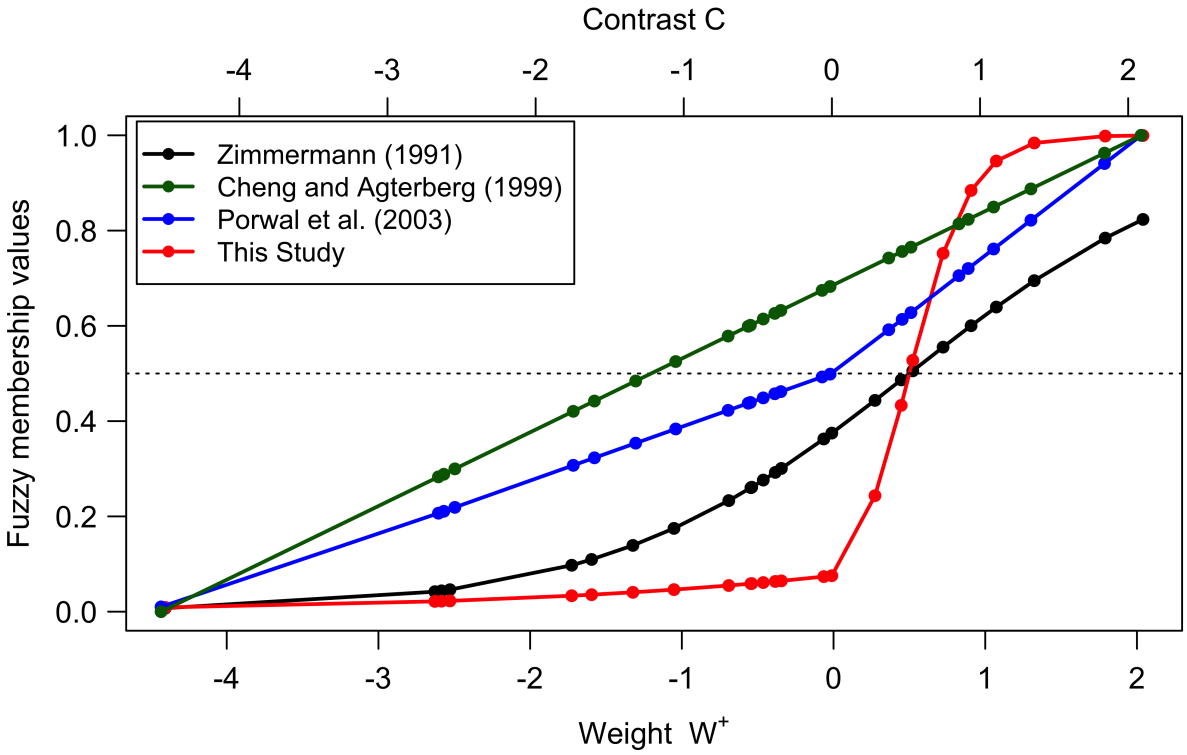

Figure 8.3: Calculation of fuzzy membership functions using different methods. The geology map (tn_geomp) was used as the example in this figure. The Weights W^+ x-axis refers to Method 1 (Zimmermann, 1991), and Method 4 developed in this study, while the Contrast C x-axis refers to Method 2 (Cheng and Agterberg, 1999) and Method 3 (Porwal et al., 2003).

Figure 8.4 plots the fuzzy membership values against the geological map units in (relative) chronological order. It shows that high fuzzy membership values were received for the Noachian age terrains, where most hydrous mineral detections were found (Carter et al., 2013). Hesperian and Noachian highland undivided (HNhu) and Hesperian transition terrains (Htu and Ht) show high Fuzzy membership values after high values seen in Early and Middle Noachian highland massifs (mHnm and eNhm). The peak observed

at the Late Noachian to Early-Hesperian transition has been proposed as an epoch of intense surface flow (Irwin et al., 2005). Carter et al. (2013) observed fever hydrous mineral exposures in Hesperian aged terrain, and a negligible number of hydrous mineral exposures in Amazonian-aged terrains. Figure 8.4 also shows a peak for Amazonian and Hesperian impacts (AHi). This might be due to the delivery of preexisting clay-rich material underneath more recent terrains to the surface by impact excavation (Barnhart and Nimmo, 2011). It is also important to note that the number of hydrous mineral occurrences corresponding to geologic units does not necessarily reflect the time of their formation. Those hydrous mineral detections can be younger (e.g., weathering) or older (e.g., transported from other place and deposited) than the outcrop (geologic unit) in which they are present (Carter et al., 2013).

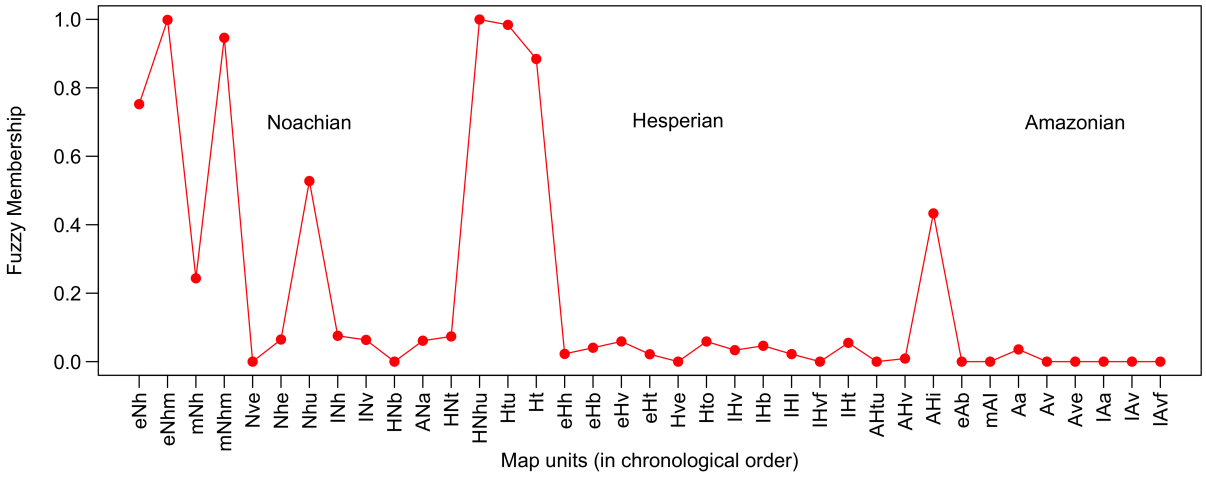

Figure 8.4: Calculated fuzzy membership values as a function of time (geological units). eNh: Early Noachian highland, eNhm: Early Noachian highland massif, mNh: Middle Noachian highland, mNhm: Middle Noachian highland massif, Nve: Noachian volcanic edifice, Nhe: Noachian highland edifice, Nhu: Noachian highland undivided, lNH: Late Noachian highland, lNv: Late Noachian volcanic, HNb: Hesperian and Noachian basin, ANa: Amazonian and Noachian apron, HNt: Hesperian and Noachian transition, HNhu: Hesperian and Noachian highland undivided, Htu: Hesperian transition undivided, Ht: Hesperian transition, eHh: Early Hesperian highland, eHb: Early Hesperian basin, eHv: Early Hesperian volcanic, eHt: Early Hesperian transition, Hve: Hesperian volcanic edifice, Hto: Hesperian transition outflow, lHv: Late Hesperian volcanic, lHb: Late Hesperian basin, lHl: Late Hesperian lowland, lHvf: Late Hesperian volcanic field, lHt: Late Hesperian transition, AHtu: Amazonian and Hesperian transition undivided, AHv: Amazonian and Hesperian volcanic, AHi: Amazonian and Hesperian impact, eAb: Early Amazonian basin, mAl: Middle Amazonian lowland, Aa: Amazonian apron, Av: Amazonian volcanic, Ave: Amazonian volcanic edifice, lAa: Late Amazonian apron, lAv: Late Amazonian volcanic, lAvf: Late Amazonian volcanic field.

Fuzzy membership function values were manually added to the factor maps of valley network (ga_vlnet) and ash thickness (lk_pyash) (Table 8.3). These membership values were chosen arbitrarily based on subjective judgment about the relative importance of each class (map unit) in each factor map.

Table 8.3: Fuzzy membership values (fzm) in map classes of maps of valley networks (ga_vlnet) and ash thickness map (lk_pyash).

ga_vlnet distance class	fzm_ga_vlnet	lk_pyash thickness class	fzm_lk_pyash
0 - 200 m	1.0	0.00 - 6.25 m	0.1
200 - 400 m	0.9	6.25 - 12.50 m	0.2
400 - 600 m	0.8	12.50 - 25.00 m	0.4
600 - 800 m	0.7	25.00 - 50.00 m	0.5
800 - 1000 m	0.6	50.00 - 100.00 m	0.6
1000 - 2500 m	0.5	100.00 - 200.00 m	0.7

ga_vlnet distance class	fzm_ga_vlnet	lk_pyash thickness class	fzm_lk_pyash
2500 - 5000 m	0.4	200.00 - 400.00 m	0.8
5000 - 10000 m	0.3	400.00 - 800.00 m	1.0
10000 - 100000 m	0.2		
> 100000 m	0.1		

Figure 5 shows the entire fuzzification process using MOLA DEM as an example. It shows the original MOLA DEM (a), classified MOLA DEM (b) and after assigning the calculated fuzzy membership values for each elevation class (c).

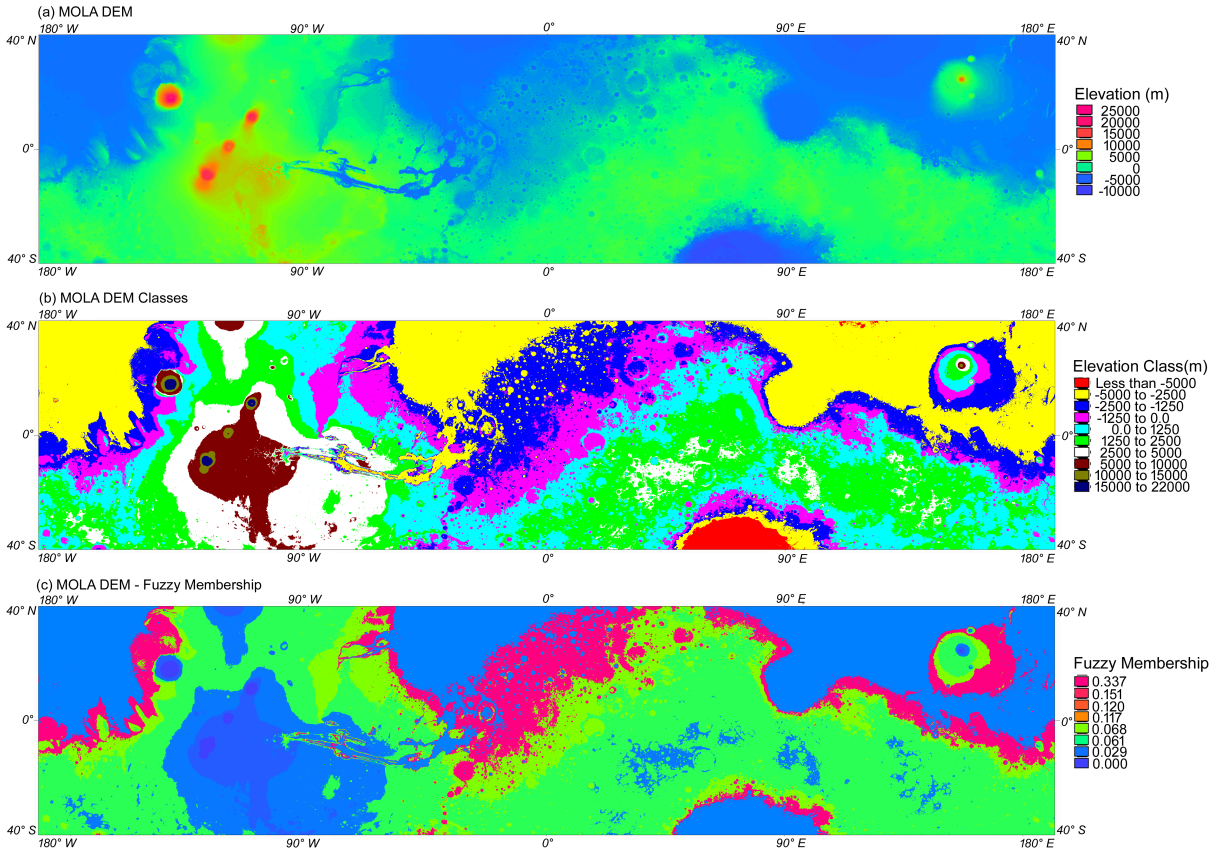

Figure 8.5: Fuzzification process showing the original MOLA DEM (a), classified MOLA DEM (b), and a map after assigning the fuzzy membership values for each elevation class (c).

Inference Engine

The inference engine, the "mind" of a fuzzy model, creates a synthesized fuzzy set from the individual fuzzy sets transmitted by the fuzzifier while filtering out the informational noise. A fuzzy inference engine consists of multiple parallel or serial networks that

sequentially combine fuzzy sets through fuzzy operators (Porwal et al., 2003). The most basic fuzzy operators are fuzzy OR, fuzzy AND, fuzzy algebraic products, fuzzy algebraic sum, and fuzzy Gamma (γ) operator.

Fuzzy OR

Fuzzy OR is equivalent to a Boolean OR (logical union) in that the output membership values are controlled by the maximum values of any of the input maps, for any particular location. The fuzzy OR is defined as,

$\mu_X = MAX(\mu_A, \mu_B, \mu_C, ...)$ ———(eq. 8.14)

using this operator, the combined membership value at a location is limited only by the most suitable of the evidence maps. As an example, several attempts were made to derive the abundance of olivine using OMEGA and TES data. This study also selected four olivine maps as factor maps and fuzzy OR operator used to integrate those maps to extract the most suitable locations for olivine. Fuzzy OR operator was used to create the maps listed below,

max_gr_clfek = MAX(fzm_gr_clmap,fzm_gr_femap,fzm_gr_kmaps)–(eq. 8.15)

max_olivine = MAX(MAX(fzm_om_osp1m,fzm_om_osp2,fzm_om_osp3), zm_ts_olvne)–(eq. 8.16)

max_pyrox = MAX(fzm_ts_lpcmp,fzm_ts_hcpmp,fzm_om_pyrox)–(eq. 8.17)

max_qtz_crb_hem = MAX(fzm_ts_quatz,fzm_ts_carbo,fzm_ts_hemat)–(eq. 8.18)

Fuzzy AND

Fuzzy AND is equivalent to a Boolean AND (logical intersection) operation on classical set values of (0,1). It is defined as

$\mu_X = MIN(\mu_A, \mu_B, \mu_C, ...)$ ————————(eq. 8.19)

where, $\mu_A m, \mu_B, \mu_C, ...$ are membership values at a particular location (x,y) of map A, map B, map C,.., respectively. The effect of Fuzzy AND is to make the output map be controlled by the smallest fuzzy membership value occurring at each location (Bonham-Carter, 1994). This rule is appropriate where two or more pieces of evidence for a hypothesis must be present together for the hypothesis to be true. In this study, as an

example, selecting the minimum albedo fuzzy membership value in each corresponding pixel in albedo fuzzy membership maps derived from both OMEGA and TES data will increase the confidence of the final albedo fuzzy membership map. Fuzzy AND operator was used to create the maps listed below,

min_dust_nnphs = MIN(fzm_ts_dustm,fzm_ts_dcimp,fzm_om_nnphs)–(eq. 8.20)

min_om_ts_albdo = MIN(fzm_om_albdo,fzm_ts_albdo)–(eq. 8.21)

min_ti_day_ngt = MIN(fzm_ts_tiday,fzm_ts_tingt)–(eq. 8.22)

min_gr_clfek = MIN(fzm_gr_clmap,fzm_gr_femap,fzm_gr_kmaps)–(eq. 8.23)

Finally, six maps were created combining above fuzzy membership maps.

min_physical = MIN(min_dust_nnphs,min_om_ts_albdo,min_ti_day_ngt)–(eq. 8.24)

max_physical = MAX(min_dust_nnphs,min_om_ts_albdo,min_ti_day_ngt)–(eq. 8.25)

min_elements = MIN(min_gr_clfek,fzm_gr_simap,fzm_gr_h2omp)–(eq. 8.26)

max_elements = MAX(max_gr_clfek,fzm_gr_simap,fzm_gr_h2omp)–(eq. 8.27)

min_minerals = MIN(max_olivine,max_pyrox,max_qtz_crb_hem)–(eq. 8.28)

max_minerals = MAX(max_olivine,max_pyrox,max_qtz_crb_hem)–(eq. 8.29)

Using either fuzzy OR or fuzzy AND, a fuzzy membership of a single piece of evidence controls the output values. Figure 8.6 shows two output maps created from two different set of fuzzy operators. Though the input maps for both sets were the same, different output maps were made based on the fuzzy operators used (eq. 8.24 and 8.25).

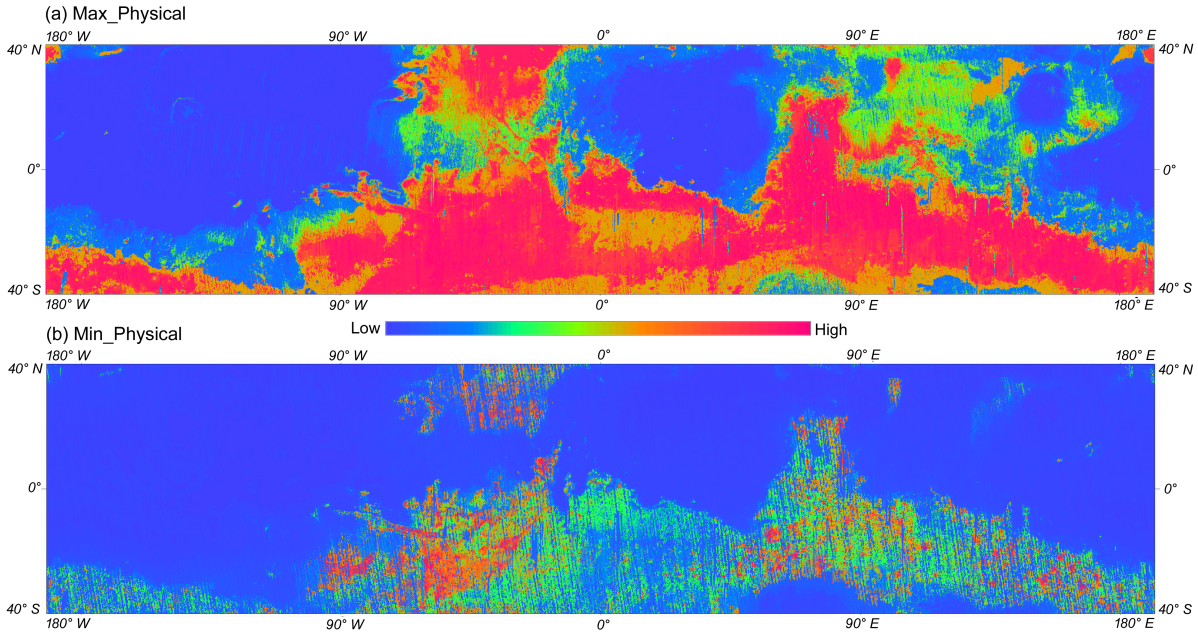

Figure 8.6: Integrated fuzzy membership maps. a) Max_physical (eq. 8.25), and b) Min_physical (eq. 8.24).

Fuzzy Algebraic Product (FAP)

The combined membership function is defined as

$\mu_X = \prod_{i=1}^{n} \mu_i$ ——————(eq. 8.30)

where μ_i is the fuzzy membership function for the i-th map and i = 1,2,3,. . . .,n maps are to be combined. The combined fuzzy membership values tend to be very small with this operator, due to the effect of multiplying several numbers less than 1. The output is always smaller than, or equal to, the smallest contributing membership value, and is therefore "decreasive".

Fuzzy Algebraic Sum (FAS)

Fuzzy algebraic sum is complementary to the fuzzy algebraic product and defined as

$\mu_X = 1 - \prod_{i=1}^{n}(1 - \mu_i)$ ——————(eq. 8.31)

The result is always larger or equal to the largest contributing fuzzy membership value. The effect is therefore "increasive." The pieces of evidence that both favor a hypothesis reinforce one another and the combined evidence is more supportive than either piece of evidence taken individually. It is also important to note that whereas

the fuzzy algebraic product is an algebraic product, the fuzzy algebraic sum is not an algebraic summation (Bonham-Carter, 1994).

Six map combinations were selected using seven input maps created during the previous step (Table 8.4). From these six map combinations, twelve maps were created calculating fuzzy algebraic product (FAP) and fuzzy algebraic sum (FAS). The resulting fuzzy algebraic products (FAP) and algebraic sum (FAS) maps for the sixth map combination (FAP_6 and FAS_6 in Table 8.4) is shown in Figure 8.7.

Table 8.4: Input map combinations used to create 12 map combinations. FAP: fuzzy algebraic product. FAS: fuzzy algebraic sum.

Map combination	FAP_1 FAS_1	FAP_2 FAS_2	FAP_3 FAS_3	FAP_4 FAS_4	FAP_5 FAS_5	FAP_6 FAS_6
min_physical	x		x	x		
max_physical		x			x	x
min_elements			x			
max_elements	x	x				
min_minerals	x		x		x	
max_minerals		x		x		x
fzm_geology	x	x	x	x	x	x

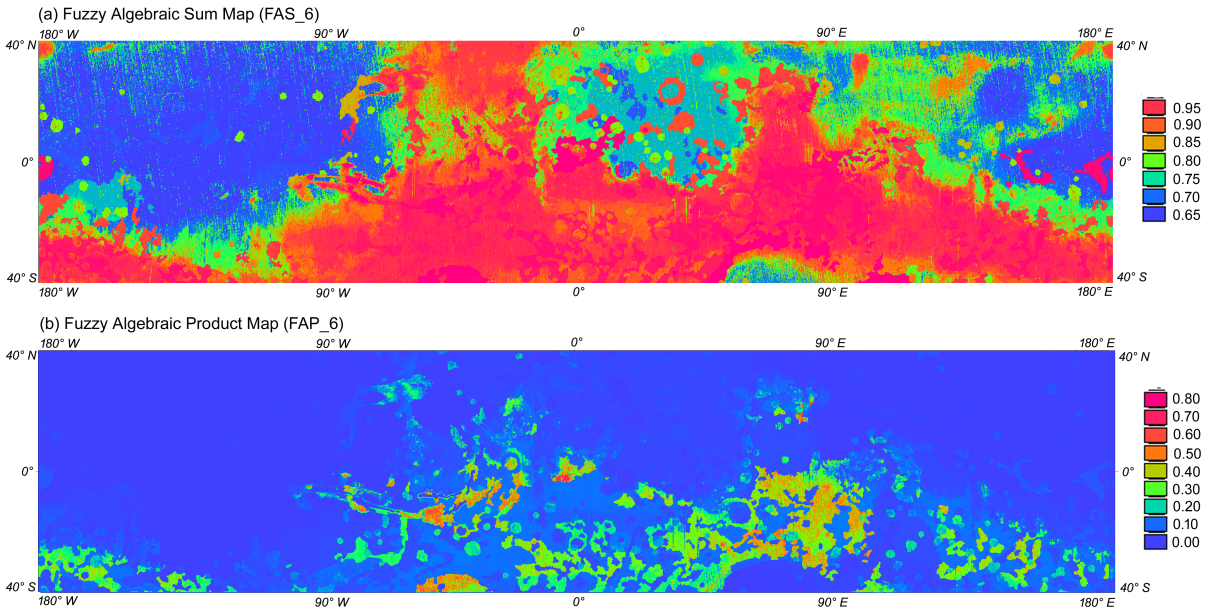

Figure 8.7: Fuzzy algebraic product (FAP) and fuzzy algebraic sum (FAS) maps of map combination 6 (FAP_6 and FAS_6) listed in Table 8.4.

Gamma (γ) operation.

Gamma operation is defined in terms of fuzzy algebraic product and the fuzzy algebraic sum by

$$\mu_X = (Fuzzyalgebraicsum)^{\gamma} * (Fuzzyalgebraicproduct)^{1-\gamma} \text{ ———(eq. 8.32)}$$

where γ is a parameter chosen in the range (0,1) (Zimmermann and Zysno, 1980). When γ is 1, the combination is the same as the fuzzy algebraic sum; and when γ is 0, the combination equals the fuzzy algebraic product. A judicious choice of γ produces output values that ensure a flexible compromise between the "increasive" tendencies of the fuzzy algebraic sum and the "decreasive" effects of the fuzzy algebraic product. The effect of choosing different values of gamma (γ) for combining two fuzzy memberships values is shown in Figure 8.8.

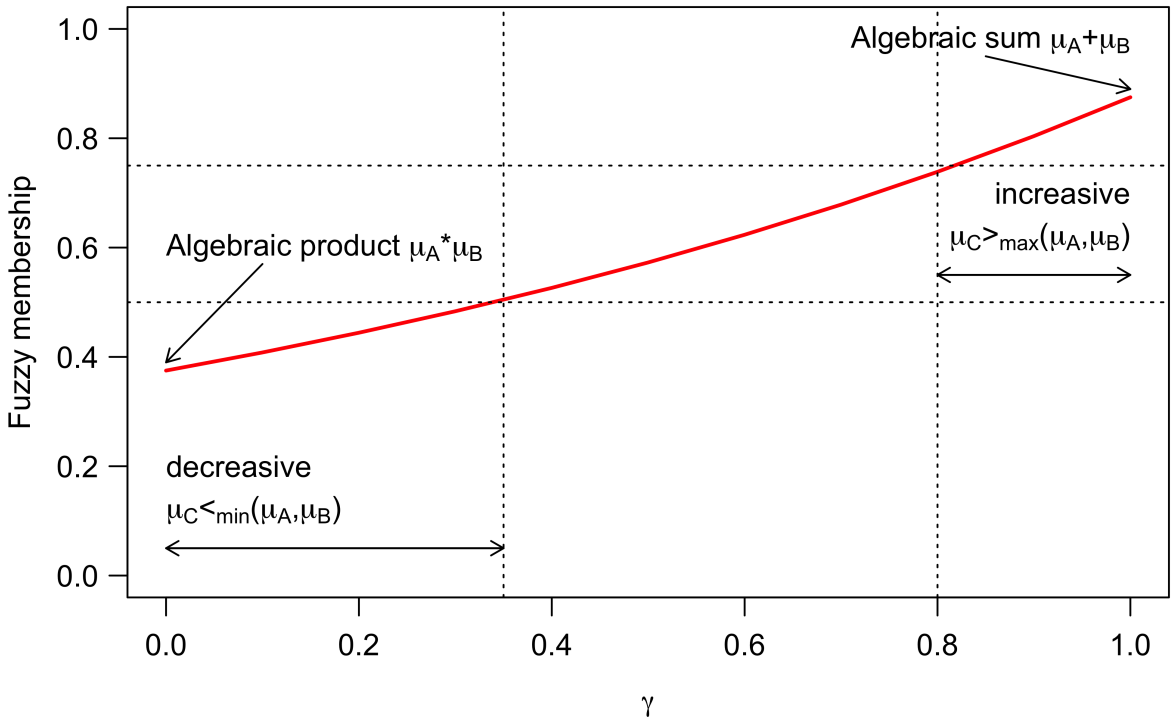

Figure 8.8: A graph of fuzzy membership obtained by combining two fuzzy membership values versus gamma.

Twenty-five (25) maps were calculated using different map combinations listed in Table 8.4 with different gamma values (Table 8.5). In other words, 25 inference network models were created. After visual and statistical analysis of all the 25 maps, map combinations 2

(Fz_02_) and 6 (Fz_06) in Table 8.4 were selected for further analysis. Figure 8.9 shows the favorability coverage and the test and train accuracy of each map combination with respect to the gamma values. Favorability coverage were calculated based on the area higher than 0.5 fuzzy membership values (pixel values) to the total map area. This shows that the percentage of (favorability) coverage and test and train accuracy of both map combinations increases with the increase of gamma values. The best predictive model in this case would be the model with the highest train and test accuracy with the lowest spatial coverage. The test and train accuracy (success rate) higher than 80% were defined as the selection criteria and based on that a 0.84 gamma value was selected. However, both map combinations (F2 and F6) scored more than 80% accuracy, though the F6 shows higher spatial coverage than F2. Four favorability map classes were created from each map (Fz_02_0.84 and Fz_06_0.84) based on the favorability index (pixel values). Classes include Unfavorable (pixel value 0 - 0.25), Less favorable (pixel value 0.25 - 0.50), Favorable (pixel value 0.50 - 0.75), and Most favorable (pixel value 0.75 - 1.00). This step is called as defuzzification. Results were validated using train and test data sets. Table 8.6 shows the results of the accuracy assessment. The values are in percentages representing the number of data points in each class with respect to the total number of points in the dataset. This shows that Fz_06_0.84 (final map created using map combination F6 with 0.84 gamma value) has the highest test and train accuracy for the most favorable class. Therefore, map F_06_0.84 was selected as the final map to depict the highest potential areas for hydrous minerals (Figure 8.10) and to identify the potential locations for zeolite in the next step.

Table 8.5: List of calculated 25 maps using different map combination and gamma values.

Map 1 - 5	Map 6 - 10	Map 11 - 15	Map 16 - 20	Map 21 - 25
Fz_01_0.65	Fz_02_0.80	Fz_02_0.85	Fz_03_0.97	Fz_06_0.82
Fz_01_0.75	Fz_02_0.81	Fz_03_0.85	Fz_04_0.85	Fz_06_0.83
Fz_01_0.85	Fz_02_0.82	Fz_03_0.90	Fz_05_0.85	Fz_06_0.84
Fz_01_0.90	Fz_02_0.83	Fz_03_0.95	Fz_06_0.80	Fz_06_0.85
Fz_01_0.95	Fz_02_0.84	Fz_03_0.96	Fz_06_0.81	Fz_06_0.86

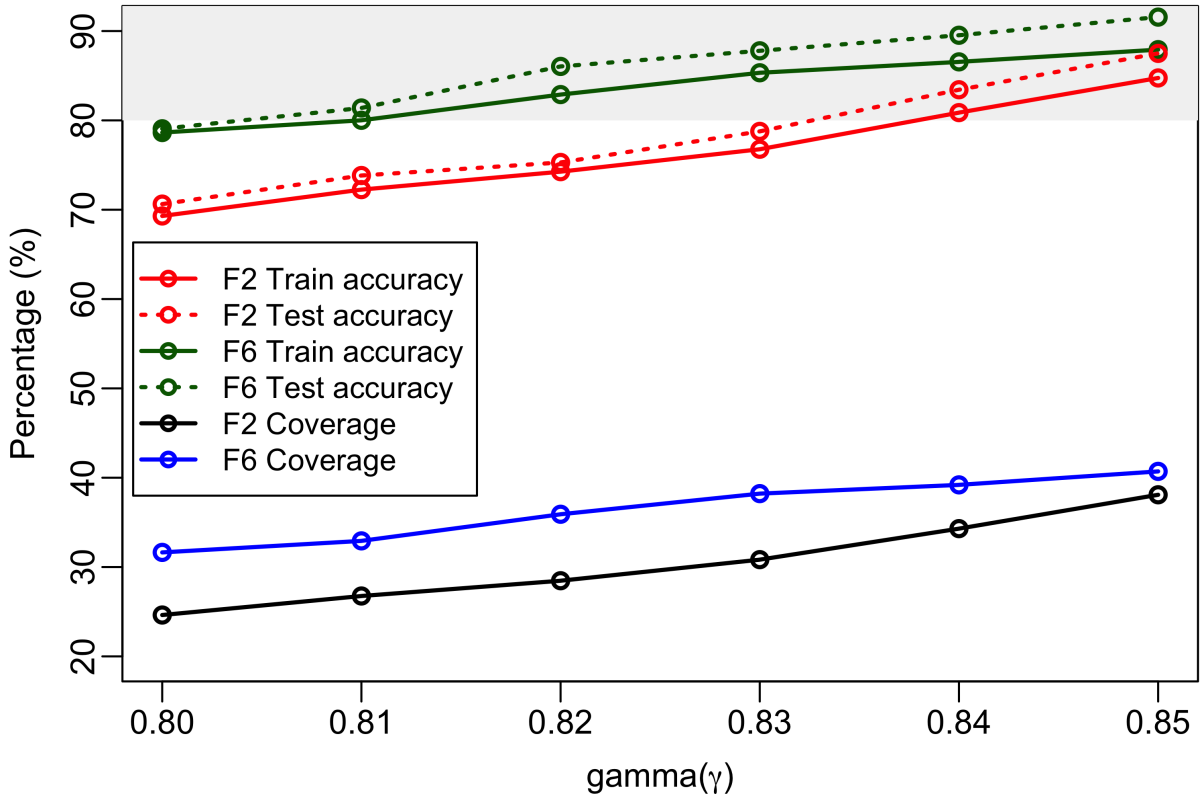

Figure 8.9: Percentage accuracy and spatial coverage in each map combination (F2 and F6) against different gamma values.

Table 8.6: Test and train accuracy (success rate) of each map combinations. This shows the number of hydrous mineral detections in each class as a percentage with respect to the total number of data points. The train dataset is indicated by letters "_trn" after the fuzzy map Fz_02_0.84 or Fz_06_0.84, while the test dataset indicated by letters "_tst".

Class	Fz_02_0.84_trn	Fz_02_0.84_tst	Fz_06_0.84_trn	Fz_06_0.84_tst
Unfavorable	0.1	0	0.3	0
Less favorable	18.9	16.5	13.1	10.4
Favorable	75.5	78.5	54.6	57.3
Most favorable	5.5	5.0	32.0	32.3

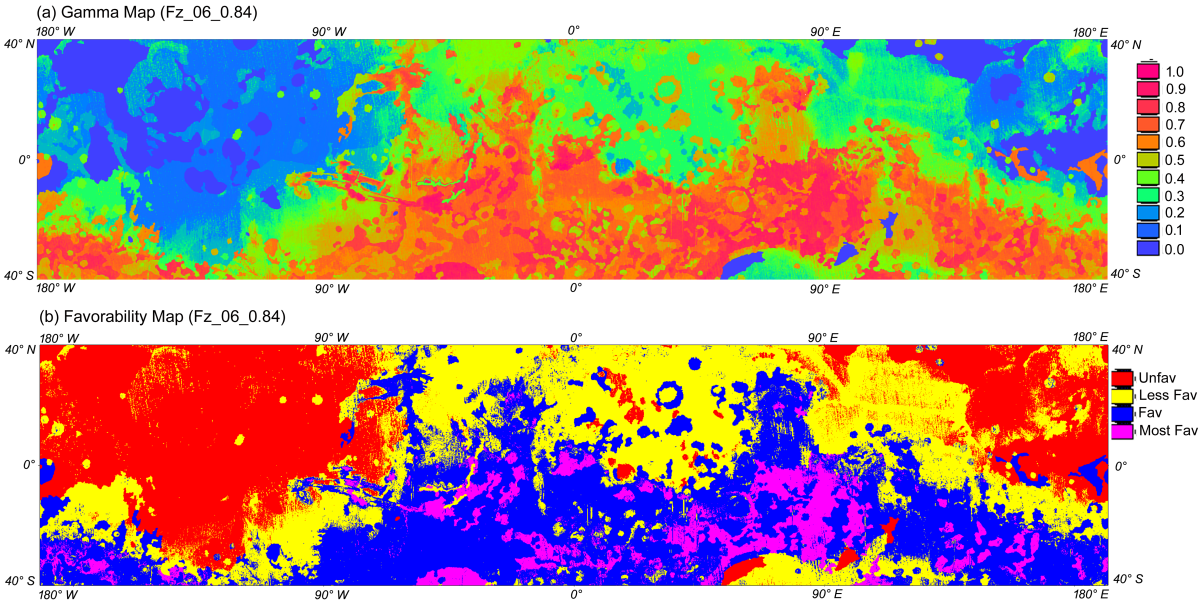

Figure 8.10: a) Favorability map for hydrous minerals (Map Fz_06_0.84). Areas ranked according to fuzzy membership values. The fuzzy set comprises those locations that satisfy the proposition favorable for hydrous minerals. Fuzzy membership ranges from 0 to 1 (less favorable to highly favorable). b) Favorability class map derived from map (a) showing the potential area for hydrous minerals on Mars up to 40 degrees latitude.

As discussed in the introduction, the highest concentrations of zeolites on Earth are found in volcaniclastic deposits. Therefore, it is hypothesized that zeolites are most likely to be found in places where pyroclastic deposits were subjected to aqueous alteration. The possible aqueous alteration areas were mapped using hydrous mineral detections in previous steps. Ash distribution patterns on Mars modeled by Kerber et al. (2013) were used to identify the most favorable areas for the presence/formation of zeolites on early Mars. Ash thickness in their model is proportional to the possibility of formation of zeolites because high thickness can reflect large amount of ash in an area or a high possibility of finding ash in the area according to the model. The map of possible pyroclastic deposits larger than $10^5 km^2$ is also used in this study to achieve more robust results. The open and closed basin paleolakes map is finally used to select the most likely paleolake basins to look for zeolites using detailed orbital studies. The ash thickness map modelled by Kerber et al. (2013), potential pyroclastic deposits (black outlines), and closed and open basin paleolakes (black filled areas) are shown in Figure 8.11. Ash thickness in the map is

represented by the fuzzy membership values. Assigned fuzzy membership values positively increase with the modeled ash thickness (Table 8.3).

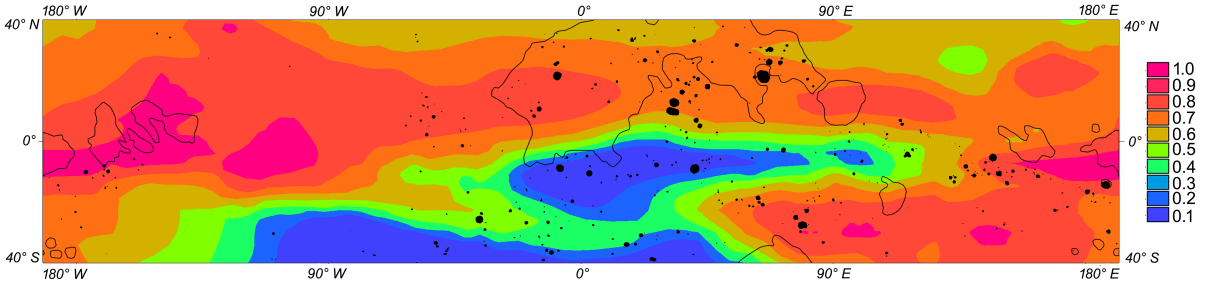

Figure 8.11: The map shows the thickness of possible ash deposits modelled by Kerber et al. (2013), pyroclastic ash deposits (black outline) compiled by Broz et al. (2020) and open and closed basins (black filled areas) compiled by Goudge et al. (2016). Values in the legend are fuzzy membership values corresponding to the thickness of the modeled ash deposits.

Figure 8.12 shows the three-stage inference engine used to create the final map. Only the inference engine (workflow) of the selected final map (Fz_06_0.84) was outlined here to make the flow chart clear and simple. At the first stage, all the fuzzified evidential maps which were created using the membership functions defined by the weight-of-evidence method were combined using fuzzy operators to yield three intermediate fuzzy evidential maps (max_physical, max_mineral, tn_geolo). These maps were later combined in the second stage using the fuzzy gamma (γ) operator to generate the synthesized fuzzy favorability map for the hydrous minerals (fav_hydrous). In the third step, the hydrous mineral favorability fuzzy membership map was combined with ash thickness (lk_pyash), pyroclastic deposits (pb_pydep), and open and closed basin (tg_basin) maps to generate a favorability map for zeolites.

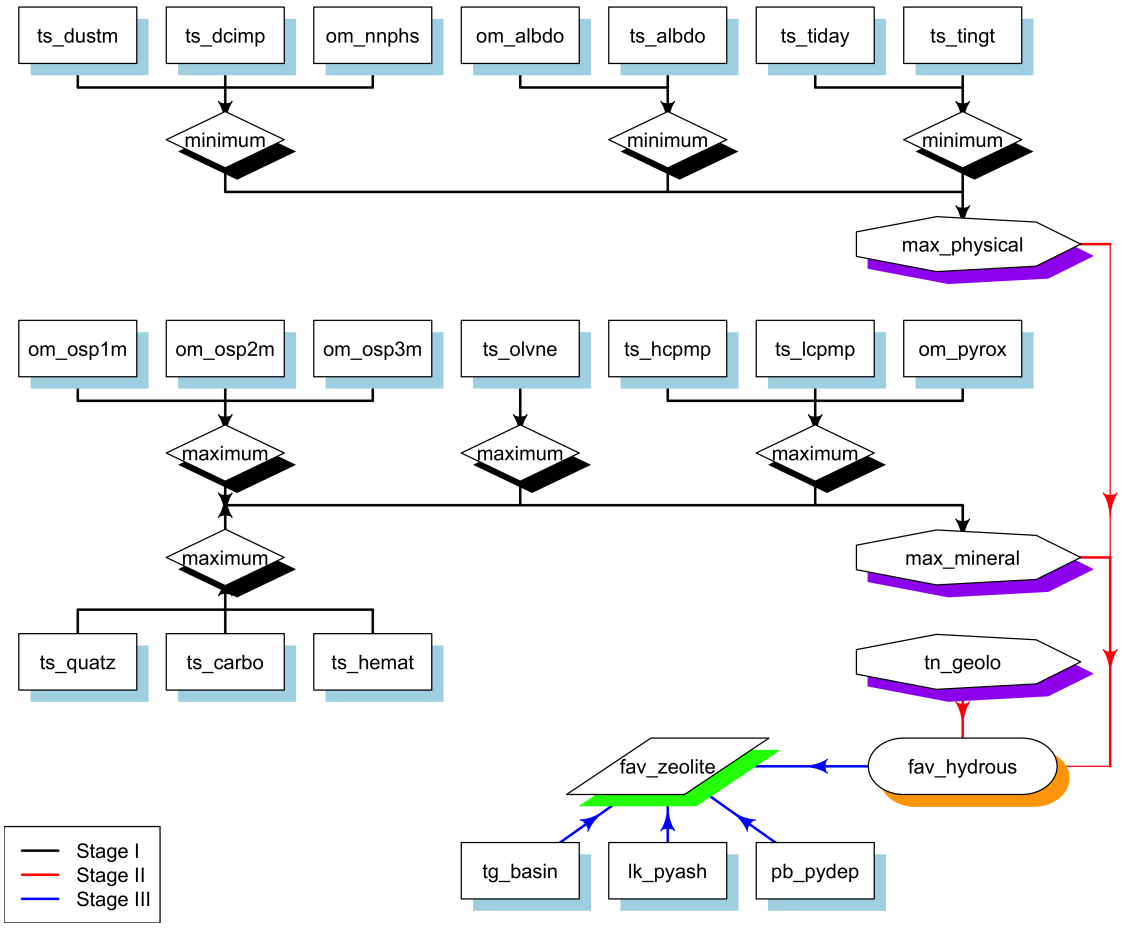

Figure 8.12: The fuzzy inference engine used to crate map Fz_06.

8.4 Results and discussion

The potential zeolite-bearing terrain map calculated using the data-driven fuzzy weights-of-evidence method is shown in Figure 8.13. This shows that the eastern and western Arabia deposits and some sites in the Medusae Fossae Formation show the highest probability for finding zeolites within the previously mapped potential pyroclastic deposits. Areas of interest outside the mapped pyroclastic deposits include certain areas of Valles Marineris, Mawrth Vallis, highlands north of Hellas, and the Terra Cimmeria and Terra Sirenum regions.

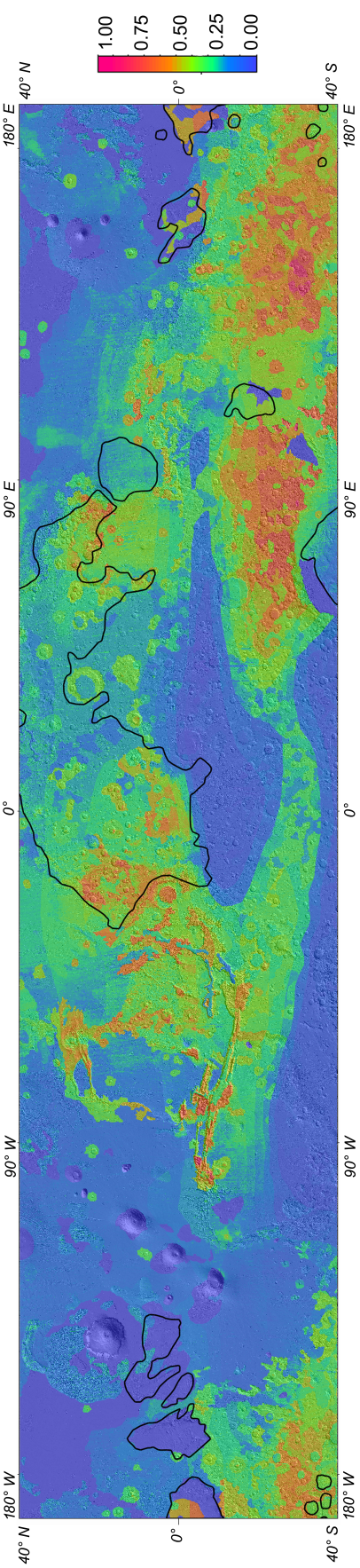

Figure 8.13: Potential zeolite bearing terrains calculated using the data driven fuzzy weights-of-evidence method. Value range indicates the possibility of finding zeolite based on the calculations. 1 = highest possibility, 0 = Lowest possibility. Background is a hillshade from MOLA DEM.

8. Data-driven Fuzzy Weights-of-Evidence model for identification of potential zeolite-bearing environments on Mars.

Arabia Terra is the most northerly region of the Martian cratered Noachian highlands and is probably composed of a mixture of volcanic deposits, impact breccias, and fluvial and aeolian sediments (Davis et al., 2019; Tanaka, 2000). Dust cover in central Arabia Terra (Ruff and Christensen, 2002) inhibited bedrock observations from orbital data and therefore most of the hydrous mineral detections are found at the western and eastern ends of Arabia Terra. The zeolite mineral analcime was first detected in the west of Nili Fossae in craters near the Antoniadi basin and in the eastern portion of the Arabia Terra by Ehlmann et al. (2009) using CRISM data. They also identified Fe/Mg-smectites, chlorite, prehnite, serpentine, kaolinite, potassium mica, hydrated silica, and magnesium carbonate in the area. These minerals are only observed in the Noachian crust and based on their spatial association and diversity, they suggested that hydrothermal alteration was a major mineral forming process. Ash dispersion modeling (e.g., Kerber et al. (2012); Kerber et al. (2013)) suggests that extensive ash deposits, carried by ancient winds, should be common throughout Arabia Terra. Fassett and Head (2007) studied the layered mantle unit in northeast Arabia Terra and observed hundreds of meters of material deposited on the surface, likely as airfall. The fretted terrain unit composed of altered, fine grained, layered sediments is suggested to be eroded ancient explosive volcanic deposits (e.g., Fassett and Head (2007); Moore (1990)). The fluvial systems in the region are consistent with formation by precipitation and runoff, and the deposits likely developed between the mid-Noachian and early-Hesperian, although it is possible that some systems may have formed later or been reactivated with localized, late-stage flows (Davis et al., 2019, 2016). Whelley et al. (2021) also identified the presence, thickness, and distribution of altered volcanic ash layers in Arabia Terra using a detailed study of their mineralogy using hyperspectral CRISM and morphology using HiRISE (High Resolution Imaging Science Experiment: McEwen et al. (2007)) and CTX (Context Camera: Malin et al. (2007)) data. They identified the interlayered sequence of volcanic ash units containing hydroxy sulfates, Fe/Mg-smectites, Al-smectites, aluminosilicates and hydrated silica. These altered ash deposits are widely distributed within Arabia Terra and at least 100 m thick as far away as 3,400 km from the potential caldera sites (Whelley et al., 2021).

8. Data-driven Fuzzy Weights-of-Evidence model for identification of potential zeolite-bearing environments on Mars.

The Medusae Fossae Formation (MFF) is a complicated and discontinuous formation located in southern Elysium and Amazonis Planitias and northern Memnonia and Aeolis Planitias (Kerber and Head, 2010). The formation is characterized by large accumulations of fine-grained, friable deposits most likely composed of volcanic ash, ignimbrites, or aeolian dust (Mandt et al., 2008; Kerber and Head, 2010). Both the Tharsis Montes and Elysium Montes could be the source of pyroclastic deposits. The detailed study by Kerber and Head (2010) suggested that the MFF is an evolving geological unit with continuous erosion and re-deposition since its initial emplacement. The initial formation age of the MFF is most likely to have been in the Hesperian and the previously assigned Amazonian ages appear to be modification ages instead of formation ages. Modified and inverted fluvial channels found within the deposit indicate that there was some fluvial activity during the emplacement or modification of the MFF (Kerber and Head, 2010).

Viviano-Beck et al. (2017) compositionally mapped the Valles Marineris wall units to constrain the formation and alteration of the martian crust in the eastern Tharsis Rise. They identified zeolites along with chlorite and associated carbonate on both the north and south walls of eastern Coprates Chasma in a confined longitudinal band. They were spatially associated with olivine-rich dikes, suggesting hydrothermal alteration from primary igneous phases to zeolite, and either alteration of saponite to chlorite and/or authigenic precipitation of chlorite from hydrothermal fluids (Viviano-Beck et al., 2017). The coexistence of zeolites and carbonates suggest that the fluids were alkaline. The walls of Valles Marineris are composed of three major groups of units, 1) Amazonian to Hesperian volcanic plains, 2) Noachian materials that form most of the upper crust in the southern highlands, and 3) deeply buried materials exposed in the lower parts of the walls (Viviano-Beck et al., 2017). A very diverse assemblage of hydrated minerals is also identified in a depression close to Noctis Labyrinthus, at the western end of the Valles Marineris where, Fig 8-13 shows high probability of finding zeolites (e.g., Thollot et al. (2012)). A detailed morphological, compositional, and stratigraphical analysis done by Thollot et al. (2012) at the site proposes an alteration sequence including formation of acid-sulfate solutions from groundwater and magmatic sulfur, and alteration of basaltic bedrock and formation of Fe-smectite and Fe-sulfate from layered sediments mainly deposited

from volcanic tephra. Mitrofanov et al. (2022) recently observed unusually high hydrogen abundances at Candor Chaos in the central area of Valles Marineris using the FREND (Fine Resolution Epithermal Neutron Detector) neutron telescope onboard ExoMars Trace Gas Orbiter (TGO). Based on these results, they concluded that the mean derived WEH (Water Equivalent Hydrogen) value of 40.3% at the Candor Chaos could be associated with the presence of either water ice permafrost or large quantities of highly hydrated minerals.

The Mawrth Vallis region, at the boundary between the southern highlands and the northern lowlands near 22-25^oN and 17 -21 ^oW (Bishop et al., 2013), hosts the largest outcrop of Al/Si-rich clays on Mars (Bishop and Rampe, 2016). It provides a unique opportunity to investigate a well-preserved record of sediments formed at the surface/shallow sub-surface during ~ 4.0-3.8 Ga ago (Loizeau et al., 2012; Bishop et al., 2013). The Al/Si-rich clay unit mainly consists of montmorillonite, opal, kaolinite/halloysite, aluminosilicates, and zeolite (Bishop et al., 2013). Bishop and Rampe (2016) have identified the poorly crystalline aluminosilicates as allophane and imogolite using CRISM and TES data. They suggested that the ash from one or many of the supervolcanoes identified in northern Arabia Terra could be the source of an allophane + imogolite unit at Mawrth Vallis. Loizeau et al. (2012) estimated the age and the time span of water activity in Mawrth Vallis region using the crater counting method. Michalski et al. (2013) developed multiple working hypotheses for the formation of the compositional stratigraphy at Mawrth Vallis region and their most favored hypothesis was that the tephra was chemically weathered in the presence of snow or ice and volcanogenic acidic aerosols and small volumes of water for the observed compositional stratigraphy.

The North Hellas highland region also shows a high favorability for the zeolites in the model. The thickest lacustrine sediments observed on Mars occur in Terby crater in the North Hellas highlands (Ansan et al., 2011). Hargitai et al. (2018) mapped potential paleolakes in the Navua-Hadriacus-Ausonia region, northeast of Hellas Basin, and identified 34 depressions that potentially hosted paleolakes, which would have contained > 2600 km^3 of water. These lakes formed during a volcanically active period in the Hesperion and may have had multiple resurfacing episodes and may have received water from different sources (Hargitai et al., 2018). Zhao et al. (2020) investigated the paleolakes in the northwest

Hellas region in detail using high-resolution imaging, topographic, and spectral data. They identified 64 paleolakes with diameters larger than 4 km, and 49 of them are newly reported. They observed lacustrine deposits, volcanic ash, aeolian sand deposits, exposures of bedrocks, and impact breccia/melts in the area. Previous studies of the northwestern Hellas region showed high concentrations of aqueous minerals such as phyllosilicates, chlorides, sulfates, and carbonates (Osterloo et al., 2010; Carter et al., 2013; Ehlmann and Edwards, 2014; Wray et al., 2016; Zhao et al., 2020; **?**).

The light-toned knobs in the Terra Cimmeria/Terra Sirenum region of Mars contains Fe/Mg-rich phyllosilicates, which appear to have been locally altered to Al-rich phyllosilicates by acid leaching. These clays are possibly formed by subaqueous alteration of the Electris Deposit. The Electris deposit, named by Grant and Schultz (1990), is a fine-grained sedimentary unit described as airfall deposit (Wendt et al., 2013). These deposits are consistent with clay formation within a network of local lakes that possibly once formed the Eridania lake in the late Noachian (Wendt et al., 2013). The mineralogical, morphological, and stratigraphic study of Terra Cimmeria/Terra Sirenum region done by Wendt et al. (2013) shows a complex and long-lasting aqueous history. The aqueous activity continued after clay formation near the Noachian-Hesperian boundary, and features valley networks, localized lakes, and possibly mineral alteration stages (Wendt et al., 2013).

Previous studies of these sites, as briefly discussed above, show the presence of zeolites and other hydrated minerals. If there are no zeolites yet observed, these areas at least contain volcaniclastic materials and signatures of palaeohydrological events that are most important for the formations of zeolites. It is important to study in detail the sites (pixels) which have the highest favorability index for zeolites. Figure 8.14 shows the open- and closed-basins cataloged by Goudge et al. (2016) in the Arabia Terra region with the favorability index for the zeolites (color range). Eight basins were selected and listed in Table 8.7, where the highest index values (pixel values) were observed. The in-depth analysis of each site identified in this study are beyond the scope of this chapter.

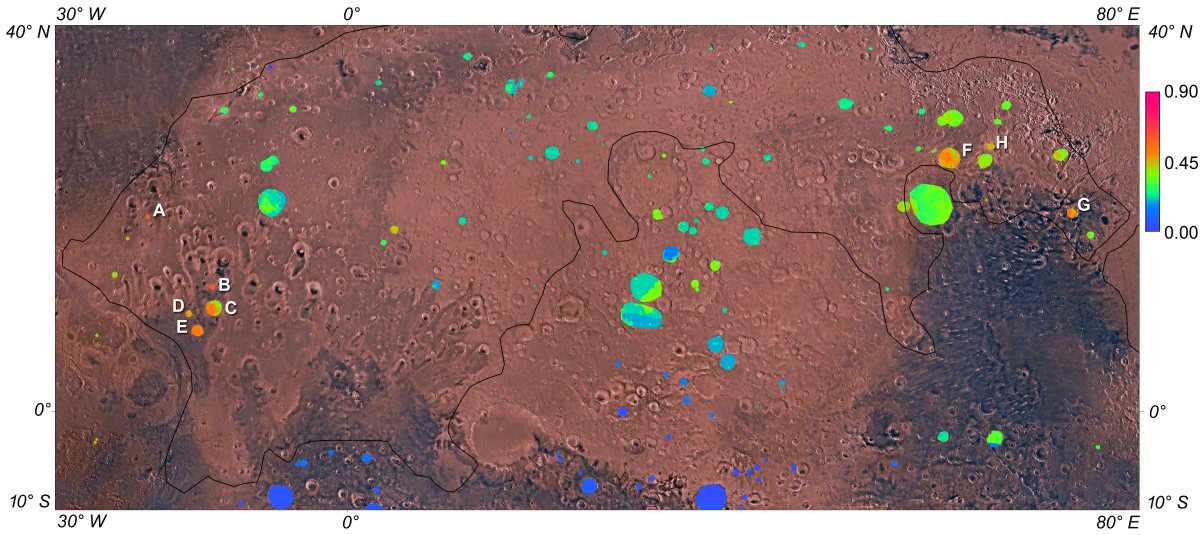

Figure 8.14: The favorability map of zeolites in open- and closed-paleolake basins cataloged by Goudge et al.(2016) in Arabia Terra region, Mars. Color range indicates the possibility of finding zeolites based on the present calculation. 0.9 = highest possibility, 0 = lowest possibility. Background is Viking color image.

Table 8.7: Selected open-closed basins in the Arabia Terra region.

Rank	Latitude	Longitude
A	$20^o21'39.12"N$	$20^o54'12.69"W$
B	$13^o02'17.61"N$	$14^o10'47.68"W$
C	$10^o53'43.86"N$	$14^o00'03.26"W$
D	$10^o11'34.46"N$	$16^o36'15.36"W$
E	$8^o29'30.65"N$	$15^o47'53.21"W$
F	$26^o35'26.81"N$	$63^o01'48.30"E$
G	$20^o41'04.53"N$	$75^o48'39.65"E$
H	$27^o41'55.92"N$	$67^o12'12.72"E$

Missing data or misinterpreted patterns are two of the major sources of uncertainty in mapping mineral favorability. This is more critical in poorly explored areas where fewer data are available than in well-explored areas. Most areas on Mars are poorly explored. The fuzzy weights-of-evidence method adopted here provides a framework for calibrating fuzzy membership functions to replace missing data for posterior probability calculations (Cheng and Agterberg, 1999). Since the weights-of-evidence method is objective, it also avoids the subjective choice of weighting factors. The objective methods are more important in poorly explored areas where little knowledge is available. One of

the main disadvantages of the weights-of-evidence method is that it is only applicable in regions where the response variable is fairly well known. If the response variable is poorly known at least for a certain region, the results must be interpreted with caution. The response variable used in this study is the locations of hydrous minerals. Carter et al. (2013) discussed several biases and limitations for hydrous mineral detections, which can directly influence the probabilistic model applied here.

1) Carter et al. (2013) demonstrated that the detection capabilities for hydrous minerals on Mars using orbital data are limited by the spatial resolution of the observations. Spots with hydrous minerals as small as the smallest footprint (~20m) can be detected. In addition, orbital spectral data from both OMEGA and CRISM exhibit a number of instrumental artifacts that can affect the identification of minerals (false positives and false negatives). Also, observational biases such as surface dust cover, ice, photometric effects, residuals in the atmospheric correction, and spectral mixing with non-hydrated minerals could affect the hydrous mineral detections from orbital data.

2) Many of the hydrated deposits detectable at the high spatial resolution of CRISM are surely left out in the 98% of the surface not observed. Though the multi-spectral CRISM observations cover almost the entire planet, hydrous mineral detection from multispectral CRISM data are mostly discarded by Carter et al. (2013) due to their low spectral sampling.

3) Some regions have been investigated more than others, yielding more detections than other regions that are less well studied.

4) The size of the hydrous mineral exposures is also a key factor as smaller exposures have fewer pixels to average on. This results in a lower S/N spectra, which makes it harder to detect.

In addition to the limitations of the response variable (hydrous mineral detection), two other types of uncertainties and errors can be identified; 1) errors and uncertainties associated with the original data or introduced during the pre-processing and processing

of vector/raster data, and 2) errors and uncertainties introduced during the information representation and digital fusion of the factor maps (Moon, 1998). Since the global maps used in this study were of different resolutions, coordinate systems, and different file formats, errors and uncertainties can be introduced during the resampling process, reclassification process, projection and transformation, and data handling. These errors and uncertainties can propagate through the entire reasoning process and into the final results. Some of the errors and uncertainties introduced during the information representation and digital fusion and the methods applied to eliminate some of these errors and uncertainties are briefly discussed below.

This study did not test the Conditional Independence (CI) among the evidential maps, though some evidential maps seem to have a conditional dependence (e.g., Albedo, Thermal inertia, dust cover index). Conditional dependence can create problems when combining maps using fuzzy algebraic product, fuzzy algebraic sum, and γ operator. However, before applying these three operators, all the similar maps were synthesized using fuzzy OR and fuzzy AND operators to eliminate the effect of CI. Therefore, it is not necessary that conditionally dependent maps are rejected in the predictive mineral mapping process using fuzzy logic, if an appropriate inference network is used (Porwal et al., 2003). However, if extremely high or low noise values are associated with some pixels in evidential maps, the fuzzy OR and fuzzy AND operators would propagate into the final synthesized fuzzy favorability map (Knox-Robinson, 2000). These noises (no data pixels and saturated pixels) were observed in most of the used image products. If fuzzy algebraic sum (FAS) and fuzzy algebraic product (FAP) operators were used individually, these noises could be amplified because of their increasive and decreasive tendencies of these two operators, respectively. The fuzzy γ operators balanced these tendencies of the FAS and FAP operators by using appropriate values of γ (Porwal et al., 2003; Knox-Robinson, 2000). One of the main advantages of fuzzy model is its capability to control the propagation of extreme-value noise to the output.

8.5 Conclusion

In this study, the data-driven fuzzy based weights-of-evidence method was applied to produce a hydrous mineral favorability map and a zeolite mineral favorability map of the surface of Mars up to 40° latitudes towards both poles. The results of this work led to the following main conclusions:

1) The methods applied in this study dealt well with qualitative, quantitative, multi-source data/information for Mars, acquired from orbital data, which may be imprecise and incomplete due to the limitations of spatial resolution, spatial coverage, surface dust, instrumental biases, and other intrinsic biases.

2) The weights-of-evidence method provided a simple statistical method for predicting mineral potential based on limited known occurrences.

3) The most important and sensitive processes in fuzzy modeling were the definition of fuzzy membership values of multiclass evidential maps and the selection of fuzzy set operators and an appropriate inference network for combining the evidential maps.

4) The favorability map for hydrous minerals obtained by a well-tuned fuzzy inference engine indicates a strong correlation (success rate) between the areas of high favorability of hydrous minerals and known hydrous mineral detections.

5) Favorability of zeolites derived from the favorability of hydrous mineral map and the pyroclastic deposits (modeled and confirmed) map agrees with previous studies conducted in those favorable areas, depicting the validity of the conceptual model used and its accuracy.

6) The favorable areas for zeolites identified in this method include the eastern and western Arabia deposits and some sites of Medusae Fossae formation within the previously mapped potential pyroclastic deposits. Favorable areas for zeolites outside the mapped pyroclastic deposits include certain areas of Valles Marineris, Mawrth Vallis, highlands north of Hellas, and the Terra Cimmeria and Terra Sirenum regions.

8. Data-driven Fuzzy Weights-of-Evidence model for identification of potential zeolite-bearing environments on Mars.

7) Based on the favorability index for zeolites, eight open- and closed-paleolake basins in Arabia Terra were selected for detail studies.

Acknowledgement

Many thanks to NASA, ESA and all the authors for making the image data and image derived products are available. Also, thanks to the developers of ILWIS, GDAL, ISIS3, R, and Rstudio for making them as free. Bas Retsios at the Faculty of ITC, the University of Twente, the Netherlands for the helpful discussions on ILWIS.

"Real knowledge is to know the extent of one's ignorance."

-Confucius-

Conclusion

This study evaluates the possible formation and evolution mechanisms of zeolites on early Mars with possible explanations for their limited detections using Earth analogs. The study focused on the formation of zeolites in the closed basin lakes where the largest relatively pure concentrations of natural zeolites are found on Earth. The study was conducted formulating five possibilities that can limit the zeolite mineral detections of Mars using orbital data.

Zeolite may not be identifiable on Mars using orbital data, if

1. they are absent, or
2. they were originally present and later removed by chemical processes (e.g., dissolution and alteration), or
3. they are present but are covered by or mixed with other materials, or
4. they are present, but the methods applied are not capable of detecting and mapping them, or
5. they are present, but we are not looking in the correct places.

Previous studies document the detection of analcime, a Na-zeolite, from orbital data, though the presence of zeolites on Mars is not yet confirmed by in situ observation or from Martian meteorites. Those identified analcime detections are hypothesized to form by hydrothermal alteration. Geochemical modeling shows that zeolites can also form at low temperatures ($0 - 25^oC$), both from basaltic and high silica starting materials. Therefore, based on the orbital detection of "analcime" and thermodynamic point of view, there is no reason to accept hypothesis 1, that "zeolites are absent". The geochemical modeling found that some zeolites (e.g., clinoptilolite) are dissolved over time while other zeolites

(e.g., analcime) precipitate, similar to a common trend observed in terrestrial zeolite-bearing paleolake systems. The most common authigenic minerals and their paragenetic relationships in zeolite-bearing paleolake systems were identified using bulk mineral assemblages of tuff samples and Self-Organizing Maps. While analcime might be the most common zeolite detected on Mars, this does not mean that other zeolites are absent, as they might be present but less abundant. The spectral mixture analysis conducted using spectral deconvolution and deep learning shows the difficulties of identifying non-analcime zeolites (clinoptilolite) from Mg-polyhydrated minerals, as discussed by several authors who mapped hydrous minerals on Mars using hyperspectral image data. This study further demonstrates that the presence of at least ~10% montmorillonite in a clinoptilolite-montmorillonite mixture can easily mask the presence of the clinoptilolite in the SWIR wavelength region of reflectance spectra. Random artifacts introduced by the noise sometimes lead to predicting completely different mineral abundances than real. Therefore, if zeolites are mixed with clay minerals, as commonly observed in Lake Tecopa and other saline-alkaline terrestrial sites, they will be difficult to identify using orbital data. The Lake Tecopa analog study area showed that most zeolite-rich tuff beds are covered by other types of beds in this depositional environment and later mixed with other beds due to erosion and/or formed as an accessory phase in claystone. Burial of thinner beds due to later deposition (e.g., layering) or dust and erosion are also common processes in sedimentary environments on Mars. The study also demonstrates that VNIR-SWIR spectroscopy is not the best method to identify non-analcime zeolite minerals due to the lack of characteristic absorption features. Further, this study demonstrates the possible reasons for limited orbital detection of zeolites using an analog study from paleolake Tecopa. Most of the hypothesized possibilities for limited detection of zeolites discussed above could be rejected using in situ observations (e.g., if the zeolite beds are covered by other materials, they cannot be observed by orbital VNIR-SWIR sensors, but could be detected by in situ rover missions). The favorability map of zeolites on Mars created using the data-driven fuzzy weights-of-evidence method could serve as a guide for further searches for zeolites using detailed orbital spectral image analysis and future in situ observations. The main conclusion of this study is that the absence (or limited detection)

of zeolites in paleolake basins on Mars does not preclude their (wider) presence, since there is no valid hypothesis to infer their absence. The best way to confirm their presence would be to "follow the zeolite on Mars" using future in situ observations.

References

Ackiss, S., Horgan, B., Seelos, F., Farrand, W., Wray, J., 2018. Mineralogic evidence for subglacial volcanism in the sisyphi montes region of mars. Icarus 311, 357–370.

Adams, J.B., Gillespie, A.R., 2006. Remote Sensing of Landscapes with Spectral Images: A Physical Modeling Approach. Cambridge University Press.

Adams, J.B., Smith, M.O., 1986. Spectral mixture modeling: A new analysis of rock and soil types at the viking lander 1 site. Journal of Geophysical Research 91, 8098–8112.

Adams, J.B., Smith, M.O., Gillespie, A.R., 1993. Imaging spectroscopy: Interpretation based on spectral mixture analysis, in: Pieters, C.M., Englert, P.A.J. (Eds.), Remote geochemical analysis: Elemental and mineralogical composition. Cambridge University Press. volume Topics in Remote Sensing 4, pp. 145–166.

Adler-Golden, S., Berk, A., Bernstein, L.S., Richtsmeier, S., Acharya, P.K., Matthew, M.W., Anderson, G.P., Allred, C.L., Jeong, L.S., Chetwynd, J.H., 1998. Flaash, a modtran4 atmospheric correction package for hyperspectral data retrievals and simulations., in: Summaries of the seventh JPL airborne earth science workshop, JPL Publication, Pasadena, CA. p. 9.

Aines, R.D., Rossman, G., 1984. Water in minerals? : A peak in the infrared. Journal of Geophysical Research 89, 4059–4071.

Alemanno, G., Orofino, V., Mancarella, F., 2018. Global map of martian fluvial systems: Age and total eroded volume estimations. Earth and Space Science 5, 560–577.

Alemanno, G., Orofino, V., Maturilli, A., Helbert, J., Mancarella, F., 2021. Detection of aqueous alteration minerals in martian open and closed paleolake basins. Planetary and Space Science 208.

Allen, C.C., Gooding, J.L., Jercinovic, M., Keil, K., 1981. Altered basaltic glass: A terrestrial analog to the soil of mars. Icarus 45, 347–369.

Anand, M., James, S., Greenwood, R.C., Johnson, D., Franchi, I.A., Grady, M.M., 2008. Mineralogy and geochemistry of shergottite rbt 04262, in: 39th Lunar and Planetary Science Conference, Lunar and Planetary Insttitute, League City, Texas. p. Abs No. 2173.

Anderson, D., 2005. Holocene fluvial geomorphology of the amargosa river through amargosa canyon, california. Earth Science Reviews 73, 291–307.

Ansan, V., Loizeau, D., Mangold, N., Mouélic, S.L., Carter, J., Poulet, F., Dromart, G., Lucas, A., Bibring, J.P., Gendrin, A., Gondet, B., Langevin, Y., Masson, P., Murchie, S., Mustard, J., Neukum, G., 2011. Stratigraphy, mineralogy, and origin of layered deposits inside terby crater, mars. Icarus 211, 273–304.

Arai, K., 2001. Early results from the vicarious calibration of terra/aster/swir. Advances in Space Research 28, 77–82.

Arai, K., Tonooka, H., 2005. Radiometric performance evaluation of aster vnir, swir, and tir. IEEE Transactions on Geoscience and Remote Seinsing Vol. 43, 2725–2732.

Armbruster, T., Gunter, M.E., 2001. Crystal structures of natural zeolites, in: Bish, D.L., Ming, D. (Eds.), Natural Zeolites: Occurrence, Properties, Applications. Reviews in Mineralogy and Geochemistry. volume Vol. 45, No. 1, pp. 1–67.

Arnold, G.E., Foerster, V., Trauth, M.H., Lamb, H., Schaebitz, F., Asrat, A., Szczech, C., Günter, C., 2021. Advanced hyperspectral analysis of sediment core samples from the chew bahir basin, ethiopian rift, in the spectral range from 0.25 to 17µm: Support for climate proxy interpretation. Frontiers in Earth Science 9.

Arvidson, R.E., Poulet, F., Bibring, J.P., Wolff, M., Gendrin, A., Morris, R.V., Freeman, J.J., Langevin, Y., Mangold, N., Bellucci, G., 2005. Spectral reflectance and morphologic correlations in eastern terra meridiani, mars. Science 307, 1591–1594.

References

Ault, C.R., 1998. Criteria of excellence for geological inquiry: The necessity of ambiguity. Journal of Research in Science Teaching 35, 189–212.

Bacao, F., Lobo, V., Painho, M., 2005. The self-organizing map,the geo-som,and relevant variants for geosciences. Computers & Geosciences 31, 155–163.

Bailly, P.A., 1972. Mineral exploration philosophy. American Mining Congress Journal 58, 31–37.

Baker, V.R., 2014. Terrestrial analogs, planetary geology, and the nature of geological reasoning. Planetary and Space Science 95, 5–10.

Bandfield, J.L., 2002. Global mineral distributions on mars. Journal of Geophysical Research Vol. 107, 10.1029/2001JE001510.

Bandfield, J.L., 2006. Extended surface exposures of granitoid compositions in syrtis major, mars. Geophysical Research Letters 33, doi:10.1029/2005GL025559.

Bandfield, J.L., 2008. High-silica deposits of an aqueous origin in western hellas basin, mars. Geophysical Research Letters Vol. 35, doi:10.1029/2008GL033807.

Bandfield, J.L., Glotch, T.D., Christensen, P.R., 2003. Spectroscopic identification of carbonate minerals in the martian dust. Science 301, 1084–1087.

Bandfield, J.L., Hamilton, V.E., Christensen, P.R., 2000. A global view of martian surface compositions from mgs-tes. Science 287, 1626–1630.

Bandfield, J.L., Rogers, A.D., 2008. Olivine dissolution by acidic fl uids in argyre planitia, mars: Evidence for a widespread process? Geology 36, 579–582.

Bandfield, J.L., Rogers, A.D., 2019. Thermal infrared spectral modeling, in: Bishop, J., III, J.B., Moersch, J. (Eds.), Remote Compositional Analysis: Techniques for Understanding Spectroscopy, Mineralogy, and Geochemistry of Planetary Surfaces. Cambridge University Press.. Cambridge Planetary Science, pp. 324–336.

Barducci, A., Pippi, I., 1996. Temperature and emissivity retrieval from remotely sensed images using the "gray body emissivity" method. IEEE Transactions on Geoscience and Remote Seinsing 34, 681–695.

Bargar, K.E., Beeson, M.H., 1981. Hydrothermal alteration in research drill hole y-2, lower geyser basin, yellowstone national park, wyoming. American Mineralogist 66, 473–490.

Barnes, R., Gupta, S., Traxler, C., Ortner, T., Bauer, A., Hesina, G., Paar, G., Huber, B., Juhart, K., Fritz, L., Nauschnegg, B., Muller, J.P., Tao, Y., 2018. Geological analysis of martian rover-derived digital outcrop models using the 3-d visualization tool, planetary robotics 3-d viewer - pro3d. Earth and Space Science 5, 285–307.

Barnhart, C.J., Nimmo, F., 2011. Role of impact excavation in distributing clays over noachian surfaces. Journal of Geophysical Research 116.

Barrows, K.J., 1980. Zeolitization of miocene voleaniclastic rocks, southern desatoya mountains, nevada. Geological Society of America Bulletin, Part 1 91, 199–210.

Bascunan, S., Kelm, U., Sanhueza, V., Alfaro, G., 2007. Zeolitization of tuffs at quinamavida, central southern chile. Clays and Clay Minerals 55, 524–533.

Basu, A., Schmitt, J., Crossey, L.J., 1998. An argument for zeolites in mars rocks and an earth analog, in: Proc. Lunar Planet Sci. Conf. 24th. Abstract No.1041.

Beck, P., Barrat, J.A., Gillet, P., Wadhwa, M., Franchi, I.A., Greenwood, R.C., Bohn, M., Cotten, J., Moortele, B.v.d., Reynard, B., 2006. Petrography and geochemistry of the chassignite northwest africa 2737 (nwa 2737). Geochemica et Cosmochimica Acta 70, 2127–2139.

Becker, F., Li, Z.L., 1990. Temperature-independent spectral indices in thermal infrared bands. Remote Sensing of Environment 32, 17–33.

Becker, F., Li, Z.L., 1995. Surface temperature and emissivity at various scales: definition, measurement and related problems. Remote Sensing Reviews 12, 225–253.

Bedford, C.C., Bridges, J.C., Schwenzer, S.P., Wiens, R.C., Rampe, E.B., Frydenvang, J., Gasda, P.J., 2019. Alteration trends and geochemical source region characteristics preserved in the fluviolacustrine sedimentary record of gale crater, mars. Geochemica et Cosmochimica Acta 246, 234–266.

Behin, J., Ghadamnan, E., Kazemian, H., 2019. Recent advances in the science and technology of natural zeolites in iran. Clay Minerals 54, 131–144.

Ben-Dor, E., Kindel, B., Goetz, A.F.H., 2004. Quality assessment of several methods to recover surface reflectance using synthetic imaging spectroscopy data. Remote Sensing of Environment 90, 389–404.

Ben-Dor, E., Kruse, F.A., Lefkoff, A.B., Banin, A., 1994. Comparison of three calibration techniques for utilization of ger 63-channel aircraft scanner data of makhtesh ramon, negev, israel. Photogrammetric Engineering & Remote Sensing 60, 1339–1354.

Berk, W.v., Fu, Y., Ilger, J.M., 2012. Reproducing early martian atmospheric carbon dioxide partial pressure by modeling the formation of mg-fe-ca carbonate identified in the comanche rock outcrops on mars. Journal of Geophysical Research 117, doi:10.1029/2012JE004173.

Berkley, J.L., Drake, M.J., 1981. Weathering of mars: Antarctic analog studies. Icarus 45, 231–249.

Bibring, J.P., Langevin, Y., Gendrin, A., Gondet, B., Poulet, F., Berthe, M., Soufflot, A., Arvidson, R., Mangold, N., Mustard, J., Drossart, P., team, O., 2005. Mars surface diversity as revealed by the omega/mars express observations. Science 307, 1576–1581.

Bibring, J.P., Langevin, Y., Mustard, J.F., Poulet, F., Arvidson, R., Gendrin, A., Gondet, B., Mangold, N., Pinet, P., Forget, F., team, O., 2006. Global mineralogical and aqueous mars history derived from omega/mars express data. Science Vol. 312, 400–404.

Bibring, J.P., Soufflot, A., Berthé, M., Langevin, Y., Gondet, B., Drossart, P., Bouyé, M., Combes, M., Puget, P., Semery, A., Bellucci, G., Formisano, V., Moroz, V., Kottsov, V., Bonello, G., Erard, S., Forni, O., Gendrin, A., Manaud, N., Poulet, F., Poulleau, G.,

Encrenaz, T., Fouchet, T., Melchiori, R., Altieri, F., Ignatiev, N., Titov, D., Zasova, L., Coradini, A., Capacionni, F., Cerroni, P., Fonti, S., Mangold, N., Pinet, P., Schmitt, B., Sotin, C., Hauber, E., Hoffmann, H., Jaumann, R., Keller, U., Arvidson, R., Mustard, J., Forget, F., 2004. Omega: Observatoire pour la minéralogie, l'eau, les glaces et l'activité. Eur. Space Agency Spec. Publ. ESA SP-1240, 37–49.

Biggar, S.F., Thome, K.J., McCorkel, J.T., D'Amico, J.M., 2005. Vicarious calibration of the aster swir sensor including crosstalk correction. Proceedings of SPIE Vol. 5882, 588217.

Bioucas-Dias, J.M., Plaza, A., Dobigeon, N., Parente, M., Du, Q., Gader, P., Chanussot, J., 2012. Hyperspectral unmixing overview: Geometrical, statistical, and sparse regression-based approaches. IEEE Journal of Selected Topics in Applied Earth Observations and Remote Sensing Vol. 5, 354–379.

Birsoy, R., 2002. Activity diagrams of zeolites: Implications for the occurances of zeolites in turkey and of erionite worldwide. Clays and Clay Minerals 50, 136–144.

Bish, D.L., Carey, J.W., 2001. Thermal behavior of natural zeolites, in: Bish, D.L., Ming, D. (Eds.), Natural Zeolites: Occurrence, Properties, Applications. Reviews in Mineralogy and Geochemistry. volume Vol. 45, No. 1, pp. 403–452.

Bish, D.L., Carey, J.W., Vaniman, D.T., Chipera, S.J., 2003. Stability of hydrous minerals on the martian surface. Icarus 164, 96–103.

Bishop, J.L., Dobrea, E.Z.N., McKeown, N.K., Parente, M., Ehlmann, B.L., Michalski, J.R., Milliken, R.E., Poulet, F., Swayze, G.A., Mustard, J.F., Murchie, S.L., Bibring, J.P., 2008. Phyllosilicate diversity and past aqueous activity revealed at mawrth vallis, mars. Science 321, 830–833.

Bishop, J.L., Fairén, A.G., Michalski, J.R., Gago-Duport, L., Baker, L.L., Velbel, M.A., Gross, C., Rampe, E.B., 2018. Surface clay formation during short-term warmer and wetter conditions on a largely cold ancient mars. Nature Astronomy 2, 206–213.

Bishop, J.L., Loizeau, D., McKeown, N.K., Saper, L., Dyar, M.D., Marais, D.J.D., Parente, M., Murchie, S.L., 2013. What the ancient phyllosilicates at mawrth vallis can tell us about possible habitability on early mars. Planetary and Space Science 86, 130–149.

Bishop, J.L., Parente, M., Weitz, C.M., Dobrea, E.Z.N., Roach, L.H., Murchie, S.L., McGuire, P.C., McKeown, N.K., Rossi, C.M., Brown, A.J., Calvin, W.M., Milliken, R., Mustard, J.F., 2009. Mineralogy of juventae chasma: Sulfates in the light-toned mounds, mafic minerals in the bedrock, and hydrated silica and hydroxylated ferric sulfate on the plateau. Journal of Geophysical Research 114.

Bishop, J.L., Pieters, C.M., Edwards, J.O., 1994. Infrared spectroscopic analysis on the nature of water in montmorillonite. Clays and Clay Minerals 42, 702–716.

Bishop, J.L., Rampe, E.B., 2016. Evidence for a changing martian climate from the mineralogy at mawrth vallis. Earth and Planetary Science Letters 448, 42–48.

Black, S.R., Hynek, B.M., 2018. Characterization of terrestrial hydrothermal alteration products with mars analog instrumentation: Implications for current and future rover investigations. Icarus 307, 235–259.

Blackburn, W.H., Dennen, W.H., 1988. Principles of Mineralogy. Wm. C. Brown Publishers.

Boardman, J.W., 1993. Automating spectral unmixing of aviris data using convex geometry concepts, in: Green, R.O. (Ed.), Summaries of the 4th Airborne Geoscience Conference, JPL Publication 93-26, Jel Propulsion Laboratory, Pasdena, CA. pp. 11–14.

Boardman, J.W., 1998. Post-atrem polishing of aviris apparent reflectance data using effort : A lesson in accuracy versus precision, in: Summaries of the Seventh JPL Airborne Earth Science Workshop, JPL Publication 97-21. p. 53.

Boardman, J.W., Kruse, F.A., 2011. Analysis of imaging spectrometer data using n-dimensional geometry and a mixture-tuned matched filtering approach. IEEE Transactions on Geoscience and Remote Seinsing 49, 4138–4152.

Bogaard, P.v.d., Schirnick, C., 1995. 40ar/39ar laser probe ages of bishop tuff quartz phenocrysts substantiate long-lived silicic magma chamber at long valley, united states. Geology 23, 759–762.

Boles, J.R., Surdam, R.C., 1979. Diagenesis of volcanogenic sediments in a tertiary saline lake; wagon bed formation, wyoming. American Journal of Science 279, 832–853.

Bonham-Carter, G.F., 1994. Geographic Information Systems for Geoscientists: Modelling with GIS. Pergamon.

Bonham-Carter, G.F., Agterberg, F.P., Wright, D.F., 1989. Weights of evidence modelling : a new approach to mapping mineral potential, in: Agterberg, F.P., Bonham-Carter, G.F. (Eds.), Statistical Applications in the Earth Sciences. Geological Survey of Canada, pp. 171–183.

Bowers, T.S., Burns, R.G., 1990. Activity diagrams for clinoptilolite: Susceptibility of this zeolite to further diagenetic reactions. American Mineralogist 75, 601–619.

Boynton, W.V., Feldman, W.C., Mitrofanov, I.G., Evans, L.G., Reedy, R.C., Squyres, S.W., Starr, R., Trombka, J.I., D'Uston, C., Arnold, J.R., Englert, P.A.J., Metzger, A.E., Wanke, H., Bruckner, J., Drake, D.M., Shinohara, C., Fellows, C., Hamara, D.K., Harshman, K., Kerry, K., Turner, C., Ward, M., Barthe, H., Fuller, K.R., Storms, S.A., Thornton, G.W., Longmire, J.L., Litvak, M.L., Ton'chev, A.K., 2004. The mars odyssey gamma-ray spectrometer instrument suite. Space Science Reviews 110, 37–83.

Boynton, W.V., Ming, D.W., Kounaves, S.P., Young, S.M.M., Arvidson, R.E., Hecht, M.H., Hoffman, J., Niles, P.B., Hamara, D.K., Quinn, R.C., Smith, P.H., Sutter, B., Catling, D.C., Morris, R.V., 2009. Evidence for calcium carbonate at the mars phoenix landing site. Science 325, 61–64.

Boynton, W.V., Taylor, G.J., Evans, L.G., Reedy, R.C., Starr, R., Janes, D.M., Kerry, K.E., Drake, D.M., Kim, K.J., Williams, R.M.S., Crombie, M.K., Dohm, J.M., Baker, V., Metzger, A.E., Karunatillake, S., Keller, J.M., Newsom, H.E., Arnold, J.R., Bruckner, J., Englert, P.A.J., Gasnault, O., Sprague, A.L., Mitrofanov, I., Squyres, S.W., Trombka,

J.I., d'Uston, L., Wanke, H., Hamara, D.K., 2007. Concentration of h, si, cl, k, fe, and th in the low- and mid-latitude regions of mars. Journal of Geophysical Research 112, doi:10.1029/2007JE002887.

Brathwaite, R.L., 2003. Geological and mineralogical characterization of zeolites in lacustrine tuffs, ngakuru, taupo volcanic zone, new zealand. Clays and Clay Minerals 51, 589–598.

Breck, D.W., 1974. Zeolite molecular sieves: structure, chemistry, and use. John Wiley and Sons, Inc.

Brierley, G., Fryirs, K., 2014. Reading the landscape in field-based fluvial geomorphology, in: Thornbush, M.J., Allen, C.D., Fitzpatrick, F.A. (Eds.), Developments in Earth Surface Processes. Elsevier. volume 18, pp. 231–257.

Bristow, T.F., Milliken, R.E., 2011. Terrestrial perspective on authigenic clay mineral production in ancient martian lakes. Clays and Clay Minerals 59, 339–358.

Brodaric, B., Gahegan, M., Harrap, R., 2004. The art and science of mapping: computing geological categories from field data. Computers & Geosciences 30, 719–740.

Brown, A.J., 2006. Spectral curve fitting for automatic hyperspectral data analysis. IEEE Transactions on Geoscience and Remote Seinsing Vol. 44, 1601–1608.

Broz, P., Bernhardt, H., Conway, S.J., Parekh, R., 2020. An overview of explosive volcanism on mars. Journal of Volcanology and Geothermal Research .

Bruckner, J., Dreibus, G., Gellert, R., Squyres, S.W., Wanke, H., Yen, A., Zipfel, J., 2008. Mars exploration rovers: chemical composition by the apxs, in: Bell, J. (Ed.), The Martian Surface: Composition, Mineralogy and Physical Properties. Cambridge University Press. Cambridge Planetary Science, pp. 58–102.

Bue, B.D., Stepinski, T.F., 2006. Automated classification of landforms on mars. Computers & Geosciences 32, 604–614.

Bultel, B., Quantin, C., Lozac'h, L., 2015. Description of cotcat (complement to crism analysis toolkit). IEEE Journal of Selected Topics in Applied Earth Observations and Remote Sensing 8, 3039–3049.

Bunch, T.E., Irving, A.J., Wittke, J.H., Rumble, D., Korotev, R.L., Gellissen, M., Palme, H., 2009. Petrology and composition of northwest africa 2990: A new type of fine-grained enriched, olivine-phyric shergottite, in: 40th Lunar and Planetary Science Conference, Lunar and Planetary Institute, The Woodlands, Texas.. p. Abs No. 2274.

Burragato, F., Cavaretta, G., Funiciello, R., 1975. The new brazillian achondrite of governador valadaras (minas gerais). Meteoritics 10, 374–375.

Cabrol, N.A., Grin, E.A., 1999. Distribution, classification, and ages of martian impact crater lakes. Icarus 142, 160–172.

Cabrol, N.A., Grin, E.A., 2002. Overview on the formation of paleolakes and ponds on mars. Global and Planetary Changes Vol. 35, 199–219.

Cabrol, N.A., Grin, E.A., 2010. 1 - searching for lakes on mars: Four decades of exploration, in: Cabrol, N.A., Grin, E.A. (Eds.), Lakes on Mars. Elsevier, pp. 1–29.

Cahill, J.T.S., Lucey, P., Stockstill-Cahill, K.R., Hawke, B.R., 2010. Radiative transfer modeling of near-infrared reflectance of lunar highland and mare soils. Journal of Geophysical Research 115, doi: 10.1029/2009JE003500.

Cahill, J.T.S., Lucey, P.G., Wieczorek, M.A., 2009. Compositional variations of the lunar crust: Results from radiative transfer modeling of central peak spectra. Journal of Geophysical Research 114.

Calvo, J.P., Blanc-Valleron, M.M., Rodriguez-Arandia, J.P., Rouchy, J.M., Sanz, M.E., 1999. Authigenic caly minerals in continental evaporitic environments, in: Thiry, M., Simon-Conicon, R. (Eds.), Palaeoweathering, Palaeosurfaces and Related Continental Deposits. volume 27, pp. 129–151.

Campbell, N.A., 1996. The decorrelation stretch transformation. International Journal of Remote Sensing 17, 1939–1949.

References

Cannon, K.M., Mustard, J.F., Salvatore, M.R., 2015. Alteration of immature sedimentary rocks on earth and mars: Recording aqueous and surface–atmosphere processes. Earth and Planetary Science Letters 417, 78–86.

Caravaca, G., Mouelic, S.L., Mangold, N., LHaridon, J., Deit, L.L., Masse, M., 2020. 3d digital outcrop model reconstruction of the kimberley outcrop (gale crater, mars) and its integration into virtual reality for simulated geological analysis. Planetary and Space Science 182.

Carr, M.H., Chuang, F.C., 1997. Martian drainage densities. Journal of Geophysical Research 102, 9145–9152.

Carr, M.H., Head, J.W., 2010. Geologic history of mars. Earth and Planetary Science Letters Vol. 294, 185–203.

Carranza, E., 2009. Predictive modeling of mineral exploration targets (chapter 01), in: Geochemical Anomaly and Mineral Prospectivity Mapping in GIS. Elsevier B.V.. volume Vol. 11 of *Handbook of Exploration and Environmental Geochemistry*, pp. 03–21.

Carranza, E.J.M., 2011. Geocomputation of mineral exploration targets. Computers & Geosciences 37, 1907–1916.

Carter, J., Poulet, F., Bibring, J.P., Mangold, N., Murchie, S., 2013. Hydrous minerals on mars as seen by the crism and omega imaging spectrometers: Updated global view. Journal of Geophysical Research. Planets 118, 831–858.

Catalano, J.G., 2013. Thermodynamic and mass balance constraints on iron-bearing phyllosilicate formation and alteration pathways on early mars. Journal of Geophysical Research. Planets 118, 2124–2136.

Chamberlin, T.C., 1897. Studies for students: The method of multiple working hypotheses. The Journal of Geology 5, 837–848.

Chamberlin, T.C., 1965. The method of multiple working hypotheses. Science 148, 754–759.

Chamley, H., 1989. Clay Sedimentology. Springer-Verlag.

Chang, H.C., Kopaska-Merkel, D.C., Chen, H.C., 2002. Identification of lithofacies using kohonen self-organizing maps. Computers & Geosciences 28, 223–229.

Cheng, Q., Agterberg, F.P., 1999. Fuzzy weights of evidence method and its application in mineral potential mapping. Natural Resources Research 8, 27–35.

Chipera, S.J., Apps, J.A., 2001. Geochemical stability of natural zeolites. Reviews in Mineralogy & Geochemistry 45, 117–161.

Chipera, S.J., Bish, D.L., 1997. Equilibrium modeling of clinoptilolite-analcime equilibria at yucca mountain, nevada, usa. Clays and Clay Minerals 45, 226–239.

Chollet, F., Allaire, J.J., 2018. Deep Learning with R. Manning Publications.

Christensen, P.R., Anderson, D.L., Chase, S.C., Clark, R.N., Kieffer, H.H., Malin, M.C., Pearl, J.C., Carpenter, J., Bandiera, N., Brown, F.G., Silverman, S., 1992. Thermal emission spectrometer experiment: Mars observer mission. Journal of Geophysical Research 97, 7719–7724.

Christensen, P.R., Bandfield, J.L., Clark, R.N., Edgett, K.S., Hamilton, V.E., Hoefen, T., Kieffer, H.H., Kuzmin, R.O., Lane, M., Malin, M.C., Morris, R.V., Pearl, J.C., Pearson, R., Roush, T.L., Ruff, S.W., Smith, M., 2000. Detection of crystalline hematite mineralization on mars by the thermal emission spectrometer: Evidence for near-surface water. Journal of Geophysical Research 105, 9623–9642.

Christensen, P.R., Bandfield, J.L., Hamilton, V.E., Ruff, S.W., Kieffer, H.H., Titus, T.N., Malin, M.C., Morris, R.V., Lane, M., Clark, R.L., Jakosky, B.M., Mellon, M.T., Pearl, J.C., Conrath, B.J., Smith, M., Clancy, R.T., Kuzmin, R.O., Roush, T., Mehall, G.L., Gorelick, N., Bender, K., Murray, K., Dason, S., Greene, E., Silverman, S., Greenfield, M., 2001. Mars global surveyor thermal emission spectrometer experiment: Investigation description and surface science results. Journal of Geophysical Research 106, 23,823 – 23,871.

Christensen, P.R., Jakosky, B.M., Kieffer, H.H., Malin, M.C., Harry Y. McSween, J., Nealson, K., Mehall, G.L., Silverman, S.H., Ferry, S., Caplinger, M., Ravine, M., 2004. The themal emission imaging system (themis) for the mars 2001 odyssey mission. Space Science Reviews 110, 85–130.

Christensen, P.R., Kieffer, H.H., Chase, S.C., LaPorte, D.D., 1986. A thermal emission spectrometer for identification of surface composition from earth orbit, in: Putnam, E.S. (Ed.), Commertial Applications and Scienctific Research Requirements for Thermal-Infrared Observations of the Terestrial Surfaces, pp. 119–132.

Clark, B.C., Baird, A.K., Weldon, R.J., Tsusaki, D.M., Schnabel, L., Candelaria, M.P., 1982. Chemical composition of martian fines. Journal of Geophysical Research 87, 10059–10067.

Clark, R.N., 1981. Water frost and ice: The near-infrared spectral reflectance 0.65 - 2.5 um. Journal of Geophysical Research 86, 3087–3096.

Clark, R.N., 1995. Reflectance spectra, in: Rock Physics and Phase Relations: A Handbook of Physical Constants. American Geophysical Union, pp. 178–188.

Clark, R.N., 1999. Spectroscopy of rocks and minerals, and principles of spectroscopy, in: Manual of Remote Sensing. U.S. Geological Survey, MS 964 Box 25046 Federal Center Denver, CO 80225-0046. volume 3, pp. 3–58.

Clark, R.N., King, T.V.V., Gorelick, N.S., 1987. Automatic continuum analysis of reflectance spectra, in: Proceedings of the Third Airborne Imaging Spectrometer Data Analysis Workshop, pp. 138–142.

Clark, R.N., King, T.V.V., Klejwa, M., Swayze, G.A., 1990. High spectral resolution reflectance spectroscopy of minerals. Journal of Geophysical Research 95, 12,653–12,680.

Clark, R.N., Roush, T.L., 1984. Reflectance spectroscopy: Quantitative analysis techniques for remote sensing applications. Journal of Geophysical Research 89, 6329–6340.

Cloutis, E.A., 1996. Hyperspectral geological remote sensing: evaluation of analytical techniques - review article. International Journal of Remote Sensing 17, 2215–2242.

Cloutis, E.A., Asher, P.M., Mertzman, S.A., 2002. Spectral reflectance properties of zeolites and remote sensing implications. Journal of Geophysical Research 107, doi:10.1029/2000JE001467.

Cloutis, E.A., Hawthorne, F.C., Mertzman, S.A., Krenn, K., Craig, M.A., Marcino, D., Methot, M., Strong, J., Mustard, J.F., Blaney, D.L., III, J.F.B., Vilas, F., 2006. Detection and discrimination of sulfate minerals using reflectance spectroscopy. Icarus 184, 121–157.

Coll, C., Caselles, V., Valor, E., Niclòs, R., Sánchez, J.M., Galve, J.M., Mira, M., 2007. Temperature and emissivity separation from aster data for low spectral contrast surfaces. Remote Sensing of Environment 110, 162–175.

Collins, E.F., Roberts, D.A., Sutton, P.C., Funk, C.C., Borel, C.C., 1999. Temperature estimation and compositional mapping using spectral mixture analysis of thermal imaging spectrometry data. Proc. SPIE 3753, Imaging Spectrometry V , 286–299.

Conel, J.E., Green, R.O., Vane, G., Bruegge, C.J., Alley, R.E., Curtiss, B.J., 1987. Airborne imaging spectrometer-2: Radiometric spectral characteristics and comparison of ways to compensate for the atmosphere. Proc. SPIE 0834, Imaging Spectroscopy II , 140–157.

Coombs, D.S., Alberti, A., Armbruster, T., Artioli, G., Colella, C., Galli, E., Grice, J.D., Liebau, F., Mandarino, J.A., Minato, H., Nickel, E.H., Passaglia, E., Peacor, D.R., Quartieri, S., Rinaldi, R., Ross, M., Sheppard, R.A., Tillmanns, E., Vezzalini, G., 1998. Recommended nomenclature for zeolite minerals: report of the subcommittee on zeolites of the international mineralogical association, commission on new minerals and mineral names. Mineralogical Magazine 62, 533–571.

Coombs, D.S., Alberti, A., Armbruster, T., Artioli, G., Colella, C., Galli, E., Grice, J.D., Liebau, F., Minato, H., Nickel, E.H., Passaglia, E., Peacor, D.R., Quartieri, S., Rinaldi, R., Ross, M., Sheppard, R.A., Tillmanns, E., Vezzalini, G., 1997. Recommended nomenclature for zeolite minerals: Report of the subcommittee on zeolites of the

international mineralogical association, commission on new minerals and mineral names. The Canadian Mineralogist 35, 1571–1606.

Cooper, S.A., 1993. Geology, development, and economics of zeolite mining in Australia. Ph.D. thesis. University of Tasmania.

Craddock, R.A., Howard, A.D., 2002. The case for rainfall on a warm, wet early mars. Journal of Geophysical Research 107, 511.

Crisp, J., Kahle, A.B., Abbott, E.A., 1990. Thermal infrared spectral character of hawaiian basaltic glasses. Journal of Geophysical Research 95, 21657–21669.

Crombie, A.C., 1994. Styles of scientific thinking in the europian tradition: The history of argument and explanation especially in the mathematical and biomedical sciences and arts. volume 1. Duckworth.

Crosta, A.P., Moore, J.M., 1989. Enhancement of landsat thematic mapper imagery for residual soil mapping in sw minais gerais state, brazil: A prospecting case history in greenstone belt terrain., in: Proceedings of the 7th (ERIM) Thematic Conference: Remote Sensing for Exploration Geology, pp. 1173–1187.

Crowley, J.K., Brickey, D.W., Rowan, L.C., 1989. Airborne imaging spectrometer data of the ruby mountains, montana: Mineral discrimination using relative absorption band-depth images. Remote Sensing of Environment 29, 121–134.

Czarnecki, S., Hardgrove, C., Gasda, P.J., Gabriel, T.S.J., Starr, M., Rice, M.S., Frydenvang, J., Wiens, R.C., Rapin, W., Nikiforov, S., Lisov, D., Litvak, M., Calef, F., Gengl, H., Newsom, H., Thompson, L., Nowicki, S., 2020. Identification and description of a silicic volcaniclastic layer in gale crater, mars, using active neutron interrogation. Journal of Geophysical Research. Planets 125, 20.

Dalton, J.B., 2003. Spectral behavior of hydrated sulfate salts: Implications for europa mission spectrometer design. Astrobiology 3, 771–784.

Daswani, M.M., Schwenzer, S.P., Reed, M.H., Wright, I.P., Grady, M.M., 2016. Alteration minerals, fluids, and gases on early mars: Predictions from 1-d flow geochemical modeling of mineral assemblages in meteorite alh 84001. Meteoritics & Planetary Science 51, 2154–2174.

Datt, B., McVicar, T.R., Niel, T.G.V., Jupp, D.L.B., Pearlman, J.S., 2003. Preprocessing eo-1 hyperion hyperspectral data to support the application of agricultural indexes. IEEE Transactions on Geoscience and Remote Seinsing Vol. 41, 1246 – 1259.

Davis, J.M., Balme, M., Grindrod, P.M., Williams, R.M.E., Gupta, S., 2016. Extensive noachian fluvial systems in arabia terra: Implications for early martian climate. Geology 44, 847–850.

Davis, J.M., Gupta, S., Balme, M., Grindrod, P.M., Fawdon, P., Dickeson, Z.I., Williams, R.M., 2019. A diverse array of fluvial depositional systems in arabia terra: Evidence for mid-noachian to early hesperian rivers on mars. Journal of Geophysical Research: Planets 124, 1913–1934.

Day, J.M.D., Taylor, L.A., Floss, C., Harry Y. McSween, J., 2006. Petrology and chemistry of mil 03346 and its significance in understanding the petrogenesis of nakhlites on mars. Meteoritics & Planetary Science 41, 581–606.

Deffeyes, K.S., 1959. Zeolites in sedimentary rocks. Journal of Sedimentary Petrology 29, 602–609.

Delany, J.M., 1985. Reaction of Topopah Spring Tuff with J-13 water: A geochemical modeling approach using the EQ3/6 Reaction Path Code. Technical Report. Lawrence Livermore National Laboratory, Livermore, California.

Delany, J.M., Puigdomenech, I., Wolery, T.J., 1986. Precipitation kinetics option for the EQ6 geochemical reaction path code. volume UCRL-53642. Livermore, California: Lawrence Livermore National Laboratory. TIC: 203008.

Dibble, W.E., Tiller, W.A., 1981. Kinetic model of zeolite paragenesis in tuffaceous sediments. Clays and Clay Minerals 29, 323–330.

Dickinson, W.W., Rosen, M.R., 2003. Antarctic permafrost: An analogue for water and diagenetic minerals on mars. Geology 31, 199–202.

Dinguirard, M., Slater, P.N., 1999. Calibration of space-multispectral imaging sensors: A review. Remote Sensing of Environment 68, 194–205.

Dixon, J.B., Weed, S.B. (Eds.), 1989. Minerals in Soil Environments. Number 1 in the Soil Science Society of America Book Series. second edition ed., Soil Science Society of America.

Dowla, F.U., Rogers, L.L., 1995. Solving Problems in Environmental Engineering and Geosciences with Artificial Neural Networks. The MIT Press.

Downes, S.M., 2021. Models and modeling in the sciences. A philosophical introduction. Taylor & Francis.

Dreibus, G., Palme, H., Rammensee, W., Spettel, B., Weckwerth, G., Wanke, H., 1982. Composition of shergotty parent body: Further evidence for a two component model of planet formation, in: Lunar and Planetary Science Conference XIII, Lunar and Planetary Institute. pp. 186–187.

Dreibus, G., Spettel, B., Haubold, R., Jochum, K.P., Palme, H., Wolf, D., Zipfel, J., 2000. Chemistry of a new shergottite: Sayh al uhaymir 005. Meteoritics & Planetary Science 35.

Du, P., Huang, D., Ning, D., Chen, Y., Liu, B., Wang, J., Xu, J., 2019. Application of bayesian model and discriminant function analysis to the estimation of sediment source contributions. International Journal of Sediment Research 34, 577–590.

Duggin, M.J., 1985. Factors limiting the discrimination and quantification of terrestrial features using remotely sensed radiance. International Journal of Remote Sensing 6, 3–27.

Duggin, M.J., Robinove, C.J., 1990. Assumptions implicit in remote sensing data acquisition and analysis. International Journal of Remote Sensing Vol. 11, 1669–1694.

Easton, A.J., Elliott, C.J., 1977. Analysis of some meteorites from the british museum (natural history) collection. Meteoritics 12, 409–416.

Edson, G.M., 1977. Some bedded zeolites, San Simon basin, Southeastern Arizona. Ph.D. thesis. The Universoty of Arizona.

Ehlmann, B.L., Berger, G., Mangold, N., Michalski, J.R., Catling, D.C., Ruff, S.W., Chassefière, E., Niles, P.B., Chevrier, V., Poulet, F., 2013. Geochemical consequences of widespread clay mineral formation in mars' ancient crust. Space Science Reviews 174, 329–364.

Ehlmann, B.L., Bish, D.L., Ruff, S.W., Mustard, J.F., 2012. Mineralogy and chemistry of altered icelandic basalts: Application to clay mineral detection and understanding aqueous environments on mars. Journal of Geophysical Research 117, 27.

Ehlmann, B.L., Edgett, K.S., Sutter, B., Achilles, C.N., Litvak, M.L., Lapotre, M.G.A., Sullivan, R., Fraeman, A.A., Arvidson, R.E., Blake, D.F., Bridges, N.T., Conrad, P.G., Cousin, A., Downs, R.T., Gabriel, T.S.J., Gellert, R., Hamilton, V.E., Hardgrove, C., Johnson, J.R., Kuhn, S., Mahaffy, P.R., Maurice, S., McHenry, M., Meslin, P.Y., Ming, D.W., Minitti, M.E., Morookian, J.M., Morris, R.V., O'Connell-Cooper, C.D., Pinet, P.C., Rowland, S.K., Schröder, S., Siebach, K.L., Stein, N.T., Thompson, L.M., Vaniman, D.T., Vasavada, A.R., Wellington, D.F., Wiens, R.C., Yen, A.S., 2017. Chemistry, mineralogy, and grain properties at namib and high dunes, bagnold dune field, gale crater, mars: A synthesis of curiosity rover observations. Journal of Geophysical Research: Planets 122, 2510–2543.

Ehlmann, B.L., Edwards, C.S., 2014. Mineralogy of the martian surface. Annual Review of Earth and Planetary Sciences 42, 291–315.

Ehlmann, B.L., Mustard, J.F., Murchie, S.L., 2010. Geologic setting of serpentine deposits on mars. Geophysical Research Letters 37, doi:10.1029/2010GL042596.

Ehlmann, B.L., Mustard, J.F., Murchie, S.L., Bibring, J.P., Meunier, A., Fraeman, A.A., Langevin, Y., 2011. Subsurface water and clay mineral formation during the early history of mars. Nature Vol. 479, 53–60.

Ehlmann, B.L., Mustard, J.F., Murchie, S.L., Poulet, F., Bishop, J.L., Brown, A.J., Calvin, W.M., Clark, R.N., Marais, D.J.D., Milliken, R.E., Roach, L.H., Roush, T.L., Swayze, G.A., Wray, J.J., 2008. Orbital identification of carbonate-bearing rocks on mars. Science 322, 1828–1832.

Ehlmann, B.L., Mustard, J.F., Swayze, G.A., Clark, R.N., Bishop, J.L., Poulet, F., Marais, D.J.D., Roach, L.H., Milliken, R.E., Wray, J.J., Barnouin-Jha, O., Murchie, S.L., 2009. Identification of hydrated silicate minerals on mars using mro-crism: Geologic context near nili fossae and implications for aqueous alteration. Journal of Geophysical Research Vol. 114, doi:10.1029/2009JE003339.

Ehsani, A.H., Quiel, F., 2009. A semi-automatic method for analysis of landscape elements using shuttle radar topography mission and landsat etm+data. Computers & Geosciences 35, 373–389.

Einsele, G., 2000. Sedimentary basins: Evolution, facies, and sedimentary budget. Springer.

Engelbrecht, A.P., 2002. Computational Intelligence. An Introduction. John Wiley and Sons, Ltd.

Engelhardt, W.v., Zimmermann, J., 1988. Theory of earth sciences. Cambridge University Press.

ENVI, 2009. Envi user's guide.

Ersoy, O., Aydar, E., Gourgaud, A., Artuner, H., Bayhan, H., 2007. Clustering of volcanic ash arising from different fragmentation mechanisms using kohonen self-organizing maps. Computers & Geosciences 33, 821–828.

Evans, L.G., Squyres, S.W., 1987. Investigation of martian h2o and co2 via orbital gamma ray spectroscopy. Journal of Geophysical Research 92, 9153–9167.

Farley, K.A., Williford, K.H., Stack, K.M., Bhartia, R., Chen, A., Torre, M.d.l., Hand, K., Goreva, Y., Herd, C.D.K., Hueso, R., Liu, Y., Maki, J.N., Martinez, G., Moeller, R.C., Nelessen, A., Newman, C.E., Nunes, D., Ponce, A., Spanovich, N., Willis, P.A., Beegle,

L.W., III, J.F.B., Brown, A.J., Hamran, S.E., Hurowitz, J.A., Maurice, S., Paige, D.A., Rodriguez-Manfredi, J.A., Schulte, M., Wiens, R.C., 2020. Mars 2020 mission overview. Space Science Reviews 216, 41.

Fassett, C.I., Head, J.W., 2005. Fluvial sedimentary deposits on mars: Ancient deltas in a crater lake in the nili fossae region. Geophysical Research Letters 32.

Fassett, C.I., Head, J.W., 2007. Layered mantling deposits in northeast arabia terra, mars: Noachian-hesperian sedimentation, erosion, and terrain inversion. Journal of Geophysical Research 112.

Fassett, C.I., Head, J.W., 2008. Valley network-fed, open-basin lakes on mars: Distribution and implications for noachian surface and subsurface hydrology. Icarus 198, 37–56.

Faye, J., 2002. Rethinking Science: A philosophical introduction to the unity of science. Ashgate.

Ferentinou, M., Hasiotis, T., Sakellariou, M., 2012. Application of computational intelligence tools for the analysis of marine geotechnical properties in the head of zakynthos canyon,greece. Computers & Geosciences 40, 166–174.

Fialips, C.I., Carey, J.W., Vaniman, D.T., Bish, D.L., Feldman, W.C., Mellon, M.T., 2005. Hydration state of zeolites, clays, and hydrated salts under present-day martian surface conditions: Can hydrous minerals account for mars odyssey observations of near-equatorial water-equivalent hydrogen? Icarus 178, 74–83.

Flint, L.E., Selker, J.S., 2003. Use of porosity to estimate hydraulic properties of volcanic tuffs. Advances in Water Resources 26, 561–571.

Folco, L., Franchi, I.A., D'orazio, M., Rocchi, S., Schultz, L., 2000. A new martian meteorite from the sahara: The shergottite dar al gani 489. Meteoritics & Planetary Science 35, 827–839.

Foley, C.N., Economou, T., Clayton, R.N., 2003. Final chemical results from the mars pathfinder alpha proton x-ray spectrometer. Journal of Geophysical Research 108, 8096.

Fraeman, A.A., Edgar, L.A., Rampe, E.B., Thompson, L.M., Frydenvang, J., Fedo, C.M., Catalano, J.G., Dietrich, W.E., Gabriel, T.S.J., Vasavada, A.R., Grotzinger, J.P., L'Haridon, J., Mangold, N., Sun, V.Z., House, C.H., Bryk, A.B., Hardgrove, C., Czarnecki, S., Stack, K.M., Morris, R.V., Arvidson, R.E., Banham, S.G., Bennett, K.A., Bridges, J.C., Edwards, C.S., Fischer, W.W., Fox, V.K., Gupta, S., Horgan, B.H.N., Jacob, S.R., Johnson, J.R., Johnson, S.S., Rubin, D.M., Salvatore, M.R., Schwenzer, S.P., Siebach, K.L., Stein, N.T., Turner, S.M.R., Wellington, D.F., Wiens, R.C., Williams, A.J., David, G., Wong, G.M., 2020a. Evidence for a diagenetic origin of vera rubin ridge, gale crater, mars : Summary and synthesis of curiosity's exploration campaign. Journal of Geophysical Research: Planets 125, 34.

Fraeman, A.A., Johnson, J.R., Arvidson, R.E., Rice, M.S., Wellington, D.F., Morris, R.V., Fox, V.K., Horgan, B.H.N., Jacob, S.R., Salvatore, M.R., Sun, V.Z., Pinet, P., III, J.F.B., Wiens, R.C., Vasavada, A.R., 2020b. Synergistic ground and orbital observations of iron oxides on mt. sharp and vera rubin ridge. Journal of Geophysical Research: Planets 125, 24.

Frodeman, R., 1995. Geological reasoning: Geology as an interpretive and historical science. GSA Bulletin 107, 960–968.

Fukushi, K., Sekine, Y., Sakuma, H., Morida, K., Wordsworth, R., 2019. Semiarid climate and hyposaline lake on early mars inferred from reconstructed water chemistry at gale. Nature Communications 10.

Futuyma, D.J., 2006. Evolution. 3rd ed., Sinauer Associates, Inc.

Gaffey, S.J., 1986. Spectral reflectance of carbonate minerals in the visible and near infrared (0.35-2.55 microns): calcite, aragonite, and dolomite. American Mineralogist 71, 151–162.

Gaffey, S.J., 1987. Spectral reflectance of carbonate minerals in the visible and nearinfrared (0.35-2.55 um): Anhydrous carbonate minerals. Journal of Geophysical Research 92, 1429–1440.

Geladi, P., MacDougall, D., Martens, H., 1985. Linearization and scatter-correction for near-infrared reflectance spectra of meat. Applied Spectroscopy 39, 491–500.

Gellert, R., Rieder, R., Bruckner, J., Clark, B.C., Dreibus, G., Klingelhofer, G., Lugmair, G., Ming, D.W., Wanke, H., Yen, A., Zipfel, J., Squyres, S.W., 2006. Alpha particle x-ray spectrometer (apxs): Results from gusev crater and calibration report. Journal of Geophysical Research 111, doi:10.1029/2005JE002555.

Gendrin, A., Mangold, N., Bibring, J.P., Langevin, Y., Gondet, B., Poulet, F., Bonello, G., Quantin, C., Mustard, J., Arvidson, R., LeMouelic, S., 2005. Sulfates in martian layered terrains: The omega/mars express view. Science 307, 1587–1591.

Gesch, D.B., 2007. Chapter 4 – the national elevation dataset, in: Maune, D. (Ed.), Digital elevationl model technologies and applications: The DEM Users Manual, (2nd ed.): Bethesda, Maryland, American Society for Photogrammetry and Remote Sensing, pp. 99–118.

Giere, R.N., 1991. Understanding Scientific Reasoning. 3 ed., Holt, Rinehart and Winston, Inc.

Giere, R.N., 1999. Using models to represent reality, in: Magnani, L., Nersessian, N.J., Thagard, p. (Eds.), Model-based reasoning in scientific discovery. Kluwer Academic/Plenum Publishers.

Gilbert, G.K., 1886. The induction of scientific method by example, with an illustration drawn from the quaternary geology of utah. American Journal of Science s3-31, 284–299.

Gilbert, G.K., 1896. The origin of yypotheses, illustrated by the discussion of a topographic problem. Science 3, 1–13.

Gillespie, A., Rokugawa, S., Matsunaga, T., Cothern, J.S., Hook, S., Kahle, A.B., 1998. A temperature and emissivity separation algorithm for advanced spaceborne thermal emission and reflection radiometer (aster) images. IEEE Transactions on Geoscience and Remote Seinsing Vol. 36, 1113–1126.

Gillespie, A.R., 1985. Lithological mapping of silicate rocks using tims, in: The TIMS Data Users' Workshop, JPL Publication 86-38, Jet Propulsion Laboratory, Pasdena, CA. pp. 29–44.

Gillespie, A.R., 1992a. Enhancement of multispectral thermal infrared images: Decorrelation contrast stretching. Remote Sensing of Environment 42, 147–155.

Gillespie, A.R., 1992b. Spectral mixture analysis of multispectral thermal infrared images. Remote Sensing of Environment 42, 137–145.

Gillespie, A.R., Kahle, A.B., Walker, R.E., 1986. Color enhancement of highly correlated images. i. decorrelation and hsi contrast stretches. Remote Sensing of Environment 20, 209–235.

Gillet, P., Barrat, J.A., Beck, P., Marty, B., Greenwood, R.C., Franchi, I.A., Bohn, M., Cotten, J., 2005. Petrology, geochemistry, and cosmic-ray exposure age of lherzolitic shergottite northwest africa 1950. Meteoritics & Planetary Science 40, 1175–1184.

Gleason, J.D., Kring, D.A., Hill, D.H., Boynton, W.V., 1997. Petrography and bulk chemistry of martian orthopyroxenite alh84001: Implications for the origin of secondary carbonates. Geochemica et Cosmochimica Acta 61, 3503–3512.

Goetz, A.F.H., Srivastava, V., 1985. Mineralogical mapping in the cuprite mining district, nevada, in: Proceedings of the Airborne Imaging Spectrometer Data Analysis Workshop, JPL Publication 85-41, Pasadena, CA. pp. 22–31.

Gondet, B., Bibring, J.P., Langevin, Y., Poulet, F., Gendrin, A., 2006. First detection of al-rich phyllosilicate on mars from omega-mex. Geophysical Research Abstracts 8, SRef–ID: 1607–7962/gra/EGU06–A–03691.

Gottardi, G., Galli, E., 1985. Natural Zeolites. volume 18 of *Minerals and Rocks*. 1 ed., Springer-Verlag Berlin Heidelberg.

Goudge, T.A., Aureli, K.L., Head, J.W., Fassett, C.I., Mustard, J.F., 2015. Classification and analysis of candidate impact crater-hosted closed-basin lakes on mars. Icarus 260, 346–367.

Goudge, T.A., Fassett, C.I., Head, J.W., Mustard, J.F., Aureli, K.L., 2016. Insights into surface runoff on early mars from paleolake basin morphology and stratigraphy. Geology , doi:10.1130/G37734.1.

Goudge, T.A., Head, J.W., Mustard, J.F., Fassett, C.I., 2012. An analysis of open-basin lake deposits on mars: Evidence for the nature of associated lacustrine deposits and post-lacustrine modification processes. Icarus 219, 211–229.

Goudge, T.A., Russell, J.M., Mustard, J.F., Head, J.W., Bijaksana, S., 2017. A 40,000 yr record of clay mineralogy at lake towuti, indonesia: Paleoclimate reconstruction from reflectance spectroscopy and perspectives on paleolakes on mars. GSA Bulletin Vol.129, 806–819.

Gould, S.J., 1989. Wonderful life: The Burgess shale and the nature of history. W. W. Norton & Company.

Grant, J.A., Schultz, P.H., 1990. Gradational epochs on mars: Evidence from west-northwest of isidis basin and electris. Icarus 84, 166–195.

Green, A.A., Berman, M., Switzer, P., Craig, M.D., 1988. A transform for ordering multispectral data in terms of image quality with implications for noise removal. IEEE Transactions on Geoscience and Remote Seinsing Vol. 26, 65–74.

Green, A.A., Craig, M.D., 1985. Analysis of aircraft spectrometer data with logarithmic residuals, in: Vane, G., Goetz, A. (Eds.), in Proceedings of the Airborne Imaging Spectrometer Data Analysis Workshop, JPL Publication 86-35. pp. 111–119.

Greensmith, J.T., 1989. Volcaniclastic deposits, in: Petrology of the sedimentary rocks. Unwin Hyman, pp. 240–255.

Grotzinger, J.P., Crisp, J., Vasavada, A.R., Anderson, R.C., Baker, C.J., Barry, R., Blake, D.F., Conrad, P., Edgett, K.S., Ferdowski, B., Gellert, R., Gilbert, J.B., Golombek, M., Gómez-Elvira, J., Hassler, D.M., Jandura, L., Litvak, M., Mahaffy, P., Maki, J., Meyer, M., Malin, M.C., Mitrofanov, I., Simmonds, J.J., Vaniman, D., Welch, R.V., Wiens,

R.C., 2012. Mars science laboratory mission and science investigation. Space Science Reviews 170, 5–56.

Grotzinger, J.P., Hayes, A.G., Lamb, M.P., McLennan, S.M., 2013. Sedimentary processes on earth, mars, titan, and venus, in: Mackwell, S.J., Simon-Miller, A.A., Harder, J.W., Bullock, M.A. (Eds.), Comparative climatology of terrestrial planets. The University of Arizona Press, pp. 439–472.

Gude, A.J., Sheppard, R.A., 1986. Zeolitic diagenesis of tuffs in an upper miocene lacustrine deposit near durkee, baker county, oregon, in: Mumpton, F.A. (Ed.), Studies in Diagenesis. U. S. Geological Survey Bulletin. volume 1578, pp. 301–333.

Gude, A.J., Sheppard, R.A., 1988. A zeolitic tuff in a lacustrine facies of the gila conglomerate near buckhorn, grant county, new mexico. U. S. Geological Survey Bulletin 1763, 27.

Gundogdu, M.N., Yalcin, H., Temel, A., Clauer, N., 1996. Geological, mineralogical and geochemical characteristics of zeolite deposits associated with borates in the bigadi , emet and kirka neogene lacustrine basins, western turkey. Mineral Deposita 31, 492–513.

Guth, P.L., 2006. Geomorphometry from srtm: Comparison to ned. Photogrammetric Engineering & Remote Sensing 72, 269–277.

Hall, A., 1998. Zeolitization of volcaniclastic sediments: The role of temperature and ph. Journal of Sedimentary Research 68, 739–745.

Hanna, K.L.D., Thomas, I.R., Bowles, N.E., Greenhagen, B.T., Pieters, C.M., Mustard, J.F., Jackson, C.R.M., Wyatt, M.B., 2012. Laboratory emissivity measurements of the plagioclase solid solution series under varying environmental conditions. Journal of Geophysical Research V. 117, doi:10.1029/2012JE004184.

Hapke, B., 1981. Bidirectional reflectance spectroscopy. Journal of Geophysical Research 86, 3039–3054.

Hapke, B., 1993. Theory of Reflectance and Emittance Spectroscopy. volume 3 of *Topics in Remote Sensing*. Cambridge University Press.

Hardie, L.A., Smoot, J.P., Eugster, H.P., 1978. Saline lakes and their deposits: a sedimentological approach, in: Matter, A., Tucker, M.E. (Eds.), Modern and Ancient Lake Sediments. John Wiley and Sons. Inc.. volume 2, pp. 7–41.

Harding, D.J., Wirth, K.R., Bird, J.M., 1989. Spectral mapping of alaskan ophiolites using landsat thematic mapper data. Remote Sensing of Environment 28, 219–232.

Hargitai, H.I., Gulick, V.C., Glines, N.H., 2018. Paleolakes of northeast hellas: Precipitation, groundwater-fed, and fluvial lakes in the navua–hadriacus–ausonia region, mars. Astrobiology 18, 1435–1459.

Harsanyi, J.C., Chang, C.I., 1994. Hyperspectral image classification and dimensionality reduction: An orthogonal subspace projection approach. IEEE Transactions on Geoscience and Remote Seinsing 32, 779–785.

Hartmann, W.K., 2005. Martian cratering 8: Isochron refinement and the chronology of mars. Icarus 174, 294–320.

Hartmann, W.K., Neukum, G., 2001. Cratering chronology and the evolution of mars. Space Science Reviews 96, 165–194.

Hausrath, E.M., Olsen, A.A., 2013. Using the chemical composition of carbonate rocks on mars as a record of secondary interaction with liquid water. American Mineralogist 98, 897–906.

Hawkins, D.B., 1981. Kinetics of glass dissolution and zeolite formation under hydrothermal conditions. Clays and Clay Minerals 29, 331–340.

Hay, R.L., 1963. Zeolitic weathering in olduvai gorge, tanganyika. Gelogical Society of America Bulletin 74, 1281–1286.

Hay, R.L., 1966. Zeolites and zeolitic reactions in sedimentary rocks. Special GSA Papers Number 85, 130.

Hay, R.L., Guldman, S.G., 1987. Diagenetic alteration of silicic ash in searles lake, california. Clays and Clay Minerals 35, 449–457.

Hay, R.L., Sheppard, R.A., 2001. Occurrence of zeolites in sedimentary rocks: An overview, in: Bish, D.L., Ming, D. (Eds.), Natural Zeolites: Occurrence, Properties, Applications. Reviews in Mineralogy and Geochemistry. volume Vol. 45, No. 1, pp. 217–234.

Hayworth, B.P., Kopparapu, R.K., Haqq-Misra, J., Batalha, N.E., Payne, R.C., Foley, B.J., Ikwut-Ukwa, M., Kasting, J.F., 2020. Warming early mars with climate cycling: The effect of co2-h2 collision-induced absorption. Icarus 345, 11.

Hazen, R.M., Papineau, D., Bleeker, W., Downs, R.T., Ferry, J.M., McCoy, T.J., Sverjensky, D.A., Yang, H., 2008. Mineral evolution. American Mineralogist 93, 1693–1720.

He, Q., Xiao, L., Balta, J.B., Baziotis, I.P., Hsu, W., Guan, Y., 2015. Petrography and geochemistry of the enriched basaltic shergottite northwest africa 2975. Meteoritics & Planetary Science 50, 2024–2044.

Hecht, M.H., Kounaves, S.P., Quinn, R.C., West, S.J., Young, S.M.M., Ming, D.W., Catling, D.C., Clark, B.C., Boynton, W.V., Hoffman, J., DeFlores, L.P., Gospodinova, K., Kapit, J., Smith, P.H., 2009. Detection of perchlorate and the soluble chemistry of martian soil at the phoenix lander site. Science 325, 64–67.

Hecker, C., Meijde, M.v.d., Werff, H.v.d., Meer, F.D.v.d., 2008. Assessing the influence of reference spectra on synthetic sam classification results. IEEE Transactions on Geoscience and Remote Seinsing Vol. 46, 4162–4172.

Helgeson, H.C., 1969. Thermodynamics of hydrothermal systems at elevated temperatures and pressures. American Journal of Science 267, 729–804.

Herd, C.D.K., Walton, E.L., Agee, C.B., Muttik, N., Ziegler, K., Shearer, C.K., Bell, A.S., Santos, A.R., Burger, P.V., Simon, J.I., Tappa, M.J., McCubbin, F.M., Gattacceca, J., Lagroix, F., Sanborn, M.E., Yin, Q.Z., Cassata, W.S., Borg, L.E., Lindvall, R.E., Kruijer, T.S., Brennecka, G.A., Kleine, T., Nishiizumi, K., Caffee, M.W., 2017. The northwest africa 8159 martian meteorite: Expanding the martian sample suite to the early amazonian. Geochemica et Cosmochimica Acta 218, 1–26.

Hernandez-Baquero, E., 2000. Characterization of the Earth's surface and atmosphere for multispectral and hyperspectral thermal imagery. Ph.D. thesis. Rochester Institute of Technology.

Hesse, M.B., 1966. Models and analogies in science. University of Notre Dame Press.

High, L.R., Picard, M.D., 1965. Sedimentary petrology and origin of analcime-rich popo agie member, chugwater (triassic) formation, west-central wyoming. Journal of Sedimentary Petrology 35, 49–70.

Hillhouse, J.W., 1987. Late tertiary and quaternary geology of the tecopa basin, southeastern california. U. S. Geological Survey Miscellaneous Investigations Map I-1728, Scale 1:48,000 , 16 p. text.

Hook, S.j., Gabell, A., Green, A., Kealy, P., 1992. A comparison of techniques for extracting emissivity information from thermal infrared data for geologic studies. Remote Sensing of Environment 42, 123–135.

Horgan, B.H., Anderson, R.B., Dromart, G., Amador, E.S., Rice, M.S., 2020. The mineral diversity of jezero crater: Evidence for possible lacustrine carbonates on mars. Icarus 339, 34.

Horn, B.K.P., Woodham, R.J., 1979. Destriping landsat mss images by histogram modification. Computer Graphics and Image Processing 10, 69–83.

Hover, V.C., Ashley, G.M., 2003. Geochemical signatures of paleodepositional and diagenetic environments: A stem/aem study of authigenic clay minerals from an arid rift basin, olduvai gorge, tanzania. Clays and Clay Minerals 51, 231–251.

Hu, B., Wan, B., Xu, Y., Tao, L., Wu, X., Qiu, Q., Wu, Y., Deng, H., 2019. Mapping hydrothermally altered minerals with ast_07xt, ast_05 and hyperion datasets using a voting-based extreme learning machine algorithm. Ore Geology Reviews 114.

Hu, R., Kass, D.M., Ehlmann, B.L., Yung, Y.L., 2015. Tracing the fate of carbon and the atmospheric evolution of mars. Nature Communications 6, doi:10.1038/ncomms10003.

Hubbard, B.E., Crowley, J.K., 2005. Mineral mapping on the chilean-bolivian altiplano using co-orbital ali, aster and hyperion imagery: Data dimensionality issues and solutions. Remote Sensing of Environment 99, 173–186.

Hunt, G.R., 1977. Spectral signatures of particulate minerals in the visible and near infrared. Geophysics Vol. 42, 501–513.

Hunt, G.R., 1979. Near-infrared (1.3-2.4 um) spectra of alteration minerals- potential for use in remote sensing. Geophysics Vol. 44, 1974–1986.

Hunt, G.R., Salisbury, J.W., 1970. Visible and near-infrared spectra of minerals and rocks: I. silicate minerals. Modern Geology 1, 283–300.

Hunt, G.R., Salisbury, J.W., Lenhoff, C.J., 1972. Visible and near-infrared spectra of minerals and rocks: V. halides, phosphates, arsenates, vanadates and borates. Modern Geology 3, 121–132.

Hunt, G.R., Salisbury, J.W., Lenhoff, C.J., 1973. Visible and near-infrared spectra of minerals and rocks: Vi. additional silicates. Modern Geology Vol. 4, 85–106.

Hurowitz, J.A., Grotzinger, J.P., Fischer, W.W., McLennan, S.M., Milliken, R.E., Stein, N., Vasavada, A.R., Blake, D.F., Dehouck, E., Eigenbrode, J.L., Fairén, A.G., Frydenvang, J., Gellert, R., Grant, J.A., Gupta, S., Herkenhoff, K.E., Ming, D.W., Rampe, E.B., Schmidt, M.E., Siebach, K.L., Stack-Morgan, K., Sumner, D.Y., Wiens, R.C., 2017. Redox stratification of an ancient lake in gale crater, mars. Science 356.

Hynek, B.M., Beach, M., Hoke, M.R.T., 2010. Updated global map of martian valley networks and implications for climate and hydrologic processes. Journal of Geophysical Research 115, doi:10.1029/2009JE003548.

Iijima, A., 1988. Chapter 3. diagenetic transformations of minerals as exemplified by zeolites and silica minerals - a japanese view, in: Chilingarian, G.V., Wolf, K.H. (Eds.), Developments in Sedimentology, Diagenesis II. volume 43, pp. 147–211.

Ikeda, Y., Kimura, M., Takeda, H., Shimoda, G., Kita, N.T., Morishita, Y., Suzuki, A., Jagoutz, E., Dreibus, G., 2006. Petrology of a new basaltic shergottite: Dhofar 378. Antarctic Meteorites Research 19, 20–44.

Irving, A.J., Bunch, T.E., Kuehner, S.M., Herd, C.D.K., Gellissen, M., Lapen, T.J., Rumble, D., Pitt, D., 2011. Petrologic, elemental and isotopic characterization of shock-melted, enriched ultramafic poikilitic shergottite northwest africa 6342, in: 42nd Lunar and Planetary Science Conference, Lunar and Planeraty Institute, The Woodlands, Texas. p. Abs No. 1612.

Irving, A.J., Bunch, T.E., Kuehner, S.M., Korotev, R.L., Classen, N.C., 2008. Unique ultramafic shergottite northwest africa 4797: A highly shocked martian wehrlite cumulate related to enriched basaltic (not "lherzolitic") shergottites, in: Lunar and Planetary Science XXXIX, Lunar and Planetary Institute, Texas. p. Abs No. 2047.

Irving, A.J., Kuehner, S.M., Herd, C.D.K., Gellissen, M., Korotev, R.L., Puchtel, I., Walker, R.J., Lapen, T.J., Rumble, D., 2010a. Petrologic, elemental and multi-isotopic characterization of permafic olivine-phyric shergottite northwest africa 5789: A primitive magma derived from depleted martian mantle, in: 41st Lunar and Planetary Science Conference, Lunar and Planetary Institute, The Woodlands, Texas. p. Abs No. 1547.

Irving, A.J., Kuehner, S.M., Herd, C.D.K., Gellissen, M., Rumble, D., Lapen, T.J., Ralew, S., Altmann, M., 2010b. Olivine-bearing diabasic shergottite northwest africa 5990: Petrology and composition of a new type of depleted martian igneous rock, in: 41st Lunar and Planetary Science Conference, Lunar and Planetary Institute, The Woodlands, Texas. p. Abs No. 1833.

Irwin, R.P., Howard, A.D., Craddock, R.A., Moore, J.M., 2005. An intense terminal epoch of widespread fluvial activity on early mars: 2. increased runoff and paleolake development. Journal of Geophysical Research 110.

ITC-ILWIS, 2001. Ilwis 3.0 academic user's guide.

Itoh, Y., Parente, M., 2021. A new method for atmospheric correction and de-noising of crism hyperspectral data. Icarus 354, doi.org/10.1016/j.icarus.2020.114024.

Iwasaki, A., Fujisada, H., Akao, H., Shindou, O., Akagi, S., 2002. Enhancement of spectral separation performance for aster/swir. Proceedings of SPIE Vol. 4486, 42–50.

Jambon, A., Barrat, J.A., Bollinger, C., Sautter, V., Boudouma, O., Greenwood, R.C., Franchi, I.A., Badia, D., 2010. Northwest africa 5790. top sequence of the nakhlite pile, in: 41st Lunar and Planetary Science Conference, Lunar and Planetary Institute, The Woodlands, Texas. p. Abs No. 1696.

James, G., Witten, D., Hastie, T., Tibshirani, R., 2017. An Introduction to Statistical Learning with Applications in R. Springer Texts in Statistics, Springer.

Johnson, B.R., Young, S.J., 1998. In-Scene Atmospheric Compensation: Application to SEBASS Data Collected at the ARM Site. Technical Report. Technical Report, Space and Environment Technology Center, The Aerospace Corporation.

Kahle, A.B., Madura, D.P., Soha, J.M., 1980. Middle infrared multispectral aircraft scanner data: analysis for geological applications. Applied Optics 19, 2279–2290.

Kahn, R., 1985. The evolution of co2 on mars. Icarus 62, 175–190.

Kalinowski, A., Oliver, S., 2004. ASTER Mineral Index Processing Manual. Technical Report. Remote Sensing Applications, Geoscience Australia.

Kasting, J.F., 1991. Co2 condensation and the climate of early mars. Icarus 94, 1–13.

Kato, S., Matsunaga, T., Tonooka, H., 2014. Statistical and in-situ validations of the aster spectral emissivity product at railroad valley, nevada, usa. Remote Sensing of Environment 145, 81–92.

Kealy, P., Gabell, A.R., 1990. Estimation of emissivity and temperature using alpha coefficients, in: Proceedings of the second TIMS Workshop, JPL Publication 90-55, Jet Propulsion Labortory, Pasdena, CA. pp. 11–15.

Kealy, P.S., Hook, S.J., 1993. Separating temperature and emissivity in thermal infrared multispectral scanner data: Implications for recovering land surface temperatures. IEEE Transactions on Geoscience and Remote Seinsing Vol. 31, 1155–1164.

Kerber, L., Forget, F., Madeleine, J.B., Wordsworth, R., Head, J.W., Wilson, L., 2013. The effect of atmospheric pressure on the dispersal of pyroclasts from martian volcanoes. Icarus 223, 149–156.

Kerber, L., Head, J.W., 2010. The age of the medusae fossae formation: Evidence of hesperian emplacement from crater morphology, stratigraphy, and ancient lava contacts. Icarus Vol. 206, 669–684.

Kerber, L., Head, J.W., Madeleine, J.B., Forget, F., Wilson, L., 2012. The dispersal of pyroclasts from ancient explosive volcanoes on mars: Implications for the friable layered deposits. Icarus 219, 358–381.

Kerrisk, J.F., 1983. Reaction-path calculations of groundwater chemistry and mineral formation at rainier mesa, nevada. Los Alamos National Laboratory Report, LA-9912-MS , 44.

Kimura, M., Imae, N., Yamaguchi, A., Haramura, H., Kojima, H., 2018. Bulk chemical compositions of antarctic meteorites in the nipr collection. Polar Science 15, 24–28.

Kind, P., Osborne, J., 2017. Styles of scientific reasoning: A cultural rationale for science education? Science Education 101, 8–31.

Kingma, D.P., Ba, J.L., 2015. Adam: A method for stochastic optimization, in: 3rd International Conference on Learning Representations, ICLR 2015, San Diego, CA, USA.

Kirkland, L.E., Herr, K.C., Adams, P.M., 2003. Infrared stealthy surfaces: Why tes and themis may miss some substantial mineral deposits on mars and implications for remote sensing of planetary surfces. Journal of Geophysical Research Vol. 108, doi:10.1029/2003JE002105.

Kirov, G., Samajova, E., Nedialkov, R., Stanimirova, T.S., 2011. Alteration processes and products of acid pyroclastic rocks in bulgaria and slovakia. Clay Minerals 46, 279–294.

Kite, E.S., Mayer, D.P., Wilson, S.A., Davis, J.M., Lucas, A.S., Quay, G.S.d., 2019. Persistence of intense, climate-driven runoff late in mars history. Science Advances 5.

Klingelhofer, G., Morris, R.V., Bernhardt, B., Schroder, C., Rodionov, D.S., Jr., P.A.d.S., Yen, A., Gellert, R., Evlanov, E.N., Zubkov, B., Foh, J., Bonnes, U., Kankeleit, E., Gutlich, P., Ming, D.W., Renz, F., Wdowiak, T., Squyres, S.W., Arvidson, R.E., 2004. Jarosite and hematite at meridiani planum from opportunity's mossbauer spectrometer. Science Vol. 306, 1740–1745.

Knight, J., Mitchell, W.A., Rose, J., 2011. Geomorphological field mapping, in: Smith, M.J., Paron, P., Griffiths, J.S. (Eds.), Developments in earth surface processes. Elsevier. volume 15, pp. 151–187.

Knott, J.R., Machette, M.N., Wan, E., Klinger, R.E., Liddicoat, J.C., Sarna-Wojcicki, A.M., Fleck, R.J., Deino, A.L., Geissman, J.W., Slate, J.L., Wahl, D.B., Wernicke, B.P., Wells, S.G., III, J.C.T., Hathaway, J.C., Weamer, V.M., 2018. Late neogene–quaternary tephrochronology, stratigraphy, and paleoclimate of death valley, california, usa. GSA Bulletin 130, 1231–1255.

Knox-Robinson, C.M., 2000. Vectorial fuzzy logic: a novel technique for enhanced mineral prospectivity mapping, with reference to the orogenic gold mineralisation potential of the kalgoorlie terrane, western australia. Australian Journal of Earth Sciences 47, 929–941.

Kodikara, G.R., McHenry, L.J., 2020. Machine learning approaches for classifying lunar soils. Icarus 345.

Kodikara, G.R.L., ray, P.K.C., Chauhan, P., Chatterjee, R.S., 2016. Spectral mapping of morphological features on the moon with mgm and sam. International Journal of Applied Earth Observation and Geoinformation Vol. 44, 31–41.

Kohler, A., Ohrnberger, M., Scherbaum, F., 2009. Unsupervised feature selection and general pattern discovery using self- organizing maps for gaining insights into the nature of seismic wavefields. Computers & Geosciences 35, 1757–1767.

Kohonen, T., 1982. Self-organized formation of topologically correct feature maps. Biological Cybernetics 43, 59–69.

Kohonen, T., 2001a. The basic som, in: Self-Organizing Maps. Springer. volume 30 of *Springer Series in Information Sciences*, pp. 105–176.

Kohonen, T., 2001b. Learning vector quantization, in: Self-Organizing Maps. 3rd ed.. Springer. volume 30 of *Springer Series in Information Science*, pp. 245–262.

Kravitz, G., 2013. The thermodynamics time arrow and the logical function of the uniformity principle in geohistorical explanation, in: Baker, V. (Ed.), Rethinking the Fabric of Geology. The Geological Society of America. volume Geological Society of America Special Paper 502, pp. 19–40.

Krieger, M.H., 1979. Zeolitization of tertiary tuffs in lacustrine and alluvial deposits in the ray-san manuel area, pinal and gila counties, arizona. Shorter contributions to mineralogy and petrology Geologocal Survey Professional Paper 1124-D, D1–D11.

Kruijer, T.S., Kleine, T., Borg, L.E., Brennecka, G.A., Irving, A.J., Bischoff, A., Agee, C.B., 2017. The early differentiation of mars inferred from hf–w chronometry. Earth and Planetary Science Letters 474, 345–354.

Kruse, F.A., 2004. Comparison of atrem, acorn, and flaash atmospheric corrections using low-altitude aviris data of boulder, colorado., in: Proceedings of 13th JPL Airborne Geoscience Workshop, Pasadena, CA, USA. p. 10.

Kruse, F.A., Boardman, J.W., Huntington, J.F., 2003. Comparison of airborne hyperspectral data and eo-1 hyperion for mineral mapping. IEEE Transactions on Geoscience and Remote Seinsing 41, 1388–1400.

Kruse, F.A., Lefkoff, A.B., Boardman, J.W., Heidebrecht, K.B., Shapiro, A.T., Barloon, P.J., Goetz, A.F.H., 1993. The spectral image processing system (sips) interactive visualization and analysis of imaging spectrometer data. Remote Sensing of Environment 44, 145–163.

Kuehner, S.M., Irving, A.J., Herd, C.D.K., Gellissen, M., Lapen, T.J., Rumble, D., 2011. Pristine olivine-phyric shergottite nwa 6162: A primitive magma with accumulated crystals derived from depleted martian mantle, in: 42nd Lunar and Planetary Science Conference, Lunar and Planetary Institute, The Woodlands, Texas. p. Abs No. 1610.

Kuhn, T.S., 1962. The structure of scientifc revolutions. The University of Chicago Press.

Kusakabe, H., 1982. An interpretation of zeolitic zoning around kuroko ore deposits on the basis of hydrothermal experiments. Mining Geology 32, 435–442.

Lagroix, F., Banerjee, S.K., 2004. The regional and temporal significance of primary aeolian magnetic fabrics preserved in alaskan loess. Earth and Planetary Science Letters 225, 379–395.

Lander, R.H., Hay, R.L., 1993. Hydrogeologie control on zeolitic diagenesis of the white river sequence. Geological Society of America Bulletin 105, 361–376.

Lane, M.D., Christensen, P.R., 1998. Thermal infrared emission spectroscopy of salt minerals predicted for mars. Icarus 135, 528–536.

Langella, A., Cappelletti, P., Gennaro, R.d., 2001. Zeolites in closed hydrologic systems, in: Bish, D.L., Ming, D. (Eds.), Natural Zeolites: Occurrence, Properties, Applications. Reviews in Mineralogy and Geochemistry. volume Vol. 45, No. 1, pp. 235–260.

Lapen, T.J., Righter, M., Andreasen, R., Irving, A.J., Satkoski, A.M., Beard, B.L., Nishiizumi, K., Jull, A.J.T., Caffee, M.W., 2017. Two billion years of magmatism recorded from a single mars meteorite ejection site. Science Advances 3.

Larsen, D., 2008. Revisiting silicate authigenesis in the pliocene–pleistocene lake tecopa beds, southeastern california: Depositional and hydrological controls. Geosphere 4, 612–639.

Larsen, D., Crossey, L.J., 1996. Depositional environments and paleolimnology of an ancient caldera lake: Oligocene creede formation, colorado. GSA Bulletin 108, 526–544.

Larsen, D., Olson, K., 2019. Evolution of the pleistocene lake tecopa beds, southeastern california: A stratigraphic and sedimentologic perspective, in: Starratt, S.W., Rosen, M.R. (Eds.), From Saline to Freshwater: The Diversity of Western Lakes in Space and Time: Geological Society of America Special Paper 536. The Geological Society of America, pp. 319–356.

Lasaga, A.C., 1998. Kinetic theory in the earth sciences. Princeton University Press.

Lawrence, D.C., 1988. Geologic field trip guide to the northern succor creek area, malheur county, oregon. Oregon Geology 50, 15–21.

LeCun, Y., Bengio, Y., Hinton, G., 2015. Deep learning (review). Nature Vol. 521, 436–444.

Lee, Y.I., 1988. Chemistry and origin of zeolites in sandstones at dsdp sites 445 and 446, daito ridge and basin province, northwest pacific. Chemical Geology 67, 261–273.

Lehnert, L.W., Meyer, H., Obermeier, W.A., Silva, B., Regeling, B., Bendix, J., 2018. Hyperspectral data analysis in r: the hsdar package. Journal of Statistical Software 89, 10.18637/jss.v089.i12.

Levenberg, K., 1944. A method for the solution of certain non-linear problems in least squares. The Quarterly of Applied Mathematics 2, 164–168.

Li, Z.L., Becker, F., Stoll, M.P., Wan, Z., 1999. Evaluation of six methods for extracting relative emissivity spectra from thermal infrared images. Remote Sensing of Environment 69, 197–214.

Lin, Y., Qi, L., Wang, G., Xu, L., 2008. Bulk chemical composition of lherzolitic shergottite grove mountains 99027 - constraints on the mantle of mars. Meteoritics & Planetary Science 43, 1179–1187.

Liu, D., Li, L., Sun, Y., 2015. An improved radiative transfer model for estimating mineral abundance of immature and mature lunar soils. Icarus 253, 40–50.

Lodders, K., 1998. A survey of shergottite, nakhlite and chassigny meteorites whole-rock compositions. Meteoritics & Planetary Science 33, A183–A190.

Loizeau, D., C.Werner, S., Mangold, N., Bibring, J.P., Vago, J.L., 2012. Chronology of deposition and alteration in the mawrth vallis region, mars. Planetary and Space Science 72, 31–43.

Love, J.D., 1970. Cenozoic geology of the granite mountains area, central wyoming. Geological Survey Professional Paper 495-C, 163.

Luo, W., Stepinski, T.F., 2009. Computer-generated global map of valley networks on mars. Journal of Geophysical Research 114.

Luo, X., Dimitrakopoulos, R., 2003. Data-driven fuzzy analysis in quantitative mineral resource assessment. Computers & Geosciences 29, 3–13.

Machiels, L., Morante, F., Snellings, R., Elsen, J., Paredes, C., 2006. Quantitative mineralogy and genetic history of the natural zeolite deposits of coastal ecuador, in: Bowman, R.S., Delap, S.E. (Eds.), Zeolite '06—7th International Conference on the Occurrence, Properties, and Utilization of Natural Zeolites, Socorro, New Mexico USA. pp. 166–167.

Madsen, B.M., 1970. Core logs of three test holes in cenozoic lake deposits near hector, california. Geological Survey Bulletin 1296, 48.

Mahaffy, P.R., Webster, C.R., Atreya, S.K., Franz, H., Wong, M., Conrad, P.G., Harpold, D., Jones, J.J., Leshin, L.A., Manning, H., Owen, T., Pepin, R.O., Squyres, S., Trainer, M., Team, M.S., 2013. Abundance and isotopic composition of gases in the martian atmosphere from the curiosity rover. Science 314, 263–266.

Malin, M.C., III, J.F.B., Cantor, B.A., Caplinger, M.A., Calvin, W.M., Clancy, R.T., Edgett, K.S., Edwards, L., Haberle, R.M., James, P.B., Lee, S.W., Ravine, M.A., Thomas, P.C., Wolff, M.J., 2007. Context camera investigation on board the mars reconnaissance orbiter. Journal of Geophysical Research 112, doi:10.1029/2006JE002808.

Mandt, K.E., Silva, S.L.d., Zimbelman, J.R., Crown, D.A., 2008. Origin of the medusae fossae formation, mars: Insights from a synoptic approach. Journal of Geophysical Research 113.

Mangold, N., Gupta, S., Gasnault, O., Dromart, G., Tarnas, J.D., Sholes, S.F., Horgan, B., Quantin-Nataf, C., Brown, A.J., Mouélic, S.L., Yingst, R.A., Bell, J.F., Beyssac, O., Bosak, T., III, F.C., Ehlmann, B.L., Farley, K.A., Grotzinger, J.P., Hickman-Lewis, K., Holm-Alwmark, S., Kah, L.C., Martinez-Frias, J., McLennan, S.M., Maurice, S., Nuñez, J.I., Ollila, A.M., Pilleri, P., Jr., J.W.R., Rice, M., Simon, J.I., Shuster, D.L., Stack, K.M., Sun, V.Z., Treiman, A.H., Weiss, B.P., Wiens, R.C., Williams, A.J., Williams, N.R., Williford, K.H., 2021. Perseverance rover reveals an ancient delta-lake system and flood deposits at jezero crater, mars. Science 374, 711–717.

Mangold, N., Schmidt, M., Fisk, M., Forni, O., McLennan, S., Ming, D., Sautter, V., Sumner, D., Williams, A., Clegg, S., Cousin, A., Gasnault, O., Gellert, R., Grotzinger, J., Wiens, R., 2017. Classification scheme for sedimentary and igneous rocks in gale crater, mars. Icarus 284, 1–17.

Mariner, R.H., Surdam, R.C., 1970. Alkalinity and formation of zeolites in saline alkaline lakes. Science 170, 977–980.

Marquardt, D.W., 1963. An algorithm for least-squares estimation of nonlinear parameters. SIAM Journal on Applied Mathematics 11, 431–441.

Mars, J.C., Rowan, L.C., 2010. Spectral assessment of new aster swir surface reflectance data products for spectroscopic mapping of rocks and minerals. Remote Sensing of Environment 114, 2011–2025.

Martin, E., Bindeman, I., 2009. Mass-independent isotopic signatures of volcanic sulfate from three supereruption ash deposits in lake tecopa, california. Earth and Planetary Science Letters 282, 102–114.

Martin, P.E., Ehlmann, B.L., Thomas, N.H., Wiens, R.C., Hollis, J.J.R., Beegle, L.W., Bhartia, R., Clegg, S.M., Blaney, D.L., 2020. Studies of a lacustrine-volcanic mars analog field site with mars-2020-like instruments. Earth and Space Science 7.

Matsubara, Y., Howard, A.D., Drummond, S.A., 2011. Hydrology of early mars: Lake basins. Journal of Geophysical Research 116.

Matsubara, Y., Howard, A.D., Gochenour, J.P., 2013. Hydrology of early mars: Valley network incision. Journal of Geophysical Research. Planets 118, 1365–1387.

Matthews, N.E., Vazquez, J.A., Calvert, A.T., 2015. Age of the lava creek supereruption and magma chamber assembly at yellowstone based on 40ar/39ar and u-pb dating of sanidine and zircon crystals. Geochemistry, Geophysics, Geosystems 16, 2508–2528.

McAdam, A.C., Zolotov, M.Y., Mironenko, M.V., Sharp, T.G., 2008. Formation of silica by low-temperature acid alteration of martian rocks: Physical-chemical constraints. Journal of Geophysical Research 113, 8.

McEwen, A.S., Eliason, E.M., Bergstrom, J.W., Bridges, N.T., Hansen, C.J., Delamere, W.A., Grant, J.A., Gulick, V.C., Herkenhoff, K.E., Keszthelyi, L., Kirk, R.L., Mellon, M.T., Squyres, S.W., Thomas, N., Weitz, C.M., 2007. Mars reconnaissance orbiter's high resolution imaging science experiment (hirise). Journal of Geophysical Research 112, doi:10.1029/2005JE002605.

McHenry, L.J., 2009. Element mobility during zeolitic and argillic alteration of volcanic ash in a closed-basin lacustrine environment: Case study olduvai gorge, tanzania. Chemical Geology 265, 540–552.

McHenry, L.J., 2010. Element distribution between coexisting authogenic mineral phases in argillic and zeolitic altered tephra, olduvai gorge, tanzania. Clays and Clay Minerals 58, 627–643.

McHenry, L.J., Kodikara, G.R.L., Stanistreet, I.G., Stollhofen, H., Njau, J.K., Schick, K., Toth, N., 2020. Lake conditions and detrital sources of paleolake olduvai, tanzania, reconstructed using x-ray diffraction analysis of cores. Palaeogeography, Palaeoclimatology, Palaeoecology 556, 24.

McKeown, N.K., Bishop, J.L., Dobrea, E.Z.N., Ehlmann, B.L., Parente, M., Mustard, J.F., Murchie, S.L., Swayze, G.A., Bibring, J.P., Silver, E.A., 2009. Characterization of phyllosilicates observed in the central mawrth vallis region, mars, their potential formational processes, and implications for past climate. Journal of Geophysical Research Vol. 114, doi:10.1029/2008JE003301.

McLane, M., 1995. Sedimentology. Oxford University Press.

McLennan, S.M., 2012. Geochemistry of sedimentary processes on mars. Sedimentary Geology of Mars SEPM Special Publication, 119–138.

McLennan, S.M., Grotzinger, J.P., Hurowitz, J.A., Tosca, N.J., 2019. The sedimentary cycle on early mars. Annual Review of Earth and Planetary Sciences 47, 91–118.

McSween, H.Y., 2015. Petrology on mars. American Mineralogist Vol. 100, 2380–2395.

McSween, H.Y., Harvey, R.P., 1998. An evaporation model for formation of carbonates in the alh84001 martian meteorite. International Geology Review 40, 774–783.

McSween, H.Y., Taylor, G.J., Wyatt, M.B., 2009. Elemental composition of the martian crust. Science Vol. 324, 736–739.

Van der Meer, F., 2004. Analysis of spectral absorption features in hyperspectral imagery. International Journal of Applied Earth Observation and Geoinformation 5, 55–68.

Mees, F., Stoops, G., Ranst, E.V., Paepe, R., Overloop, E.V., 2005. The nature of zeolite occurances in deposits of the olduvai basin, northern tanzania. Clays and Clay Minerals 53, 659–673.

Mellon, M.T., Jakosky, B.M., Kieffer, H.H., 2000. High-resolution thermal inertia mapping from the mars global surveyor thermal emission spectrometer. Icarus 148, 437–455.

Michalski, J.R., Fergason, R.L., 2009. Composition and thermal inertia of the mawrth vallis region of mars from tes and themis data. Icarus 199, 25–48.

Michalski, J.R., Kraft, M.D., Sharp, T.G., Williams, L.B., Christensen, P.R., 2005. Mineralogical constraints on the high-silica martian surface component observed by tes. Icarus 174, 161–177.

Michalski, J.R., Niles, P.B., Cuadros, J., Baldridge, A.M., 2013. Multiple working hypotheses for the formation of compositional stratigraphy on mars: Insights from the mawrth vallis region. Icarus 226, 816–840.

Milliken, R.E., Grotzinger, J.P., Thomson, B.J., 2010. Paleoclimate of mars as captured by the stratigraphic record in gale crater. Geophysical Research Letters 37, doi:10.1029/2009GL041870.

Milliken, R.E., Mustard, J.F., 2005. Quantifying absolute water content of minerals using near-infrared reflectance spectroscopy. Journal of Geophysical Research 110, doi:10.1029/2005JE002534.

Ming, D.W., Gellert, R., Morris, R.V., Arvidson, R.E., Bruckner, J., Clark, B.C., Cohen, B.A., d'Uston, C., Economou, T., Fleischer, I., Klingelhofer, G., McCoy, T.J., Mittlefehldt, D.W., Schmidt, M.E., Schroder, C., Squyres, S.W., Treguier, E., Yen, A.S., Zipfel, J., 2008. Geochemical properties of rocks and soils in gusev crater, mars: Results of the alpha particle x-ray spectrometer from cumberland ridge to home plate. Journal of Geophysical Research 113, doi:10.1029/2008JE003195.

Ming, D.W., Gooding, J.L., 1988. Zeolites on mars: Possible environmental indicators in soils and sediments, in: Workshop on Mars Sample Return Science, Lunar and Planetary Institute. pp. 124–125.

Mitrofanov, I., Malakhov, A., Djachkova, M., Golovin, D., Litvak, M., Mokrousov, M., Sanin, A., Svedhem, H., Zelenyi, L., 2022. The evidence for unusually high hydrogen abundances in the central part of valles marineris on mars. Icarus 374.

Moon, W.M., 1998. Integration and fusion of geological exploration data: a theoretical review of fuzzy logic approach. Geoscience Journal 2, 175–183.

Moore, J.M., 1990. Nature of the mantling deposit in the heavily cratered terrain of northeastern arabia, mars. Journal of Geophysical Research 95, 14,279–14,289.

Mormone, A., Piochi, M., 2020. Mineralogy, geochemistry and genesis of zeolites in cenozoic pyroclastic flows from the asuni area (central sardinia, italy). Minerals 10, doi:10.3390/min10030268.

Morris, R.V., Klingelho¨fer, G., Schro¨der, C., Rodionov, D.S., Yen, A., Ming, D.W., Jr., P.A.d.S., Fleischer, I., Wdowiak, T., Gellert, R., Bernhardt, B., Evlanov, E.N., Zubkov, B., Foh, J., Bonnes, U., Kankeleit, E., Gutlich, P., Renz, F., Squyres, S.W., Arvidson, R.E., 2006. Mossbauer mineralogy of rock, soil, and dust at gusev crater, mars: Spirit's journey through weakly altered olivine basalt on the plains and pervasively altered basalt in the columbia hills. Journal of Geophysical Research 111, doi:10.1029/2005JE002584.

Morris, R.V., Vaniman, D.T., Blake, D.F., Gellert, R., Chipera, S.J., Rampe, E.B., Ming, D.W., Morrison, S.M., Downs, R.T., Treiman, A.H., Yen, A.S., Grotzinger, J.P., Achilles, C.N., Bristow, T.F., Crisp, J.A., Marais, D.J.D., Farmer, J.D., Fendrich, K.V., Frydenvang, J., Graff, T.G., Morookian, J.M., Stolper, E.M., Schwenzer, S.P., 2016. Silicic volcanism on mars evidenced by tridymite in high-sio2 sedimentary rock at gale crater. PNAS 113, 7071–7076.

Morrison, R.B., 1999. Lake tecopa: Quaternary geology of tecopa valley; california, a multimillion-year record and its relevance to the proposed nuclear-waste repository at yucca mountain, nevada, in: Wright, L.A., Troxel, B.W. (Eds.), Cenozoic Basins of the Death Valley Region. The Geological Society of America. volume Special Paper 333, pp. 301–344.

Mumpton, F.A., 1977. Natural zeolites, in: Mumpton, F.A. (Ed.), Mineralogy and Geology of Natural Zeolites. Mineralogy Society of America. volume 4, pp. 1–17.

Murai, I., 1964. Homogeneous characteristics of the particle size distribution and mineral composition of a tuff bed. International Geology Review 6, 1903–1919.

Murchie, S., Arvidson, R., Bedini, P., Beisser, K., Bibring, J.P., Bishop, J., Boldt, J., Cavender, P., Choo, T., Clancy, R.T., Darlington, E.H., Marais, D.D., Espiritu, R., Fort, D., Green, R., Guinness, E., Hayes, J., Hash, C., Heffernan, K., Hemmler, J., Heyler, G., Humm, D., Hutcheson, J., Izenberg, N., Lee, R., Lees, J., Lohr, D., Malaret, E., Martin, T., McGovern, J.A., McGuire, P., Morris, R., Mustard, J., Pelkey, S., Rhodes, E., Robinson, M., Roush, T., Schaefer, E., Seagrave, G., Seelos, F., Silverglate, P., Slavney, S., Smith, M., Shyong, W.J., Strohbehn, K., Taylor, H., Thompson, P., Tossman, B., Wirzburger, M., Wolff, M., 2007. Compact reconnaissance imaging spectrometer for mars (crism) on mars reconnaissance orbiter (mro). Journal of Geophysical Research Vol. 112, doi:10.1029/2006JE002682.

Murtagh, F., Legendre, P., 2014. Ward's hierarchical agglomerative clustering method: Which algorithms implement ward's criterion? Journal of Classification 31, 274–295.

Mushkin, A., Balick, L.K., Gillespie, A.R., 2005. Extending surface temperature and emissivity retrieval to the mid-infrared (3-5 [mu]m) using the multispectral thermal imager (mti). Remote Sensing of Environment 98, 141–151.

Mustard, J.F., Murchie, S.L., Pelkey, S.M., Ehlmann, B.L., Milliken, R.E., Grant, J.A., Bibring, J.P., Poulet, F., Bishop, J., Dobrea, E.N., Roach, L., Seelos, F., Arvidson, R.E., Wiseman, S., Green, R., Hash, C., Humm, D., Malaret, E., McGovern, J.A., Seelos, K., Clancy, T., Clark, R., Marais, D.D., Izenberg, N., Knudson, A., Langevin, Y., Martin, T., McGuire, P., Morris, R., Robinson, M., Roush, T., Smith, M., Swayze, G., Taylor, H., Titus, T., Wolff, M., 2008. Hydrated silicate minerals on mars observed by the mars reconnaissance orbiter crism instrument. Nature Vol. 454, 305–309.

Mustard, J.F., Pieters, C.M., 1989. Photometric phase functions of common geologic minerals and applications to quantitative analysis of mineral mixture reflectance spectra. Journal of Geophysical Research 94, 13619–13634.

Nelson, S.T., Karlsson, H.R., Paces, J.B., Tingey, D.G., Ward, S., Peters, M.T., 2001. Paleohydrologic record of spring deposits in and around pleistocene pluvial lake tecopa, southeastern california. GSA Bulletin 113, 659–670.

Neuhäuser, B., Terhorst, B., 2007. Landslide susceptibility assessment using "weights-of-evidence" applied to a study area at the jurassic escarpment (sw-germany). Geomorphology 86, 12–24.

Ninomiya, Y., Fu, B., 2019. Thermal infrared multispectral remote sensing of lithology and mineralogy based on spectral properties of materials. Ore Geology Reviews 108, 54–72.

Ninomiya, Y., Fu, B., Cudahy, T.J., 2005. Detecting lithology with advanced spaceborne thermal emission and reflection radiometer (aster) multispectral thermal infrared "radiance-at-sensor" data. Remote Sensing of Environment 99, 127–139.

Noble, S.K., Pieters, C.M., Hiroi, T., Taylor, L.A., 2006. Using the modified gaussian model to extract quantitative data from lunar soils. Journal of Geophysical Research 111, doi:10.1029/2006JE002721.

Noh, J.H., Boles, J.R., 1989. Diagenetic alteration of perlite in the guryongpo area, republic of korea. Clays and Clay Minerals 37, 47–58.

Nordstrom, D.K., 2012. Models, validation, and applied geochemistry: Issues in science, communication, and philosophy. Applied Geochemistry 27, 1899–1919.

Nova, D., Estevez, P.A., 2014. A review of learning vector quantization classifiers. Neural Computing & Applications 25, 511–521.

Ody, A., Poulet, F., Langevin, Y., Bibring, J.P., Bellucci, G., Altieri, F., Gondet, B., Vincendon, M., Carter, J., Manaud, N., 2012. Global maps of anhydrous minerals at the surface of mars from omega/mex. Journal of Geophysical Research 117, doi:10.1029/2012JE004117.

Ogihara, S., 1996. Diagenetic transformation of clinoptilolite to analcime in silicic tufts of hokkaido, japan. Mineral Deposita 31, 548–553.

Ontiveros-Cuadras, J.F., Ruiz-Fernández, A.C., Sanchez-Cabeza, J.A., Pérez-Bernal, L.H., Preda, M., Páez-Osuna, F., 2018. Mineralogical signatures and sources of recent sediment in a large tropical lake. International Journal of Sediment Research 33, 183–190.

Oreskes, N., 2000. Why believe a computer? models, measures, and meaning in the natural world, in: Schneiderman, J.S. (Ed.), The earth around us: Maintaining a livable planet. W. H. Freeman and Company, p. 455.

Osborne, J., 2018. Styles of scientific reasoning: What can we learn from looking at the product, not the process, of scientific reasoning?, in: Fischer, F., Chinn, C.A., Engelmann, K., Osborne, J. (Eds.), Scientific reasoning and argumentation: The roles of domain-specific and domain-general knowledge. Taylor & Francis, pp. 162–186.

Osterloo, M.M., Anderson, F.S., Hamilton, V.E., Hynek, B.M., 2010. Geologic context of proposed chloride-bearing materials on mars. Journal of Geophysical Research 115, doi:10.1029/2010JE003613.

Ostrooumov, M., Ostrooumova, I., 2006. First reported occurrence of clinoptiloliterich tuff deposits in the mexican volcanic belt (state of michoacan, southwestern mexico), in: Bowman, R.S., Delap, S.E. (Eds.), Zeolite '06—7th International Conference on the Occurrence, Properties, and Utilization of Natural Zeolites, Socorro, New Mexico USA. pp. 199–200.

Oyuntseteg, J., Lkhagvajav, R., 2006. Analysis of physical and chemical properties of natural zeolite in the southeast region of mongolia, in: Bowman, R.S., Delap, S.E. (Eds.), Zeolite '06—7th International Conference on the Occurrence, Properties, and Utilization of Natural Zeolites, Socorro, New Mexico USA. p. 201.

Pablo-Galan, L.D., Chavez-Garcia, M.D.L., 1996. Diagenesis of oligocene vitric tuffs to zeolites, mexican volcanic belt. Clays and Clay Minerals 44, 324–338.

Palandri, J.L., Kharaka, Y.K., 2004. A compilation of rate parameters of water-mineral interaction kinetics for application to geochemical modeling. U. S. Geological Survey Open file report 2004-1068, 70.

Palumbo, A.M., Head, J.W., Wilson, L., 2020. Rainfall on noachian mars: Nature, timing, and influence on geologic processes and climate history. Icarus 347.

Pan, G., Harris, D.P., 2000. Information synthesis for mineral exploration. Oxford University Press.

Pan, J.J., Chang, C.I., 1992. Destriping of landsat mss images by filtering techniques. Photogrammetric Engineering & Remote Sensing 58, 1417–1423.

Parente, M., Makarewicz, H.D., Bishop, J.L., 2011. Decomposition of mineral absorption bands using nonlinear least squares curve fitting: Application to martian meteorites and crism data. Planetary and Space Science 59, 423–442.

Park, D.Y., Park, M., 2013. Examining the features of earth science logical reasoning and authentic scientific inquiry demonstrated in a high school earth science curriculum: A case study. Journal of Geoscience Education 61, 364–377.

Parker, A., Sellwood, B.W. (Eds.), 1981. Sediment Diagenesis. volume 115 of *NATO ASI Series. Mathematical and Physical Sciences*. D. Reidel Publishing Company.

Passaglia, E., Sheppard, R.A., 2002. The crystal chemistry of zeolites, in: Bish, D.L., Ming, D. (Eds.), Natural Zeolites: Occurrence, Properties, Applications. Reviews in Mineralogy and Geochemistry. volume Vol. 45, No. 1, pp. 69–116.

Passaglia, E., Vezzalini, G., 1985. Crystal chemistry of diagenetic zeolites in volcanoclastic deposits of italy. Contributions to Mineralogy and Petrology 90, 190–198.

Pearlman, J.S., Barry, P.S., Segal, C.C., Shepanski, J., Beiso, D., Carman, S.L., 2003. Hyperion, a space-based imaging spectrometer. IEEE Transactions on Geoscience and Remote Seinsing 41, 1160–1173.

Penn, B.S., 2005. Using self-organizing maps to visualize high-dimensional data. Computers & Geosciences 31, 531–544.

Petrov, P.I., 2006. On the geology of the zeolite deposit beli plast in ne rhodopes, bulgaria, in: Bowman, R.S., Delap, S.E. (Eds.), Zeolite '06—7th International Conference on the Occurrence, Properties, and Utilization of Natural Zeolites, Socorro, New Mexico USA. p. 205.

Phillips-Lander, C.M., Parnell, S., McGraw, L., Madden, M.E., 2018. Carbonate dissolution rates in high salinity brines: Implications for post-noachian chemical weathering on mars. Icarus 307, 281–293.

Pleskot, L.K., Miner, E.D., 1981. Time variability of martian bolometric albedo. Icarus 45, 179–201.

Pokrovsky, O.S., Schott, J., 2001. Kinetics and mechanism of dolomite dissolution in netureal to alkaline solutions revisited. American Journal of Science 301, 597–626.

Polgari, M., Forizs, I., Mathe, Z., Toth, M., Pecsi-Donath, E., 1997. Geoautoclave-type zeolitization in the miocene rhyolite tuff, mecsek mts., sw hungary. Natural Zeolites - Sofia '95 , 227–240.

Pommerol, A., Schmitt, B., 2008. Strength of the h2o near-infrared absorption bands in hydrated minerals: Effects of particle size and correlation with albedo. Journal of Geophysical Research 113, 33.

Pommerol, A., Schmitt, B., Beck, P., Brissaud, O., 2009. Water sorption on martian regolith analogs: Thermodynamics and near-infrared reflectance spectroscopy. Icarus 204, 114–136.

Popov, N., Yanev, Y., Iliev, T., Popova, T., 2006. Clinoptilolitized pyroclastic rocks from oaxaca (south mexico): A mineralogical and technological study, in: Bowman, R.S., Delap, S.E. (Eds.), Zeolite '06—7th International Conference on the Occurrence, Properties, and Utilization of Natural Zeolites, Socorro, New Mexico USA. pp. 208–209.

Popper, K.R., 1959. The logic of scientific discovery. Martino Fine Books.

Porwal, A., Carranza, E.J.M., Hale, M., 2003. Knowledge-driven and data-driven fuzzy models for predictive mineral potential mapping. Natural Resources Research 12, 1–25.

Poulet, F., Bibring, J.P., Mustard, J.F., Gendrin, A., Mangold, N., Langevin, Y., Arvidson, R.E., Gondet, B., Gomez, C., Team, O., 2005. Phyllosilicates on mars and implications for early martian climate. Nature Vol. 438, 623–627.

Poulet, F., Gomez, C., Bibring, J.P., Langevin, Y., Gondet, B., Pinet, P., Belluci, G., Mustard, J., 2007. Martian surface mineralogy from observatoire pour la mine´ralogie, l'eau, les glaces et l'activite´ on board the mars express spacecraft (omega/mex): Global mineral maps. Journal of Geophysical Research 112, doi:10.1029/2006JE002840.

Pozo, M., Casas, J., Medina, J.A., Carretero, M.I., Rubí, J.A.M., 2006. Pedogenic origin of clinoptilolite and heulandite in magnesium rich sedimentary deposits (madrid basin, spain), in: Bowman, R.S., Delap, S.E. (Eds.), Zeolite '06—7th International Conference on the Occurrence, Properties, and Utilization of Natural Zeolites, Socorro, New Mexico USA. pp. 210–211.

Putzig, N.E., Mellon, M.T., 2007. Apparent thermal inertia and the surface heterogeneity of mars. Icarus 191, 68–94.

Quay, G.S.d., Goudge, T.A., Fassett, C.I., 2020. Precipitation and aridity constraints from paleolakes on early mars. Geology 48, 1189–1193.

Quay, G.S.d., Goudge, T.A., Kite, E.S., Fassett, C.I., Guzewich, S.D., 2021. Limits on runoff episode duration for early mars: Integrating lake hydrology and climate models. Geophysical Research Letters 48.

Rabus, B., Eineder, M., Roth, A., Bamler, R., 2003. The shuttle radar topography mission - a new class of digital elevation models acquired by spaceborne radar. ISPRS Journal of Photogrammetry and Remote Sensing 57, 241–262.

Rajendran, S., Nasir, S., 2019. Aster capability in mapping of mineral resources of arid region: A review on mapping of mineral resources of the sultanate of oman. Ore Geology Reviews 108, 33–53.

Ramirez, R.M., 2017. A warmer and wetter solution for early mars and the challenges with transient warming. Icarus 297, 71–82.

Ramirez, R.M., Craddock, R.A., 2018. The geological and climatological case for a warmer and wetter early mars. Nature Geoscience 11, 230–237.

Ramirez, R.M., Craddock, R.A., Usui, T., 2019. Climate simulations of early mars with estimated precipitation, runoff, and erosion rates. Journal of Geophysical Research. Planets 125.

Ramirez, R.M., Kopparapu, R., Zugger, M.E., Robinson, T.D., Freedman, R., Kasting, J.F., 2014. Warming early mars with co2 and h2. Nature Geoscience 7, 59–63.

Rampe, E.B., Ming, D.W., Blake, D.F., Bristow, T.F., Chipera, S.J., Grotzinger, J.P., Morris, R.V., Morrison, S.M., Vaniman, D.T., Yen, A.S., Achilles, C.N., Craig, P.I., Marais, D.J.D., Downs, R., Farmer, J.D., Fendrich, K.V., Gellert, R., Hazen, R.M., Kah, L.C., Morookian, J.M., Peretyazhko, T.S., Sarrazin, P., Treiman, A.H., Berger, J.A., Eigenbrode, J., Fairén, A.G., Forni, O., Gupta, S., Hurowitz, J.A., Lanza, N.L., Schmidt, M.E., Siebach, K., Sutter, B., Thompson, L.M., 2017. Mineralogy of an ancient lacustrine mudstone succession from the murray formation, gale crater, mars. Earth and Planetary Science Letters 471, 172–185.

Rautman, C.A., Flint, L.E., Flint, A.L., Istok, J.D., 1995. Physical and hydrologic properties of outcrop samples from a nonwelded to welded tuff transition, Yucca Mountain, Nevada. Technical Report. U.S. Geological Survey.

Raymond, W.H., Bush, A.L., Gude, A.J., 1982. Zeolites in the pine ridge indian reservation, south dakota. U. S. Geological Survey Open-File Report 82-959 , 16.

Reed, J.K., Gipson, M., Vass, D., 1993. Hydrocarbon potential of sandstone reservoirs inn the east slovakian basin, part 2: Zeolites and clay minerals. Journal of Petroleum Geology 16, 223–236.

Reheis, M.C., Caskey, J., Bright, J., Paces, J.B., Mahan, S., Wan, E., 2020. Pleistocene lakes and paleohydrologic environments of the tecopa basin, california: Constraints on the drainage integration of the amargosa river. GSA Bulletin 132, 1537–1565.

Renaut, R.W., 1993. Zeolitic diagenesis of late quaternary fluviolacustrine sediments and associated calcrete formation in the lake bogoria basin, kenya rift valley. Sedimentology 40, 271–301.

Rezende, N., Angélica, R.S., 1999. Sedimentary zeolites in brazil. Mineralogia et Petrographica Acta 42, 71–82.

Rice, M., Cloutis, E., III, J.B., Bish, D., Horgan, B., Mertzman, S., Craig, M., Renaut, R., Gautason, B., Mountain, B., 2013. Reflectance spectra diversity of silica-rich materials: Sensitivity to environment and implications for detections on mars. Icarus Vol. 223, 499–533.

Richter, R., 1996. A spatially adaptive fast atmospheric correction algorithm. International Journal of Remote Sensing 17, 1201–1214.

Richter, R., Schlapfer, D., 2002. Geo-atmospheric processing of airborne imaging spectrometry data. part 2: atmospheric/topographic correction. International Journal of Remote Sensing 23, 2631–2649.

Rieder, R., Economou, T., Wanke, H., Turkevich, A., Crisp, J., Bruckner, J., Dreibus, G., McSween, H.Y., 1997. The chemical composition of martian soil and rocks returned by the mobile alpha proton x-ray spectrometer: Preliminary results from the x-ray mode. Science 278, 1771–1774.

Rieder, R., Gellert, R., Anderson, R.C., Bruckner, J., Clark, B.C., Dreibus, G., Economou, T., Klingelhofer, G., Lugmair, G.W., Ming, D.W., Squyres, S.W., d'Uston, C., Wanke, H., Yen, A., Zipfel, J., 2004. Chemistry of rocks and soils at meridiani planum from the alpha particle x-ray spectrometer. Science Vol. 306, 1746–1749.

Rivard, B., Petroy, S.B., Miller, J.R., 1993. Measured effects of desert varnish on the mid-infrared spectra of weathered rocks as an aid to tims imagery interpretation. IEEE Transactions on Geoscience and Remote Seinsing Vol. 31, 284–291.

Roach, L.H., Mustard, J.F., Murchie, S.L., Bibring, J.P., Forget, F., Lewis, K.W., Aharonson, O., Vincendon, M., Bishop, J.L., 2009. Testing evidence of recent hydration state change in sulfates on mars. Journal of Geophysical Research 114, doi:10.1029/2008JE003245.

Robert, C., Goffe, B., 1993. Zeolitization of basalts in subaqueous freshwater settings: Field observations and experimental study. Geochemica et Cosmochimica Acta 57, 3597–3612.

Robertson, K.M., Milliken, R.E., Li, S., 2016. Estimating mineral abundances of clay and gypsum mixtures using radiative transfer models applied to visible-near infrared reflectance spectra. Icarus 277, 171–186.

Rolim, S.B.A., Grondona, A., Hackmann, C.L., Rocha, C., 2016. A review of temperature and emissivity retrieval methods: Applications and restrictions. American Journal of Environmental Engineering 6, 119–128.

Romero-Calcerrada, R., Luque, S., 2006. Habitat quality assessment using weights-of-evidence based gis modelling: The case of picoides tridactylus as species indicator of the biodiversity value of the finnish forest. Ecological Modelling 196, 62–76.

Rosenblueth, A., Wiener, N., 1945. The role of models in science. Philosophy of Science 12, 316–321.

Rossman, G.R., 1988. Vibrational spectroscopy of hydrous components, in: Hawthorne, F.C. (Ed.), Spectroscopic methods in mineralogy and geology. Mineralogical Society of America. volume Reviews in mineralogy. No.18., pp. 193–206.

Roush, T.L., Bishop, J.L., Brown, A.J., Blake, D.F., Bristow, T.F., 2015. Laboratory reflectance spectra of clay minerals mixed with mars analog materials: Toward enabling quantitative clay abundances from mars spectra. Icarus 258, 454–466.

Roush, T.L., Singer, R.B., 1986. Gaussian analysis of temperature effects on the reflectance spectra of mafic minerals in the 1-um region. Journal of Geophysical Research 91, 10,301–10,308.

Rousseeuw, P.J., 1987. Silhouettes: a graphical aid to the interpretation and validation of cluster analysis. Journal of Computational and Applied Mathematics 20, 53–65.

Rowan, L.C., Mars, J.C., 2003. Lithologic mapping in the mountain pass, california area using advanced spaceborne thermal emission and reflection radiometer (aster) data. Remote Sensing of Environment 84, 350–366.

Rowan, L.C., Mars, J.C., Simpson, C.J., 2005. Lithologic mapping of the mordor, nt, australia ultramafic complex by using the advanced spaceborne thermal emission and reflection radiometer (aster). Remote Sensing of Environment Vol. 99, 105 – 126.

Rubin, A.E., Warren, P.H., Greenwood, J.P., S.Verish, R., Leshin, L.A., Hervig, R.L., Clayton, R.N., 2000. Los angeles: The most differentiated basaltic martian meteorite. Geology 28, 1011–1014.

Ruff, S.W., 2004. Spectral evidence for zeolite in the dust on mars. Icarus 168, 131–143.

Ruff, S.W., Christensen, P.R., 2002. Bright and dark regions on mars: Particle size and mineralogical characteristics based on thermal emission spectrometer data. Journal of Geophysical Research 107, doi:10.1029/2001JE001580.

Ruff, S.W., Niles, P.B., Alfano, F., Clarke, A.B., 2014. Evidence for a noachian-aged ephemeral lake in gusev crater, mars. Geology 42, 359–362.

Sabol, D.E., Adams, J.B., Smith, M.O., 1992. Quantitative subpixel spectral detection of targets in multispectral images. Journal of Geophysical Research 97, 2659–2672.

Salisbury, J.W., D'Aria, D.M., 1992. Emissivity of terrestial materials in the 8-14um atmospheric window. Remote Sensing of Environment 42, 83–106.

Salisbury, J.W., Hapke, B., Eastes, J.W., 1987. Usefulness of weak bands in midinfrared remote sensing of particulate planetary surfaces. Journal of Geophysical Research Vol. 92, 702–710.

Salisbury, J.W., Wald, A., D'Aria, D.M., 1994. Thermal-infrared remote sensing and kirchhoff's law 1. laboratory measurements. Journal of Geophysical Research 99, 11,897–11,911.

Salisbury, J.W., Walter, L.S., 1989. Thermal infrared (2.5-13.5 um) spectroscopic remote sensing of igneous rock types on particulate planetary surfaces. Journal of Geophysical Research Vol. 94, 9192–9202.

Sarbadhikari, A.B., Day, J.M.D., Liu, Y., Rumble, D., Taylor, L.A., 2009. Petrogenesis of olivine-phyric shergottite larkman nunatak 06319: Implications for enriched components in martian basalts. Geochemica et Cosmochimica Acta 73, 2190–2214.

Savitzky, A., Golay, M.J.E., 1964. Smoothing and differentiation of data by simplified least squares procedures. Analytical Chemistry 36, 1627–1639.

Schmidhuber, J., 2015. Deep learning in neural networks: An overview. Neural Networks 61, 85–117.

Schmidt, M.E., Campbell, J.L., Gellert, R., Perrett, G.M., Treiman, A.H., Blaney, D.L., Olilla, A., III, F.J.C., Edgar, L., Elliott, B.E., Grotzinger, J., Hurowitz, J., King, P.L., Minitti, M.E., Sautter, V., Stack, K., Berger, J.A., Bridges, J.C., Ehlmann, B.L., Forni, O., Leshin, L.A., Lewis, K.W., McLennan, S.M., Ming, D.W., Newsom, H., Pradler, I., Squyres, S.W., Stolper, E.M., Thompson, L., VanBommel, S., Wiens, R.C., 2014. Geochemical diversity in first rocks examined by the curiosity rover in gale crater: Evidence for and significance of an alkali and volatile-rich igneous source. Journal of Geophysical Research. Planets 119, doi:10.1002/2013JE004481.

Schumm, S.A., 1991. To Interpret the Earth: Ten ways to be wrong. Cambridge University Press.

Scott, G.R., Deino, A.L., 2014. The jaramillo subchron: New magnetostratigraphy and 40ar/39 ar dating in the death valley region, california, in: AGU Fall Meeting, San Francisco.

Shaw, P.A., Thomas, D.S.G., 1989. Playas, pans and salt lakes, in: Thomas, D.S.G. (Ed.), Arid Zone Geomorphology. John Wiley and Sons, pp. 184–205.

Sheppard, R.A., 1973. Zeolites in sedimentary rocks, in: United States Mineral Resources. Geological Survey Professional Paper. volume 820, pp. 689–695.

Sheppard, R.A., 1974. Zeolites in sedimentary deposits of the united states—a review. Molecular Sieve Zeolites-I, Advances in Chemistry 101, 279–310.

Sheppard, R.A., 1991. Zeolitic diagenesis of tuffs in the miocene chalk hills formation, western snake river plain, idaho. U. S. Geological Survey Bulletin 1963, 35.

Sheppard, R.A., 1994. Zeolitic diagenesis of tuffs in miocene lacustrine rocks near harney lake, harney county, oregon. U. S. Geological Survey Bulletin 2108, 36.

Sheppard, R.A., Gude, A.J., 1968. Distribution and genesis of authigenic silicate minerals in tuffs of pleistocene lake tecopa, inyo county california. Geological Survey Professional Paper, United States Government Printing Office, Washington 597, 38 pp.

Sheppard, R.A., Gude, A.J., 1969a. Authigenic fluorite in pliocene lacustrine rocks near rome, malheur county, oregon. U. S. Geological Survey Professional Paper 650-D , D69–D74.

Sheppard, R.A., Gude, A.J., 1969b. Diagenesis of tuffs in the barstow formation, mud hills, san bernardino county, california. Geological Survey Professional Paper 634, 35.

Sheppard, R.A., Gude, A.J., 1973. Zeolites and associated authigenic silicate minerals in tuffaceous rocks of the big sandy formation, mohave county, arizona. Geological Survey Professional Paper 830, 36.

Sheppard, R.A., Gude, A.J., 1980. Diagenetic fluorite in the eastgate zeolite deposit, churchill county, nevada. U. S. Geological Survey Open-File Report 80-506, 9.

Sheppard, R.A., Gude, A.J., 1983. Zeolites in tertiary tuffs along the little humboldt river, humboldt and elko counties, nevada. U. S. Geological Survey Open-File Report 83-458, 12.

Sheppard, R.A., Gude, A.J., Fitzpatrick, J.J., 1988. Distribution, characterization, and genesis of mordenite in miocene silicic tuffs at yucca mountain, nye county, nevada. U. S. Geological Survey Bulletin 1777, 27.

Sheppard, R.Y., Milliken, R.E., Robertson, K.M., 2021a. Presence of clay minerals can obscure spectral evidence of mg sulfates: Implications for orbital observations of mars, in: 52nd Lunar and Planetary Science Conference.

Sheppard, R.Y., Thorpe, M.T., Fraeman, A.A., Fox, V.K., Milliken, R.E., 2021b. Merging perspectives on secondary minerals on mars: A review of ancient water-rock interactions in gale crater inferred from orbital and in-situ observations. Minerals 11.

Sheridan, M.F., 1971. Particle-size characteristics of pyroclastic tuffs. Journal of Geophysical Research 76, 5627–5634.

Shi, C., Wang, L., 2014. Incorporating spatial information in spectral unmixing: A review. Remote Sensing of Environment 149, 70–87.

Shkuratov, Y.G., Kreslavsky, M.A., Ovcharenko, A.A., Stankevich, D.G., Zubko, E.S., Pieters, C., Arnold, G., 1999. Opposition effect from clementine data and mechanisms of backscatter. Icarus 141, 132–155.

Shortridge, A., Messina, J., 2011. Spatial structure and landscape associations of srtm error. Remote Sensing of Environment 115, 1576–1587.

Sibley, D.F., 2009. A cognitive framework for reasoning with scientific models. Journal of Geoscience Education 57, 255–263.

Siegel, R., Howell, J.R., 1981. Thermal radiation heat transfer. Second edition ed., Hemisphere Publishing Corporation.

Smith, D.E., Zuber, M.T., Frey, H.V., Garvin, J.B., Head, J.W., Muhleman, D.O., Pettengill, G.H., Phillips, R.J., Solomon, S.C., Zwally, H.J., Banerdt, W.B., Duxbury, T.C., Golombek, M.P., Lemoine, F.G., Neumann, G.A.., Rowlands, D.D., Aharonson, O., Ford, P.G., Ivanov, A.B., Johnson, C.L., McGovern, P.J., Abshire, J.B., Afzal, R.S.,

Sun, X., 2001. Mars orbiter laser altimeter: Experiment summary after the first year of global mapping of mars. Journal of Geophysical Research 106, 23,689–23,722.

Smith, G.I., 1979. Subsurface stratigraphy and geochemistry of late quaternary evaporites, searles lake, california. Geological Survey Professional Paper 1043 , 137.

Smoot, J.P., Lowenstein, T.K.., 1991. Depositional environments of non-marine evaporites, in: Melvin, J.L. (Ed.), Developments in Sedimentology. Elsevier. volume 50, pp. 189–347.

Smykatz-Kloss, W., Roy, P.D., 2010. Evaporite mineralogy and major element geochemistry as tools for palaeoclimatic investigations in arid regions: A synthesis. Boletín de la Sociedad Geológica Mexicana 62, 379–390.

Soha, J.M., Schwartz, A.A., 1978. Multispectral histogram normalization contrast enhancement, in: Proc. 5th Canadian Symposium on Remote Sensing, Victoria, BC, Canada. pp. 86–93.

Somers, B., Asner, G.P., Tits, L., Coppin, P., 2011. Endmember variability in spectral mixture analysis: A review. Remote Sensing of Environment 115, 1603–1616.

Squyres, S.W., Arvidson, R.E., Ruff, S., Gellert, R., Morris, R.V., Ming, D.W., Crumpler, L., Farmer, J.D., Marais, D.J.D., Yen, A., McLennan, S.M., Calvin, W., III, J.F.B., Clark, B.C., Wang, A., McCoy, T.J., Schmidt, M.E., Jr., P.A.d.S., 2008. Detection of silica-rich deposits on mars. Science 320, 1063–1067.

Stack, K.M., Edwards, C.S., Grotzinger, J.P., Gupta, S., Sumner, D.Y., III, F.J.C., Edgar, L.A., Edgett, K.S., Fraeman, A.A.., Jacob, S.R., Deit, L.L., Lewis, K.W., Rice, M.S., Rubin, D., Williams, R.M.E., Williford, K.H., 2016. Comparing orbiter and rover image-based mapping of an ancient sedimentary environment, aeolis palus, gale crater, mars. Icarus 280, 3–21.

Stack, K.M., Milliken, R.E., 2015. Modeling near-infrared reflectance spectra of clay and sulfate mixtures and implications for mars. Icarus Vol. 250, 332–356.

Stamatakis, M.G., 1989a. Authigenic silicates and silica polymorphs in the miocene saline-alkaline deposits of the karlovassi basin, samos, greece. Economic Geology 84, 788–798.

Stamatakis, M.G., 1989b. A boron-bearing potassium feldspar in volcanic ash and tuffaceous rocks from miocene lake deposits, samos islando greece. American Mineralogist 74, 230–235.

Starkey, H.C., Blackmon, P.D., 1979. Clay mineralogy of pleistocene lake tecopa, inyo country, california. Geological Survey Professional Paper 1061, 34.

Starkey, H.C., Blackmon, P.D., 1984. Sepiolite in pleistocene lake tecopa, inyo county, california, in: Singer, A., Galan, E. (Eds.), Palygorskite - Sepiolite: Occurrences, Genesis and Uses, Developments in Sedimentology. Elsevier. volume 37, pp. 137–147.

Stefánsson, A., Stefánsdóttir, G., Keller, N.S., Barsotti, S., Sigurdsson, Á., Thorláksdóttir, S.B., Pfeffer, M.A., Eiríksdóttir, E.S., Jónasdóttir, E.B., Löwis, S.v., Gíslason, S.R., 2017. Major impact of volcanic gases on the chemical composition of precipitation in iceland during the 2014–2015 holuhraun eruption. Journal of Geophysical Research: Atmospheres 122, 1971–1982.

Stein, N., Grotzinger, J.P., Schieber, J., Mangold, N., Hallet, B., Newsom, H., Stack, K.M., Berger, J.A., Thompson, L., Siebach, K.L., Cousin, A., Mouélic, S.L., Minitti, M., Sumner, D.Y., Fedo, C., House, C.H., Gupta, S., Vasavada, A.R., Gellert, R., Wiens, R.C., Frydenvang, J., Forni, O., Meslin, P.Y., Payré, V., Dehouck, E., 2018. Desiccation cracks provide evidence of lake drying on mars, sutton island member, murray formation, gale crater. Geology 46, 515–518.

Sultan, M., Arvidson, R.E., Sturchio, N.C., Guinness, E.A., 1987. Lithologic mapping in arid regions with landsat thematic mapper data: Meatiq dome, egypt. Geological Society of America Bulletin 99, 748–762.

Sun, L., Neville, R., Staenz, K., White, H.P., 2008. Automatic destriping of hyperion imagery based on spectral moment matching. Canadian Journal of Remote Sensing 34, S68–S81.

Sun, V.Z., Milliken, R.E., 2015. Ancient and recent clay formation on mars as revealed from a global survey of hydrous minerals in crater central peaks. Journal of Geophysical Research. Planets 120, 2293–2332.

Sunshine, J.M., Pieters, C.M., 1993. Estimating modal abundances from the spectra of natural and laboratory pyroxene mixtures using the modified gaussian model. Journal of Geophysical Research 98, 9075–9087.

Sunshine, J.M., Pieters, C.M., Pratt, S.F., 1990. Deconvolution of mineral absorption bands: An improved approach. Journal of Geophysical Research 95, 6955–6966.

Surdam, R., Eugster, H., 1976. Mineral reactions in the sedimentary deposits of the lake magadi region, kenya. Geological Society of America Bulletin 87, 1739–1752.

Surdam, R.C., Parker, R.D., 1972. Authigenic aluminosilicate minerals in the tuffaceous rocks of the green river formation, wyoming. Gelogical Society of America Bulletin 83, 689–700.

Swayze, G.A., Clark, R.N., Goetz, A.F.H., Chrien, T.G., Gorelick, N.S., 2003. Effects of spectrometer band pass, sampling, and signal-to-noise ratio on spectral identification using the tetracorder algorithm. Journal of Geophysical Research 108.

Swayze, G.A., Ehlmann, B.L., Milliken, R.E., Poulet, F., Wray, J.J., Rye, R.O., Clark, R.N., Desborough, G.A., Crowley, J.K., Gondet, B., Mustard, J.F., Seelos, K.D., Murchie, S.L., 2008. Discovery of the acid-sulfate mineral alunite in terra sirenum, mars, using mro crism: Possible evidence for acid-saline lacustrine deposits? American Geophysical Union, Fall Meeting abstract id.P44A-04.

Tanaka, K.L., 2000. Dust and ice deposition in the martian geologic record. Icarus 144, 254–266.

Tanaka, K.L., A.SkinnerJr., J., S.Crumpler, L., M.Dohm, J., 2009. Assessment of planetary geologic mapping techniques for mars using terrestrial analogs:the sp mountain area of the san francisco volcanic field, arizona. Planetary and Space Science 57, 510–532.

Tanaka, K.L., Robbins, S.J., Fortezzo, C.M., SkinnerJr., J.A., Hare, T.M., 2014a. The digital global geologic map of mars: Chronostratigraphic ages topographic and crater morphologic characteristics, and updated resurfacing history. Planetary and Space Science 95, 11–24.

Tanaka, K.L., Skinner, J.A., Dohm, J.M., Irwin, R.P., Kolb, E.J., Fortezzo, C.M., Platz, T., Michael, G.G., Hare, T.M., 2014b. Geologic map of mars. U.S. Geological Survey Scientific Investigations Map 3292, scale 1:20,000,000, pamphlet , 43.

Tanre, D., Herman, M., Deschamps, P.Y., Leffe, A.d., 1979. Atmospheric modeling for space measurements of ground reflectances, including bidirectional properties. Applied Optics 18, 3587–3594.

Tarantola, A., Valette, B., 1982. Generalized nonlinear inverse problems solved using the least squares criterion. Reviews of Geophysics and Space Physics Vol. 20, 219–232.

Taylor, F.W., Svedhem, H., Head, J.W., 2018. Venus: The atmosphere, climate, surface, interior and near-space environment of an earth-like planet. Space Science Reviews 214.

Taylor, L.A., Nazarov, M.A., Shearer, C.K., McSween, H.Y., Cahill, J., Neal, C.R., Ivanova, M.A., Barsukova, L.D., Lentz, R.C., Clayton, R.N., Mayeda, T.K., 2002. Martian meteorite dhofar 019: A new shergottite. Meteoritics & Planetary Science 37, 1107–1128.

Taylor, M.W., Surdam, R.C., 1981. Zeolite reactions in the tuffaceous sediments at teels marsh, neveda. Clays and Clay Minerals 29, 341–352.

Taylor, S.R., McLennan, S.M., 2009. Mars: crustal composition and evolution, in: Planetary Crusts: Their Composition, Origin and Evolution. Cambridge University Press, pp. 141–180.

Teillet, P.M., 1986. Image correction for radiometric effects in remote sensing. International Journal of Remote Sensing 7, 1637–1651.

Temel, A., Giindogdu, M.N., 1996. Zeolite occurrences and the erionite-mesothelioma relationship in cappadocia, central anatolia, turkey. Mineral Deposita 31, 539–547.

Thollot, P., Mangold, N., Ansan, V., Mouélic, S.L., Milliken, R.E., Bishop, J.L., Weitz, C.M., Roach, L.H., Mustard, J.F., Murchie, S.L., 2012. Most mars minerals in a nutshell: Various alteration phases formed in a single environment in noctis labyrinthus. Journal of Geophysical Research Vol. 117, doi:10.1029/2011JE004028.

Thorndike, R.L., 1953. Who belongs in the family? Phychometrika 18, 267–276.

Thorpe, M.T., Hurowitz, J.A., Siebach, K.L., 2021. Source-to-sink terrestrial analogs for the paleoenvironment of gale crater, mars. Journal of Geophysical Research: Planets 126, 14.

Tibbetts, G.G., 2013. How the great scientists reasoned: The scientific method in action. Elsevier.

Tibshirani, R., Walther, G., Hastie, T., 2001. Estimating the number of clusters in a data set via the gap statistic. Journal of the Royal Statistical Society 63, 411–423.

Tokano, T., Bish, D.L., 2005. Hydration state and abundance of zeolites on mars and the water cycle. Journal of Geophysical Research 110, doi:10.1029/2005JE002410.

Tonooka, H., 2005. Inflight straylight analysis for aster thermal infrared bands. IEEE Transactions on Geoscience and Remote Seinsing Vol. 43, 2752–2762.

Tonooka, H., Sakuma, F., Kudoh, M., Iwafune, K., 2004. Aster/tir onboard calibration status and user-based recalibration, in: Meynart, R., Neeck, S.P., Shimoda, H., Lurie, J.B., Aten, M.L. (Eds.), Proc. SPIE 5234, Sensors, Systems, and Next-Generation Satellites VII, pp. 191–201.

Trainer, M.G., Wong, M.H., McConnochie, T.H., Franz, H.B., Atreya, S.K., Conrad, P.G., Lefevre, F., Mahaffy, P.R., Malespin, C.A., Manning, H.L., Martin-Torres, J., Martinez, G.M., McKay, C.P., Navarro-Gonzalez, R., Vicente-Retortillo, A., Webster, C.R., Zorzano, M.P., 2019. Seasonal variations in atmospheric composition as measured in gale crater, mars. Journal of Geophysical Research: Planets 124, 3000–3024.

Trang, D., Lucey, P.G., 2019. Improved space weathering maps of the lunar surface through radiative transfer modeling of kaguya multiband imager data. Icarus 321, 307–323.

Trauth, M.H., Denio, A., Strecker, M.R., 2001. Response of the east african climate to orbital forcing during the last interglacial (130–117 ka) and the early last glacial (117–60 ka). Geology 29, 499–502.

Treiman, A.H., Irving, A.J., 2008. Petrology of martian meteorite northwest africa 998. Meteoritics & Planetary Science 43, 829–854.

Treiman, A.H., Mckay, G.A., Bogard, D.D., Mittlefehldt, D.W., Wang, M.S., Keller, L., Lipschutz, M.E., Lindstrom, M.M., Garrison, D., 1994. Comparison of the lew88516 and alba77005 martian meteorites: Similar but distinct. Meteoritics 29, 581–592.

Trickett, S.B., Trafton, J.G., 2007. "what if. . .": The use of conceptual simulations in scientific reasoning. Cognitive Science 31, 843–875.

Tsolis-Katagas, P., Katagas, C., 1990. Zeolitic diagenesis of oligocene pyroclastic rocks of the metaxades area, thrace, greece. Mineralogical Magazine 54, 95–103.

Tumenbayar, B., Grayson, R., Petrova, V., Enkhsaikhan, R., 2019. Natural zeolite formation in mongolia. Mongolian Geoscientist 49, 35–40.

Turbet, M., Boulet, C., Karman, T., 2020. Measurements and semi-empirical calculations of co2 thch4 and co2 thh2 collision-induced absorption across a wide range of wavelengths and temperatures. application for the prediction of early mars surface temperature. Icarus 346, 6.

Turenne, N., Parkinson, A., Applin, D.M., Mann, P., Cloutis, E.A., Mertzman, S.A., 2022. Spectral reflectance properties of minerals exposed to martian surface conditions: Implications for spectroscopy-based mineral detection on mars. Planetary and Space Science 210.

Turner, C.E., Fishman, N.S., 1991. Jurassic lake t'oo'dichi': A large alkaline, saline lake, morrison formation, eastern colorado plateau. Gelogical Society of America Bulletin 103, 538–558.

Vaniman, D.T., Bish, D.L., Chipera, S.J., Fialips, C.I., Carey, J.W., Feldman, W.C., 2004. Magnesium sulphate salts and the history of water on mars. Nature 431, 663–665.

Vaniman, D.T., Bish, D.L., Ming, D.W., Bristow, T.F., Morris, R.V., Blake, D.F., Chipera, S.J., Morrison, S.M., Treiman, A.H., Rampe, E.B., Rice, M., Achilles, C.N., Grotzinger, J., McLennan, S.M., Williams, J., III, J.B., Newsom, H., Downs, R.T., Maurice, S., Sarrazin, P., Yen, A.S., Morookian, J.M., Farmer, J.D., Stack, K., Milliken, R.E., Ehlmann, B., Sumner, D.Y., Berger, G., Crisp, J.A., Hurowitz, J.A., Anderson, R., DesMarais, D., Stolper, E.M., Edgett, K.S., Gupta, S., Spanovich, N., Team, M.S., 2014. Mineralogy of a mudstone at yellowknife bay, gale crater, mars. Science 343.

Vaniman, D.T., Martinez, G.M., Rampe, E.B., Bristow, T.F., Blake, D.F., Yen, A.S., Ming, D.W., Rapin, W., Meslin, P.Y., Morrison, J.M., Downs, R.T., Chipera, S.J., Morris, R.V., Morrison, S.M., Treiman, A.H., Achilles, C.N., Robertson, K., Grotzinger, J.P., Hazen, R.M., Wiens, R.C., Sumner, D.Y., 2018. Gypsum, bassanite, and anhydrite at gale crater, mars. American Mineralogist 103, 1011–1020.

Varnes, D.J., 1974. The Logic of Geological Maps, With Rcference toTheir Interpretation and Use for Engineerirg Purposes. volume Geological Survey Professional Paper 837. United States Government Printing Office, Washington.

Vermote, E., Tanré, D., Deuzé, J.L., Herman, M., Morcrette, J.J., Kotchenova, S.Y., 2006. Second Simulation of a Satellite Signal in the Solar Spectrum - Vector (6SV). Technical Report. http://6s.ltdri.org.

Vermote, E.F., Tanre, D., Deuze, J.L., Herman, M., Morcrette, J.J., 1997. Second simulation of the satellite signal in the solar spectrum, 6s: An overview. IEEE Transactions on Geoscience and Remote Seinsing 35, 675–686.

Viennet, J.C., Bultel, B., Riu, L., Werner, S.C., 2017. Dioctahedral phyllosilicates versus zeolites and carbonates versus zeolites competitions as constraints to understanding early mars alteration conditions. Journal of Geophysical Research: Planets 122, 2328–2343.

Viviano-Beck, C.E., Murchie, S.L., Beck, A.W., Dohm, J.M., 2017. Compositional and structural constraints on the geologic history of eastern tharsis rise, mars. Icarus 284, 43–58.

Wagner, C., Schade, U., 1996. Measurements and calculations for estimating the spectrometric detection limit for carbonates in martian soil. Icarus 123, 256–268.

Wang, A., Jolliff, B.L., Liu, Y., Connor, K., 2016. Setting constraints on the nature and origin of the two major hydrous sulfates on mars: Monohydrated and polyhydrated sulfates. Journal of Geophysical Research. Planets 121, 678–694.

Wanke, H., Bruckner, J., Dreibus, G., Rieder, R., Ryabchikow, I., 2001. Chemical compostion of rocks and soils at the pathfinder site. Space Science Reviews 96, 317–330.

Warren, J.K., 2016. Evaporites: A Geological Compendium. Springer International Publishing.

Warren, P.H., 1998. Petrologic evidence for low-temperature, possibly flood evaporitic origin of carbonates in the alh84001 meteorite. Journal of Geophysical Research 103, 16,759–16,773.

Warren, P.H., Kallemeyn, G.W., 1997. Yamato-793605, eet79001, and other presumed martian meteorites: Compositional clues to their origins. Antarctic Meteorites Research 10, 61–81.

Watson, K., 1992. Spectral ratio method for measuring emissivity. Remote Sensing of Environment 42, 113–116.

Way, D.S., 1978. Terrain Analysis: A guide to site selection using aerial photographic interpretation. Dowden, Hutchinson & Ross, Inc.

Wehrens, R., Buydens, L.M.C., 2007. Self- and super-organizing maps in r: The kohonen package. Journal of Statistical Software 21, 19.

Wehrens, R., Kruisselbrink, J., 2018. Flexible self-organizing maps in kohonen 3.0. Journal of Statistical Software 87, 18.

Weisberg, M., 2015. Simulation and Similarity: Using models to understand the world. Oxford University Press.

Weisenberger, T., Spurgin, S., 2009. Zeolites in alkaline rocks of the kaiserstuhl volcanic complex, se germany- new microprobe investigation and the relationship of zeolite mineralogy to the host rock. Geologica Belgica 12, 75–91.

Weitz, C.M., Dobrea, E.N., Wray, J.J., 2015. Mixtures of clays and sulfates within deposits in western melas chasma, mars. Icarus 251, 291–314.

Weitz, C.M., Sullivan, R.J., Lapotre, M.G.A., Rowland, S.K., Grant, J.A., Baker, M., Yingst, R.A., 2018. Sand grain sizes and shapes in eolian bedforms at gale crater, mars. Geophysical Research Letters 45, 9471–9479.

Wendt, L., Bishop, J.L., Neukum, G., 2013. Knob fields in the terra cimmeria/terra sirenum region of mars: Stratigraphy, mineralogy and morphology. Icarus 225, 200–215.

Wharton, R.A., Crosby, J.M., McKay, C.P., Rice, J.W., 1995. Paleolakes on mars. Journal of Paleolimnology 13, 267–283.

Whelley, P., Novak, A.M., Richardson, J., Bleacher, J., Mach, K., Smith, R.N., 2021. Stratigraphic evidence for early martian explosive volcanism in arabia terra. Geophysical Research Letters 48.

White, A.F., Brantley, S.L., 2003. The effect of time on the weathering of silicate minerals: why do weathering rates differ in the laboratory and field? Chemical Geology 202, 479–506.

Williams, R.M.E., Grotzinger, J.P., Dietrich, W.E., Gupta, S., Sumner, D.Y., Wiens, R.C., Mangold, N., Malin, M.C., Edgett, K.S., Maurice, S., Forni, O., Gasnault, O., Ollila, A., Newsom, H.E., Dromart, G., Palucis, M.C., Yingst, R.A., Anderson, R.B., Herkenhoff, K.E., Mouélic, S.L., Goetz, W., Madsen, M.B., Koefoed, A., Jensen, J.K., Bridges, J.C., Schwenzer, S.P., Lewis, K.W., Stack, K.M., Rubin, D., Kah, L.C., III, J.F.B., Farmer, J.D., Sullivan, R., Beek, T.V., Blaney, D.L., Pariser, O., Deen, R.G., Team‡, M.S., 2013. Martian fluvial conglomerates at gale crater. Science 340, 1068–1972.

Williford, K.H., Farley, K.A., Stack, K.M., Allwood, A.C., Beaty, D., Beegle, L.W., Bhartia, R., Brown, A.J., Juarez, M.d.l.T., Hamran, S.E., Hecht, M.H., Hurowitz, J.A., Rodriguez-Manfredi, J.A., Maurice, S., Milkovich, S., Wiens, R.C., 2018. The nasa mars 2020 rover mission and the search for extraterrestrial life, in: Cabrol, N.A., Grin, E.A. (Eds.), From Habitability to Life on Mars. Elsevier, pp. 275–308.

Wilson, L., Head, J.W., 2007. Explosive volcanic eruptions on mars: Tephra and accretionary lapilli formation, dispersal and recognition in the geologic record. Journal of Volcanology and Geothermal Research 163, 83–97.

Wolery, T.W., 2013. EQ3/6 - Software for Geochemical Modeling, Version 8.0a, LLNL-CODE-2013-683958. Technical Report. Lawrence Livermore National Laboratory, Livermore, California.

Wolf, K.H., Ellison, B., 1971. Sedimentary geology of the zeolitic volcanic lacustrine pliocene rome beds, oregon, 1. Sedimentary Geology 6, 271–302.

Wordsworth, R., Forget, F., Millour, E., Head, J.W., Madeleine, J.B., Charnay, B., 2013. Global modelling of the early martian climate under a denser co2 atmosphere: Water cycle and ice evolution. Icarus 222, 1–19.

Wordsworth, R., Kalugina, Y., Lokshtanov, S., Vigasin, A., Ehlmann, B., Head, J., Sanders, C., Wang, H., 2017. Transient reducing greenhouse warming on early mars. Geophysical Research Letters 44, 665–671.

Wordsworth, R., Knoll, A.H., Hurowitz, J., Baum, M., Ehlmann, B.L., Head, J.W., Steakley, K., 2021. A coupled model of episodic warming, oxidation and geochemical transitions on early mars. Nature Geoscience 14, 127–132.

Wray, J.J., Ehlmann, B.L., Squyres, S.W., Mustard, J.F., Kirk, R.L., 2008. Compositional stratigraphy of clay-bearing layered deposits at mawrth vallis, mars. Geophysical Research Letters 35.

Wray, J.J., Milliken, R.E., Dundas, C.M., Swayze, G.A., Andrews-Hanna, J.C., Baldridge, A.M., Chojnacki, M., Bishop, J.L., Ehlmann, B.L., Murchie, S.L., Clark, R.N., Seelos, F.P., Tornabene, L.L., Squyres, S.W., 2011. Columbus crater and other possible groundwater-fed paleolakes of terra sirenum, mars. Journal of Geophysical Research 116, 41.

Wray, J.J., Murchie, S.L., Bishop, J.L., Ehlmann, B.L., Milliken, R.E., Wilhelm, M.B., Seelos, K.D., Chojnacki, M., 2016. Orbital evidence for more widespread carbonatebearing rocks on mars. Journal of Geophysical Research. Planets 121, 625–677.

Wray, J.J., Murchie, S.L., Squyres, S.W., Seelos, F.P., Tornabene, L.L., 2009. Diverse aqueous environments on ancient mars revealed in the southern highlands. Geology 37, 1043–1046.

Wray, J.J., Squyres, S.W., Roach, L.H., Bishop, J.L., Mustard, J.F., Dobrea, E.Z.N., 2010. Identification of the ca-sulfate bassanite in mawrth vallis, mars. Icarus Vol. 209, 416–421.

Wright, S.P., Ramsey, M.S., 2006. Thermal infrared data analyses of meteor crater, arizona: Implications for mars spaceborne data from the thermal emission imaging system. Journal of Geophysical Research 111.

Yamaguchi, Y., Kahle, A.B., Tsu, H., Kawakami, T., Pniel, M., 1998. Overview of advanced spaceborne thermal emission and reflection radiometer (aster). IEEE Transactions on Geoscience and Remote Seinsing 36, 1062–1071.

Yang, L., Meng, X., Zhang, X., 2011. Srtm dem and its application advances : Review article. International Journal of Remote Sensing 32, 3875–3896.

Yang, X.Q., Kodikara, G.R., Luedeling, E., Yang, X.F., He, J., Liu, P.g., Xu, J.C., 2012. Looking below the ground: Prediction of tuber indicum habitat using the weights of evidence method. Ecological Modelling Vol. 247, 27–39.

Yoleva, A., Petrov, O., Djambazov, S., Malinov, O., Stoycheva, D., 2006. Clinoptilolite in volcanic neck structure near kralevo deposit, haskovo region (bulgaria), in: Bowman, R.S., Delap, S.E. (Eds.), Zeolite '06—7th International Conference on the Occurrence, Properties, and Utilization of Natural Zeolites, Socorro, New Mexico USA. pp. 256–257.

Young, S.J., Johnson, B.R., Hackwell, J.A., 2002. An in-scene method for atmospheric compensation of thermal hyperspectral data. Journal of Geophysical Research 107, doi:10.1029/2001JD001266.

Zadeh, L.A., 1965. Fuzzy sets. Inform. Control vol. 8, 338–353.

Zhao, J., Xiao, L., Glotch, T.D., 2020. Paleolakes in the northwest hellas region, mars: Implications for the regional geologic history and paleoclimate. Journal of Geophysical Research: Planets 125.

Zimmermann, H.J., 1991. Fuzzy Set Theory and Its Applications. volume 1. Springer.

Zimmermann, H.J., Zysno, P., 1980. Latent connectives in human decision making. Fuzzy Sets and Systems 4, 37–51.

Zolotov, M.Y., Mironenko, M.V., 2007. Timing of acid weathering on mars: A kinetic-thermodynamic assessment. Journal of Geophysical Research 112, doi:10.1029/2006JE002882.

Zolotov, M.Y., Mironenko, M.V., 2016. Chemical models for martian weathering profiles: Insights into formation of layered phyllosilicate and sulfate deposits. Icarus 275, 203–220.

Appendices

A

Non-Marine Tuff Deposits

Table A.1: Database of non-marine tuff deposits from literature.

Lake/basin	Country	Time	Reference
Congo Basin	Africa	lJU-eCr	Hay (1966)
Chubutiano Group	Argentina	lCr	Hay (1966)
Dark Victor Formation	Argentina	lTr	Hay (1966)
Rio Sali Formation	Argentina	uMi	Hay (1966)
Mendoza	Argentina	Tr	Deffeyes (1959)
Tamworth Belt	Australia	lCa	Cooper (1993)
Drummond Basin	Australia	eCa	Cooper (1993)
Otway Basin	Australia	eCr	Cooper (1993)
Currabubula Formation	Australia	lCa	Cooper (1993)
Corda Formation	Brazil	Cr	Rezende and Angélica (1999)
Adamantina Formation	Brazil	Cr	Rezende and Angélica (1999)
Botucatu Formation	Brazil	Ju	Rezende and Angélica (1999)
Kralevo deposit	Bulgariya	Ol	Yoleva et al. (2006)
Beli Plast	Bulgariya	Ol	Petrov (2006)
Gorna Krepost	Bulgariya	Ol	Petrov (2006)
Most	Bulgariya	Ol	Petrov (2006)
Golobradovo	Bulgariya	Ol	Petrov (2006)
Belia Bair	Bulgariya	Ol	Petrov (2006)
Ljaskovetz	Bulgariya	Ol	Petrov (2006)
Colbun Formation	Chile	lEo-mMi	Bascunan et al. (2007)
Kivu	Congo	lPl	Hay (1966)
Cayo formation	Ecuador	Cr	Machiels et al. (2006)
Plateau des Coirons	France	Mi-Pi	Robert and Goffe (1993)
Coirons	France	Mi	Robert and Goffe (1993)
Kutais-Gelatsk Region	Georgia	Ju	Hay (1966)
Western Georgia	Georgia	Ju	Deffeyes (1959)
Germany	Germany	eCa	Hay (1966)
Karlovassi Basin	Greece	uMi	Stamatakis (1989a)

Lake/basin	Country	Time	Reference
Metaxades Area	Greece	Ol	Tsolis-Katagas and Katagas (1990)
Honolulu Series	Hawaii	lPl	Hay (1966)
Mecsek Mts.	Hungary	Mi	Polgari et al. (1997)
Basic Tuffs	Iceland	Pl	Hay (1966)
South of Central Alborz	Iran	Eo	Behin et al. (2019)
Sartakht area	Iran	Eo	Behin et al. (2019)
Karaj Formation	Iran	Eo	Behin et al. (2019)
Meyamey area, Shahrood	Iran	Eo	Behin et al. (2019)
Mianeh City	Iran	Eo	Behin et al. (2019)
Karaj Formation, Central Alborz	Iran	Eo	Behin et al. (2019)
NW of Bardsir City	Iran	Eo	Behin et al. (2019)
Baft Region	Iran	Eo	Behin et al. (2019)
Qom Province	Iran	Eo	Behin et al. (2019)
Parandak City	Iran	Eo	Behin et al. (2019)
Erjenan Region	Iran	Eo	Behin et al. (2019)
NE Zanjan City	Iran	Eo	Behin et al. (2019)
Taleghan region	Iran	Eo	Behin et al. (2019)
Northern Zahedan	Iran	Eo	Behin et al. (2019)
Cinerite of central northern Apennines	Italy	Ol-Mi	Passaglia and Vezzalini (1985)
Asuni Area	Italy	Ol-Mi	Mormone and Piochi (2020)
Campania	Italy	Qu	Passaglia and Vezzalini (1985)
MITI-Toyokoro	Japan	Mi-Pi	Ogihara (1996)
Lake Magadi	Kenya	Pl-Ho	Surdam and Eugster (1976)
Lake Bogoria Basin	Kenya	lQu	Renaut (1993)
Guryongpo area	Korea	Mi	Noh and Boles (1989)
La Bufa	Mexico	Eo-Ol	Pablo-Galan and Chavez-Garcia (1996)
Chichindaro	Mexico	Ol	Pablo-Galan and Chavez-Garcia (1996)
Oaxaca	Mexico	Ol	Popov et al. (2006)

Lake/basin	Country	Time	Reference
Laguna de Cuitzeo	Mexico	uMi-lPi	Ostrooumov and Ostrooumova (2006)
East Mongolian Volcanic Belt	Mongolia	uJu-eCr	Oyuntseteg and Lkhagvajav (2006)
Tsagaansav	Mongolia	lJU-eCr	Tumenbayar et al. (2019)
Tushleg East	Mongolia	lJU-eCr	Tumenbayar et al. (2019)
Tushleg West	Mongolia	lJU-eCr	Tumenbayar et al. (2019)
Tushleg North	Mongolia	lJU-eCr	Tumenbayar et al. (2019)
Urgen	Mongolia	lJU-eCr	Tumenbayar et al. (2019)
Sugir	Mongolia	lJU-eCr	Tumenbayar et al. (2019)
Ngakuru	New Zealand	lQu	Brathwaite (2003)
North Onega Bauxite Deposite	Russia	eCr	Hay (1966)
Continental Intercalaire	Sahara	eCr	Hay (1966)
Tuva	Siberia	eCa	Hay (1966)
East Slovakian Basin	Slovakia	Pi-pNe	Reed et al. (1993)
Madrid Basin	Spain	Mi	Pozo et al. (2006)
Lake Natron	Tanzania	Re	Hay (1966)
Lake Natron	Tanzania	mPl	Hay (1966)
Olduvai Gorge	Tanzania	mPl	Hay (1966)
Olduvai Gorge	Tanzania	ePl-mPl	Hay (1966)
Olduvai Gorge	Tanzania	ePl-mPl	Hay (1966)
Olduvai Gorge	Tanzania	lPl	Hay (1966)
Olduvai Gorge	Tanzania	Re	Hay (1966)
Degirmenli	Turkey	Mi	Gundogdu et al. (1996)
Emirler	Turkey	Mi	Gundogdu et al. (1996)
Kopenez	Turkey	Mi	Gundogdu et al. (1996)
Karaoren	Turkey	Mi	Gundogdu et al. (1996)
Urgup formation	Turkey	uMi	Temel and Giindogdu (1996)
Coal Measures	UK	Ca	Hay (1966)
Arizona	USA	Mi	Hay (1966)
Black Point Volcano	USA	lPl	Hay (1966)

Lake/basin	Country	Time	Reference
Central Nevada	USA	Pi	Hay (1966)
Central Nevada	USA	lMi-Pi	Hay (1966)
Central Nevada	USA	pMi-lMi	Hay (1966)
China Lake	USA	lPl	Hay (1966)
Chinle Formation	USA	lTr	Hay (1966)
Chugwater Formation	USA	Tr	High and Picard (1965)
Columbia River Basalt	USA	Mi-Pi	Hay (1966)
Esmeralda Formation	USA	lPl/ePl	Hay (1966)
Esmeralda Formation	USA	lPl-Pl	Hay (1966)
Esmeralda Formation	USA	Pi	Hay (1966)
Esmeralda Formation	USA	Mi-Pi	Hay (1966)
Green River Formation	USA	Eo	Surdam and Parker (1972)
Grizzly Peak Formation	USA	ePi	Hay (1966)
Hay Ranch Formation	USA	mPi-MPl	Hay (1966)
John Day Formation	USA	lOl-eMi	Hay (1966)
Kramer	USA	Mi	Hay (1966)
Livingstone Formation	USA	lCr-Pa	Hay (1966)
Lockatong Formation	USA	Tr	Hay (1966)
Lysite Mountain	USA	mEo-lEo	Hay (1966)
New South Wales	USA	Pe	Hay (1966)
Newark	USA	lTr	Hay (1966)
North Central Nevada	USA	Ol-ePi	Hay (1966)
Oak Spring Formation	USA	Pi	Hay (1966)
Owens Lake	USA	lPl	Hay (1966)
San Joaquin Valley	USA	Re	Hay (1966)
Searles Lake	USA	lPl	Hay and Guldman (1987)
Siesta Formation	USA	ePi	Hay (1966)
Southern California	USA	Pi	Hay (1966)
Teels Marsh	USA	Ho	Taylor and Surdam (1981)

Lake/basin	Country	Time	Reference
Tepee Creek Formation	USA	Pe	Deffeyes (1959)
Tongue River Formation	USA	Pa	Deffeyes (1959)
Upper Kuttunf	USA	lCa	Hay (1966)
Wagon Bed Formation	USA	mEo-lEo	Boles and Surdam (1979)
Waucoba Lake	USA	ePl	Hay (1966)
White River Formation	USA	Ol	Lander and Hay (1993)
Wind River Formation	USA	Pa	Love (1970)
Popo Agie Formation	USA	Tr	Deffeyes (1959)
Chinle Formation	USA	Tr	Deffeyes (1959)
Tepee Trail Formation	USA	Eo	Deffeyes (1959)
Big Sandy Formation	USA	Pi	Sheppard and Gude (1973)
Hector	USA	Pi	Deffeyes (1959)
Salt Lake Group	USA	Pi	Deffeyes (1959)
Pierre Shale	USA	Cr	Deffeyes (1959)
Elko Oil Shale	USA	Ol	Deffeyes (1959)
Pine Valley	USA	Pi-ePl	Deffeyes (1959)
Reese Valley	USA	ePi	Deffeyes (1959)
Jersey Valley	USA	lMi	Deffeyes (1959)
Blackleaf Sandy member of Colorado Shale	USA	Cr	Deffeyes (1959)
Chalk Hills Formation	USA	Mi	Sheppard (1991)
Lake Tecopa	USA	Pl	Sheppard and Gude (1968)
Little Humboldt River	USA	Mi	Sheppard and Gude (1983)
Durkee	USA	Mi	Gude and Sheppard (1986)
Harney Lake	USA	Mi	Sheppard (1994)
Buckhorn	USA	Pi	Gude and Sheppard (1988)
Barstow Formation	USA	Mi	Sheppard and Gude (1969b)
Succor Creek	USA	Mi	Lawrence (1988)
Southern Desatoya Mountains	USA	Mi	Barrows (1980)

Lake/basin	Country	Time	Reference
Creede Formation	USA	Ol	Larsen and Crossey (1996)
Ray San Manuel	USA	Mi	Krieger (1979)
Near Hector	USA	Mi-Pi	Madsen (1970)
Pine Ridge Reservation	USA	Ol	Raymond et al. (1982)
Rome Beds	USA	Pi	Wolf and Ellison (1971)
San Simon basin	USA	Pi-Pl	Edson (1977)
Eastgate Zeolite deposit	USA	Pi	Sheppard and Gude (1980)
Chkalova district	USSR	Pe	Deffeyes (1959)

Time Abbreviations: Re = Recent, Ho = Holocene, Pl = Pleistocene, Pi = Pliocene, Mi = Miocene, Ol = Oligocene, Eo = Eocene, Pa = Paleocene, Cr = Cretaceous, Ju = Jurassic, Tr = Triassic, Pe = Permian, Ca = Carboniferous, Letter l, m, and e suffix to the time period indicate Late, Middle, and Early, respectively.

B

Spectral Angle Mapper Results

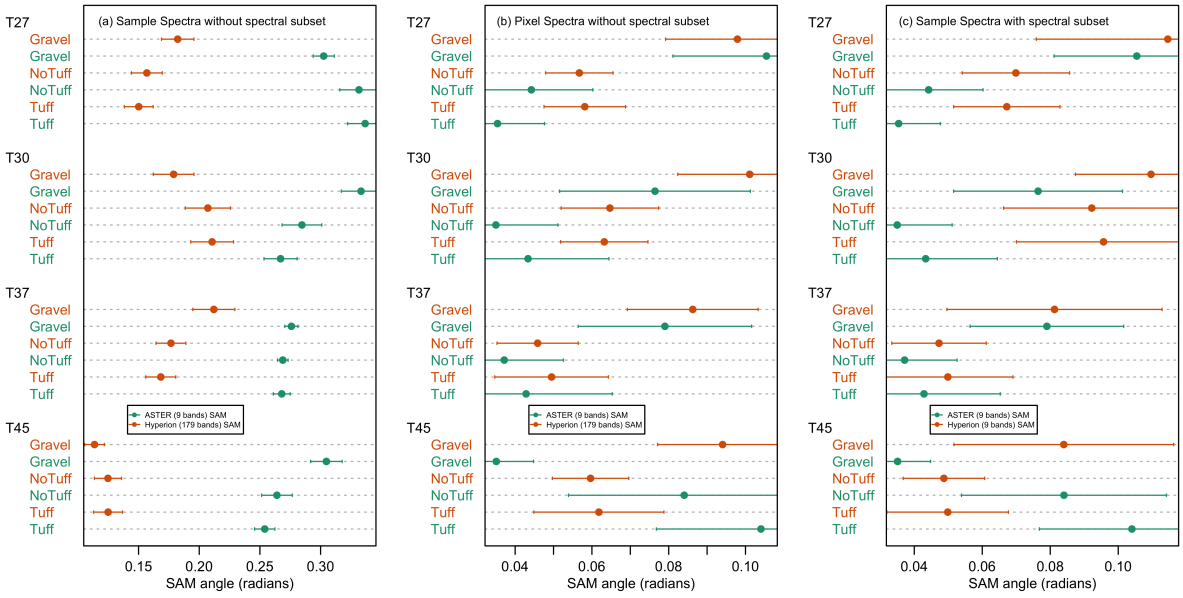

Figure B.1: Spectral Angle Mapper classification results from ASTER and Hyperion images, using sample spectra for classification without spectral subset (a), using pixel spectra for classification without spectral subset (b), and using sample spectra after spectral subset (c).

Three different mapping scenarios were studied in this SAM analysis area discussed here. Those are, 1) SAM classification using field sample spectra (T27, T30, T37, T45) for both ASTER and Hyperion images with all bands, 2) SAM classification using the corresponding pixel spectra (T27P, T30P, T37P, T45P) for both images with all bands, 3) SAM classification using 9 bands of the Hyperion image, which are comparable to

the ASTER bands, with their corresponding pixel spectra (T27P, T30P, T37P, T45P). SAM results were assessed using the Class point map. Figure S1 shows the results of these three scenarios. The mean spectral angle value of each class is represented by a data point, whereas the standard deviation associated with each class is represented by the "bar" of each point. Figure S1 (a) shows the SAM angles calculated from all bands of Hyperion (179 bands) and ASTER (9 bands) data using the sample spectra. Figure S1 (a) does not show any meaningful correlation between the sample spectra with the surface types except for T27. The Hyperion full band spectra were able to identify T27 as Tuff. However, Figure S1 (a) shows the opposite trend in SA values for ASTER and Hyperion for samples T27, T30, and T45. The SAM classification using image spectra with full spectral bands is shown in Figure S1 (b). The overall spectral angles decreased around three times compared to the first scenario. From the ASTER SAM results, T27 is classified as Tuff, while T30 and T37 are classified as NoTuff areas based on their low SA values. T45 is identified as Gravel, most probably due to its less intense absorption features. SAM results from the Hyperion image do not show as high performance as in the ASTER image. Figure S1 (c) compares the SAM results of 9 ASTER bands with the SAM classification performed using Hyperion 9 bands, at band locations similar to those of ASTER, with their image spectra. The result shows that even though the SA values are relatively lower than using all the Hyperion bands, none of the sample spectra could differentiate the Tuff beds from the NoTuff beds. This might be due to the higher SNR in the Hyperion data than in ASTER and/or due to the noise remaining after atmospheric correction. Therefore, this study shows that for the SAM classification, the image spectra give better results than the sample spectra and ASTER gives better results than Hyperion, likely because of the high noise inherent with the Hyperion image.

C
Deep Leaning Model

The mineral abundances (weight percentage) of each end member mineral in each mixture.

Sample ID	Clinoptilolite	Montmorillonite	Epsomite
T00	0	100	0
T01	0	90	10
T02	0	80	20
T03	0	70	30
T04	0	60	40
T05	0	50	50
T06	0	40	60
T07	0	30	70
T08	0	20	80
T09	0	10	90
T10	0	0	100
T11	10	90	0
T12	10	80	10
T13	10	70	20
T14	10	60	30
T15	10	50	40
T16	10	40	50
T17	10	30	60
T18	10	20	70
T19	10	10	80
T20	10	0	90
T21	20	80	0
T22	20	70	10
T23	20	60	20
T24	20	50	30

C. Deep Leaning Model

Sample ID	Clinoptilolite	Montmorillonite	Epsomite
T25	20	40	40
T26	20	30	50
T27	20	20	60
T28	20	10	70
T29	20	0	80
T30	30	70	0
T31	30	60	10
T32	30	50	20
T33	30	40	30
T34	30	30	40
T35	30	20	50
T36	30	10	60
T37	30	0	70
T38	40	60	0
T39	40	50	10
T40	40	40	20
T41	40	30	30
T42	40	20	40
T43	40	10	50
T44	40	0	60
T45	50	50	0
T46	50	40	10
T47	50	30	20
T48	50	20	30
T49	50	10	40
T50	50	0	50
T51	60	40	0
T52	60	30	10
T53	60	20	20
T54	60	10	30
T55	60	0	40
T56	70	30	0
T57	70	20	10
T58	70	10	20
T59	70	0	30
T60	80	20	0
T61	80	10	10
T62	80	0	20
T63	90	10	0
T64	90	0	10
T65	100	0	0

C. Deep Leaning Model

Basic tools (codes) used to create deep learning models.

1. Setup python environment

```
library(reticulate)
virtualenv_create("rstudio")
use_virtualenv("rstudio")
use_python("/Users/kodi/opt/miniconda3/bin/python")
matplotlib <- import("matplotlib")
matplotlib$use("Agg", force = TRUE)
```

2. Multiplicative Scatter Correction (MSC) algorithm

```
def msc(input_data, reference=None):
    # mean center correction
    for i in range(input_data.shape[0]):
        input_data[i,:] -= input_data[i,:].mean()
    # Get the reference spectrum.
    if reference is None:
        # Calculate mean
        ref = np.mean(input_data, axis=0)
    else:
        ref = reference
    # Define a new array.
    data_msc = np.zeros_like(input_data)
    for i in range(input_data.shape[0]):
        # Run regression
        fit = np.polyfit(ref, input_data[i,:], 1, full=True)
        # Apply correction
        data_msc[i,:] = (input_data[i,:] - fit[0][1]) / fit[0][0]
    return (data_msc, ref)
```

3. Savitzky Golay Filter

```
from math import factorial
def savitzky_golay(y, window_size, order, derive = 0, rate =1):
  order_range = range(order + 1)
  half_window = (window_size -1) // 2
  b = np.mat([[k**i for i in order_range] for
              k in range(-half_window, half_window + 1)])
  m = np.linalg.pinv(b).A[derive]* rate**derive * factorial(derive)
  firstvals = y[0] - np.abs(y[1:half_window +1][::-1] -y[0])
  lastvals = y[-1] + np.abs(y[-half_window-1:-1][::-1] -y[-1])
  y = np.concatenate((firstvals, y, lastvals))
  return np.convolve(m[::-1], y, mode='valid')
```

4. Gaussian Models

```
from lmfit.models import GaussianModel
F2 = np.genfromtxt('F2_cont.csv',delimiter = ',')
del(y)
del(x)
y = -np.log10(F2[5,4:])
x = 10000/F2[0,4:]
plt.clf()
gauss1 = GaussianModel(prefix='g1_')
pars = gauss1.guess(y, x=x)
pars['g1_center'].set(value=6.8475, min = 6.7, max = 6.9)
pars['g1_sigma'].set(value=0.09, min=0.02)
pars['g1_amplitude'].set(value=0.00195, min=0.0002)
gauss2 = GaussianModel(prefix='g2_')
pars.update(gauss2.make_params())
pars['g2_center'].set(value=7.082, min = 7.0, max =7.2)
```

C. Deep Leaning Model

```
pars['g2_sigma'].set(value=0.075, min=0.01)
pars['g2_amplitude'].set(value=0.0063, min=0.001)
mod = gauss1 + gauss2
init = mod.eval(pars, x=x)
out = mod.fit(y, pars, x=x)
comps = out.eval_components(x=x)
residual = y - (comps['g1_'] + comps['g2_'])
with plt.style.context(('fast')):
    fig, ax = plt.subplots(figsize=(9, 5))
    ax.plot(x, y, 'r', label='Spectrum ID05')
    ax.plot(x, comps['g1_'], 'g--', label='Gaussian 1')
    ax.plot(x, comps['g2_'], 'b--', label='Gaussian 2')
    ax.plot(x, residual, 'k', label='Residuals')
    ax.set_xlabel("Wave number (cm-1)")
    ax.set_ylabel("Apparent absorbance")
    ax.legend(loc = 'best')
    plt.savefig('F105.png', dpi =1000)
plt.show()
print(out.fit_report(min_correl=0.005))
```

5. Deep Leaning Module A. Import basic python libraries

```
import numpy as np
import torch
from numpy import vstack
from numpy import sqrt
from sklearn.metrics import mean_squared_error
from torch.utils.data import Dataset
from torch.utils.data import DataLoader
from torch.utils.data import random_split
```

C. Deep Leaning Model

```
from torch import Tensor
from torch.nn import Linear
from torch.nn import Sigmoid
from torch.nn import ReLU
from torch.nn import Module
from torch.optim import SGD
from torch.optim import Adam
from torch.nn import MSELoss
from torch.nn.init import xavier_uniform_
```

B. Import dataset

```
path = 'Gauss_DL10_Train.csv'
```

C. Data set definition

```
class CSVDataset(Dataset):
    # load the dataset
    def __init__(self, path):
        # load the csv file as a dataframe
        df = np.genfromtxt(path, delimiter = ',', skip_header=True)
        # store the inputs and outputs
        self.X = np.asarray(df[:, 4:12], dtype = 'float32')
        self.y = np.asarray(df[:, 1:4], dtype='float32')
        # ensure target has the right shape
        self.y = self.y.reshape((len(self.y), 3))
    # number of rows in the dataset
    def __len__(self):
        return len(self.X)
    # get a row at an index
    def __getitem__(self, idx):
        return [self.X[idx], self.y[idx]]
    # get indexes for train and test rows
```

C. Deep Leaning Model

```
    def get_splits(self, n_test=0.33):
        # determine sizes
        test_size = round(n_test * len(self.X))
        train_size = len(self.X) - test_size
        # calculate the split
        return random_split(self, [train_size, test_size])
```

D. Prepare the dataset

```
def prepare_data(path):
    # load the dataset
    dataset = CSVDataset(path)
    # calculate split
    train, test = dataset.get_splits()
    # prepare data loaders
    train_dl = DataLoader(train, batch_size=5, shuffle=True)
    test_dl = DataLoader(test, batch_size=5, shuffle=False)
    return train_dl, test_dl
train_dl,test_dl = prepare_data(path)
print(len(train_dl.dataset), len(test_dl.dataset))
```

E. Model Definition

```
class MLP(Module):
    # define model elements
    def __init__(self, n_inputs):
        super(MLP, self).__init__()
        # input to first hidden layer
        self.hidden1 = Linear(n_inputs, 6)
        xavier_uniform_(self.hidden1.weight)
        self.act1 = Sigmoid()
        #self.act1 = ReLU()
        # second hidden layer
```

```
        self.hidden2 = Linear(6, 6)
        xavier_uniform_(self.hidden2.weight)
        self.act2 = Sigmoid()
        #self.act2 = ReLU()
        # third hidden layer and output
        self.hidden3 = Linear(6, 3)
        xavier_uniform_(self.hidden3.weight)
    # forward propagate input
    def forward(self, X):
        # input to first hidden layer
        X = self.hidden1(X)
        X = self.act1(X)
         # second hidden layer
        X = self.hidden2(X)
        X = self.act2(X)
        # third hidden layer and output
        X = self.hidden3(X)
        return X
```

F. Train the model

```
def train_model(train_dl, model):
    # define the optimization
    criterion = MSELoss()
    #optimizer = SGD(model.parameters(), lr=0.1, momentum=0.9)
    optimizer = Adam(model.parameters(), lr=0.001, betas=(0.9, 0.999),
                     eps=1e-08, weight_decay=0, amsgrad=False)
    # enumerate epochs
    for epoch in range(10000):
        # enumerate mini batches
        for i, (inputs, targets) in enumerate(train_dl):
```

```
            # clear the gradients
            optimizer.zero_grad()
            # compute the model output
            yhat = model(inputs)
            # calculate loss
            loss = criterion(yhat, targets)
            # credit assignment
            loss.backward()
            # update model weights
            optimizer.step()
```

G. Evaluate the model

```
def evaluate_model(test_dl, model):
    predictions, actuals = list(), list()
    for i, (inputs, targets) in enumerate(test_dl):
        # evaluate the model on the test set
        yhat = model(inputs)
        # retrieve numpy array
        yhat = yhat.detach().numpy()
        actual = targets.numpy()
        actual = actual.reshape((len(actual), 3))
        # store
        predictions.append(yhat)
        actuals.append(actual)
    predictions, actuals = vstack(predictions), vstack(actuals)
    # calculate mse
    mse = mean_squared_error(actuals, predictions)
    return mse
# make a class prediction for one row of data
def predict(row, model):
```

```
    # convert row to data
    row = Tensor([row])
    # make prediction
    yhat = model(row)
    # retrieve numpy array
    yhat = yhat.detach().numpy()
    return yhat
```

H. Define the network

```
model = MLP(8)
# train the model
train_model(train_dl, model)
# evaluate the model
mse = evaluate_model(test_dl, model)
print('MSE: %.3f, RMSE: %.3f' % (mse, sqrt(mse)))
```

I. Model parameters

```
# Print model's state_dict
print("Model's state_dict:")
for param_tensor in model.state_dict():
    print(param_tensor, "\t", model.state_dict()[param_tensor])
# Print optimizer's state_dict
print("Optimizer's state_dict:")
for var_name in optimizer.state_dict():
    print(var_name, "\t", optimizer.state_dict()[var_name])
```

J. Save the model

```
torch.save(model, 'AS_10000E2.pt')
torch.save(model.state_dict(),'AS_10000E2_weights.pt')
```

K. Predictions for new dataset

C. Deep Leaning Model

```
df_pred = np.genfromtxt('Gauss_DL10_Predi.csv',
                        delimiter = ',', skip_header=True)
pred = np.asarray(df_pred[:, 4:12], dtype = 'float32')
```

C. Deep Leaning Model

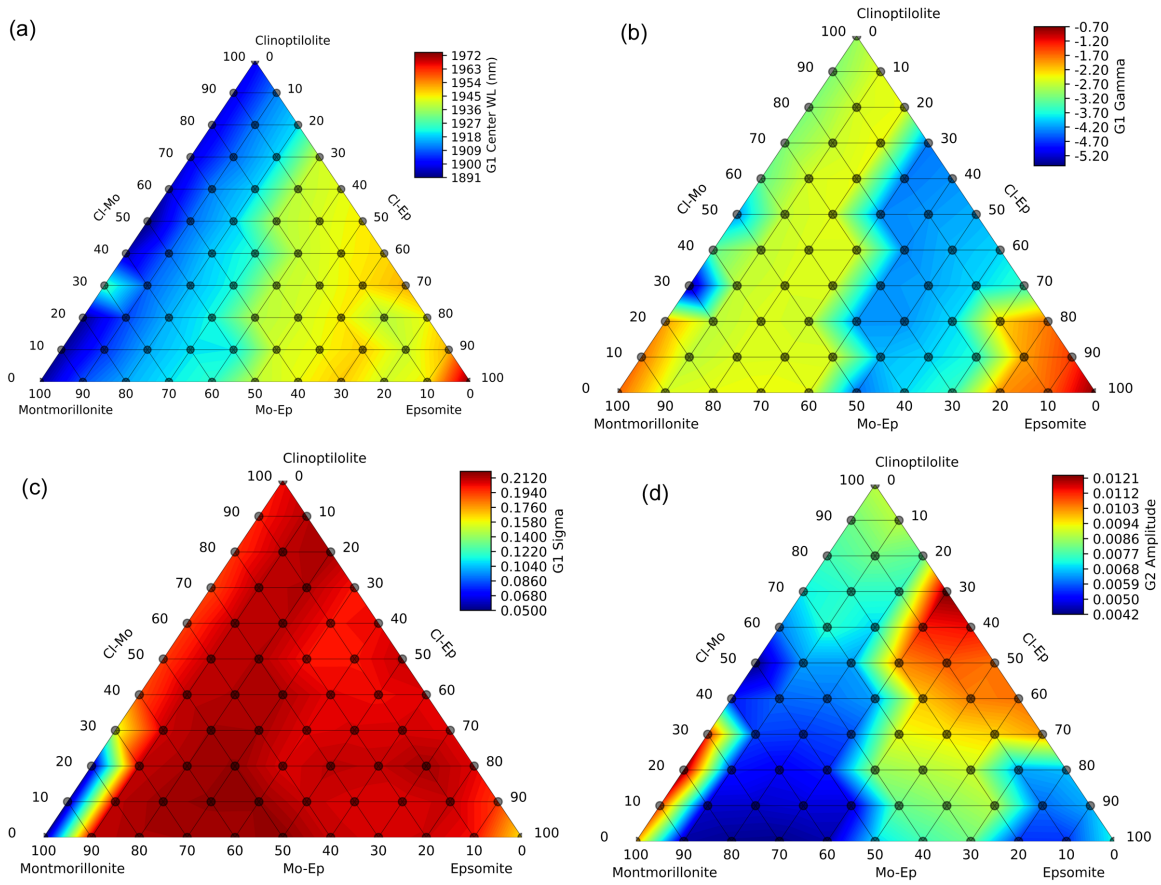

Figure C.1: Ternary plots showing the center wavelength of Gaussian curve 1 of feature 2 (a), gamma value of Gaussian curve 1 of feature 2 (b), sigma value of Gaussian curve 1 of feature 2 (c), amplitude of Gaussian curve 2 of feature 2 (d). Linear interpolation was applied between the sample points to fill the colors in small triangles in the plots.

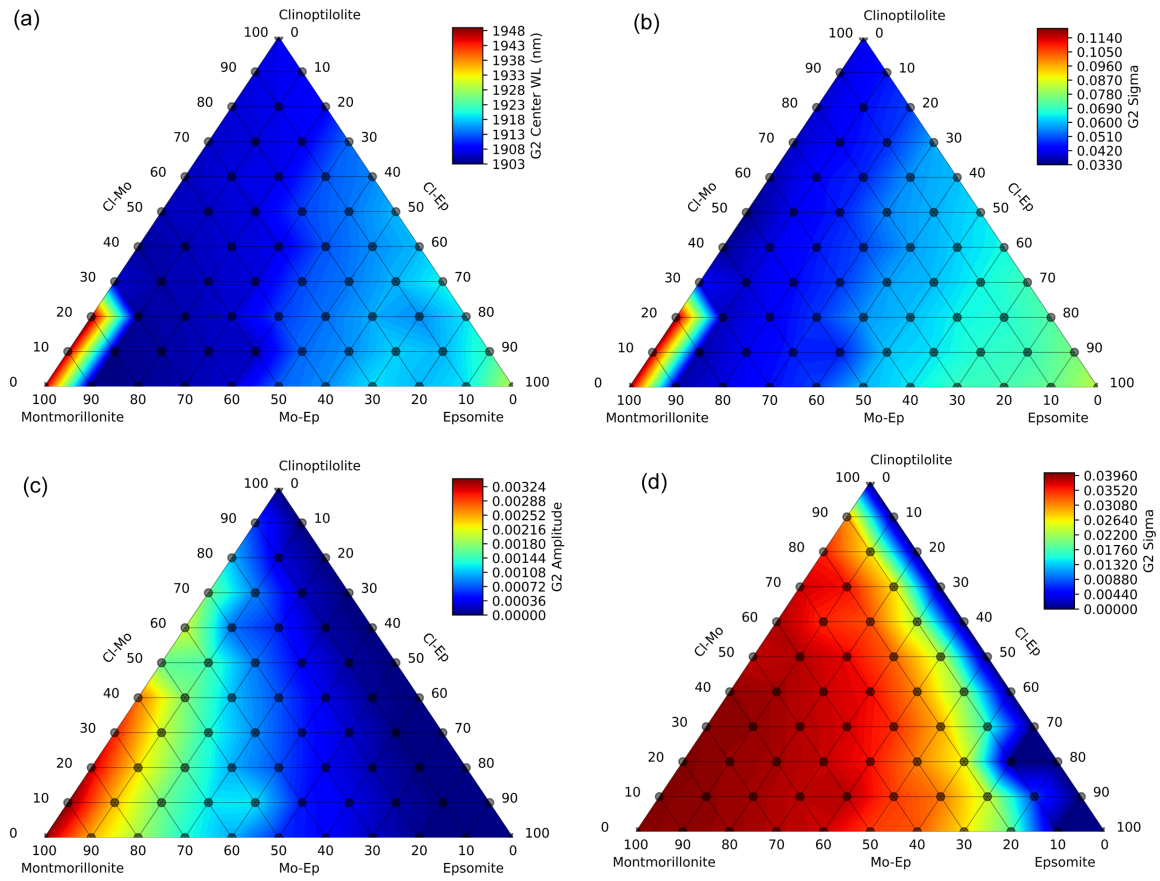

Figure C.2: Ternary plots showing the center wavelength of Gaussian curve 2 of feature 2 (a), gamma value of Gaussian curve 2 of feature 2 (b), amplitude of Gaussian curve 2 of feature 3 (c), sigma value of Gaussian curve 2 of feature 3 (d). Linear interpolation was applied between the sample points to fill the colors in small triangles in the plots.

Table C.2: Deep leaning prediction results

Type	Spec ID	EPS_{or}	EPS_{pr}	CLN_{or}	CLN_{pr}	MOT_{or}	MOT_{pr}
Mix	MIX_89	43	40	13	11	43	49
Mix	MIX_120	33	35	33	31	33	34
Mix	MIX_131	13	12	43	44	43	44
Mix	MIX_134	43	42	43	44	13	14
Mix	MIX_155	17	13	67	73	17	14
Cln	T27U	0	40	100	46	0	14
Cln	GDS152_5841	0	27	100	60	0	13
Cln	GDS2_5896	0	27	100	60	0	13
Cln	laze27	0	22	100	65	0	13
Cln	laze28	0	29	100	58	0	13
Eps	gds149_7646	100	98	0	0	0	2
Eps	c1cc19	100	98	0	0	0	2
Eps	c1cc31	100	98	0	0	0	2

C. Deep Leaning Model

Type	Spec ID	EPS_{or}	EPS_{pr}	CLN_{or}	CLN_{pr}	MOT_{or}	MOT_{pr}
Eps	c1jb366	100	86	0	12	0	2
Eps	c1jb711	100	33	0	54	0	13
Mot	c1gr02	0	3	0	15	100	82
Mot	c1jb186	0	0	0	20	100	80
Mot	cdjb13	0	4	0	68	100	28
Mot	c1jb899	0	28	0	59	100	13
Mot	cm27_14440	0	0	0	37	100	63
Nos	T53_05	20	23	60	56	20	21
Nos	T53_10	20	5	60	74	20	21
Nos	T53_25	20	34	60	60	20	6
Nos	T53_50	20	3	60	67	20	30
Nos	T53_75	20	11	60	0	20	89

Abbreviations: Mix = spectra of mineral mixtures, Cln = clinoptilolite spectra, Eps = epsomite spectra, Mot = montmorillonite spectra, Nos = noise added spectra, EPS_{or} = epsomite real weight percentage, EPS_{pr} = epsomite predicted weight percentage, CLN_{or} = clinoptilolite real weight percentage, CLN_{pr} = clinoptilolite predicted weight percentage, MOT_{or} = montmorillonite real weight percentage, MOT_{pr} = montmorillonite predicted weight percentage.

D

Self-Organizing Maps

Basic tools (codes) used to create a SOM.

1. Import libraries

```
library(magrittr)
library(tidyverse)
library(kohonen)
Zeolite <- read.csv("ZeoliteDB.csv", header = TRUE)
data <- Zeolite[,4:17]
```

2. Data Preparation

```
numerics <- summarise_all(data, is.numeric) %>% as.logical()
factors <- names(data) %>% .[!numerics]
data_list <- list()
distances <- vector()

for (fac in factors) {
  data_list[[fac]] <- kohonen::classvec2classmat(data[[fac]])
```

```
  distances <- c(distances, 'tanimoto')
}
str(data_list)
```

3. Create a grid onto which the SOM will be mapped

```
map_dimension <- 10
n_iterations <- 1000
som_grid <- kohonen::somgrid(xdim = map_dimension, ydim = map_dimension,
                             topo = "hexagonal")
m <- kohonen::supersom(data_list, grid = som_grid, rlen = n_iterations,
                       alpha = 0.05, whatmap = c(factors, 'numerics'),
                       dist.fcts = distances)
save(m, file = 'som.Rdata')
Changes <- as.data.frame(m$changes)
Changes$Iteration <- seq(1,1000)
```

4. Fuse all layers into one dataframe

```
codes = tibble(layers = names(m$codes), codes = m$codes) %>%
  mutate(codes = purrr::map(codes, as_tibble)) %>%
  spread(key = layers, value = codes) %>%
  apply(1, bind_cols) %>%
  .[[1]] %>% as_tibble()
```

5. Generate distance matrix for codes

```
# Generate distance matrix for codes
dist_m = dist(codes) %>% as.matrix()
# Generate separate distance matrix for map location
dist_on_map = kohonen::unit.distances(som_grid)
```

D. Self-Organizing Maps

```
# Exponentiate euclidean distance by distance on map
dist_adj = dist_m ^ dist_on_map
```

6. Determine the optimal number of clusters

```
# Ellow method
factoextra::fviz_nbclust(dist_adj, factoextra::hcut,
              method = "wss", hc_method = 'ward.D2', k.max = 15)
# Silhouette method
factoextra::fviz_nbclust(dist_adj, factoextra::hcut,
              method = "silhouette", hc_method = "ward.D2", k.max = 15)
# Gap statistic
set.seed(123)
gap_stat = cluster::clusGap(dist_adj, FUN = factoextra::hcut,
              K.max = 15, B = 50, hc_method = "ward.D2")
factoextra::fviz_gap_stat(gap_stat)
```

7. Hierarchical Clustering

```
png("Fig Cluster_All.png", width=4000, height=14000, res=500)
par(mfrow = c(7,2))
par(mar = c(0.5, 0.5, 0.5, 0.2), xpd=NA, mgp = c(2.0,0.7,0), las = 1)

dist_adj =  dist_m ^ dist_on_map
clust_adj = hclust(as.dist(dist_adj), 'ward.D2')
som_cluster_adj = cutree(clust_adj, 5)
plot(m, type="codes", main=colnames(getCodes(m)),
     bgcol = col_vector[som_cluster_adj], pchs = NA)
```

8. Cluster Summary

```
link = tibble( map_loc = names(som_cluster_adj) %>% as.integer()
               ,cluster = som_cluster_adj)


pred = tibble( map_loc = m$unit.classif) %>%
  left_join(link)
data_pred = data %>% bind_cols(pred)
d_plot = data_pred %>%
  as_tibble() %>%
  select( one_of(factors), cluster ) %>%
  gather(key = 'key', value = 'value', one_of(factors) )
d_order = data_pred %>%
  as_tibble() %>%
  select( one_of(factors), cluster ) %>%
  mutate_all( as.integer ) %>%
  gather(key = 'key', value = 'order', one_of(factors) ) %>%
  mutate( order = stringr::str_c(key, order))
d_plot = d_plot %>%
  bind_cols( select(d_order, order) )%>%
  arrange( order ) %>%
  mutate( value = forcats::as_factor(value))
ggplot(d_plot ) +
  geom_bar( aes( x = forcats::as_factor(value)
                 , y = ..prop..
                 , fill = key
                 , group = key)
            )+
  facet_wrap(~ cluster
             ,ncol = 1)+
  labs(title = 'Percentages for each level of
       each factor level\n of each cluster',
```

```
       fill = 'factors')+
  theme(axis.text.x = element_text(angle = 90))
ggplot(data_pred, aes(x = as.factor(cluster)
                      , fill = as.factor(cluster))
       ) +
  geom_bar(show.legend = F)
```

9. Decision Tree Analysis

```
library(rpart.plot)
png("Fig_DTA.png", width=13500, height=5000, res=500)
data_pred_tree = data_pred

data_pred_tree$cluster = as.factor(data_pred_tree$cluster)

m_tree = rpart::rpart(cluster~.-map_loc
                      , data_pred_tree
                      , maxdepth = 30)

rpart.plot::prp(m_tree
                , branch.type   = 5
                , box.palette   ="RdYlGn"
                , faclen        = 0
                , extra         = 6
                , fallen.leaves = T
                , tweak         = 2
                #, gap           = input$gap
                #, space         = input$space
                )
```

E

Geochemical Modeling

Table E.1: Database used to create Total alkali vs. SiO_2 diagram (TAS diagram) in Chapter 7.

Type	Sample	Study_Area	Country/Region	Reference
TE	T1	Lake Tecopa	USA	Sheppard and Gude (1968)
TE	T2a	Lake Tecopa	USA	Sheppard and Gude (1968)
TE	T2b	Lake Tecopa	USA	Sheppard and Gude (1968)
TE	H10-1	Little Humboldt River	USA	Sheppard and Gude (1983)
TE	CC-46D	Chalk Hills Formation	USA	Sheppard (1991)
TE	CC-32	Chalk Hills Formation	USA	Sheppard (1991)
TE	Rhyolite Tuff	E-Mecsek	Hungary	Polgari et al. (1997)
TE	Dacite Tuff	E-Mecsek	Hungary	Polgari et al. (1997)
TE	HL-40A	Harney Lake	USA	Sheppard (1994)
TE	HL-66-2	Harney Lake	USA	Sheppard (1994)
TE	HL-48-13	Harney Lake	USA	Sheppard (1994)
TE	9D	Durkee	USA	Gude and Sheppard (1986)
TE	SD-8-11C	Durkee	USA	Gude and Sheppard (1986)
TE	SD-8-9A	Durkee	USA	Gude and Sheppard (1986)
TE	M4-32B	Barstow Formation	USA	Sheppard and Gude (1969b)
TE	ME-1	Mexican Volcanic Belt	Mexico	Pablo-Galan and Chavez-Garcia (1996)
TE	ME-2	Mexican Volcanic Belt	Mexico	Pablo-Galan and Chavez-Garcia (1996)
TE	Gl-1	Digirmenli	Turkey	Gundogdu et al. (1996)
TE	Gl-2	Emirler	Turkey	Gundogdu et al. (1996)
TE	Gl-3	Emirler	Turkey	Gundogdu et al. (1996)
TE	Gl-4	Kopenez	Turkey	Gundogdu et al. (1996)
TE	Gl-5	Kopenez	Turkey	Gundogdu et al. (1996)
TE	Gl-6	Kopenez	Turkey	Gundogdu et al. (1996)
TE	Gl-7	Kopenez	Turkey	Gundogdu et al. (1996)
TE	Gl-8	Kopenez	Turkey	Gundogdu et al. (1996)
TE	Gl-9	Kopenez	Turkey	Gundogdu et al. (1996)
TE	Gl-10	Karaoren	Turkey	Gundogdu et al. (1996)
TE	Gl-11	Karaoren	Turkey	Gundogdu et al. (1996)

Type	Sample	Study_Area	Country/Region	Reference
TE	Kralevo	Eastern Rhodopes	Bulgaria	Kirov et al. (2011)
TE	Oreske	Eastern Rhodopes	Bulgaria	Kirov et al. (2011)
TE	FG-1	Wagon Bed Formation	USA	Boles and Surdam (1979)
TE	FG-2	Wagon Bed Formation	USA	Boles and Surdam (1979)
TE	FG-3	Wagon Bed Formation	USA	Boles and Surdam (1979)
TE	FG-4	Wagon Bed Formation	USA	Boles and Surdam (1979)
TE	FG-5	Wagon Bed Formation	USA	Boles and Surdam (1979)
TE	Rhyolitic Glass	Teels Marsh	USA	Taylor and Surdam (1981)
TE	Tuff-4	White River	USA	Lander and Hay (1993)
TE	Tuff-5	White River	USA	Lander and Hay (1993)
TE	Tuff07	White River	USA	Lander and Hay (1993)
TE	Tuff-6c	White River	USA	Lander and Hay (1993)
TE	02-T103	Olduvai Gorge	Tanzania	McHenry (2009)
TE	T45-1	Lake Tecopa	USA	**?**
TE	T45-2	Lake Tecopa	USA	**?**
TE	T45-3	Lake Tecopa	USA	**?**
TE	T45-4	Lake Tecopa	USA	**?**
TE	T3	Lake Tecopa	USA	Sheppard and Gude (1968)
TE	VME-KFH-07	Kit Fox Hills	USA	Knott et al. (2018)
TE	CIT-NOV-01	Nova Formation	USA	Knott et al. (2018)
TE	JRK-DV-211	Kit Fox Hills	USA	Knott et al. (2018)
TE	JCH-KFH-005	Kit Fox Hills	USA	Knott et al. (2018)
TE	JRK-DV-42	Natural Bridge	USA	Knott et al. (2018)
TE	JRK-DV-93	Bishop-Death Valley	USA	Knott et al. (2018)
TE	BT-8A	Bishop-Death Valley	USA	Knott et al. (2018)
TE	OL92-1021	Bishop-Death Valley	USA	Knott et al. (2018)
MT	ALH77005	Allan Hills		Treiman et al. (1994)
MT	ALH84001			Gleason et al. (1997)
MT	Chassigny			Lodders (1998)

Type	Sample	Study_Area	Country/Region	Reference
MT	DaG489			Folco et al. (2000)
MT	Dhofar019			Taylor et al. (2002)
MT	Dhofar378			Ikeda et al. (2006)
MT	EETA79001 A			Lodders (1998)
MT	Governador Valadares			Burragato et al. (1975)
MT	Grove Mountains99027			Lin et al. (2008)
MT	Lafayette			Lodders (1998)
MT	LAR06319			Sarbadhikari et al. (2009)
MT	LAR12095			Kruijer et al. (2017)
MT	LEW88516			Lodders (1998)
MT	Los Angeles			Rubin et al. (2000)
MT	MIL 03346			Day et al. (2006)
MT	Nakhla			Day et al. (2006)
MT	NWA1950			Gillet et al. (2005)
MT	NWA2737			Beck et al. (2006)
MT	NWA2975			He et al. (2015)
MT	NWA2990			Bunch et al. (2009)
MT	NWA4480			Irving et al. (2010b)
MT	NWA4797			Irving et al. (2008)
MT	NWA4925			Kuehner et al. (2011)
MT	NWA5298			Irving et al. (2011)
MT	NWA5789			Irving et al. (2010a)
MT	NWA5790			Jambon et al. (2010)
MT	NWA5990			Irving et al. (2010b)
MT	NWA6162			Kuehner et al. (2011)
MT	NWA6342			Irving et al. (2011)
MT	NWA7635			Lapen et al. (2017)
MT	NWA8159			Herd et al. (2017)
MT	NWA998			Treiman and Irving (2008)

Type	Sample	Study_Area	Country/Region	Reference
MT	QUE94201			Warren and Kallemeyn (1997)
MT	RBT04262			Anand et al. (2008)
MT	Sayh al Uhaymir			Dreibus et al. (2000)
MT	Shergotty			Dreibus et al. (1982)
MT	Y000749			Kimura et al. (2018)
MT	Y793605			Warren and Kallemeyn (1997)
MT	Y980459			Irving et al. (2010a)
MT	Zagami			Easton and Elliott (1977)
MS	Tarmac		Meridiani Planum	Rieder et al. (2004)
MS	Hema2		Meridiani Planum	Rieder et al. (2004)
MS	Hema trench1		Meridiani Planum	Rieder et al. (2004)
MS	Hema trenchwall2		Meridiani Planum	Rieder et al. (2004)
MS	Les Hauches		Meridiani Planum	Rieder et al. (2004)
MS	Jack Russell		Meridiani Planum	Rieder et al. (2004)
MS	Beagle Burrow		Meridiani Planum	Rieder et al. (2004)
MS	Nougat		Meridiani Planum	Rieder et al. (2004)
MS	Robert E	Stone Mountain	Meridiani Planum	Rieder et al. (2004)
MS	middleRAT	McKittrick	Meridiani Planum	Rieder et al. (2004)
MS	middleRAT	McKittrick	Meridiani Planum	Rieder et al. (2004)
MS	GuadalupeRAT	Guadalupe	Meridiani Planum	Rieder et al. (2004)
MS	King3	Guadalupe	Meridiani Planum	Rieder et al. (2004)
MS	Makar	Last Chance	Meridiani Planum	Rieder et al. (2004)
MS	Hi-Ho	Dells	Meridiani Planum	Rieder et al. (2004)
MS	Mojo2	Flat rock	Meridiani Planum	Rieder et al. (2004)
MS	Mojo2	Flat rock	Meridiani Planum	Rieder et al. (2004)
MS	Rubel	Berry Bowl	Meridiani Planum	Rieder et al. (2004)
MS	Empty	Berry Bowl	Meridiani Planum	Rieder et al. (2004)
MS	Enamel1	Real Sharks Tooth	Meridiani Planum	Rieder et al. (2004)
MS	Glanz	Bounce rock	Meridiani Planum	Rieder et al. (2004)

Type	Sample	Study_Area	Country/Region	Reference
MS	Case	Bounce rock	Meridiani Planum	Rieder et al. (2004)
MS	RedHerringMaggie	Bounce rock	Meridiani Planum	Rieder et al. (2004)
MS	Golf	Pilbara	Meridiani Planum	Rieder et al. (2004)
MS	A-2	After deploy	Pathfinder	Rieder et al. (1997)
MS	A-4	Next to Yogi	Pathfinder	Rieder et al. (1997)
MS	A-5	Dark next to Yogi	Pathfinder	Rieder et al. (1997)
MS	A-8	Scooby Doo	Pathfinder	Rieder et al. (1997)
MS	A-10	Next to Lamb	Pathfinder	Rieder et al. (1997)
MS	A-15	Mermaid Dune	Pathfinder	Rieder et al. (1997)
MS	A-3	Barnacle Bill	Pathfinder	Rieder et al. (1997)
MS	A-7	Yogi	Pathfinder	Rieder et al. (1997)
MS	A-16	Wedge	Pathfinder	Rieder et al. (1997)
MS	A-17	Shark	Pathfinder	Rieder et al. (1997)
MS	A-18	Half Dome	Pathfinder	Rieder et al. (1997)
MS	Soil-free rock	Calculated	Pathfinder	Rieder et al. (1997)
MS	A475_OB	Cumberland Ridge	Gusev Crater	Ming et al. (2008)
MS	A477_SU	Cumberland Ridge	Gusev Crater	Ming et al. (2008)
MS	A481_OB	Cumberland Ridge	Gusev Crater	Ming et al. (2008)
MS	A484_OB	Cumberland Ridge	Gusev Crater	Ming et al. (2008)
MS	A494_OU	Cumberland Ridge	Gusev Crater	Ming et al. (2008)
MS	A495_OU	Cumberland Ridge	Gusev Crater	Ming et al. (2008)
MS	A496_OB	Cumberland Ridge	Gusev Crater	Ming et al. (2008)
MS	A499_OU	Cumberland Ridge	Gusev Crater	Ming et al. (2008)
MS	A502_SU	Cumberland Ridge	Gusev Crater	Ming et al. (2008)
MS	A511_RB	Cumberland Ridge	Gusev Crater	Ming et al. (2008)
MS	A512_RU	Cumberland Ridge	Gusev Crater	Ming et al. (2008)
MS	A532_OU	Cumberland Ridge	Gusev Crater	Ming et al. (2008)
MS	A533_OB	Cumberland Ridge	Gusev Crater	Ming et al. (2008)
MS	A542_OS	Cumberland Ridge	Gusev Crater	Ming et al. (2008)

Type	Sample	Study_Area	Country/Region	Reference
MS	A552_OU	Summit Region	Gusev Crater	Ming et al. (2008)
MS	A553_OB	Summit Region	Gusev Crater	Ming et al. (2008)
MS	A557_OU	Summit Region	Gusev Crater	Ming et al. (2008)
MS	A560_OB	Summit Region	Gusev Crater	Ming et al. (2008)
MS	A563_OU	Summit Region	Gusev Crater	Ming et al. (2008)
MS	A566_OU	Summit Region	Gusev Crater	Ming et al. (2008)
MS	A571_OU	Summit Region	Gusev Crater	Ming et al. (2008)
MS	A587_SU	Summit Region	Gusev Crater	Ming et al. (2008)
MS	A588_SD	Summit Region	Gusev Crater	Ming et al. (2008)
MS	A600_RU	Summit Region	Gusev Crater	Ming et al. (2008)
MS	A607_SD	Summit Region	Gusev Crater	Ming et al. (2008)
MS	A611_SU	Summit Region	Gusev Crater	Ming et al. (2008)
MS	A630_RU	Summit Region	Gusev Crater	Ming et al. (2008)
MS	A633_RU	Summit Region	Gusev Crater	Ming et al. (2008)
MS	A646_RB	Haskin Ridge	Gusev Crater	Ming et al. (2008)
MS	A660_RB	Haskin Ridge	Gusev Crater	Ming et al. (2008)
MS	A672_OB	Haskin Ridge	Gusev Crater	Ming et al. (2008)
MS	A675_OB	Haskin Ridge	Gusev Crater	Ming et al. (2008)
MS	A687_OU	Haskin Ridge	Gusev Crater	Ming et al. (2008)
MS	A688_OB	Haskin Ridge	Gusev Crater	Ming et al. (2008)
MS	A699_OB	Haskin Ridge	Gusev Crater	Ming et al. (2008)
MS	A700_OB	Haskin Ridge	Gusev Crater	Ming et al. (2008)
MS	A709_SU	El Dorado	Gusev Crater	Ming et al. (2008)
MS	A710_SD	El Dorado	Gusev Crater	Ming et al. (2008)
MS	A723_SD	El Dorado	Gusev Crater	Ming et al. (2008)
MS	A724	El Dorado	Gusev Crater	Ming et al. (2008)
MS	A726_RU	El Dorado	Gusev Crater	Ming et al. (2008)
MS	A749_OU	Home Plate	Gusev Crater	Ming et al. (2008)
MS	A750_OU	Home Plate	Gusev Crater	Ming et al. (2008)

Type	Sample	Study_Area	Country/Region	Reference
MS	A754_OB	Home Plate	Gusev Crater	Ming et al. (2008)
MS	A763_OB	Home Plate	Gusev Crater	Ming et al. (2008)
MS	A764_OB	Home Plate	Gusev Crater	Ming et al. (2008)
MS	A770_RU	Home Plate	Gusev Crater	Ming et al. (2008)
MS	A809_RU	Low Ridge	Gusev Crater	Ming et al. (2008)
MS	A814_SU	Low Ridge	Gusev Crater	Ming et al. (2008)
MS	A823_SU	Low Ridge	Gusev Crater	Ming et al. (2008)
MS	A831_SD	Low Ridge	Gusev Crater	Ming et al. (2008)
MS	A833_SU	Low Ridge	Gusev Crater	Ming et al. (2008)
MS	A847_SD	Low Ridge	Gusev Crater	Ming et al. (2008)
MS	A875_RU	Low Ridge	Gusev Crater	Ming et al. (2008)
MS	A901_RU	Low Ridge	Gusev Crater	Ming et al. (2008)
MS	A927_RU	Low Ridge	Gusev Crater	Ming et al. (2008)
MS	A942_RU	Low Ridge	Gusev Crater	Ming et al. (2008)
MS	A1013_SD	Low Ridge	Gusev Crater	Ming et al. (2008)
MS	A1017_SD	Low Ridge	Gusev Crater	Ming et al. (2008)
MS	A1027_RU	Low Ridge	Gusev Crater	Ming et al. (2008)
MS	A1031_RB	Low Ridge	Gusev Crater	Ming et al. (2008)
MS	A1035_RB	Low Ridge	Gusev Crater	Ming et al. (2008)
MS	A1055_RU	Low Ridge	Gusev Crater	Ming et al. (2008)
MS	A1072_RU	Low Ridge	Gusev Crater	Ming et al. (2008)
MS	A1079_RB	Low Ridge	Gusev Crater	Ming et al. (2008)
MS	A1081_RU	Low Ridge	Gusev Crater	Ming et al. (2008)
MS	A1098_SU	Low Ridge	Gusev Crater	Ming et al. (2008)
MS	A1143_RB	Mitcheltree Ridge	Gusev Crater	Ming et al. (2008)
MS	A1157_RU	Eastern Valley	Gusev Crater	Ming et al. (2008)
MS	A1168_RU	Eastern Valley	Gusev Crater	Ming et al. (2008)
MS	A1173_RD	Eastern Valley	Gusev Crater	Ming et al. (2008)
MS	A1177_RB	Eastern Valley	Gusev Crater	Ming et al. (2008)

Type	Sample	Study_Area	Country/Region	Reference
MS	A1179_RU	Eastern Valley	Gusev Crater	Ming et al. (2008)
MS	A1190_SD	Eastern Valley	Gusev Crater	Ming et al. (2008)
MS	A1194_SD	Eastern Valley	Gusev Crater	Ming et al. (2008)
MS	A1199_SD	Eastern Valley	Gusev Crater	Ming et al. (2008)
MS	A1206_OB	Home Plate	Gusev Crater	Ming et al. (2008)
MS	A1209_OB	Home Plate	Gusev Crater	Ming et al. (2008)
MS	A1211_OB	Home Plate	Gusev Crater	Ming et al. (2008)
MS	A1216_RB	Home Plate	Gusev Crater	Ming et al. (2008)
MS	A1225_RU	Eastern Valley	Gusev Crater	Ming et al. (2008)
MS	A1226_RBFd	Eastern Valley	Gusev Crater	Ming et al. (2008)
MS	A1230_SU	Eastern Valley	Gusev Crater	Ming et al. (2008)
MS	A1235_SU	Eastern Valley	Gusev Crater	Ming et al. (2008)
MS	A1239_SD	Eastern Valley	Gusev Crater	Ming et al. (2008)
MS	A1246_SD	Eastern Valley	Gusev Crater	Ming et al. (2008)
MS	A1251_RD	Eastern Valley	Gusev Crater	Ming et al. (2008)
MS	A1252_RD	Eastern Valley	Gusev Crater	Ming et al. (2008)
MS	A1288_RU	Eastern Valley	Gusev Crater	Ming et al. (2008)
MS	A1325_RU	Home Plate	Gusev Crater	Ming et al. (2008)
MS	A1326_RB	Home Plate	Gusev Crater	Ming et al. (2008)
MS	A1340_RU	Home Plate	Gusev Crater	Ming et al. (2008)
MS	A1341_RB	Home Plate	Gusev Crater	Ming et al. (2008)
MS	A1360_SD	Home Plate	Gusev Crater	Ming et al. (2008)
MS	A1368_RB	Home Plate	Gusev Crater	Ming et al. (2008)
MS	Adirondack	Husband Hill	Gusev Crater	Ming et al. (2008)
MS	Watchtower	Husband Hill	Gusev Crater	Ming et al. (2008)
MS	Backstay	Husband Hill	Gusev Crater	Ming et al. (2008)
MS	Irvine	Husband Hill	Gusev Crater	Ming et al. (2008)
MS	Independence subclass	Husband Hill	Gusev Crater	Ming et al. (2008)
MS	Assemblee subclass	Husband Hill	Gusev Crater	Ming et al. (2008)

Type	Sample	Study_Area	Country/Region	Reference
MS	Descartes	Husband Hill	Gusev Crater	Ming et al. (2008)
MS	Algonquin series	Husband Hill	Gusev Crater	Ming et al. (2008)
MS	Barnhill subclass	Husband Hill	Gusev Crater	Ming et al. (2008)
MS	Pesapallo subclass	Husband Hill	Gusev Crater	Ming et al. (2008)
MS	Fuzzy Smith	Husband Hill	Gusev Crater	Ming et al. (2008)
MS	Elizabeth Mahon	Husband Hill	Gusev Crater	Ming et al. (2008)
MS	Innocent Bystander	Husband Hill	Gusev Crater	Ming et al. (2008)
MS	Everett	Husband Hill	Gusev Crater	Ming et al. (2008)
MS	Good Question	Husband Hill	Gusev Crater	Ming et al. (2008)
MS	Halley subclass	Husband Hill	Gusev Crater	Ming et al. (2008)
MS	Graham Land subclass	Husband Hill	Gusev Crater	Ming et al. (2008)
MS	Montalva	Husband Hill	Gusev Crater	Ming et al. (2008)
MS	Torquas	Husband Hill	Gusev Crater	Ming et al. (2008)
MS	JM1	Jake_Matijevic	Gale Crater	Schmidt et al. (2014)
MS	JM2-daytime	Jake_Matijevic	Gale Crater	Schmidt et al. (2014)
MS	JM2-night time	Jake_Matijevic	Gale Crater	Schmidt et al. (2014)
MS	BI_For_Real	Bthurst_Inlet	Gale Crater	Schmidt et al. (2014)
MS	BI_Top	Bthurst_Inlet	Gale Crater	Schmidt et al. (2014)
MS	Et_Then	Et_Then	Gale Crater	Schmidt et al. (2014)
MS	Rocknest_3	Rocknest	Gale Crater	Schmidt et al. (2014)
MS	Best mix	Best mix	Gale Crater	Schmidt et al. (2014)
MS	Portage	Portage	Gale Crater	Schmidt et al. (2014)
MS	Bradbury		Gale Crater	Bedford et al. (2019)
MS	Mt Sharp		Gale Crater	Bedford et al. (2019)
MS	Buckskin	Gale Crater	Gale Crater	Morris et al. (2016)
MS	Gobabeb_DumpE	Gale Crater	Gale Crater	Ehlmann et al. (2017)

Abbreviation: TE = Tuff of the Earth, MT = Martian Meteorites, MS = Mars rock/soil

Table E.2: Thermodynamic Database (from EQ3/6 software).

No	Mineral	Chemical formula	log k
001	Albite	$NaAlSi_3O_8$	2.8495
002	Albite_high	$NaAlSi_3O_8$	4.1682
003	Albite_low	$NaAlSi_3O_8$	2.8495
004	Alunite	$KAl_3(OH)_6(SO_4)_2$	-2.4018
005	Analcime	$Na_{0.96}Al_{0.96}Si_{2.04}O_6 : H_2O$	6.0057
006	Analcime_dehy	$Na_{0.96}Al_{0.96}Si_{2.04}O_6$	12.3685
007	Anhydrite	$CaSO_4$	-4.3064
008	Anorthite	$CaAl_2(SiO_4)_2$	25.7219
009	Antarcticite	$CaCl_2.6H_2O$	4.0933
010	Aragonite	$CaCO_3$	1.9931
011	Bassanite	$CaSO_4 : 0.5H_2O$	-3.6615
012	Beidellite-Ca	$Ca_{0.165}Al_{2.33}Si_{3.67}O_{10}(OH)_2$	4.9352
013	Beidellite-H	$H_{0.33}Al_{2.33}Si_{3.67}O_{10}(OH)_2$	3.9773
014	Beidellite-K	$K_{0.33}Al_{2.33}Si_{3.67}O_{10}(OH)_2$	4.6522
015	Beidellite-Mg	$Mg_{0.165}Al_{2.33}Si_{3.67}O_{10}(OH)_2$	4.8971
016	Beidellite-Na	$Na_{0.33}Al_{2.33}Si_{3.67}O_{10}(OH)_2$	4.9911
017	Bischofite	$MgCl_2 : 6H_2O$	4.3923
018	Bloedite	$Na_2Mg(SO_4)_2 : 4H_2O$	-2.4777
019	Burkeite	$Na_6CO_3(SO_4)_2$	9.4866
020	Ca-Al-Pyroxene	$CaAl_2SiO_6$	34.8632
021	Calcite	$CaCO_3$	1.8487
022	Carnallite	$KMgCl_3 : 6H_2O$	4.2721
023	Celadonite	$KMgAlSi_4O_{10}(OH)_2$	7.8372
024	Chabazite	$K_{0.6}Na_{0.2}Ca_{1.50}Al_{3.8}Si_{8.2}O_{24} : 10H_2O$	10.3714
025	Chalcedony	SiO_2	-3.4715
026	Clinoptilolite-Ca	$Ca_{1.7335}Al_{3.45}Fe_{0.017}Si_{14.533}O_{36} : 10.922H_2O$	-5.6428
027	Clinoptilolite-K	$K_{3.467}Al_{3.45}Fe_{0.017}Si_{14.533}O_{36} : 10.922H_2O$	-9.5819
028	Clinoptilolite-Na	$Na_{3.467}Al_{3.45}Fe_{0.017}Si_{14.533}O_{36} : 10.922H_2O$	-5.7696
029	Cristobalite (alpha)	SiO_2	-3.1922
030	Cristobalite (beta)	SiO_2	-2.7488
031	Dawsonite	$NaAlCO_3(OH)_2$	3.6618
032	Dolomite	$CaMg(CO_3)_2$	2.5135
033	Dolomite-dis	$CaMg(CO_3)_2$	4.0579
034	Dolomite-ord	$CaMg(CO_3)_2$	2.5135
035	Enstatite	$MgSiO_3$	11.5835
036	Epsomite	$MgSO_4 : 7H_2O$	-1.9623
037	Erionite	$K_{1.5}Na_{0.9}Ca_{0.9}Al_{14.2}Si_{13.8}O_{36} : 13.0H_2O$	-4.8296
038	Gaylussite	$CaNa_2(CO_3)_2 : 5H_2O$	11.1641
039	Gibbsite	$Al(OH)_3$	6.9666
040	Glauberite	$Na_2Ca(SO_4)_2$	-5.4690
041	Goethite	$FeOOH$	0.5347
042	Greenalite	$Fe_3Si_2O_5(OH)_4$	23.1624

No	Mineral	Chemical formula	log k
043	Gypsum	$CaSO_4 : 2H_2O$	-4.4823
044	Halite	$NaCl$	1.5855
045	Hematite	Fe_2O_3	0.1086
046	Hexahydrite	$MgSO_4 : 6H_2O$	-1.7268
047	Huntite	$CaMg_3(CO_3)_4$	10.3010
048	Jarosite	$KFe_3(SO_4)_2(OH)_6$	-9.3706
049	Jarosite-Na	$NaFe_3(SO_4)_2(OH)_6$	-5.4482
050	K-feldspar	$KAlSi_3O_8$	-0.1903
051	Kainite	$KMgClSO_4 : 3H_2O$	-0.3114
052	Kaolinite	$Al_2Si_2O_5(OH)_4$	5.9539
053	Kieserite	$MgSO_4 : H_2O$	-0.2670
054	Leonite	$K_2Mg(SO_4)_2 : 4H_2O$	-4.1123
055	Magnesite	$MgCO_3$	2.2936
056	Magnetite	Fe_3O_4	10.4724
057	Maximum_Microcline	$KAlSi_3O_8$	-0.1903
058	Melanterite	$FeSO_4 : 7H_2O$	-2.3490
059	Minnesotaite	$Fe_3Si_4O_{10}(OH)_2$	15.0002
060	Mirabilite	$Na_2SO_4 : 10H_2O$	-1.1398
061	Montmorillonite-Ca	$Ca_{0.165}Mg_{0.33}Al_{1.67}Si_4O_{10}(OH)_2$	2.4024
062	Montmorillonite-H	$H_{0.33}Mg_{0.33}Al_{1.67}Si_4O_{10}(OH)_2$	1.4445
063	Montmorillonite-K	$K_{0.33}Mg_{0.33}Al_{1.67}Si_4O_{10}(OH)_2$	2.1194
064	Montmorillonite-Mg	$Mg_{0.495}Al_{1.67}Si_4O_{10}(OH)_2$	2.3643
065	Montmorillonite-Na	$Na_{0.33}Mg_{0.33}Al_{1.67}Si_4O_{10}(OH)_2$	2.4583
066	Nahcolite	$NaHCO_3$	-0.7061
067	Natron	$Na_2CO_3 : 10H_2O$	9.6102
068	Nontronite-Ca	$Ca_{0.165}Fe_2Al_{0.33}Si_{3.67}H_2O_{12}$	-11.1001
069	Nontronite-H	$H_{0.33}Fe_2Al_{0.33}Si_{3.67}H_2O_{12}$	-12.0580
070	Nontronite-K	$K_{0.33}Fe_2Al_{0.33}Si_{3.67}H_2O_{12}$	-11.3831
071	Nontronite-Mg	$Mg_{0.165}Fe_2Al_{0.33}Si_{3.67}H_2O_{12}$	-11.1382
072	Nontronite-Na	$Na_{0.33}Fe_2Al_{0.33}Si_{3.67}H_2O_{12}$	-11.0442
073	Pentahydrite	$MgSO_4 : 5H_2O$	-1.3872
074	Phillipsite	$K_{0.7}Na_{0.7}Ca_{1.1}Al_{13.6}Si_{12.4}O_{32} : 12.6H_2O$	-6.7617
075	Picromerite	$K_2Mg(SO_4)_2 : 6H_2O$	-4.4396
076	Pirssonite	$Na_2Ca(CO_3)_2 : 2H_2O$	11.3230
077	Polyhalite	$K_2MgCa_2(SO_4)_2 : 2H_2O$	-14.3124
078	Pyrite	FeS_2	-24.6534
079	Quartz	SiO_2	-3.7501

No	Mineral	Chemical formula	log k
080	Sanidine_high	$KAlSi_3O_8$	1.0089
081	Saponite-Ca	$Ca_{0.165}Mg_3Al_{0.33}Si_{3.67}O_{10}(OH)_2$	27.0032
082	Saponite-H	$H_{0.33}Mg_3Al_{0.33}Si_{3.67}O_{10}(OH)_2$	26.0453
083	Saponite-K	$K_{0.33}Mg_3Al_{0.33}Si_{3.67}O_{10}(OH)_2$	26.7202
084	Saponite-Mg	$Mg_{3.165}Al_{0.33}Si_{3.67}O_{10}(OH)_2$	26.9651
085	Saponite-Na	$Na_{0.33}Mg_3Al_{0.33}Si_{3.67}O_{10}(OH)_2$	27.0591
086	Sepiolite	$Mg_4Si_6O_{15}(OH)_2 : 6H_2O$	30.4439
087	Sepiolite (am)	$Mg_4Si_6O_{15}(OH)_2 : 6H_2O$	37.5600
088	Palygorskite	$Mg_{2.84}Al_{11.8}Si_{7.73}O_{20}(OH)_2(OH_2)_4 : 4H_2O$	26.4078
089	$SiO_2(am)$	SiO_2	-2.7136
090	Siderite	$FeCO_3$	-0.1920
091	Smectite-high-Fe-Mg	$Ca_{0.025}Na_{0.1}K_{0.2}Fe^{2+}_{0.5}Fe^{3+}_{0.2}Mg_{1.15}Al_{1.25}Si_{3.5}H_2O_{12}$	17.4595
092	Smectite-low-Fe-Mg	$Ca_{0.02}Na_{0.15}K_{0.2}Fe^{2+}_{0.29}Fe^{3+}_{0.16}Mg_{0.9}Al_{1.25}Si_{3.75}H_2O_{12}$	11.1541
093	Sylvite	KCl	0.8459
094	Syngenite	$K_2Ca(SO_4)_2 : H_2O$	-7.4484
095	Tachyhydrite	$Mg_2CaCl_6 : 12H_2O$	17.1439
096	Thenardite	Na_2SO_4	-0.3091
097	Thermonatrite	$Na_2CO_3 : H_2O$	10.9623
098	Tridymite	SiO_2	-3.8278
099	Trona-K	$K_2NaH(CO_3)_2 : 2H_2O$	11.5891

Table E.3: Secondary minerals formed in models (Thermodynamic data are from EQ36 database).

Mineral	Formula	log K
Alunite	$KAl_3(OH)_6(SO_4)_2 + 6H^+ \rightarrow K^+ + 3Al^{3+} + 2SO_4^- + H_2O$	-2.40
Analcime	$Na_{0.96}Al_{0.96}Si_{2.04}O_6 : H_2O + 3.84H^+ \rightarrow 0.96Al^{3+} + 0.96Na^+ + 2.04SiO_{2(aq)} + 2.92H_2O$	6.00
Calcite	$CaCO_3 + H^+ \rightarrow Ca^{2+} + HCO_3^-$	1.84
Chabazite	$K_{0.6}Na_{0.2}Ca_{1.5}Al_{13.8}Si_{8.2}O_{24} : 10H_2O + 15.2H^+ \rightarrow$ $0.2Na^+ + 0.6K^+ + 1.5Ca^{2+} + 3.8Al^{3+} + 8.2SiO_{2(aq)} + H_2O$	10.37
Chalcedony	$SiO_2 \rightarrow SiO_{2(aq)}$	-3.47
Clinoptilolite Ca	$Ca_{1.7335}Al_{3.45}Fe_{0.017}Si_{14.533}O_{36} : 10.922H_2O + 13.6H^+ \rightarrow$ $0.0170Fe^{3+} + 1.7335Ca^{2+} + 3.45Al^{3+} + 14.533SiO_{2(aq)} + 17.856H_2O$	-5.64
Gibbsite	$Al(OH)_3 + 3H^+ \rightarrow Al^{3+} + 3H_2O$	6.96
Gypsum	$CaSO_4.2H_2O \rightarrow Ca^{2+} + SO_4^{2-} + 2H_2O$	-4.48
Hematite	$Fe_2O_3 + 6H^+ \rightarrow 2Fe^{3+} + 3H_2O$	0.10
Kaolinite	$Al_2Si_2O_5(OH)_4 + 6H^+ \rightarrow 2Al^{3+} + 2SiO_{2(aq)} + 5H_2O$	5.95
Magnesite	$MgCO_3 + H^+ \rightarrow Mg^{2+} + HCO_3^-$	2.29
Montmorillonite Ca	$Ca_{0.165}Mg_{0.33}Al_{1.67}Si_4O_{10}(OH)_2 + H^+ \rightarrow$ $0.33Mg^{2+} + 1.67Al^{3+} + 0.165Ca^{2+} + 4SiO_{2(aq)} + 4H_2O$	2.40
Nontronite H	$H_{0.33}Fe_2Al_{0.33}Si_{3.67}H_2O_{12} + 6.99H^+ \rightarrow 0.33Al^{3+} + Fe^{3+} + SiO_{2(aq)} + 4.66H_2O$	-12.05
Nontronite Ca	$Na_{0.33}Fe_2Al_{0.33}Si_{3.67}H_2O_{12} + 7.32H^+ \rightarrow$ $0.165Ca^{2+} + 0.33Al^{3+} + 2Fe^{3+} + 3.67SiO_{2(aq)} + 4.66H_2O$	-11.10
Nontronite Mg	$Mg_{0.165}Fe_2Al_{0.33}Si_{3.67}H_2O_{12} + 7.32H^+ \rightarrow$ $0.165Mg^{2+} + 0.33Al^{3+} + 2Fe^{3+} + 3.67SiO_{2(aq)} + 4.66H_2O$	-11.13
Pyrite	$FeS_2 + H_2O \rightarrow 0.25H^+ + Fe^{2+} + 0.25SO_4^{2-} + 1.75HS^-$	-24.65
Saponite Ca	$Ca_{0.165}Mg_3Al_{0.33}Si_{3.67}O_{10}(OH)_2 + 7.32H^+ \rightarrow$ $0.165Ca^{2+} + 0.33Al^{3+} + 3Mg^{2+} + 3.67SiO_{2(aq)} + 4.66H_2O$	27.00
Saponite Mg	$Mg_{3.165}Al_{0.33}Si_{3.67}O_{10}(OH)_2 + 7.32H^+ \rightarrow 0.33Al^{3+} + 3.165Mg^{2+} + 3.67SiO_{2(aq)} + 4.66H_2O$	26.96
Siderite	$FeCO_3 + H^+ \rightarrow Fe^{2+} + HCO_3^-$	-0.19